Multi-platform Integrated Positioning and Attitude Determination using GNSS



P.J. Buist

Multi-platform Integrated Positioning and Attitude Determination using GNSS

PROEFSCHRIFT

ter verkrijging van de graad van doctor
aan de Technische Universiteit Delft,
op gezag van de Rector Magnificus prof. ir. K.Ch.A.M. Luyben,
voorzitter van het College voor Promoties,
in het openbaar te verdedigen op donderdag 20 juni 2013 om 12.30 uur

door

Peter Jacob BUIST

ingenieur luchtvaart- en ruimtevaart
Technische Universiteit Delft, Delft, Nederland
geboren te Grijpskerk, Nederland

Dit proefschrift is goedgekeurd door de promotor: Prof. dr. ir. P.J.G. Teunissen

Samenstelling promotiecommissie:

Rector Magnificus,	voorzitter
Prof. dr. ir. P.J.G. Teunissen,	Technische Universiteit Delft, promotor
Dr. ir. A.A. Verhagen,	Technische Universiteit Delft, copromotor
Prof. dr. -ing.habil. R. Klees,	Technische Universiteit Delft
Prof. dr. E.K.A. Gill,	Technische Universiteit Delft
Prof. dr. M. Menenti,	Technische Universiteit Delft
Dr. M.J. Unwin,	Surrey Satellite Technology Ltd.
Ir. F.J. Abbink,	Nationaal Lucht- en Ruimtevaartlaboratorium (gepensioneerd), Technische Universiteit Delft (gepensioneerd)
Prof. dr. ir. R.F. Hanssen,	Technische Universiteit Delft, Reserve

Buist, Peter Jacob

Multi-platform Integrated Positioning and Attitude Determination using GNSS

Delft University of Technology

Keywords: Global Navigation Satellite Systems (GNSS), precise GNSS (relative) positioning, attitude determination, ambiguity resolution, constrained LAMBDA

Citation: Buist, P.J. (2013). Multi-platform Integrated Positioning and Attitude Determination using GNSS. PhD thesis, Delft University of Technology,

ISBN 978-94-6191-785-0
Typeset by the author with the LaTeXDocumentation System.
Printed by Ipskamp, Rotterdam, the Netherlands.

Copyright ©2013 by Buist, P.J.
All rights reserved. No part of the material protected by this copyright notice may be reproduced or utilized in any form or by any means, electronic or mechanical, including photocopying, recording or by any information storage and retrieval system, without the prior permission of the author.
Cover contains a photo of the 2009 launch of the Balloon-based Operation Vehicle (BOV) [©JAXA]. More details can be found in appendix A.6.

This dissertation is dedicated to:
Yuka and the two HendRiks.

In memory of Piety Buist-Veldkamp
(19 January 1946 - 26 December 2012)
and Jaap Veldkamp
(20 September 1913 - 29 January 1997)

Abstract

Multi-platform Integrated Positioning and Attitude Determination using GNSS

There is trend in spacecraft engineering toward distributed systems where a number of smaller spacecraft work as a larger satellite. However, in order to make the small satellites work together as a single large platform, the precise relative positions (*baseline*) and orientations (*attitude*) of the elements of the formation have to be estimated. Global Navigation Satellite System (GNSS, the general term for systems as GPS and Galileo) receivers can be utilized to provide baseline estimates with centimeter to millimeter level accuracy. These precise GNSS applications utilize the carrier phase observations, which are inherently ambiguous.
While precise relative positioning using GNSS for surveying has been around for some time, precise relative navigation for moving applications on land, on water, in the air and even in space is still under development. The methods developed in this thesis can be applied for all these applications as no model for the user dynamics is applied (the methods are independent of the user motion).
A functional model was developed, in which the difference between the topocentric distance at the GNSS system time and at the GNSS receiver time is taken into account. For users with high dynamics and/or large clock offsets, not taking this affect into account can cause time-varying offsets in the baseline estimate.
The Doppler observation was reviewed and analysed for different types of applications. In most GNSS receivers, as the Doppler observation is generated from carrier phase observations, these observations are highly correlated with carrier-phase observations. For relative positioning applications, it was shown that inclusion of the Doppler observations in the model is only desirable

1. if the GNSS receivers have large clock offsets. Especially in a dynamic environment, the standard Double Difference model will result in an offset in the baseline estimation.

2. for applications were the relative position between two platforms is actively controlled, the relative velocity is generally required as input for the control loop.

The Doppler observation will not improve the float solution of the relative positioning problem and therefore will not improve ambiguity resolution. The drawback of using the Doppler for relative velocity estimation is that the effect from the relative motion and the clock drift cannot be separated. If the relative velocity can be obtained offline, taking the time derivative of the baseline estimate can provide a more accurate relative velocity estimation.

A single and multi-epoch data processing strategy was introduced that exploits the capability of the current GPS system, however, the tests are focused on its stand-alone, unaided, single-frequency, single-epoch performance, as this is the most challenging case for ambiguity resolution. A stronger model (larger number of observations, lower observation noise) will improve the performance of the developed approach in terms of the probability of correctly fixing the ambiguities.
Multiple GNSS antennas mounted on one platform may be used to determine the attitude of the platform as well. In terms of accuracy not much room for improvement is expected in GNSS attitude determination, as the theoretical limit has been reached by the available techniques. However, for ambiguity resolution still a number of open challenges remain. Ideally, one would like to have an ambiguity resolution method with a high probability of correctly fixing the ambiguities even when a limited number of observations is available (weak models) which could work instantaneously, eliminating the need for a dynamics model, and is computational efficient. The method applied in this thesis is based on a constrained extension of the popular LAMBDA method, known as the Multivariate Constrained (MC-) LAMBDA method.
The MC-LAMBDA method is a nontrivial modification of the standard LAMBDA method. In contrast to existing methods that make use of the known baseline length, the MC-LAMBDA method does full justice to the given information by fully integrating the nonlinear baseline constraint into the ambiguity objective function. As a result, the a priori information receives a proper weighting in the ambiguity objective function, thus leading to higher success rates.
The method was tested, using simulated as well as actual GPS data. The simulations cover a large number of different measurement scenarios, where the impact of measurement precision and receiver-GNSS satellite geometry was analysed.
GNSS-based precise relative positioning between spacecraft normally requires dual frequency observations, whereas attitude determination of the spacecraft can be performed precisely using only single frequency observations. In this contribution, the possibility was investigated to use multi-antenna data in an integrated approach, not only for attitude determination, but also to improve the relative positioning between spacecraft.
The rigorous inclusion of the known geometry of the antennas at the platform into the ambiguity objective function shows

- dramatic improvements in the ambiguity resolution success rates for the baselines at and between the spacecraft.
- improved precision of the baseline estimation for the baseline between the platforms.

The theoretical improvement achievable for the baseline between the platforms as a function of the number of antennas on each platform was shown, both for ambiguity resolution and accuracy of the baseline solution. The obtained mathematical relationship was verified by software based, hardware-in-the-loop simulations and field experiments.
The improved instantaneous ambiguity resolution will result in an even stronger reduction in time to fix (TTF). An additional benefit of the method is an improved robustness against multipath.

Samenvatting

Geïntegreerde plaats- en standbepaling voor meerdere platforms mbv GNSS

Er is een trend in de ruimtevaart om gedistribueerde systemen te gebruiken waarbij een aantal kleinere satellieten werken als een grotere satelliet. Hiervoor is het noodzakelijk om de relatieve plaats (*basislijn*) en oriëntatie (*stand*) van de elementen van de formatie te bepalen. Global Navigation Satellite System (GNSS, de generieke term voor systemen als GPS en Galileo) ontvangers kunnen gebruikt worden om deze basislijnen met een nauwkeurigheid van centimeter tot millimeter niveau te bepalen. Voor deze precieze GNSS toepassingen worden de fasemetingen gebruikt die inherent een onbekende meerduidigheid bevatten.
Hoewel precieze relatieve plaatsbepaling met behulp van GNSS voor landmeten al een tijd gebruikt wordt, is precieze plaatsbepaling voor bewegende voertuigen op het land, in het water, in de lucht en zelfs in de ruimte, nog altijd in ontwikkeling. De methoden ontwikkeld in dit proefschrift kunnen voor al deze toepassingen gebruikt worden omdat er geen gebruik gemaakt wordt van bewegingsvergelijkingen voor de gebruiker (de ontwikkelde methoden zijn toepasbaar onafhankelijk van de bewegingen van de gebruiker).
Een functioneel model is ontwikkeld dat rekening houdt met de verschil in de topocentrische afstand op GNSS systeemtijd en GNSS ontvangertijd. Voor gebruikers in een erg dynamische omgeving en/of met grote ontvangerklokfouten kan het niet meenemen van dit effect leiden tot tijdsvariabele afwijkingen in de basislijn schatting.
De Doppler waarneming was onderzocht en geanalyseerd voor verschillende toepassingen. In de meeste GNSS ontvangers wordt de Doppler waarnemingen gegenereerd van de fasemetingen en daardoor zijn deze waarnemingen sterk gecorreleerd met de fasemetingen. Voor relatieve plaatsbepaling is vastgesteld dat het meenemen van de Doppler waarnemingen in het model alleen gewenst is

1. indien de GNSS ontvangers grote klokfouten hebben. Met name in een dynamische omgeving kan de het standaard *Double Difference model* resulteren in afwijkingen in de basislijn schatting.

2. voor toepassingen waarbij de relatieve afstand tussen de twee platforms actief gecontroleerd wordt. De relatieve snelheid is voor dit soort toepassingen, in het algemeen, vereist als input voor de *control loop*.

Het meenemen van de Doppler waarnemingen in het model zal de *float solution* van het relatieve plaatsbepalingsprobleem niet verbeteringen, en daardoor ook niet de mate van succes in het correct oplossen van de meerduidigheden. Het nadeel van het gebruik van de Doppler waarnemingen voor relatieve snelheidbepaling is dat de effecten van de relatieve beweging en de klokdrift niet van elkaar gescheiden kunnen worden. Als niet vereist is

dat de relatieve snelheid in *real-time* beschikbaar is, is het daarom aan te raden om de tijdsafgeleide van de schatting van de basislijn te gebruiken als een preciezer benadering van de relatieve snelheidsvector.
Een dataverwerkingstrategie voor enkele en meerdere epochen is ontwikkeld dat gebruik maakt van de capaciteiten van het GPS systeem maar de testen zijn voornamelijk gericht op het analyseren van *stand-alone*, enkele frequentie en enkele epoche prestaties omdat dit de meest uitdagende toepassing is voor het schatten van meerduidigheden. Een sterker model (meer en/of nauwkeurige waarnemingen) zullen de prestaties van de ontwikkelde aanpak verbeteren in termen van de waarschijnlijkheid dat de meerduidigheid correct opgelost wordt.
Meerdere GNSS antennes geplaatst op een enkel platform kunnen ook gebruikt worden om de stand van het platform te bepalen. Op het gebied van nauwkeurigheid is het niet te verwachten dat er veel verbeteringen mogelijk zijn voor de GNSS standbepaling's toepassing omdat de theoretische nauwkeurigheid bereikt wordt met de bestaande technieken, maar voor het oplossen van de meerduidigheden zijn er nog een aantal uitdagingen. Men zou graag een methode willen hebben met een hoge waarschijnlijkheid om de meerduidigheden correct op te lossen, zelfs als er weinig waarnemingen beschikbaar (zwak model) zijn, die instantaan kan werken en daarom een dynamisch model overbodig maakt en ook nog weinig rekenkracht vereist. De methode beschreven in dit proefschrift is gebaseerd op een uitbreiding met *constraints* van de populaire LAMBDA methode, die bekend staat als de *Multivariate Constrained* (MC-) LAMBDA methode. De MC-LAMBDA methode is een niet-triviale aanpassing aan de standaard LAMBDA methode. Anders dan de bestaande technieken die gebruik maken van de bekende lengte van de basislijn, doet de MC-LAMBDA methode recht aan de gegeven informatie door het volledig integreren van de niet-lineaire *constraints* in de meerduidigheidsdoelfunctie. Het resultaat is dat de a-priori informatie het juiste gewicht krijgt in de meerduidigheidsdoelfunctie en daarmee een hogere mate van succes bereikt. De methode is getest met gesimuleerd en echte GPS data. De simulaties beslaan verschillende scenario's waarmee de invloed van nauwkeurigheid van de waarnemingen en de ontvanger-GNSS satelliet geometrie onderzocht werd.
Relatieve plaatsbepaling tussen satellieten met behulp van GNSS vereist normaalgesproken waarnemingen op twee frequenties, terwijl de standbepaling van de satelliet gedaan kan worden met waarnemingen op een enkele frequentie. In dit onderzoek zijn de mogelijkheden onderzocht om data van meerdere antennes te gebruiken door middel van een geïntegreerde aanpak, niet voor alleen de standbepaling, maar ook om de relatieve plaatsbepaling te verbeteren. De systematische toevoeging van de geometrie van meerdere antennes in de meerduidigheids-doelfunctie resulteert in

1. een dramatisch verbetering in de mate van succes in het oplossen van meerduidigheden voor de basislijnen op en tussen de platforms

2. verbeterde precisie van de schatting van de basislijn tussen de platforms.

De theoretische verbetering mogelijk voor de basislijn tussen de platforms als functie van het aantal antennes op beide platforms was ontwikkeld, zowel voor het oplossen van de meerduidigheden als de nauwkeurigheid van de schatting van de basislijn. De gevonden wiskundige relatie is getest met *software-based*, *hardware-in-the-loop* simulaties maar ook met data verzameld in het veld. De verbeterde instantane oplossing van meerduidigheden resulteert in een nog sterkere afname van de time to fix (TTF). Een ander voordeel van de methode is een verbeterde weerstand tegen multipath.

Acknowledgments

This thesis could not have been realized without the support of many people. In the first place, I would like to thank my promotor, Prof. Peter Teunissen, for giving me the opportunity to perform my PhD research and the theory behind ambiguity resolution. Sandra Verhagen is thanked for her daily guidance and discussions. Gabriele Giorgi is acknowledged for the pleasant and fruitful cooperation during this research and his work on multivariate constrained LAMBDA. Lennard Huisman and Roel van Bree are thanked for their technical support during the experiments described in this thesis.

Part of this work was done at JAXA-ISAS, Japan during a research visit with professor Tatsuaki Hashimoto and the support of his group is acknowledged. The MicroNed-MISAT framework is kindly thanked for their support.

The GPS simulators and receivers used for the experiment with PROBA-3 characteristics have been provided by the navigation laboratory of the European Space Agency (ESA-ESTEC). I would like to thank the people from this laboratory, especially Alberto Garcia-Rodriguez and David Jemenez Banos, for their support.

The GAIN team, a cooperation between the chairs of Control and Simulation, Physical and Space Geodesy and Mathematical Geodesy and Positioning at the Delft University of Technology is acknowledged for the cooperation during the experiments with the Cessna Citation II.

I would like to thank Mohammad Choudhury from the University of New South Wales for providing the Garada data set used in this work. Part of the work has been done in the context of the Australian Space Research Program Garada project.

A number of people I would like to thank for inspiring discussions over the years: Yoshi Hashida, Martin Unwin, Hiroaki Maeda, Susumu Kumagai, Oliver Montenbruck, Christian Tiberius and all other (PhD) researchers I have been in contact with in Delft. To Alessandro Atzei, Michel van Pelt (finally I have the chance to thank you in the preface of a book), Sander Goossens, Colinda Francke, Ron Noteborn and Dennis Gerrits I express my thanks for inspiration. Lastly I would like to thank the National Aerospace Laboratory NLR for allowing me time off to finish this thesis.

Peter Buist
Delft, 4 April 2013

Notation and Symbols

GNSS Models

$P_{r,f}^{s,j}$	code observation
$\Phi_{r,f}^{s,j}$	carrier phase observation
$D_{r,f}^{s,j}$	Doppler observation
s	GNSS satellite
r	receiver
f	frequency
j	platform
t	time of observation in GNSS system time
$\rho_{P,r,f}^{s}$	the geometric distance for code between r at time t and s at time $t - \tau_r^s$
$\rho_{\Phi,r,f}^{s}$	the geometric distance for carrier phase between r at time t and s at time $t - \tau_r^s$
τ_r^s	the signal traveling time
$I_{r,f}^{s}$	ionospheric error at f
T_r^s	tropospheric error
ζ_r	clock error of r
ζ^s	clock error of s
d_f^s	instrumental code delay for s on f
$d_{r,f}$	instrumental code delay for r on f
$\epsilon_{r,f}^{s}$	residual unmodelled error terms for the code observations
λ_f	wavelength of frequency f
$\phi_{r,f}(t_{r,0})$	initial phase for r on f
$\phi_f^s(t_0^s)$	initial phase for s on f
δ_f^s	instrumental phase delay for s on f
$\delta_{r,f}$	instrumental phase delay for r on f
$z_{r,f}^{s}$	number of complete carrier phase cycles
$\varepsilon_{r,f}^{s}$	residual unmodelled error terms on the carrier phase observations
ξ^s	satellite's ephemeris error
φ	latitude
λ	longitude
Λ	the diagonal matrix of wavelengths: $\Lambda = diag\left(\lambda_1, \ldots, \lambda_{N_f}\right)$
c	speed of light $\approx 299792458\ m/s$
R_e or a	the radius of the earth $\approx 6371.2\ km$
$n+1$	number of locked GNSS satellites
n	number of double difference observations

C	Total number of constrained baselines at all platforms
N^j	Total bumber of constrained baselines at platform j
N_f	Number of frequencies
N_b	Number of baselines
N_e	Number of epochs
u_r^s	line-of-sight vector between the GNSS satellite s and user r
μ_f	coefficient for the Ionospheric delays
ZTD	Zenith Tropospheric Delay
STD	Slant Tropospheric Delay
TID	Traveling Ionospheric Disturbances
M	Mapping function
b	Baseline vector
β	Baseline vector and its derivative
υ	undifferenced code, carrier phase and Doppler observations
y	undifferenced code and carrier phase observations
υ^{sd}	SD code, carrier phase and Doppler observations
y^{sd}	SD code and carrier phase observations
υ^{dd}	DD code, carrier phase and Doppler observations
y^{dd}	DD code and carrier phase observations
Z	$n \times N$ matrix of DD integer ambiguity vectors
Y	$2n \times N$ matrix of observation vectors
B	$3 \times N$ matrix of baseline vectors
F	$3 \times N$ matrix of body frame vectors f
f	body frame vector
R	rotation matrix

GNSS receiver models

d	early-late chip spacing
$R(d)$	correlation peak evaluated at d
α	slope of the correlation peak
B	Loop Bandwidth r
$\{.\}_p$	code indicator
$\{.\}_\phi$	carrier indicator
C/N_0	Carrier-to-Noise value
T_c	chip duration

Mathematical and Statistical Notation and Operators

$\arg(.)$	argument is a vector that minimize the term within the brackets
$\sum(.)$	summation
$div(.)$	divergence operator
$\nabla(.)$	gradient operator
$H_f(...)$	the hessian matrix of the function f
$\|.\|$	absolute value of a scalar
$\|.\|$	norm of a vector
$\|..\|_Q^2$	weighted squared norm $(..)^T Q^{-1}(..)$
$\langle ..., ... \rangle$	Inner product
$E\{.\}$	mathematical expectation operator
$D\{.\}$	mathematical dispersion operator
σ	standard deviation
ρ	correlation coefficient
$\mathbb{R}^m$	real Euclidean space of dimension m
$\mathrm{rank}(.)$	rank of a matrix (independent columns or rows of a matrix)
$(.)$	vector $(.)$ (lowercase boldface)
trace$(.)$	sum of elements on the main diagonal of a square matrix
dim$(.)$	dimension of a matrix or vector
$\perp$	orthogonal complement (is orthogonal to)
$(.)^T$	transpose of a matrix
$(.)^{-1}$	inverse of a matrix
N(x, Q_x)	normal distribution with mean x and covariance matrix Q_x
$Q_{\hat{z}\hat{z}}$	covariance matrix of $\hat{z}$
λ_v	Lagrange multiplier
e_n	$n \times 1$ vector with all elements equal one
vec	vec operator

Acronyms

ADOP	Ambiguity Dilution Of Precision
ADP	Attitude Determination Package
AGPS	Assisted GPS
AttDOP	Attitude Dilution of Precision
BOC	Binary Offset Carrier
BPSK	Binary Phase Shift Keying
C/A	Coarse/Acquisition code
C-LAMBDA	Constrained-LAMBDA
CS	Commercial Service
DD	Double Differenced
DEOS	Department of Earth Observation and Space system
DIA	Detection, Identification and Adaptation
DLL	Delay lock loop
DPB	Differential Phase Bias
DSP	Digital Signal Processor
ECEF	Earth Central Earth Fixed
ECI	Earth Central Inertial
EGNOS	European Geostationary Navigation Overlay Service
ESA	European Space Agency
GAS	Geomagnetic Aspect Sensor
GEO	GEOstationary orbit satellite
GLONASS	GLObal NAvigation Satellite Systems (Russian)
GNSS	Global Navigation Satellite Systems
GPS	Global Positioning System
ICD-GPS-200C	GPS Interface Control Document
IGS	International GPS Service
ILS	Integer Least Squares
ISS	International Space Station
IRNSS	Indian Regional Navigation Satellite System
ISAS	Institute of Space and Astronautical Science
ITAR	International Traffic in Arms Regulations
JAXA	Japan Aerospace eXploration Agency
LAMBDA	Least Squares AMBiguity Decorrelation Adjustment
LEO	Low Earth Orbit
LOM	Local Overall Model

MC-LAMBDA	Multivariate-Constrained-LAMBDA
MGP	Mathematical Geodesy and Positioning
MSE	Mean Squared Error
NASA	National Aeronautics and Space Administration
NASDA	National Space Development Agency of Japan (Since 2003 JAXA)
NEDO	New Energy and industrial technology Development Organization
OS	Open Service
P	Precision code
PDF	Probability Distribution Function
PLL	Phase Lock loop
PRS	Public Regulated Service
PRN	Pseudo Random Noise
QZSS	Quazi Zenith Satellite System
RINEX	Receiver INdependent EXchange format
RF	Radio Frequency
RMS	Root-Mean-Squared error
RTCM	Radio Technical Commission for Maritime Service
RTK	Real-Time Kinematic
SAS	Sun Aspect Sensor
SBAS	Satellite Based Augmentation System
SD	Single Differenced
SIS-ICD	Galileo open service, Signal In Space Interface Control Document
SPP	Single Point Positioning
SPS	Standard Positioning Service
STD	STandard Deviation
STS	Space Transportation System
SoL	Safety of Life
sps	symbols per second
TD-X	TanDEM-X
TEC	Total Electron Content
TECU	Total Electron Content Unit
TR-X	Terrasar-X
TTF	Time To Fix
UD	Undifferenced
USEF	Unmanned Space Experiment Free Flyer
UT	Universal Time
UTC	Coordinated Universal Time (UTC, French: Temps Universel Coordonn)
VTEC	Vertical Total Electron Content
WAAS	Wide Area Augmentation System
WGS84	World Geodetic System 1984
WLSE	Weighted Least Squares Estimator

Contents

Abstract i

Samenvatting iii

Acknowledgments v

Notation and Symbols vii

Acronyms x

1 Introduction 1
- 1.1 Background . . . 1
- 1.2 Research objectives and contributions . . . 3
- 1.3 Outline of the thesis . . . 5

2 GNSS Observation Model 7
- 2.1 Global Navigation Satellite Systems . . . 7
  - 2.1.1 Legacy and Modernized GPS . . . 8
  - 2.1.2 Galileo . . . 9
  - 2.1.3 GLONASS . . . 10
  - 2.1.4 Other GNSSs . . . 10
- 2.2 Observation Model . . . 11
- 2.3 Range rate and Doppler shift . . . 16
  - 2.3.1 Relationship between range rate and Doppler shift . . . 17
  - 2.3.2 Doppler observations . . . 19
  - 2.3.3 Derivative of the topocentric distance with respect to time . . . 20
  - 2.3.4 RINEX instructions for correcting observations . . . 23
  - 2.3.5 Receiver clock offset for different kinds of applications . . . 23
  - 2.3.6 Range rate and range rate rate for different kinds of applications . . . 24
- 2.4 Functional model . . . 28
  - 2.4.1 Undifferenced equations . . . 28
  - 2.4.2 Single difference equations . . . 33
  - 2.4.3 Double difference equations . . . 38
  - 2.4.4 Functional model for one receiver with multi-antennas . . . 40
  - 2.4.5 Implementation aspects of the functional model . . . 43
- 2.5 Atmospheric model . . . 46

2.5.1 Tropospheric model . . . 46
2.5.2 Ionospheric model . . . 51
2.5.3 Redundancy of the models . . . 53
2.6 Stochastic Properties of GNSS . . . 57
2.6.1 Space GNSS Receivers: Literature Study . . . 59
2.6.2 Space GNSS Receivers: Analysis of thermal noise . . . 60
2.6.3 Stochastic Model . . . 61
2.6.4 Assessment of receiver noise and correlation . . . 65
2.6.5 Weighting schemes . . . 65
2.7 Concluding remarks . . . 66

3 Absolute and Relative Positioning 67
3.1 Research relevance . . . 67
3.2 Absolute Positioning . . . 69
3.2.1 Model using code observations: standard SPP . . . 70
3.2.2 Model using code and Doppler observations . . . 72
3.3 Relative Positioning . . . 77
3.3.1 Applied relative positioning approaches on some missions . . . 79
3.3.2 Single Epoch Solution . . . 82
3.3.3 Multi-epoch Solution . . . 93
3.4 Data Quality and Validation . . . 96
3.4.1 DIA procedure . . . 96
3.4.2 Lower bound success rate ambiguity resolution . . . 98
3.4.3 Ratio Test on Resolved Ambiguities . . . 99
3.5 Verification by simulation . . . 99
3.6 Verification by hardware-in-the-loop and field experiments . . . 101
3.6.1 Satellite Formation Flying: PROBA-3 . . . 101
3.6.2 Satellite Formation Flying: PROBA-3 with external reference clock 109
3.6.3 Satellite formation flying: Garada . . . 112
3.6.4 Short Baseline with Large Clock Error: BOV 2008 . . . 117
3.7 Concluding remarks . . . 119

4 Attitude Determination using GNSS Signals 121
4.1 Overview of Previous Work/ Methods . . . 121
4.1.1 Compass: Heading and elevation . . . 123
4.1.2 Full attitude determination . . . 123
4.1.3 Ambiguity Resolution . . . 124
4.1.4 Experience onboard Spacecraft . . . 127
4.1.5 Research relevance . . . 132
4.2 C-LAMBDA . . . 133
4.2.1 Constrained Model . . . 133
4.2.2 The constrained float solution . . . 136
4.2.3 Multi-epoch Model . . . 137
4.3 MC-LAMBDA . . . 138
4.3.1 Attitude from combining Single Baseline Estimates . . . 138

4.3.2 Constrained Multi-baseline Model . . . 139
4.3.3 Influence of baseline and satellite geometry on attitude estimation . 145
4.3.4 Influence of baseline geometry on ambiguity resolution . . . 148
4.3.5 The constrained float solution . . . 149
4.3.6 Multi-epoch model . . . 151
4.4 Verification by simulations . . . 154
4.5 Verification by field experiments . . . 156
4.5.1 Multi-Antenna experiment (MAx) . . . 156
4.5.2 Vessel Application: Schie 2003 . . . 158
4.5.3 Aircraft Application: Cessna Citation II 2005 and 2007 . . . 160
4.5.4 Aerospace application: BOV 2009 . . . 160
4.5.5 Satellite Formation Flying: PROBA-3 and Garada . . . 166
4.6 Concluding remarks . . . 166

5 Integrated Positioning and Attitude Determination 169
5.1 Overview of Previous Work/Methods . . . 169
5.2 Triple and Quadruple-antenna configurations . . . 170
5.2.1 Multi-baseline setup . . . 170
5.2.2 Model and unconstrained float solution . . . 171
5.2.3 Optimal solution of the fully integrated approach . . . 174
5.2.4 Vectorial bootstrapping of the fully integrated approach . . . 180
5.2.5 Uncoupled approach using unconstrained and constrained baselines 182
5.2.6 Verification by simulation . . . 182
5.2.7 Concluding remarks . . . 186
5.3 General Model with both constrained and unconstrained baselines . . . 186
5.3.1 Multi-baseline Setup . . . 186
5.3.2 Vectorial bootstrapping using C-LAMBDA . . . 188
5.3.3 MC-LAMBDA bootstrapped relative positioning . . . 197
5.3.4 Discussion . . . 201
5.3.5 Multi-frequency, multi-antenna relative positioning . . . 202
5.3.6 Multi-epoch, multi-antenna relative positioning . . . 204
5.4 Verification by simulation . . . 205
5.4.1 Multi-platform Ambiguity resolution . . . 205
5.4.2 Bootstrapped Relative Positioning . . . 207
5.4.3 Influence of geometry . . . 216
5.4.4 Dual Frequency . . . 216
5.5 Verification by field experiments . . . 219
5.5.1 MAx Experiment . . . 219
5.5.2 Satellite Formation Flying: PROBA-3 . . . 225
5.5.3 Satellite formation flying: Garada mission . . . 226
5.6 Concluding remarks . . . 228

6 Conclusions and recommendations 229
6.1 Kinematic relative positioning . . . 229
6.2 Attitude Determination . . . 230

6.3 Attitude bootstrapped relative positioning . . . 231
6.4 Recommendations for future work . . . 232

A Simulation and field experiments 233
A.1 Simulations, observation accuracy, number of GNSS satellites and baselines 233
A.2 Simulations, influence of geometry . . . 233
A.3 Static Experiment: Multi-Antenna experiment (MAx) . . . 237
A.4 Vessel Application: Schie 2003 . . . 243
A.5 Aircraft Application: . . . 243
A.5.1 Cessna 2005 . . . 243
A.5.2 Cessna 2007 . . . 243
A.6 Aerospace application: Balloon-based Operation Vehicle . . . 245
A.6.1 Balloon-based Operation Vehicle . . . 245
A.6.2 Attitude Determination and Control for Balloon Gondolas . . . 246
A.6.3 Background GPS Experiment . . . 246
A.6.4 Initial Flights performed in 2008 . . . 247
A.6.5 Gondola Experimental Flight performed in 2009 . . . 248
A.7 Satellite Formation Flying: PROBA-3 . . . 249
A.8 Satellite Formation Flying: Garada . . . 251

B Orbits of GNSS Satellites 253
B.1 $r(t), \dot{r}(t), \ddot{r}(t)$ in ECEF WGS-84 . . . 253

C Scaling Factor 256
C.1 Derivation of the Scaling Factor for the v-c Matrix . . . 256
C.2 Inverse of Tridiagonal Matrix P . . . 256

D Mathematics 258
D.1 vec Operator . . . 258
D.2 Kronecker product . . . 258
D.3 Trigonometric functions . . . 259
D.4 Inverse of block matrices . . . 259

E Transformations 260
E.1 ECEF to ECI . . . 260
E.2 ECEF to ENU . . . 260
E.3 ECEF to Local Orbit . . . 261
E.4 Attitude representation: Euler . . . 261
E.5 Attitude representation: quaternions . . . 261
E.6 Attitude rotation . . . 262

F Test Procedure 263

Curriculum Vitae 267

Bibliography 268

1 Introduction

There is a trend in spacecraft engineering toward distributed systems where a number of smaller spacecraft work as a larger satellite. However, in order to make the small satellites work together as a single large platform, the precise relative positions and orientations of the elements of the formation have to be estimated. Global Navigation Satellite System (GNSS) receivers can be utilized to provide baseline estimates with centimeter to millimeter level accuracy.
This chapter starts with background information on the foreseen space missions where this research could be applied, but will also describe terrestrial and aviation applications were this research could be of interest. Moreover, this chapter will summarize the research objectives and contributions, and will provide an outline of the thesis.
Extracts of this chapter were published in (Buist et al., 2006) and (Buist et al., 2010).

1.1 Background

In the United States, Europe and Japan, there are or have been a number of missions requiring relative positioning between elements of the mission and it is expected that this number will continue to increase (Buist et al., 2006). We will start with an overview of the most significant missions using the terms chaser and target. The target is the main satellite and, in formation flying the chaser is positioning itself relative to the target and, in case of rendezvous, the chaser is approaching the target. The very first mission to use GNSS (GPS) signals for relative navigation in space was ETS-7 (Kawano et al., 1999). The ETS-7 experiment used four space qualified L1 GPS receivers: two redundant receivers on each sub-satellite. Delft University of Technology and the German Aerospace Center DLR showed results using orbital data from the GRACE formation where mm level accuracy (1-dimensional) for relative positioning were obtained (Kroes, 2006). Recent transport missions to the International Space Station (ISS) utilizing a rendezvous by GPS were performed by the ATV of Europe, and the Japanese HTV. The European PRISMA mission demonstrated formation flying techniques in space (Gill et al., 2006).
If satellites have a number of antennas in a typical configuration as is shown in Fig. 1.1, GNSS can be used to determine the attitude besides the relative position. In general three antennas are required, and four antennas are common, for platforms using GNSS for full attitude determination (Buist et al., 2003). This attitude solution can enhance the relative positioning between satellites as we will show in this research.
A number of missions, applying GNSS for relative positioning between elements, have more than one antenna on the individual satellites. For the ETS-7 mission, the chaser satellite had two antennas and the target satellite one, and therefore this configuration of three

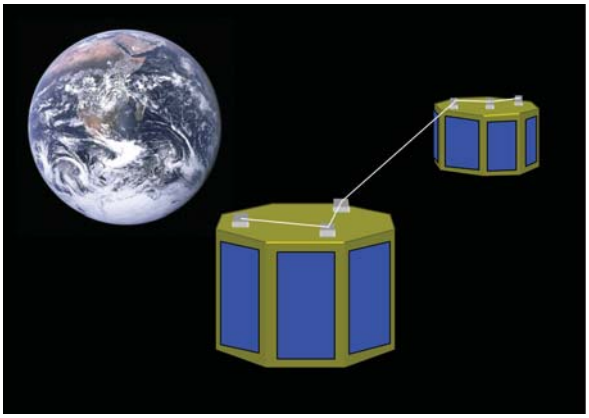


Figure 1.1: Artist impression of two satellites with multi- GNSS antennas flying in formation

antennas made a two baseline system (Ishijima et al., 2000). The ATV has two redundant receivers but they are not used at the same time (Narmada, 2005), therefore only one antenna is used for relative positioning (Marcille et al., 1997). The space station has a number of receivers (Saunders and Barton, 1995)(SSTL, 2009)(Svehla et al., 2009) with one of them being applied for attitude determination (Gomez and Lammers, 2004). The HTV has three redundant "Space Integrated GPS/INS" (SIGI) units and the Japanese Experiment Module on the ISS has another two of these units, with each SIGI having its own antenna (Tsukui et al., 2003). Other examples of missions with multiple antennas at some of their elements are Terrasar-X (TR-X) and TanDEM-X (TD-X) (Montenbruck et al., 2007), and FFAST (Mitani et al., 2009). On the TR-X/TD-X mission two receivers are used on each satellite, with one receiver connected to two antennas. For FFAST, GPS will also be applied for attitude determination of the detector spacecraft and therefore this satellite will have three antennas. The PRISMA mission has two antennas at opposite sides of each spacecraft. During the flight the spacecraft will select automatically the antenna to be used (Ardaens et al., 2010). The number of antennas on the elements of these missions are summarized in Table. 1.1.

Table 1.1: Number of Antennas on the Individual Elements of Missions utilizing GNSS-based Relative Positioning

Mission	Number of Antennas at	
	Target	Chaser
ETS7	1	2
GRACE	1	1
ATV	> 4	1
HTV	> 4	3
PRISMA	1	1
TR-X/TD-X	3	3
FFAST	3	1

For relative positioning in spaceborne applications, often an extensive dynamics model in combination with a (Kalman type of) filter and GNSS observations are used. This type of approach is discussed in detail in section 3.3.1. In this study a pure kinematic relative positioning approach for space applications is developed. The main advantage of

the kinematic approach is that information about dynamics of the system is not applied, which gives more flexibility and furthermore could improve the scientific interest of the observations made by the mission (see for example (Gerlach et al., 2003)(Svehla and Rothacher, 2005)). Therefore a functional kinematic approach could be of high importance for future space missions, but also for terrestrial applications and aviation. While precise relative positioning using GNSS for surveying has been around for some time, precise relative navigation for moving applications on land, on water, in the air and even in space is still under development. The automotive industry shows interest in this application for relative navigation between vehicles and reference stations, but also between vehicles. Maritime applications, especially inshore relative navigation, require precise and robust methods. Obviously this kind of technique is required for a swarm of Unmanned Aerial Vehicles (UAV), but also could be beneficial for swarms of manned vehicles. Other aircraft applications are aerial refueling as well as, potentially, landing on airports but also on aircraft carriers.

1.2 Research objectives and contributions

This research has the following objectives:

- Develop a functional model that accounts for large receiver clock biases and high dynamics, allowing the use of non-dedicated GNSS receivers on spacecraft for relative positioning.
- Develop a ambiguity resolution method -by including additional constraints- for attitude determination. This ambiguity resolution method should be computational efficient and have a high probability of correctly fixing the ambiguities, even when a limited number of observations is available.
- Investigate if the ambiguity resolution method could work instantaneously, eliminating the need for a dynamics model.
- Develop an optimal method for multi-platform integrated positioning and attitude determination.
- Develop a mathematically relationship between expected improvement for ambiguity resolution and baseline precision as function of the number of antennas at each platform.

Three restrictions were applied during the research:

- Atmospheric effects are described, but only short baseline experiments are analyzed.
- Focus is on the improvement of the multi-antenna relative positioning and attitude determination problem. This improvement is demonstrated with single epoch, single frequency solutions -the most challenging case- as the difference in performance is a good indication of the strength of the underlying models.

- Multi-antenna data from spacecraft flying relatively close to each other was not available (only multi-antenna from a single platform or single antenna from multi-platform), therefore hardware-in-the-loop simulations are applied for testing multi-antenna relative positioning.

The main contributions of this research can be summarized as follows:

- This research shows that, with multi-frequency, multi-constellation (spaceborne) GNSS receivers -which are expected to become more common in the near future- an instantaneous kinematic approach for relative navigation over short baselines could become feasible.

- The number of observations on the L1 frequency will increase in the near future and these observations from the Galileo system and modernized GPS are more precise than legacy GPS. This will result in a stronger model for single frequency relative positioning. When multiple GNSSs become available, single frequency instantaneous ambiguity resolution will become feasible for many short baseline applications.

- The legitimate spaceborne receivers cannot be applied on smaller satellites due to various restrictions, and therefore non-dedicated receivers are lately being used. A functional model was developed, in which the difference between the topocentric distance at the GNSS system time and at the GNSS receiver time is taken into account. For users with high dynamics and/or large clock offsets, not taking this affect into account can cause time-varying offsets in the baseline estimate. In the proposed functional model, this error can be corrected and the accuracy of the baseline estimate approaches the theoretical limitation resulting from the carrier phase accuracy.

- The derived functional and stochastic models were applied for absolute and relative positioning. In the analysis, emphasis was on the effects of large receiver clock errors and user dynamics on absolute and relative positioning. It was demonstrated that the Doppler is not an independent observation and is correlated with the carrier phase observations.

- For relative positioning applications, it was shown that inclusion of the Doppler observations in the model is only desirable.

    1. if the GNSS receivers have large clock offsets. Especially in a dynamic environment, the standard Double Difference model will result in an offset in the baseline estimation.
    2. for applications were the relative position between two platforms is actively controlled, the relative velocity is generally required as input for the control loop.

- The Doppler observation will not improve the float solution of the relative positioning problem and therefore will not improve ambiguity resolution. If the relative velocity can be obtained offline, taking the time derivative of the baseline estimate can provide a more accurate relative velocity estimation.

- Literature and experience have shown that in terms of accuracy not much room for improvement is expect for GNSS attitude determination. However, for ambiguity resolution still a number of open challenges remain. Ideally, the ambiguity resolution method should -working instantaneously- have a high probability of correctly fixing the ambiguities even when a limited number of observations is available. A constrained extension of the popular LAMBDA method, known as the Multivariate Constrained (MC-) LAMBDA method was investigated.

- The method was tested, using simulated as well as actual GPS data. The simulations cover a large number of different measurement scenarios, where the impact of measurement precision and receiver-satellite geometry was analysed.

- The rigorous inclusion of the baseline length constraint into the ambiguity objective function shows dramatic improvements in the success rates and more reliable attitude estimations. The improved instantaneous ambiguity resolution will result in an even stronger reduction in time to fix (TTF). Additionally, it was demonstrated that this also resulted in an increase in robustness against multipath and receiver-satellite geometry changes.

- Traditionally, the relative positioning and attitude determination problems are treated independently. In this research, the possibility of using multi-antenna data from multi-platform for relative positioning is investigated.

- The integrated method makes use of the following information to determine the relative position and orientation of a multi-antenna system with unconstrained and constrained baselines: the integerness of the ambiguities, the relationship between the ambiguities on the different baselines and the known geometry of the baselines at the platforms. The outcome of the attitude determination problem is applied in the ambiguity constrained solution on the unconstrained baseline between the platforms.

- The theoretical improvement achievable for the unconstrained baseline between the platforms was derived as a function of the number of antennas on each platform, both for ambiguity resolution and accuracy of the baseline solution. Again, the improved instantaneous ambiguity resolution will result in an even stronger reduction in TTF. The obtained mathematical relationship between the achievable improvement and the number of antennas was verified by software based and hardware-in-the-loop simulations.

1.3 Outline of the thesis

This thesis consists of 6 chapters, *Chapter 1* is an introduction.
Chapter 2 deals with the observation model for GNSS. The functional model describing the relationship between the observations (the code, carrier phase and Doppler) and the unknown parameters is developed, and a stochastic model describing the noise characteristic of the observables.
In *Chapter 3*, algorithms are developed for absolute and relative positioning and velocity

estimation using a single antenna at each platform.
If a platform has multiple antenna, GNSS could potentially be utilized for attitude determination. In *Chapter 4*, algorithms are developed for attitude determination using multiple antennas/receivers at a single platform.
Chapter 5 investigates the possibility of using multi-antenna data, not only for attitude determination, but also to improve relative positioning between platforms containing multiple antennas.
Finally, in *Chapter 6*, the conclusions of this thesis are summarized and recommendation are given for future research.

2 GNSS Observation Model

This chapter deals with the observation model for the different GNSSs and signals. An observation model contains a functional model, describing the relationship between the observations and the unknown parameters, and a stochastic model, describing the noise characteristics of the observables.
The chapter starts in section 2.1 with an introduction to GNSS systems and an overview of the signals. Section 2.2 describes the GNSS observations in general. As Doppler observations will be applied -which is less common in kinematic positioning- section 2.3 will review the Doppler observation and analyse the Doppler values expected for different types of applications. The first half of section 2.4 develops the undifferenced functional model. Subtracting carrier phase measurements from two receivers or antennas will give a range difference and a fraction of carrier phase cycle, which is the precise observable exploited for GNSS-based relative positioning and attitude determination. The second half of section 2.4 develops the single and double difference models for these applications. Section 2.5 describes atmospheric models, in section 2.6, after a review of expected accuracies of the GNSS observations for terrestrial and spaceborne applications, the stochastic model is described.
Extracts of this chapter were published in (Buist et al., 2010b), (Buist et al., 2010c) and (Buist et al., 2011).

2.1 Global Navigation Satellite Systems

Global Navigation Satellite System (GNSS) is the general term for satellite-based navigation systems. The Global Positioning System (GPS) was the first of a new generation of these systems that became available. Other examples of global systems are GLONASS, Beidou/COMPASS and Galileo. What all GNSS have in common is that they make use of three segments: the space segment, the control segment and the user segment. The space segment are the satellites, the control segment is responsible for the management of the satellite operations, the user segments covers all user equipment. GNSS is generally a one way system: the user receives the GNSS signals and there is no direct interaction from the user to the satellites operators. The key parameters of the GNSS systems, as there are number of spacecraft, the altitude, orbital period and inclination of the spacecraft's orbits, are summarized in Table 2.1.

Table 2.2 introduces the GNSS signal parameters of the different GNSSs. GPS originally utilized a single civilian signal on a single frequency, besides two military signals on

Table 2.1: GNSS System Parameters

GNSS	Nominal Altitude [km]	Number of SC	Orbit Period [h]	Inclination [°]
GPS	20,180	$\geq$ 24	12	55
Galileo	23,223	30(TBC)	14.1	56
GLONASS	19,100	24	11.3	64.8

Table 2.2: GNSS Signal Parameters

GNSS	Signal	Frequency [MHz]	Nominal Power[dBW][1]	Bandwidth [MHz]	Chiprate [Mcps][2]	Symbol rate [sps]
GPS	L1C/A	1575.42	-158.5	20.46	1.023	50
	L1C		-157.0	24.0		100
	L2C(ML)	1227.60	-159.3	20.46	1.023	50/-
	L5(I/Q)	1176.45	-157.9	24.0	10.23	100/-
Galileo	E1 (E1BC)	1575.42	-157.0	24.552	1.023	250
	E5a (I/Q)	1176.45	-155	20.46	10.23	50/-
	E5b (I/Q)	1207.14				250/-
	E5 (a+b)	1191.795	-152	51.150	10.23	-/-

two frequencies, but over the years the number of available signals and frequencies has increased and will continue to increase in the coming period. For precise single frequency relative positioning and attitude determination, one could use the civil signals in the L1/E1 band with carrier frequency $f_{L_1} = 1575.42$ MHz. For GPS, the legacy L1C/A and the future L1C signals are in this band, whereas for Galileo there will be the E1A, E1B and E1C signals. For multi-frequency precise relative positioning one could use the civil signals on GPS L2, L5, and Galileo E5, in addition to L1/E1. The specifications of these signals are shown in Table 2.2 and also transmit bandwidths and nominal received power levels are included. Next, the different GNSSs and their signals -in terms of modulations, chip and symbol rates- will be discussed in more detail.

2.1.1 Legacy and Modernized GPS

For GPS the nominal number of satellites in the constellation is 24 but for the last years the number of working satellites in orbit has been higher: up to 32 which is the maximum number that can be used in the system due to the designation of the PRN numbers. The GPS satellites are in six different orbital planes with nominal altitude of 20,180 kilometer. The six planes have approximately 55° inclination and are separated by about 60° right ascension of the ascending node.
The modulation on the GPS C/A-code is Binary Phase Shift Keying (BPSK). From the

[1]dBW: decibel Watt
[2]Mcps: Mega-chips per second
[3]sps: Symbols per second

launch of the first block III, GPS will also apply a L1C signal (IS-GPS-800, 2007), which will become the common signal between most GNSSs. It became available first, with the launch of the first QZSS satellite in 2010, on the Japanese QZSS system (IS-QZSS, 2009). The L1C signal will use a Binary Offset Carrier (BOC) modulation and consists of two main components: a pilot signal without any data message, which is spread by a ranging code, and a carrier that is spread by a ranging code and modulated by a data message. L1C/A contains a data message of 50 sps and therefore the integration time is limited to 20 ms. L1C will contain 100 sps, only on the data-channel.
L2C was the first modernized GPS signal that came available (Fontana et al., 2001)(Yamamoto et al., 2006). The civilian signal on L2 contains two multiplexed signals: the Civilian Moderate length code (called CM), and the Civilian Long length code (called CL). The CM code is 10,230 chips long, repeating every 20 ms and the CL code is 767,250 chips long, repeating every 1500 ms. Hence, each signal is transmitted at 0.5115 Mcps and, as they are multiplexed together, the chiprate becomes the same as L1C/A. The CM signal is modulated with the CNAV Navigation Message, whereas CL does not contain any modulated data and is called a dataless or pilot channel. Compared to the L1 C/A signal, L2C's transmission power is 2.3 dB weaker. The CNAV messages uses Forward Error Correction (FEC) in a rate 1/2 convolution code, so while the navigation message is 25 bps, a 50 sps signal is transmitted.
Two PRN ranging codes are transmitted on L5: the in-phase code (denoted as the L5I); and the quadrature-phase code (denoted as the L5Q). Both codes are 10,230 bits long and transmitted at 10.23 MHz. The signal has a higher transmitted power than L1C/A and L2C signal and wider bandwidth. The L5 signals contains 50 bps data that is coded in a rate 1/2 convolution coder which resulting 100 sps symbol stream is modulo-2 added to the L5I-code only. L5Q is therefore also a dataless or pilot channel.
For completeness, the military signals and capabilities of GPS are mentioned. Together with the C/A-code, the military P(Y)-code is known as legacy GPS signals, as they predate the modernization program. The encrypted P(Y) code comprises the publicly available P-code multiplied by an encrypted Y-code. The encryption makes it difficult to deceive GPS user equipment by transmitting replica signals on the GPS frequencies, and therefore this is known as anti-spoofing (AS). The new military (M)-code signals are the first to use BOC modulation to provide spectral separation from the civil GPS signals.
During the 90s, the accuracy of GPS was deliberately degraded on a global scale using a technique called selective availability (S/A). S/A was deactivated on May 1, 2000, showing the commercial importance of GPS, but still the capability remains an option. The United States is working on regional denial of service, minimizing the impact to peaceful users outside the area of conflict.

2.1.2 Galileo

Galileo is planned to have 10 satellites in each of the three orbital planes. For Galileo the altitude will be about 23,222 km and inclination about 56°. The satellites will be in three orbital planes with ascending nodes separated by 120° longitude. There will be 9 operational satellites and one active spare per orbital plane.
E1C from Galileo is the Open Service (OS) pilot-channel, E1B is, besides the OS data-channel, a Safety of Life service (SoL), and E1A the Commercial Service (CS). The signals

from the OS are free of user charges. In the SoL service, currently under revision, there is an integrity function i.e. a warning of system malfunction that will reach the user in a given alarm time. CS provides access to two additional signals to allow for a higher data rate and improved accuracy. For completeness we will mention that on the E1A signal there is also the Public Regulated Service (PRS), which is not part of this research. The modulation on the B and C-component is a BOC modulation. The symbol rate of E1B is 250 sps, therefore the maximum integration time for this data-channel is 4 ms, and E1C is the pilot-channel.
The other OS frequency is E5, where a wideband signal generated following a modified BOC modulation called AltBOC(15,10) is transmitted (Sleewaegen and De Wilde, 2004)(Shivaramaiah and Dempster, 2009). Each signal in E5a and E5b itself is a BPSK signal. This signal is then amplified through a very wideband amplifier before transmission at the medium carrier frequency between E5a and E5b at 1191.795 MHz. Since the minimum received power from E5a and E5b is -155 dBHz, the minimum signal power for the wideband E5 is -152 dBHz (ESA, 2006).

2.1.3 GLONASS

In this research, we are not using data from the GLONASS satellites. Nevertheless an overview of GNSSs cannot be complete without at least mentioning this system as it was the second GNSSs deployed at a worldwide scale. In 2011, GLONASS was restored as 24 satellites were operational. The GLONASS system has three orbital planes, which ascending nodes are separated by 120°. For a full constellation, each plane will contain eight equally spaced satellites. The orbits have an inclination of about 64.8° and an altitude of about 19,100 km. Therefore the orbital period is approximately 11 hours, 15 minutes.

2.1.4 Other GNSSs

Other GNSSs are also under development or already deployed in different parts of the world, some of them are global, others are local systems. The Chinese Beidou/COMPASS system is an example of a global system, but as official information is not or limited available this system is not part of this research. Beidou/COMPASS is scheduled to have five geostationary satellites, three inclined geosynchronous and 30 Medium-Earth-Orbit satellites.
Satellite Based Augmentation Systems (SBAS) like WAAS in the United States, EGNOS in Europe and MSAS in Japan are examples of regional systems that together have almost a global coverage. The main goal of SBAS is augmentation of GPS.
The Quasi Zenith Satellite System (QZSS) is another Japanese contribution to GNSS, which -as the name suggests- is in an inclined geosynchronous orbit. The QZSS consists of at least three satellites, one of which is always located directly above, and most of the time at the zenith, of the service area. Therefore, radio-waves from the satellites will be received without being blocked by buildings or other obstructions. The signals will be completely compatible with modernized GPS, thus interoperability between the systems in insured. There is coordination in signal design between Galileo and QZSS.
The Indian regional navigation satellite system (IRNSS) is planned to comprise three ordinary and four inclined geosynchronous satellites.

2.2 Observation Model

An observation model contains a functional model, describing the relationship between the observations y and the unknown parameters x, and a stochastic model, describing the noise characteristics of the observables. The observation equations can be collected in the system

$$\underline{y} = Ax + \underline{e} \tag{2.1}$$

where $\underline{y}$ and $\underline{e}$ are random vectors. $\underline{e}$ is the discrepancy between $\underline{y}$ and Ax. The expectation of $\underline{y}$ is

$$E(\underline{y}) = Ax \tag{2.2}$$

Model (2.2) is referred to as the functional model.

The dispersion of $\underline{y}$ is

$$D(\underline{y}) = E(\underline{e}\underline{e}^T) = Q_{yy} \tag{2.3}$$

Model (2.3) is the stochastic model with Q_{yy} is the variance-covariance (vc-) matrix. Eq. (2.2) and (2.3) are also known as the Gauss-Markov model. In this section the Gauss-Markov model for the GNSS observations is developed.

GNSS Observations Most GNSS receivers can provide code (i.e. pseudo range), carrier phase and Doppler observations for each tracked satellite. A code observation is equal to the difference between the receiver time at signal reception and satellite time at signal transmission, multiplied by the speed of light. A carrier phase measurement is the difference between the received GNSS satellite's carrier phase ϕ^s and the locally generated carrier phase ϕ_r of the internal oscillator of the GNSS receiver (Teunissen and Kleusberg, 1998)(Leick, 2003). A Doppler observation is a measurement of the change in apparent frequency of the received signal due to relative motion between the GNSS satellite and the user (Misra and Enge, 2001).
The code, phase and Doppler observation can be expressed by equations (2.4), (2.5) and (2.6) in meters.

$$\begin{aligned} P^s_{r,f}(t) = \;& \rho^s_{P,r,f}(t, t-\tau^s_r) + I^s_{r,f} + T^s_r + c\left[\zeta_r(t) - \zeta^s(t-\tau^s_r)\right] + \\ & + c\left[d_{r,f}(t) + d^s_f(t-\tau^s_r)\right] + \epsilon^s_{r,f} \end{aligned} \tag{2.4}$$

$$\begin{aligned} \Phi^s_{r,f}(t) = \;& \rho^s_{\Phi,r,f}(t, t-\tau^s_r) - I^s_{r,f} + T^s_r + c\left[\zeta_r(t) - \zeta^s(t-\tau^s_r)\right] + \\ & + c\left[\delta_{r,f}(t) + \delta^s_f(t-\tau^s_r)\right] + \lambda_f[\phi_{r,f}(t_{r,0}) - \phi^s_f(t^s_0)] + \lambda_f z^s_{r,f} + \varepsilon^s_{r,f} \end{aligned} \tag{2.5}$$

$$D^s_{r,f}(t) = \quad \dot{\rho}^s_{\dot{\Phi},r,f}(t, t-\tau^s_r) - \dot{I}^s_{r,f} + \dot{T}^s_r + c\left[\dot{\zeta}_r(t) - \dot{\zeta}^s(t-\tau^s_r)\right] + \dot{\varepsilon}^s_{r,f} \tag{2.6}$$

where $(..)^s_{r,f}$ means between receiver r and satellite s on frequency f

$P^s_{r,f}$	code observation
t	time of observation in GNSS system time
$\rho^s_{P,r,f}$	the geometric distance for code between r at time t and s at time $t-\tau^s_r$
$\rho^s_{\Phi,r,f}$	the geometric distance for carrier phase between r at time t and s at time $t-\tau^s_r$
τ^s_r	the signal traveling time
$I^s_{r,f}$	ionospheric error at f
T^s_r	tropospheric error
ζ_r	clock error of r
ζ^s	clock error of s
d^s_f	instrumental code delay for s on f
$d_{r,f}$	instrumental code delay for r on f
$\epsilon^s_{r,f}$	residual unmodelled error terms for the code observations
λ_f	wavelength of frequency f
$\Phi^s_{r,f}$	carrier phase observation
$\phi_{r,f}(t_{r,0})$	initial phase for r on f
$\phi^s_f(t^s_0)$	initial phase for s on f
δ^s_f	instrumental phase delay for s on f
$\delta_{r,f}$	instrumental phase delay for r on f
$z^s_{r,f}$	number of complete carrier phase cycles
$\varepsilon^s_{r,f}$	residual unmodelled error terms on the carrier phase observations
$D^s_{r,f}$	Doppler observation

The notation $\dot{(..)}$ indicates the time derivatives of quantity $(..)$, and the considered quantities are geometric distance $\rho^s_{\Phi,r,f}$, ionospheric $I^s_{r,f}$ and tropospheric T^s_r errors, the receiver ζ_r and satellite clock ζ^s error and residual error $\varepsilon^s_{r,f}$.

The time of observation is generally referred to as the GNSS time, which is the time as maintained by the GNSS control segment. The relationship between the time of observation t, the receiver time t_r and the clock error of the receiver ζ_r (in seconds), under the assumption that the timescales are not too different, is

$$t = t_r(t) - \zeta_r(t) \tag{2.7}$$

between satellite time t^s and GNSS time t is

$$t^s(t) - t = \zeta^s(t) \tag{2.8}$$

and between the time of transmission $t-\tau^s_r$, the satellite time t^s and the clock error of the satellite ζ^s is

$$t - \tau^s_r = t^s(t) - \tau^s_r - \zeta^s(t) \tag{2.9}$$

The receiver time must be within some small tolerance of GNSS time, typically <30 ms, for the receiver to function properly (Ray and Senior, 2005), therefore the requirement for similar timescales is fulfilled.
An approximation for the satellite clock error ζ^s is provided by the GNSS satellite data message (see section 2.4.5.4).

$\phi_{r,f}(t_{r,0})$ and $\phi^s_f(t^s_0)$ indicate initial phase at the receiver and GNSS satellite respectively. Of course in general this t_0 is different for any GNSS satellite and receiver. However for a proper designed GNSS receiver (and for GNSS payloads generating multiple signals) this $\phi_{r,f}(t_{r,0})$ should be the same or at least the difference between initial phase offsets should be an integer number for all received signals from all GNSS satellites (see also (Psiaki and Mohiuddin, 2007)). Depending on the receiver design this might not be straightforward, especially for multi-frequency receivers that make use of different analog parts for the different signals in the RF-front end.
The requirement for the design of a Phase Lock Loop (PLL) for static terrestrial applications is not very stringent as the dynamics involved are due to the GNSS satellite traveling through its orbit. For satellite or rocket applications a higher order tracking loop is required as the vehicle's acceleration and jerk will cause offsets in the estimated phase (Kaplan and Hegarty, 2006).
Moreover the receiver has to solve the so-called half cycle ambiguity problem, which is the result of the transmitted navigation bits on the GNSS signal. The tracking loop itself cannot distinguish between positive and negative bit patterns. After decoding the known bit patterns for the Hand Over Word (HOW), these bits can be applied -if required- for adjustment of the half cycle ambiguities. Nowadays RTK receivers take care of this initial phase offset in a proper way, but there are examples of receivers that did not and therefore making ambiguity resolution more challenging.

The Doppler observation is normally generated from carrier phase observations, therefore the last term of Eq. (2.6), the unmodelled error term $\dot{\varepsilon}^s_{r,f}$, is the derivative of the error $\varepsilon^s_{r,f}$ in Eq. (2.5). The Doppler observation is -in general- not an independent observation and correlated with carrier (or code). How much it is correlated will depend on the GNSS receiver's implementation. This will be discussed more in section 2.3.2 and analyzed in section 2.6.4.
In Eq. (2.6), the term $\left[\dot{\delta}_{r,f}(t) + \dot{\delta}^s_f(t - \tau^s_r)\right]$ is neglected as the variation of these biases -even over longer time periods- are known to be small (Lightsey, 1997). (Liu et al., 2004) reported values for the receiver hardware delay change rates under normal conditions below 0.1 mm/s. Satellite hardware delay change rates are assumed to be constrained to even smaller values.

The equations (2.4), (2.5) and (2.6) are linear in the GNSS satellite clock error, hardware and atmospheric delays and the ambiguities, but non-linear in the GNSS satellite and user positions and in the receiver clock bias and drift error as these are part of the geometric range (Tiberius, 1998). Eq. (2.6) is also linear in the GNSS satellite's and user's velocities. The distance ρ between the satellite s and the receiver r can be described as a sum of

different factors for the pseudorange observation in Eq. (2.4):

$$\rho^s_{P,r,f}(t, t-\tau^s_r) = \|\mathbf{r}^s(t-\tau^s_r) + d\mathbf{r}^s_f(t-\tau^s_r) - \mathbf{r}_r(t) - d\mathbf{r}_{r,f}(t)\| \tag{2.10}$$

where $\mathbf{r}$ represents the position vector of the satellite/receiver (center of mass) in for example an Earth Centered Inertial (ECI) frame, and $d\mathbf{r}$ describes the eccentricity vector between the center of mass and the antenna. Since the phase observations are related to different eccentricities than the ones relative to the pseudorange measurements as the effective antenna centers are different (e.g. in general the phase centers of antennas for code and carrier phase observation differ), the geometrical distance is written for the carrier phase observation in Eq. (2.5) as

$$\rho^s_{\Phi,r,f}(t, t-\tau^s_r) = \|\mathbf{r}^s(t-\tau^s_r) + \delta\mathbf{r}^s_f(t-\tau^s_r) - \mathbf{r}_r(t) - \delta\mathbf{r}_{r,f}(t)\| \tag{2.11}$$

And, as indicated in the equations, these phase centers also depend on the frequency of the observation. We assume that the eccentricities $d\mathbf{r}_f$ for code and $\delta\mathbf{r}_f$ for carrier phase of the different frequencies to be either known -and therefore the code and carrier observations can be corrected -as described in section 2.4.5.1- or negligibly small. Therefore $\rho^s_{P,r,f}$ and $\rho^s_{\Phi,r,f}$ are replaced with ρ^s_r from hereon.
For the equations (2.4) till (2.6) the receiver and GNSS satellite positions, clock errors as well as the tropospheric delay effect are independent of the signal frequency. All other terms, including the eccentricity vectors as the effective antenna centers also differ for frequencies, will -in general- depend on the signal frequencies.

We will collect the set of code, phase and Doppler observations at the receiver r into a vector of dimension $3(n+1)N_f$, with $n+1$ is the number of locked GNSS satellites, and N_f is the number of frequencies:

$$y_r = \begin{pmatrix} P_r \\ \Phi_r \\ D_r \end{pmatrix} \tag{2.12}$$

where

$$P_r = \left[P^1_{r,1} \dots P^{n+1}_{r,1} \dots\dots P^1_{r,N_f} \dots P^{n+1}_{r,N_f}\right]^T \tag{2.13}$$

$$\Phi_r = \left[\Phi^1_{r,1} \dots \Phi^{n+1}_{r,1} \dots\dots \Phi^1_{r,N_f} \dots \Phi^{n+1}_{r,N_f}\right]^T \tag{2.14}$$

$$D_r = \left[D^1_{r,1} \dots D^{n+1}_{r,1} \dots\dots D^1_{r,N_f} \dots D^{n+1}_{r,N_f}\right]^T \tag{2.15}$$

are all the code, phase and Doppler observations referred to a certain epoch collected at receiver r.
Equations (2.4) and (2.5) need to be linearized, which is normally done using the Taylor expansion over an initial point $\mathbf{x}_o$ (Teunissen, 1990a):

$$f(\mathbf{x}) = f(\mathbf{x}_o) + \bigtriangledown f(\mathbf{x}_o)^T(\mathbf{x}-\mathbf{x}_o) + \overbrace{\frac{1}{2}(\mathbf{x}-\mathbf{x}_o)^T H_f(\mathbf{x}_o)(\mathbf{x}-\mathbf{x}_o)}^{R_2(\mathbf{x}-\mathbf{x}_o)} + R_3(\mathbf{x}-\mathbf{x}_o) \tag{2.16}$$

where $\bigtriangledown f(\mathbf{x}_o) = \partial_x f = \left[\frac{\partial f}{\partial x_1}, \ldots, \frac{\partial f}{\partial x_n}\right]^T$ is the gradient, $H_f(\mathbf{x}_o)$ the Hessian matrix of the function f, $R_2(\mathbf{x}-\mathbf{x}_o)$ and $R_3(\mathbf{x}-\mathbf{x}_o)$ is the 2^{nd} and 3^{rd} order remainder of the Taylor expansion respectively. The geometrical distance between the satellite s and the receiver r (given by Eq.(2.10)) is

$$\begin{aligned}\rho_r^s(t, t-\tau_r^s) = &\ \|\mathbf{r}^s(t-\tau_r^s) - \mathbf{r}_r(t)\| \\ = &\sqrt{\langle \mathbf{r}^s(t-\tau_r^s) - \mathbf{r}_r(t), \mathbf{r}^s(t-\tau_r^s) - \mathbf{r}_r(t)\rangle}\end{aligned} \tag{2.17}$$

where we left out the eccentricities and $\langle\ ,\ \rangle$ indicates an inner product. (Leick, 2003) shows that this equation can be written in ECEF coordinates as:

$$\rho_r^s(t, t-\tau_r^s) = \ \|R_{ECEF}^{ECI}(t-\tau_r^s)\mathbf{r}^s(t-\tau_r^s)_{ECEF} - R_{ECEF}^{ECI}(t)\mathbf{r}_r(t)_{ECEF}\| \tag{2.18}$$

where R_{ECEF}^{ECI} is a rotation matrix from the ECEF to the ECI frame. For more information about this rotation, see appendix E.1.

Applying the Taylor expansion to expression Eq. (2.17) gives (we will limit the expansion to the first order approximation):

$$\rho_r^s \approx \ \|\mathbf{r}_o^s - \mathbf{r}_{r,o}\| - \mathbf{u_r^s}(\mathbf{r}^s - \mathbf{r}_o^s) + \mathbf{u_r^s}(\mathbf{r}_r - \mathbf{r}_{r,o}) + \dot{\rho}_r^s(\zeta_r - \zeta_{r,o}) \tag{2.19}$$

with the following gradient components:

$$\frac{\partial \rho_r^s(t, t-\tau_r^s)}{\partial \mathbf{r}^s}\Big|_0 = \mathbf{u}_r^s \tag{2.20}$$

$$\frac{\partial \rho_r^s(t, t-\tau_r^s)}{\partial \mathbf{r}_r}\Big|_0 = -\mathbf{u}_r^s \tag{2.21}$$

$$\frac{\partial \rho_r^s(t, t-\tau_r^s)}{\partial \zeta_r(t)}\Big|_0 = \frac{\partial \rho_r^s(t, t-\tau_r^s)}{\partial t}\Big|_0 \frac{\partial t}{\partial \zeta_r(t)} = -\dot{\rho}_r^s(t, t-\tau_r^s) \tag{2.22}$$

and the derivative of Eq. (2.7):

$$\frac{\partial t}{\partial \zeta_r(t)} = \frac{\partial(t_r - \zeta_r)}{\partial \zeta_r(t)} = -1 \tag{2.23}$$

$\mathbf{u_r^s}$ is the unit vector containing the line-of-sight coordinates:

$$\mathbf{u_r^s} = \begin{bmatrix} \frac{x^s - x_r}{\sqrt{(x^s-x_r)^2+(y^s-y_r)^2+(z^s-z_r)^2}} \\ \frac{y^s - y_r}{\sqrt{(x^s-x_r)^2+(y^s-y_r)^2+(z^s-z_r)^2}} \\ \frac{z^s - z_r}{\sqrt{(x^s-x_r)^2+(y^s-y_r)^2+(z^s-z_r)^2}} \end{bmatrix}^T = \left[\frac{\mathbf{r}^s - \mathbf{r}_r}{\|\mathbf{r}^s - \mathbf{r}_r\|}\right]^T \tag{2.24}$$

and $\mathbf{r}_{r,o}$, $\mathbf{r}_o^s$ are the initial approximate values for the user and GNSS satellite positions, $\zeta_{r,o}$ the initial approximate value of the user clock.
The line-of-sight vector from Eq. (2.24) between the GNSS satellite and the user can be expressed as:

$$\mathbf{u}_r^s = \left[\frac{\mathbf{r}^s(t-\tau_r^s) - \mathbf{r}_r(t)}{\|\mathbf{r}^s(t-\tau_r^s) - \mathbf{r}_r(t)\|}\right]^T = \left[\frac{\mathbf{r}^s(t-\tau_r^s) - \mathbf{r}_r(t)}{\rho_r^s(t-\tau_r^s, t)}\right]^T \tag{2.25}$$

We can rewrite Eq. (2.19) in terms of increments $\triangle\mathbf{r}^s = \mathbf{r}^s - \mathbf{r}_o^s$, $\triangle\mathbf{r}_r = \mathbf{r}_r - \mathbf{r}_{r,o}$ and $\triangle\zeta_r = \zeta_r - \zeta_{r,o}$:

$$\triangle\rho_r^s = \rho_r^s - \|\mathbf{r}_o^s - \mathbf{r}_{r,o}\| \approx \quad -\mathbf{u}_r^s\triangle\mathbf{r}^s + \mathbf{u}_r^s\triangle\mathbf{r}_r + \dot{\rho}_r^s\triangle\zeta_r \tag{2.26}$$

Now, we can write the model equations as a sum of increments from an initial estimation of the unknown parameters.

The linearized code and carrier phase observations equations are:

$$\begin{aligned}\triangle P_{r,f}^s(t) = \; & \frac{\partial\rho_r^s(t,t-\tau_r^s)}{\partial\mathbf{r}^s}\Big|_0\triangle\mathbf{r}^s + \frac{\partial\rho_r^s(t,t-\tau_r^s)}{\partial\mathbf{r}_r}\Big|_0\triangle\mathbf{r}_r + \frac{\partial\rho_r^s(t,t-\tau_r^s)}{\partial\zeta_r(t)}\Big|_0\triangle\zeta_r(t) + \\ & + \triangle I_{r,f}^s + \triangle T_r^s + c\left[\triangle\zeta_r(t) - \triangle\zeta^s(t-\tau_r^s)\right] + c\left[\triangle d_{r,f}(t) + \triangle d_f^s(t-\tau_r^s)\right] + \\ & + \epsilon_{r,f}^s\end{aligned} \tag{2.27}$$

$$\begin{aligned}\triangle\Phi_{r,f}^s(t) = \; & \frac{\partial\rho_r^s(t,t-\tau_r^s)}{\partial\mathbf{r}^s}\Big|_0\triangle\mathbf{r}^s + \frac{\partial\rho_r^s(t,t-\tau_r^s)}{\partial\mathbf{r}_r}\Big|_0\triangle\mathbf{r}_r + \frac{\partial\rho_r^s(t,t-\tau_r^s)}{\partial\zeta_r(t)}\Big|_0\triangle\zeta_r(t) + \\ & - \triangle I_{r,f}^s + \triangle T_r^s + c\left[\triangle\zeta_r(t) - \triangle\zeta^s(t-\tau_r^s)\right] + c\left[\triangle\delta_{r,f}(t) + \triangle\delta_f^s(t-\tau_r^s)\right] + \\ & + \lambda_f[\phi_{r,f}(t_{r,0}) - \phi_f^s(t_0^s)] + \lambda_f z_{r,f}^s + \varepsilon_{r,f}^s\end{aligned} \tag{2.28}$$

In these equations $\frac{\partial}{\partial x}\Big|_0\triangle x$ indicates that apriori approximate values of parameter x_0 are -in general- not available or of low quality, therefore the least-squares adjustment needs to be iterated and the linearized observation equation for the observable for the current iteration step is based on values of the parameters from the previous iteration step. $\triangle$ represents the parameter increments.

Before we continue to derive the functional model, we first will have a closer look at the Doppler equation as it is generally not included in functional models for precise relative positioning for static applications as described in (Teunissen and Kleusberg, 1998).

2.3 Range rate and Doppler shift

In this section, we will review Doppler observations and analyse the Doppler values expected for different types of applications. A geocentric coordinate system is an Earth-centered

system where objects are located in three-dimensions along the Cartesian X, Y and Z axes. They are different from topocentric coordinates which use the user's location as the origin. Both systems, however, share a common difficulty that the Earth, the GNSS satellites, and for some applications also the user(s), are constantly moving, which requires the addition of a time component to define the position of the users. The topocentric distance is the distance between the user and the GNSS satellite. The difference in the topocentric distance at the GNSS system time and at the receiver time is currently neglected in most applications: in other words the assumption is made that there is no motion of the receiver between the epoch at system time and the epoch at the receiver time. Especially for most terrestrial applications, the variation due to the motion of user itself is very small. For a terrestrial user this effect is in the order of millimeters, especially if the receiver clock offset is actively steered. For space applications, as will be discussed in section 2.6.1, the influence of the effect is normally kept small by keeping the clock offset small, which is generally done in dedicated space receivers as the Blackjack receiver (Kroes, 2006) and the receiver developed for the Japanese space agency (Kumagai et al., 2001)(Buist et al., 2004).

Non-dedicated receivers often do not have this option and, especially for spacecraft in eccentric orbits, the effect has to be taken into account for precise absolute and relative positioning.

In section 2.3.1, the relationship between the range rate and Doppler shift is discussed, section 2.3.2 explains the different techniques to estimate Doppler shift in a GNSS receiver. The section 2.3.3 provides models for range rate and range rate rate, section 2.3.4 goes over the RINEX instruction regarding clock corrections as, discussed in the introduction, the influence of clock offset and range rate are closely related. In the last two sections, expected receiver clock offsets, range rate and range rate rate values for different applications are discussed.

2.3.1 Relationship between range rate and Doppler shift

The Doppler effect (or Doppler shift) is named after the Austrian physicist Christian Doppler. In his work, Doppler postulated his principle (later coined the Doppler effect) that the observed frequency of a wave depends on the relative speed of the source and the observer, and he tried to use this concept for explaining the colour of binary stars. The Doppler effect of sound was first verified by Buys Ballot, a Dutch chemist and meteorologist, in 1845 by using a group of musicians playing a calibrated note on a train traveling from Utrecht to Amsterdam (Buys-Ballot, 1857).
The received (Doppler shifted) frequency can be written as (Wells, 1974)(Seeber, 2003):

$$f_r = f_f \left(\frac{1 - \left[\frac{(\dot{\mathbf{r}}^s(t-\tau^s_{r,f}) - \dot{\mathbf{r}}_r(t))^T}{c} \mathbf{u}^s_r \right]}{\sqrt{1 - \frac{\|\dot{\mathbf{r}}^s(t-\tau^s_{r,f}) - \dot{\mathbf{r}}_r(t)\|^2}{c^2}}} \right) \tag{2.29}$$

where $\dot{\mathbf{r}}^s(t-\tau^s_r)$ and $\dot{\mathbf{r}}_r(t)$ are the GNSS satellite s and user r velocity vectors respectively, c is the speed of light, f_f is the transmitted carrier frequency and $\mathbf{u^s_r}$ is the unit vector

containing the line-of-sight coordinates (see Eq. (2.24)). The term $\frac{\|\dot{\mathbf{r}}^s(t-\tau^s_{r,f})-\dot{\mathbf{r}}_r(t)\|^2}{c^2}$ is the relativistic effect (Vanicek and Krakiwsky, 1986).
The inverse of the denominator term can be expanded using a binomial series:

$$\frac{1}{\sqrt{1-\frac{\|\dot{\mathbf{r}}^s(t-\tau^s_{r,f})-\dot{\mathbf{r}}_r(t)\|^2}{c^2}}} = 1+\frac{\|\dot{\mathbf{r}}^s(t-\tau^s_{r,f})-\dot{\mathbf{r}}_r(t)\|^2}{2c^2}+ \\ +\frac{3\|\dot{\mathbf{r}}^s(t-\tau^s_{r,f})-\dot{\mathbf{r}}_r(t)\|^4}{8c^2}+\dots \tag{2.30}$$

The relative motion between a GNSS satellite and user results in a Doppler shift. In general, when the higher order terms in Eq. (2.30) are ignored, which is valid if relative velocity between the GNSS satellite and the receiver is slow compared to the speed of light ($\dot{\mathbf{r}}^s(t-\tau^s_{r,f})-\dot{\mathbf{r}}_r(t) \ll c$) and the distance between the GNSS satellite and receiver is large relative to the wavelength ($\mathbf{r}^s(t-\tau^s_{r,f})-\mathbf{r}_r(t) \gg \lambda_f$), this Doppler shift can be expressed as:

$$f_d = -(f_r - f_f) = \left[\frac{(\dot{\mathbf{r}}^s(t-\tau^s_{r,f})-\dot{\mathbf{r}}_r(t))^T}{c}\mathbf{u}^s_r\right] f_f \tag{2.31}$$

So the Doppler shift can be written as a projection of the relative velocity vector on the satellite line-of-sight vector.
For notational convenience later on, the Doppler shift is defined as positive when a GNSS satellite and the user receiver are approaching each other, while a departing GNSS satellite and user receiver has a negative Doppler shift. This is opposite from Eq. (2.31) and the definition applied in (Hofmann-Wellenhoff et al., 2001)(Seeber, 2003) but the same as applied in (Zhang et al., 2006), the RINEX format (Gurtner and Estey, 2006b) and a receiver frequently utilized in this research (Septentrio, 2007).

For the Doppler observations obtained from the GNSS receiver, the distinction between the Doppler effect from the relative motion and the clock drift at the receiver and/or the GNSS satellite cannot be made. By definition we normally distinguish between pseudo range rate and range rate. $\dot{\rho}^s_r(t, t-\tau^s_r)$ is the range rate: the change in the range between the user and the GNSS satellite at time t and $t-\tau^s_r$, respectively. The pseudo range rate is the rate of change of the signal delay (i.e. range plus clock errors at the GNSS satellite and user receiver).
The Doppler shift, which is the pseudo range rate expressed in frequency, is related to the change in the range and the clock drift by:

$$f_d = \frac{\overbrace{\overbrace{\dot{\rho}^s_r(t,t-\tau^s_r)}^{\text{range rate}}+c(\dot{\zeta}_r(t)-\dot{\zeta}^s(t-\tau^s_r))}^{\text{pseudo range rate}}}{\lambda_f} \tag{2.32}$$

The following conversion can be applied if one would like to express Doppler shift in meters per second instead of Hz:

$$D^s_{r,f}(t) = \lambda_f f_d = +\dot{\rho}^s_r(t, t - \tau^s_r) + c\left[\dot{\zeta}_r(t) - \dot{\zeta}^s(t - \tau^s_r)\right] \tag{2.33}$$

2.3.2 Doppler observations

The Doppler shift is estimated by a GNSS receiver in both the signal acquisition and tracking processes. In the acquisition process, the receiver searches bins of Doppler frequency and code phase shifts. For a spaceborne application, the Doppler range is much wider than for the terrestrial application and therefore the signal acquisition in space might take considerably longer than on Earth. The acquisition process might consist of coarse and fine searching which differ in frequency steps. During the acquisition, the accuracy of the Doppler estimate depends on the size of the Doppler bin.

The two most common approaches to obtain Doppler observations after acquisition are:

1. time differencing of carrier phase observations
2. Doppler estimation as provided by a tracking loop

For all known approaches currently applied in GNSS receivers to obtain the Doppler observation, the same drawback exists that the observation is not independent and always correlated with the code or carrier phase observations as it is either based on the same (integrated) measurements or a product of the same tracking loops. In section 2.6.4, this correlation is analyzed for actual GPS data.

A property that could make it interesting for some applications to use Doppler in combination with range observations is that it is less sensitive to spoofing, jamming and multipath (Bahrami, 2009)(Harper, 2009), but this is beyond the scope of the research.

2.3.2.1 Differencing of carrier phase observations

This observation is called delta range when the carrier phase is integrated over a short time interval, and divided by the integration period (Braasch and Van Dierendonck, 2002). To be more precise, the approach takes the difference of two carrier phase observations collected at two different epochs separated by an interval over which the carrier phase is integrated. The first carrier phase observation is collected at $t - \Delta t$ and the second at t, where t is the observation epoch of the code and carrier observations and $t - \Delta t$ is a short time before this epoch, typically 0.1 or 0.05 seconds. The delta range observation is

$$\frac{\Phi^s_r(t) - \Phi^s_r(t - \Delta t)}{\Delta t} \tag{2.34}$$

So the carrier phase is differenced over $t - \Delta t$ till t. In general this observation's accuracy will improve if the integration time is longer, however with longer integration times, the estimate will not completely capture the current dynamics (thus at t).

2.3.2.2 Byproduct of tracking loop

For this approach, Kubo and Pullen (2008) provide the following typical accuracies, categorized by the tracking loop that is applied to obtain the observation (the units are corrected after correspondence with the authors of (Kubo and Pullen, 2008)):

1. delta pseudo ranges obtained from a Code (or Delay) Lock Loop ($\approx$ 1.0 m/s)
2. Doppler measurements obtained from a Frequency Lock Loop ($\approx$ 0.1 m/s)
3. delta carrier phases obtained from a Phase Lock Loop ($\approx$ 0.01 m/s)

2.3.3 Derivative of the topocentric distance with respect to time

In this section, we will develop a model for the derivative of the topocentric distance with respect to time for users traveling with non-negligible velocity. The model will make use of parameters in the ECEF (WGS84) frame, as induced in the Galileo ICD (ESA, 2006), for straightforward implementation. More information on the derivation for terrestrial applications can be found in (Jin, 1995)(de Jonge, 1998). We will make use of the time of transmission $t - \tau_r^s$ as described by Eq. (2.9), as a function of $\rho_r^s(t, t - \tau_r^s)$:

$$t - \tau_r^s = t - \frac{\rho_r^s(t, t - \tau_r^s)}{c} \tag{2.35}$$

Details on the calculation of $\rho_r^s(t, t - \tau_r^s)$ are provided in section 2.4.5.

In Eq. (2.17) we have obtained the geometrical distance between satellite s and receiver r as:

$$\rho_r^s(t, t - \tau_r^s) = \sqrt{\langle \mathbf{r}^s(t - \tau_r^s) - \mathbf{r}_r(t), \mathbf{r}^s(t - \tau_r^s) - \mathbf{r}_r(t) \rangle} \tag{2.36}$$

The time derivative of $\langle x, x \rangle$ and $\sqrt{\langle x, x \rangle}$ is $2 \langle \dot{x}, x \rangle$ and $\frac{\langle \dot{x}, x \rangle}{\sqrt{\langle x, x \rangle}}$ respectively. Therefore for the time derivative of the topocentric distance we can write in ECI frame:

$$\dot{\rho}_r^s(t, t - \tau_r^s) = \frac{1}{\rho_r^s(t, t - \tau_r^s)} \left\langle \frac{\partial(\mathbf{r}^s(t - \tau_r^s)_{ECI} - \mathbf{r}_r(t)_{ECI})}{\partial t}, \mathbf{r}^s(t - \tau_r^s)_{ECI} - \mathbf{r}_r(t)_{ECI} \right\rangle \tag{2.37}$$

In the ECI frame, the time derivative of $\mathbf{r}_r(t)$ is of course non-zero even for stationary receivers. The general formula for the time derivative of satellite position is:

$$\frac{\partial \mathbf{r}^s(t-\tau_r^s)_{ECI}}{\partial t} = \frac{\partial \mathbf{r}^s(t-\tau_r^s)_{ECI}}{\partial (t-\tau_r^s)} \frac{\partial (t-\tau_r^s)}{\partial t}$$
$$= \dot{\mathbf{r}}^s(t-\tau_r^s)_{ECI} \frac{\partial (t - \frac{\rho_r^s(t,t-\tau_r^s)}{c})}{\partial t} = \dot{\mathbf{r}}^s(t-\tau_r^s)_{ECI}(1 - \frac{\dot{\rho}_r^s(t,t-\tau_r^s)}{c}) \tag{2.38}$$

We will coin the difference between satellite and user position $A0$:

$$A0 = \mathbf{r}^s(t-\tau_r^s)_{ECI} - \mathbf{r}_r(t)_{ECI} = R_{ECEF}^{ECI}(t-\tau_r^s)\mathbf{r}^s(t-\tau_r^s)_{ECEF} - R_{ECEF}^{ECI}(t)\mathbf{r}_r(t)_{ECEF} \tag{2.39}$$

Next, we will write the satellite's and the user's velocity in the ECEF frame as:

$$A1 = \dot{\mathbf{r}}^s(t-\tau_r^s)_{ECI} = R_{ECEF}^{ECI}(t-\tau_r^s)\dot{\mathbf{r}}^s(t-\tau_r^s)_{ECEF} + \dot{R}_{ECEF}^{ECI}(t-\tau_r^s)\mathbf{r}^s(t-\tau_r^s)_{ECEF} \tag{2.40}$$

$$A2 = \dot{\mathbf{r}}_r(t)_{ECI} = R_{ECEF}^{ECI}(t)\dot{\mathbf{r}}_r(t)_{ECEF} + \dot{R}_{ECEF}^{ECI}(t)\mathbf{r}_r(t)_{ECEF} \tag{2.41}$$

Hence for the time derivative of the topocentric distance described by Eq. (2.37), we can write in both the ECI and ECEF frame:

$$\dot{\rho}_r^s(t,t-\tau_r^s) = \frac{\langle A1 - A2, A0\rangle}{\rho_r^s(t,t-\tau_r^s) + \langle \frac{A1}{c}, A0\rangle} \tag{2.42}$$

In order to calculate this range rate, the position and velocity of the GNSS satellite and the user are required.

In the model described in (de Jonge, 1998), the derivation of the satellite time is simplified from Eq. (2.38) to

$$\frac{\partial \mathbf{r}^s(t-\tau_r^s)_{ECI}}{\partial t} = \dot{\mathbf{r}}^s(t-\tau_r^s)_{ECI} \tag{2.43}$$

Furthermore the receiver is assumed to be stationary in the ECEF frame, which is of course only valid for stationary users (the application in (de Jonge, 1998)), thus $\dot{\mathbf{r}}_r(t)_{ECEF} = 0$.

Hence for the time derivative of the topocentric distance, we can write in the ECEF frame, if the effect of the difference between the time at the GNSS satellite, $t-\tau_r^s$, and the user, t, is ignored (thus Eq. (2.38) becomes: $\frac{\partial \mathbf{r}^s(t-\tau_r^s)_{ECI}}{\partial t} \approx \dot{\mathbf{r}}^s(t-\tau_r^s)_{ECI}$):

$$\dot{\rho}_r^s(t, t-\tau_r^s) = \frac{1}{\rho_r^s(t, t-\tau_r^s)} \langle A1 - A2, A0 \rangle \tag{2.44}$$

And for a static user the model as described in (de Jonge, 1998) is obtained, hence for the time derivative of the topocentric we can write in the ECEF frame:

$$\dot{\rho}_r^s(t, t-\tau_r^s) = \frac{1}{\rho_r^s(t, t-\tau_r^s)} \left\langle A1 - \dot{R}_{ECEF}^{ECI}(t)\mathbf{r}_r(t)_{ECEF}, A0 \right\rangle \tag{2.45}$$

We will follow the same approach to develop a model for the second derivative of the topocentric distance with respect to time. We can write:

$$\ddot{\rho}_r^s(t, t-\tau_r^s) = \frac{\partial \dot{\rho}_r^s(t, t-\tau_r^s)}{\partial t} = \frac{\partial}{\partial t}\left(\frac{\langle A1 - A2, A0 \rangle}{\rho_r^s(t, t-\tau_r^s) + \left\langle \frac{A1}{c}, A0 \right\rangle} \right) \tag{2.46}$$

We introduce

$$A3 = \langle A1 - A2, A0 \rangle = \left\langle \dot{A0}, A0 \right\rangle \tag{2.47}$$

and

$$A4 = \rho_r^s(t, t-\tau_r^s) + \left\langle \frac{A1}{c}, A0 \right\rangle \tag{2.48}$$

and thus:

$$\ddot{\rho}_r^s(t, t-\tau_r^s) = \frac{\partial}{\partial t}\left(\frac{A3}{A4}\right) = \frac{\left(\left\langle \ddot{A0}, A0 \right\rangle + \left\langle \dot{A0}, \dot{A0} \right\rangle\right)(A4) - (A3)(\dot{A4})}{(A4)^2} \tag{2.49}$$

In order to calculate this range rate rate, the position, velocity and acceleration of the GNSS satellite and the user are required. Appendix B shows how to calculate position, velocity and acceleration of the GNSS satellite from ephemeris data based on the steps described in (GPS-ICD-200, 1993) and the derivations from (de Jonge, 1998), but acceleration of the user is normally not available as a GNSS receiver does not provide an observation that is the derivative of the Doppler shift. Therefore range rate rate $\ddot{\rho}_r^s(t, t-\tau_r^s)\triangle\zeta_r(t)$ is in general unobservable, and the user's acceleration cannot be estimated directly.
In (Zhang, 2006) an attempt is made to develop a differentiator to obtain this quantity in post-processing and potentially also in real-time. However, as this kind of approach is based on assumptions on the user's dynamics and introduces time-correlation in the observations, it is beyond the scope of this research.

2.3.4 RINEX instructions for correcting observations

As we will see later on ideally for space applications the receiver clocks are actively steered, rather than through discrete adjustments once in a while (the so-called *clock jumps*). If this is not done, the absolute navigation result can be applied for correcting the GNSS observations a posteriori: the observations are checked for clock offset and can be corrected using the RINEX instructions (Gurtner and Estey, 2006a) (Gurtner and Estey, 2006b). In section 3.3 of (Gurtner and Estey, 2006b) the instructions are that if the receiver or the converter software adjusts the measurements using the real-time-derived receiver clock offsets *dT(r)*, the consistency of the 3 quantities phase / pseudo-range / epoch must be maintained, i.e. the receiver clock correction should be applied to all 3 observables (using the RINEX notation):

Time(corr) = *Time(r)* - *dT(r)*

PR(corr) = *PR(r)* - *dT(r)*c*

phase(corr) = *phase(r)* - *dT(r)*freq*

where the *Time(r)* is the receiver time and *Time(corr)* is time corrected for offset from the GNSS time; *PR* is the pseudo range, *phase* is the carrier phase and *freq* is the observation frequency. *c* is the speed of light. There are no instructions what to do with Doppler observations when the measurements are adjusted for the receiver clock offset. However, for large clock offsets and/or high user dynamics, this correction will only reduce the effects that later on in this report will be described. So the general discussion will remain valid if the RINEX corrections are applied on the observations.

2.3.5 Receiver clock offset for different kinds of applications

For a well-designed receiver, the receiver clock can be steered within at least 1 μs from GNSS time and nominally the clock offset can be 100 times smaller. For a typical navigational type of receiver the clock offset can be up to 0.5 or 1 ms, with a clock drift up to 2 μs/s.

As an example the Phoenix receiver from DLR can steer its clock with the GPS time (Montenbruck et al., 2004)(Montenbruck and Markgraf, 2008), after a valid position solution has been calculated (thus satellite signals and navigation data are acquired, and a position solution has been calculated which fulfills certain requirements). The typical error amounts to about 0.2 μs and is determined by the limited resolution of the correlator timing (175 ns) and the accuracy with which the modeled GPS time of the receiver matches the true GPS system time ($<$0.1 μs with S/A off). The measurements and navigation solution of the receiver are aligned to the integer GPS second, whenever a continuous 3D navigation solution has been achieved.

2.3.6 Range rate and range rate rate for different kinds of applications

In this section we will analyze the amplitude of range rate and range rate rate for four different users;

1. a terrestrial User
2. a LEO user at 400 km altitude
3. a LEO user at 80 km altitude
4. an User in a very eccentric orbit

The amplitude of the range rates will be different for the different GNSSs as GPS, Galileo and GLONASS. From these 3 GNSSs, the Galileo satellites are in the highest orbit (see discussion in section 2.1) and therefore their maximum relative velocity to the user will be lowest, the GLONASS satellites are in the lowest orbit and therefore the relative velocity to an Earthbound user will be highest.
The difference in range rate and range rate rate for the three scenarios and a GPS constellation using data collected from a Spirent GNSS simulator will be analyzed next.

2.3.6.1 Static user at the Earth Surface

For this user the velocity is by definition zero in an Earth Centred Earth Fixed frame. Therefore the variation in range is solely depending on the motion of the GNSS satellites. In Fig. 2.1 the range rate for a user at longitude $0\,^{\circ}N$ and latitude $0\,^{\circ}E$ is shown over a 24 hours period. The maximum absolute value for range rate during this period is 666.75 m/s and for range rate rate 0.12 m/s^2. The maximum negative value for range rate rate is smaller than the maximum positive value (i.e. the figure is asymmetric in the x-axis). This can be explained by plotting the elevation angle vs the range rate and range rate rate in Fig. 2.2. The figure shows the distinct paths of the GNSS satellites in different orbits, slowly shifting over the day. If the GNSS satellite moves directly through the zenith (elevation angle is 90°), the range rate becomes zero, but the change of the range rate reaches its maximum value and is always positive.

2.3.6.2 User in Low Earth Orbit

We simulated two different circular Low Earth Orbits (LEO) to investigate the range rate for this kind of application. The first orbit has an altitude of 400 kilometer, the second an altitude of 80 kilometer. Note that the scale of the range rate rate axis in these figures is also 100 times larger than in Fig. 2.1.
For the 400-km orbit (Fig. 2.3), the maximum range rate is less than 7845.33 m/s and the maximum range rate rate is less than 12.39 m/s^2. For a satellite with an altitude of 80 kilometer (very low and unstable orbit), the maximum range rate is 8027.55 m/s, the maximum range rate rate is less than 13.32 m/s^2 (see Fig. 2.5). So the maximum range rate is for the LEO user more than 10 times larger than for the terrestrial user, the maximum range rate rate is more than 100 times larger.

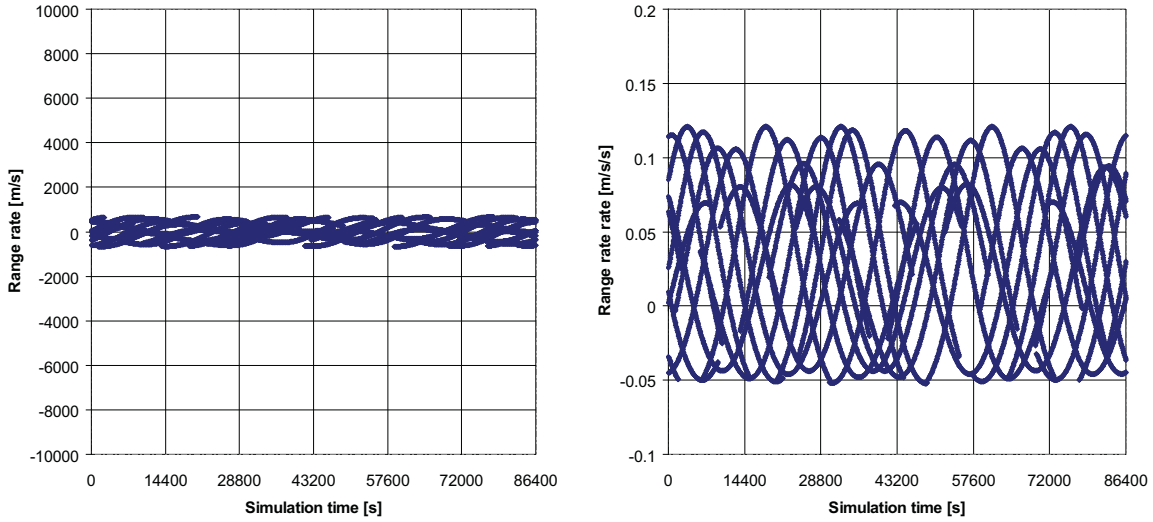


Figure 2.1: Range rate and Range rate rate of observation between terrestrial user and GPS spacecraft

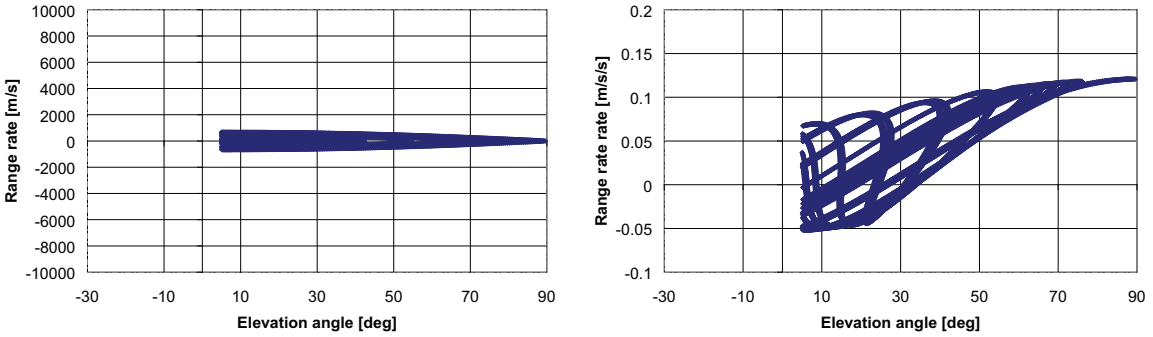


Figure 2.2: Range rate and Range rate rate vs elevation angle of observation between terrestrial user and GPS spacecraft

Moreover note the increase in range rate rate is much larger in the positive direction: the negative values on the right side of Fig. 2.3 are at most -2 m/s^2 whereas the positive values has increased up to more than 12 m/s^2. This can be understood from Fig. 2.4, where the range and range rate rate are shown as function of elevation angle. Although different from the static user in Fig. 2.2, the user's velocity in orbit is higher than the velocity of the GNSS satellites, still if the GNSS satellite moves through the zenith, the range rate becomes zero, the change of the range rate reaches its maximum value and is always positive.

2.3.6.3 User in Eccentric Orbit

For this user, we will use the orbit of the European formation flying mission PROBA-3 currently developed under a contract with ESA. The mission and orbit is described in appendix A.7 based on (Llorente et al., 2008)(Peters et al., 2008). For the PROBA-3 scenario a whole orbit is simulated but only the part of orbit where the satellites are below the GPS constellation is of importance. According to (Peters et al., 2008), the mission requirements are that GPS receivers will be used for relative positioning during the period where the altitude of the satellites are below 5000 km. The velocity of the PROBA-3

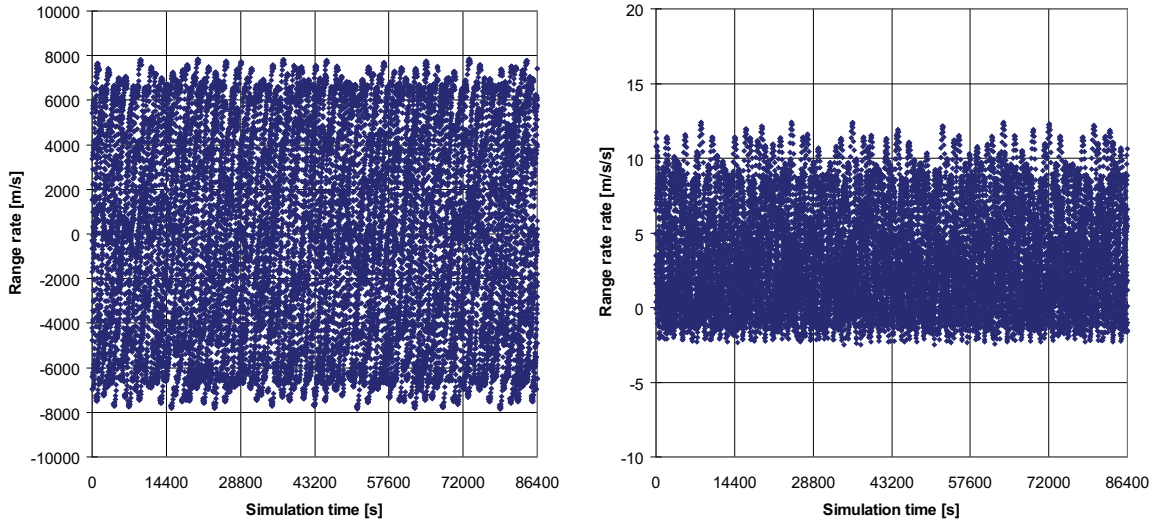


Figure 2.3: Range rate and range rate rate of observations between LEO (400 km) and GPS spacecraft

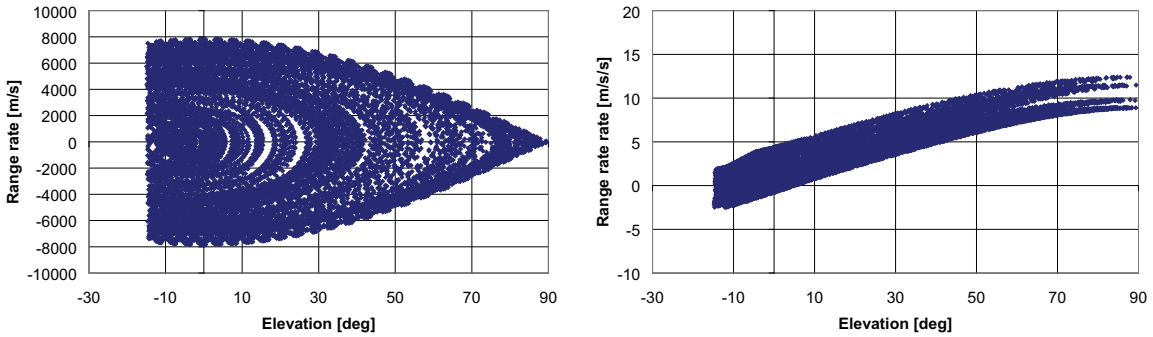


Figure 2.4: Range rate and range rate rate vs elevation angle of observations between LEO (400 km) and GPS spacecraft

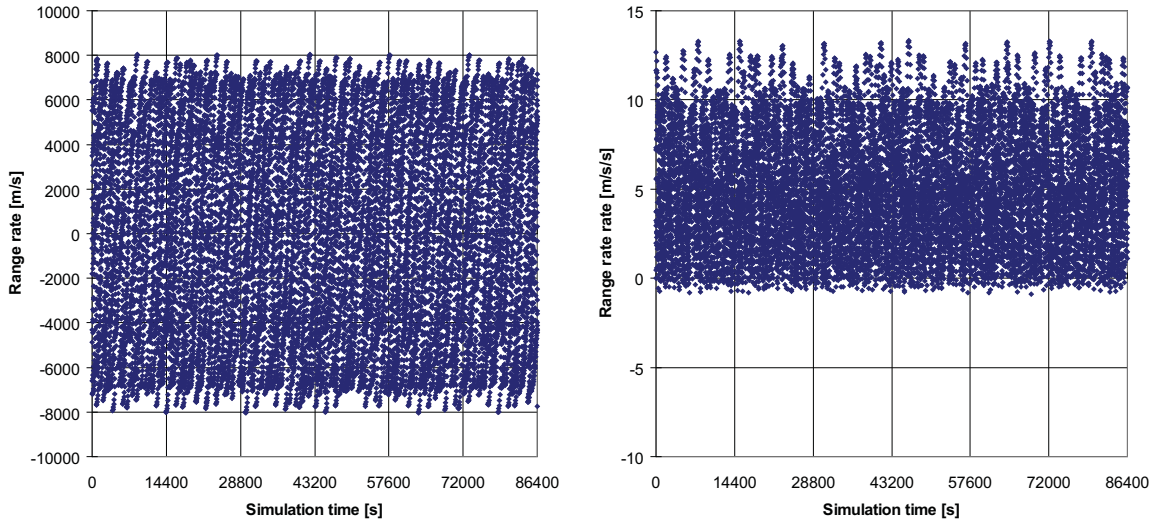


Figure 2.5: Range rate and range rate rate of observations between LEO (80 km) and GPS spacecraft

satellites when passing through the perigee is about 10 km/s (≈40.000 km/hr). For this orbit, as is shown in Fig. 2.6, the maximum range rate at the perigee is 8739.59 m/s and the maximum range rate rate is less than 11.84 m/s^2. So the order of maximum range rate and range rate rate is the about the same as the LEO user and respectively 10 and 100 times larger as for the static terrestrial user.

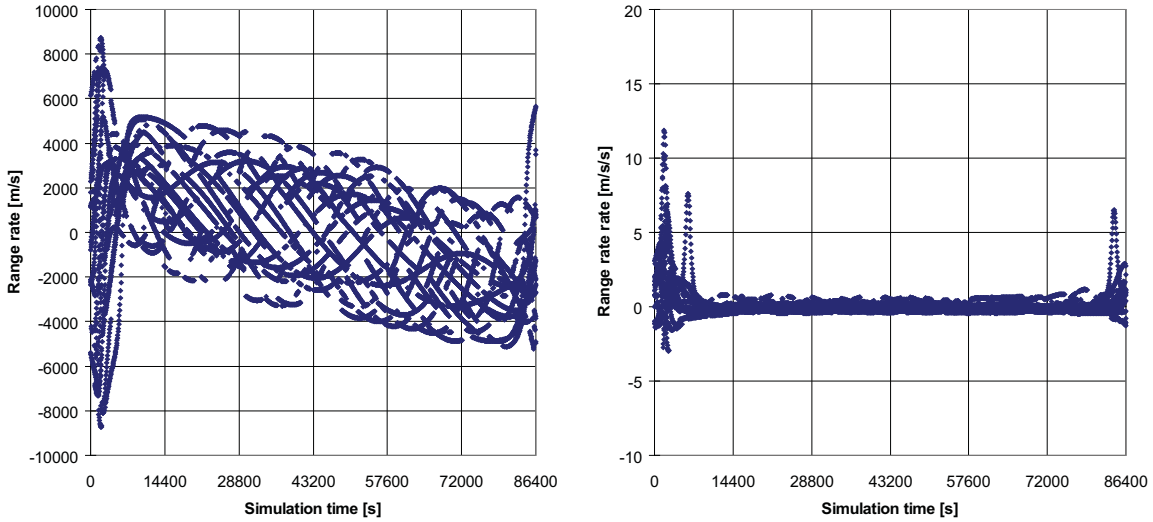


Figure 2.6: Range rate and range rate rate of observations between Proba-3 and GPS spacecraft (SC)

2.3.6.4 Discussion

The discussed examples show that, especially for users in space, the values of range rate and range rate rate can become very large due to the larger relative velocities and accelerations between the user and the GNSS spacecraft. This can become critical when the receiver clock is not steered close to the GNSS time. In the next sections, a model will be developed were large clock offsets and high dynamics at the user receiver are taken into account.

2.4 Functional model

2.4.1 Undifferenced equations

For convenience the observation equations for pseudorange, carrier phase and Doppler are repeated once again at the start of this section. Under the assumptions made in section 2.2, code, phase and Doppler observation can be expressed by the equations (2.50),(2.51) and (2.52).

$$\begin{aligned} P^s_{r,f}(t) = \; & \rho^s_r(t, t-\tau^s_r) + I^s_{r,f} + T^s_r + c\,[\zeta_r(t) - \zeta^s(t-\tau^s_r)] + \\ & + c\left[d_{r,f}(t) + d^s_f(t-\tau^s_r)\right] + \epsilon^s_{r,f} \end{aligned} \tag{2.50}$$

$$\begin{aligned} \Phi^s_{r,f}(t) = \; & \rho^s_r(t, t-\tau^s_r) - I^s_{r,f} + T^s_r + c\,[\zeta_r(t) - \zeta^s(t-\tau^s_r)] + \\ & + c\left[\delta_{r,f}(t) + \delta^s_f(t-\tau^s_r)\right] + \lambda_f[\phi_{r,f}(t_{r,0}) + \phi^s_f(t^s_0)] + \lambda_f z^s_{r,f} + \varepsilon^s_{r,f} \end{aligned} \tag{2.51}$$

$$D^s_{r,f}(t) = \quad \dot\rho^s_r(t, t-\tau^s_r) - \dot I^s_{r,f} + \dot T^s_r + c\left[\dot\zeta_r(t) - \dot\zeta^s(t-\tau^s_r)\right] + \dot\varepsilon^s_{r,f} \tag{2.52}$$

The derived linearized code and carrier observation equations are:

$$\begin{aligned} \triangle P^s_{r,f}(t) = \; & \frac{\partial \rho^s_r(t, t-\tau^s_r)}{\partial \mathbf{r}^s}\Big|_0 \triangle \mathbf{r}^s + \frac{\partial \rho^s_r(t, t-\tau^s_r)}{\partial \mathbf{r}_r}\Big|_0 \triangle \mathbf{r}_r + \frac{\partial \rho^s_r(t, t-\tau^s_r)}{\partial \zeta_r(t)}\Big|_0 \triangle\zeta_r(t) + \\ & + \triangle I^s_{r,f} + \triangle T^s_r + c\,[\triangle\zeta_r(t) - \triangle\zeta^s(t-\tau^s_r)] + c\left[\triangle d_{r,f}(t) + \triangle d^s_f(t-\tau^s_r)\right] + \\ & + \epsilon^s_{r,f} \end{aligned}$$

$$\begin{aligned} \triangle \Phi^s_{r,f}(t) = \; & \frac{\partial \rho^s_r(t, t-\tau^s_r)}{\partial \mathbf{r}^s}\Big|_0 \triangle \mathbf{r}^s + \frac{\partial \rho^s_r(t, t-\tau^s_r)}{\partial \mathbf{r}_r}\Big|_0 \triangle \mathbf{r}_r + \frac{\partial \rho^s_r(t, t-\tau^s_r)}{\partial \zeta_r}(t)\Big|_0 \triangle\zeta_r(t) + \\ & - \triangle I^s_{r,f} + \triangle T^s_r + c\,[\triangle\zeta_r(t) - \triangle\zeta^s(t-\tau^s_r)] + c\left[\triangle\delta_{r,f}(t) + \triangle\delta^s_f(t-\tau^s_r)\right] + \\ & + \lambda_f[\phi_{r,f}(t_{r,0}) + \phi^s_f(t^s_0)] + \lambda_f z^s_{r,f} + \varepsilon^s_{r,f} \end{aligned} \tag{2.53}$$

These two equations can be rewritten, by applying Eq. (2.20) till Eq. (2.23) to:

New UD Model: code and phase

$$\begin{aligned} \triangle P^s_{r,f}(t) = \; & \mathbf{u}^s_r \triangle \mathbf{r}^s - \mathbf{u}^s_r \triangle \mathbf{r}_r - \dot\rho^s_r(t, t-\tau^s_r)\triangle\zeta_r(t) + \triangle I^s_{r,f} + \triangle T^s_r + \\ & + c\,[\triangle\zeta_r(t) - \triangle\zeta^s(t-\tau^s_r)] + c\left[\triangle d_{r,f}(t) + \triangle d^s_f(t-\tau^s_r)\right] + \epsilon^s_{r,f} \end{aligned} \tag{2.54}$$

$$\begin{aligned} \triangle \Phi^s_{r,f}(t) = \; & \mathbf{u}^s_r \triangle \mathbf{r}^s - \mathbf{u}^s_r \triangle \mathbf{r}_r - \dot\rho^s_r(t, t-\tau^s_r)\triangle\zeta_r(t) - \triangle I^s_{r,f} + \triangle T^s_r + \\ & + c\,[\triangle\zeta_r(t) - \triangle\zeta^s(t-\tau^s_r)] + c\left[\triangle\delta_{r,f}(t) + \triangle\delta^s_f(t-\tau^s_r)\right] + \\ & + \lambda_f[\phi_{r,f}(t_{r,0}) - \phi^s_f(t^s_0)] + \lambda_f z^s_{r,f} + \varepsilon^s_{r,f} \end{aligned} \tag{2.55}$$

The standard undifferenced model used for single point positioning, as the term $\dot{\rho}_r^s(t, t - \tau_r^s)\triangle\zeta_r(t)$ is neglected for most terrestrial applications, is:

Standard UD Model

$$\begin{aligned}\triangle P_{r,f}^s(t) = \; & \mathbf{u}_r^s\triangle\mathbf{r}^s - \mathbf{u}_r^s\triangle\mathbf{r}_r + \triangle I_{r,f}^s + \triangle T_r^s + \\ & + c\left[\triangle\zeta_r(t) - \triangle\zeta^s(t - \tau_r^s)\right] + c\left[\triangle d_{r,f}(t) + \triangle d_f^s(t - \tau_r^s)\right] + \epsilon_{r,f}^s \end{aligned} \tag{2.56}$$

$$\begin{aligned}\triangle\Phi_{r,f}^s(t) = \; & \mathbf{u}_r^s\triangle\mathbf{r}^s - \mathbf{u}_r^s\triangle\mathbf{r}_r - \triangle I_{r,f}^s + \triangle T_r^s + \\ & + c\left[\triangle\zeta_r(t) - \triangle\zeta^s(t - \tau_r^s)\right] + c\left[\triangle\delta_{r,f}(t) + \triangle\delta_f^s(t - \tau_r^s)\right] + \\ & + \lambda_f[\phi_{r,f}(t_{r,0}) - \phi_f^s(t_0^s)] + \lambda_f z_{r,f}^s + \varepsilon_{r,f}^s \end{aligned} \tag{2.57}$$

The difference between equations (2.56)-(2.57) and the model found in (Psiaki and Mohiuddin, 2007) is that the latter evaluates the observations at receiver time $t_r(t)$, instead of GNSS system time t, and assumes that $t^s(t) - t = \zeta^s$. For real-time applications, ζ^s is a prediction provided by the navigation message, for post-processing applications it can be a very good approximation.

2.4.1.1 Equations for Doppler based on differencing Carrier Phase Observations

In this section, the Doppler equation Eq. (2.52) is not linearized itself (this will be done in the next section), instead we obtain the time derivative of the linearized geometric distance as applied in the Eq. (2.55):

$$\begin{aligned}\triangle D_{r,f}^s(t) = \; & \frac{\partial(\triangle\Phi_{r,f}^s(t))}{\partial t} \\ = & \frac{\partial}{\partial t}\left(\frac{\partial\rho_r^s(t, t - \tau_r^s)}{\partial\mathbf{r}^s}\Big|_0\triangle\mathbf{r}^s\right) + \frac{\partial}{\partial t}\left(\frac{\partial\rho_r^s(t, t - \tau_r^s)}{\partial\mathbf{r}_r}\Big|_0\triangle\mathbf{r}_r\right) + \\ & + \frac{\partial}{\partial t}\left(\frac{\partial\rho_r^s(t, t - \tau_r^s)}{\partial\zeta_r(t)}\Big|_0\triangle\zeta_r(t)\right) - \triangle\dot{I}_{r,f}^s + \triangle\dot{T}_r^s + \\ & + c\left[\triangle\dot{\zeta}_r(t) - \triangle\dot{\zeta}^s(t - \tau_{r,f}^s)\right] + \dot{\varepsilon}_{r,f}^s \end{aligned} \tag{2.58}$$

For this equation using Eq. (2.21), (2.25) and (2.38)

$$\frac{\partial}{\partial t}\left(\frac{\partial\rho_r^s(t, t - \tau_r^s)}{\partial\mathbf{r}^s}\Big|_0\triangle\mathbf{r}^s\right) = \frac{\partial(\mathbf{u}_r^s\triangle\mathbf{r}^s)}{\partial t} = \dot{\mathbf{u}}_r^s\triangle\mathbf{r}^s + \mathbf{u}_r^s\triangle\dot{\mathbf{r}}^s \tag{2.59}$$

$$\frac{\partial}{\partial t}\left(\frac{\partial\rho_r^s(t, t - \tau_r^s)}{\partial\mathbf{r}_r}\Big|_0\triangle\mathbf{r}_r\right) = -\frac{\partial(\mathbf{u}_r^s\triangle\mathbf{r}_r)}{\partial t} = -\dot{\mathbf{u}}_r^s\triangle\mathbf{r}_r - \mathbf{u}_r^s\triangle\dot{\mathbf{r}}_r \tag{2.60}$$

$$\begin{aligned}\dot{\mathbf{u}}_r^s &= \frac{\partial}{\partial t}\left(\left[\frac{\mathbf{r}^s(t-\tau_r^s)-\mathbf{r}_r(t)}{\rho_r^s(t-\tau_r^s,t)}\right]^T\right)\\ &= \frac{\left(\dot{\mathbf{r}}^s(t-\tau_r^s)(1-\frac{\dot{\rho}_r^s(t,t-\tau_r^s)}{c})-\dot{\mathbf{r}}_r(t)\right)\rho_r^s(t,t-\tau_r^s)-(\mathbf{r}^s(t-\tau_r^s)-\mathbf{r}_r(t))\,\dot{\rho}_r^s(t,t-\tau_r^s)}{(\rho_r^s(t,t-\tau_r^s))^2}\\ &= \frac{\left(\dot{\mathbf{r}}^s(t-\tau_r^s)(1-\frac{\dot{\rho}_r^s(t,t-\tau_r^s)}{c})-\dot{\mathbf{r}}_r(t)\right)-\mathbf{u}_r^s\dot{\rho}_r^s(t,t-\tau_r^s)}{\rho_r^s(t,t-\tau_r^s)}\end{aligned} \tag{2.61}$$

and using Eq. (2.22)

$$\begin{aligned}\frac{\partial}{\partial t}\left(\frac{\partial\rho_r^s(t,t-\tau_r^s)}{\partial\zeta_r(t)}\Big|_0\triangle\zeta_r(t)\right) &= \frac{\partial}{\partial t}\left(-\dot{\rho}_r^s(t,t-\tau_r^s)\triangle\zeta_r(t)\right)\\ &= -\ddot{\rho}_r^s(t,t-\tau_r^s)\triangle\zeta_r(t)-\dot{\rho}_r^s(t,t-\tau_r^s)\triangle\dot{\zeta}_r(t)\end{aligned} \tag{2.62}$$

Eq. (2.61) describes $\dot{\mathbf{u}}_r^s$ as the difference in velocity between the receiver and the GNSS satellite minus the range rate component in the direction of the line-of-sight vector divided by the geometric distance between the receiver and GNSS satellite. This relationship was also derived in (van Diggelen, 2009).
The Doppler equation becomes:

New UD Model: Doppler 1

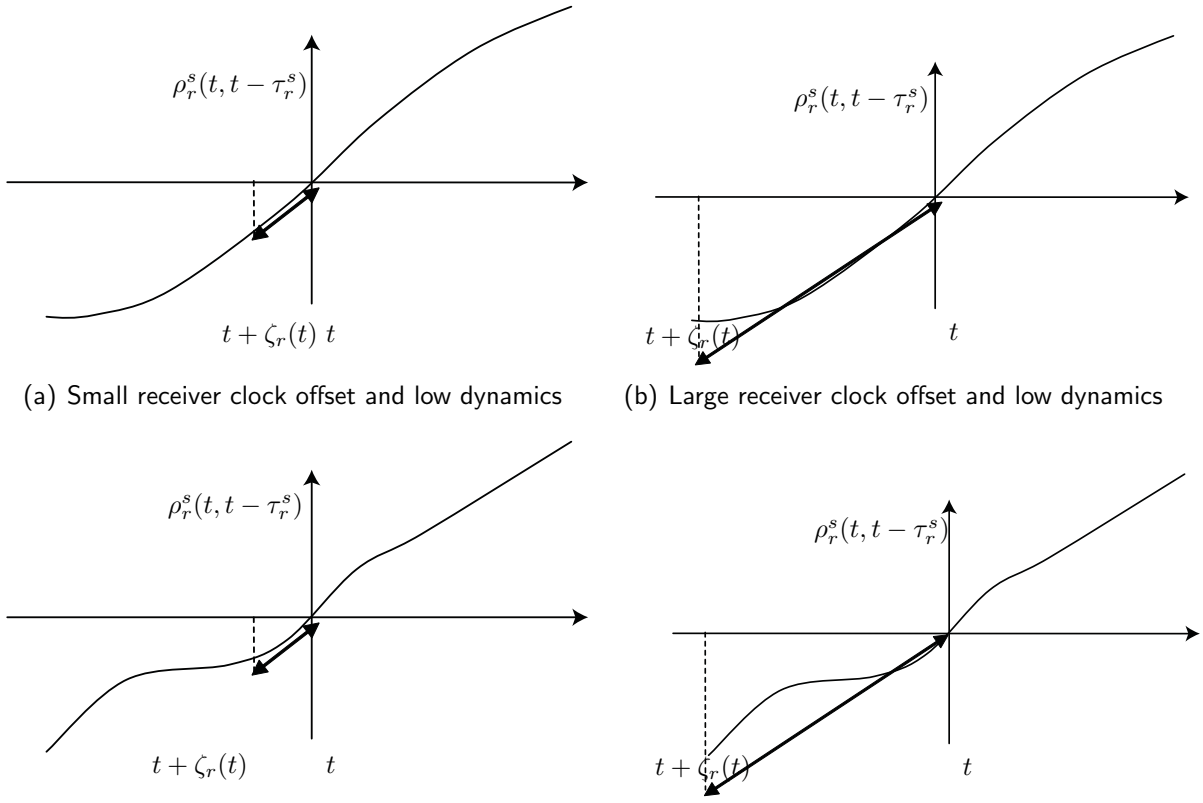
$$\begin{aligned}\triangle D_{r,f}^s(t) = \;& \mathbf{u}_r^s\triangle\dot{\mathbf{r}}^s+\dot{\mathbf{u}}_r^s\triangle\mathbf{r}^s-\mathbf{u}_r^s\triangle\dot{\mathbf{r}}_r-\dot{\mathbf{u}}_r^s\triangle\mathbf{r}_r-\ddot{\rho}_r^s(t,t-\tau_r^s)\triangle\zeta_r(t)-\dot{\rho}_r^s(t,t-\tau_r^s)\triangle\dot{\zeta}_r(t)+\\ & -\triangle\dot{I}_{r,f}^s+\triangle\dot{T}_r^s+c\left[\triangle\dot{\zeta}_r(t)-\triangle\dot{\zeta}^s(t-\tau_r^s)\right]+\dot{\varepsilon}_{r,f}^s\end{aligned} \tag{2.63}$$

For these equations, we will analyze the order of magnitude of the terms for the applications discussed in section 2.3.6. It follows from Eq. (2.54)-(2.55) and (2.63) that the effect of the amplitude of $\dot{\rho}_r^s(t,t-\tau_r^s)$ and $\ddot{\rho}_r^s(t,t-\tau_r^s)$ on the observations is depending of the relative dynamics between the users and the GNSS satellites as these determine $\dot{\rho}_r^s(t,t-\tau_r^s)$ and $\ddot{\rho}_r^s(t,t-\tau_r^s)$ itself and the time offset/drift of the receivers as $\dot{\rho}_r^s(t,t-\tau_r^s)$ and $\ddot{\rho}_r^s(t,t-\tau_r^s)$ are multiplied with this time offset/drift.

Fig. 2.7 shows a sketch of the range as a function of time. The range at GNSS system time t and receiver time $t_r(t) = t+\zeta_r(t)$ (see Eq. (2.7)) is indicated, so the sketches illustrate the variations in range between the time of observation and the receiver time. The four cases considered are:
(a) the nominal case with small receiver clock offset and low dynamics
(b) the case with large receiver clock offset and low dynamics
(c) the case with small receiver clock offset and high dynamics

(d) the case with large receiver clock offset and high dynamics

where the small clock offset case represents a receiver that actively controls its clock at every epoch, and the large clock offset case represents the receiver that applies clock jumps of -for example- 0.5 or 1 ms.
Only for the first case the relationship between range and receiver clock offset can be considered linear. The most challenging application is the one with large clock offsets and high dynamics, but even for the cases of large clock offset with low dynamics and small clock offset and high dynamics, the linear relationship might not be appropriate. This is investigated next for the simulation results described in section 2.3.6.



(a) Small receiver clock offset and low dynamics

(b) Large receiver clock offset and low dynamics

(c) Small receiver clock offset and high dynamics

(d) Large receiver clock offset and high dynamics

Figure 2.7: Four cases with different receiver clock offsets and dynamics

Static user at the Earth Surface The maximum absolute value for range rate during the 24 hours period simulated for the terrestrial user in section 2.3.6 is 666.75 m/s which results in range error of $\dot{\rho}_r^s(t, t-\tau_r^s)\triangle\zeta_r(t)$ =0.33 m for a receiver with a maximum clock offset of 0.5 ms. The maximum contributions from the product of range rate rate and clock offset to the Doppler is $\ddot{\rho}_r^s(t, t-\tau_r^s)\triangle\zeta_r(t)$ =0.12× 0.5 ms=0.060 mm/s and from the range rate and clock drift is $\dot{\rho}_r^s(t, t-\tau_r^s)\triangle\dot{\zeta}_r(t)$ =666.75× 2 μs/s=1.3 mm/s. Both terms are about 100 times smaller then the contribution of range rate, more importantly below the noise level of the Doppler observation and therefore can be neglected in the functional model. For a receiver where the clock is steered within 1 μs (this number is still conservative, normally it could be 100 times smaller), the contribution of the range rate to the pseudo range and carrier phase is negligible.

User in Low Earth Orbit For the 400 kilometers orbit (Fig. 2.3 in section 2.3.6), the maximum range rate is less than 7845.33 m/s and maximum range rate rate is less than 12.39 m/s^2. For a maximum clock offset of 0.5 ms, this would result in a contribution of 3.92 meters to the pseudo range and carrier phase observation. The maximum contributions from the product of range rate rate and clock offset $\ddot{\rho}_r^s(t, t-\tau_r^s)\triangle\zeta_r(t)$ =12.39$\times$ 0.5 ms=6.2 mm/s and range rate and clock drift, respectively $\dot{\rho}_r^s(t, t-\tau_r^s)\triangle\dot{\zeta}_r(t)$ =7845.33$\times$ 2 μs/s=15.6 mm/s, more than 100 times smaller, but of the order of the noise level of the Doppler observations and therefore cannot be neglected in the functional model. For a receiver, with a clock offset within 1 μs, (again this a pessimistic value) this would be about 7.84 mm, so even for this kind of receiver significantly higher than the noise level on the carrier phase observations. For a satellite with a altitude of 80 kilometer (very low and unstable orbit), the maximum range rate is 8027.55 m/s (see Fig. 2.5 in section 2.3.6)), which will result in a contribution to the observation of 4.01 m for the typical navigation and 8.0 mm to the steered receiver respectively. The maximum contributions from the range rate rate times clock offset and range rate times clock drift are 13.32$\times$ 0.5 ms=6.7 mm/s and, respectively 8027.55$\times$ 2 μ s/s=16.1 mm/s.

User in Eccentric Orbit For this orbit the maximum range rate at the perigee is 8739.59 m/s. This maximum range rate would result in a contribution to the pseudo range and carrier phase observation of about 4.37 m for the free-running clock receiver with a maximum clock offset of 0.5 ms, and 8.74 mm for the clock-steered receiver with a clock offset of 1 μs (as said before this value is pessimistic). The maximum contributions from the range rate rate times clock offset and range rate times clock drift are again not negligible: 11.84$\times$ 0.5 ms=5.92 mm/s and, respectively 8739.59$\times$ 2 μs/s=17.48 mm/s.

As described in section 2.3.3, $\ddot{\rho}_r^s(t, t-\tau_r^s)$ can in general not be determined. With the simplification $\ddot{\rho}_r^s(t, t-\tau_r^s)\triangle\zeta_r(t) \approx 0$, we obtain a linear equation relating the receiver position, velocity vectors and the clock drift to the Doppler observations:

New UD Model 1: Doppler (simplified)

$$\begin{aligned}\triangle D_{r,f}^s(t) = \; & \mathbf{u}_r^s\triangle\dot{\mathbf{r}}^s + \dot{\mathbf{u}}_r^s\triangle\mathbf{r}^s - \mathbf{u}_r^s\triangle\dot{\mathbf{r}}_r - \dot{\mathbf{u}}_r^s\triangle\mathbf{r}_r - \dot{\rho}_r^s(t, t-\tau_r^s)\triangle\dot{\zeta}_r(t) - \triangle\dot{I}_{r,f}^s + \triangle\dot{T}_r^s + \\ & + c\left[\triangle\dot{\zeta}_r(t) - \triangle\dot{\zeta}^s(t-\tau_r^s)\right] + \dot{\varepsilon}_{r,f}^s \end{aligned} \tag{2.64}$$

In this linearization, we relate seven unknowns to the Doppler observations. The similarity of the first terms of the equations (2.54), (2.55) and (2.63), might give the idea that they are linearly dependent. However it can be shown that pseudorange and Doppler observations are orthogonal (Jorgensen, 1980)(Hofmann-Wellenhoff et al., 2001), as the former are measured along the line-of-sight between user and GNSS satellite, the latter provide information along the direction of the component of relative velocity that is perpendicular to this line-of-sight vector.

2.4.1.2 Doppler Equations for Observations obtained from Tracking Loop

We can show that the Doppler equation (2.63) is different from what we would obtain if we would manipulate Eq. (2.52) itself, by writing it as:

$$D^s_{r,f}(t) = \quad \langle \dot{\mathbf{r}}^s(t-\tau^s_r) - \dot{\mathbf{r}}_r(t), \mathbf{u}^s_r \rangle - \dot{I}^s_{r,f} + \dot{T}^s_r + c\left[\dot{\zeta}_r(t) - \dot{\zeta}^s(t-\tau^s_r)\right] + \dot{\varepsilon}^s_{r,f} \quad (2.65)$$

then the linearized model becomes:

New UD Model: Doppler 2

$$\triangle D^s_{r,f}(t) = \ \mathbf{u}^s_r \triangle \dot{\mathbf{r}}^s - \mathbf{u}^s_r \triangle \dot{\mathbf{r}}_r - \triangle \dot{I}^s_{r,f} + \triangle \dot{T}^s_r + c\left[\triangle \dot{\zeta}_r(t) - \triangle \dot{\zeta}^s(t-\tau^s_r)\right] + \dot{\varepsilon}^s_{r,f} \quad (2.66)$$

This is the approach described in (Misra and Enge, 2001)(Gleason and Gebre-Egziabher, 2009). This equation is linear in the user velocity $\dot{\mathbf{r}}_r(t)$ and the GNSS satellite's velocity $\dot{\mathbf{r}}^s(t-\tau^s_r)$ is known. Therefore this equation could be written as:

$$D^s_{r,f}(t) - \langle \dot{\mathbf{r}}^s(t-\tau^s_r), \mathbf{u}^s_r \rangle = \quad -\langle \dot{\mathbf{r}}_r(t), \mathbf{u}^s_r \rangle - \dot{I}^s_{r,f} + \dot{T}^s_r + c\left[\dot{\zeta}_r(t) - \dot{\zeta}^s(t-\tau^s_r)\right] + \dot{\varepsilon}^s_{r,f} \quad (2.67)$$

In this linear equation only four states, namely the receiver velocity vector and the clock drift, are related to the Doppler observations. There is no direct dependence on the position of the receiver (other than the line-of-sight vector) and in this model we could solve for the absolute position and velocity independently using Eq. (2.54) and (2.67).

2.4.2 Single difference equations

Since later on we will primarily deal with relative positioning between receivers, we can simplify our observation equations by eliminating explicitly the common error terms $\phi^s_f(t^s_0)$ and ξ^s. Differencing of observations has its origin in interferometry (Counselman III et al., 1972).
The differences in geometric distance $\triangle\rho^s_r$ as described by Eq. (2.26) between receivers 1 and r are:

$$(-\triangle\rho^s_1) - (-\triangle\rho^s_r) = (\mathbf{u}^s_1 \triangle \mathbf{r}_1 - \mathbf{u}^s_1 \triangle \mathbf{r}^s - \dot{\rho}^s_1 \triangle \zeta_1) - (\mathbf{u}^s_r \triangle \mathbf{r}_r - \mathbf{u}^s_r \triangle \mathbf{r}^s - \dot{\rho}^s_r \triangle \zeta_r) \quad (2.68)$$

Adding and subtracting the term $\mathbf{u}^s_r \triangle \mathbf{r}_1$ to this expression and applying $\mathbf{r}_{1r} = \mathbf{r}_r - \mathbf{r}_1$ and $\mathbf{u}^s_{1r} = \mathbf{u}^s_r - \mathbf{u}^s_1$ leads to:

$$(-\triangle\rho^s_1) - (-\triangle\rho^s_r) = -\mathbf{u}^s_r \triangle \mathbf{r}_{1r} - \mathbf{u}^s_{1r} \triangle \mathbf{r}_1 + \mathbf{u}^s_{1r} \triangle \mathbf{r}^s - \dot{\rho}^s_1 \triangle \zeta_1 + \dot{\rho}^s_r \triangle \zeta_r \quad (2.69)$$

Next, we will make use of the following relations.

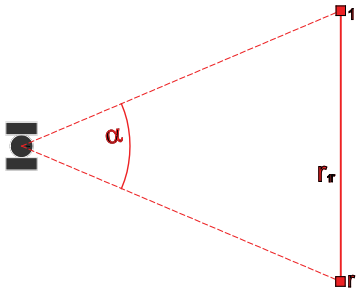


Figure 2.8: The angle α between the two line-of-sight vectors of the two antennas forming the baseline

$$\|\mathbf{u}_{1r}^s\|^2 = 2\left[1 - \mathbf{u}_1^s(\mathbf{u}_r^s)^T\right] = 2(1 - \cos(\alpha)) \tag{2.70}$$

with α, as shown in Fig. 2.8, is the angle between the two unit vectors $\mathbf{u}_1^s$ and $\mathbf{u}_r^s$. Applying the cosine rule on the baseline gives:

$$\|\mathbf{r}_{1r}\|^2 = \|\mathbf{r}_1^s\|^2 + \|\mathbf{r}_r^s\|^2 - \|\mathbf{r}_1^s\|\|\mathbf{r}_r^s\|\cos(\alpha) \tag{2.71}$$

Since for short baselines $\|\mathbf{r}_1^s\| \cong \|\mathbf{r}_r^s\|$, we can write $\|\mathbf{r}_{1r}\|^2 \cong 2\|\mathbf{r}_1^s\|^2(1 - \cos(\alpha))$ and therefore that $\|\mathbf{u}_{1r}^s\|^2 \cong \frac{\|\mathbf{r}_{1r}\|^2}{\|\mathbf{r}_1\|^2}$, and $\|\mathbf{u}_{1r}^s\| \cong \frac{\|\mathbf{r}_{1r}\|}{\|\mathbf{r}_1\|}$

The term $\mathbf{u}_{1r}^s \triangle \mathbf{r}^s$ can be demonstrated to be small as long as the baseline is much shorter than the distance between user receivers and the GNSS satellite (Teunissen and Kleusberg, 1998):

$$|\mathbf{u}_{1r}^s \triangle \mathbf{r}^s| \leq \left\{\frac{\|\mathbf{r}_{1r}\|}{\|\mathbf{r}_r^s\|}\right\} \|\triangle \mathbf{r}^s\| \tag{2.72}$$

The same can be said about the absolute receiver positioning error:

$$|\mathbf{u}_{1r}^s \triangle \mathbf{r}_1| \leq \left\{\frac{\|\mathbf{r}_{1r}\|}{\|\mathbf{r}_r^s\|}\right\} \|\triangle \mathbf{r}_1\| \tag{2.73}$$

Therefore the baseline increment can be written as

$$\triangle\rho_{1r}^s = \quad - \mathbf{u}_r^s \triangle \mathbf{r}_{1r} - \dot{\rho}_1^s \triangle\zeta_1 + \dot{\rho}_r^s \triangle\zeta_r \tag{2.74}$$

This means that it is sufficient to take one of the two antennas as a reference to calculate the line-of-sight vectors, even for distances between the receivers of dozens of kilometers.

Expression (2.73) is the upper limit of the influence of absolute navigation error on the relative solution. Assuming four values of moderate accuracy for the absolute positioning solution of 10, 1, 0.1 and 0.01 meters the upper limit as function of the baseline length is shown in Fig. 2.9. So for baseline vectors up to 10 km, the upper limit is smaller than mm level. In RTK applications, the position of the reference station is generally known with an accuracy of cm level or even better. For baselines of the order of 100 kms, the linearization

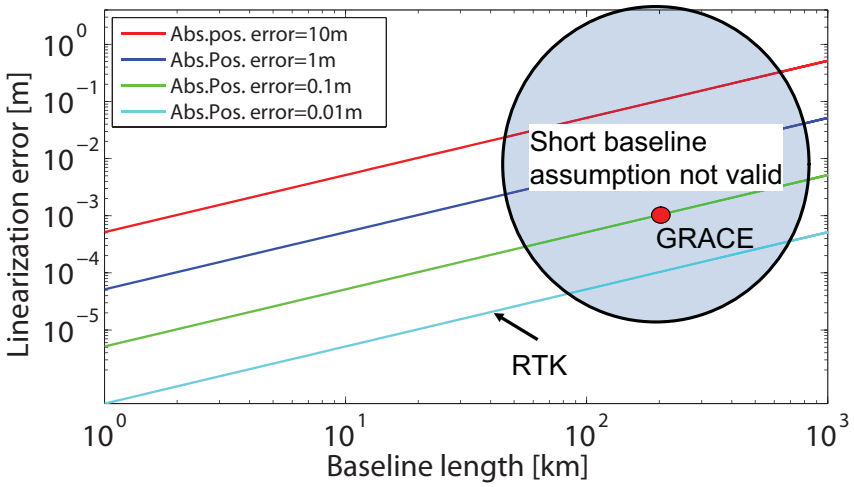


Figure 2.9: Upper limit for the relative positioning error for four values of absolute positioning error, the shade area indicates where short baseline assumption is not valid

error becomes critical and, as Eq. (2.74) is no longer valid, other processing strategies are required.

In (Kroes, 2006), in which an algorithm is developed for the GRACE mission with a baseline of about 220 km, in order to reduce errors induced by this effect, the trajectory of the reference spacecraft is estimated with high precision, e.g. a 3-dimensional position accuracy of 10 cm or better.

From here on we will use y_r as the observation vector that contains code P_r and carrier Φ_r observations, and υ_r as the observation vector that contains code P_r, carrier Φ_r and Doppler D_r observations on the $(n+1)$ satellites and N_f frequencies. Hence,

$$y_r = \begin{pmatrix} P_r^T & \Phi_r^T \end{pmatrix}^T \tag{2.75}$$

and

$$\upsilon_r = \begin{pmatrix} P_r^T & \Phi_r^T & D_r^T \end{pmatrix}^T = \begin{pmatrix} y_r^T & D_r^T \end{pmatrix}^T \tag{2.76}$$

The single differences between receivers are formed as follows:

$$\upsilon = \begin{pmatrix} \upsilon_1^T & \upsilon_r^T \end{pmatrix}^T = \begin{pmatrix} P_1^T & \Phi_1^T & D_1^T & P_r^T & \Phi_r^T & D_r^T \end{pmatrix}^T \tag{2.77}$$

the vector of single differences (SD) between receivers is

$$\upsilon^{SD} = \begin{bmatrix} \mathbf{I}_{(n+1)N_f} & \mathbf{0} & \mathbf{0} & -\mathbf{I}_{(n+1)N_f} & \mathbf{0} & \mathbf{0} \\ \mathbf{0} & \mathbf{I}_{(n+1)N_f} & \mathbf{0} & \mathbf{0} & -\mathbf{I}_{(n+1)N_f} & \mathbf{0} \\ \mathbf{0} & \mathbf{0} & \mathbf{I}_{(n+1)N_f} & \mathbf{0} & \mathbf{0} & -\mathbf{I}_{(n+1)N_f} \end{bmatrix} \begin{pmatrix} P_1 \\ \Phi_1 \\ D_1 \\ P_r \\ \Phi_r \\ D_r \end{pmatrix} =$$

$$= H^{SD} \begin{pmatrix} \upsilon_1 \\ \upsilon_r \end{pmatrix} \tag{2.78}$$

where $\mathbf{I}_{(n+1)N_f}$ is an identity matrix with dimension $(n+1)N_f \times (n+1)N_f$.
When the atmosphere parameters are not estimated, but an a-priori correction is applied based on a model, the terms y_r refer to the corrected observations. Some models for correcting tropospheric T_r^s and ionospheric $I_{r,f}^s$ delays and their derivatives are described in section 2.5.

Making use of the previous considerations and applying Eq. (2.54) and (2.55), the linearized code and phase SD observation are

$$\begin{aligned}\triangle P_{1r,f}^s(t) = \quad & -\mathbf{u}_r^s \triangle \mathbf{r}_{1r} - \dot{\rho}_1^s(t, t-\tau_1^s)\triangle\zeta_1(t) + \dot{\rho}_r^s(t, t-\tau_r^s)\triangle\zeta_r(t) + \\ & + \triangle I_{1r,f}^s + \triangle T_{1r}^s + c\triangle\zeta_{1r}(t) + c\triangle d_{1r,f} + \epsilon_{1r,f}^s \end{aligned} \tag{2.79}$$

$$\begin{aligned}\triangle \Phi_{1r,f}^s(t) = \quad & -\mathbf{u}_r^s \triangle \mathbf{r}_{1r} - \dot{\rho}_1^s(t, t-\tau_1^s)\triangle\zeta_1(t) + \dot{\rho}_r^s(t, t-\tau_r^s)\triangle\zeta_r(t) + \\ & - \triangle I_{1r,f}^s + \triangle T_{1r}^s + c\triangle\zeta_{1r}(t) + c\delta_{1r,f}(t) + \\ & + \lambda_f \phi_{1r,f}(t_{1r,0}) + \lambda_f z_{1r,f}^s + \varepsilon_{1r,f}^s \end{aligned} \tag{2.80}$$

where the initial phase at the GNSS satellite $\lambda_f \phi_f^s(t_0^s)$ is explicitly canceled from the equation, and the difference in initial phase of the receivers is written as $\lambda_f \phi_{1r,f}(t_{1r,0}) = \lambda_f \phi_{1,f}(t_{1,0}) - \lambda_f \phi_{r,f}(t_{r,0})$.
For Doppler we can apply both models Eq. (2.63) and (2.66), and the linearized Doppler SD observation become

Doppler 1:

$$\begin{aligned}\triangle D_{1r,f}^s(t) = \quad & -\mathbf{u}_r^s \triangle \dot{\mathbf{r}}_{1r} - \dot{\mathbf{u}}_r^s \triangle \mathbf{r}_{1r} - \ddot{\rho}_1^s(t, t-\tau_1^s)\triangle\zeta_1(t) + \ddot{\rho}_r^s(t, t-\tau_r^s)\triangle\zeta_r(t) + \\ & - \dot{\rho}_r^s(t, t-\tau_r^s)\triangle\dot{\zeta}_r(t) + \dot{\rho}_r^s(t, t-\tau_r^s)\triangle\dot{\zeta}_r(t) - \triangle \dot{I}_{1r,f}^s + \triangle \dot{T}_{1r}^s + \\ & + c\triangle\dot{\zeta}_{1r}(t) + \dot{\varepsilon}_{1r,f}^s \end{aligned} \tag{2.81}$$

and

Doppler 2:

$$\triangle D_{1r,f}^s(t) = \quad -\mathbf{u}_r^s \triangle \dot{\mathbf{r}}_{1r} - \triangle \dot{I}_{1r,f}^s + \triangle \dot{T}_{1r}^s + c\triangle\dot{\zeta}_{1r}(t) + \dot{\varepsilon}_{1r,f}^s \tag{2.82}$$

respectively.

Applying $\zeta_{1r}(t) = \zeta_1(t) - \zeta_r(t)$ and $\dot{\zeta}_{1r}(t) = \dot{\zeta}_1(t) - \dot{\zeta}_r(t)$ provide us with the following expression, in which $\zeta_1(t)$ is known from the absolute navigation, $\dot{\zeta}_1(t)$ and $\dot{\rho}_1^s(t, t-\tau_1^s) - \dot{\rho}_r^s(t, t-\tau_r^s)$ from the absolute velocities of the GNSS satellites and user receivers:

New SD Model

$$\begin{aligned}\triangle P^s_{1r,f}(t) = &- \mathbf{u}^s_r \triangle \mathbf{r}_{1r} + [c - \dot{\rho}^s_r(t, t-\tau^s_r)]\,\triangle\zeta_{1r}(t) + \\ &- [\dot{\rho}^s_1(t, t-\tau^s_1) - \dot{\rho}^s_r(t, t-\tau^s_r)]\,\triangle\zeta_1(t) + \triangle I^s_{1r,f} + \triangle T^s_{1r} + \\ &+ c\triangle d_{1r,f} + \epsilon^s_{1r,f} \end{aligned} \tag{2.83}$$

$$\begin{aligned}\triangle \Phi^s_{1r,f}(t) = &- \mathbf{u}^s_r \triangle \mathbf{r}_{1r} + [c - \dot{\rho}^s_r(t, t-\tau^s_r)]\,\triangle\zeta_{1r}(t) + \\ &- [\dot{\rho}^s_1(t, t-\tau^s_1) - \dot{\rho}^s_r(t, t-\tau^s_r)]\,\triangle\zeta_1(t) - \triangle I^s_{1r,f} + \triangle T^s_{1r} + c\triangle\delta_{1r,f} + \\ &+ \lambda_f \phi_{1r,f}(t_{1r,0}) + \lambda_f z^s_{1r,f} + \varepsilon^s_{1r,f} \end{aligned} \tag{2.84}$$

New SD Model: Doppler 1

$$\begin{aligned}\triangle D^s_{1r,f}(t) = &- \mathbf{u}^s_r \triangle \dot{\mathbf{r}}_{1r} - \dot{\mathbf{u}}^s_r \triangle \mathbf{r}_{1r} + \ddot{\rho}^s_r(t, t-\tau^s_r)\triangle\zeta_{1r}(t) + \\ &- [\ddot{\rho}^s_1(t, t-\tau^s_1) - \ddot{\rho}^s_r(t, t-\tau^s_r)]\,\triangle\zeta_1(t) + [c - \dot{\rho}^s_r(t, t-\tau^s_r)]\,\triangle\dot{\zeta}_{1r}(t) + \\ &- [\dot{\rho}^s_1(t, t-\tau^s_1) - \dot{\rho}^s_r(t, t-\tau^s_r)]\,\triangle\dot{\zeta}_1(t) - \triangle \dot{I}^s_{1r,f} + \triangle \dot{T}^s_{1r} + \dot{\varepsilon}^s_{1r,f} \end{aligned} \tag{2.85}$$

New SD Model: Doppler 2

$$\triangle D^s_{1r,f}(t) = - \mathbf{u}^s_r \triangle \dot{\mathbf{r}}_{1r} - \triangle \dot{I}^s_{1r,f} + \triangle \dot{T}^s_{1r} + c\triangle\dot{\zeta}_{1r}(t) + \dot{\varepsilon}^s_{1r,f} \tag{2.86}$$

These equations show that we will have to change the clock offset coefficient in the design matrix of the standard model for single differences from c to $c - \dot{\rho}^s_r(t, t-\tau^s_r)$ and include $[\dot{\rho}^s_1(t, t-\tau^s_1) - \dot{\rho}^s_r(t, t-\tau^s_r)]\,\triangle\zeta_r(t)$.
The standard SD model used in surveying is:

Standard SD Model

$$\triangle P^s_{1r,f}(t) = - \mathbf{u}^s_r \triangle \mathbf{r}_{1r} + \triangle I^s_{1r,f} + \triangle T^s_{1r} + c\triangle\zeta_{1r}(t) + c\triangle d_{1r,f} + \epsilon^s_{1r,f} \tag{2.87}$$

$$\begin{aligned}\triangle \Phi^s_{1r,f}(t) = &- \mathbf{u}^s_r \triangle \mathbf{r}_{1r} - \triangle I^s_{1r,f} + \triangle T^s_{1r} + c\triangle\zeta_{1r}(t) + c\triangle\delta_{1r,f} + \\ &+ \lambda_f \phi_{1r,f}(t_{1r,0}) + \lambda_f z^s_{1r,f} + \varepsilon^s_{1r,f} \end{aligned} \tag{2.88}$$

The difference with Eq. (2.83) and (2.84) is the result of not neglecting the range rate.

2.4.3 Double difference equations

Writing the vector of observation as Eq. (2.77), the DD observations vector (of dimension $3nN_f$) is built as

$$\upsilon^{DD} = \; DH^{SD}\upsilon^{SD} = \begin{bmatrix} D & -D \end{bmatrix} \begin{pmatrix} P_1 \\ \Phi_1 \\ D_1 \\ P_r \\ \Phi_r \\ D_r \end{pmatrix} \tag{2.89}$$

The D matrix is

$$D = \; \left(\mathbf{I}_{3N_f} \otimes \bar{D}\right) \tag{2.90}$$

where $\bar{D}$ is the matrix which forms the differences between satellites at the same frequency/observation type. If one satellite is chosen as a reference, say k, the $\bar{D}$ matrix has the form

$$\bar{D} = \; \left[\begin{bmatrix} \mathbf{I}_{k-1} \\ 0 \end{bmatrix}; \; -\mathbf{e}_{n-1} \; ; \begin{bmatrix} 0 \\ \mathbf{I}_{n-k} \end{bmatrix} \right] \tag{2.91}$$

$\otimes$ is the Kronecker product (see Appendix D.2), $\mathbf{I}_{3N_f}$ is an identity matrix with dimension $3N_f \times 3N_f$, $\mathbf{e}_{n-1}$ is a vector with $n-1$ ones.
The general expressions for the DD are:

$$\begin{aligned} \triangle P^{1s}_{1r,f}(t) = \; & -\mathbf{u}^{1s}_r \triangle \mathbf{r}_{1r} - \left[\dot{\rho}^1_1(t, t-\tau^1_1) - \dot{\rho}^s_1(t, t-\tau^s_r)\right] \triangle\zeta_1(t) + \\ & + \left[\dot{\rho}^1_r(t, t-\tau^1_r) - \dot{\rho}^s_r(t, t-\tau^s_r)\right] \triangle\zeta_r(t) + \triangle I^{1s}_{1r,f} + \triangle T^{1s}_{1r} + \epsilon^{1s}_{1r,f} \end{aligned} \tag{2.92}$$

$$\begin{aligned} \triangle \Phi^{1s}_{1r,f}(t) = \; & -\mathbf{u}^{1s}_r \triangle \mathbf{r}_{1r} - \left[\dot{\rho}^1_1(t, t-\tau^1_1) - \dot{\rho}^s_1(t, t-\tau^s_1)\right] \triangle\zeta_1(t) + \\ & + \left[\dot{\rho}^1_r(t, t-\tau^1_r) - \dot{\rho}^s_r(t, t-\tau^s_r)\right] \triangle\zeta_r(t) - \triangle I^{1s}_{1r,f} + \triangle T^{1s}_{1r} + \\ & + \lambda_f z^{1s}_{1r,f} + \varepsilon^{1s}_{1r,f} \end{aligned} \tag{2.93}$$

and thus the initial phase at the receivers' side $\lambda_f \phi_{1r,f}(t_{1r,0})$ is also explicitly eliminated from the equation.

For Doppler we will again derive two expressions:

Doppler 1:

$$\begin{aligned} \triangle D^{1s}_{1r,f}(t) = \; & -\mathbf{u}^{1s}_r \triangle \dot{\mathbf{r}}_{1r} - \dot{\mathbf{u}}^{1s}_r \triangle \mathbf{r}_{1r} - \left[\ddot{\rho}^1_1(t, t-\tau^1_1) - \ddot{\rho}^s_1(t, t-\tau^s_1)\right] \triangle\zeta_1(t) + \\ & + \left[\ddot{\rho}^1_r(t, t-\tau^1_r) - \ddot{\rho}^s_r(t, t-\tau^s_r)\right] \triangle\zeta_r(t) + \\ & - \left[\dot{\rho}^1_1(t, t-\tau^1_1) - \dot{\rho}^s_1(t, t-\tau^s_1)\right] \triangle\dot{\zeta}_1(t) + \\ & + \left[\dot{\rho}^1_r(t, t-\tau^1_r) - \dot{\rho}^s_r(t, t-\tau^s_r)\right] \triangle\dot{\zeta}_r(t) - \triangle \dot{I}^{1s}_{1r,f} + \triangle \dot{T}^{1s}_{1r} + \dot{\varepsilon}^{1s}_{1r,f} \end{aligned} \tag{2.94}$$

and
Doppler 2:

$$\triangle D^{1s}_{1r,f}(t) = \; -\mathbf{u}^{1s}_r \triangle \dot{\mathbf{r}}_{1r} - \triangle \dot{I}^{1s}_{1r,f} + \triangle \dot{T}^{1s}_{1r} + \dot{\varepsilon}^{1s}_{1r,f} \tag{2.95}$$

In this model, we make use of the following notation to write the single difference range rate:

$$\dot{\rho}_1^{1s} = [\dot{\rho}_1^1(t, t-\tau_1^1) - \dot{\rho}_1^s(t, t-\tau_1^s)]$$

$$\dot{\rho}_r^{1s} = [\dot{\rho}_r^1(t, t-\tau_r^1) - \dot{\rho}_r^s(t, t-\tau_r^s)]$$

New Linearized DD Model

$$\begin{aligned}\triangle P_{1r,f}^{1s} = \; & -\mathbf{u}_r^{1s}\triangle\mathbf{r}_{1r} - \dot{\rho}_1^{1s}\triangle\zeta_1(t) + \dot{\rho}_r^{1s}\triangle\zeta_r(t) + \\ & + \triangle I_{1r,f}^{1s} + \triangle T_{1r}^{1s} + \epsilon_{1r,f}^{1s} \end{aligned} \tag{2.96}$$

$$\begin{aligned}\triangle \Phi_{1r,f}^{1s} = \; & -\mathbf{u}_r^{1s}\triangle\mathbf{r}_{1r} - \dot{\rho}_1^{1s}\triangle\zeta_1(t) + \dot{\rho}_r^{1s}\triangle\zeta_r(t) + \\ & - \triangle I_{1r,f}^{1s} + \triangle T_{1r}^{1s} + \lambda_f z_{1r,f}^{1s} + \varepsilon_{1r,f}^{1s} \end{aligned} \tag{2.97}$$

New Linearized DD Model: Doppler 1

$$\begin{aligned}\triangle D_{1r,f}^{1s} = \; & -\mathbf{u}_r^{1s}\triangle\dot{\mathbf{r}}_{1r} - \dot{\mathbf{u}}_r^{1s}\triangle\mathbf{r}_{1r} - \ddot{\rho}_1^{1s}\triangle\zeta_1(t) + \ddot{\rho}_r^{1s}\triangle\zeta_{r(t)} + \\ & - \dot{\rho}_1^{1s}\triangle\dot{\zeta}_1(t) + \dot{\rho}_r^{1s}\triangle\dot{\zeta}_r(t) - \triangle\dot{I}_{1r,f}^{1s} + \triangle\dot{T}_{1r}^{1s} + \dot{\varepsilon}_{1r,f}^{1s} \end{aligned} \tag{2.98}$$

New Linearized DD Model: Doppler 2

$$\triangle D_{1r,f}^{1s} = \; -\mathbf{u}_r^{1s}\triangle\dot{\mathbf{r}}_{1r} - \triangle\dot{I}_{1r,f}^{1s} + \triangle\dot{T}_{1r}^{1s} + \dot{\varepsilon}_{1r,f}^{1s} \tag{2.99}$$

These equations show that, different from the standard DD model, in our new model the clock error does not completely disappear from the equations (2.96) and (2.97). The standard DD model used in surveying is:

Standard Linearized DD Model

$$\triangle P_{1r,f}^{1s} = \; -\mathbf{u}_r^{1s}\triangle\mathbf{r}_{1r} + \triangle I_{1r,f}^{1s} + \triangle T_{1r}^{1s} + \epsilon_{1r,f}^{1s} \tag{2.100}$$

$$\triangle \Phi_{1r,f}^{1s} = \; -\mathbf{u}_r^{1s}\triangle\mathbf{r}_{1r} - \triangle I_{1r,f}^{1s} + \triangle T_{1r}^{1s} + \lambda_f z_{1r,f}^{1s} + \varepsilon_{1r,f}^{1s} \tag{2.101}$$

For comparison and later use the non-linearized DD equations are also given here:

$$\begin{aligned} P^{1s}_{1r,f} = & \|\mathbf{r}^s(t-\tau^1_r) - \mathbf{r}_r(t)\| - \|\mathbf{r}^s(t-\tau^s_1) - \mathbf{r}_1(t)\| + \\ & + \|\mathbf{r}^1(t-\tau^1_1) - \mathbf{r}_1(t)\| - \|\mathbf{r}^1(t-\tau^1_r) - \mathbf{r}_r(t)\| + \\ & + I^{1s}_{1r,f} + T^{1s}_{1r} + \epsilon^{1s}_{1r,f} \\ = & \ \rho^{1s}_{1r}(t, t-\tau^{1s}_{1r}) + I^{1s}_{1r,f} + T^{1s}_{1r} + \epsilon^{1s}_{1r,f} \end{aligned} \tag{2.102}$$

$$\begin{aligned} \Phi^{1s}_{1r,f} = & \quad \|\mathbf{r}^s(t-\tau^1_r) - \mathbf{r}_r(t)\| - \|\mathbf{r}^s(t-\tau^s_1) - \mathbf{r}_1(t)\| + \\ & + \|\mathbf{r}^1(t-\tau^1_1) - \mathbf{r}_1(t)\| - \|\mathbf{r}^1(t-\tau^1_r) - \mathbf{r}_r(t)\| + \\ & - I^{1s}_{1r,f} + T^{1s}_{1r} + \lambda_f z^{1s}_{1r,f} + \varepsilon^{1s}_{1r,f} \\ = & \ \rho^{1s}_{1r}(t, t-\tau^{1s}_{1r}) - I^{1s}_{1r,f} + T^{1s}_{1r} + \epsilon^{1s}_{1r,f} \end{aligned} \tag{2.103}$$

$$D^{1s}_{1r,f} = \dot{\rho}^{1s}_{1r}(t, t-\tau^{1s}_{1r}) - \dot{I}^{1s}_{1r,f} + \dot{T}^{1s}_{1r} + \dot{\varepsilon}^{1s}_{1r,f} \tag{2.104}$$

For double differencing between GNSS systems two major approaches exist:

1. Combining the systems where only DD between the satellites of the same system are used (Verhagen and Joosten, 2003).
2. The cross-coupling approach where the DD between satellites of different systems are also included (Julien et al., 2003, 2004).

In a mixed GNSS model, additional between-receiver inter-system bias (ISB) parameters could be present for all observations. In (Odijk and Teunissen, 2012), the size and variability for GPS L1 - GIOVE E1 and GPS L5 - GIOVE E5a ISBs were investigated. From this analysis, it followed that differential ISBs are only significant for receivers of different types and manufacturers. In case of different receiver types, the phase and code ISBs may be calibrated as they appear to be very stable in time.
Nadarajah et al. (2012) indicated that the same conclusion appears to be valid for ISBs between Galileo, GPS and the Chinese Beidou/COMPASS system.

2.4.4 Functional model for one receiver with multi-antennas

If the baseline length between the antennas is limited -which is a reasonable assumption for receivers placed on a single platform- we can neglect the differential ionospheric, $\triangle I^s_{1r,f}$ and $\triangle I^{1s}_{1r,f}$, and tropospheric delays, $\triangle T^s_{1r}$ and $\triangle T^{1s}_{1r}$, and assume that $\dot{\rho}^s_1(t, t-\tau^s_1) = \dot{\rho}^s_r(t, t-\tau^s_r)$ in the single and double difference model.

The SD model of Eq. (2.79), (2.80) and (2.81)/(2.82) for receivers without a common clock is then reduced to:

$$\triangle P^s_{1r,f}(t) = -\mathbf{u}^s_r\triangle\mathbf{r}_{1r} + [c+\dot\rho^s_1(t,t-\tau^s_1)]\,\triangle\zeta_{1r}(t) + c\triangle d_{1r,f} + \epsilon^s_{1r,f} \tag{2.105}$$

$$\begin{aligned}\triangle\Phi^s_{1r,f}(t) = &-\mathbf{u}^s_r\triangle\mathbf{r}_{1r} + [c+\dot\rho^s_1(t,t-\tau^s_1)]\,\triangle\zeta_{1r}(t) + c\triangle\delta_{1r,f} + \\ &+\lambda_f\phi_{1r,f}(t_{1r,0}) + \lambda_f z^s_{1r,f} + \varepsilon^s_{1r,f}\end{aligned} \tag{2.106}$$

Doppler 1:

$$\begin{aligned}\triangle D^s_{1r,f}(t) = &-\mathbf{u}^s_r\triangle\dot{\mathbf{r}}_{1r} - \dot{\mathbf{u}}^s_r\triangle\mathbf{r}_{1r} + [c+\ddot\rho^s_1(t,t-\tau^s_1)]\,\triangle\zeta_{1r}(t) + \\ &+[c+\dot\rho^s_1(t,t-\tau^s_1)]\,\triangle\dot\zeta_{1r}(t) + \dot\varepsilon^s_{1r,f}\end{aligned} \tag{2.107}$$

Doppler 2:

$$\triangle D^s_{1r,f}(t) = -\mathbf{u}^s_r\triangle\dot{\mathbf{r}}_{1r} + c\triangle\dot\zeta_{1r}(t) + \dot\varepsilon^s_{1r,f} \tag{2.108}$$

The unknowns in the code and carrier equations are $\triangle\mathbf{r}_{1r}$, ζ_{1r}, $\triangle d_{1r,f}$, $\triangle\zeta_{1r}$, $\triangle\delta_{1r,f}$ $\phi_{1r,f}(t_{1r,0})$ and $\lambda_f z^s_{1r,f}$. Therefore one may think that the redundancy (see section 2.5.3) is lower in the SD than in the DD model. One method to overcome this apparent redundancy issue is using the reparametrization described in (de Jonge, 1998)(Jong, 2000) where the single difference ambiguity of a reference satellite is subtracted from all other carrier SD observations. In this way we can express the carrier ambiguities in terms of double difference ambiguities, since these can be resolved to their integer values, whereas the single difference ambiguities cannot. Therefore, assuming both receivers are tracking satellites 1 and s, and assuming satellite s is the reference satellite, we may write for a SD code and carrier observation:

$$\triangle P^1_{1r,f}(t) = -\mathbf{u}^1_r\triangle\mathbf{r}_{1r} + \overbrace{\left[c+\dot\rho^1_1(t,t-\tau^1_1)\right]\triangle\zeta_{1r}(t) + c\triangle d_{1r,f}}^{\triangle\eta_{d_{1r,f}}} + \epsilon^1_{1r,f} \tag{2.109}$$

$$\begin{aligned}\triangle\Phi^1_{1r,f}(t) = &-\mathbf{u}^1_r\triangle\mathbf{r}_{1r} + \left[c+\dot\rho^1_1(t,t-\tau^1_1)\right]\triangle\zeta_{1r}(t) + c\triangle\delta_{1r,f} + \lambda_f\phi_{1r,f}(t_{1r,0}) + \\ &+\lambda_f(\underbrace{z^1_{1r,f} - z^s_{1r,f}}_{z^{1s}_{1r,f}} + z^s_{1r,f}) + \varepsilon^1_{1r,f}\end{aligned} \tag{2.110}$$

$$\begin{aligned}= &-\mathbf{u}^1_r\triangle\mathbf{r}_{1r} + \\ &+\overbrace{\left[c+\dot\rho^1_1(t,t-\tau^1_1)\right]\triangle\zeta_{1r}(t) + c\triangle\delta_{1r,f} + \lambda_f\phi_{1r,f}(t_{1r,0}) + \lambda_f z^s_{1r,f}}^{\triangle\eta_{\delta_{1r,f}}} + \\ &+\lambda_f z^{1s}_{1r,f} + \varepsilon^1_{1r,f}\end{aligned} \tag{2.111}$$

where $z^{1s}_{1r,f}$ is the double difference ambiguity. The parameters $\triangle\eta_{d_{1r,f}}$ and $\triangle\eta_{\delta_{1r,f}}$ can be treated as receiver clock biases for the code and carrier observation. Therefore the SD model has the same redundancy as the DD model. This is in line with the described equivalence of the undifferenced, single difference and double difference models in (de Jonge, 1998)(Odijk, 2002).

For one receiver connected to multiple antennas (or multiple receivers synchronized by a common clock) there is no timing difference between observations from the different antennas (except for a hardware delay, generally known as the line bias for the GNSS-based attitude determination problem (Ward, 1996), which also could be considered as a timing error).

The SD model of Eq. (2.105) till (2.114)/(2.115) for receivers with a common clock is further reduced to:

$$\triangle P^s_{1r,f}(t) = \quad -\mathbf{u}^s_r\triangle\mathbf{r}_{1r} + c\triangle d_{1r,f} + \epsilon^s_{1r,f} \tag{2.112}$$

$$\triangle \Phi^s_{1r,f}(t) = \quad -\mathbf{u}^s_r\triangle\mathbf{r}_{1r} + c\triangle\delta_{1r,f} + \lambda_f\phi_{1r,f}(t_{1r,0}) + \lambda_f z^s_{1r,f} + \varepsilon^s_{1r,f} \tag{2.113}$$

Doppler 1

$$\triangle D^s_{1r,f}(t) = \quad -\mathbf{u}^s_r\triangle\dot{\mathbf{r}}_{1r} - \dot{\mathbf{u}}^s_r\triangle\mathbf{r}_{1r} + \dot{\varepsilon}^s_{1r,f} \tag{2.114}$$

Doppler 2

$$\triangle D^s_{1r,f}(t) = \quad -\mathbf{u}^s_r\triangle\dot{\mathbf{r}}_{1r} + \dot{\varepsilon}^s_{1r,f} \tag{2.115}$$

In general the redundancy of the model described by Eq. (2.105)-(2.106) is the same as Eq. (2.112)-(2.113). A careful calibration may reduce the instrumental delays (d and δ) in this model, although these biases are known to be dependent on the temperature of the receiver hardware and therefore - especially in a thermally challenging environment as a spacecraft- calibration is difficult (Buist et al., 2003). Moreover the initial phase term $\phi_{1r,f}(t_{1r,0})$ is coupled with the carrier bias δ which makes calibration even more challenging. However as discussed in section 2.2, a proper designed GNSS receiver should keep the difference between initial phase offsets $\phi_{r,f}(t_{r,0})$ an integer number for all received signals from all GNSS satellites, even if the signals are tracked at different antennas. Then Eq. (2.113) is reduced to

$$\triangle \Phi^s_{1r,f}(t) = \quad -\mathbf{u}^s_r\triangle\mathbf{r}_{1r} + c\triangle\delta_{1r,f} + \lambda_f z^s_{1r,f} + \varepsilon^s_{1r,f} \tag{2.116}$$

where $z^s_{1r,f}$ is a different integer number than in Eq. (2.113).

The DD model of Eq. (2.92),(2.93) and (2.95) are reduced for the multi-antenna/receivers model placed at the same platform to:

$$\triangle P^{1s}_{1r,f}(t) = \quad - \mathbf{u}^{1s}_{r} \triangle \mathbf{r}_{1r} + \epsilon^{1s}_{1r,f} \tag{2.117}$$

$$\triangle \Phi^{1s}_{1r,f}(t) = \quad - \mathbf{u}^{1s}_{r} \triangle \mathbf{r}_{1r} + \lambda_f z^{1s}_{1r,f} + \varepsilon^{1s}_{1r,f} \tag{2.118}$$

$$\triangle D^{1s}_{1r,f}(t) = \quad - \mathbf{u}^{1s}_{r} \triangle \dot{\mathbf{r}}_{1r} + \dot{\varepsilon}^{1s}_{1r,f} \tag{2.119}$$

This is the standard functional model as can be found in (Teunissen and Kleusberg, 1998) without the atmospheric errors. This model is valid if both receivers are connected to different clocks but also if they are connected to the same clock.

From the discussion above one might think that there is no advantage to synchronize GNSS receivers with a common clock. However, the advantage comes from the fact that

1. the receiver's thermal noise is to some extent determined by the clock of the system.
2. the measurements are done at the same time for the different antennas.

For observations collected at multiple receivers connected to a common clock, the noise variance of the single and double differences is considerably smaller than for observations from receivers with individual clocks.

2.4.5 Implementation aspects of the functional model

2.4.5.1 Phase center variations for code and carrier phase observations at different frequencies

As described in section 2.2, the phase centers of GNSS antennas depend on the type and frequency of the observation. For most popular antennas, the patterns are known from calibrations and therefore the code and carrier observations can be corrected for each frequency. In general for single frequency relative positioning and attitude determination -especially between two antennas of the same type-, the corrections are not required as both antennas will have similar phase center offsets. So corrections for the phase center variations are especially important for the multi-frequency approach, and of course when different antennas are applied (Gurtner et al., 1989)(Geiger, A., 1990).

2.4.5.2 Phase wind-up

The phase wind-up effect is described in (Leick, 2003), (Kim et al., 2005) and (Le and Tiberius, 2006). A model to analyze the phase wind-up effect for space applications is

presented in (Psiaki and Mohiuddin, 2007). The phase wind-up effect occurs in carrier phase measurements due to changes in the relative orientation between the transmitting and the receiving antenna.
For static receivers, the phase wind-up error is only caused by rotation of the GNSS satellites and the slow motion of the Earth and thus relatively small and slowly varying, and relatively simple to correct in post-processing as long as the GNSS satellites do not make maneuvers. In general, the phase wind-up effect at the GNSS satellite side can be corrected knowing the satellite's body frame, and can be corrected using the procedure described in (Wu et al., 1992).
However, with a kinematic receiver, the phase wind-up effect is mainly the result of the motion of the receiver. According to (Psiaki and Mohiuddin, 2007), it is the difference in attitude between two antennas (transmit and receive) at a large distance the reason why phase wind-up effects for spacecraft application are not negligible, as this effect may grow to be significant. If this happens, the attitude knowledge must be used to compensate for this term; otherwise it may not be possible to resolve the integer ambiguities. One full turn is equivalent to one cycle, hence about two decimeters in range for the L-band signals of GNSS.
For correcting the phase wind-up effect at the receiver side, it involves attitude knowledge of the antenna which makes it rather difficult to estimate and correct, especially in real-time.

2.4.5.3 Signal traveling time

The commonly applied way to calculate the signal traveling time of the observations is (Parkinson et al., 1996):

$$\tau_r^s = P_{r,f}^s(t)/c \tag{2.120}$$

However, as this is not a robust approach, the iterative loop described below will be applied (Tiberius, 1998). In the loop, the latest estimate of the user's position is used, and the GNSS satellite's position, velocity and acceleration in ECEF at time t are calculated using the approach described in appendix B.

$$\begin{aligned}
&\rho_{old} = \|r^s(t-\tau_r^s) - r_r(t)\| \\
&\tau_r^s = \frac{\rho_{old}}{c} \\
&while \quad d > \epsilon \\
&\quad \kappa = \zeta_r(t) + \tau_r^s \\
&\quad \rho_r^s = \|R_{ECEF}^{ECI}(-\tau_r^s)(r^s(t) - \kappa\dot{r}^s(t) + \frac{1}{2}\kappa^2\ddot{r}^s(t)) - r_r(t)\| \\
&\quad \tau_r^s = \frac{\rho_r^s}{c} \\
&\quad d = \|\rho_r^s - \rho_{old}\| \\
&\quad \rho_{old} = \rho_r^s
\end{aligned} \tag{2.121}$$

2.4.5.4 GNSS spacecraft's clock correction

For the GNSS spacecraft's clock correction, a polynomial to approximate ζ^s, as defined in (GPS-ICD-200, 1993), is applied, plus the relativistic correction from the same reference. The code phase offset can be calculated using

$$t^s(t) - t = \triangle t_{sv} = \overbrace{a_{f_0} + a_{f_1}(t - t_{oc}) + a_{f_2}(t - t_{oc})^2}^{\text{Approximation of } \zeta^s} + \triangle t_r \tag{2.122}$$

where the a_f are the polynomial coefficients provided by the GNSS navigation messages, t_{oc} is the effective spacecraft PRN code phase time at the message transition time, $\triangle t_r$ is the relativistic correction term in seconds which is given by:

$$\triangle t_r = Fe\sqrt{A}sin(E_k) \tag{2.123}$$

where e, A, E_k are orbital parameters - eccentricity, semi major axis, eccentric anomaly -of the GNSS satellite, and $F = \frac{-2\sqrt{\mu}}{c^2} = -4.442807633 \cdot 10^{-10}$ with $\mu = 3.986005 \cdot 10^{14}$ is the value of Earth's universal gravitational parameter and c is the speed of light in vacuum.

The derivatives of these equations are applied when we make use of the Doppler observations:

$$\frac{\partial \triangle t_{sv}}{\partial t} = a_{f_1} + 2a_{f_2}(t - t_{oc}) \tag{2.124}$$

$$\frac{\partial \triangle t_r}{\partial t} = Fe\sqrt{A}cos(E_k)\dot{E}_k \tag{2.125}$$

Due to rotation of the Earth during the time of signal transmission, a relativistic error is introduced, known as the *Sagnac effect*. The phenomenon, named after the French physicist Georges Sagnac who did some of the first experiments demonstrating the effect (Sagnac, 1913), is the basis of interferometers and ring laser gyroscopes.
The effect, if only the GNSS spacecraft is moving with large velocity, can be corrected using the equation below in which the effect is absorbed in corrected x and y position of the GNSS spacecraft (appendix E.1).

$$\begin{bmatrix} x_{after} \\ y_{after} \end{bmatrix} = \dot{R}^{ECI}_{ECEF}(-\tau^s_r)r^s(t) = \begin{bmatrix} cos(\dot{\Omega}\tau^s_r) & sin(\dot{\Omega}\tau^s_r) \\ -sin(\dot{\Omega}\tau^s_r) & cos(\dot{\Omega}\tau^s_r) \end{bmatrix} \begin{bmatrix} x_{before} \\ y_{before} \end{bmatrix} \tag{2.126}$$

where $\dot{\Omega}$ is the rotation rate of the Earth, which is defined in (GPS-ICD-200, 1993) as $7.2921151467 \cdot 10^{-5}$ rad/s.

The Sagnac correction, if both the GNSS spacecraft and the user are moving with large velocities, for the range observation can be calculate by (Ashby and Spilker, 1996):

$$\triangle t_s = \frac{2\omega}{c}\frac{r_r \times r^s}{2} = \frac{\dot{\Omega}}{c}(x_r y^s - y_r x^s) \tag{2.127}$$

where $\omega = \left[0, 0, \dot{\Omega}\right]^T$

The Sagnac correction for the Doppler observations can be obtained by differencing this equation with respect to time:

$$\frac{\partial(\triangle t_s)}{\partial t} = \frac{\omega}{c}\frac{\partial(r_r \times r^s)}{\partial t} = \frac{\dot{\Omega}}{c}(\dot{x}_r y^s + x_r \dot{y}^s - \dot{y}_r x^s - y_r \dot{x}^s) \tag{2.128}$$

Of course, if one works entirely in the non-rotating ECI frame (i.e. apply Eq. (2.18) and Eq. (2.121)), there is no Sagnac effect and the corrections given here should not be applied.

2.5 Atmospheric model

The atmospheric effects on GNSS observations can be divided into two different categories: tropospheric and ionospheric delay. The troposphere is a dominant error source for users on or close to the Earth's surface, whereas the ionosphere is a dominant error source both for users in the atmosphere and in LEO.

2.5.1 Tropospheric model

As is well known, different from the ionospheric delays, the tropospheric delays are the same for code and carrier observations at all frequencies and therefore cannot be directly removed or estimated by a linear combination from the GNSS signals. The troposphere stretches to an altitude of about 16 kilometers at the equator and 9 kilometers above the poles (Misra and Enge, 2001), and as this is the altitude where aircraft are flying, the tropospheric delays cannot be disregarded for these applications, especially for relative navigation between two GNSS receivers at different heights.
The troposphere contains both dry air and water vapor. Dry air has no significant variation in composition with latitude and height. The amount of water vapor, contained mostly in the lowest 2 km of the troposphere, varies both spatially and temporally. The troposphere is made up of different layers with distinct temperature, air pressure and humidity. A GNSS signal traveling trough the troposphere suffers a change in direction due to refraction. The total change in direction, or bending, can be calculated by repeatedly applying the Snell's law for each layer (Kleijer, 2004):

$$n_{i+1} \sin z_{i+1} = n_i \sin z_i \tag{2.129}$$

where z_i and z_{i+1} are the zenith angles of the GNSS signal in layer i and $i+1$, and n_i and n_{i+1} are the corresponding refractive indexes. By applying Snell's law for each layer, one finds

$$n_0 \sin z_0 = \sin z_m \tag{2.130}$$

where n_0 and z_0 are the refractive index and zenith angle in the lowest layer and z_m is the zenith angle in the highest layer where the refractive index is 1.
The tropospheric effect is one of the main differences in the functional model between space and aircraft applications. In an all-purpose relative positioning procedure, which could be applied for both types of applications, the decreasing effect of the tropospheric delay with the users' altitude has to be taken into account.
The difference in zenith delay is about 40 centimeter for the reference station on the ground and the aircraft at 1400 m altitude for the aircraft experiment described in appendix A.5. For the balloon experiment described in appendix A.6, the difference in zenith delay between the reference station on the ground and the balloon is even larger.
In (Kleijer, 2004) a good overview of tropospheric models is provided. Section 2.5.1.1 describes the standard procedure based on the Saastamoinen model, section 2.5.1.2 describes an improved model based on the Neill mapping function. For both models also the time derivatives are obtained required for the aproiri corrections for the Doppler observations.

2.5.1.1 Tropospheric model based on Saastamoinen

In this procedure, the Zenith Tropospheric Delay (ZTD) is computed using the Saastamoinen's model (Saastamoinen, 1972) with average meteorological conditions at the user's location. These are obtained from a model of the standard atmosphere, and the saturated vapor pressure is calculated using a modified Hopfield model as described in (Goad and Goodman, 1974a). Based on the ZTD, an a priori correction is calculated for all (code and carrier) range observations (Odijk, 2002).

Dry temperature T_K, pressure ρ and relative humidity H in degrees Celsius, millibar and $[\%]$ respectively, are calculated using the following equations (Gurtner et al., 1987):

$$\begin{aligned} T_K &= T_{K,0} - 0.0065(h - h_0) \\ \rho &= \rho_0 \left(1 - 0.0000226(h - h_0)\right)^{5.225} \\ H &= H_0 e^{(-0.0006396(h-h_0))} \end{aligned} \tag{2.131}$$

where $T_{K,0}$, ρ_0 and H_0 are the meteorological values from the standard atmosphere at the reference height h_0 which is chosen as the sea level.

With the computed meteorological values the tropospheric zenith delay is computed using the Saastamoinen's model mentioned. In general, however, a GNSS signal will not arrive from the zenith direction, but from slant directions, and therefore we will make use of the Slant Tropospheric Delay (STD). In this model the range correction for troposphere to be subtracted from the observed range is given by the formula:

$$T = 0.002277 \sec(z) \left(p + (\frac{1255}{T_K} + 0.05) e_{wv} - 1.16 \tan^2(z) \right) \tag{2.132}$$

where T is the slant delay in meters, $\sec(z) = \frac{1}{\cos(z)}$ with z is zenith angle, p is the total barometric pressure and e_{wv} is the partial pressure of water vapor, both in millibars, and T_K is the absolute temperature in degrees Kelvin. The zenith angle is defined as:

$$\cos(z) = \frac{\mathbf{u}_r^s}{\mathbf{u}_r^z} \tag{2.133}$$

where $\mathbf{u}_r^s$ was given in Eq. (2.24) and $\mathbf{u}_r^z$ is the normalized vector from the receiver in the zenith direction.

The partial pressure of water vapor is computed using the equation for saturated vapor pressure from (Goad and Goodman, 1974b) and the relative humidity. The saturated vapor pressure is:

$$\rho_{sv} = 6.11 \cdot 10^{(7.5t/(t+273.3))} = e^{(7.5\ln(10)t/(t+273.3))} \cong e^{(17.27t/(t+273.3))} \tag{2.134}$$

With t is temperature in degrees Celsius. The partial pressure of water vapor is:

$$e_{wv} = H_{rel}\rho_{sv} \tag{2.135}$$

where H_{rel} is the relative humidity.

Assuming that the zenith delay changes much slower than the mapping function, the tropospheric delay rate can be expressed by the time derivative of the tropospheric delay function (i.e. the time derivative of the zenith delay is neglected):

$$\dot{T} = \frac{\partial T}{\partial z}\frac{\partial z}{\partial t} \tag{2.136}$$

where using the trigonometric functions from appendix D.3

$$\frac{\partial T}{\partial z} = 0.002277\sec(z)\tan(z)\left(p + \frac{1255}{T_K} + 0.05e_{wv} - 1.16\tan^2(z)\right) - 0.005283\sec^3(z) \tag{2.137}$$

and by applying Eq. (2.133)

$$\frac{\partial z}{\partial t} = \frac{\partial \arccos(\frac{\mathbf{u}_r^z}{\mathbf{u}_r^s})}{\partial t} = -\frac{1}{\mathbf{u}_r^s}\frac{\dot{\mathbf{u}}_r^z - \frac{\mathbf{u}_r^z}{\mathbf{u}_r^s}\dot{\mathbf{u}}_r^s}{\sqrt{1-(\frac{\mathbf{u}_r^z}{\mathbf{u}_z^s})^2}} \tag{2.138}$$

2.5.1.2 Tropospheric Model using the Neill mapping functions

Ifadis (Ifadis, 1992) and Neill (Neill, 1996) mapping functions for the troposphere can improve the Saastamoinen's model. In this section a tropospheric model is described based on the literature research summarized in (Kleijer, 2004).

Troposphere delay models often use standard values for the temperature and pressure in different layers of the atmosphere as for example the 1976 US standard atmosphere (Stull, 1995) where h is the (geopotential) height above the mean sea level, T_K is temperature

in Kelvin and P_d is the dry air pressure :

Troposphere (0< h ≤11 km):

$$\begin{aligned} T_K &= 288.15 - 6.5h \\ P_d &= 1013.25(\frac{288.15}{T_K})^{-5.255877} \end{aligned} \tag{2.139}$$

Tropopause(11< h ≤20 km):

$$\begin{aligned} T_K &= 216.65 \\ P_d &= 226.32e^{-0.1568(h-11)} \end{aligned} \tag{2.140}$$

Stratosphere(20< $h \leq 32$ km):

$$\begin{aligned} T_K &= 216.65 + h - 20 \\ P_d &= 54.749(\frac{216.65}{T_K})^{34.16319} \end{aligned} \tag{2.141}$$

An empirical relation between partial pressure of water vapor and temperature is (Baby et al., 1988) for $T_K > T_{K,0}$:

$$e_{wv} = e^{\left(24.3702 - \frac{6162.3496}{T_K}\right)} \tag{2.142}$$

The general form of a mapping function is (Marini, 1972):

$$M(z_0) = \frac{1}{\cos(z_0) + \frac{a}{\cos(z_0) + \frac{b}{\cos(z_0) + \frac{c}{\cdots}}}} \tag{2.143}$$

with z_0 the zenith angle at the lowest layers. This angle is defined as $z_0 = 90^\circ - el$, with el is the elevation angle, and, as $\cos(z_0) = \cos(90^\circ - el) = \sin(el)$, can also be applied with by substituting $\cos(z_0)$ with $\sin(el)$.

In (Ifadis, 1992) and Neill (Neill, 1996) use the following type of mapping function:

$$M_i(z_0) = \frac{1 + \frac{a_i}{1 + \frac{b_i}{1 + \frac{c_i}{\cdots}}}}{\cos(z_0) + \frac{a_i}{\cos(z_0) + \frac{b_i}{\cos(z_0) + \frac{c_i}{\cdots}}}} = \frac{M_0}{M_e} \tag{2.144}$$

where subscript $i = h$ or w, and the coefficients a_i, b_i, and c_i are empirically determined functions of variables which will be discussed next.

In (Ifadis, 1992) a hydrostatic mapping function (*dry model*) is introduced that can be applied to observations from high to low elevation angles (till 2°). The hydrostatic mapping function M_h has the following constants:

$$
\begin{aligned}
a_h &= 0.1237 \cdot 10^{-2} + 0.1316\ 10^{-6}(P_0 - 1000) + 0.8057 \cdot 10^{-5}\sqrt{e_0} + 0.1378 \cdot 10^{-5}(T_0 - 15) \\
b_h &= 0.333 \cdot 10^{-2} + 0.1946\ 10^{-6}(P_0 - 1000) + 0.1747 \cdot 10^{-6}\sqrt{e_0} + 0.1040 \cdot 10^{-6}(T_0 - 15) \\
c_h &= 0.078
\end{aligned}
\tag{2.145}
$$

where e_0 is the partial pressure of water vapor at reference height h_0. This mapping function N_w can be used in combination with non-hydrostatic mapping function (*wet model*) with the following constants (Mendes, 1999):

$$
\begin{aligned}
a_w &= 0.5236 \cdot 10^{-3} + 0.2471 \cdot 10^{-6}(P_0 - 1000) + 0.1328 \cdot 10^{-4}\sqrt{e_0} - 0.1724 \cdot 10^{-6}(T_0 - 15) \\
b_w &= 0.1705 \cdot 10^{-2} + 0.7384 \cdot 10^{-6}(P_0 - 1000) + 0.2147 \cdot 10^{-4}\sqrt{e_0} + 0.3767 \cdot 10^{-6}(T_0 - 15) \\
c_w &= 0.05917
\end{aligned}
\tag{2.146}
$$

The model then contains a hydrostatic and wet part, thus the total slant delay becomes:

$$T_{total} = M_h D_h + M_w D_w \tag{2.147}$$

where (Kleijer, 2004)

$$D_h = 0.002277 \frac{P_0}{1 - 0.002266\cos(2\phi) - 0.00000028h} \tag{2.148}$$

where P_0 is in [mbar], ϕ is the latitude in [Rad], h is the height above mean sea level (msl) in [km] and D_h is in [m].

$$D_w = 0.002277 \left(P_0 + (\frac{1255}{T_{K,0}} + 0.05)e_0 \right) \tag{2.149}$$

where e_0 is in [mbar], $T_{K,0}$ is in [K], and D_w is in [m].

Assuming that the zenith delay changes much slower than the mapping function, the tropospheric delay rate can be expressed by the time derivatives of the mapping function (Simsky and Boon, 2003):

$$\dot{T}_{total} = \dot{M}_h D_h + \dot{M}_w D_w \tag{2.150}$$

$$\dot{M}_i = \frac{\partial M_i(z_0)}{\partial z_0} \frac{\partial z_0}{\partial t} \tag{2.151}$$

with $\frac{\partial z_0}{\partial t}$ as defined in Eq.(2.138) and

$$\frac{\partial M_i(z_0)}{\partial z_0} = \frac{M_0 \sin(z_o)}{M_e^2} \left(1 - \left(\frac{a_i}{(\cos(z_0) + \frac{b_i}{\cos(z_0)+c_i})^2}\right)\left(1 - \frac{b_i}{(\cos(z_0)+c_i)^2}\right)\right) \tag{2.152}$$

2.5.2 Ionospheric model

2.5.2.1 Background

The ionosphere, extending from a height of about 50 km to 1000 km above the earth, is a region with free electrons and ions. The ionization is caused by the sun's activity and therefore there are daily and yearly variations in the state of the ionosphere, and even longer periodic variations due to the 11th year solar cycle (Misra and Enge, 2001).
For terrestrial applications with baseline lengths of less than ten kilometers, relative positioning without ionospheric corrections and/or estimation of the ionospheric delays is known to work well (Tiberius et al., 1997). For applications with longer baselines often a network of reference stations is utilized to estimate the (relative) ionospheric delays between the permanent stations (Odijk, 2001). Obviously such a reference network is not available for space applications and therefore a different approach is necessary as the ionospheric delays are not negligible for longer baselines, especially for LEO orbits. Like the tropospheric models, which were introduced in the previous section, an a-priori model as the Klobuchar model (Klobuchar, 1987) for ionospheric delay can be applied, but these kind of models normally do not have enough accuracy for precise formation flying in real-time.
Instead, we can make use of a so-called ionosphere-weighted model as described in (Odijk, 2001), which is believed to be more flexible than physical models as for each satellite and observation epoch an ionospheric delay parameter is estimated. This model is called ionosphere-weighted model as it makes use of the ionospheric corrections as a pseudo observation and these are treated stochastically: i.e. their uncertainly in the stochastic model is propagated with a proper variance-covariance matrix.
The two extreme values for the variance factor of the ionospheric pseudo-observables are *zero* and *infinity*. For the ionosphere-weighted model we refer to these models respectively as:

1. the ionosphere-fixed model ($\sigma = 0$)
2. the ionosphere-float model ($\sigma = \infty$)

The general model is referred to as the ionosphere-weighted model. We first will discuss the two extremes before we will discuss the general model in more detail.
For completeness, we like to mention that physical models to describe small-scale features in the ionospheric delays, such as Traveling Ionospheric Disturbances or *TIDs* were recently developed in (Memarzadeh, 2009).

2.5.2.2 Ionosphere-fixed Model ($\sigma = 0$)

In this model the ionospheric delays are assumed to be known beforehand, hence they are treated as deterministic quantities instead of stochastic variables. There are two variants for this model: in the first the assumption is that the ionospheric information available is exact, in the second the distance between the GNSS receivers is so short that the assumption can be made that the ionospheric delays are exactly the same for both receivers and hence cancel out.

2.5.2.3 Ionosphere-float Model ($\sigma = \infty$)

In the ionosphere-float model, the unknown DD ionospheric delays are estimated simultaneously with the baseline vectors and DD ambiguities. This kind of model is closely related to the widely used ionospheric-free combinations of dual frequency observations, where the linear combination eliminates the unknown first-order ionospheric delays. The ionosphere-float model, explicitly determines the DD ionospheric delays.

2.5.2.4 Ionosphere-weighted Model (0$< \sigma < \infty$)

The ionosphere-weighted model make uses of the ionospheric corrections as a pseudo observation and treat them stochastically. i.e. their uncertainly in the stochastic model is propagated with a proper variance-covariance matrix. The vector of observations (UD,SD or DD) can be corrected according to

$$\begin{aligned} y_{corr} =& y + \begin{Bmatrix} -\mu \otimes I_{L_1} \\ \mu \otimes I_{L_1} \end{Bmatrix} \\ y^{SD}_{corr} =& y^{SD} + \begin{Bmatrix} -\mu \otimes I^{SD}_{L_1} \\ \mu \otimes I^{SD}_{L_1} \end{Bmatrix} \\ y^{DD}_{corr} =& y^{DD} + \begin{Bmatrix} -\mu \otimes I^{DD}_{L_1} \\ \mu \otimes I^{DD}_{L_1} \end{Bmatrix} \end{aligned} \tag{2.153}$$

where y indicates the set of code and phase observations from one (or two if SD and DD) receiver(s).

Due to the dispersiveness of the ionosphere, it is sufficient to model the ionospheric delay on the L1 frequency and relate the delays at the other frequencies to this delay with a coefficient. These coefficients are collected in the vector μ:

$$\mu = [\mu_1, \ldots, \mu_f]^T \tag{2.154}$$

where $\mu_f = \frac{\lambda_f^2}{\lambda_1^2}$ is the coefficient for the ionospheric delays. As an example the ionospheric coefficient vector for modernized GPS becomes:

$$\mu = [\mu_{L_1}, \mu_{L_2}, \mu_{L_5}]^T = [1, \left(\frac{77}{60}\right)^2, \left(\frac{154}{115}\right)^2]^T \tag{2.155}$$

I_{L_1}, $I_{L_1}^{SD}$ and $I_{L_1}^{DD}$ indicate the vector (of dimension $n+1$ for UD and SD, or n for DD respectively) of ionospheric corrections on the L_1 frequency with respect to the given satellite(s)-receiver(s) geometry. When applying these corrections, a proper weight function must be used in the stochastic model (see section 2.6).

If the vector of observations (UD,SD or DD) also contains Doppler observations it can be corrected, both for the ionosphere-float and -weighted model, according to

$$\begin{aligned} \upsilon_{corr} &= \upsilon + \begin{Bmatrix} \mu \otimes I_{L_1} \\ -\mu \otimes I_{L_1} \\ -\mu \otimes \dot{I}_{L_1} \end{Bmatrix} \\ \upsilon_{corr}^{SD} &= \upsilon^{SD} + \begin{Bmatrix} \mu \otimes I_{L_1}^{SD} \\ -\mu \otimes I_{L_1}^{SD} \\ -\mu \otimes \dot{I}_{L_1}^{SD} \end{Bmatrix} \\ \upsilon_{corr}^{DD} &= \upsilon^{DD} + \begin{Bmatrix} \mu \otimes I_{L_1}^{DD} \\ -\mu \otimes I_{L_1}^{DD} \\ -\mu \otimes \dot{I}_{L_1}^{DD} \end{Bmatrix} \end{aligned} \tag{2.156}$$

Ionospheric Model using Klobuchar The GPS system provides ionospheric corrections to the single frequency user through its navigation messages. This model has in general an accuracy of around 50 % (Misra and Enge, 2001) for terrestrial users. For terrestrial users at mid-latitudes, the model error in zenith delay can be up to 10 m during the day, and much more during periods with high solar activity. As this model does not take the altitude of the user into account, the applicability to users at different height (aircraft, high altitude platforms and especially spacecraft) is questionable: for spacecraft the ionospheric delay itself would be different, for aviation applications the elevation angles to the GNSS satellites are dissimilar from the elevation for the terrestrial user.

Ionospheric Model for Space Applications Even though the differential ionospheric effects are commonly considered to be small for formations with short baselines, they may still produce effects when dealing with high accuracy carrier phase measurements (Montenbruck et al., 2011). To account at least partly for such effects, DLR makes use of a simplified ionospheric path delay model, which describes the differential path delay based on (Lear, 1987). This Lear mapping function has been specifically designed for spaceborne applications and takes into account that the ionospheric electron density maximum is at or below the orbital altitude of common LEO spacecraft. So instead of estimating a differential delay for each GPS satellite, a single vertical delay I_0 is estimated in the relative navigation process. The work on ionospheric path delay models for spaceborne GPS receivers flying in formation with large baselines is recently extended in (Tancredi et al., 2011).

2.5.3 Redundancy of the models

For any model, where y is an $m \times 1$ vector and x is an $w \times 1$ vector,

$$y = Ax \tag{2.157}$$

the redundancy of this system of equations is defined as $m - rank(A)$. For the system with $m - rank(A) < w$ there is not a unique solution. The system with $m - rank(A) = w$ is consistent having a unique solution. For a system with $m - rank(A) > w$ we have an overdetermined system that we solve using the least squares principle. The discussion below is based on the assumption that A has full column rank, thus $rank(A) = w$ and therefore the redundancy of the model becomes the number of observations minus the number of parameters of the model $(m - w)$.

In this section, we will evaluate the above defined redundancy as function of the number of baselines N_b, the number of DD code and carrier observations $2n$ (thus $(n+1)$ is the number of tracked GNSS satellites), the number of frequencies N_f, the number of observation epochs N_e and the selected number of estimated parameters w in the model (Odijk, 2002). This w consists of the three components of the baseline vector, plus one parameter if the Zenith Tropospheric Delay (ZTD) is estimated (e.g. longer baseline(s) in terrestrial applications).
Note that for dynamic applications a baseline vector is estimated for every observation epoch, while it is not necessary to estimate the ZTD for every observation epoch as typically one time per hour should suffice (Odijk, 2002). The assumption is made in this discussion that all receivers track the same GNSS satellites and both code and carrier observations are available. For our geometry-based model, we need at least 3 DD observations of both code and carrier -thus from 4 GNSS satellites- to have a unique solution, therefore $(n + 1 \geq 4)$.

2.5.3.1 Ionosphere-fixed model

General Multi-baseline Model In the ionosphere-fixed model, the number of observations is $2nN_bN_fN_e$, and the number of unknowns $wN_bN_e + nN_bN_f$ where the second term nN_bN_f is related to the number of DD integer ambiguities, thus the redundancy is

$$N_b\,[N_f(2N_e - 1)n - wN_e] = N_bN_f(2N_e - 1)n - wN_bN_e \tag{2.158}$$

For the static application, the wN_bN_e part of the number of unknowns is reduced to wN_b as the baseline vector(s) will not vary. Then the redundancy of the model is reduced to the function given in (Odijk, 2002):

$$N_b\,[N_f(2N_e - 1)n - w] = N_bN_f(2N_e - 1)n - wN_b \tag{2.159}$$

Important general conclusion for the multi-baseline model is that the minimum number of required GNSS satellites is independent of the number of baselines applied in the model if all antennas collect data at the same number of frequencies.
The redundancy for the ionosphere-fixed model using single epoch $(N_e = 1)$ observations and $w = 3$ is:

$$N_b(N_fn - 3) \tag{2.160}$$

This redundancy as function of the number of baselines is shown in Fig. 2.10(a) and 2.11(a) for 5 and 8 GNSS satellites respectively. For single $(N_f = 1)$ and dual $(N_f = 2)$

frequency this function is shown in the first two rows ($N = 1, 2$) of Table 2.3. Hence every additional frequency will improve the redundancy with $N_b n$.
From the redundancy function, we can conclude that the number of satellites required to solve the problem using a single epoch, single frequency observations, is 5 if the ZTD is estimated, and 4 if not. This is shown in Table 2.3 for the instantaneous ($N_e = 1$) single ($N_f = 1$) and dual ($N_f = 2$) frequency case where $w = 3$: i.e. containing only the baseline vector.
For the ionosphere-fixed model, observations from a single frequency are enough to solve the model instantaneously. If observations from two frequencies are available at all the receivers, we can solve the problem instantaneously with observations from only four satellites (see also Table 2.3), both with and without estimating ZTD, again independently of the number of baselines in the model.

From the discussion above we conclude that for the ionosphere-fixed, multi-baseline model - if all receivers collect data at the same frequencies - the minimum number of required GNSS satellites is the same as the single baseline model, however the redundancy is improved compared to the single baseline model.

Two Platform Multi-baseline Model If not all the receivers of the model collect multi-frequency observations but only the receivers forming the baseline between the platforms - implying the assumption that the ionospheric delays for all antennas for the same platform can be considered the same - the number of observations $2nN_bN_fN_e$ is reduced to $2nN_fN_e + 2n(N_b - 1)N_e$, the number of unknown ambiguities is reduced from nN_bN_f to $nN_f + n(N_b - 1)$, and the redundancy becomes:

$$(N_b + N_f - 1)(2N_e - 1)n - wN_bN_e \tag{2.161}$$

From this equation -included on the third row ($N = 3$) of Table 2.3-, we can observe directly that, for the in-between single frequency baseline, the number of GNSS satellites required is independent of the number of baselines. Also for a configuration of any number of baselines, where only the two receivers of the in-between baselines are double frequency, we still require at least observations from four GNSS satellites to have a unique solution.
The redundancy for the ionosphere-fixed model as function of the number of baselines is shown in Fig. 2.10(b) and 2.11(b) for 5 and 8 GNSS satellites respectively using $w = 3$ and $N_e = 1$. For a single frequency in-between baseline, the redundancy is the same as Eq. (2.158), for a multi-frequency in-between baseline the redundancy is always reduced compared to the general multi-baseline model described in section 2.5.3.1.

2.5.3.2 Ionosphere float model

General Multi-baseline Model In the ionosphere float model the number of observations is of course again $2nN_bN_fN_e$, but now the number of unknowns is increased to $wN_bN_e + nN_bN_f + nN_bN_e$ where the second term nN_bN_f is related to the number of DD integer ambiguities and the third term nN_bN_e to the DD ionospheric delays. Thus the redundancy

function of this model becomes

$$N_b\left[\left[N_f(2N_e-1)-N_e\right]n-wN_e\right]=N_b\left[N_f(2N_e-1)-N_e\right]n-wN_bN_e \tag{2.162}$$

Compared with Eq. (2.158), we observe that for the ionosphere float model always the redundancy is reduced with N_bnN_e compared to the ionosphere fixed model. This is of course as expected as the number of observations remains the same while the number of unknowns is increased with N_bnN_e.

For the static application, the redundancy of the model is again reduced to the function given in (Odijk, 2002) for the ionosphere float model:

$$N_b\left[\left[N_f(2N_e-1)-N_e\right]n-w\right]=N_b\left[N_f(2N_e-1)-N_e\right]n-wN_b \tag{2.163}$$

For the ionosphere-float model, observations from at least two frequencies are necessary since no a priori information on the ionospheric delays are applied. This is shown in the fifth row ($N=5$) of Table 2.3 as n/a for the single frequency case. With dual frequency observations, at least 4 GNSS satellites are required to solve the system of equations.
The redundancy for the ionosphere-float model as function of the number of baselines is shown in fifth and sixth row ($N=5,6$) of Table 2.3 for the single ($N_f=1$) and dual frequency ($N_f=2$) case. This redundancy as function of the number of baselines is also shown in Fig. 2.10(a) and 2.11(a) for 5 and 8 GNSS satellites respectively using again $w=3$ and $N_e=1$. From the table and figures, we observe that the dual frequency ionosphere float model has the same redundancy as the single frequency ionosphere fixed model. This is as expected, as in Eq. (2.162), we observed that for the ionosphere float model always the redundancy is reduced with nN_e compared to the ionosphere fixed model. Therefore Eq. (2.162) is reduced for $N_e=1$, $N_f=2$ and $w=3$ to the redundancy function as given in the sixth row ($N=6$) of Table 2.3.

Two Platform Multi-baseline Model If again not all the receivers collect multi-frequency observations but only the two receivers forming the in-between baseline, the number of observations $2nN_bN_fN_e$ is reduced to $2nN_fN_e+2n(N_b-1)N_e$, the second or ambiguity term nN_bN_f in the unknowns is reduced to $nN_f+n(N_b-1)$ and the third or ionosphere delay term nN_bN_e is reduced to nN_e, and the redundancy becomes:

$$(N_b+N_f-1)(2N_e-1)n-nN_e-wN_bN_e \tag{2.164}$$

From this equation we can observe directly that, if the in-between baseline is single frequency, than the number of GNSS satellites required is not independent of the number of baselines (see the seventh row ($N=7$) in Table 2.3 representing the single frequency case on the in-between baseline). For a single baseline, the problem is not solvable. With two, three, or more baselines, the number of GNSS satellites required is 7, 6, and 5 respectively. This is an important result as it shows that for two platforms with at least 2 antennas (one constrained baseline) at one of the platforms, single frequency observations are sufficient to estimate the ionospheric delays as long as at least 7 GNSS satellites are tracked.
If for any configuration of baselines, only from the two receivers forming the in-between

Table 2.3: Minimum number of GNSS satellites $(n+1)$ required as function of the number of baselines N_b ($N_e = 1$, $w = 3$), antenna distribution is total number of antennas at each platform

N	Model	Multibaseline	N_f	redundancy	N_b											
					1	2	3	4	5	6	7	8	9	10	100	1000
	Ionosphere	Mode			Antenna distribution (platform 1 - platform 2)											
					(1-1)	(2-1)	(2-2)	(3-2)	(3-3)	(4-3)	(4-4)	(5-4)	(5-5)	(6-5)	(51-50)	(501-500)
1	Fixed	General	1	$N_b(n-3)$	4											
2			2	$N_b(2n-3)$	4											
3		Two platforms	1	$N_b(n-3)$	4											
4			2	$N_b(n-3)+n$	4											
5	Float	General	1	-	n/a											
6			2	$N_b(n-3)$	4											
7		Two platforms	1	$N_b(n-3)-n$	n/a	7	6	5	5	5	5	5	5	5	5	5
8			2	$N_b(n-3)$	4											

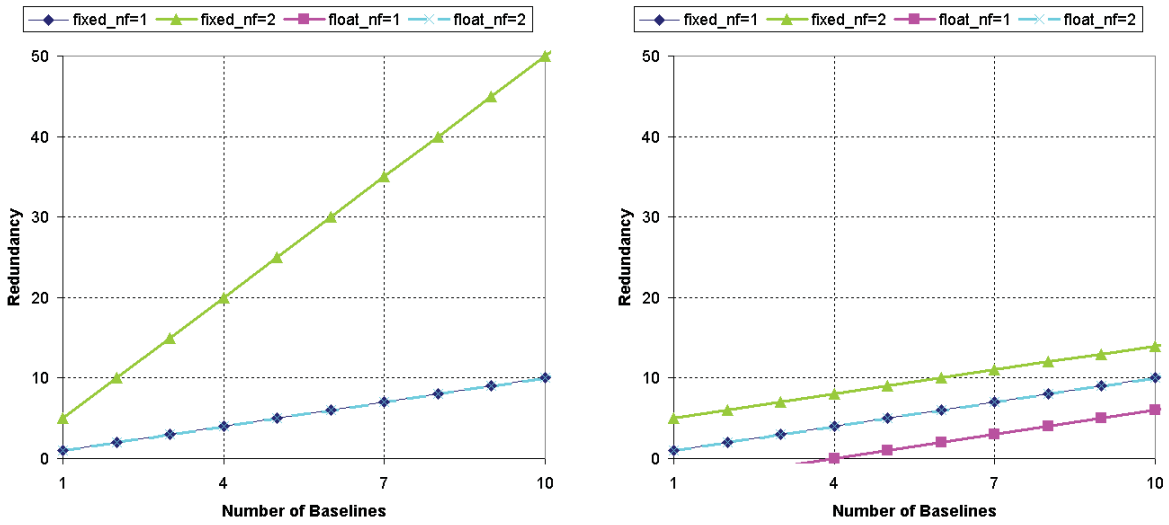
baselines dual frequency observations are available, observations from at least four GNSS satellites are required to have a unique solution.
The table also shows that, even for a large number of baselines, the single frequency multi-baseline system always requires at least one more observation compared to a system with dual frequency observations for the in-between baseline (5 vs. 4 for $N_b \geq 4$).
The redundancy of the system is shown in Fig. 2.10(b) and 2.11(b) as function of the number of baselines for $w = 3$ and $N_e = 1$.

2.5.3.3 Conclusion

It is concluded that for the ionosphere-fixed model, where the in-between baseline is multi-frequency, the multi-baseline model is stronger than the single baseline model: it has an improved redundancy. However, the required number of GNSS satellites for a solution is not reduced.
For the ionosphere-float model where the in-between baseline is multi-frequency, the multi-baseline model is stronger than the single baseline model: it has an improved redundancy. For a single frequency in-between baseline, the system can be solved if there is at least one platform with two antennas and sufficient observations. With the traditional set-up with one antenna at each platform, the system cannot be solved if only observations at a single frequency are available.

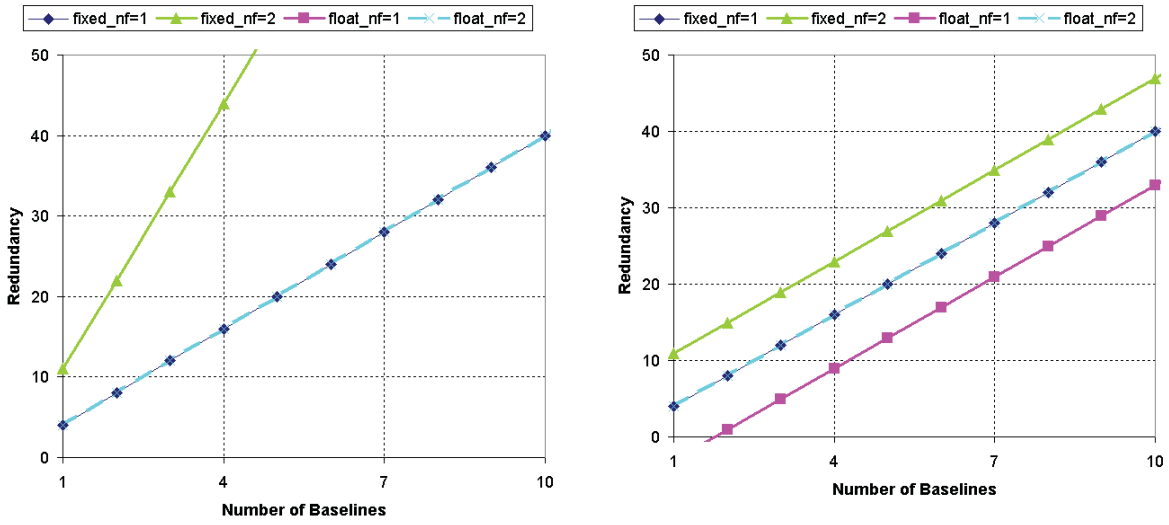
2.6 Stochastic Properties of GNSS

In estimation, beside the functional model as described in section 2.4, the stochastic model is of great importance as GNSS observations are realisations of stochastic variables and therefore the random and non-random errors cannot be modeled in a functional model. This stochastic model describes the statistical properties of the observables in the form of variance-covariance matrices. In this section, we will develop a stochastic model by starting with a literature review on noise values found for the space applications in section 2.6.1. In section 2.6.2, this followed by a theoretical discussion on noise values for the legacy and modernized GNSS signals which were described in section 2.1. In section 2.6.3,



(a) General Multi-baseline Model (b) Two platform Multi-baseline Model

Figure 2.10: Redundancy as function of number of baselines for $(n+1=5)$, single epoch $(N_e=1)$



(a) General Multi-baseline Model (b) Two platform Multi-baseline Model

Figure 2.11: Redundancy as function of number of baselines for $(n+1=8)$, single epoch $(N_e=1)$

the stochastic model is derived, in section 2.6.4 receiver noise and especially correlation between observation is assessed, and finally in section 2.6.5 general weighing schemes for the observations are introduced.

2.6.1 Space GNSS Receivers: Literature Study

Signal noise values for space qualified receivers on space missions, as reported in literature, will be briefly discussed in this section. One difficulty is that relevant laboratory test data or in-flight performance data have often not been publicly released (Montenbruck et al., 2006). GNSS receivers developed for space applications and known to have been utilized as mission critical equipment are the Viceroy and Monarch developed by General Dynamics (General Dynamics C4, 2005b)(General Dynamics C4, 2005a) and the Blackjack/IGOR receiver from JPL in the United States of America. In Japan there is a receiver series used on, among others, the ADEOS and ALOS mission (Kumagai et al., 2001). In Europe there is the SGR-series from Surrey Satellite Technology and the Phoenix receiver from DLR.
For the Blackjack receiver on the GRACE mission, a L1 code noise of 0.2 meter and 2-3 millimeter for carrier phase was reported (Kroes, 2006). More recently, JPL has licensed core technology to Broadreach Engineering, which now manufactures the IGOR receiver as a BlackJack follow-on version with improved space hardness. For this receiver on the TerraSAR-X satellite, noise values are not yet reported but on the same satellite there is a second receiver called MosiacGNSS on its maiden flight (Krauss et al., 2008). For this receiver, developed by EADS in Germany, the reported noise values for L1 code is 4-5 meter and 2-3 millimeter for carrier phase (Montenbruck et al., 2008). This receiver experienced interference, interestingly enough from the IGOR receiver (Montenbruck et al., 2008). European manufacturers experience difficulties to acquire electronic parts with the required radiation tolerance because of the International Traffic in Arms Regulations (ITAR) of the United States of America. With no radiation hardened hardware correlators for space applications available at the European market, the MosiacGNSS design is based on software correlation using a DSP board (Krauss et al., 2008).
The Surrey receiver is designed using a different approach based on the use of commercial parts. The testing of the core components under radiation demonstrated the suitability of the technology for spaceborne applications while maintaining the low cost approach (Unwin et al., 1998). The specification sheet of the SGR-10 reports typical measurement precision of 0.9 meter for code observations and 1.5 millimeter for carrier phase (SSTL, 2010). In (Ebinuma et al., 2005), raw observation accuracy of this receiver was confirmed to be 1-2 meter for pseudorange and 2-3 millimeter for carrier phase using a GPS simulator.
The miniaturized GPS receiver SGR-05U is based on the Zarlink Semiconductor's GPS4020 chip which incooperates a 12-channels correlator module for GPS L1C/A code and carrier tracking and a 32-bit AMR7TDMI processor onto the same chip (Ebinuma et al., 2004). The Phoenix receiver from DLR is based on the same chip (Montenbruck et al., 2004).
The mentioned Japanese receiver has specifications of 3.3 meter for L1 code and 3.3 millimeter for carrier (Buist et al., 2004), but these values are not noise values in nominal conditions. Instead they are based on the practice in space mission design to include large safety margins on the specifications as the GPS receiver is critical equipment for the success of the mission.
The relative large difference in code noise compared with the static, surveying environment

as will be discussed in the next section, should be explained by the fact that a legitimate space receiver is using space qualified components, which by definition have lower specifications than terrestrial components. One of the reasons for this is the time consuming process required to qualify the components for the space environment (Larson and Wertz, 1992). Furthermore these receivers typically do not use a narrow chip space and have a tracking loop design that keeps the code and carrier observations independent. Both the current versions of the Japanese and German space receivers have only eight channels and therefore a limited number of observations.
Next, we will discuss how these reported noise values compare with theoretically lower bounds for the legacy and modernized GPS and Galileo signals.

2.6.2 Space GNSS Receivers: Analysis of thermal noise

The following discussion on nominal noise values for code and carrier is based on the theoretical lower bounds given by the formulas from (Sleewaegen and De Wilde, 2004) with parameters from (Tiberius et al., 2009). For code tracking noise, the standard deviation for either BPSK and BOC modulations, can be expressed in meters as:

$$\sigma_{P_f} = \frac{cT_c}{\alpha}\sqrt{\frac{1-R(d)}{2C/N_0}B_p} \tag{2.165}$$

The carrier tracking noise can be expressed in meters, keeping in mind that the BOC signals will not improve the carrier noise, as:

$$\sigma_{\phi_f} = \frac{\lambda_f}{2\pi}\sqrt{\frac{B_\phi}{C/N_0}} \tag{2.166}$$

where d is the early-late chip spacing, $R(d)$ is the correlation peak evaluated at a delay of d, α is the slope of the correlation peak evaluated at $\tau = \frac{-d}{2}$ (thus α is 1 for BSPK, 3 for BOC(1,1) and 9 for the AltBOC with 70 MHz bandwidth (Sleewaegen and De Wilde, 2004)), B_p is the DLL loop bandwidth in Hz, C/N_0 is the carrier-to-noise density ratio, c is the speed of light, T_c is the chip duration, B_ϕ is the PLL loop bandwidth in Hz and λ_f is the carrier wavelength at frequency f. In these expressions the squaring loss has been neglected.

In our calculation we will apply a conservative nominal received signal level of $C/N_0 = 45$ dB-Hz but from Table 2.2, it is clear that both Galileo E1BC and GPS L1C have a signal that is 1.5 dB stronger than legacy GPS and therefore their expected performance will be better than reported here. Two applications are included in Table 2.4: the first is the static application in which the high-end receivers are placed in static, surveying type of environment with surveying-grade antennas, limited multipath and nominal values for received signal strength. In these circumstances the receiver noise approaches the theoretical lower bounds (Tiberius et al., 2009). The second case is the dynamic environment onboard a spacecraft in which we make use of a space receiver with significantly higher noise values, (sometimes) lower received signal strength depending on altitude and orientation of the

Table 2.4: Noise Characteristics

GNSS	Signal	Static / surveying		Dynamic / space	
		σ_ϕ [m]	σ_p [m]	σ_ϕ [m]	σ_p [m]
GPS	L1C/A	$5.4 \cdot 10^{-4}$	0.18	$3.0 \cdot 10^{-3}$	0.90
	L1C	$5.4 \cdot 10^{-4}$	0.11	$3.0 \cdot 10^{-3}$	0.55
	L2C	$6.9 \cdot 10^{-4}$	0.18	$3.9 \cdot 10^{-3}$	0.90
	L5	$7.2 \cdot 10^{-4}$	0.06	$4.0 \cdot 10^{-3}$	0.28
Galileo	E1 (E1BC)	$5.4 \cdot 10^{-4}$	0.11	$3.0 \cdot 10^{-3}$	0.55
	E5 (AltBOC)	$7.2 \cdot 10^{-4}$	$0.04 \cdot 10^{-1}$	$4.0 \cdot 10^{-3}$	0.02

spacecraft, (most of the times) a patch antenna directly mounted on the surface of the spacecraft, interference from other electronic equipment on the spacecraft and inherently significant code and carrier multipath from the local metal objects near the antenna.
For the legacy GPS L1C/A and modernized L2C signal, we observe that the lower bound at 45 dB-Hz for the code noise is 0.18 meter and for the carrier noise around 0.5 and 0.7 millimeter respectively. For modernized GPS L1C and Galileo E1BC, we see that accuracy of the code noise is improved to 0.11 meter and the carrier is not improved as is expected keeping in mind that BOC signals do not improve carrier noise. For the GPS L5 signal, the code noise at this signal is 0.06 meter, mainly due to the 10 times higher chiprate compared to L1C/A (see Table 2.2). The carrier noise expressed in meters is higher than L1C/A because of the longer wavelength. For the AltBOC signal on E5, we observe a sub-centimeter level for code. These values are shown in Table 2.4 as the typical values for the static surveying type of application.
Based on the literature research in section 2.6.1, we assume that for a space GPS receiver a typical code noise value is 0.9 meter and carrier noise is 3 millimeter. For the improvement with modernized GPS and Galileo signals, we assume that this is proportional to the improvement as we observed for the surveying application and thus we come to a value of 0.55 meter for L1C and E1BC code, 0.28 meter for L5, 0.02 meter for the AltBOC on E5 and again no improvement for carrier phase. These values are shown in Table 2.4 as the typical values for the space application in the dynamic environment of a spacecraft. We will use these noise values in sections 3.5, 4.4 and 5.4 to discuss our simulation results.

2.6.3 Stochastic Model

It is common practice in GNSS applications to assume that the observations are *normally distributed* (Borre and Tiberius, 1999). The normal distribution is often also referred to as Gaussian distribution. The symmetric $2(n+1)N_f \times 2(n+1)N_f$ variance-covariance matrix of observations from a single receiver is:

$$Q_{yy,r} = \begin{bmatrix} Q_{P^s_{r,f}P^s_{r,f}} & Q_{P^s_{r,f}\Phi^s_{r,f}} \\ Q_{\Phi^s_{r,f}P^s_{r,f}} & Q_{\Phi^s_{r,f}\Phi^s_{r,f}} \end{bmatrix} \tag{2.167}$$

The vc-matrices $Q_{P^s_{r,f}P^s_{r,f}}$ and $Q_{\Phi^s_{r,f}\Phi^s_{r,f}}$ on the diagonal are related to the code and phase observables, the off-diagonal matrix $Q_{P_r\Phi_r}$ contains the correlation term between the code

and phase observations.
Cross-correlation between different types of observations can be present, especially between code or carrier phase observations from different frequencies: notable correlation between L1 and L2 observations are known to be present in legacy GPS receivers. The reason for this is aiding of the tracking loop for L2P(Y) with L1C/A rate-change for code and carrier (Braasch and Van Dierendonck, 2002). Correlation between code and phase is practically absent (Bona, 2000).
Time-correlation is also known to be present in GNSS observation, especially for code observations, due to internal smoothing to reduce thermal noise, multipath mitigation and multipath itself. Time-correlation on 1 Hz data or larger sampling rates might be significant for certain GNSS receivers (Bona, 2000)(Bona and Tiberius, 2000).
In this study the main focus is on instantaneous applications, for which time-correlation is not relevant as processing is performed using observations from a single epoch.

As described in section 2.4, we will make use of an observation vector containing pseudo range, carrier phase and Doppler observations which we will call υ. Dispersion of this observation vector is:

$$Q_{\upsilon\upsilon,r} = \begin{bmatrix} Q_{P^s_{r,f}P^s_{r,f}} & Q_{P^s_{r,f}\Phi^s_{r,f}} & Q_{P^s_{r,f}D^s_{r,f}} \\ Q_{\Phi^s_{r,f}P^s_{r,f}} & Q_{\Phi^s_{r,f}\Phi^s_{r,f}} & Q_{\Phi^s_{r,f}D^s_{r,f}} \\ Q_{D^s_{r,f}P^s_{r,f}} & Q_{D^s_{r,f}\Phi^s_{r,f}} & Q_{D^s_{r,f}D^s_{r,f}} \end{bmatrix} \tag{2.168}$$

If the correlation between Doppler and both the code and carrier phase observations is maintained, the vc-matrices become:

New UD Model

$$\begin{aligned} Q_{\upsilon\upsilon,r} &= \begin{bmatrix} Q_{P^s_{r,f}P^s_{r,f}} & \mathbf{0} & Q_{P^s_{r,f}D^s_{r,f}} \\ \mathbf{0} & Q_{\Phi^s_{r,f}\Phi^s_{r,f}} & Q_{\Phi^s_{r,f}D^s_{r,f}} \\ Q_{D^s_{r,f}P^s_{r,f}} & Q_{D^s_{r,f}\Phi^s_{r,f}} & Q_{D^s_{r,f}D^s_{r,f}} \end{bmatrix} \\ &= \begin{bmatrix} \sigma^2_{P^s_{r,f}} I_{(n+1)N_f\times(n+1)N_f} & \mathbf{0} & \rho_{P^s_{r,f}D^s_{r,f}}\sigma_{P^s_{r,f}}\sigma_{D^s_{r,f}} I_{(n+1)N_f\times(n+1)N_f} \\ & \sigma^2_{\Phi^s_{r,f}} I_{(n+1)N_f\times(n+1)N_f} & \rho_{\Phi^s_{r,f}D^s_{r,f}}\sigma_{\Phi^s_{r,f}}\sigma_{D^s_{r,f}} I_{(n+1)N_f\times(n+1)N_f} \\ & & \sigma^2_{D^s_{r,f}} I_{(n+1)N_f\times(n+1)N_f} \end{bmatrix} \end{aligned} \tag{2.169}$$

where ρ is a correlation coefficient and σ is standard deviation.

Assuming no correlation between code and carrier phase observations, the vc-matrices become:

Standard UD Model

$$Q_{yy,r} = \begin{bmatrix} Q_{P^s_{r,f}P^s_{r,f}} & \mathbf{0} \\ \mathbf{0} & Q_{\Phi^s_{r,f}\Phi^s_{r,f}} \end{bmatrix} \tag{2.170}$$

The vc-matrix associated to the vector of observations from two receivers $y = \begin{pmatrix} y_1 \\ y_r \end{pmatrix}$ is written as

$$Q_{yy,1r} = \begin{bmatrix} Q_{yy,1} & Q_{yy,1r} \\ Q_{yy,1r} & Q_{yy,r} \end{bmatrix} \tag{2.171}$$

where $Q_{yy,1r}$ is the covariance matrix between the two receivers. Under the assumption of no correlation between the observations from the two receivers we obtain:

$$Q_{yy,1r} = \begin{bmatrix} Q_{yy,1} & \mathbf{0} \\ \mathbf{0} & Q_{yy,r} \end{bmatrix} \tag{2.172}$$

Following the same approach the vc-matrix for the observation vector including Doppler, again under the assumption of no correlation between the two receivers, can be obtained as:

$$Q_{vv,1r} = \begin{bmatrix} Q_{vv,1} & \mathbf{0} \\ \mathbf{0} & Q_{vv,r} \end{bmatrix} \tag{2.173}$$

The vc-matrix of the SD between receivers, as explained in section 2.4.2, is derived by applying the propagation law of variances on Eq. (2.78):

$$\begin{aligned} Q^{SD}_{vv} &= H^{SD} Q_{vv,1r} (H^{SD})^T = \\ &= \begin{bmatrix} Q_{P^s_{1,f}P^s_{1,f}} + Q_{P^s_{r,f}P^s_{r,f}} & \mathbf{0} & Q_{P^s_{1,f}D^s_{1,f}} + Q_{P^s_{r,f}D^s_{r,f}} \\ \mathbf{0} & Q_{\Phi^s_{1,f}\Phi^s_{1,f}} + Q_{\Phi^s_{r,f}\Phi^s_{r,f}} & Q_{\Phi^s_{1,f}D^s_{1,f}} + Q_{\Phi^s_{r,f}D^s_{r,f}} \\ Q_{D^s_{1,f}P^s_{1,f}} + Q_{D^s_{r,f}P^s_{r,f}} & Q_{D^s_{1,f}\Phi^s_{1,f}} + Q_{D^s_{r,f}\Phi^s_{r,f}} & Q_{D^s_{1,f}D^s_{1,f}} + Q_{D^s_{r,f}D^s_{r,f}} \end{bmatrix} \end{aligned} \tag{2.174}$$

If the standard deviations are assumed equal for all the observations at both receivers, then the vc-matrix of the SD is the vc-matrix of the undiffferenced observations multiplied by 2:

New SD Model

$$\begin{aligned} Q^{SD}_{vv} &= \begin{bmatrix} 2Q_{P^s_{r,f}P^s_{r,f}} & \mathbf{0} & 2Q_{P^s_{r,f}D^s_{r,f}} \\ \mathbf{0} & 2Q_{\Phi^s_{r,f}\Phi^s_{r,f}} & 2Q_{\Phi^s_{r,f}D^s_{r,f}} \\ 2Q_{D^s_{r,f}P^s_{r,f}} & 2Q_{D^s_{r,f}\Phi^s_{r,f}} & 2Q_{D^s_{r,f}D^s_{r,f}} \end{bmatrix} \\ &= \begin{bmatrix} 2\sigma^2_{P^s_{r,f}} I_{(n+1)N_f \times (n+1)N_f} & \mathbf{0} & 2\rho_{P^s_{r,f}D^s_{r,f}} \sigma_{P^s_{r,f}} \sigma_{D^s_{r,f}} I_{(n+1)N_f \times (n+1)N_f} \\ & 2\sigma^2_{\Phi^s_{r,f}} I_{(n+1)N_f \times (n+1)N_f} & 2\rho_{\Phi^s_{r,f}D^s_{r,f}} \sigma_{\Phi^s_{r,f}} \sigma_{D^s_{r,f}} I_{(n+1)N_f \times (n+1)N_f} \\ & & 2\sigma^2_{D^s_{r,f}} I_{(n+1)N_f \times (n+1)N_f} \end{bmatrix} \end{aligned} \tag{2.175}$$

Hence the differencing operator increases the measurement noise with the factor $\sqrt{2}$ compared to the original observation.
For the vc-matrix of the SD y observations we obtain:

Standard SD Model

$$Q_{yy}^{SD} = \begin{bmatrix} 2\sigma^2_{P^s_{r,f}} I_{(n+1)N_f \times (n+1)N_f} & \mathbf{0} \\ \mathbf{0} & 2\sigma^2_{\Phi^s_{r,f}} I_{(n+1)N_f \times (n+1)N_f} \end{bmatrix} \tag{2.176}$$

The vc-matrix of the double difference equations, which were derived in section 2.4.3, are obtained applying the variance propagation law:

$$Q_{vv}^{DD} = DQ_{vv}^{SD}D^T = DH^{SD}Q_{vv,r_{1r}}(H^{SD}D)^T \tag{2.177}$$

If we assume no correlation between receivers, between observations from different satellites and the same standard deviations for all the observations, the vc-matrix of the double difference observations becomes:

New DD Model

$$Q_{vv}^{DD} = \begin{bmatrix} 2\bar{D}\bar{D}^T\sigma^2_{P^s_{r,f}} & \mathbf{0} & 2\bar{D}\bar{D}^T\rho_{P^s_{r,f}D^s_{r,f}}\sigma_{P^s_{r,f}}\sigma_{D^s_{r,f}} \\ \mathbf{0} & 2\bar{D}\bar{D}^T\sigma^2_{\Phi^s_{r,f}} & 2\bar{D}\bar{D}^T\rho_{\Phi^s_{r,f}D^s_{r,f}}\sigma_{\Phi^s_{r,f}}\sigma_{D^s_{r,f}} \\ 2\bar{D}\bar{D}^T\rho_{D^s_{r,f}P^s_{r,f}}\sigma_{D^s_{r,f}}\sigma_{P^s_{r,f}} & 2\bar{D}\bar{D}^T\rho_{D^s_{r,f}\Phi^s_{r,f}}\sigma_{D^s_{r,f}}\sigma_{\Phi^s_{r,f}} & 2\bar{D}\bar{D}^T\sigma^2_{D^s_{r,f}} \end{bmatrix} \tag{2.178}$$

where

$$\bar{D}\bar{D}^T = \begin{bmatrix} 2 & 1 & \dots & 1 \\ 1 & 2 & & \vdots \\ \vdots & & & \vdots \\ 1 & & \ddots & 1 \\ 1 & \dots & 1 & 2 \end{bmatrix} \tag{2.179}$$

Hence the differencing between both satellites and receivers increases the measurement noise with factor 4 compared to the original observation and introduces correlation.
For the standard model, the following is obtained:

Standard DD Model

$$Q_{yy}^{DD} = \begin{bmatrix} 2\bar{D}\bar{D}^T\sigma^2_{P^s_{r,f}} & \mathbf{0} \\ \mathbf{0} & 2\bar{D}\bar{D}^T\sigma^2_{\Phi^s_{r,f}} \end{bmatrix} \tag{2.180}$$

Table 2.5: Standard deviation of DD code and carrier phase residuals

$\sigma_{P^s_{r,f}}$ [m]	0.2799	0.3058	0.3182	0.3306	0.3601	0.4167	0.4671
$\sigma_{\Phi^s_{r,f}}$ [m]	0.0038	0.0036	0.0030	0.0028	0.0031	0.0031	0.0027

Table 2.6: Standard deviation of DD Doppler residuals and the correlation with code and carrier phase

$\sigma_{D^s_{r,f}}$ [m/s]	0.0371	0.0343	0.0371	0.0397	0.0460	0.0506	0.0514
$\rho_{D^s_{r,f}P^s_{r,f}}$	-0.02	-0.01	0.00	0.01	0.00	-0.01	0.02
$\rho_{D^s_{r,f}\Phi^s_{r,f}}$	0.76	0.70	0.69	0.70	0.62	0.54	0.56

2.6.4 Assessment of receiver noise and correlation

As a last step we will show noise characteristics of a surveying type of receiver. The main purpose is to demonstrate the expected correlation between Doppler and carrier phase observations. For a static setup of two Trimble receivers (one R7 and one SSA both connected to a Geodectic W groundplane), the fixed ambiguity vector and baseline are subtracted from the observation vector. The data was collected at a favorable location with clear sky.
The results are shown in Table 2.5 for eight channels of the receivers. The DD code noise varies between 0.5 and 0.3 [m], and DD carrier phase noise is around 3 [mm].
In Table 2.4, the undifferenced code and carrier phase noise was given as 0.18 and $5.4 \cdot 10^{-4}$ [m] respectively. Following the propagation described in Eq. (2.177), a DD code and carrier phase noise of 0.36 and $1 \cdot 10^{-4}$ [m] is expected.
Table 2.6 shows the standard deviation of the DD Doppler observations and the correlation coefficients $\rho_{D^s_{r,f}\Phi^s_{r,f}}$ and $\rho_{D^s_{r,f}P^s_{r,f}}$. It is clear that the code and Doppler observations are uncorrelated but the carrier phase and Doppler are highly correlated. By comparing Eq. (2.169), Eq. (2.175) and Eq. (2.178), it is observed that the correlation coefficient for UD, SD and DD observations are the same and therefore the same values can be applied in the UD and DD models applied in chapter 3.

2.6.5 Weighting schemes

Since the GNSS signals arriving at the receiver from satellites at lower elevation angles are -in general- weaker than signals from satellites at higher elevation, traveled a longer path through the atmosphere before arriving at the antenna and are more likely to be affected by multipath, a weighting scheme in the stochastic model could be implemented to take these effects into account. Examples of such models are the elevation-dependent model (Euler and Goad, 1991) or a C/N_0-dependent model (Liu, 2002). The C/N_0 dependency is rather obvious as Eqs. (2.165) and (2.166) showed the direct relationship between the accuracy of the observation and its carrier-to-noise density ratio.

Assuming an elevation dependent noise characteristics (Euler and Goad, 1991), the standard

deviations of the observations can be written as

$$\sigma_{\phi^s_{r,f}(t)} = \sigma_r \sigma_f \sigma_{\phi 0} \nu^i \tag{2.181}$$

$$\sigma_{p^s_{r,f}(t)} = \sigma_r \sigma_f \sigma_{p0} \nu^i \tag{2.182}$$

$$\sigma_{D^s_{r,f}(t)} = \sigma_r \sigma_f \sigma_{D0} \nu^i \tag{2.183}$$

$$\nu^s(t) = \left(1 + a_0 \exp\left(\frac{-\gamma^s(t)}{\gamma_0}\right)\right) \tag{2.184}$$

where $\gamma^s(t)$ is the elevation angle of the sth satellite, a_0 and γ_0 are elevation dependent model parameters, σ_r and σ_f are the receiver and frequency dependent weightings, respectively, and $\sigma_{\phi 0}$, σ_{p0} and σ_{D0} are observation dependent weightings. For completeness, it is mentioned that the elevation dependence could be different for the code, carrier phase and Doppler observations.
In this research, we will apply elevation independent models, as for correct elevation weighting the attitude of the platforms has to be taking into account.

2.7 Concluding remarks

In this chapter, functional and stochastic models for GNSS observations were derived. In the next three chapters, these models will be applied in absolute and relative positioning, attitude determination and integrated positioning and attitude determination, respectively. These models are different from what is commonly applied in GNSS based relative positioning: they include Doppler observations and take into account large receiver clock offsets and high dynamics. In this chapter it was demonstrated that the Doppler is not an independent observation and correlated with the carrier phase. For relative positioning, the usefulness of including the Doppler observations in the model is investigated in Chapter 3. For attitude determination, the baseline between receivers has most of the time a fixed length, and this length is limited. When a receiver with multiple antennas, or multiple receivers with a common clock are applied, the simplified models described in section 2.4.4 will suffice.

3 Absolute and Relative Positioning

In this chapter, algorithms are developed for absolute and relative positioning and velocity estimation using a single antenna at each platform. If the platforms have multiple antennas, GNSS could potentially be used for attitude determination of the platform(s). Traditionally the relative positioning and attitude determination problems are treated as independent. In this research, the possibility of using multi-antenna data is investigated, not only for attitude determination, but also to improve the relative positioning. In Fig. 3.1, the relationship between the topics covered in the chapters 3 to 5 is explained. Absolute and relative positioning is the topic of the current chapter. Attitude determination and attitude bootstrapped relative positioning of two platforms each equipped with $N+1$ GNSS receivers r, which are tracking common $n+1$ satellites s at N_f frequencies f will be considered in chapters 4 and 5. A dedicated (multi-variate) constrained (M)C-LAMBDA processing (Chapter 4) at each platform is performed to estimate attitude matrix ($\check{R}^j(\check{Z}^j)$) and integer ambiguity matrix ($\check{Z}^j$) using N_f frequency code ($P_{r,f}^{s,j}$), carrier phase ($\Phi_{r,f}^{s,j}$) and Doppler observations ($D_{r,f}^{s,j}$). Then, attitude bootstrapping is performed using each platform's ambiguity matrices to estimate precisely the baseline between the platforms in Chapter 5. The superscript $j = 1$ or 2 indicates the platform number, the baseline $\check{b}^{12}$ is between platforms 1 and 2, therefore the superscript contains the indicator of both platforms.
Extracts of this chapter were published in (Buist et al., 2006), (Buist, 2008), (Buist et al., 2010a), (Giorgi et al., 2010) and (Buist et al., 2010b).

3.1 Research relevance

While precise relative positioning using GNSS for *static* applications (i.e. in the surveying applied Real-Time-Kinematic (RTK) approach) has been around for some time, precise relative navigation for *moving* applications on land, on water, in the air and even in space is still under development. The automotive industry shows interest in this application for relative navigation between vehicles and reference stations, but also between vehicles (Nguyen et al., 1997). Maritime applications, especially inshore relative navigation, require precise and robust methods (Kleusberg, 1986). Obviously this kind of technique is required for a swarm of Unmanned Aerial Vehicles (UAV) (Campa et al., 2004)(Khanafseh and Pervan, 2007) or spacecraft (Buist, 2008), but also could be beneficial for swarms of manned vehicles (Vachon et al., 2003). Other aircraft applications are aerial refueling as well as, potentially, landing (Hansen et al., 2004). For relative navigation between aircraft and vessels, landing on aircraft carriers is an important application (Pervan et al., 2003).

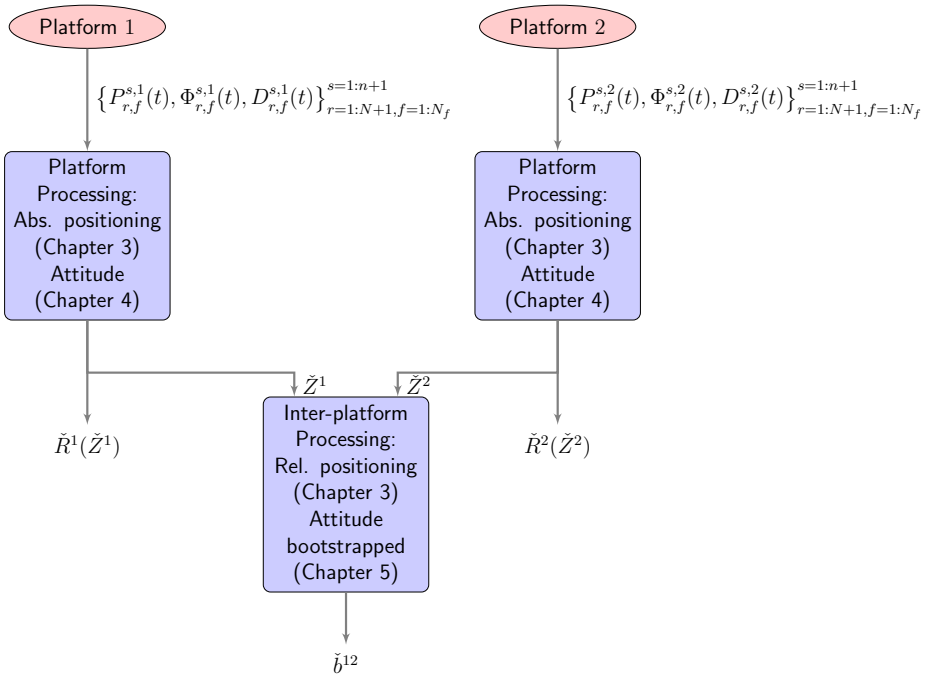


Figure 3.1: Flow diagram of joint absolute positioning, attitude determination and (attitude bootstrapped) relative positioning ($N+1$ GNSS receivers, $n+1$ GNSS satellites, N_f frequencies)

Currently there is a trend in space mission design towards payload distribution: one satellite, integrally carrying the entire payload, is replaced by a cluster or swarm of smaller satellites. Implementation of a formation flying concept is being considered by the European Space Agency (ESA) for the Darwin, the Lisa Path finder, and the PROBA-3 mission. Also national programs in Europe are developing formation flying missions, as for example the SIMBOL-X, and the COSMO-SkyMed-SABRINA missions. Moreover, universities are developing formation flying missions. One example is the plan of Delft University of Technology to develop a formation mission consisting of at least two satellites (Gill et al., 2012).

All these missions have in common that they will depend on GNSS or GNSS-like sensors, autonomously or in combination with other sensors, for relative navigation. As a matter of fact, one of the key technologies for formation flying of spacecraft is relative positioning between the elements of the formation. GNSS can be applied for relative positioning but in order to do this precisely, the ambiguity on the carrier phase observations has to be resolved, preferably in a short time span. In this study the challenge is to achieve the shortest possible time for ambiguity resolution: the single epoch or instantaneous approach. For spaceborne applications, often an extensive dynamics model in combination with a filter is used to resolve the ambiguities of the GNSS observations. In this study a pure kinematic relative positioning approach for space applications is developed. This kinematic approach has a number of advantages which will be briefly discussed.

The main advantage of the kinematic over the filtering approach is that information about dynamics of the system is not applied, which gives more flexibility and furthermore could improve the scientific interest of the observations made by the mission (see for example (Gerlach et al., 2003)(Svehla and Rothacher, 2005)). Therefore a functional kinematic approach could be of high importance for future space missions.

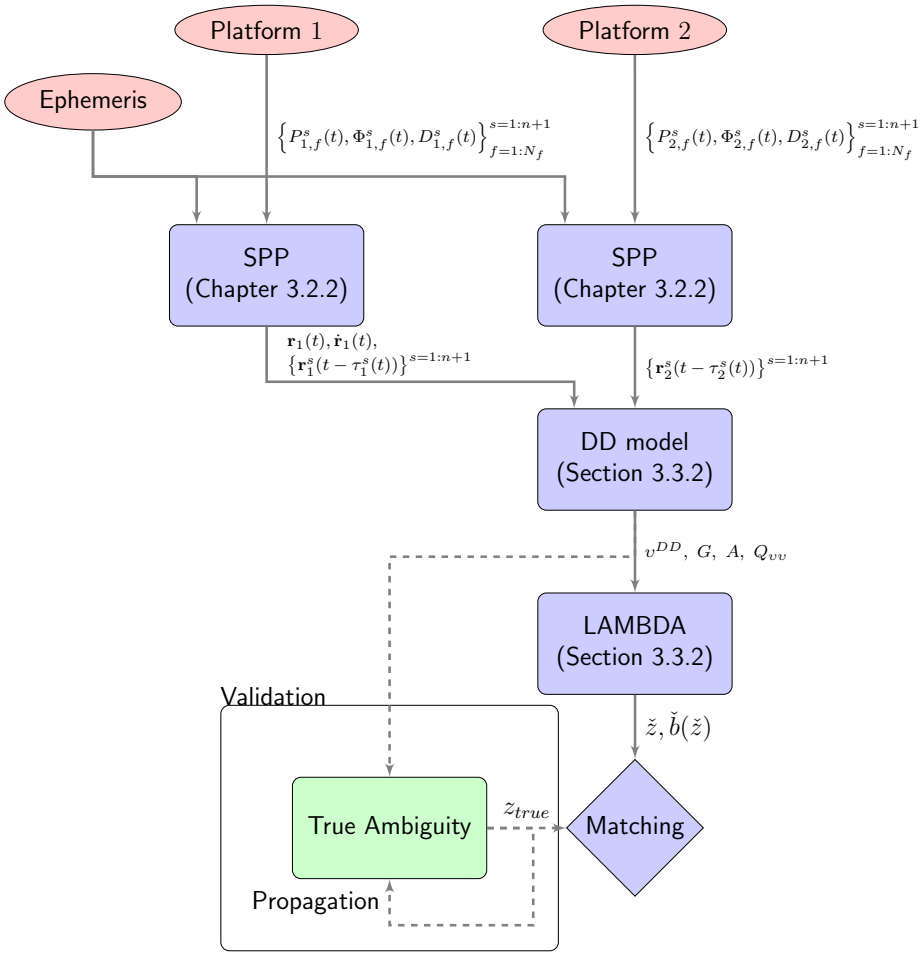


Figure 3.2: Inter-Platform Processing (Relative positioning)

Velocity estimation is important for formation flying for three reasons: first of all the user velocity is required in order to incorporate large clock biases in the functional model (see section 3.3.2.2).
The second reason is that the Doppler observations contain relevant information for absolute and relative positioning and thus could be utilized -besides velocity estimation- as well for positioning. This will be investigated in this chapter.
Moreover the relative velocity is important for formation flying in real-time as the velocity is the main input for the control logic used for formation keeping (Alfriend et al., 2010).
These are the reasons why we will investigate absolute and relative velocity estimation in this chapter.

3.2 Absolute Positioning

Although the main research topic is relative positioning, absolute positioning is important as some or even all platforms in this research are moving. This is different from the standard RTK solution were one of the GNSS receivers -the reference station- is static and located at a precisely known position. So the problem in RTK is to determine the precise relative

position of the rover towards the reference station.
In this research, absolute positioning is performed for each platform. The standard concept of absolute positioning is commonly referred to as *Single Point Positioning* (SPP).
Figure 3.2 shows the relationship between SSP at a single platform and relative positioning between the platforms. The validation block is utilized later on to validate the ambiguity resolution process.

3.2.1 Model using code observations: standard SPP

The SPP is performed for each receiver to compute the absolute position of the receiver, $\mathbf{r}_r(t)$, and the positions of the satellites, $\{\mathbf{r}_r^s(t-\tau_r^s(t))\}^{s=1:n+1}$, using the pseudorange observations. After linearizing the pseudorange observations in Eq. (2.56), the system reads:

Standard SPP using code observations

$$E(\Delta y_r) = H_r \begin{bmatrix} \Delta\mathbf{r}_r(t) \\ c\Delta\zeta_r(t) \end{bmatrix} \tag{3.1}$$

where $\Delta y_r = [\Delta P_{r,f}^1(t) \ \ldots \ \Delta P_{r,f}^{n+1}(t)]^T$, $\Delta P_{r,f}^s(t) = P_{r,f}^s(t) - P_{r,f}^{s-}(t)$ is the observed-minus-computed observation, $\Delta\mathbf{r}_r(t)$ and $\Delta\zeta_r(t)$ are the position and receiver clock corrections in the iterative least-squares estimation, $H_r = [h_r^1 \ldots \ h_r^{n+1}]^T$, and $h_r^s = [-\mathbf{u}_r^s(t)^T \ 1]^T$. The normalized line-of-sight vector $\mathbf{u}_r^s(t)$ from receiver at time t to satellite at time $t-\tau_r^s(t)$ is given as (Eq. (2.25)):

$$\mathbf{u}_r^s(t) = \left[\frac{\mathbf{r}^s\left(t-\tau_r^s(t)\right) - \mathbf{r}_r(t)}{\rho_r^s(t, t-\tau_r^s(t))}\right]^T \tag{3.2}$$

The computed observation $P_{r,f}^{s-}(t)$ is calculated with respect to the approximate values from the previous iteration:

$$P_{r,f}^{s-}(t) = [\rho_r^s(t, t-\tau_r^s(t)) + c\zeta_r(t) - c\zeta^s(t-\tau_r^s(t))]|_{\mathbf{r}_r^-(t),\zeta_r^-(t)} \tag{3.3}$$

where $\mathbf{r}_r^-(t)$ and $\zeta_r^-(t)$ are the estimates for receiver position and clock bias from the previous iteration. Note that the atmospheric delays are ignored in the above computation. More general information on absolute positioning can be found in chapter 5 of (Teunissen and Kleusberg, 1998).

3.2.1.1 Implementation

The iterative SPP procedure can be summarized as:

1. Initialize receiver position $\mathbf{r}_r(t) = \mathbf{r}_{r,0}(t)$ (estimate from previous epoch or approximate position from RINEX header) and receiver clock error $\zeta_r(t) = \zeta_{r_0}(t)$ (estimate from previous epoch or zero), where t is the observation time.

2. Compute satellite states (position $\mathbf{r}^s(t)$, velocity $\dot{\mathbf{r}}^s(t)$, and acceleration $\ddot{\mathbf{r}}^s(t)$) at observation time t for $s = 1, \ldots, n+1$ using navigation data (see Appendix B).

3. Compute propagation time $\tau_r^s(t)$ and satellite position $\mathbf{r}^s\left(t - \tau_r^s(t)\right)$ at transmission time for $s = 1, \ldots, n+1$.

   (a) Initialize $\tau_r^s(t)$.

   (b) Compute satellite position (applying the iteration steps described by Eq. (2.121)):

$$\begin{aligned} \mathbf{r}^s\left(t - \tau_r^s(t)\right) &= \mathbf{r}^s(t) - \dot{\mathbf{r}}^s(t)\left(\zeta_r(t) + \tau_r^s(t)\right) + \\ &\quad + \ddot{\mathbf{r}}^s(t)\left(\zeta_r(t) + \tau_r^s(t)\right)^2/2 \end{aligned} \tag{3.4}$$

   (c) Compute new value for propagation time:

$$\tau_r^{s'}(t) = \rho_r^s(t, t - \tau_r^s(t))/c \tag{3.5}$$

   where c is the speed of light.

   (d) If $|\tau_r^s(t) - \tau_r^{s'}(t)| < \textit{threshold}$, return with $\tau_r^s(t)$ and $\mathbf{r}^s\left(t - \tau_r^s(t)\right)$.

   (e) Otherwise $\tau_r^s(t) = \tau_r^{s'}(t)$ and go to step (b).

4. Compute satellite clock correction $\zeta^s\left(t - \tau_r^s(t)\right)$ at transmission time $t - \tau_r^s(t)$ using Eq. (2.122) and navigation data for $s = 1, \ldots, n+1$.

5. Calculate observed-minus-computed measurement for each satellite,

$$\Delta y = [\Delta y^1, \ \ldots, \ \Delta y^{n+1}]^T \tag{3.6}$$

$$\Delta y^s = P_{r,f}^s(t) - P_{r,f}^{s-}(t) \tag{3.7}$$

6. Construct design matrix H_r from Eq. (3.1).

7. Construct variance-covariance matrix Q_{yy} from Eq. (2.184) using the model parameters a_0, γ_0 and $\sigma_{p_0^s}$.

8. Least-squares adjustment:

$$\Delta\mathbf{r} = \left(H_r^T Q_{yy}^{-1} H_r\right)^{-1} H_r^T Q_{yy}^{-1} \Delta y \tag{3.8}$$

$$Q_{\Delta\mathbf{r},\Delta\mathbf{r}} = \left(H_r^T Q_{yy}^{-1} H_r\right)^{-1} \tag{3.9}$$

9. If $\Delta\mathbf{r}^T Q_{\Delta\mathbf{r},\Delta\mathbf{r}}^{-1} \Delta\mathbf{r} \leq \textit{threshold}$ return with $\mathbf{r}_r(t)$ and $\{\mathbf{r}_r^s(t - \tau_r^s(t))\}^{s=1:n+1}$.

10. Otherwise, update parameters $\mathbf{r}_r(t) = \mathbf{r}_r(t) + \Delta\mathbf{r}_{1:3}$, $\zeta_r(t) = \zeta_r(t) + \Delta\mathbf{r}_4$ and go to step 3.

The above procedure is repeated for each receiver to obtain an approximate position (linearization point) $\mathbf{r}_r(t)$, and satellite positions $\{\mathbf{r}_r^s(t - \tau_r^s(t))\}_{r=1:N+1}^{s=1:n+1}$.

3.2.2 Model using code and Doppler observations

As described in section 2.4.1, the Doppler observation can be considered as the time derivative of the *range* observation. Therefore the system of observation equations could be written as

$$\begin{aligned} E(y) &= Ax \\ E(\dot{y}) &= A\dot{x} + \dot{A}x \end{aligned} \tag{3.10}$$

Different from the pseudo range and carrier phase observations which provide position information along the line-of-sight vector to the GNSS satellite (i.e. the term Ax in Eq. (3.10)), the Doppler observation provides position information perpendicular to this line-of-sight vector (i.e. the term $\dot{A}x$ in Eq. (3.10))(Jorgensen, 1980). In other words it provides information along the direction of the component of the relative velocity that is perpendicular to the line-of-sight vector.
Velocity information of the user is provided by Doppler along the line-of-sight vector to the GNSS satellite (i.e. the term $A\dot{x}$ in Eq. (3.10)).
This section will start with a literature review on previous work on Doppler-based absolute and relative positioning.

3.2.2.1 Literature review

The Doppler effect has been exploited for space-based ranging, positioning and radionavigation since the launch of Sputnik 1 at the beginning of the space age in 1957 (Guier and Weiffenbach, 1960).
Transit was the first operational satellite-based navigation system. It contained some essential elements of the current GNSSs including satellites broadcasting radio signals, ground stations tracking these satellites and facilities to update satellite orbital parameters. Different than the current GNSSs, the satellites were in polar orbit and the Transit user's determined their position by measuring the Doppler shift of the signals transmitted by the satellites.
Nowadays, still some GPS receivers make use of the Doppler observations for positioning. Ashjaee (Ashjaee et al., 1989) suggests that Ashtech receivers apply Doppler observations in their positioning algorithm and this expands, especially, the usage of GNSS in areas with low satellite visibility as forests or urban canyons. This is the type of application, for which Assisted-GPS (AGPS) -discussed later on in this section- is developed. In (Ashjaee, 1986)(Ashjaee et al., 1989), Doppler (absolute) positioning is introduced for static applications, but no details about the implementation -as for example the time derivative of the geometry matrix in the model- are provided. The unknowns in their research were three position coordinates, receiver clock bias and clock drift. The velocity was not estimated as the Doppler positioning was developed for static applications.
Jorgensen (1980) used the relation between Doppler and absolute position for positioning but his approach did not apply the time derivative of line-of-sight vectors but instead takes the difference between two line-of-sight vectors at two epochs, therefore this approach is not instantaneous.

Weill (1992) makes use of the relationship between Doppler shift and a GNSS satellite's velocity. For a stationary user, the four unknowns are the user position vector and the clock bias, so the user position vector can be obtained from the line-of-sight vectors: this relationship is later on derived as Eq. (3.16).
In (Simsky and Boon, 2003) the general relationship between range rate observations and position and velocity is derived but then the assumption is made that the magnitude of the time derivative of the Jacobian, $\dot{A}$ in Eq. (3.10), is negligible: hence the Doppler observations are only used for velocity estimation.
van Diggelen (2009) described Doppler based positioning for AGPS in detail, especially for applications where a best effort approach based on a limited number of observations -even with poor data quality- is acceptable. Often for AGPS applications, the assumption is made that the altitude is known, and that the user is moving slowly: thus reducing the number of unknowns in the model.
For relative positioning, the number of publications describing the use of Doppler is limited. In (Kubo and Pullen, 2008) and (Kubo, 2009), a velocity estimation based on Doppler observations is used to propagate the baseline vector from the previous fixed baseline coordinates. As information from the previous epoch(s) is applied, the method is strictly speaking not instantaneous, but more related to a Kalman filter approach.

3.2.2.2 Algorithm

For absolute positioning, the undifferenced linearized code and Doppler observations are utilized as described in section 2.4. Applying Eq. (2.54) and (2.63), a set of $2(n+1)$ undifferenced linear equations can be written in matrix notation as:

New SPP using code and Doppler observations

$$E(\triangle \upsilon) = E \begin{bmatrix} \triangle P^1_{r,f} \\ \triangle P^2_{r,f} \\ \vdots \\ \triangle P^{n+1}_{r,f} \\ \triangle D^1_{r,f} \\ \triangle D^2_{r,f} \\ \vdots \\ \triangle D^{n+1}_{r,f} \end{bmatrix} = \begin{bmatrix} -\mathbf{u}^1_r & 1-\dot{\rho}^1_r/c & 0 & 0 \\ -\mathbf{u}^2_r & 1-\dot{\rho}^2_r/c & 0 & 0 \\ \vdots & \vdots & & \\ -\mathbf{u}^{n+1}_r & 1-\dot{\rho}^{n+1}_r/c & 0 & 0 \\ -\dot{\mathbf{u}}^1_r & 0 & -\mathbf{u}^1_r & 1-\dot{\rho}^1_r/c \\ -\dot{\mathbf{u}}^2_r & 0 & -\mathbf{u}^2_r & 1-\dot{\rho}^2_r/c \\ \vdots & \vdots & \vdots & \vdots \\ -\dot{\mathbf{u}}^{n+1}_r & 0 & -\mathbf{u}^{n+1}_r & 1-\dot{\rho}^{n+1}_r/c \end{bmatrix} \begin{bmatrix} \triangle \mathbf{r}_r \\ \triangle \zeta_r(t) \\ \triangle \dot{\mathbf{r}}_r \\ \triangle \dot{\zeta}_r(t) \end{bmatrix} = \qquad (3.11)$$

$$= \begin{bmatrix} \mathbf{U}_r & p_{n+1} & \mathbf{0}_{3\times(n+1)} & 0_{m+1} \\ \dot{\mathbf{U}}_r & 0_{n+1} & \mathbf{U}_r^s & p_{n+1} \end{bmatrix} \begin{bmatrix} \triangle \mathbf{r}_r \\ \triangle \zeta_r(t) \\ \triangle \dot{\mathbf{r}}_r \\ \triangle \dot{\zeta}_r(t) \end{bmatrix} = \underbrace{\begin{bmatrix} H_r & 0 \\ \dot{H}_r & H_r \end{bmatrix}}_{\mathcal{H}_r} \begin{bmatrix} \triangle \mathbf{r}_r \\ \triangle \zeta_r(t) \\ \triangle \dot{\mathbf{r}}_r \\ \triangle \dot{\zeta}_r(t) \end{bmatrix} \tag{3.12}$$

and

$$D(\triangle v) = Q_{vv} \tag{3.13}$$

with E is the expected value and D is the dispersion of $\triangle v$, the vector of observed minus computed undifferenced code ($\Delta P^s = P^s_{r,f}(t) - P^{s-}_{r,f}(t)$) and Doppler ($\Delta D^s = D^s_{r,f}(t) - D^{s-}_{r,f}(t)$) observations. The normalized line-of-sight vectors and their derivatives are collected in the matrices $\mathbf{U}_r = \begin{bmatrix} -\mathbf{u}_r^1 & -\mathbf{u}_r^2 & \dots & -\mathbf{u}_r^{n+1} \end{bmatrix}^T$, $\dot{\mathbf{U}}_r = \begin{bmatrix} -\dot{\mathbf{u}}_r^1 & -\dot{\mathbf{u}}_r^2 & \dots & -\dot{\mathbf{u}}_r^{n+1} \end{bmatrix}^T$ and $\mathbf{0}_{3\times(n+1)}$ is a $3 \times (n+1)$ matrix with all entries being zero, 0_{n+1} is a vector with $n+1$ zeros and p_{n+1} is a vector with $(1 - \dot{\rho}_r^{n+1}/c)$ as its entries for $n+1$ GNSS satellites. $\dot{\mathbf{u}}_r^s$ is obtained using Eq. (2.61).

The computed observation $P^{s-}_{r,f}(t)$ is calculated with respect to the approximate values from the previous iteration:

$$P^{s-}_{r,f}(t) = [\rho^s_r(t - \tau^s_r(t), t) + c\zeta_r(t) - c\zeta^s(t - \tau^s_r(t))]|_{\mathbf{r}^-_r(t), \zeta^-_r(t)} \tag{3.14}$$

where $\mathbf{r}^-_r(t)$ and $\zeta^-_r(t)$ are the estimates for receiver position and clock bias from previous iteration. Note that the atmospheric delays are again ignored in the above computation. Similarly the computed observation $D^{s-}_{r,f}(t)$ is calculated with respect to the approximate values from the previous iteration:

$$D^{s-}_{r,f}(t) = \left[\dot{\rho}^s_r(t - \tau^s_r(t), t) + c\dot{\zeta}_r(t) - c\dot{\zeta}^s(t - \tau^s_r(t))\right]\Big|_{\mathbf{r}^-_r(t), \dot{\mathbf{r}}^-_r(t), \dot{\zeta}^-_r(t)} \tag{3.15}$$

where $\mathbf{r}^-_r(t)$, $\dot{\mathbf{r}}^-_r(t)$ and $\dot{\zeta}^-_r(t)$ are the estimates for receiver position, velocity and clock drift from previous iteration.

For the observations, a-priori available information on atmospheric delays can be applied based on models developed in section 2.5. Other a-priori corrections include the relativistic and clock effects described in section 2.4.5 and their derivatives which are necessary for the velocity estimation.

3.2.2.3 Initialization

In the SPP approach, the equations are linearized about the previous estimates of the user state (in this section: position, velocity, receiver clock bias and drift) and iterated until the change in the estimation is smaller than a selected threshold. In order for the estimation to converge to a solution, in each iteration step the change should be smaller than the

previous step. The difference in initialization for SPP between using only code and code and Doppler observation is discussed next.

Absolute positioning using code observations The iteration loop applied in absolute positioning using pseudorange observations converges quickly when the starting point of the iteration is chosen somewhere inside the orbit of the GNSS constellation. Often the centre of the Earth, the position in the header of the RINEX file or the last obtained position solution is applied as the starting point of the iteration.

Absolute positioning and velocity estimation using Doppler observations Absolute positioning using only Doppler observations requires a fairly accurate knowledge of the user's position to guarantee convergence.
For stationary users ($\dot{\mathbf{r}}_r = 0$), the Doppler observations could be used to do positioning using the following model (Weill, 1992)(Misra and Enge, 2001), by manipulating Eq. (2.67) to:

$$\begin{aligned} E\begin{bmatrix} D^1_{r,f} + \dot{\zeta}^1(t-\tau^1_r) \\ D^2_{r,f} + \dot{\zeta}^2(t-\tau^2_r) \\ \vdots \\ D^{n+1}_{r,f} + \dot{\zeta}^{n+1}(t-\tau^{n+1}_r) \end{bmatrix} &= \begin{bmatrix} \mathbf{u}^1_r \\ \mathbf{u}^2_r \\ \vdots \\ \mathbf{u}^{n+1}_r \end{bmatrix} \begin{bmatrix} \dot{\mathbf{r}}^1 \\ \dot{\mathbf{r}}^2 \\ \vdots \\ \dot{\mathbf{r}}^{n+1} \end{bmatrix} + \begin{bmatrix} \dot{\zeta}_r(t) \\ \dot{\zeta}_r(t) \\ \vdots \\ \dot{\zeta}_r(t) \end{bmatrix} \\ &= \begin{bmatrix} -\mathbf{U}_r \end{bmatrix} \begin{bmatrix} \dot{\mathbf{r}}^1 \\ \dot{\mathbf{r}}^2 \\ \vdots \\ \dot{\mathbf{r}}^{n+1} \end{bmatrix} + \begin{bmatrix} e_{n+1} \end{bmatrix} \dot{\zeta}_r(t) \end{aligned} \tag{3.16}$$

The unknowns are the user position $\mathbf{r}_r$ (in $\mathbf{U}_r$) and the receiver clock drift $\dot{\zeta}_r(t)$. Similar to the approach applied in SPP using code observations, one could linearize about the initial position and clock drift and solve the equation iteratively. However this model -as it is not very sensitive to small changes in the estimate of the user position (the user position is only applied in the line-of-sight vectors)- is weaker than the model of Eq. (3.11). Moreover for applications of moving platforms, the assumption that the user velocity is negligible is inappropriate.

Absolute positioning and velocity estimation using code and Doppler observations If Doppler observations are applied in combination with pseudo range observations, convergence is generally guaranteed under the condition that the initial user position is within the GNSS constellation.
Alternatively for velocity, a fairly accurate initial estimate can be obtained by manipulating the equation Eq. (2.67) (Misra and Enge, 2001) (Gleason and Gebre-Egziabher, 2009). The set of linear equations is:

$$E\begin{bmatrix} D^1_{r,f} - \dot{\mathbf{r}}^1\mathbf{u}^1_r + \dot{\zeta}^1(t-\tau^1_r) \\ D^2_{r,f} - \dot{\mathbf{r}}^2\mathbf{u}^2_r + \dot{\zeta}^2(t-\tau^2_r) \\ \vdots \\ D^{n+1}_{r,f} - \dot{\mathbf{r}}^{n+1}\mathbf{u}^{n+1}_r + \dot{\zeta}^{n+1}(t-\tau^{n+1}_r) \end{bmatrix} = \begin{bmatrix} -\mathbf{u}^1_r & 1 \\ -\mathbf{u}^2_r & 1 \\ \vdots & \vdots \\ -\mathbf{u}^{n+1}_r & 1 \end{bmatrix} \begin{bmatrix} \dot{\mathbf{r}}_r \\ \dot{\zeta}_r(t) \end{bmatrix} = \begin{bmatrix} \mathbf{U}_r & e_{n+1} \end{bmatrix} \begin{bmatrix} \dot{\mathbf{r}}_r \\ \dot{\zeta}_r(t) \end{bmatrix}$$

(3.17)

where e_{n+1} is a vector with $n+1$ ones.

This is the approach applied for initialization of the user velocity in the SPP using code and Doppler observations.

3.2.2.4 Implementation

The iterative SPP procedure with velocity estimation can be summarized as:

1. Initialize receiver position $\mathbf{r}_r(t) = \mathbf{r}_{r,0}(t)$ (estimate from previous epoch, approximate position from RINEX header or center of the Earth), receiver velocity $\dot{\mathbf{r}}_r(t) = \dot{\mathbf{r}}_{r,0}(t)$ (estimate from previous epoch, the linearized equation described by Eq. (3.17) or initial value), receiver clock bias $\zeta_r(t) = \zeta_{r,0}(t)$ and clock drift $\dot{\zeta}_r(t) = \dot{\zeta}_{r,0}(t)$ (both are the estimates from previous epochs or zero), where t is the observation time.
2. Compute satellite states (position $\mathbf{r}_r^s(t)$, velocity $\dot{\mathbf{r}}_r^s(t)$, and acceleration $\ddot{\mathbf{r}}_r^s(t)$) at observation time t for $s = 1, \ldots, n+1$ using navigation data (see Appendix B).
3. Compute propagation time $\tau_r^s(t)$, satellite position $\mathbf{r}^s\left(t - \tau_r^s(t)\right)$ and satellite velocity $\ddot{\mathbf{r}}^s\left(t - \tau_r^s(t)\right)$ at transmission time for $s = 1, \ldots, n+1$.
   (a) Initialize $\tau_r^s(t)$.
   (b) Compute satellite position (applying iteration described by Eq. (2.121)):
   $$\begin{aligned} \mathbf{r}^s\left(t - \tau_r^s(t)\right) &= \mathbf{r}^s(t) - \dot{\mathbf{r}}^s(t)\left(\zeta_r(t) + \tau_r^s(t)\right) + \\ &\quad + \ddot{\mathbf{r}}^s(t)\left(\zeta_r(t) + \tau_r^s(t)\right)^2/2 \end{aligned} \tag{3.18}$$
   (c) Compute satellite velocity:
   $$\dot{\mathbf{r}}^s\left(t - \tau_r^s(t)\right) = -\dot{\mathbf{r}}^s(t) + 2\ddot{\mathbf{r}}^s(t)\left(\zeta_r(t) + \tau_r^s(t)\right) \tag{3.19}$$
   (d) Compute new value for propagation time:
   $$\tau_r^{s'}(t) = \rho_r^s(t - \tau_r^s(t), t)/c \tag{3.20}$$
   where c is the speed of light.
   (e) If $|(\tau_r^s(t) - \tau_r^{s'}(t))|$ *threshold*, return with $\tau_r^s(t)$ and $\mathbf{r}^s\left(t - \tau_r^s(t)\right)$.
   (f) Otherwise $\tau_r^s(t) = \tau_r^{s'}(t)$ and go to step (b).
4. Compute satellite clock correction $\zeta^s\left(t - \tau_r^s(t)\right)$ and $\dot{\zeta}^s\left(t - \tau_r^s(t)\right)$ at transmission time $t - \tau_r^s(t)$ using Eq. (2.122) and navigation data for $s = 1, \ldots, n+1$.
5. Calculate observed-minus-computed measurement for each satellite,
   $$\Delta v = [\Delta P^1, \ \ldots, \ \Delta P^{n+1}, \Delta D^1, \ \ldots, \ \Delta D^{n+1}]^T \tag{3.21}$$
   $$\Delta P^s = P_{r,f}^s(t) - P_{r,f}^{s-}(t) \tag{3.22}$$
   $$\Delta D^s = D_{r,f}^s(t) - D_{r,f}^{s-}(t) \tag{3.23}$$

6. Construct design matrix $\mathcal{H}_i$ from Eq. (3.11).
7. Construct variance-covariance matrix Q_{vv} from Eq. (2.184) using the model parameters a_0, γ_0, $\sigma_{p_0^s}$ and $\sigma_{D_0^s}$.
8. Least-squares adjustment:

$$\Delta\mathbf{r} = \left(\mathcal{H}_r^T Q_{vv}^{-1} \mathcal{H}_r\right)^{-1} \mathcal{H}_r^T Q_{vv}^{-1} \Delta\upsilon \tag{3.24}$$

$$Q_{\Delta\mathbf{r},\Delta\mathbf{r}} = \left(\mathcal{H}_r^T Q_{vv}^{-1} \mathcal{H}_r\right)^{-1} \tag{3.25}$$

9. If $\Delta\mathbf{r}_{1:4}^T Q_{\Delta P,\Delta P}^{-1} \Delta\mathbf{r}_{1:4} \leq$ *threshold* and $\Delta\mathbf{r}_{5:8}^T Q_{\Delta D,\Delta D}^{-1} \Delta\mathbf{r}_{5:8} \leq$ *threshold* return with $\mathbf{r}_r(t)$, $\dot{\mathbf{r}}_r(t)$ and $\{\mathbf{r}_r^s(t-\tau_r^s(t))\}_{s=1}^{n+1}$.
10. Otherwise, update parameters ($\mathbf{r}_r(t) = \mathbf{r}_r(t) + \Delta\mathbf{r}_{1:3}$, $\zeta_r(t) = \zeta_r(t) + \Delta\mathbf{r}_4$, $\dot{\mathbf{r}}_r(t) = \dot{\mathbf{r}}_r(t) + \Delta\mathbf{r}_{5:7}$, $\dot{\zeta}_r(t) = \dot{\zeta}_r(t) + \Delta\mathbf{r}_8$) and go to step 3.

The above procedure is repeated with each receiver to obtain the approximate position (linearization point) $\mathbf{r}_r(t)$, velocity $\dot{\mathbf{r}}_r(t)$ and satellite positions $\{\mathbf{r}_r^s(t-\tau_r^s(t))\}_{r=1:N+1}^{s=1:n+1}$.

3.3 Relative Positioning

This section starts with a discussion on the approaches applied on the space missions introduced in section 1.1. Table 3.1 provides a summary including the most important parameters of these approaches which will be covered in this section. This section is divided in two main subsections: in the first one single epoch solutions are developed, in the second multi-epoch solutions. Both subsections are then subdivided into parts focusing on the standard model using code and carrier observations, and a model using code, carrier and Doppler observations. Moreover single and multi-frequency models are discussed.

Table 3.1: Overview of missions using GNSS for relative positioning

Mission (Agency)	ETS-7 (JAXA)	GRACE (NASA)	PRISMA (SSC)	TanDEM-X (GFZ)
Relative positioning	JAXA	TUDelft/DLR	DLR	GFZ/DLR
Relative distance [km]	0 - 0.5	220	0.05 - 2	0.2 - 0.45
Real-time (R), Postprocessed (P)	R,P	P	R,P	R,P
Observation frequency (channels)	L1 (6)	L1+L2 (24)	L1 (12)	L1+L2 (24)
Rendezvous (R), Formation Flying (F)	R	F	R,F	F
Kalman filter state [1] (dimensions)	p, v, b, d (8)[3] p, v, b, d, nA (float) (12)[4]	p, v, a, rd, s, b, d, 2nA, nI (12+3n)	p, v, a, rd, b, nA, I_0 (13+n)	p, v, a, rd, s, b, 2nA, nI (12+3n)
Observations [2]	L1 PR, L1CP L1DR	L1 PR, L1CP	L1 PR, L1CP	
Integration of position	Hill equations	'Pseudo' relative dynamics	'Pseudo' relative dynamics	'Pseudo' relative dynamics
Other sensors	accelerometers	KBR/accelerometers	FFRF, VBS	
Reported accuracy [m]	<10 (R)[3] <10 (R)[4] <5 (P)	<0.01 (R)	<0.1 (R) <0.01 (P)	<0.01 (P)

[1] p: position, v: velocity, a: acceleration, b: clock bias, d: clock drift, A: ambiguities, I: ionospheric delay, I_0: vertical ionospheric delay, rd: relative drag, s: relative solar radiation pressure coefficient

[2] PR: Pseudo range, DR: Delta Range, CP: Carrier Phase

[3] First onboard experiment in 1997

[4] Second onboard experiment in 1998

3.3.1 Applied relative positioning approaches on some missions

3.3.1.1 ETS-7

JAXA (formerly NASDA) has been developing rendezvous and docking techniques since the 90s, especially targeting this technology to utilize it for docking the H2A Transfer Vehicle (HTV) with the International Space Station (ISS). The ETS-7 experiment -a demonstration mission for relative positioning in the space environment- used 4 space qualified L1 GPS receivers (2 redundant receivers on each satellite) developed by Toshiba (Kawano et al., 1999). The original goal of the experiment was to use the GPS receiver until the two sub-satellites arrived at a relative distance of 500 meter. The conservative requirement for relative position and velocity was 21 m and 5 cm/s respectively. Because of the relative small distance between the satellites, the difference in ionospheric delay on the observations at the two sub-satellites were negligible.
The original implementation used for the onboard relative navigation experiment estimated a 8-element state vector (3 relative position elements, 3 relative velocity elements, difference of clock bias and clock drift between the GPS receiver of the chaser and target satellite).
The performance could be determined when the two satellites were mated and the distance between the antennas was known. The reported accuracy was 10 m and 1 cm/s for relative position and velocity estimation respectively. During rendez-vous, the GPS based relative positioning result was compared with the rendezvous laser radar. The difference was reported a few meters.
In the second part of the experiment (Kawano et al., 2000), a carrier phase based relative navigational experiment was performed in which the carrier phase ambiguities estimations (float) were added to the state vector, and therefore the state vector dimension became 14: 8 original states plus 6 carrier phase ambiguities for the 6 channel GPS receivers. The onboard accuracy for relative position and velocity was reported to be better than 10 meters and 2 cm/s respectively. After post-processing, the accuracy improved to 5 meters and 1 cm/s respectively. The float ambiguities were calculated from the residual of the single difference carrier phase.
Besides GPS, also data from the accelerometer was used for state propagation, and this made it possible to keep the relative errors small even when the thrusters were used to correct the approach of the chaser satellite. The state vector was updated every 10 seconds. An interpolation model was used to calculate the observations from the 2 satellites at the same epoch as the GPS receivers were not time-synchronized.

3.3.1.2 GRACE

The Gravity Recovery and Climate Experiment (GRACE) mission from NASA/DLR, consists of two identical formation flying spacecraft in a near polar, near circular orbit with an initial altitude of approximately 500 km (Kroes, 2006). The spacecraft have a nominal separation of 220 km. The primary mission objective is to measure the time-variable gravity field, which is accomplished by the mission's key instruments: the Ka-Band Ranging System (KBR) and the accelerometers. The GPS receiver, based on the Blackjack developed

by JPL, is not used for real-time relative navigation by the satellites. Research at Delft University of Technology and DLR has proved that -using orbital data from the GRACE formation- mm level of accuracy is achievable for GNSS-based relative navigation between spacecraft in post-processing. The strategy processes differential GPS pseudorange and carrier phase observations and uses (pseudo) relative spacecraft dynamics to propagate the relative satellite state over the observation epochs. It can resolve and incorporate the integer double difference carrier phase ambiguities.
There are a number of differences between the work described in (Kroes, 2006) and the approaches developed for real-time, rendezvous missions (e.g. ETS-7). The major differences are the use of dual frequency observations, processing of the measurements in forward and backward direction, smoothing of the relative position estimates, the actual estimation of the ambiguities, the propagation model for the state vector describing the relative position, the much extended state vector including states for the ionospheric delay, and the 5-dimensional vector of relative force model parameters. This last vector contains the relative drag and solar radiation pressure coefficient as well as the relative empirical accelerations. Furthermore note that different from the real-time rendezvous approaches, the relative clock drift is not modeled in (Kroes, 2006), but only the clock bias. The processing strategy applied a state dimension of 42 ($= 12 + 3n$ with for n the maximum number of 10 channels of the GPS receiver, but the actual number depending on the outcome of the quality control algorithm).
GRACE data was also used by (Bertiger et al., 2002)(Wu and Bar-Sever, 2006), which applied a similar EKF approach using a reference and differential orbit and the LAMBDA method for ambiguity fixing. (Jaggi et al., 2007) compared the KBR baselines with solutions based on the Bernese software and found a similar accuracy as Kroes.

3.3.1.3 PRISMA

PRISMA is a Swedish mission and provides a demonstration for critical technologies related to formation flying and In-Orbit-Servicing (rendezvous) (Persson et al., 2009). The PRISMA test bed comprises a fully maneuverable micro-satellite as well as a smaller sub-satellite, similar to the chaser and target sub-satellites used for the ETS-7 mission. Within PRISMA, the German DLR has responsibility for providing a GPS-based onboard navigation system offering absolute and relative orbit information in real-time. An intersatellite link is applied to transmit GPS and telemetry data from the sub-satellite to the micro-satellite and to relay telecommands through the micro-satellite to the sub-satellite. For relative navigation, a double-difference carrier phase difference between the chaser and target satellite is applied (Gill et al., 2006). As was shown in section 2.4.2 and 2.4.3, differencing across receivers reduces broadcast ephemeris and ionospheric errors, the differencing across GNSS satellites explicitly eliminates the user clock error. The onboard processing strategy estimates the spacecraft position and velocity components, the empirical accelerations, clock errors and biases along with carrier phase ambiguities as float values and differential ionospheric path delays. The relative empirical accelerations in radial, along-track and cross-track direction (see appendix E.3 for the definition) are used to capture any discrepancies or mismodeling of the relative spacecraft dynamics.

The PRISMA project also demonstrated autonomous formation flying and rendezvous

based on RF-based and vision based sensors. The RF-based navigation instrument (Formation Flying Radio Frequency sensor or FFRF), under CNES development, was tested for the first time on PRISMA, both for instrument performance, but also in closed loop as main sensor for formation flying. The vision based experiments utilized the Vision Based Sensor (VBS), a modified star camera provided by the Technical University of Denmark (DTU).
The mission was launched in June 2010 into a sun-synchronous 700 km orbit. An intersatellite S-band link transmits telecommand, GPS and telemetry data. Due to computational limitations of the onboard processor a time and measurement update step requires 10 seconds of computational time, if no other computations are taking place. Therefore new observations are only processed every 30 seconds.
In real-time, the PRISMA mission demonstrated sub-decimeter relative navigation accuracy, and post-processed GPS results have shown a consistency with FFRF at the level of 1 cm standard deviation but the results include notable and partly time-varying biases (Montenbruck et al., 2011).

3.3.1.4 TanDEM-X (TR-X) and TerraSAR-X (TD-X)

The TanDEM-X mission is the first SAR mission using close formation flying (Fig. 3.3). It is a mission both from DLR and the German Research Centre for Geosciences (GFZ). The TanDEM-X (TD-X) spacecraft was launched on the 21st of June 2010 to complement the existing TerraSAR-X (TR-X). The two almost identical satellites are in a helix orbit with an altitude of 515 km and an 11 days revisiting period (Krieger et al., 2007)(Krieger et al., 2010). A helix orbit combines a radial separation at the poles with a lateral separation at the equator. The satellites have an intersatellite distance of about 250 meter.
For real-time relative navigation the MosaicGNSS single-frequency receivers are used (see also section 2.6.1) with accuracies (RMS errors) of 30 m and 4 m for along-track and cross track respectively. Precise orbit determination and baseline estimation are based on the IGOR dual frequency receivers which is the commercial version of the Blackjack receivers used onboard GRACE. The receiver has 16 channels for L1 C/A and semi-codeless L2 tracking of which 12 can be used for navigation, the other 4 are reserved for radio occultation observations.
For this mission, baselines are generated by DLR using the same approach as applied for the GRACE mission (Montenbruck et al., 2011)(Montenbruck et al., 2010). Independently GFZ is also generating baselines using the BERNESE software (Moon et al., 2008).
Different than the GRACE mission, which carries a high-precision Ka-band ranging system, the TanDEM-X does not have an independent sensor of similar quality to verify the precision and accuracy of the GPS-based relative navigation products. Therefore a variety of self-consistency tests and performance metrics were applied to have a basic quality check and performance assessment which indicate an similar accuracy as achieved on the GRACE mission (Montenbruck et al., 2011).

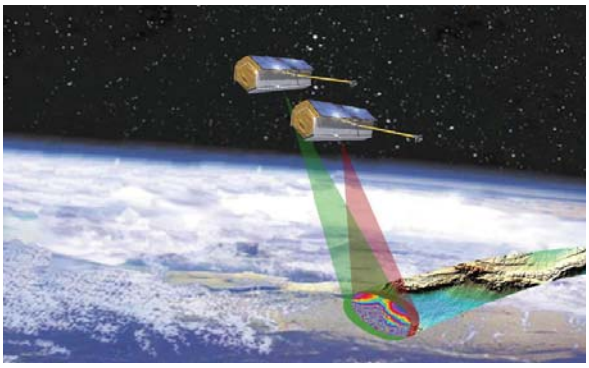


Figure 3.3: Artist impression of TanDEM-X (TD-X) and TerraSAR-X (TR-X) in orbit (Courtesy of DLR)

3.3.2 Single Epoch Solution

3.3.2.1 Model using Code and Carrier Observations

Most GNSS receivers make use of at least two types of observations: pseudo range and carrier phase. The pseudo range observations typically have an accuracy of decimeters for surveying type of receivers. However, as discussed in section 2.6.1, for space receivers this can be up to meters. The carrier phase observations have accuracies down to millimeter level.

Linearized Double-Difference Model For long baselines where atmospheric delays cannot be neglected, the following extended model based on Eq. (2.100) and (2.101) can be applied:

$$E(P^{1s}_{12,f}(t)) = \rho^{1s}_{12}(t) + I^{1s}_{12,f} + T^{1s}_{12} \quad (3.26)$$

$$E(\Phi^{1s}_{12,f}(t)) = \rho^{1s}_{12}(t) + \lambda_f z^{1s}_{12,f} - I^{1s}_{12,f} + T^{1s}_{12} \quad (3.27)$$

where the DD topocentric distance $\rho^{1s}_{r_{12}}(t)$ was given in Eq. (2.102) as

$$\begin{aligned}\rho^{1s}_{12}(t) = {} & \|\mathbf{r}^s(t-\tau^s_2(t)) - \mathbf{r}_2(t)\| - \|\mathbf{r}^s(t-\tau^s_1(t)) - \mathbf{r}_1(t)\| \\ & -\|\mathbf{r}^1(t-\tau^1_1(t)) - \mathbf{r}_1(t)\| - \|\mathbf{r}^1(t-\tau^1_2(t)) - \mathbf{r}_2(t)\|\end{aligned} \quad (3.28)$$

Linearization about $\mathbf{r}_1(t)$ yields (see discussion in section 2.4.2 and 2.4.3),

$$\rho^{1s}_{12}(t) = \rho^{1s-}_{12}(t) + \left(\mathbf{u}^1_1(t) - \mathbf{u}^s_1(t)\right)\mathbf{b} \quad (3.29)$$

where $\mathbf{b}$ is the baseline vector, the unit vector $\mathbf{u}^s_1(t)$ is given by Eq. (3.2) and the computed DD topocentric distance $\rho^{1s-}_{12}(t)$. Hence, the linearized DD observation equations read

$$E(\Delta P^{1s}_{12,f}) = {g^{1s}_1}^T\mathbf{b} + \Delta I^{1s}_{12,f} + \Delta T^{1s}_{12} \quad (3.30)$$

$$E(\Delta \Phi^{1s}_{12,f}) = {g^{1s}_1}^T\mathbf{b} + \lambda_f z^{1s}_{12,f} - \Delta I^{1s}_{12,f} + \Delta T^{1s}_{12} \quad (3.31)$$

where

$$\Delta P^{1s}_{12,f} = P^{1s}_{12,f} - \rho^{1s-}_{12}(t) - \Delta I^{1s}_{12,f} - \Delta T^{1s}_{12} \quad (3.32)$$

$$\Delta \Phi^{1s}_{12,f} = \Phi^{1s}_{12,f} - \rho^{1s-}_{12}(t) + \Delta I^{1s}_{12,f} - \Delta T^{1s}_{12} \quad (3.33)$$

$$g^{1s}_1 = \mathbf{u}^1_1(t) - \mathbf{u}^s_1(t) \quad (3.34)$$

The vectorial form of the DD observation equation for the fth frequency reads

$$E(y_P^{DD}) = G_1\mathbf{b} + \mu_f \Delta I_{12,1}^{1s} + \Delta T_{12}^{1s} \quad (3.35)$$

$$E(y_\Phi^{DD}) = G_1\mathbf{b} + \lambda_f I_n z_{12,f} - \mu_f \Delta I_{12,1}^{1s} + \Delta T_{12}^{1s} \quad (3.36)$$

with $y_P^{DD} = [\Delta P_{12,f}^{12} \ \dots \ \Delta P_{12,f}^{1(n+1)}]^T$, $y_\Phi^{DD} = [\Delta \Phi_{12,f}^{12} \ \dots \ \Delta \Phi_{12,f}^{1(n+1)}]^T$, $G_1 = [g_1^{12} \ \dots \ g_1^{1(n+1)}]^T$, and $z_{12,f} = [z_{12,f}^{12} \ \dots \ z_{12,f}^{1(n+1)}]^T$. Arranging the observations, the observation model of the baseline then reads

Standard DD model for long baseline

$$E(y^{DD}) = Az + Gb + T_{total} + \begin{Bmatrix} -\mu_f I_{L_1}^{DD} \\ \mu_f I_{L_1}^{DD} \end{Bmatrix}, \quad D(y^{DD}) = Q_{yy} \quad (3.37)$$

Where T_{total} is the total slant delay described by Eq. (2.147), μ_f is a coefficient and $I_{L_1}^{DD}$ is a $n \times 1$ vector of DD ionospheric delays on L1 as described in section 2.5.2.4.

Next, the assumption is made that the antennas are close to each other and thus that atmospheric effects can be neglected. Ignoring the atmospheric delays in Eq. (2.100) and (2.101), the double-difference (DD) observation equations can be written as (Teunissen and Kleusberg, 1998):

Standard DD model for short baseline

$$E(y^{DD}) = Az + Gb, \quad D(y^{DD}) = Q_{yy}, \quad z \in \mathbb{Z}^{n \times N_f}, \ b \in \mathbb{R}^3 \quad (3.38)$$

y^{DD} is the vector of observed minus computed DD carrier phases and code observations of the order $m = 2n$, z is the unknown vector of ambiguities of the order $n \times N_f$ expressed in cycles rather than range to maintain their integer character. b is the baseline vector of order three. G is the geometry matrix containing normalized line-of-sight vectors $\left[\mathbf{U}_r^{DD}, \mathbf{U}_r^{DD}\right]^T$, A is a design matrix that links the data vector to the unknown vector z. The variance matrix of y^{DD} is given by the positive definite matrix Q_{yy} which is assumed to be known.

The construction of the linearized DD model is summarized as:

1. Calculate the observed-minus-computed observations defined in Eq. (3.32) and Eq. (3.33).
2. Compute geometry vectors (difference of unit line-of-sight vectors) defined in Eq. (3.34).
3. Construct DD observation model in Eq. (3.35) and Eq. (3.36).
4. Construct the baseline model in Eq. (3.38).
5. Construct the corresponding dispersion matrix in (2.184).

Single Frequency The double difference (DD) observation equations as described in the standard DD model of Eq. (2.100)-(2.101) can be written for a single baseline as the system of linearized observation equations of Eq. (3.38). It is important to note that the ambiguities z are integers, thus ($z \in \mathbb{Z}^n$) with $\mathbb{Z}^n$ being the n dimensional space of integer and $b \in \mathbb{R}^3$. The solution of the linear system of observation equations is therefore an integer least-squares problem. Of course it would be possible to express the integer ambiguities in the space of reals, after all the space of integers is a subset of the space of reals. In that case the solution could be found by an ordinary least-squares solution. However this would imply that the ambiguities would not be integers anymore and thus not all available information to solve the problem is utilized. This information could have, if used in an appropriate way, a very beneficial impact on the accuracy obtainable.

The least-squares criterion for the unconstrained problem reads as (Teunissen, 1995)(Teunissen and Kleusberg, 1998):

$$\min_{z\in\mathbb{Z}^n, b\in\mathbb{R}^3} \|y^{DD} - Az - Gb\|^2_{Q_{yy}} = \|\hat{e}\|^2_{Q_{yy}} + \min_{z\in\mathbb{Z}^n, b\in\mathbb{R}^3} \left(\|\hat{z} - z\|^2_{Q_{\hat{z}\hat{z}}} + \|\hat{b}(z) - b\|^2_{Q_{\hat{b}(z)\hat{b}(z)}} \right) \tag{3.39}$$

where $\hat{e} = y - A\hat{z} - G\hat{b}$ is the least-squares residual vector of the float solution $\hat{z}, \hat{b}$, and $\hat{b}(z)$ is the least-squares solution for b, assuming that z is known and $Q_{\hat{b}(z)\hat{b}(z)} = Q_{\hat{b}\hat{b}} - Q_{\hat{b}\hat{z}}Q^{-1}_{\hat{z}\hat{z}}Q_{\hat{z}\hat{b}}$. The last term of Eq. (3.39) can be made zero for any z. In our notation we will make use of the weighted squared norm $\|..\|^2_{Q_{yy}} = (..)^T Q^{-1}_{yy}(..)$.

The set of linear observation equations is solved by applying the well-known Integer Least-Squares (ILS) principle for which the solution can be obtained from the following three steps (Teunissen, 1995):
1) First the so-called float solution $\hat{z}$ and $\hat{b}$ is obtained, i.e. the least-squares solution disregarding the integer nature of the ambiguities:

$$\begin{bmatrix} \hat{z} \\ \hat{b} \end{bmatrix} = \begin{bmatrix} Q_{\hat{z}\hat{z}} & Q_{\hat{z}\hat{b}} \\ Q_{\hat{b}\hat{z}} & Q_{\hat{b}\hat{b}} \end{bmatrix} \left[\begin{bmatrix} A & G \end{bmatrix}^T Q^{-1}_{yy} y^{DD} \right] \tag{3.40}$$

for which the variance-covariance (or v-c) matrix is derived as:

$$\begin{bmatrix} Q_{\hat{z}\hat{z}} & Q_{\hat{z}\hat{b}} \\ Q_{\hat{b}\hat{z}} & Q_{\hat{b}\hat{b}} \end{bmatrix} = \left[\begin{bmatrix} A & G \end{bmatrix}^T Q^{-1}_{yy} \begin{bmatrix} A & G \end{bmatrix} \right]^{-1} \tag{3.41}$$

With the float solutions ($\hat{z} \in \mathbb{R}^n, \hat{b} \in \mathbb{R}^3$), the squared norm of the least-squares residual vector becomes the solution of the linear system of observations:

$$\|y^{DD} - A\hat{z} - G\hat{b}\|^2_{Q_{yy}} = \|\hat{e}\|^2_{Q_{yy}} \tag{3.42}$$

2) We solve the vector of integer least-squares estimates of the ambiguities $\check{z}$:

$$\check{z} = \arg(\min_{z\in\mathbb{Z}^n} \|\hat{z} - z\|^2_{Q_{\hat{z}\hat{z}}}) \tag{3.43}$$

where $\check{z}$ is the vector of integers that minimizes the term within the brackets ($\arg$ or $argument$). This integer ambiguity vector is estimated by means of an extensive search

for the integer vector which minimizes the distance with respect to the float solution in the metric of the v-c matrix of the float ambiguities. The search space for this problem is defined as:

$$\Psi(\chi^2) = \left\{ z \in \mathbb{Z}^n | \ \|\hat{z} - z\|^2_{Q_{\hat{z}\hat{z}}} \leq \chi^2 \right\} \tag{3.44}$$

where χ^2 is a properly chosen constant. The LAMBDA method is an efficient way to find the minimizer of Eq.(3.43) (Teunissen, 1993, 1994, 1995, 1999).
For GNSS applications the search space, which elongation is determined by the variance matrix of the float solution of z, is very much influenced by the high correlation between the ambiguities. However, a transformation can be applied that decorrelates the ambiguities and therefore can improve the computational efficiency of the search dramatically. This will be discussed in more detail next.

Fig. 3.4 shows the spectrum of the original and decorrelated float ambiguity v-c matrix for a single frequency observation epoch with eight locked GPS satellites. The original spectrum contained a large discontinuity when passing from the third to the fourth conditional standard deviation. The discontinuity is determined by the dimension of the unknown baseline vector (i.e. three in the model applied in this section). If at least three ambiguities are fixed, the baseline can be determined by the very precise carrier phase observations and -with the baseline vector known- the remaining ambiguities can be determined with high precision using the remaining $n-3$ double difference observations: therefore the conditional standard deviations of these ambiguities have to be very small.
The improvement in the decorrelated spectrum is clearly visible in the figure as the discontinuity has disappeared and all the conditional standard deviations are of the same order. Therefore the search for the integer ambiguity vector can be performed much more efficiently. More information on the spectrum of the conditional standard deviations of the DD ambiguities can be found in (Teunissen et al., 1994)(Teunissen and Kleusberg, 1998)(Teunissen et al., 2011).
As will be discussed in chapter 4, some ambiguity resolution methods developed for attitude determination make use of the described relationship between the first three and remaining $n-3$ ambiguities.

3) The fixed baseline solution is obtained using the estimated integer ambiguities. As the constraint that the solution of z has to be an integer ($\check{z} \in \mathbb{Z}^n, \check{b} = \hat{b}(\check{z}) \in \mathbb{R}^3$) is applied, the minimum solution becomes:

$$\|y^{DD} - A\check{z} - G\check{b}\|^2_{Q_{yy}} = \|\check{e}\|^2_{Q_{yy}} = \|\hat{e}\|^2_{Q_{yy}} + \|\hat{z} - \check{z}\|^2_{Q_{\hat{z}\hat{z}}} \tag{3.45}$$

The minimum of this equation is clearly equal to or larger than the float solution Eq. (3.42). The residual $\hat{z} - \check{z}$ is used to adjust the float solution $\hat{b}$ of the first step, which is $\check{b} = \hat{b}(\check{z})$. This final fixed baseline solution is obtained as:

$$\check{b} = \hat{b}(\check{z}) = \hat{b} - Q_{\hat{b}\hat{z}} Q^{-1}_{\hat{z}\hat{z}} (\hat{z} - \check{z}) \tag{3.46}$$

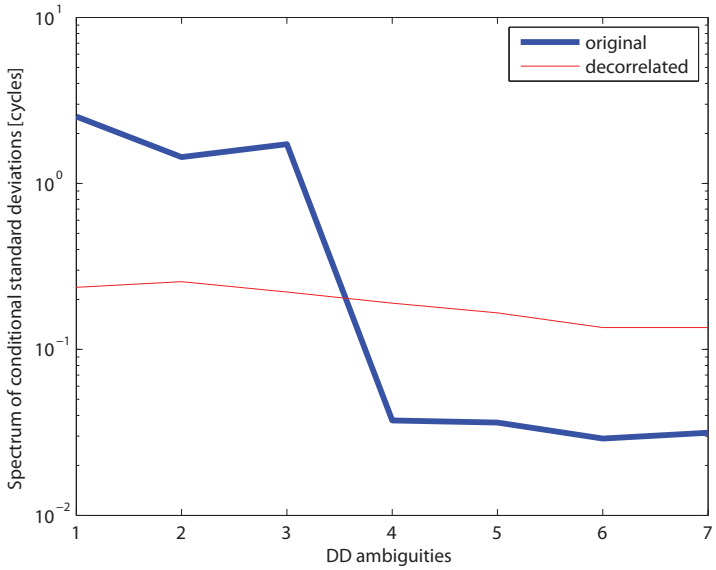


Figure 3.4: Spectrum of conditional standard deviations of the DD float ambiguities

This equation shows the relation that exists between the float and fixed solution, $\hat{b}$ and $\check{b}$. It shows that the difference between the two baseline estimates depends on the difference between float and the fixed least-squares ambiguity estimate $\hat{z}$ and $\check{z}$. Then, by applying the variance propagation law, the v-c matrix for the least-squares solution for b assuming that z is known and therefore deterministic, becomes:

$$Q_{\check{b}\check{b}} = Q_{\hat{b}(z)\hat{b}(z)} = Q_{\hat{b}\hat{b}} - Q_{\hat{b}\hat{z}}Q_{\hat{z}\hat{z}}^{-1}Q_{\hat{z}\hat{b}} \tag{3.47}$$

This fixed baseline estimate is much more accurate (as $Q_{\check{b}\check{b}} < Q_{\hat{b}\hat{b}}$) than the float solution as long as the ambiguities are fixed correctly. However if the ambiguities are fixed incorrectly, the result might be that the fixed solution is worse than the float solution. Therefore a validation method as described in section 3.4.3 is required in order to be sure that only correctly fixed ambiguities are used.

Intermezzo Next, the difference between $Q_{\check{b}\check{b}}$ and $Q_{\hat{b}\hat{b}}$ is quantified. The design matrices A and G and the v-c matrix Q_{yy} can be written as:

$$A = \begin{bmatrix} \lambda_f I_n \\ 0 \end{bmatrix} \qquad G = \begin{bmatrix} U \\ U \end{bmatrix} \qquad Q_{yy} = \begin{bmatrix} \sigma_\phi^2 Q & 0 \\ 0 & \sigma_p^2 Q \end{bmatrix} \tag{3.48}$$

where λ_f is the carrier wavelength, U is the differenced line-of-sight vectors, Q is variance matrix of the DD phase and code observations.

The v-c matrix given in Eq. (3.41) can be rewritten as

$$\begin{bmatrix} Q_{\hat{z}\hat{z}} & Q_{\hat{z}\hat{b}} \\ Q_{\hat{b}\hat{z}} & Q_{\hat{b}\hat{b}} \end{bmatrix} = \begin{bmatrix} A^T Q_{yy}^{-1} A & A^T Q_{yy}^{-1} G \\ G^T Q_{yy}^{-1} A & G^T Q_{yy}^{-1} G \end{bmatrix}^{-1} \tag{3.49}$$

By applying the mathematical properties described in Appendix D.4, the projectors P_A and P_G and the orthogonal projectors $P_A^{\perp}$ and $P_G^{\perp}$, the following v-c matrices are obtained:

$$\begin{aligned} Q_{\hat{z}\hat{z}} &= [A^T Q_{yy}^{-1} A - A^T Q_{yy}^{-1} G [G^T Q_{yy}^{-1} G]^{-1} G^T Q_{yy}^{-1} A]^{-1} \\ &= [\overline{A}^T Q_{yy}^{-1} \overline{A}]^{-1} \\ Q_{\hat{z}\hat{b}} &= -[A^T Q_{yy}^{-1} A]^{-1} A^T Q_{yy}^{-1} G [\overline{G}^T Q_{yy}^{-1} \overline{G}]^{-1} \\ Q_{\hat{b}\hat{z}} &= Q_{\hat{z}\hat{b}}^T \\ Q_{\hat{b}\hat{b}} &= [\overline{G}^T Q_{yy}^{-1} \overline{G}]^{-1} \end{aligned} \tag{3.50}$$

where

$$\begin{aligned} \overline{G} &= P_A^{\perp} G = [I - P_A] G = [I - A[A^T Q_{yy}^{-1} A]^{-1} A^T Q_{yy}^{-1}] G \\ \overline{A} &= P_G^{\perp} A = [I - P_G] A = [I - G[G^T Q_{yy}^{-1} G]^{-1} G^T Q_{yy}^{-1}] A \end{aligned} \tag{3.51}$$

and P_A and P_G are projectors that project orthogonally onto the range space of A and G, respectively.

By substituting Eq. (3.48) into Eq. (3.50), the precision of the float solution $\hat{z}$ can be related to the precision of the code and carrier observations:

$$Q_{\hat{z}\hat{z}} = \frac{\sigma_p^2}{\lambda_f^2} \left(\frac{\sigma_\phi^2}{\sigma_p^2} Q + U (U^T Q^{-1} U)^{-1} U^T \right) \approx \frac{\sigma_p^2}{\lambda_f^2} \left(U (U^T Q^{-1} U)^{-1} U^T \right) \tag{3.52}$$

As described in section 2.6.2, the code observations are typically hundred times less accurate than the carrier phase, thus $\frac{\sigma_\phi^2}{\sigma_p^2} \approx 10^{-4}$, it is clear that the precision of the float solution $\hat{z}$ is driven by the less precise code observations.

Furthermore, it can be shown that the precision of the baseline float solution $\hat{b}$ is only driven by the precision of the code observations:

$$Q_{\hat{b}\hat{b}} = \sigma_p^2 (U^T Q^{-1} U)^{-1} \tag{3.53}$$

The conditional baseline variance matrix can be derived by applying Eq. (3.47) as:

$$Q_{\check{b}\check{b}} = Q_{\hat{b}(z)\hat{b}(z)} = [G^T Q_{yy}^{-1} G]^{-1} = \frac{\sigma_\phi^2}{1 + \sigma_p^2} \left(U^T Q^{-1} U \right)^{-1} \approx \sigma_\phi^2 \left(U^T Q^{-1} U \right)^{-1} \tag{3.54}$$

This shows that the precision of the conditional baseline solution is driven by the much more precise carrier phase observations, where $Q_{\hat{b}\hat{b}}$ was driven by the code observations.

Multi-frequency Similar to the single frequency model described in the previous section, the DD multi-frequency observation equations can be written for a single baseline as a system of linearized observation equations:

$$
\begin{aligned}
E\begin{bmatrix} y_{L_1}^{DD} \\ \vdots \\ y_{N_f}^{DD} \end{bmatrix} &= \begin{bmatrix} A_{L_1} & \dots & 0 \\ \vdots & \ddots & \vdots \\ 0 & \dots & A_{L_{N_f}} \end{bmatrix} \begin{bmatrix} z_{L_1} \\ \vdots \\ z_{L_{N_f}} \end{bmatrix} + (e_{2N_f} \otimes G)b \\
&= \left(\begin{bmatrix} \Lambda \\ \mathbf{0} \end{bmatrix} \otimes I_{n-1} \right) \begin{bmatrix} z_{L_1} \\ \vdots \\ z_{L_{N_f}} \end{bmatrix} + (e_{2N_f} \otimes G)b \qquad (3.55) \\
D\begin{bmatrix} y_{L_1}^{DD} \\ \vdots \\ y_{N_f}^{DD} \end{bmatrix} &= P_{L_1 \dots L_{N_f}} \otimes Q_{yy}
\end{aligned}
$$

where e_{2N_f} is a vector containing only ones with dimension $2N_f$, A_{L_i} is a design matrix containing L_i wavelengths that links the data vector to the unknown vector z_{L_i}, $z = \begin{bmatrix} z_{L_1}, \dots, z_{L_{N_f}} \end{bmatrix}^T$ and Λ is the diagonal matrix of wavelengths: $\Lambda = diag\left(\lambda_1, \dots, \lambda_{N_f}\right)$.

The variance matrix of y_{L_i} is given by the positive definite matrix Q_{yy} which is assumed to be known and there is assumed to be no cross correlation between the frequencies.

The set of linear observation equations is again solved by applying the ILS principle for which the solution:

$$
\min_{z \in \mathbb{Z}^{n \times N_f}, b \in \mathbb{R}^3} \left\| \begin{matrix} y_{L_1}^{DD} - A_{L1} z_{L_1} - Gb \\ \vdots \\ y_{L_{N_f}}^{DD} - A_{L_{N_f}} z_{L_{N_f}} - Gb \end{matrix} \right\|^2_{P_{L_1 \dots L_{N_f}} \otimes Q_{yy}} \qquad (3.56)
$$

can be obtained from the following three steps:
1) First the so-called float solution $\hat{z}$ and $\hat{b}$ is obtained, i.e. the least-squares solution disregarding the integer nature of the ambiguities:

$$
\begin{bmatrix} \hat{z}_{L_1} \\ \vdots \\ \hat{z}_{L_{N_f}} \\ \hat{b} \end{bmatrix} = \begin{bmatrix} & Q_{\hat{z}\hat{z}} & & Q_{\hat{z}_{L_1}\hat{b}} \\ & & & \vdots \\ & & & Q_{\hat{z}_{L_{N_f}}\hat{b}} \\ Q_{\hat{b}\hat{z}_{L_1}} & \dots & Q_{\hat{b}\hat{z}_{L_{N_f}}} & Q_{\hat{b}\hat{b}} \end{bmatrix} M^T (P^{-1}_{L_1 \dots L_{N_f}} \otimes Q^{-1}_{yy}) \begin{bmatrix} y_{L_1}^{DD} \\ \vdots \\ y_{L_{N_f}}^{DD} \end{bmatrix} \qquad (3.57)
$$

with

$$
M = \begin{bmatrix} A_{L_1} & \dots & 0 & G \\ \vdots & & & \vdots \\ 0 & \dots & A_{L_{N_f}} & G \end{bmatrix} \qquad (3.58)
$$

The associated v-c matrix is derived as:

$$\begin{bmatrix} & Q_{\hat{z}\hat{z}} & & Q_{\hat{z}_{L_1}\hat{b}} \\ & & & \vdots \\ & & & Q_{\hat{z}_{L_{N_f}}\hat{b}} \\ Q_{\hat{b}\hat{z}_{L_1}} & \cdots & Q_{\hat{b}\hat{z}_{L_{N_f}}} & Q_{\hat{b}\hat{b}} \end{bmatrix} = \left[M^T (P^{-1}_{L_1 \ldots L_{N_f}} \times Q^{-1}_{yy}) M \right]^{-1} \tag{3.59}$$

and

$$Q_{\hat{z}\hat{z}} = \begin{bmatrix} Q_{\hat{z}_{L_1}\hat{z}_{L_1}} & \cdots & Q_{\hat{z}_{L_1}\hat{z}_{L_{N_f}}} \\ \vdots & & \vdots \\ Q_{\hat{z}_{L_{N_f}}\hat{z}_{L_1}} & \cdots & Q_{\hat{z}_{L_{N_f}}\hat{z}_{L_{N_f}}} \end{bmatrix} \tag{3.60}$$

From $Q_{\hat{z}\hat{z}}$ it is obvious that, although the observations on the two frequencies were assumed to be uncorrelated, the ambiguities are not. This will be important later on when we combine the unconstrained baseline between platforms with information from constrained baselines at the platforms.
2) We solve the vector of integer least-squares estimates of the ambiguities $\check{z}$:

$$\begin{bmatrix} \check{z}_{L_1} \\ \vdots \\ \check{z}_{L_{N_f}} \end{bmatrix} = \arg \left(\min_{z \in \mathbb{Z}^{n \otimes N_f}} \left\| \begin{matrix} \hat{z}_{L_1} - z_{L_1} \\ \vdots \\ \hat{z}_{L_{N_f}} - z_{L_{N_f}} \end{matrix} \right\|^2_{Q_{\hat{z}\hat{z}}} \right) \tag{3.61}$$

3) The fixed baseline solution is obtained by using the estimated integer ambiguities, similar to Eq. (3.46).

3.3.2.2 Model using Code, Carrier and Doppler Observations

In the previous section, the standard relative positioning models were introduced using two types of observations: code and carrier phase. In this section, a model is introduced that makes use of these two observations plus Doppler. The general DD observation equations were derived in section 2.4. As said before the pseudo range observations can have an accuracy of decimeters and the carrier phase observations have accuracies down to millimeter level. The Doppler observations have an accuracy worse than carrier phase but normally better than centimeter level (see sections 2.3.2 and 2.6.4).
The model described by the Eq. (2.96) - (2.99) as developed in section 2.4.3 and again assuming that either the atmospheric delays are corrected apriori or are negligible due to the short baseline setup, becomes:

$$\triangle P^{1s}_{12,f} = \quad - \mathbf{u}^{1s}_2 \triangle \mathbf{r}_{12} - \dot{\rho}^{1s}_1 \triangle \zeta_1 + \dot{\rho}^{1s}_2 \triangle \zeta_2 + \epsilon^{1s}_{12,f} \tag{3.62}$$

$$\triangle \Phi^{1s}_{12,f} = \quad - \mathbf{u}^{1s}_2 \triangle \mathbf{r}_{12} - \dot{\rho}^{1s}_1 \triangle \zeta_1 + \dot{\rho}^{1s}_2 \triangle \zeta_2 + \lambda_f z^{1s}_{12,f} + \varepsilon^{1s}_{12,f} \tag{3.63}$$

$$\triangle D^{1s}_{12,f} = \quad - \mathbf{u}^{1s}_2 \triangle \dot{\mathbf{r}}_{12} - \dot{\mathbf{u}}^{1s}_2 \triangle \mathbf{r}_{12} - \dot{\rho}^{1s}_1 \triangle \dot{\zeta}_1 + \dot{\rho}^{1s}_2 \triangle \dot{\zeta}_2 + \dot{\varepsilon}^{1s}_{12,f} \tag{3.64}$$

In the Doppler equation, the range rate rate is ignored as it was shown in section 2.3 that the user acceleration is required to determine this term. Compared with the model developed in section 3.3.2.1, for code and carrier phase the same number of DD observations is available but with two extra unknowns, namely the clock biases $\triangle\zeta_1$ and $\triangle\zeta_2$. Therefore this is a weaker model with consequently a lower expected success rate for ambiguity fixing. Another drawback of this model is that clock drifts $\triangle\dot{\zeta}_1$ and $\triangle\dot{\zeta}_2$ are not linearly independent from velocity, which is easy to see if the velocity terms are expressed in orbital coordinates: the clock drift cannot be uncoupled from the velocity along track of both the platforms.
A way to cope with these issues is to correct the code and carrier observations with the product of the clock biases $\triangle\zeta_1$ and $\triangle\zeta_2$ -which are known from the absolute navigation of both platforms (see section 3.2.2)- and the range rates $\dot{\rho}^{1s}_1$ and $\dot{\rho}^{1s}_2$ which are known from the absolute velocity estimation for both platforms in combination with the GNSS ephemeris. Moreover the Doppler observations can be corrected with the product of the clock drifts $\triangle\dot{\zeta}_1$ and $\triangle\dot{\zeta}_2$ and the range rates $\dot{\rho}^{1s}_1$ and $\dot{\rho}^{1s}_2$ both of which are known from the absolute velocity estimation for both platforms. The model then becomes:

$$\triangle P^{1s}_{12,f} + \dot{\rho}^{1s}_1 \triangle\zeta_1 - \dot{\rho}^{1s}_2 \triangle\zeta_2 = -\mathbf{u}^{1s}_2 \triangle \mathbf{r}_{12} + \epsilon^{1s}_{12,f} \tag{3.65}$$

$$\triangle \Phi^{1s}_{12,f} + \dot{\rho}^{1s}_1 \triangle\zeta_1 - \dot{\rho}^{1s}_2 \triangle\zeta_2 = -\mathbf{u}^{1s}_2 \triangle \mathbf{r}_{12} + \lambda_f z^{1s}_{12,f} + \varepsilon^{1s}_{12,f} \tag{3.66}$$

$$\triangle D^{1s}_{12,f} + \dot{\rho}^{1s}_1 \triangle\dot{\zeta}_1 - \dot{\rho}^{1s}_2 \triangle\dot{\zeta}_2 = -\mathbf{u}^{1s}_2 \triangle \dot{\mathbf{r}}_{12} - \dot{\mathbf{u}}^{1s}_2 \triangle \mathbf{r}_{12} + \dot{\varepsilon}^{1s}_{12,f} \tag{3.67}$$

Linearized Double-Difference Model The double-difference (DD) observation equations can be written as

$$\begin{aligned} E(P^{1s}_{12,f}(t)) &= \rho^{1s}_{12}(t) && (3.68)\\ E(\Phi^{1s}_{12,f}(t)) &= \rho^{1s}_{12}(t) + \lambda_f z^{1s}_{12,f} && (3.69)\\ E(D^{1s,f}_{12}(t)) &= \dot{\rho}^{1s}_{12}(t) && (3.70) \end{aligned}$$

The linearized DD observation equations read (Buist et al., 2010b)

$$\begin{aligned} E(\Delta P^{1s}_{12,f} + \dot{\rho}^{1s}_1 \triangle\zeta_2 - \dot{\rho}^{1s}_2 \triangle\zeta_2) &= g^{1s^T}_1 \mathbf{b} && (3.71)\\ E(\Delta \Phi^{1s}_{12,f} + \dot{\rho}^{1s}_1 \triangle\zeta_1 - \dot{\rho}^{1s}_2 \triangle\zeta_2) &= g^{1s^T}_1 \mathbf{b} + \lambda_f z^{1s}_{12,f} && (3.72)\\ E(\Delta D^{1s}_{12,f} + \dot{\rho}^{1s}_1 \triangle\dot{\zeta}_1 - \dot{\rho}^{1s}_2 \triangle\dot{\zeta}_2) &= (\dot{g}^{1s}_1)^T \mathbf{b} + g^{1s^T}_1 \dot{\mathbf{b}} && (3.73) \end{aligned}$$

where

$$\Delta P^{1s}_{12,f} = p^{1s}_{12,f} - \rho^{1s-}_{12}(t), \tag{3.74}$$
$$\Delta \Phi^{1s}_{12,f} = \phi^{1s}_{12,f} - \rho^{1s-}_{12}(t), \tag{3.75}$$
$$\Delta D^{1s}_{12,f} = D^{1s}_{12,f} - \dot{\rho}^{1s-}_{12}(t), \tag{3.76}$$
$$g^{1s}_1 = \mathbf{u}^1_1(t) - \mathbf{u}^s_1(t) \tag{3.77}$$
$$\dot{g}^{1s}_1 = \dot{\mathbf{u}}^1_1(t) - \dot{\mathbf{u}}^s_1(t) \tag{3.78}$$

The vectorial form of the DD observation equation for the ith baseline and the fth frequency read

$$E(\upsilon^{DD}_{P;corr}) = G_1\mathbf{b} \tag{3.79}$$
$$E(\upsilon^{DD}_{\phi;corr}) = G_1\mathbf{b} + \lambda_f I_n z_{12,f} \tag{3.80}$$
$$E(\upsilon^{DD}_{D;corr}) = \dot{G}_1\mathbf{b} + G_1\dot{\mathbf{b}} \tag{3.81}$$

with $\upsilon^{DD}_{P;corr} = [\Delta P^{12}_{12,f} + \dot{\rho}^{12}_1\triangle\zeta_1 - \dot{\rho}^{12}_2\triangle\zeta_2 \ \ldots \ \Delta P^{1(n+1)}_{12,f} + \dot{\rho}^{1(n+1)}_1\triangle\zeta_1 - \dot{\rho}^{1(n+1)}_2\triangle\zeta_2]^T$, $\upsilon^{DD}_{\Phi;corr} = [\Delta \Phi^{12}_{12,f} + \dot{\rho}^{12}_1\triangle\zeta_1 - \dot{\rho}^{12}_2\triangle\zeta_2 \ \ldots \ \Delta \Phi^{1(n+1)}_{12,f} + \dot{\rho}^{1(n+1)}_1\triangle\zeta_1 - \dot{\rho}^{1(n+1)}_2\triangle\zeta_2]^T$, $\upsilon^{DD}_{D;corr} = [\Delta D^{12}_{12,f} + \dot{\rho}^{12}_1\triangle\zeta_1 - \dot{\rho}^{12}_2\triangle\zeta_2 \ \ldots \ \Delta D^{1(n+1)}_{12,f} + \dot{\rho}^{1(n+1)}_1\triangle\zeta_1 - \dot{\rho}^{1(n+1)}_2\triangle\zeta_2]^T$, $G_1 = [g^2_1 \ \ldots \ g^{n+1}_1]^T$, $\dot{G}_1 = [\dot{g}^2_1 \ \ldots \ \dot{g}^{n+1}_1]^T$, and $z_{12,f} = [z^{12}_{12,f} \ \ldots \ z^{1(n+1)}_{12,f}]^T$. Arranging the observations, the observation model of the baseline then reads

New DD model for short baseline

$$E(\upsilon^{DD}_{corr}) = Az + \Gamma\beta, \quad z \in \mathbb{Z}^{n\times N_f}, \ \beta \in \mathbb{R}^6 \tag{3.82}$$

In this section, a new notation is introduced that will allow us to use the notation of the general model as developed in section 3.3.2.1. y^{DD} was the vector of observed minus computed DD carrier phases and code observations of the order $m = 2n$, here the vector υ^{DD}_{corr} of observed minus computed DD carrier phases, code and Doppler observations is used -corrected for receiver clock biases and drifts- of the order $m = 3n$. β contains the baseline vector b of order three, and its derivative $\dot{b}$, which is the relative velocity between the two platforms, thus $\beta = [b, \dot{b}]^T$. Γ is the geometry matrix containing normalized line-of-sight vectors $\mathbf{U}^{DD}_r$ and its derivative $\dot{\mathbf{U}}^{DD}_r$: $\Gamma = \begin{bmatrix} \mathbf{U}^{DD}_r & 0 \\ \mathbf{U}^{DD}_r & 0 \\ \dot{\mathbf{U}}^{DD}_r & \mathbf{U}^{DD}_r \end{bmatrix}$. A is the original design matrix that links the data vector to the unknown vector z. It is important to note that the ambiguities are again integers and therefore z and β are ($z \in \mathbb{Z}^n, \beta \in \mathbb{R}^6$) with $\mathbb{Z}$ being the dimensional space of integers.

The construction of the linearized DD model for baseline between platforms is summarized as:

1. Calculate the observed-minus-computed observations defined in Eq. (3.74) and Eq. (3.75).

2. Compute geometry vectors (difference of unit line-of-sight vectors) defined in Eq. (3.77).

3. Construct DD observation model for each baseline in Eq. (3.79), Eq. (3.80) and Eq. (3.81).

4. Construct baseline model in Eq. (3.82).

5. Construct the corresponding dispersion matrix.

The least-squares criterion for the unconstrained problem reads as:

$$\min_{z\in\mathbb{Z}^n,\beta\in\mathbb{R}^6} \|v^{DD} - Az - \Gamma\beta\|^2_{Q_{vv}} \tag{3.83}$$

Now, again the ILS can be obtained from the three steps as described in section 3.3.2.1.

Intermezzo For later use, two variations on model described in Eq. (3.82) are introduced here. In the first, the observations are not corrected for large receiver clock offsets:

New DD model for short baseline 2

$$E(v^{DD}) = Az + \Gamma\beta, \quad z \in \mathbb{Z}^{n\times N_f},\ \beta \in \mathbb{R}^6 \tag{3.84}$$

with $v^{DD}_{P;} = [\Delta P^{12}_{12,f} \ \dots \ \Delta P^{1(n+1)}_{12,f}]^T$, $v^{DD}_{\Phi;} = [\Delta \Phi^{12}_{12,f} \ \dots \ \Delta \Phi^{1(n+1)}_{12,f}]^T$, $v^{DD}_{D;} = [\Delta D^{12}_{12,f} \ \dots \ \Delta D^{1(n+1)}_{12,f}]^T$.

In the second variation, the code and carrier phase observations are corrected for large clock offsets (using the clock bias and absolute velocity estimated by the new SPP using code and Doppler observations as described in section 3.2.2), but the Doppler observations are not utilized for relative positioning:

New DD model for short baseline 3

$$E(y^{DD}_{corr}) = Az + Gb, \quad z \in \mathbb{Z}^{n\times N_f},\ b \in \mathbb{R}^3 \tag{3.85}$$

with $y^{DD}_{P;corr} = [\Delta P^{12}_{12,f} + \dot\rho^{12}_1 \triangle\zeta_1 - \dot\rho^{12}_2 \triangle\zeta_2 \ \dots \ \Delta P^{1(n+1)}_{12,f} + \dot\rho^{1(n+1)}_1 \triangle\zeta_1 - \dot\rho^{1(n+1)}_2 \triangle\zeta_2]^T$, $y^{DD}_{\Phi;corr} = [\Delta \Phi^{12}_{12,f} + \dot\rho^{12}_1 \triangle\zeta_1 - \dot\rho^{12}_2 \triangle\zeta_2 \ \dots \ \Delta \Phi^{1(n+1)}_{12,f} + \dot\rho^{1(n+1)}_1 \triangle\zeta_1 - \dot\rho^{1(n+1)}_2 \triangle\zeta_2]^T$.

3.3.3 Multi-epoch Solution

3.3.3.1 Model using Code and Carrier Observations

Especially for single epoch, single frequency observations, the model described by Eq. (3.38) is often not strong enough to fix the ambiguities. In which case, one might consider a multi-epoch solution which will improve the accuracy of the float solution and therefore increase the probability of fixing the correct integer vector. When observations from N_e epochs are available, the model described by Eq. (3.40) can be written as (Giorgi and Teunissen, 2009)(Giorgi et al., 2010):

$$\begin{aligned} E\begin{bmatrix} y_1^{DD} \\ y_2^{DD} \\ \vdots \\ y_{N_e}^{DD} \end{bmatrix} &= \begin{bmatrix} A & G_1 & 0 & \dots & 0 \\ A & 0 & G_2 & \dots & \vdots \\ \vdots & & & \ddots & 0 \\ A & 0 & \dots & 0 & G_{N_e} \end{bmatrix} \begin{bmatrix} z_{N_e} \\ b_1 \\ \vdots \\ b_{N_e} \end{bmatrix} = M_{N_e} \begin{bmatrix} z_{N_e} \\ b_1 \\ \vdots \\ b_{N_e} \end{bmatrix} \\ D\begin{bmatrix} y_1^{DD} \\ y_2^{DD} \\ \vdots \\ y_{N_e}^{DD} \end{bmatrix} &= I_{N_e} \otimes Q_{yy} \end{aligned} \tag{3.86}$$

where z_{N_e} is ambiguity float solution obtained using observations from N_e-epochs.
In this model, every epoch is considered independent from previous and following epochs, so there is no time correlation, in the stochastic model. The model holds as long as no cycle slips and changes in the number of tracked GNSS satellites occur.

The associated v-c matrix for this multi-epoch float solution is derived as:

$$\begin{bmatrix} Q_{\hat{z}_{N_e}\hat{z}_{N_e}} & Q_{\hat{z}_{N_e}\underline{\hat{b}}} \\ Q_{\underline{\hat{b}}\hat{z}_{N_e}} & Q_{\underline{\hat{b}}\underline{\hat{b}}} \end{bmatrix} = \begin{bmatrix} & M_{N_e}^T (I_{N_e} \otimes Q_{yy}^{-1}) M_{N_e} \end{bmatrix}^{-1} \tag{3.87}$$

where $Q_{\underline{\hat{b}}\underline{\hat{b}}}$ is the $3N_e \times 3N_e$ v-c matrix for the float baseline estimates of N_e epochs:

$$Q_{\underline{\hat{b}}\underline{\hat{b}}} = \begin{bmatrix} Q_{\hat{b}_1\hat{b}_1} & Q_{\hat{b}_1\hat{b}_2} & \dots & Q_{\hat{b}_1\hat{b}_{N_e}} \\ Q_{\hat{b}_2\hat{b}_1} & Q_{\hat{b}_2\hat{b}_2} & \dots & Q_{\hat{b}_2\hat{b}_{N_e}} \\ \vdots & & \ddots & \vdots \\ Q_{\hat{b}_{N_e}\hat{b}_1} & Q_{\hat{b}_{N_e}\hat{b}_2} & \dots & Q_{\hat{b}_{N_e}\hat{b}_{N_e}} \end{bmatrix} \tag{3.88}$$

and

$$Q_{\hat{z}_{N_e}\underline{\hat{b}}} = \begin{bmatrix} Q_{\hat{z}_{N_e}\hat{b}_1} & Q_{\hat{z}_{N_e}\hat{b}_2} & \dots & Q_{\hat{z}_{N_e}\hat{b}_{N_e}} \end{bmatrix} \tag{3.89}$$

The notation $(\underline{\cdot})$ is introduced to distinguish between this v-c matrix and the single epoch v-c matrix.

The sum-of-squares decomposition of the squared norm of the residuals is obtained for the multi-epoch model Eq. (3.86) as:

$$\begin{aligned}\left\| \begin{matrix} y_1^{DD} - Az_1 - G_1 b_1 \\ \vdots \\ y_{N_e}^{DD} - Az_{N_e} - G_{N_e} b_{N_e} \end{matrix} \right\|^2_{I_{N_e} \otimes Q_{yy}} &= \left\| \begin{matrix} \hat{e}_1 \\ \vdots \\ \hat{e}_{N_e} \end{matrix} \right\|^2_{I_{N_e} \otimes Q_{yy}} + \\ &+ \|\hat{z}_{N_e} - z\|^2_{Q_{\hat{z}_{N_e}\hat{z}_{N_e}}} + \left\| \begin{matrix} \hat{b}_1(z) - b_1 \\ \vdots \\ \hat{b}_{N_e}(z) - b_{N_e} \end{matrix} \right\|^2_{Q_{\underline{\hat{b}}(z)\underline{\hat{b}}(z)}}\end{aligned} \tag{3.90}$$

where the baseline solution assuming the integer ambiguities z as known is applied:

$$\begin{bmatrix} \hat{b}_1(z) \\ \hat{b}_2(z) \\ \vdots \\ \hat{b}_{N_e}(z) \end{bmatrix} = \begin{bmatrix} \hat{b}_1 \\ \hat{b}_2 \\ \vdots \\ \hat{b}_{N_e} \end{bmatrix} - Q_{\underline{\hat{b}}\hat{z}_{N_e}} Q^{-1}_{\hat{z}_{N_e}\hat{z}_{N_e}} (\hat{z}_{N_e} - z) \tag{3.91}$$

with

$$Q_{\underline{\hat{b}}(z)\underline{\hat{b}}(z)} = Q_{\underline{\hat{b}}\underline{\hat{b}}} - Q_{\underline{\hat{b}}\hat{z}_{N_e}} Q^{-1}_{\hat{z}_{N_e}\hat{z}_{N_e}} Q_{\hat{z}_{N_e}\underline{\hat{b}}} \tag{3.92}$$

This last matrix has a block diagonal structure

$$Q_{\underline{\hat{b}}(z)\underline{\hat{b}}(z)} = \begin{bmatrix} Q_{\hat{b}_1(z)\hat{b}_1(z)} & 0 & \dots & 0 \\ 0 & Q_{\hat{b}_2(z)\hat{b}_2(z)} & \dots & 0 \\ \vdots & & \ddots & \vdots \\ 0 & 0 & \dots & Q_{\hat{b}_{N_e}(z)\hat{b}_{N_e}(z)} \end{bmatrix} \tag{3.93}$$

$$Q_{\underline{\hat{b}}_i(z)\underline{\hat{b}}_i(z)} = (G_i^T Q_{yy}^{-1} G_i)^{-1} \tag{3.94}$$

The least-squares criterion for this multi-baseline problem reads, written in the same form as Eq. (3.39), as:

$$\begin{aligned}\min_{z \in \mathbb{Z}^n, \underline{b} = \left[b_1 \dots b_{N_e}\right] \in \mathbb{R}^{3 \times N_e}} \left\| \begin{matrix} y_1^{DD} - Az_{N_e} - G_1 b_1 \\ \vdots \\ y_{N_e}^{DD} - Az_{N_e} - G_{N_e} b_{N_e} \end{matrix} \right\|^2_{I_{N_e} \otimes Q_{yy}} &= \sum_{i=1}^{N_e} \|\hat{e}_i\|^2_{Q_{yy}} + \\ + \min_{z \in \mathbb{Z}^n, \underline{b} = \left[b_1 \dots b_{N_e}\right] \in \mathbb{R}^{3 \times N_e}} \left(\|\hat{z}_{N_e} - z\|^2_{Q_{\hat{z}_{N_e}\hat{z}_{N_e}}} + \sum_{i=1}^{N_e} \|\hat{b}_i(z) - b_i\|^2_{Q_{\underline{\hat{b}}_i(z)\underline{\hat{b}}_i(z)}} \right)\end{aligned} \tag{3.95}$$

Without a constraint on the baseline length (in chapter 4, the attitude model is introduced for which this assumption is not valid), the last term can be made zero for any ambiguity vector, and thus the minimizer is obtained by minimizing the second term by the LAMBDA method.
As the entries of $Q_{\hat{z}_{N_e}\hat{z}_{N_e}}$ for the multi-epoch solution are reduced compared to the single-epoch case, the probability of correctly fixing the integer ambiguity vector increases.

The baseline solutions can be obtained using the same approach as applied in Eq. (3.46):

$$\begin{bmatrix} \check{b}_1 \\ \check{b}_2 \\ \vdots \\ \check{b}_{N_e} \end{bmatrix} = \begin{bmatrix} \hat{b}_1(\check{z}_{N_e}) \\ \hat{b}_2(\check{z}_{N_e}) \\ \vdots \\ \hat{b}_{N_e}(\check{z}_{N_e}) \end{bmatrix} = \begin{bmatrix} \hat{b}_1 \\ \hat{b}_2 \\ \vdots \\ \hat{b}_{N_e} \end{bmatrix} - Q_{\underline{\hat{b}}\hat{z}_{N_e}} Q^{-1}_{\hat{z}_{N_e}\hat{z}_{N_e}} (\hat{z}_{N_e} - \check{z}) \tag{3.96}$$

The improvement using a multi-epoch solution compared to the single-epoch solution can be quantified. For the single-epoch model described by Eq. (3.38), the v-c matrix of the ambiguity float solution was derived as (see Eq. (3.50):

$$Q_{\hat{z}\hat{z}} = [\overline{A}^T Q_{yy}^{-1} \overline{A}]^{-1} \tag{3.97}$$

The multi-epoch model described by Eq. (3.86), under the assumption that the geometry between the user and GNSS satellites does not change, can be rewritten to:

$$\begin{aligned} E \begin{bmatrix} y_1^{DD} \\ y_2^{DD} \\ \vdots \\ y_{N_e}^{DD} \end{bmatrix} &= \left[e_{N_e} \otimes A\right] z_{N_e} + \left[I_{N_e} \otimes G\right] \begin{bmatrix} b_1 \\ \vdots \\ b_{N_e} \end{bmatrix} \\ D \begin{bmatrix} y_1^{DD} \\ y_2^{DD} \\ \vdots \\ y_{N_e}^{DD} \end{bmatrix} &= I_{N_e} \otimes Q_{yy} \end{aligned} \tag{3.98}$$

For this model,the v-c matrix of the ambiguity float solution can be derived as:

$$Q_{\hat{z}_{N_e}\hat{z}_{N_e}} = \frac{1}{N_e} [\overline{A}^T Q_{yy}^{-1} \overline{A}]^{-1} \tag{3.99}$$

So it is observed that the v-c matrix is scaled by $\frac{1}{N_e}$. Thus a multi-epoch solution based on four epochs has the same v-c matrix as a solution using observations with two times smaller standard deviations for both code and carrier.
Note that the assumption was made that the geometry does not change between the epochs. In reality, especially for space application where the user moves with high velocity, the geometry will change considerably making the multi-epoch solution even stronger.

3.3.3.2 Model using Code, Carrier and Doppler Observations

When code, carrier phase and Doppler observations from N_e epochs are available, the model described in section 3.3.2.2 by the Eq. (3.82) can be written as:

$$
\begin{aligned}
E\begin{bmatrix} v_1^{DD} \\ v_2^{DD} \\ \vdots \\ v_{N_e}^{DD} \end{bmatrix} &= \begin{bmatrix} A & \Gamma_1 & 0 & \dots & 0 \\ A & 0 & \Gamma_2 & \dots & 0 \\ \vdots & & & \ddots & \vdots \\ A & 0 & 0 & \dots & \Gamma_{N_e} \end{bmatrix} \begin{bmatrix} z \\ \beta_1 \\ \vdots \\ \beta_{N_e} \end{bmatrix} \\
D\begin{bmatrix} v_1^{DD} \\ v_2^{DD} \\ \vdots \\ v_{N_e}^{DD} \end{bmatrix} &= I_{N_e} \otimes Q_{vv}
\end{aligned}
\tag{3.100}
$$

This model does not include all the information as the change in baseline vector is depending on the baseline vectors at two consecutive epochs. This information could be included in the model as a system of constraints or as a pseudo observation.

3.4 Data Quality and Validation

Fig. 3.5 shows the data quality and validation process applied in this research. For precise relative navigation but also attitude determination it is important to use only data with a certain quality. The GNSS community has developed methods based on Receiver Autonomous Integrity Monitoring (RAIM) for integrity monitoring but also for exclusion of erroneous data. One example of such an approach is the DIA procedure which will be introduced next. The DIA procedure can be applied both in SPP and relative positioning, for the latter both on the float and fixed solution.
The fixed baseline estimate is only more accurate than the float solution as long as the ambiguities are fixed correctly. However if the ambiguities are fixed incorrectly, the result might be that the fixed solution is worse than the float solution. A lower bound of the probability of obtaining the correct integer ambiguity vector can be used to check apriori whether the ambiguity estimator guarantees sufficient success of obtaining the correct integer ambiguity vector. When the lower bound is lower than these values, no attempt is made to solve the ambiguities. After fixing the ambiguities, the ratio test is applied to validate the solution.

3.4.1 DIA procedure

Delft University of Technology has developed a method for quality control of GNSS data (Teunissen, 1990b). The DIA procedure, which stands for Detection, Identification and Adaptation, is commonly applied in GNSS data processing. In the DIA procedure the following three steps are applied:
1 *Detection*: The Local Overall Model (LOM) test statistic is calculated to detect if unspecified model errors have occurred

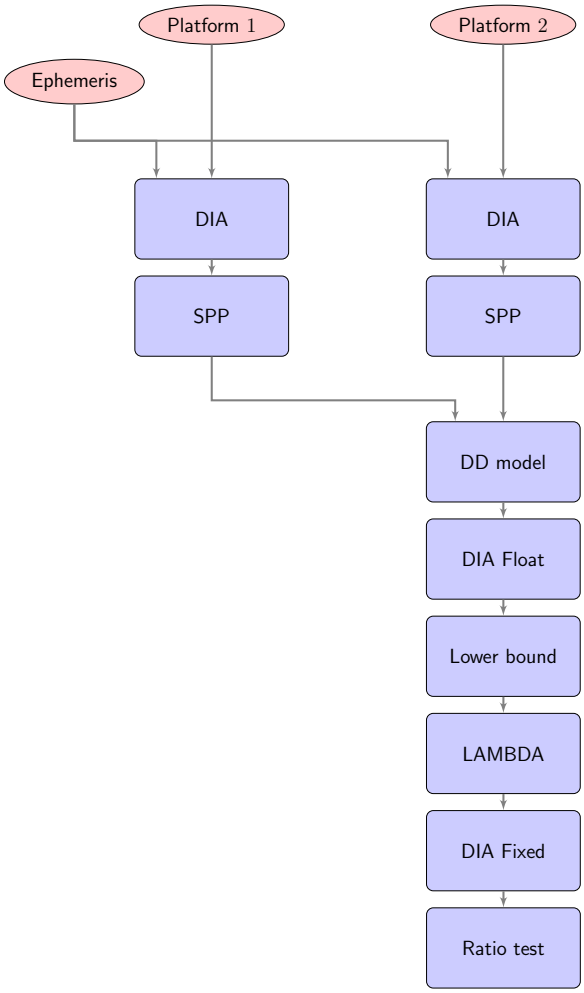


Figure 3.5: Data quality and validation

2 *Identification*: If the LOM test is not passed, potential model error(s) are identified
3 *Adaptation*: After identification of the most likely source for the model error, the observation model is adapted to eliminate the error source

The LOM equation at epoch *k* is:

$$T_{m-w} = \frac{\hat{e}_k^T Q_{yy}^{-1} \hat{e}_k}{m - w} \tag{3.101}$$

With Q_{yy} is the variance covariance matrix of observation y, $\hat{e}$ are the least-squares residuals, *m* is the number of observations, and *w* is the number of unknown parameters (see also discussion in section 2.5.3). The LOM test can be performed on the undifferenced, the single difference and double difference observations -which should all return the same test characteristic, see the discussion on Eq. (2.109) and (2.110)- for either the float or the fixed solution.
The main difference between the fixed and the float LOM test is the degree of freedom. Consider the example of 6 dual frequency observations, both code and carrier, and thus 24 single difference observations or 20 double difference observations. The single difference case has 17 unknowns (10 double difference ambiguities, position vector and code and

carrier clock error per frequency), the double difference case 13 unknowns (10 ambiguities and the position vector). Hence in both cases the float LOM test has 7 degrees of freedom. After fixing the ambiguities, the degrees of freedom for the double difference model is (20-3=)17, which is of course equivalent to the single difference model (with 24-7).
The LOM test statistic has a central F-distribution with $m_k - w_k$ degrees of freedom: $F_{\alpha_k}(m_k - w_k, \infty, 0)$ with α_k is the level of significance of the test. If the float LOM test is not passed, potential erroneous observations are identified. To identify the observation(s) that is (are) contaminated by model error(s), the so-called outlier test statistic is used:

$$t_i = \frac{c_i^T Q_{yy}^{-1} \hat{e}_k}{\sqrt{c_i^T Q_{yy}^{-1} Q_{\hat{e}\hat{e}} Q_{yy}^{-1} c_i}} \tag{3.102}$$

With the vector c_i is used to select the current observation and the following v-c matrices using the general notation of Eq. (2.2) and (2.3):

$$Q_{\hat{x}\hat{x}} = (A^T Q_{yy}^{-1} A)^{-1},\ Q_{\hat{y}\hat{y}} = A Q_{\hat{x}\hat{x}} A^T,\ Q_{\hat{e}\hat{e}} = Q_{yy} - Q_{\hat{y}\hat{y}} \tag{3.103}$$

The outlier test statistic is normally distributed. In order to identify all model errors, the procedure contains a cycle to identify all multiple error identifications. In this cycle, each time the LOM test statistic is updated after an erroneous observation is identified. This procedure is continued until the LOM test is passed -in which case the erroneous observation was eliminated from the solution- or the number of observations reaches the minimum acceptable number. This is a good approach if a large number of observations is available and only a limited number of observations contain outliers.

3.4.2 Lower bound success rate ambiguity resolution

The ambiguity success rate, i.e. probability of correct integer estimation, depends on three factors: the observation equations (functional model), the precision of the observations (the stochastic model), and the chosen method for ambiguity resolution (Teunissen, 1999). The theoretical success rate can be calculated once the functional and stochastic models are available, even before the actual measurements are obtained. As described in (Teunissen, 1998b), a lower bound of the probability of obtaining the correct integer ambiguity vector of dimension n, is:

$$P(\check{z} = z) \geq \prod_{i=1}^{n} \left(2\Phi(\frac{1}{2\sigma_{\hat{z}_{i|I}}} - 1) \right) \tag{3.104}$$

where $\Phi(x)$ is the cumulative normal distribution given as,

$$\int_{-\infty}^{x} \frac{1}{\sqrt{2\pi}} exp(-\frac{1}{2}z^2) dz \tag{3.105}$$

$\hat{z}_i$ stands for the i^{th} least-squares ambiguity, $\sigma_{\hat{z}_{i|I}}$ is the standard deviation of the i^{th} ambiguity obtained through a conditioning on the previous ambiguities. Hence from this equation it is clear that as the probability of obtaining the correct integer value increases as the standard deviation of $\hat{z}_{i|I}$ gets smaller. The diagonal entries of the variance-covariance matrix depends on the standard deviation of the observations and on the satellite-user geometry. The lower bound becomes sharper when it is applied to decorrelated ambiguities as utilized in the LAMBDA method. This lower bound can be used to check apriori whether the ambiguity estimator guarantees sufficient success of obtaining the correct integer ambiguity vector. When the lower bound is lower than these values, no attempt is made to solve the ambiguities.

3.4.3 Ratio Test on Resolved Ambiguities

Once the ambiguities are estimated, the ratio test can be applied to decide whether or not to accept the found integer solution (Teunissen and Verhagen, 2004). For the ratio test the best and second best integer solutions are utilized as follows;

Accept $\check{z}$ if

$$\frac{\|\hat{z} - \check{z}_2\|^2_{Q_{\hat{z}\hat{z}}}}{\|\hat{z} - \check{z}\|^2_{Q_{\hat{z}\hat{z}}}} \geq \mu, \mu \leq 1 \tag{3.106}$$

Where z is the ambiguity vector, $Q_{\hat{z}\hat{z}}$ is the v-c matrix of the float ambiguity vector $\hat{z}$, $\check{z}$ is the fixed ambiguity vector and μ is a threshold.
In this research, the traditional approach using a fixed threshold of 2 (Wei and Schwarz, 1995) is applied, which was found to give good results for multi-frequency (dual or more) data, after the low elevation satellites are eliminated with an elevation mask of 15 degrees (Buist, 2008).
In (Teunissen and Verhagen, 2004), it was shown that a model-dependent threshold value should be used rather than a fixed threshold value. The value is then determined based on a maximum allowable failure rate, to be chosen by the user. This failure rate is the probability of accepting the wrong ambiguity.
In (Verhagen and Teunissen, 2012), the model-driven ratio test is analysed and it is explained how a look-up table can be used to determine the appropriate threshold value depending on the user-defined failure rate, the number of ambiguities and the integer least-squares failure rate. The latter equals the failure rate without applying the ratio test, for which the upper bound can be used equal to $1 - P(\hat{z} = z)$, see Eq. (3.104).

3.5 Verification by simulation

In this section, ambiguity resolution for a single baseline configuration is analyzed by simulation. We will focus on single and dual frequency observations models using Eq. (3.38) to demonstrate that dual frequency observations are required for precise relative positioning using instantaneous ambiguity resolution.

Table 3.2: Single baseline simulation results for single-frequency, single-epoch success rates

N_{SV}	σ_ϕ=3 [mm]			σ_ϕ=1 [mm]		
	σ_p [cm]			σ_p [cm]		
	30	15	5	30	15	5
5	0.03	0.20	0.87	0.06	0.27	0.95
6	0.25	0.67	0.97	0.49	0.87	1.00
7	0.50	0.77	0.99	0.74	0.93	1.00
8	0.86	0.94	1.00	1.00	1.00	1.00

Table 3.3: Single baseline simulation results for dual-frequency, single-epoch success rates

N_{SV}	σ_ϕ=3 [mm]			σ_ϕ=1 [mm]		
	σ_p [cm]			σ_p [cm]		
	30	15	5	30	15	5
5	1.00	1.00	1.00	1.00	1.00	1.00
6	1.00	1.00	1.00	1.00	1.00	1.00
7	1.00	1.00	1.00	1.00	1.00	1.00
8	1.00	1.00	1.00	1.00	1.00	1.00

The simulation conditions are provided in Appendix A.1. The stochastic model does not apply elevation weighting and -as code and carrier phase noise- the same values as the simulations are used. The results are presented in two tables (Tables 3.2 and 3.3) containing empirical success rates as a function of the number of tracked satellites (N_{SV}) and the undifferenced phase and code noise (σ_ϕ, σ_p). The presented results are of the LAMBDA method applied to the single baseline for 3 and 1 mm undifferenced carrier phase noise. In Table 3.2 and Table 3.3 the results are for single and dual frequency models respectively, both for the most challenging instantaneous application. The empirical success rate is defined as the ratio of occurrences that the computed integer solution is equal to the known true integer vector.
For the weaker models (single frequency, larger code and phase noise), more than 8 GNSS satellites are required to obtain 100% success rates. Normally only if the lower bound of the success rate is higher than a certain threshold an attempt will be made to fix the ambiguities. In the tables, the cases are colored grey for which success rate are higher than a threshold of 95%. It has to be noted that for most applications a success rate of 95% will not be acceptable.
For the dual frequency case, even the weakest simulated model achieves 100% success rate. This result is as expected as dual frequency observations, which is a stronger model due to more redundancy, are generally required for precise relative positioning.

Time-To-Fix

In this section, Time-To-Fix (TTF) is defined as the number of epochs required to obtain a success rate of 100% for ambiguity resolution. TTF is an important number for real world applications as only after fixing the ambiguities, the higher accuracy of the carrier phase observations can be exploided. After the ambiguities are correctly fixed and as long as no cycle slips occur, the ambiguities vectors will not change. As was shown in Eq.

Table 3.4: Simulation results for single-frequency, single-epoch Time-To-Fix

N_{SV}	σ_ϕ=3 [mm]			σ_ϕ=1 [mm]		
	σ_p [cm]			σ_p [cm]		
	30	15	5	30	15	5
5	$\geq$36	$\geq$9	$\geq$1	$---Same---$		
6	$\geq$36	$\geq$9	$\geq$1			
7	36	9	1			
8	36	9	1			

(3.99), a multi-epoch solution based on four epochs has the same v-c matrix as a solution using observations with two times smaller standard deviations for both code and carrier phase observations.
Applying this relationship, an approximation of the Time-To-Fix will be provided based on the simulation results for relative positioning. Tables 3.4 show the expected Time-To-Fix for the simulation results presented in Table 3.2. It is observed that for the weakest models more than 30 epochs are required to fix the ambiguities.

3.6 Verification by hardware-in-the-loop and field experiments

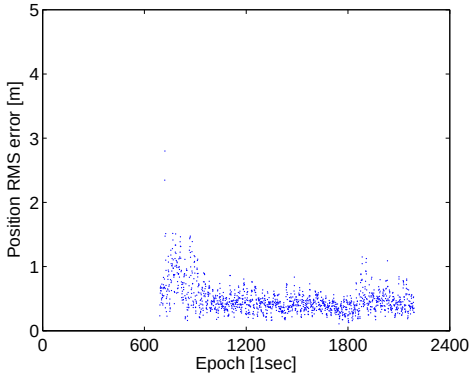
In the next section, we will discuss various cases in which the functional models described in this chapter could be applied. The emphasis is on the usefulness of including the Doppler observations in the functional model.

3.6.1 Satellite Formation Flying: PROBA-3

This section contains results obtained from a hardware-in-the-loop experiment for the PROBA-3 mission, described in detail in appendix A.7. This data is collected with non-dedicated receivers (Septentrio PolaRx2) with (section 3.6.2) and without (this section) an external reference clock. The later is important to enable analysis of data collected with GNSS receivers with large receiver clock biases and high dynamics to evaluate the functional model described in section 3.3.2.2. For this purpose, the GPS signal strength of the simulator was set about 5 dB above nominal resulting in a success rate of 100% for ambiguity fixing on the baseline between the platforms. The reference positions and velocities from the Spirent simulator are used to calculate absolute and relative position and velocity errors. For these simulations, ionospheric delays were not included. The relative distance between the two spacecraft is 150 meters.
First, the absolute positioning models using code observations (introduced in section 3.2.1) and code and Doppler observations (section 3.2.2) are analysed. The absolute position and velocity error are summarized in Table 3.5. The transformation from inertial to FNR frame is described in Appendix E.3, the definition of the FNR frame is shown in Fig. E.1.

3.6.1.1 Absolute positioning using code observations

Here results, Fig. 3.6(a), are analysed of absolute positioning using only code observations. As described in section 2.4 there are four unknowns and therefore at least that number of locked GNSS satellites are required to obtain a position estimation. In this experiment, the GPS receivers were initialised with a cold start. The initially locked GPS satellites are not of a favorable geometry, therefore the position error during the first 10 minutes is larger than the remaining epochs. The user velocity cannot be instantaneously calculated in this model and therefore is not included in the figure.



(a) Absolute Positioning Error

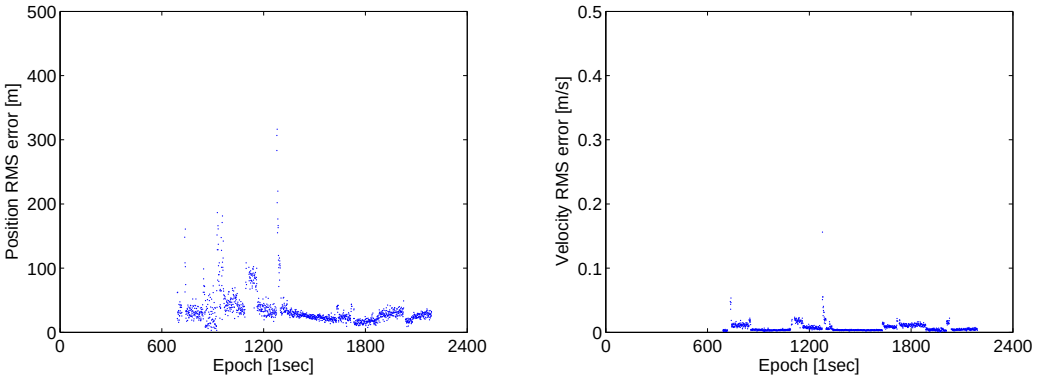
Figure 3.6: Results using code observations (PROBA-3)

3.6.1.2 Absolute positioning using Doppler observations

Next, the results of absolute positioning using only Doppler observations are analysed. As described in section 2.4, there are seven unknowns and therefore at least the same number of locked GNSS satellites are required to obtain a position estimation. If less than seven GNSS satellite are tracked, no solution is obtained.
For Doppler only positioning, the convergence of the least-squares is not guaranteed: we have to be careful with the initial value for position coordinates.
Figures 3.7(a) and 3.7(b) show the RMS error of the absolute position and velocity estimation using only Doppler observations. Note that scale on the y-axis in Fig. 3.7(a) is 100 $\times$ the scale of this axis in Fig. 3.6(a) and Fig. 3.8(a). The much lower accuracy is as expected as the Doppler based absolute positioning is known to be much less accurate.
By comparing Fig. 3.7(b) with Fig. 3.7(a), the influence of the absolute positioning error on the velocity estimation, as a direct consequence of the error in the line-of-sight vector, is clear.

3.6.1.3 Absolute Positioning using code and Doppler observations

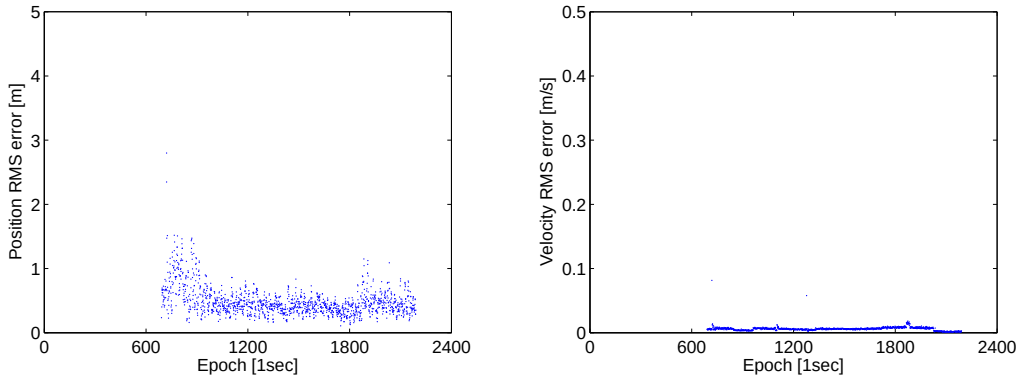
This last section contains the results of absolute positioning using both code and Doppler observations. As described in section 2.4 there are eight unknowns, but as both pseudo range and Doppler observations are collected at least four locked (if both code and Doppler



(a) Absolute Positioning Error (b) Absolute Velocity Error

Figure 3.7: Results using Doppler observations (PROBA-3)

are tracked) GNSS satellites are required to obtain a position, clock bias and velocity, clock drift estimation.
For the PolaRx2 receiver, the clock offset was at most 0.5 ms, which resulted in a small offset in the Nadir and Forward direction.
From Table 3.5, it is clear that the absolute positioning results is exactly the same as obtained with code observations. So, it can be concluded that the inclusion of the Doppler observations did not improve the absolute position accuracy. This can be explained by the weak relationship between the Doppler observations and position as was also observed in Fig. 3.7(a).
In this stronger model using both code and Doppler observations, the position and velocity errors have decreased compared to model using only Doppler observations (Fig. 3.8(a) and 3.8(b) vs. 3.7(a) and 3.7(b)).



(a) Absolute Positioning Error (b) Absolute Velocity Error

Figure 3.8: Results using both Pseudo range and Doppler observations (PROBA-3)

Table 3.5: Mean $\hat{\mu}$ and Standard deviation $\hat{\sigma}$ for the absolute positioning (PROBA-3)

		$\hat{\mu}$		$\hat{\sigma}$	
Observations	Coordinate	Position [m]	Velocity [m/s]	Position [m]	Velocity [m/s]
code	Forward	-0.34	-	0.15	-
	Right	0.06	-	0.18	-
	Nadir	-0.17	-	0.29	-
Doppler	Forward	-1.85	0.00	19.76	0.004
	Right	9.00	0.00	10.80	0.004
	Nadir	-12.02	0.00	40.81	0.008
code and Doppler	Forward	-0.34	-0.00	0.15	0.002
	Right	0.06	-0.00	0.18	0.002
	Nadir	-0.17	-0.00	0.29	0.004

3.6.1.4 Relative Positioning using standard DD model with code and carrier phase observations

Fig. 3.9 shows the clock offsets for the receivers obtained from the absolute position estimate for receiver 1 (Clk1) and receiver 2 (Clk2). It is observed that the clocks of the two receivers in this experiment behave very differently. The clock drift of Clk2 is much larger than the drift of Clk1. The clocks of the two receivers are controlled within 0.5 ms; if one of the two clock errors exceeds this threshold it is actively steered by the receiver.
Fig. 3.10(a) shows the error in the baseline estimation if the standard DD model, as described by Eq. (3.38), is applied. By comparing Fig. 3.9 and Fig. 3.10(a), it is observed that the baseline error is related to the relative clock error (described by Clk1-Clk2). But the relationship is not linear; there is a second effect in the baseline error that is related to the relative dynamics between the GNSS satellite and the user(s). This will be investigated next.
At the instant the clock is steered, also the baseline error is changing. The maximum baseline error is around 16 centimeter with the standard DD model and the error depends on the difference between clock offsets of the two receivers and the user dynamics. This results in a time-varying offset in the relative position or baseline estimate between the two receivers. Table 3.6 shows that the mean error $\hat{\mu}$ and standard deviation $\hat{\sigma}$ on the baseline estimate are 14.90 mm and 42.07 mm respectively.

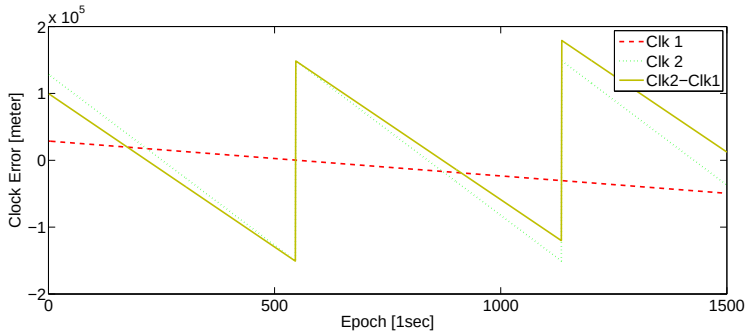


Figure 3.9: Clock errors (absolute and the difference) for the two GPS receivers (PROBA-3)

3.6.1.5 Relative Positioning using the proposed DD Model with code, carrier phase and Doppler Observations

In the presented result in Fig. 3.10(b), Fig. 3.10(c) and Fig. 3.10(d), the proposed DD Model is applied as described by Eq. (3.82). In Fig. 3.10(b) only corrections, based on clock error and range rate, are made for receiver 1, in Fig. 3.10(c) only for receiver 2 and in Fig. 3.10(d) for both receivers. As receiver 1 has only a small clock offset, in Fig. 3.10(b)

Table 3.6: Mean $\hat{\mu}$ and Standard deviation $\hat{\sigma}$ for the fixed baseline estimate [mm] (PROBA-3)

	$\hat{\mu}$	$\hat{\sigma}$
Standard Model	14.90	42.07
Proposed Model	0.05	0.70

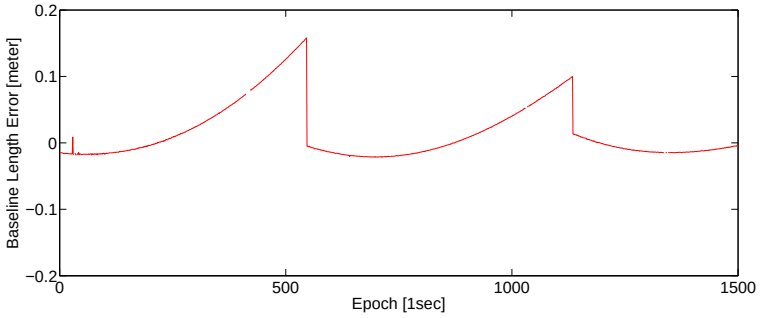
not much difference is observed compared to Fig. 3.10(a). Receiver 2 has a much larger time offset, therefore the baseline estimate in Fig. 3.10(c) is much improved and a small error - almost linearly depending on the clock offset of receiver 1 - becomes apparent. In Fig. 3.10(d), corrections are applied for both receivers and the time-varying offset error in the baseline estimate is completely removed. By comparing Fig. 3.10(d) with Fig. 3.10(a), it is concluded that the proposed DD model can correct the clock behavior and dynamics of the receivers well.

The results, if corrections from both receivers are applied, are summarized in Table 3.6. The mean error $\hat{\mu}$ and standard deviation $\hat{\sigma}$ on the baseline estimate are 0.05 mm and 0.7 mm respectively. So the mean of the error is almost zero and the standard deviation is approaching the theoretical limit of GNSS relative positioning. Inclusion of the Doppler observation did not improve the float solution, thus did not improve ambiguity resolution.

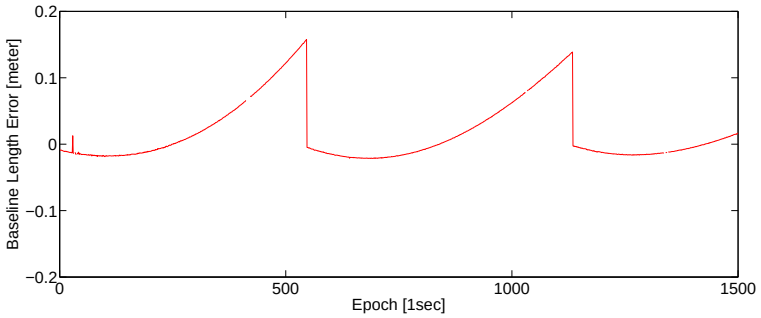
Next, the relative velocity estimation is analysed. Fig. 3.11(a) shows the true relative velocity based on the output of the Spirent simulator. Fig. 3.11(b) shows the relative velocity as estimated by the proposed model without (Eq. (3.84)), and Fig. 3.11(c) for the proposed model with the correction for large clock offsets (Eq. (3.82)).

For the standard model, offsets for all three velocity components are present. For the proposed model this offset is much reduced, however an offset in the forward direction is visible related to the clock offset (see Fig. 3.9) as the velocity estimation is coupled with the receiver clock offset and cannot be separated. This was discussed in section 2.3.1 as for the Doppler observations, the distinction between the Doppler effect from the relative motion and the clock drift at the receiver and/or the GNSS satellite cannot be made.

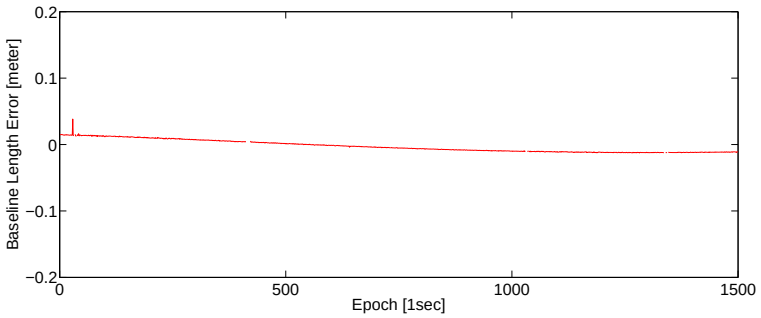
Fig. 3.11(d) shows the relative velocity obtained from differencing between adjacent elements of fixed baseline coordinates. It is clear that this is a more precise result than what was obtained from the Doppler observations using the standard and the proposed model.



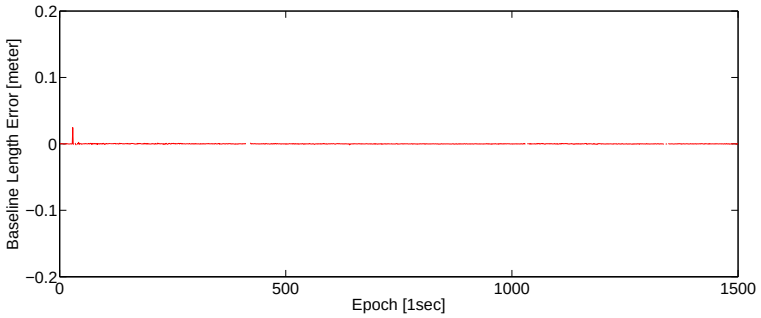
(a) Standard DD model



(b) Proposed DD model only for receiver 1

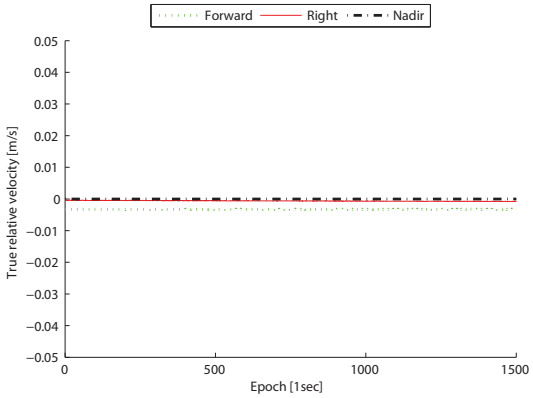


(c) Proposed DD model only for receiver 2

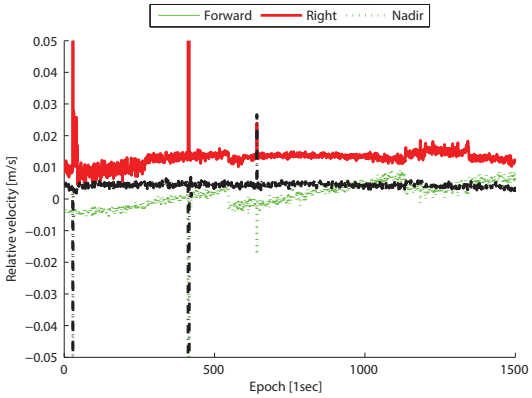


(d) Proposed DD model for both receivers

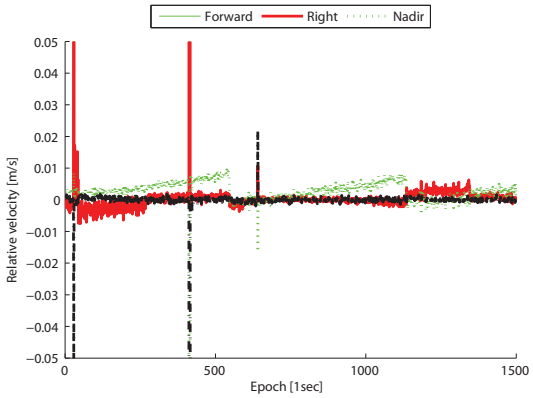
Figure 3.10: Baseline error (PROBA-3)



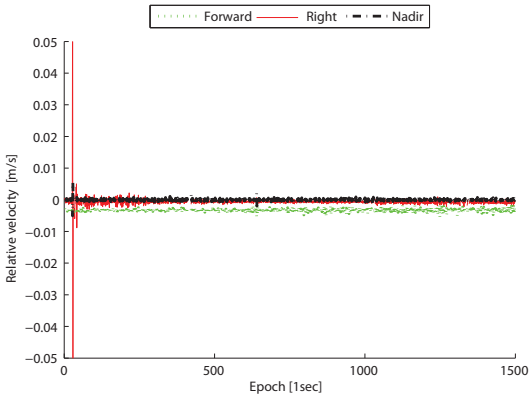
(a) True relative velocity



(b) Doppler based proposed model (Eq. (3.84))



(c) Doppler based proposed model (Eq. (3.82))



(d) Differencing relative positioning

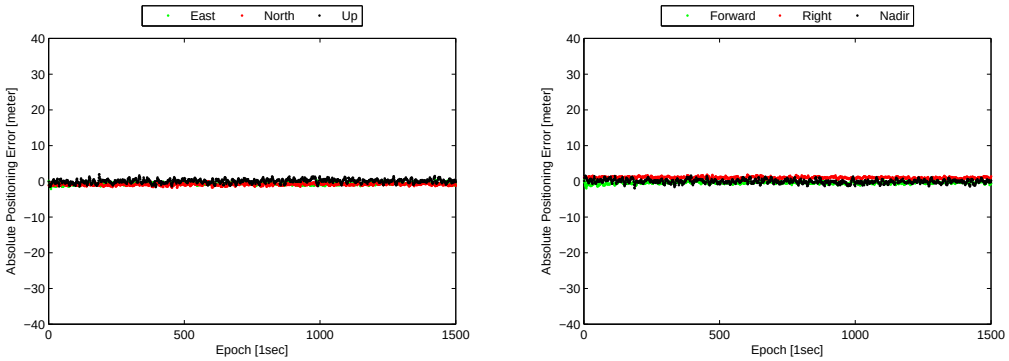
Figure 3.11: Relative velocity (PROBA-3)

3.6.2 Satellite Formation Flying: PROBA-3 with external reference clock

In this section, an external reference clock is applied to control the internal clock of the receivers. Fig. 3.12 show the absolute positioning errors in both East North Up and Forward Nadir Right Coordinates. Table 3.7 show the same results expressed in mean $\hat{\mu}$ and standard deviation $\hat{\sigma}$ of the error for FNR coordinates.
Fig. 3.13(a) shows the clock offsets of the two receivers obtained from the absolute position estimate. Both receivers have an offset of about 0.3 ms and this offset remains constant. The clock offset of both receivers is not exactly the same: a relative clock error of 0.01 ms is present.
Fig. 3.13(b) shows the error on the length of the float baseline and Fig. 3.14 on the fixed baseline solution using the standard DD model and the proposed DD model respectively. From Fig. 3.14 it is clear that even with a small relative clock offset of 0.01 ms, the standard model will result in a small offset (in the order of 2 mm but clearly visible in the figure) in the baseline estimate. The proposed model shows an error with zero mean.
These results are also summarized in Table 3.8 using the mean $\hat{\mu}$ and standard deviation $\hat{\sigma}$ of the float and fixed baseline lengths.
An empirical success rate for instantaneous ambiguity fixing of 85% was obtained. Inclusion of the Doppler observation did not improve the float solution, thus did not improve ambiguity resolution.
Again, the relative velocity estimation is analysed. Fig. 3.15(b) shows the relative velocity as estimated by the proposed model without (Eq. 3.84), and Fig. 3.15(c) for the proposed model with the correction for large clock offsets (Eq. 3.82). Note that the scale is 20 times larger than Fig. 3.11(b) and 3.11(c). For this hardware-in-the-loop simulation, the random error on the estimation is much larger than the errors in the functional model, which are not even visible in these figures.
Fig. 3.15(d) shows the relative velocity obtained from differencing between adjacent elements of fixed baseline coordinates. As was observed in Fig. 3.11(d), differencing baseline estimates from two subsequent epochs is more precise than what is obtained from the Doppler observations using the proposed model.

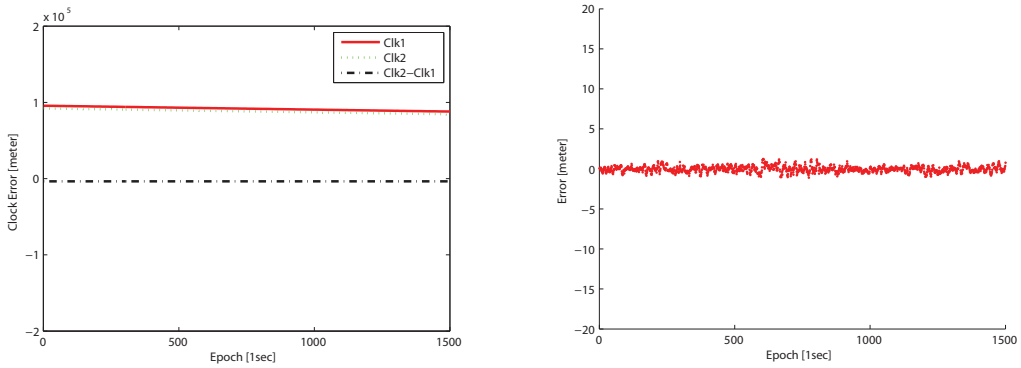
Table 3.7: Mean $\hat{\mu}$ and Standard deviation $\hat{\sigma}$ for the absolute positioning (PROBA-3 with external reference clock)

	$\hat{\mu}$		$\hat{\sigma}$	
Coordinate	Position [m]	Velocity [m/s]	Position [m]	Velocity [m/s]
Forward	-0.64	0.00	0.30	0.07
Right	-0.88	0.00	0.28	0.07
Nadir	0.03	0.00	0.54	0.12



(a) ENU coordinates (b) FNR coordinates

Figure 3.12: Absolute positioning errors (PROBA-3 with external reference clock)



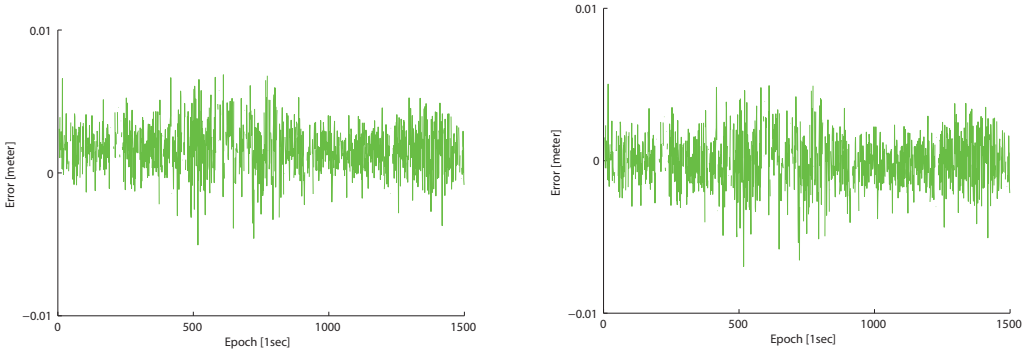
(a) Clock errors (absolute and the difference) for the two GPS receivers

(b) Error on float baseline length

Figure 3.13: PROBA-3 with external reference clock

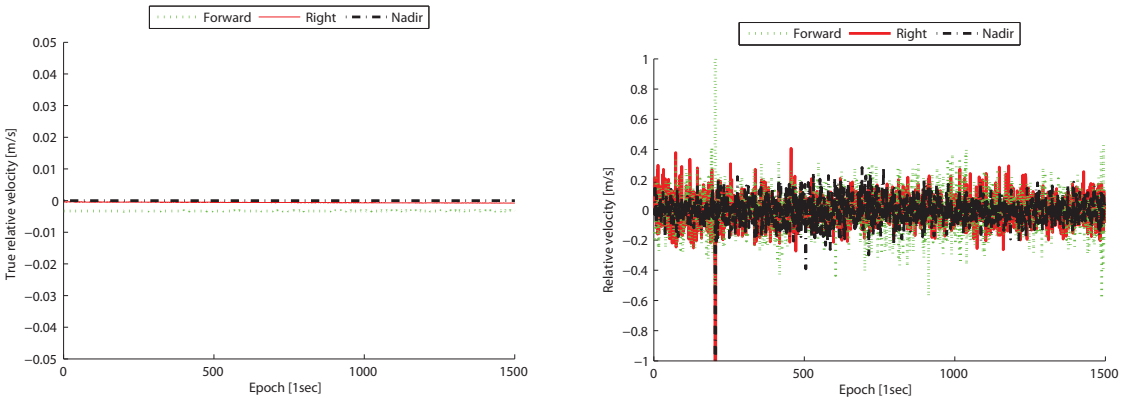
Table 3.8: Mean $\hat{\mu}$ and Standard deviation $\hat{\sigma}$ for the baseline estimate (PROBA-3 with external reference clock)

	Relative Positioning Error [mm]	
	$\hat{\mu}$	$\hat{\sigma}$
Float	-32.00	370.04
Fixed (Standard Model)	1.69	1.62
Fixed (Proposed Model)	-0.03	1.62

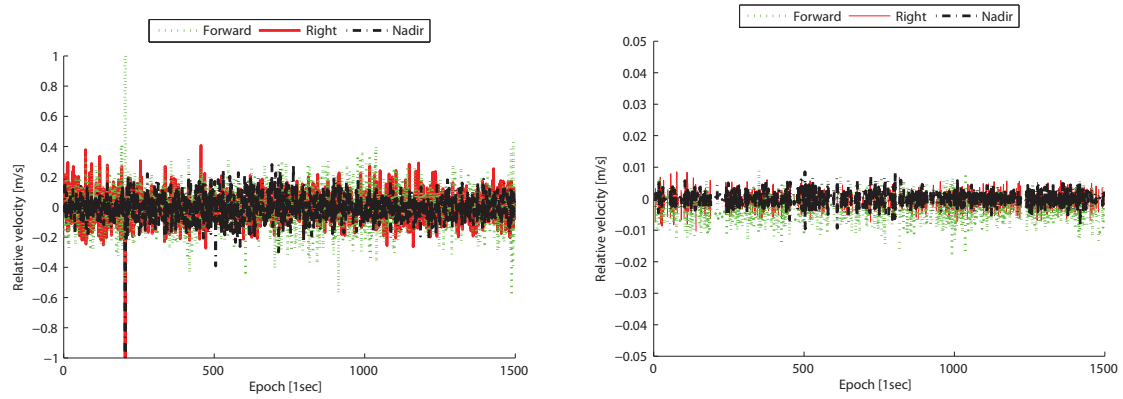


(a) Standard DD model (b) Proposed DD model

Figure 3.14: Error on fixed baseline length (PROBA-3 with external reference clock)



(a) True relative velocity (b) Doppler based proposed model (Eq. (3.84))



(c) Doppler based proposed model (Eq. (3.82)) (d) Differencing relative positioning

Figure 3.15: Relative velocity (PROBA-3 with external clock)

3.6.3 Satellite formation flying: Garada

3.6.3.1 Absolute positioning

The Garada mission, introduced in Appendix A.8, is utilized to evaluate absolute and relative positioning for a SAR formation flying mission. GPS data was collected, in a hardware-in-the-loop experiment using a Spirent simulator, from two Namuru receivers at two platforms flying 500 meters behind each other in the Garada orbit. An experimental version of the Namuru receiver (version 2.4) with some known issues (Buist et al., 2011a) was used in these experiments. The reference data provided by the Spirent simulator is applied to evaluate the accuracy of the estimated absolute position. Fig. 3.16 shows the absolute positioning errors in East, North, Up (ENU) coordinates for the master antenna at the first platform. The same errors in Forward, Nadir and Right (FNR) coordinates are shown on the right hand side in the same figure. The transformation from inertial to the FNR frame is described in Appendix E.3, the definition of the FNR frame is shown in Fig. E.1.

Fig. 3.16 shows on the right side an increasing error in the Forward direction which reset at fixed intervals. In the Nadir direction there is a more or less constant offset. This offset in the Nadir direction can be explained by the ionospheric delays on the observations: all GNSS signals experience a ionospheric delay, and because of the geometry (i.e. there are no GNSS satellites located between the user and the Earth), the altitude of the orbit is estimated too high. The time varying offset in the Forward direction can be explained by the receiver time offset, as will be demonstrated next.

Fig. 3.17 shows on the left hand side both the receiver clock offset and the absolute positioning error in the Forward direction as function of time. It is clear from the figure that the Forward error resets at the same time as the receiver clock. On the right side of the same figure, the error in the Forward direction is shown as function of the receiver clock error. It can be observed that the relationship between clock error and position error in the Forward direction is linear. Fig. 3.18 shows the absolute position error in the Forward direction as function of the error in the Right direction.

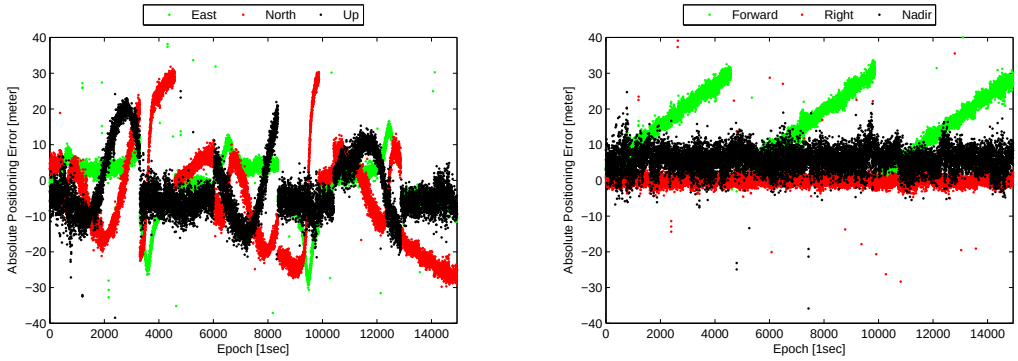
The order of the positioning error in the Forward direction can be explained as follows: the spacecraft has a velocity of about 7.5 km/s in the simulated orbit, and therefore moves with 7.5 meter in 1 ms. When the time offset of the receiver reaches the maximum 4 ms, the position error in the Forward direction becomes about (7.5x4=) 30 meters (see right hand side of Fig. 3.16). The same relationship between the receiver clock offset and absolute positioning error in Forward direction was also discussed in (Nakamura et al., 2004).

As reported in (Buist et al., 2012), there are erroneous pseudorange observations in the data of the Namuru receivers. These errors typically occur on a few (up to three) subsequent epochs and at more than one channel at the same time.

The LOM test was introduced in section 3.4.1 as part of the DIA procedure and can be applied in the absolute positioning process. As there are erroneous pseudoranges on more than one channel, the identification step of the DIA procedure is not applied.

The 3-5th row of Table 3.9 shows the results without the LOM test. Excluding the epochs with erroneous pseudoranges, the mean $\hat{\mu}$ and the standard deviation $\hat{\sigma}$ of the absolute positioning errors are shown in the 6-8th row of Table 3.9. By excluding these epochs, the

standard deviation of the absolute positioning is improved.



(a) ENU coordinates (b) FNR coordinates

Figure 3.16: Absolute position errors (Garada)

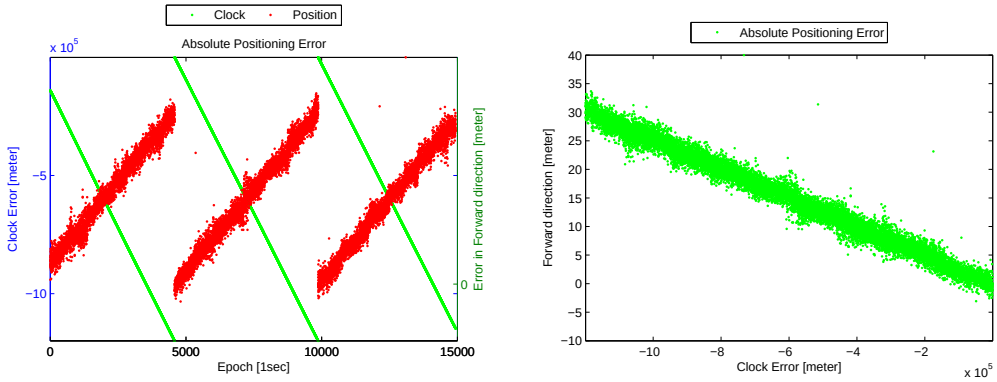


Figure 3.17: Absolute position error in Forward direction and clock error (Garada)

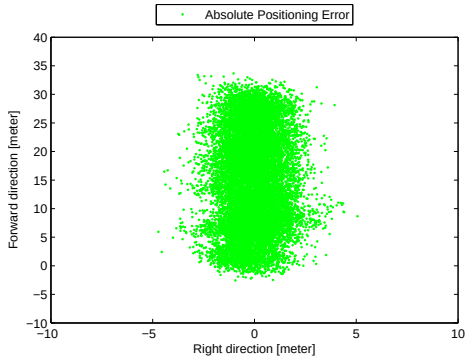


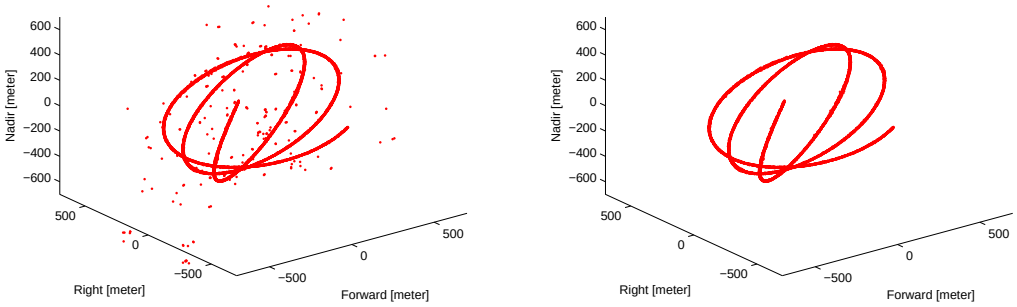
Figure 3.18: Absolute position error in Forward direction as function of the error in Right direction (Garada)

3.6.3.2 Relative positioning

The float baseline estimates are shown in Fig. 3.19 in a 3D plot, Fig. 3.20 also shows the error on the distance of the float baseline estimate between the two platforms. The left hand side are results without LOM test on absolute positioning, the right hand side are results after applying the LOM test in the absolute positioning process. The 3D figures shows clearly the relative geometry of the baseline between the two platforms. Fig. 3.21 show the fixed baseline estimate on the left hand side and the error on the distance between the two platforms after fixing on the right.
The single epoch ambiguity resolution empirical success rate for this data is 18%. The relative positioning results are summarized in Table 3.10. The mean error $\hat{\mu}$ and standard deviation $\hat{\sigma}$ on the baseline estimate are 42 mm (float), 2.7 mm (fixed) and 1770 mm (float) and 1.56 mm (fixed) respectively. So for the fixed solution, the mean of the error is almost zero and the standard deviation is approaching the theoretical limit of GNSS relative positioning.
The same results as for the PROBA-3 experiment was obtained: inclusion of the Doppler observation did not improve the float solution, thus did not improve ambiguity resolution. The float solution of the Namuru receiver has a five times larger standard deviation than the Septentrio PolaRx2 receivers applied in the PROBA-3 experiment described in section 3.6.1. The success rate found in the PROBA-3 experiment was 85% which as expected as the float solution is much more accurate.
The relative large code noise makes the Namuru receiver very suitable to investigate the improvement feasible with the multi-antenna relative positioning (chapter 5) compared to the single baseline result presented in this chapter.

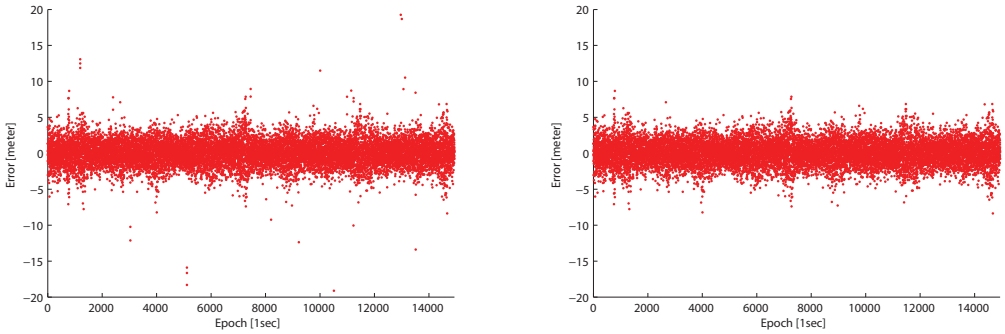
Table 3.9: Mean $\hat{\mu}$ and Standard deviation $\hat{\sigma}$ for the absolute positioning [mm] (Garada)

		$\hat{\mu}$		$\hat{\sigma}$	
Test	Coordinate	Position [m]	Velocity [m/s]	Position [m]	Velocity [m/s]
without LOM	Forward	16.63	-0.52	21.92	0.21
	Nadir	0.02	-0.04	5.46	0.55
	Right	6.54	3.51	24.79	0.73
with LOM	Forward	15.37	-0.52	8.46	0.21
	Right	-0.05	-0.04	1.06	0.55
	Nadir	5.81	3.51	2.99	0.73



(a) without LOM (b) with LOM

Figure 3.19: Float baseline solutions for the in-between baseline (Garada)

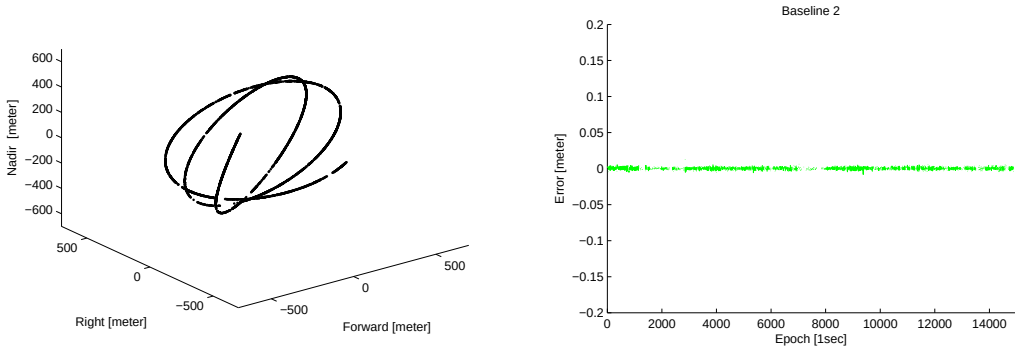


(a) without LOM (b) with LOM

Figure 3.20: Error on baseline length for the in-between baseline (Garada)

Table 3.10: Mean $\hat{\mu}$ and Standard deviation $\hat{\sigma}$ for the baseline estimate [mm] (Garada)

$\hat{\mu}$		$\hat{\sigma}$	
Float	Fixed	Float	Fixed
42	2.7	1770	1.56



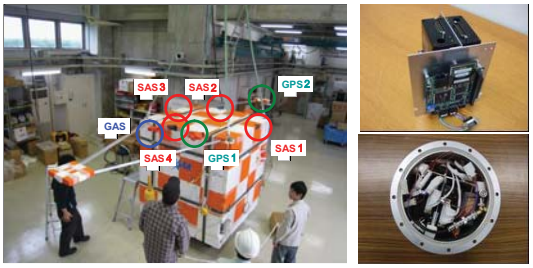
(a) Baseline estimate

(b) Error on baseline length

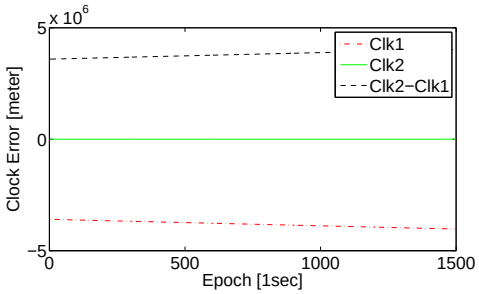
Figure 3.21: Fixed solution for the in-between baseline (Garada)

3.6.4 Short Baseline with Large Clock Error: BOV 2008

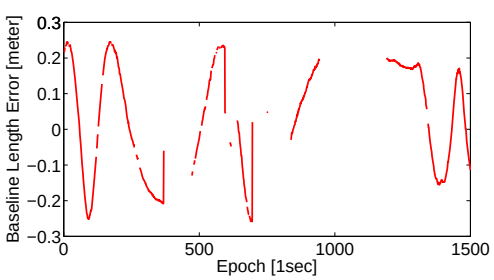
In the last example, it will be demonstrated that the proposed functional model is not only of importance for space application where the platforms have extreme large velocities, but also for other applications where receiver clocks have large offsets from the GNSS time frame.
In this example, data is used collected onboard a gondola hanging under a high altitude balloon (see Fig. 3.22(a)). More details about the experiment can be found in appendix A.6.4. In this experiment, the baseline length between two navigational receivers is constant but the clock of receiver 1 (Clk1 in Fig. 3.22(b)) was experiencing odd behavior and became larger than 13 ms.
Fig. 3.22(c) show the error in the norm of the baseline estimate if the standard DD model as described in section 3.3.2.1 is applied. The baseline error is only plotted if the ambiguity vector is correctly fixed and therefore the plotted line is discontinuous. As is shown in Table 3.11, the instantaneous empirical success rate for the standard DD model is 61%. The table also contains the mean $\hat{\mu}$ and standard deviation $\hat{\sigma}$ of the baseline estimate and these values are respectively more than 35 and 149 mm.
Fig. 3.22(d) shows the baseline error when the proposed model of this section is applied. If this figure is compared with Fig. 3.22(c), it is observed that the baseline error is much smaller and that the plotted line appears to be continuous: this indicates a much higher success rate for ambiguity resolution. This is also confirmed with an empirical success rate of 94% in Table 3.11. The table shows a much more accurate solution for the baseline with a mean $\hat{\mu}$ and standard deviation $\hat{\sigma}$ of respecitvely 0.0 and 3.4 mm.
From the higher success rate, one might think that the proposed model (where Doppler is applied to calculate a float solution) is stronger than the standard model. However, this is not the case. The offset on the code and carrier phase observations is simply so large that without correcting these observations, the probability of obtaining the correct integer ambiguity vector is reduced. This can be demonstrated by applying the model of Eq. (3.85), where the code and carrier observations are adjusted by the product of the range rate and the estimation of the receiver clock bias, but the Doppler observations themselves are not used for relative positioning. The obtained success rate with this model is exactly the same as the proposed model (see Table 3.11).



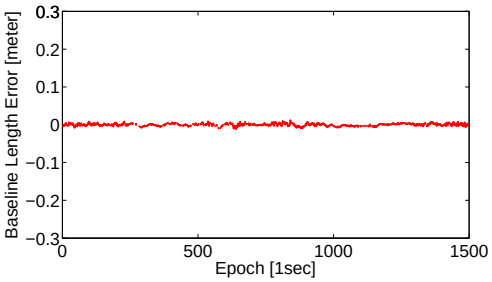
(a) BOV Gondola in 2008 experiment



(b) Clock errors and the difference for the two GPS receivers



(c) standard DD model



(d) proposed DD model

Figure 3.22: Baseline error (BOV)

Table 3.11: Mean $\hat{\mu}$ and Standard deviation $\hat{\sigma}$ for the baseline estimate (BOV)

	Relative Positioning Error [mm]		Success rate [%]
	$\hat{\mu}$	$\hat{\sigma}$	
Standard Model	35.56	149.40	0.61
Proposed Model Eq. (3.82)	0.0	3.4	0.94
Proposed Model Eq. (3.85)	0.0	3.4	0.94

3.7 Concluding remarks

In this chapter, the functional and stochastic models derived in chapter 2 were applied for absolute and relative positioning. In the analysis, emphasis was on the effects of large receiver clock errors and dynamics on absolute and relative positioning. For relative positioning applications, it was shown that inclusion of the Doppler observations in the model is desirable

1. if the GNSS receivers forming a baseline have large clock offsets -especially in a dynamic environment- the standard DD model will result in an offset in the baseline estimation. In order to correct the clock offset, the Doppler observations can be applied.

2. for an application were the relative position between two platforms is actively controlled, the relative velocity is generally required as input for the control loop.

The Doppler observation will not improve the float solution of the relative positioning problem and therefore will not improve ambiguity resolution. The drawback of using the Doppler for relative velocity estimation is the effect from the relative motion and the clock drift at the receiver cannot be separated. If the relative velocity can be obtained offline, taking the time derivative of the baseline estimate can provide a more accurate estimation of this quantity.
In the next two chapters, the main focus is on improving the ambiguity resolution using multi-antenna models, therefore the inclusion of the Doppler observation in the models will not have an advantage and we will apply the standard GNSS models without the Doppler observations.
The obtained results for ambiguity resolution in the PROBA-3 and Garada hardware-in-the-loop simulations are shown in Table 3.12 for later reference.

Table 3.12: Hardware-in-the-loop simulation results: single-frequency, single-epoch success rates for the baseline b^{12} using standard LAMBDA

	PROBA-3	*Garada (v2.4)*
Success rate	0.85	0.18

4 Attitude Determination using GNSS Signals

Attitude determination using GNSS signals is discussed in this chapter. The structure is the following: section 4.1 will start with an introduction on attitude determination and an overview of methods applied for ambiguity resolution for this application. The third part of section 4.1 describes the state of the art GNSS-based attitude determination for space applications, and ends with the relevance of the research described in this chapter. Next, in section 4.2, the Constrained-LAMBDA method is introduced in which a single constrained baseline is applied to strengthen the model described in section 3.3.2.1. The more general Multivariate Constrained LAMBDA method is the topic of section 4.3. Both models will be extensively tested in sections 4.4 and 4.5 using both simulations and field data.
Fig. 4.1 shows the relationship between the different elements of the single platform processing, including SSP for each GNSS receiver and attitude determination using data from all GNSS receivers at the platform.
Extracts of this chapter were published in (Buist, 2007), (Giorgi and Buist, 2008), (Teunissen et al., 2010), (Buist et al., 2010), (Giorgi et al., 2010), (Buist et al., 2011), (Giorgi et al., 2011), (Giorgi et al., 2012) and (Nadarajah et al., 2012). For a detailed discussion on the methods described in this chapter, see also (Giorgi, 2011).

4.1 Overview of Previous Work/ Methods

The attitude of a vehicle is its orientation with respect to a defined frame of reference. The aim of attitude determination is to estimate this orientation with respect to the given reference frame. Typical sensors applied for attitude determination are horizon sensors (or Earth sensors), gyroscopes, sun sensors, star trackers and magnetometers.
Two or more GNSS antennas mounted on one platform may be used to determine the attitude of the platform as well: with two antennas the application is called GNSS compass, with more than two GNSS-based attitude determination. Although less precise than some of the sensors mentioned above, GNSS-based attitude determination is relatively inexpensive and, unlike inertial sensors, drift-free. One example of a sensor that, like the compass, does not provide full attitude information is the sun sensor as it cannot detect any rotation of the spacecraft around the vector pointing toward the sun. The sun and horizon sensor provide a single vector measurement, GNSS generally provides multiple vector measurements at any time instance (namely vector measurements toward all the locked GNSS satellites).
Chapter 3 demonstrated how baseline vectors can be estimated precisely from GNSS observations. These can be translated into angular estimations of attitude, the accuracy

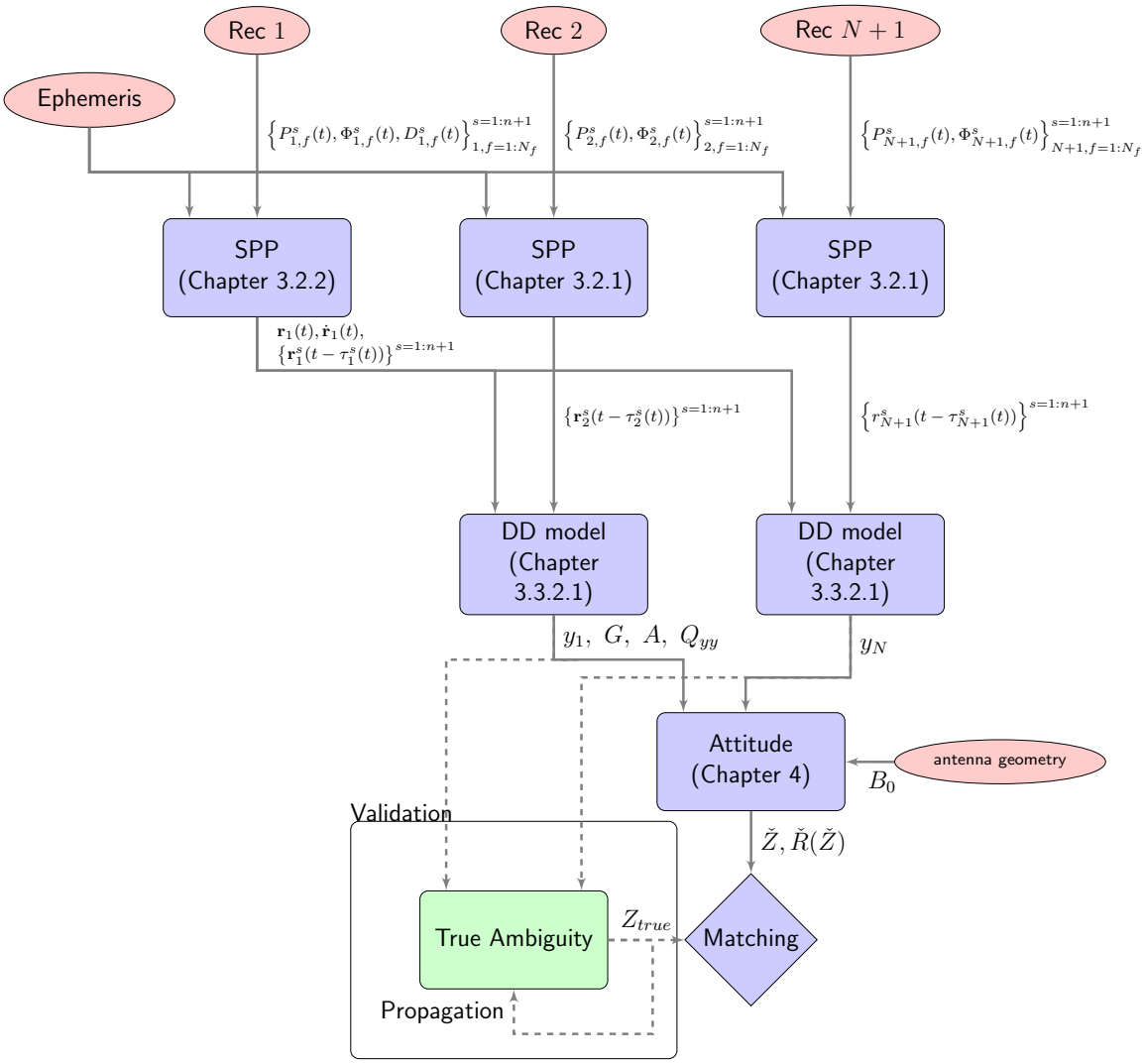


Figure 4.1: Platform Processing (Attitude determination)

of which depends primarily on two factors: the GNSS observation quality and the length of the baselines between antennas on the platform. This relationship, which will be discussed in section 4.3.3, is shown in Fig. 4.2 for three different carrier phase noise values. This figure is included to give an idea of the achievable attitude accuracy as function of baseline length and it can be concluded that the accuracy of GNSS attitude determination could reach 0.1° for baselines of more than one meter long. The required accuracy for space missions depends on the application. The different missions indicated in the figure will be discussed in detail in section 4.1.4.
Often one has no control over the baseline length, because the size and geometry of the platform limit the maximum distance at which the antennas can be placed. Thus, the challenge of obtaining precise angular estimates relies on observation accuracy and the attitude determination method itself.

Two types of applications for GNSS-based attitude determination are described in literature and will be introduced next.

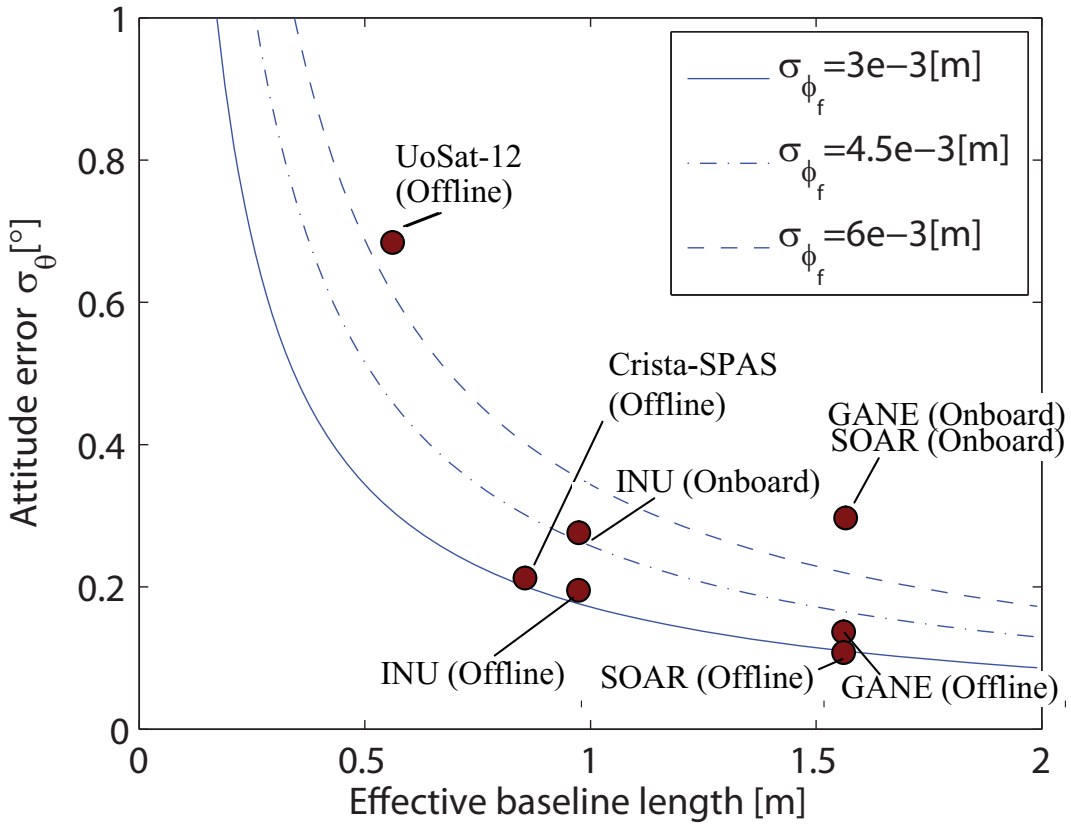


Figure 4.2: Relationship baseline length vs. attitude accuracy for different values of observation accuracy σ_{ϕ_f}, dots indicate reported accuracy for various space missions for the applied baseline length(s) (the experiments shown were performed under different conditions, see section 4.1.4 for details)

4.1.1 Compass: Heading and elevation

In the GNSS compass application, two nearby antennas track GNSS satellites. By expressing the baseline vector $b = (b_1, b_2, b_3)^T$ between the two antennas with respect to the local North-East-Up frame (see appendix E.2) the heading (or azimuth) and elevation angle can be computed.

$$Heading = \arctan \frac{b_2}{b_1} \tag{4.1}$$

$$Elevation = \arctan \frac{b_3}{\sqrt{b_1^2 + b_2^2}} \tag{4.2}$$

4.1.2 Full attitude determination

The goal of attitude determination is to determine the orientation of a vehicle with respect to some user-defined frame. The sensor (or sensors) applied for attitude determination is mounted on the platform with known orientation in the body frame: i.e. for GNSS the

Table 4.1: Ambiguity Resolution Methods applied in GNSS Attitude/ Short Baseline Applications

Motion-based	Search-based	
	Bayesian	Non-Bayesian
Cohen (Cohen, 1996) Crassidis (Crassidis et al., 1999)	GSF (Turner and Faruqi, 1997)	LAMBDA (Teunissen, 1993, 1995), Knight (Knight, 1994) ARCE (Park et al., 1996), Sutton (Sutton, 1997) Brown (Brown, 1992), LSAST (Hatch, 1990) OMEGA (Kim and Langley, 1999), INU (Buist et al., 2003) SSTL (Hodgart and Purivigraipong, 2000)

baseline vectors $F = \left[f_1, \ldots, f_N\right]$ between the antennas on the platform are generally known in this body frame. The same baselines can be expressed in a navigational frame such as e.g. the ECEF-frame (Earth Centred Earth Fixed) or the ENU-frame (East North Up). In this navigational frame, the baseline vectors are written as $B = \left[b_1, \ldots, b_N\right]$. These two different expressions are related by a rotation matrix R (Wertz, 1978). The relation between the baseline coordinates B and F in the different frames is

$$B = RF \tag{4.3}$$

with $R^T R = I_3$ and $\det R = 1$.
The attitude determination problem in general is finding this matrix R. For full three-axis attitude knowledge, at least two vector measurements, ideally orthogonal, are required.

4.1.3 Ambiguity Resolution

For GNSS-based attitude determination, we make use of the carrier phase observations as introduced in chapter 2, which are inherently ambiguous. As we saw in chapter 3, carrier phase ambiguity resolution is the key to high precision relative positioning, as it is for attitude determination. We will start this chapter with a literature overview of previous work on GNSS-based attitude determination with emphasis on ambiguity resolution.
Ambiguity resolution for attitude determination is different from the integer ambiguity search for kinematic positioning as described in chapter 3 because for attitude determination the baseline is generally speaking relatively short and often the baseline length is precisely known in advance.
In this section, a short overview of the different ambiguity resolution techniques is provided, which were developed up until now. Table 4.1 summarizes the different ambiguity resolution techniques and divides them into different sub-groups.
A possible division for ambiguity resolution methods is between motion-based and search-based. Examples of motion-based methods are introduced in (Cohen and Parkinson, 1992)(Cohen, 1996) and (Crassidis et al., 1999). The motion-based methods are by definition not instantaneous as they make use of the abundance of information provided by the platform or GNSS satellite motion. This motion will result in relative carrier phase variations that can be exploited to identify the cycle ambiguities. In the method developed by Cohen (Cohen, 1996), the Cartesian position of the slave antenna relative to its unknown starting points is determined without knowledge of the integer ambiguities. If the platform moves by a large angle (or for a static platform if data is collected for a long time), a set of displacement vectors can be used to calculate an initial solution to initialize

a nonlinear least-squares fit, which is a batch solution for a data set in which the integer terms remain constant over the collection period. By using the baseline constraints in the case of non-coplanar baseline configurations, motion about a single axis of rotation is adequate for ambiguity resolution. Hence, drawbacks are that this method is not instantaneous, a significant amount of memory is required for storage of the batch data, a motion of the baseline is required (or data has to be collected for even a longer time), a priori attitude information is required and in case of a coplanar baseline configuration, motion about two axes is required.
In (Crassidis et al., 1999), some of the disadvantages of the motion-based method are overcome by resolving the integer ambiguities without any a priori attitude knowledge, requiring less computational effort and a noniterative implementation, but the method requires three noncoplanar baselines, and, since user motion is still required, cannot be used instantaneously.
The search-based methods are motionless and therefore can be used instantaneously (i.e. using only observations from a single epoch). These methods find a solution that minimizes the error residuals at a specific time by searching through a list of all potential integers and rejecting all candidate solutions for which the weight function of the residual errors becomes too large. For the search-based approach, one would like to limit the number of potential solutions as much as possible and reject unlikely candidates as early as possible in the search process.
According to (Verhagen and Teunissen, 2006), the search-based GNSS ambiguity resolution methods themselves can be divided into two different approaches: the Bayesian approach and the non-Bayesian approach. In the Bayesian approach, not only the vector observable y is assumed to be random but also the two vectors of unknown parameters, for example the integer vector and baseline or attitude solution. In the non-Bayesian approach only the y vector is considered to be a random vector.
In (Teunissen, 2001), a review is given on the Bayesian approach and its relation with the non-Bayesian approach. In (Turner and Faruqi, 1997), a Bayesian approach is developed specifically for the GNSS-based attitude determination application. For this kind of approach the ambiguity resolution and attitude filtering is not being performed separately but a unified approach is proposed in which the ambiguity resolution and filtering processes are combined under a Gaussian Sum Filter (GSF).
Although the Bayesian approach has not yet found a wide-spread use in any of the GNSS applications, the concept itself is of interest to justify further research in this field. An example of an experimental implementation of a Bayesian approach for formation flight is (Draganov et al., 2002).
For completeness, it is mentioned that the LAMBDA method, and especially the decorrelation step of the LAMBDA method can be applied in the Bayesian approach (Gundlich and Koch, 2002).
For the non-Bayesian approaches, the LAMBDA method is well known and was explained in detail in section 3.3.2.1. The LAMBDA method is using an Integer Least-Squares (ILS) approach, however not all search-based methods make use of this approach. The Knight method (Knight, 1994) and ARCE (Ambiguity Resolution using Constraint Equation) (Park et al., 1996) search for the relative positions of the GNSS antennas, whereas in the method applied in the Integrated Navigation Unit (INU) the attitude space is searched (Buist et al., 2003). These methods could work very well if some information about baseline length and/or initial attitude is known. In that case their search space could be

much reduced and therefore the search time would be shortened while the success rate would increase.
The Knight method was originally developed for aircraft applications and it requires some initial knowledge of the attitude of the platform. In applications where the initial attitude is not known, it is reported not to work optimally (Gomez and Lammers, 2004). The novelty of this method is partially the way the large number of potential solutions for the integer ambiguity is reduced by eliminating all unlikely solutions in an early stage of the search process.

For attitude determination systems, the initial integer cycle ambiguity search is often performed in the solution space instead of the measurement space (Sutton, 1997). This paper from Sutton states that in other words the initial search is based on baseline length instead of the phase residual. The fundamental equation relating the GNSS phase difference measurements from two antennas can be solved independently for each antenna separation vector (i.e. baseline vector). Two baseline vectors can be used to compute the attitude associated with the plane containing the two vectors. A better approach (Brown, 1992) is to take advantage of the geometry constraint that the two vectors are coplanar. Given that the two vectors lie in the same plane only one angle is required to specify the direction of the two vectors relative to each other.
Another method that makes use of the same principle is ARCE (Park et al., 1996). It divides the n-dimensional integer ambiguity vector into independent and dependent parts. If the carrier phase observations are accurate enough it assumes that not n-dimensional but a 3 dimensional space can be searched to find the proper integer ambiguities (see also the discussion on the spectrum of conditional standard deviation of the DD float ambiguities in section 3.3.2.1). If knowledge of the baseline vector is applied as a pseudo-measurement, the search space is reduced to 2-dimensional. Because of the errors on the carrier-phase observations, it is not straightforward to determine an appropriate search space and there is no theoretical guide to divide the search space into independent and dependent parts. Park et al. (1996) showed an improvement compared to standard LAMBDA, although it will be shown in this work that even better performance is feasible by applying a constrained version of LAMBDA. Algorithms like Least-Squares Ambiguity Search Technique or LSAST (Hatch, 1990) and Optimal Method for Estimating GPS Ambiguities or OMEGA (Kim and Langley, 1999) can also be classified as independent-ambiguity-search methods, but they also apply the variance-covariance matrix obtained from the float solution.
For the INU experiment (Buist et al., 2003) onboard the SERVIS-1 satellite, the ambiguity search is performed in combination with an initial attitude search. In order to limit the ambiguity search space, coarse attitude is estimated using information of visible satellites. The fact that one GNSS satellite is visible for an antenna provides information about the pointing direction of the antenna: the angle between the antenna boresight and line-of-sight vector should be less than than half of the antenna's field of view. By combining this information from all visible and non-visible GNSS satellites, a coarse pointing direction of the antenna can be estimated. By simply applying information in which direction the GNSS antennas are pointing, the computational time required for the ambiguity search was reduced. This is a variation on the methods applied for attitude determination using the signal strength of observations discussed later, but here applied to initialize an ambiguity search method. A similar method is described in (Pasetti et al., 1997).

Another example of an attitude-based search method, developed at Surrey Satellite Technology (SSTL), is (Hodgart and Purivigraipong, 2000), which makes use of the Gram-Schmidt orthogonalization procedure in order to find individual baseline solutions. The second step of this method narrows the search space by identifying the most likely combination of baselines by employing the known orientation of the baselines. The third step finds the initial attitude and employs an integrity check for the found solution. This integer ambiguity resolution method was improved in newer work as described in (Duncan, 2010).
For the search-based approaches, the LAMBDA method is well known. (Lin et al., 2004), (Kuylen et al., 2006) and (Hauschild and Montenbruck, 2007) did use the standard LAMBDA method in combination with a Kalman Filter for attitude determination. Kuylen et al. (2006) applied the baseline length constraint to validate the found solution. Similarly in (Kim and Langley, 2007), an ILS approach is applied for ambiguity resolution on individual baselines, the baseline length information is only applied after ambiguity resolution for validation.
The standard LAMBDA method has been modified in previous work (see e.g.(Monikes et al., 2005) and (Wang et al., 2009)) but these modifications did not integrally exploit all a-priori information. In both publications, the baseline length constraint was used to modify the standard LAMBDA search for a subset of the unknown integer ambiguities.
In this chapter, a nontrivial extension of the LAMBDA method by a rigorous inclusion of the nonlinear constraint(s) is introduced, which in case of a single baseline, is the length of the baseline, and in case of multiple baselines, is the multi-baseline geometry described in the platform-fixed frame.

4.1.4 Experience onboard Spacecraft

In this section a short overview of several experiments of GNSS-based attitude determination onboard spacecraft is provided. The reported accuracy of the attitude determination as function of the applied baseline length was shown in Fig. 4.2. The discussed missions are summarized in Table 4.2, which is an extension of a table in (Purivigraipong, 2000) with information from (Lightsey et al., 1996)(Buist et al., 1998)(Lisano et al., 1999)(Um and Lighsey, 2000).
These GNSS attitude determination experiments are indicated in Fig. 4.2 as a function of the baseline length used in the experiment. In case baseline vectors of different lengths were used in the experiment, the shortest baseline vector is plotted in the figure as it is the limiting factor in the achievable accuracy. Each point is plotted using root mean square (RMS) attitude error for all axes. The experimental results shown in this figure are all different in terms of antenna configuration, multipath environment, reference attitude sensor, etc. This has to be kept in mind when interpreting the results.
The first experiment onboard a satellite was RADCAL (Ward, 1996) which stands for RADar CALibration. Ambiguity resolution was performed using a motion-based method as described in (Cohen, 1996) and as the mission did not have other precise attitude determination sensors onboard, the accuracy assessment was reported difficult. This is also the most likely reason why the RMS error is much off from the expected accuracy given the baseline length in Fig. 4.2.
The CRISTA-SPAS (Cryogenic Infrared Spectrometers and Telescopes for the Atmosphere-Shuttle Pallet Satellite) was a 3-axis stabilized flight experiment launched with, released

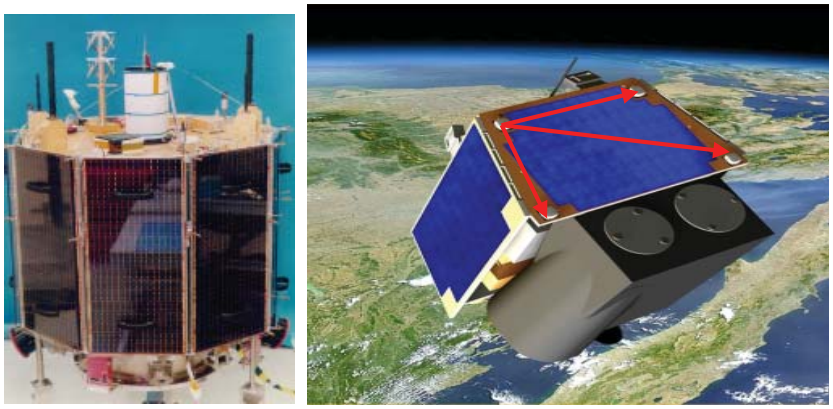


Figure 4.3: Image of UoSAT-12 and artist impression of Topsat in space (Courtesy of SSTL)

from and subsequently recovered by Space Shuttle Atlantis, STS 66. This experimental platform was the first real-time space operation of GPS-based attitude determination. An accurate IMU and star tracker were carried on the CRISTA-SPAS for providing the reference attitude within 0.05° error (Brock et al., 1995).
REX (Radiation Experiment Satellite) II was a gravity gradient stabilized spacecraft which demonstrated real-time onboard attitude estimation and closed loop control using GPS measurements, but only after nadir pointing control was achieved. The GPS attitude solution was always checked with the attitude derived from magnetometer measurements before being applied for attitude control (Freesland et al., 1996). The reference sensors were magnetometers and coarse sun sensor that provided a reference attitude with an RMS error of 3° making it difficult to evaluate the GPS attitude error: it could validated to be within 3° RMS (Lightsey et al., 1996).
A number of experiments were performed onboard the Space Shuttle in the SIGI Orbital Attitude Readiness (SOAR) (Um and Lighsey, 2000) and GPS Attitude and Navigation Experiment (GANE) (Lisano et al., 1999) experiments with relative long baseline vectors (1.5 and more than 3 meters baseline length respectively). On these flights the difference between GPS and reference attitude was found to be smaller than 0.5°. Onboard SOAR, both GPS only and a combination of INS with GPS attitude determination was demonstrated. GPS only resulted in an error between 0.4° and 0.1° for the different axes respectively (Um and Lighsey, 2000). Using data collected with GANE and SOAR experiments, a better accuracy was achieved offline; about 0.2 and 0.1° respectively for all axes (Um and Lighsey, 2000)(Lisano et al., 1999). In these experiments the ambiguity estimation was done by a search-based method as described in (Knight, 1994). These experiments led to the use of GPS onboard the International Space Station (ISS) for attitude determination.
Purivigraipong (Purivigraipong, 2000) showed that 1° RMS for all three attitude angles is achievable (offline) with relative short baselines of 0.65 meter onboard a small satellite, UoSAT-12. This attitude estimation method was improved in newer work as described in (Duncan et al., 2007)(Duncan, 2010) and validated using data from TOPSAT. Images of both Surrey satellites are shown in Fig. 4.3.
(Hauschild and Montenbruck, 2007) and (Kim and Langley, 2007), as discussed in the previous section, applied an ILS approach for a satellite project. For both missions in-flight results are not reported yet.

The drawback of the RADCAL, REX II and UoSAT-12 missions was that no reference data from another attitude sensor more accurate than the GPS attitude was available. The GANE, SOAR and Crista SPAS experiment were done onboard or controlled by the space shuttle and therefore very limited in duration (a space shuttle mission was at most 17 days). The experiment that will be described next did not have these drawbacks as a star sensor was available to provide reference attitude information and the experiment was conducted for a duration of two years in orbit.
The SERVIS-1 spacecraft performed a technology demonstration mission of GPS-based attitude determination in the space environment (Buist et al., 2003). The satellite, developed by the Institute for Unmanned Space Experiment Free Flyer (USEF) under a contract from the New Energy and industrial technology Development Organization (NEDO), was launched on 30th of October 2003 as a technology demonstration experiment. The satellite was in a sun-synchronous orbit with an altitude of 1000 kilometer, alternating two weeks Earth-pointing and sun-pointing (see right hand side of Fig. 4.4 for the definition of these attitude modes). The star sensor was pointing in the same direction as the antenna-boresight of the GPS antennas (see Fig. 4.4). For two years, the GPS receiver was operated continuously to collect GPS data and perform attitude determination in real-time. Attitude accuracy was assessed off-line using the star sensor as reference sensor (Buist et al., 2004)(Buist et al., 2005). Some of the lessons learnt from this mission will be discussed in section 5.1.

Another GNSS attitude determination concept makes use of the fact that measured signal strength is provided by the GNSS receiver in a local antenna-fixed reference frame (right side of Fig. 4.5). This concept, first proposed by Hashida (Hashida and Unwin, 1993), enables attitude determination using data from only one antenna. Although the achievable accuracy of this method is lower than with the carrier phase difference concept, it has the advantage of relatively simple implementation, which does not require any hardware adjustments of the GPS navigation system. In this type of approach, the known relationship between elevation angle and antenna gain is utilized.
Behre (Behre, 1997)(Axelrad and Behre, 1999) did research on single axis attitude determination using symmetric antenna patterns and demonstrated the concept with data collected from a number of satellites and concluded that the achievable accuracy is around 3° till 10° (RMS), much lower than the accuracy achievable by applying carrier phase observations.
Under special circumstances it is possible to do full attitude determination with data from a single GPS antenna. For example, Buist et al. (1998) used data from a satellite called PoSAT-1, where the antenna pattern was disturbed by the presence of a gravity gradient boom (see bottom-right hand side of Fig. 4.5) to demonstrate full attitude determination with an accuracy of 10° for yaw and around 3° for pitch and roll.
Full attitude determination using signal strength measurements is also possible if non-aligned antennas are used. For example the SOAR experiment also used a variation of this method to find initial ambiguities (Um and Lighsey, 2000), similar to the approach based on visibility in the INU experiment.

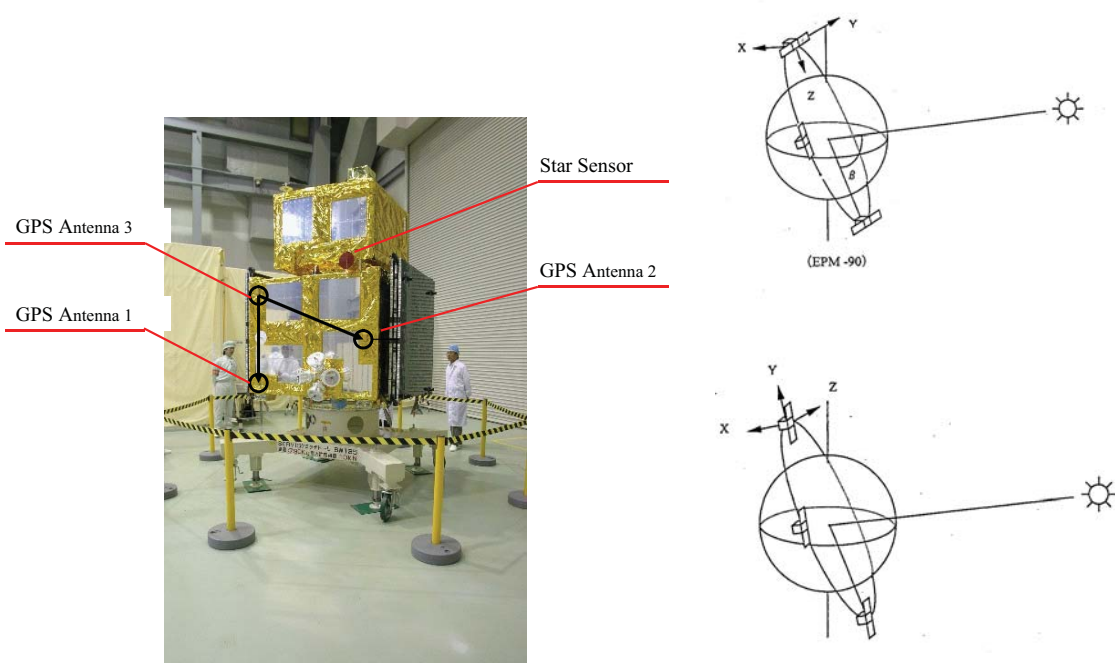


Figure 4.4: (Left) GPS Antenna configuration and Star sensor's location on the SERVIS-1 satellite (Courtesy of USEF), (right) Earth- and Sun pointing modes of the SERVIS-1 satellite

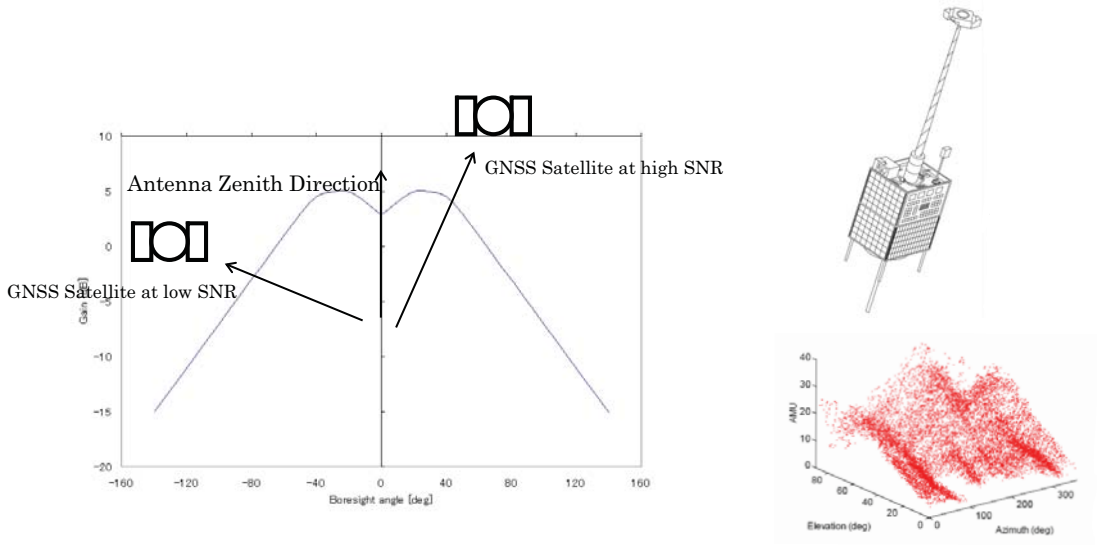


Figure 4.5: (Left) Relationship between antenna boresight and antenna gain, (right) UoSAT satellite with gravity gradient boom, antenna pattern of POSAT-1 (PoSAT-1 Image is courtesy of SSTL)

Table 4.2: Overview of Significant Missions for GPS Full Attitude Determination

Launch	Mission	GPS receiver	# Antennas	Baseline lengths [meter]	RMS Attitude error [°] [3]	Offline or Onboard result	Reference attitude sensor
1993	RADCAL	Trimble Quadrex	4	0.67, 0.67,0.67	2	Offline	Magnetometers
1993	PoSAT-1	Trimble TANS	1	-	(r 3, p 3, y 10)	Offline	Magnetometers and sun sensors
1994	CRISTA SPAS	Trimble Vector	4	1, 1.2,0.8	2 0.21 (r 0.21, p 0.18, y 0.23)	Onboard Offline	Star Tracker and IMU
1996	REX II	Trimble Vector	4	0.67, 0.67, 0.67	2	Onboard	Magnetometers
1996	GANE (Space Shuttle)	Trimble Vector	4	1.5, 3, 3.4	0.28 (p 0.2 , y 0.2, r 0.4) 0.14 (p 0.1, y 0.1, r 0.2)	Onboard Offline	Star Tracker and IMU
1999	UoSAT-12	SGR	4	0.65, 0.65, 0.8	0.75 (p 0.9, r 0.9, y 0.2)	Offline	Magnetometer and horizon sensor
2000	SOAR (Space Shuttle)	SIGI (GPS+INS)	4	1.5, 3.6, 3.2	0.28 (p 0.40, r 0.24, y 0.10) 0.09 (p 0.10, r 0.11, y 0.07)	Onboard (GPS only) Offline GPS only	Star Tracker
2003	SERVIS-1	INU	3	1.38,0.97	0.28 (p 0.23, r 0.34, y 0.25) 0.19 (p 0.17, r 0.20, y 0.21)	Onboard Offline	Star sensor

[3] r: roll, p: pitch, y: yaw

4.1.5 Research relevance

As can be concluded from the discussion in the previous section, in terms of accuracy not much room for improvement is expected in GNSS attitude determination, as the theoretical limit has been reached by the available techniques. However, for ambiguity resolution still a number of open challenges remain.
Based on experience from the SERVIS-1 mission, ambiguity resolution can still be challenging for attitude determination, especially for space applications. The INU experiment would restart once in two weeks time on average, although during some periods more frequent as part of the scheduled experiments. Only during the initialization process after restart, it would perform ambiguity resolution. After successfully resolving the integer ambiguities, it would update these as part of the Kalman filter based attitude determination algorithm (Buist et al., 2003). In Earth Pointing Mode with good visibility of GPS satellites, the INU was always able to find the correct integer ambiguities, however occasionally it would reject the obtained solution and reinitialize the search with data from the next epoch. For integer ambiguity resolution, it required rough attitude information from visible GNSS satellites and -on average- 10 seconds processing time on the CPU of the GPS receiver (Buist et al., 2005).
When the SERVIS-1 satellite was not Earth-pointing but Sun-pointing (or in transition between these two modes), the number of available satellites could drop significantly and ambiguity resolution become a challenge.
During transition, the pitch rate of about $-0.05^\circ/s$ in Earth pointing mode (the orbital rate for this orbit) would decrease to zero (the Sun pointing mode is inertial), while the yaw rotation could reach $0.5^\circ/s$ during the repointing towards the Sun. During these transitions the dynamics model applied in the Kalman filter would be inconsistent with reality and the attitude error increased from the reported 0.2° for all angles to 1° for roll and pitch and 3° for yaw (Buist et al., 2005). The larger yaw error was a result of the delay in response from the Kalman filter, which onboard would have been running for two weeks continuously. Similar behavior of the Kalman filter would occur during regular firing of the thrusters for attitude control.
Hence three areas were identified in GNSS attitude determination, especially in ambiguity resolution, where significant improvement is desired and could be achieved. For this type of applications we would like to develop:

1. An ambiguity resolution method with a high probability of correctly fixing the ambiguities even when a limited number of observations is available (weak models).

2. Ideally the method should work instantaneously, eliminating the need for a dynamics model.

3. the method should be computational efficient, enabling real-time integer ambiguity resolution on spaceborne CPUs.

In the remainder of this chapter, we will describe such a method based on a constrained extension of the popular LAMBDA method.

4.2 C-LAMBDA

In this section constrained models are developed as an extension of the standard unconstrained model described in section 3.3.2.1. It is expected that a constrained method achieves higher performance due to the rigorous inclusion of the nonlinear constraint into the integer estimation process, as given by the known distance between the GNSS antennas.
In section 3.3.2.1, we wrote explicitly y^{DD} to indicate double differenced observations. In this section, it is assumed that a double difference model is applied and therefore the DD is dropped from the notation.

4.2.1 Constrained Model

For baselines whose length $||b|| = l$ is known, the observation equations, Eq. (3.38), become (Teunissen, 2006):

$$E(y) = Az + Gb, \quad D(y) = Q_{yy}, \quad ||b||_{I_3} = l, \quad z \in \mathbb{Z}^n, \quad b \in \mathbb{R}^3 \tag{4.4}$$

Using this modification the minimization problem, Eq. (3.83), is reformulated as:

$$\begin{aligned} &\min_{z\in\mathbb{Z}^n, b\in\mathbb{R}^3, ||b||=l} \|y - Az - Gb\|^2_{Q_{yy}} \\ &= \|\hat{e}\|^2_{Q_{yy}} + \min_{z\in\mathbb{Z}^n, b\in\mathbb{R}^3, ||b||=l} \left(\|\hat{z} - z\|^2_{Q_{\hat{z}\hat{z}}} + \|\hat{b}(z) - b\|^2_{Q_{\hat{b}(z)\hat{b}(z)}} \right) \\ &= \|\hat{e}\|^2_{Q_{yy}} + \min_{z\in\mathbb{Z}^n} \left(\|\hat{z} - z\|^2_{Q_{\hat{z}\hat{z}}} + \min_{b\in\mathbb{R}^3, ||b||=l} (\|\hat{b}(z) - b\|^2_{Q_{\hat{b}(z)\hat{b}(z)}}) \right) \end{aligned} \tag{4.5}$$

where $\hat{b}(z)$ is the least-squares solution for b, assuming that z is known. This solution follows the same steps as described in section 3.3.2.1, with the exception that the search for the integer vector is now done with the constrained (C-) LAMBDA method (Teunissen, 2006, 2008, 2010), (Buist, 2007) and (Teunissen et al., 2010):

The minimization problem of C-LAMBDA

$$\check{z} = \arg\min_{z\in\mathbb{Z}^n} (||\hat{z} - z||^2_{Q_{\hat{z}\hat{z}}} + ||\hat{b}(z) - \check{b}(z)||^2_{Q_{\hat{b}(z)\hat{b}(z)}}) \tag{4.6}$$

$$\check{b}(z) = \arg(\min_{b\in\mathbb{R}^3, ||b||=l} \|\hat{b}(z) - b\|^2_{Q_{\hat{b}(z)\hat{b}(z)}}) \tag{4.7}$$

where $\check{b}(z)$ is the fixed solution for b, assuming that z is known.

This method integrates the nonlinear baseline constraint into the search for the integer minimizer. The C-LAMBDA method is a nontrivial modification of the LAMBDA method in which we have to search for the integer least-squares ambiguity vector $\check{z}$ in the integer search space:

$$\Psi(\chi^2) = \left\{ z \in \mathbb{Z}^n | \ \|\hat{z} - z\|^2_{Q_{\hat{z}\hat{z}}} + ||\hat{b}(z) - \check{b}(z))\|_{Q_{\hat{b}(z)\hat{b}(z)}} \leq \chi^2 \right\} \tag{4.8}$$

The auxiliary ellipsoidal integer search space was introduced in section 3.3.2.1 as

$$\Psi_0(\chi^2) = \left\{ z \in \mathbb{Z}^n | \ \|\hat{z} - z\|^2_{Q_{\hat{z}\hat{z}}} \leq \chi^2 \right\} \tag{4.9}$$

where $\Psi(\chi^2) \subset \Psi_0(\chi^2)$, thus $\Psi_0(\chi^2)$ contains all the integer vectors of $\Psi(\chi^2)$ including the float solution $\hat{z}$.

Note that this search space of Eq. (4.8) is not ellipsoidal anymore due to the presence of the residual baseline term. It is shown in (Teunissen, 2006) how to perform such a search in an efficient way. Here we will describe one approach that was successfully applied in (Park and Teunissen, 2003)(Buist, 2007).
The problem is to minimize Eq. (4.7), where

$$\begin{aligned} ||\hat{b}(z) - b(z))\|^2_{Q_{\hat{b}(z)\hat{b}(z)}} &= c^2 \\ &= \hat{b}(z)^T Q^{-1}_{\hat{b}(z)\hat{b}(z)} \hat{b}(z) - 2\hat{b}(z)^T Q^{-1}_{\hat{b}(z)\hat{b}(z)} b(z) + b(z)^T Q^{-1}_{\hat{b}(z)\hat{b}(z)} b(z) \end{aligned} \tag{4.10}$$

is the equation of an ellipsoid centred at $\hat{b}(z)$ and where

$$||b||^2_{I_3} = b^T b = l^2 \tag{4.11}$$

is the equation of a sphere centred in its origin with radius l (i.e. the baseline length). Thus the minimization problem is equal to finding the smallest ellipsoid that just touches the sphere, at which point the sphere and the ellipsoid will have the same normal vector.

These two normal vectors can be written in the form of the normal equations:

$$(Q^{-1}_{\hat{b}(z)\hat{b}(z)} - \mu I_3) b = Q^{-1}_{\hat{b}(z)\hat{b}(z)} \hat{b}(z) \tag{4.12}$$

where μ is the Lagrange multiplier.

The Lagrange multiplier can also be obtained by applying the Lagrangian method for the solution of Eq. (4.7) utilizing the Lagrange function defined by

$$\Lambda(b(z),\mu) = \hat{b}(z)^T Q^{-1}_{\hat{b}(z)\hat{b}(z)} \hat{b}(z) - 2\hat{b}(z)^T Q^{-1}_{\hat{b}(z)\hat{b}(z)} b(z) + b(z)^T Q^{-1}_{\hat{b}(z)\hat{b}(z)} b(z) - \mu(b^T b - l^2) \tag{4.13}$$

The search method applied in this research, and in (Park and Teunissen, 2003) and (Buist, 2007), is referred to as "Expansion approach". In the Expansion approach, we first use the standard LAMBDA method to collect integer vectors inside the search space $\Psi_0(\chi^2)$ and store all those that fulfill the inequality:

$$||\hat{b}(z) - \check{b}(z)||^2_{Q_{\hat{b}(z)\hat{b}(z)}} \leq \chi^2 - ||\hat{z} - z||^2_{Q_{\hat{z}\hat{z}}} \tag{4.14}$$

Of course one would like the search space $\Psi_0(\chi^2)$ to be as small as possible in order to finish the search in a reasonable time which is especially important for real-time applications. However, in order to guarantee that the search space is not empty, the search space should neither be chosen to be too small. The initial search space is defined by the value $\chi_1^2 = ||\hat{z} - \check{z}_B||^2_{Q_{\hat{z}\hat{z}}}$ where $\check{z}_B$ is the bootstrapped solution of z (see section 3.3.2.1). This initial value χ_1^2 is increased k times until the search space $\Psi(\chi_k^2)$ is non-empty, using the logic visualized in Fig. 4.6. For every step, we enumerate all the integer vectors contained in $\Psi_0(\chi_i^2)$ with $i = 1, \ldots, k$. If the set is non-empty, we pick up the minimizer, otherwise we increase χ_i^2 and thus the size of the search space $\Psi_0(\chi_i^2)$. The increment of χ^2 is empirically set: a good choice is to double at each step (Buist, 2007).
In Fig. 4.6, the search space $\Psi_0(\chi_1^2)$ is non-empty, but $\Psi(\chi_1^2)$ is, and thus χ_1^2 is increased. The same holds for the second step. For χ_3^2, both $\Psi_0(\chi_3^2)$ and $\Psi(\chi_3^2)$ are non-empty, and a solution is obtained. If more than one candidate would be available in $\Psi(\chi_3^2)$, all would be enumerated and the minimizer selected.
The computation of $\check{b}(z)$ can be very time consuming if it has to be done for many integer candidates z. In Eq. (4.5) the ambiguity residual in $\left(\|\hat{z} - z\|^2_{Q_{\hat{z}\hat{z}}}\right)$ is weighted by the inverse of the ambiguity variance matrix, while the residuals of $\left(\|\hat{b}(z) - b\|^2_{Q_{\hat{b}(z)\hat{b}(z)}}\right)$ are weighted by the inverse conditional baseline variance matrix. As the example in section 3.3.2.1 showed, these weights differ by typically 2 or 3 orders of magnitude.

It can be shown that the original search space can be bounded by a search space expressed by the largest eigenvalue (λ_{max}) and larger than a search space expressed by the smallest eigenvalue (λ_{min}) (Teunissen, 2006). Thus the function $F(z) = ||\hat{z} - z||^2_{Q_{\hat{z}\hat{z}}} + ||\hat{b}(z) - \check{b}(z)||^2_{Q_{\hat{b}(z)\hat{b}(z)}}$ from Eq. (4.6) can be bounded by functions that are easier to evaluate, by applying the following inequalities:

$$\begin{aligned} &F_1(z) \leq F(z) \leq F_2(z) \\ &F_1(z) = ||\hat{z} - z||^2_{Q_{\hat{z}\hat{z}}} + \lambda_{min}(||\hat{b}(z)||_{I_3} - l)^2 \\ &F_2(z) = ||\hat{z} - z||^2_{Q_{\hat{z}\hat{z}}} + \lambda_{max}(||\hat{b}(z)||_{I_3} - l)^2 \end{aligned} \tag{4.15}$$

With the functions $F_1(z)$ and $F_2(z)$ the following search spaces can be obtained:

$$\begin{aligned} &\Psi_1(\chi^2) = \{z \in \mathbb{Z}^n | F_1(z) \leq \chi^2\} \\ &\Psi_2(\chi^2) = \{z \in \mathbb{Z}^n | F_2(z) \leq \chi^2\} \end{aligned} \tag{4.16}$$

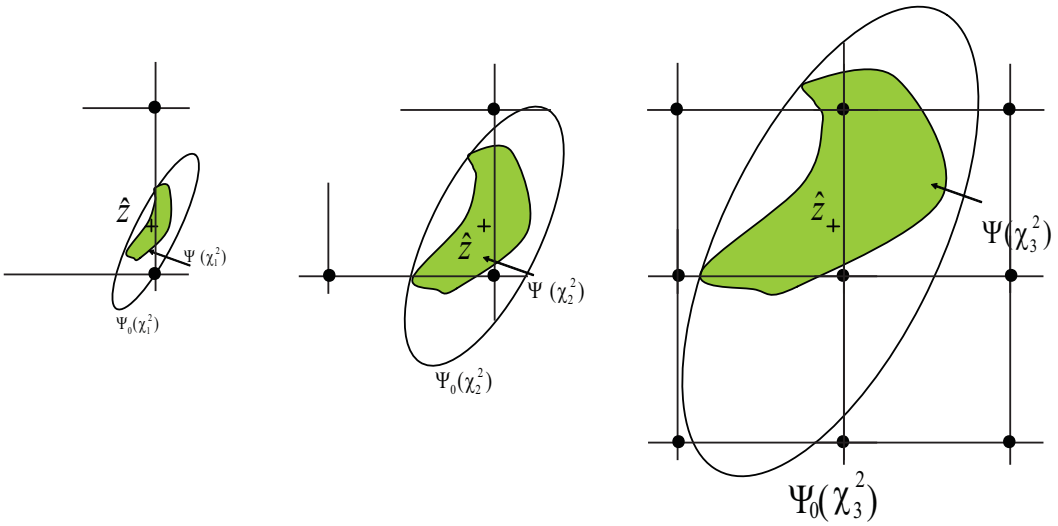


Figure 4.6: Expansion procedure implemented for C-LAMBDA

where

$$\Psi_2(\chi^2) \subset \Psi(\chi^2) \subset \Psi_1(\chi^2) \tag{4.17}$$

The functions F_1 and F_2 do not require solving a non-linear least-squares problem, hence resulting in a much lower computational burden compared to the calculation of $\check{b}(z)$ in $F(z)$ with the weighted squared norm $Q^{-1}_{\hat{b}(z)\hat{b}(z)}$.
For completeness, we would like to mention another method, the so called "Search and Shrink approach". This approach was already mentioned in (de Jonge and Tiberius, 1996) and developed to solve the same problem in (Giorgi et al., 2008)(Teunissen, 2010). The "Expansion approach" and "Search and Shrink approach" will obtain the same solution and thus have the same performance for ambiguity resolution, although the required computational effort might differ.

4.2.2 The constrained float solution

A viable way to improve the float solution is by applying the a-priori known baseline length in what is called a constrained float solution. The float solution $\hat{z}$ in Eq. (3.40) derived in section 3.3.2.1 is not based on the baseline constraint, hence the improved float solution can be obtained by incorporating this information in the float solution. Then the baseline constrained least-squares problem can be written as (Teunissen, 2006):

$$\min_{z\in\mathbb{R}^n, b\in\mathbb{R}^3, ||b||=l} \|y - Az - Gb\|^2_{Q_{yy}} \tag{4.18}$$

The difference with Eq. (4.5) is that z is not an integer number but a real-valued number.

Similar to Eq. (4.5) the minimization problem can be reformulated as:

$$\begin{aligned}
&\min_{z\in\mathbb{R}^n, b\in\mathbb{R}^3, ||b||=l} \|y - Az - Gb\|^2_{Q_{yy}} \\
&= \|\hat{e}\|^2_{Q_{yy}} + \min_{z\in\mathbb{R}^n, b\in\mathbb{R}^3, ||b||=l} \left(\|\hat{b} - b\|^2_{Q_{\hat{b}\hat{b}}} + \|\hat{z}(b) - z\|^2_{Q_{\hat{z}(b)\hat{z}(b)}} \right) \\
&= \|\hat{e}\|^2_{Q_{yy}} + \min_{b\in\mathbb{R}^3, ||b||=l} \left(\|\hat{b} - b\|^2_{Q_{\hat{b}\hat{b}}} + \min_{z\in\mathbb{R}^n} (\|\hat{z}(b) - z\|^2_{Q_{\hat{z}(b)\hat{z}(b)}}) \right)
\end{aligned} \tag{4.19}$$

where $\hat{z}(b)$ is the least-squares solution for z, assuming that b is known. Then, by applying again the variance propagation law, the v-c matrix for the least-squares solution for z assuming that b is known, becomes:

$$Q_{\hat{z}(b)\hat{z}(b)} = Q_{\hat{z}\hat{z}} - Q_{\hat{z}\hat{b}} Q^{-1}_{\hat{b}\hat{b}} Q_{\hat{b}\hat{z}} \tag{4.20}$$

Similar to Eq. (3.39), the last term of the third equation can be made zero -as there is no integer requirement- for any b, the constrained float solution is given as:

$$\begin{aligned}
\hat{b}_l &= \min_{b\in\mathbb{R}^3, ||b||=l} \left(\|\hat{b} - b\|^2_{Q_{\hat{b}\hat{b}}} \right) \\
\hat{z}_l &= \hat{z}(\hat{b}_l) = \hat{z} - Q_{\hat{z}\hat{b}} Q^{-1}_{\hat{b}\hat{b}} (\hat{b} - \hat{b}_l) = (A^T Q^{-1}_{yy} A)^{-1} A^T Q^{-1}_{yy} (y - G\hat{b}_l)
\end{aligned} \tag{4.21}$$

It follows from this equation that the *constrained float solution* $\hat{b}_l, \hat{z}_l$ is related to the *unconstrained float solution* $\hat{b}, \hat{z}$ as was described in Eq. (3.40). Once $\hat{b}_l$ is solved as a nonlinear (i.e. quadratically constrained) least-squares problem, only a linear correction $\hat{b} - \hat{b}_l$ on $\hat{z}$ is required to obtain $\hat{z}_l$. Since $\hat{z}_l$ can be expected to be an improvement over $\hat{z}$, the constrained float solution in the metric of $Q_{\hat{z}\hat{z}}$ can be expected to be closer to the true integer vector. Of course this does not mean that the success rate of ambiguity fixing will increase if we apply the constrained float solution, as both minimization problems will find the same solution, but instead it will generally make the ambiguity search step more time efficient.

4.2.3 Multi-epoch Model

Next a multi-epoch model for C-LAMBDA is derived as an extension of the multi-epoch model described in section 3.3.3.1. For clarity we will repeat the least-squares criterion for the multi-epoch model obtained in section 3.3.3.1:

$$\begin{aligned}
&\min_{z\in\mathbb{Z}^n, \underline{b}\in\mathbb{R}^{3\times N_e}} \left\| \begin{matrix} y_1 - Az_{N_e} - G_1 b_1 \\ \vdots \\ y_{N_e} - Az_{N_e} - G_{N_e} b_{N_e} \end{matrix} \right\|^2_{I_{N_e}\otimes Q_{yy}} = \sum_{i=1}^{N_e} \|\hat{e}_i\|^2_{Q_{yy}} + \\
&+ \min_{z\in\mathbb{Z}^n, \underline{b}\in\mathbb{R}^{3\times N_e}} \left(\|\hat{z}_{N_e} - z\|^2_{Q_{\hat{z}_{N_e}\hat{z}_{N_e}}} + \sum_{i=1}^{N_e} \|\hat{b}_i(z) - b_i\|^2_{Q_{\underline{\hat{b}}_i(z)\underline{\hat{b}}_i(z)}} \right)
\end{aligned} \tag{4.22}$$

where $\underline{b} = \left[b_1 \dots b_{N_e}\right]$.

For the constrained solution, the baseline length is known and assumed constant over time, therefore the nonlinear geometrical constraints $\|b_i\| = l$ have to be respected for $i = 1, \dots, N_e$.
The unconstrained float solution $\hat{z}_{N_e}$ and $\hat{b}_1, \dots, \hat{b}_{N_e}$ are obtained as explained in section 3.3.3.1. As we saw in section 4.2.1, the last term on the right-hand side of the least-squares criterion cannot be made zero for any choice of the ambiguity vector z, and thus the sought integer vector not only minimizes the distance to the float solution in the metric $Q_{\hat{z}_{N_e}\hat{z}_{N_e}}$, but also the distance to the float baseline solution.

The baseline solutions at the different epochs $i = 1, \dots, N_e$ after solving the set of nonlinear least-squares problems can be obtained from:

$$\check{b}_i = \arg \min_{b_i \in \mathbb{R}^3, \|b_i\| = l} \|\hat{b}_i(\check{z}) - b_i\|^2_{Q_{\hat{b}_i(z)\hat{b}_i(z)}} \tag{4.23}$$

4.3 MC-LAMBDA

In this section a multivariate extension of the C-LAMBDA approach is introduced. We will solve the multi-baseline problem on a single platform by the multivariate generalization of the method coined the Multivariate Constrained (MC-)LAMBDA method. We will start with a demonstration why calculating attitude from multiple single baseline solutions is suboptimal.

4.3.1 Attitude from combining Single Baseline Estimates

If a platform has more than one baseline, its attitude can be determined by combining the single baseline estimates. In this case the relationship Eq. (4.3) is not applied to solve the multivariate model as we will do in section 4.3.2, it is only applied to compute the attitude matrix R after the individual baselines are fixed. The simplest way to obtain three axis attitude from two directions is by the TRIAD (Three-axis Attitude Determination) algorithm (Shuster and Oh, 1981). The drawback of this method is that it can be applied to only two baselines.
A more general approach is achieved by the following solution:

$$\check{R} = \arg \min_{R \in \mathbb{O}^{3\times q}} \|vec(\check{B} - RF)\| \tag{4.24}$$

The body frame vectors of coordinates are denoted as f_i and collected in the matrix $F = \left[f_1, \dots, f_N\right]$. The orthogonality requirement is formulated as $R \in \mathbb{O}^{3\times q}$ and will be discussed in more detail in section 4.3.2.

A well-known method to calculate an attitude estimation from two or more baselines is called Wahba method after one of the first authors to publish it (Wahba, 1965). This is the method applied in (Giorgi and Buist, 2008) to calculate the attitude from N baselines estimated by the C-LAMBDA method using:

$$\check{R} = \arg \min_{R \in \mathbb{O}^{3\times 3}} \sum_{i=1}^{N} \|b_i - Rf_i\|^2 = trace(B^T B) + trace(F^T F) - 2trace(R^T B F^T) \quad (4.25)$$

Minimizing this equation equals to maximizing the third term on the right-hand side. If the product BF^T is non-singular it can be decomposed, using Singular Value Decomposition, as two orthonormal matrices U and V and a diagonal matrix D: $BF^T = UDV^T$. In (Giorgi and Buist, 2008) it was shown that the minimizer of Eq. (4.25) is

$$\check{R} = U\hat{X}V^T \quad (4.26)$$

with

$$\check{X} = \begin{bmatrix} det(V^T U) & 0 \\ 0 & I_{N-1} \end{bmatrix} \quad (4.27)$$

The accuracy on the estimation of the matrix $\check{R}$ depends on two factors, the length of the baseline and the precision of the baselines solution: lower variances on the baseline components and longer baselines produce higher angular accuracies. As was shown in section 3.3.2.1 for the conditional baseline solution, the former depends on the carrier phase observations. This is a relationship that will be discussed in section 4.3.3.

The above approach is clearly a suboptimal way to combine observations from multiple baselines as not all available information is applied, a better way will be introduced next.

4.3.2 Constrained Multi-baseline Model

Next a matrix formulation for the multi-baseline problem based on (Teunissen, 2007) is introduced. We will make use of a $2n \times N$ data matrix $Y = [y_1, \ldots, y_N]$, an $n \times N$ matrix $Z = [z_1, \ldots, z_N]$ of N DD integer ambiguity vectors and a $3 \times N$ matrix $B = [b_1, \ldots, b_N]$ of N unknown baseline vectors. The linear multi-baseline model can be formulated as:

$$E(Y) = AZ + GB \quad (4.28)$$

Two definitions of the baselines in a four antenna example are shown in Fig. 4.7. In order to apply the integer least-squares principle to Eq. (4.28), this equation is written in the form of Eq. (3.38) using the vec-operator. The vec-operator is a linear transformation which transforms a matrix into a vector by stacking the columns of the matrix one underneath

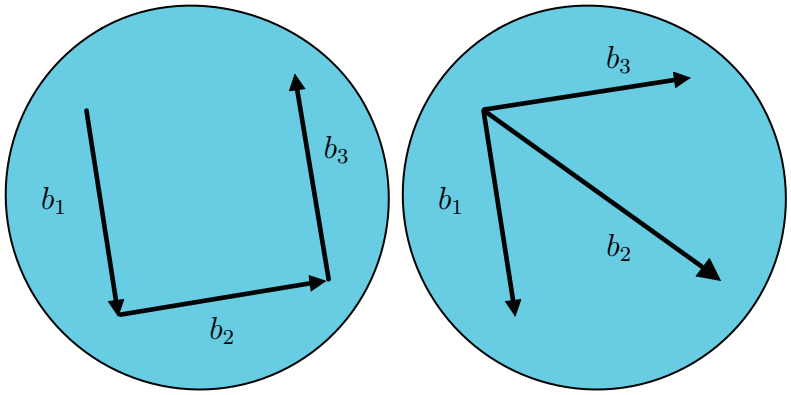


Figure 4.7: Two definitions for multi-baseline model

the other (Appendix D.1). Application of the vec-operator and the Kronecker product $\otimes$ to Eq. (4.28) gives:

$$\begin{aligned} E(vec(Y)) &= (I_N \otimes A)vec(Z) + (I_N \otimes G)vec(B) \\ D(vec(Y)) &= P_B \otimes Q_{yy} = Q_{YY} \end{aligned} \tag{4.29}$$

To describe the dispersion of the observations at all baselines, we make use of $P_B \otimes Q_{yy}$, where matrix P_B takes care of the correlation that follows from the fact that the baselines have one antenna in common in the baseline definitions shown in Fig. 4.7. In Chapter 5, the matrix P_B will be discussed in detail. As an example of a four antenna configuration at a single platform (shown on the left-side in Fig. 4.7) using the identity matrix I_{2n} with the dimension $2n$ of the double differenced observation vector y, the dispersion becomes:

$$\begin{aligned} D\begin{bmatrix} y_1 \\ y_2 \\ y_3 \end{bmatrix} &= \begin{bmatrix} -I_{2n} & I_{2n} & 0 & 0 \\ 0 & -I_{2n} & I_{2n} & 0 \\ 0 & 0 & -I_{2n} & I_{2n} \end{bmatrix} \begin{bmatrix} \frac{1}{2}Q_{yy} & 0 & 0 & 0 \\ 0 & \frac{1}{2}Q_{yy} & 0 & 0 \\ 0 & 0 & \frac{1}{2}Q_{yy} & 0 \\ 0 & 0 & 0 & \frac{1}{2}Q_{yy} \end{bmatrix} \begin{bmatrix} -I_{2n} & 0 & 0 \\ I_{2n} & -I_{2n} & 0 \\ 0 & I_{2n} & -I_{2n} \\ 0 & 0 & I_{2n} \end{bmatrix} \\ &= \begin{bmatrix} Q_{yy} & -\frac{1}{2}Q_{yy} & 0 \\ -\frac{1}{2}Q_{yy} & Q_{yy} & -\frac{1}{2}Q_{yy} \\ 0 & -\frac{1}{2}Q_{yy} & Q_{yy} \end{bmatrix} = P_B \otimes Q_{yy} \end{aligned} \tag{4.30}$$

In this matrix we recognize the DD v-c matrix on the diagonal and the single difference v-c matrix on the off-diagonal entries (see sections 2.4.2 and 2.4.3).

In attitude determination, normally the baselines are chosen to have one master antenna in common (shown on the right hand side in Fig. 4.7), and therefore the dispersion becomes:

$$D\begin{bmatrix} y_1 \\ y_2 \\ y_3 \end{bmatrix} = \begin{bmatrix} -I_{2n} & I_{2n} & 0 & 0 \\ -I_{2n} & 0 & I_{2n} & 0 \\ -I_{2n} & 0 & 0 & I_{2n} \end{bmatrix} \begin{bmatrix} \frac{1}{2}Q_{yy} & 0 & 0 & 0 \\ 0 & \frac{1}{2}Q_{yy} & 0 & 0 \\ 0 & 0 & \frac{1}{2}Q_{yy} & 0 \\ 0 & 0 & 0 & \frac{1}{2}Q_{yy} \end{bmatrix} \begin{bmatrix} -I_{2n} & -I_{2n} & -I_{2n} \\ I_{2n} & 0 & 0 \\ 0 & I_{2n} & 0 \\ 0 & 0 & I_{2n} \end{bmatrix}$$
$$= \begin{bmatrix} Q_{yy} & \frac{1}{2}Q_{yy} & \frac{1}{2}Q_{yy} \\ \frac{1}{2}Q_{yy} & Q_{yy} & \frac{1}{2}Q_{yy} \\ \frac{1}{2}Q_{yy} & \frac{1}{2}Q_{yy} & Q_{yy} \end{bmatrix} = P_B \otimes Q_{yy} \tag{4.31}$$

Next, we will introduce a model for which we can apply the MC-LAMBDA method. As we will see, this method cannot only make use of known baseline lengths of multi-baseline configurations, but also the relative geometry between the baselines. We assume that the constrained baselines are rigidly fixed on the platform and the their geometry is known in the body frame integral with the platform. The body frame vectors of coordinates are denoted as f_i and collected in the $3 \times N$ matrix $F = \begin{bmatrix} f_1, \ldots, f_N \end{bmatrix}$. The relationship between the baselines b and f, as discussed in section 4.1.2, is given by the rotation matrix R:

$$B = RF \tag{4.32}$$

It is clear that R is underdetermined for a single baseline configuration, although in that case an attitude information can be obtained (for a single baseline heading and elevation as explained in section 4.1.1). To be able to include the single baseline case, the structure for body frame representation introduced in (Teunissen, 2007) is followed. The baselines of the body frame are represented as a special sort of triangular matrix:

$$N \geq 3, q = 3 : RF = \begin{bmatrix} r_1, r_2, r_3 \end{bmatrix} \begin{bmatrix} f_{11} & f_{21} & f_{31} & \ldots & f_{N1} \\ 0 & f_{22} & f_{32} & \ldots & f_{N2} \\ 0 & 0 & f_{33} & \ldots & f_{N3} \end{bmatrix} \tag{4.33}$$

$$N = q = 2 : RF = \begin{bmatrix} r_1, r_2 \end{bmatrix} \begin{bmatrix} f_{11} & f_{21} \\ 0 & f_{22} \end{bmatrix} \tag{4.34}$$

$$N = q = 1 : RF = r_1 f_{11} \tag{4.35}$$

In the applied definition, the first axis of the local coordinate frame is aligned with the first baseline, the second axis is perpendicular to the first axis in the plane that is formed by the first two baselines, the third axis is directed in the direction of the outer product of the first two baselines forming a right-handed orthogonal frame.

For notational convenience the parameter q is introduced to indicate the number of columns in R. Then it follows directly that

$q = 3$ for $N \geq 3$
$q = N$ for $N < 3$

And thus for $q = N = 1$, the model of Eq. (4.28) is reduced to the model of section 4.2 with a scaling factor for the baseline length. This will be discussed in more detail later.
Applying the rotation matrix R, Eq. (4.28) can be rewritten to:

$$E(Y) = AZ + GRF \tag{4.36}$$

in which the unknowns are Z and R. Again application of the vec-operator gives (Teunissen, 2007):

$$\begin{aligned} E(vec(Y)) &= (I_N \otimes A)vec(Z) + (F^T \otimes G)vec(R) \\ D(vec(Y)) &= P_B \otimes Q_{yy} \end{aligned} \tag{4.37}$$

Now we can solve the multi-baseline problem on a single platform by the multivariate generalization in which an arbitrary number of baselines can be included in the model and solved integrally as we will discuss next based on (Teunissen, 2007)(Giorgi et al., 2009, 2010).

The least-squares solution of Eq. (4.37) disregarding the integer and orthonormality constraints on Z and R respectively is:

$$\begin{bmatrix} vec(\hat{Z}) \\ vec(\hat{R}) \end{bmatrix} = \begin{bmatrix} Q_{\hat{Z}\hat{Z}} & Q_{\hat{Z}\hat{R}} \\ Q_{\hat{R}\hat{Z}} & Q_{\hat{R}\hat{R}} \end{bmatrix} \left[\begin{bmatrix} I_N \otimes A & F^T \otimes G \end{bmatrix}^T [P_B \otimes Q_{yy}]^{-1} vec(Y) \right] \tag{4.38}$$

for which the v-c matrix is derived as:

$$\begin{aligned} \begin{bmatrix} Q_{\hat{Z}\hat{Z}} & Q_{\hat{Z}\hat{R}} \\ Q_{\hat{R}\hat{Z}} & Q_{\hat{R}\hat{R}} \end{bmatrix} &= \left[\begin{bmatrix} I_N \otimes A & F^T \otimes G \end{bmatrix}^T [P_B \otimes Q_{yy}]^{-1} \begin{bmatrix} I_N \otimes A & F^T \otimes G \end{bmatrix} \right]^{-1} \\ &= \begin{bmatrix} P_B^{-1} \otimes A^T Q_{yy}^{-1} A & F P_B^{-1} \otimes G^T Q_{yy}^{-1} A \\ P_B^{-1} F^T \otimes A^T Q_{yy}^{-1} G & F P_B^{-1} F^T \otimes G^T Q_{yy}^{-1} G \end{bmatrix}^{-1} \end{aligned} \tag{4.39}$$

If we assume that the integer ambiguity matrix Z is known, then the float estimation of the rotation matrix with the corresponding v-c matrix is:

$$\begin{aligned} vec(\hat{R}(Z)) &= vec(\hat{R}) - Q_{\hat{R}\hat{Z}} Q_{\hat{Z}\hat{Z}}^{-1} vec(\hat{Z} - Z) \\ Q_{\hat{R}(Z)\hat{R}(Z)} &= Q_{\hat{R}\hat{R}} - Q_{\hat{R}\hat{Z}} Q_{\hat{Z}\hat{Z}}^{-1} Q_{\hat{Z}\hat{R}} \end{aligned} \tag{4.40}$$

The minimization problem that has to be solved is:

The minimization problem of MC-LAMBDA

$$vec(\check{Z}) = \arg\min_{Z\in\mathbb{Z}^{n\times N}} \left(\left\| vec(\hat{Z}-Z) \right\|^2_{Q_{\hat{Z}\hat{Z}}} + \min_{R\in\mathbb{O}^{3\times q}} \left\| vec(\hat{R}(Z)-R(Z)) \right\|^2_{Q_{\hat{R}(Z)\hat{R}(Z)}} \right) \tag{4.41}$$

The solution of this problem which accounts for both the integer and attitude matrix, is named the Multivariate-Constrained (MC-)LAMBDA.
The model of Eq. (4.29) did not explicitly account for the geometrical constraints on the attitude matrix R. For this rotation matrix it is known that it belongs to the class of orthonormal matrices for which $R^TR = I_q$ (see section 4.3.1). For platforms with three or more baselines, this results in six constraints, namely three orthogonality and three unit length constraint of the three columns of the rotation matrix. If our platform contains only a single baseline, the result is one constraint on the rotation matrix, namely the unit length, thus the MC-LAMBDA is reduced to C-LAMBDA as described in Section 4.2.1 with a scaling factor for the baseline length. We formulate the orthonormality requirement as $R_q \in \mathbb{O}^{3\times q}$.

The orthonormal attitude matrix has to be numerically extracted by solving for the last term in problem Eq. (4.41), for which three schemes are briefly reviewed.
The solution based on the Lagrangian Multipliers Method was described for the single baseline in section 4.2. For the multi-baseline problem, this solution will be discussed for the constrained float solution in section 4.3.5.

Euler angles and quaternions can also be used to reparametrize the rotation matrix R and solve for Eq. (4.41). After reparameterizing the attitude matrix in terms of the Euler angles, the matrix $R(\theta)$ implicitly fulfills the constraint $R^TR = I_q$

$$\check{\theta} = \arg\min_{\theta\in\mathbb{R}^3} \|h(\theta)\|^2_I \tag{4.42}$$

with $h(\theta) = Q^{-\frac{1}{2}}_{\hat{R}\hat{R}} vec(\hat{R}(Z) - R(\theta))$ as the vector of $3q$ nonlinear functions of θ.

The Euler angles parameterization approach has the advantage of working with only three unknowns, and in general converges to the sought minimizer if an accurate initial guess is used. The disadvantage is that trigonometric functions have to be evaluated, increasing the computational load.

For quaternions, the minimization problem becomes:

$$\check{\overline{q}} = \arg\min_{\overline{q}\in\mathbb{R}^4, \|\overline{q}\|=1} \|vec(\hat{R}(Z) - R(\overline{q}))\|^2_{Q_{\hat{R}\hat{R}}} \tag{4.43}$$

The orthogonality constraint for R is guaranteed by the normality of the quaternion (see appendix E.5). The Lagrangian function can be written as:

$$\Lambda(\overline{q},\mu) = vec(\hat{R}(Z) - R(\overline{q}))^T Q^{-1}_{\hat{R}\hat{R}} vec(\hat{R}(Z) - R(\overline{q})) - trace\left[\mu(\overline{q}^T\overline{q} - 1)\right] \tag{4.44}$$

with μ is the Lagrangian multiplier. This approach appears to be the best of the three, as it makes use of a small number of unknowns and no trigonometric functions have to be evaluated (Giorgi et al., 2012).

The same bounding functions as discussed in section 4.2.1 can be applied to perform the search in a more efficient way. A list of alternative bounding functions has been studied in (Nadarajah et al., 2011), some of which provide tighter bounds and thus speeding up the search process.

Intermezzo By applying the same reasoning as in the example given in section 3.3.2.1, the v-c matrices of Eq. (4.39) can be rewritten, with the following intermediate step:

$$\begin{aligned}
Q_{\hat{R}\hat{R}} &= [FP_B^{-1}F^T]^{-1} \otimes [\overline{G}^T Q_{yy}^{-1}\overline{G}]^{-1} \\
Q_{\hat{Z}\hat{R}} &= -F^T[FP_B^{-1}F^T]^{-1} \otimes \left[[A^T Q_{yy}^{-1}A]^{-1}A^T Q_{yy}^{-1}G[\overline{G}^T Q_{yy}^{-1}\overline{G}]^{-1}\right] \\
Q_{\hat{R}\hat{Z}} &= Q_{\hat{Z}\hat{R}}^T \\
Q_{\hat{Z}\hat{Z}} &= \big[P_B^{-1} \otimes A^T Q_{yy}^{-1}A + \\
&\quad -[P_B^{-1}F^T \otimes A^T Q_{yy}^{-1}G][FP_B^{-1}F^T \otimes G^T Q_{yy}^{-1}G]^{-1}[FP_B^{-1} \otimes G^T Q_{yy}^{-1}A]\big]^{-1}
\end{aligned} \tag{4.45}$$

to:

$$Q_{\hat{R}\hat{R}} = \sigma_p^2\left[[FP_B^{-1}F^T]^{-1} \otimes [U^T Q^{-1}U]^{-1}\right] \tag{4.46}$$

$$Q_{\hat{Z}\hat{Z}} = \frac{\sigma_\phi^2}{\lambda_f^2}\left[P_B \otimes \frac{\sigma_\phi^2}{{\sigma_P}^2}Q + F^T[FP_B^{-1}F^T]^{-1}F \otimes U[U^T Q^{-1}U]^{-1}U^T\right] \tag{4.47}$$

As was observed for the baseline float solution, the attitude float solution R is only driven by the precision of the code observations (for a give baseline configuration), and as the code observations are much less accurate than the carrier phase, the precision of the float ambiguity Z is also dominated by the code precision.

The conditional attitude variance matrix can be derived by applying Eq. (4.40) to

$$\begin{aligned}
Q_{\hat{R}(Z)\hat{R}(Z)} &= [FP_B^{-1}F^T]^{-1} \otimes [G^T Q_{yy}^{-1}G]^{-1} \\
&= [FP_B^{-1}F^T]^{-1} \otimes \frac{\sigma_\phi^2}{\frac{\sigma_\phi^2}{\sigma_P^2} + 1}[U^T Q^{-1}U]^{-1} \\
&\approx [FP_B^{-1}F^T]^{-1} \otimes \sigma_\phi^2[U^T Q^{-1}U]^{-1}
\end{aligned} \tag{4.48}$$

This shows again that the precision of the conditional solution is driven by the much more precise carrier phase observation and, different from the conditional baseline solution, also by the baseline geometry as defined by F. This will be discussed in more detail in the next section.

4.3.3 Influence of baseline and satellite geometry on attitude estimation

A well-known term in GNSS is dilution of precision (DOP), defined as:

$$DOP = \sqrt{\sum_{i=1}^{n} (A^T A)_{ii}^{-1}} = trace([A^T A]^{-1}) \tag{4.49}$$

where the subscripts refer to the diagonal elements of the matrix $[A^T A]^{-1}$, or in other words the $trace$. The DOP values indicate the influence of the geometry on the precision of the parameters to be estimated. Well-known DOP factors are Geometric DOP (GDOP), Position DOP (PDOP), Horizontal DOP, Vertical DOP (VDOP) and Time DOP (TDOP) where

$$\begin{aligned} GDOP &= \sqrt{PDOP^2 + TDOP^2} \\ PDOP &= \sqrt{HDOP^2 + VDOP^2} \end{aligned} \tag{4.50}$$

The horizontal DOP and the vertical DOP, are both dependent on the coordinate system applied (for example North, East, Down).

Deriving a DOP value for attitude, based on the precision of the conditional attitude of Eq, (4.48) is not straightforward. In literature simpler models are available (Sullivan, 1995)(Cohen, 1996)(Gomez, 2000)(Yoon and Lundberg, 2001)(Buist et al., 2003)(Park et al., 2006), all based on the assumption that the attitude estimation is solely determined by the carrier phase observation.

Cohen made use of the following cost function:

$$J(A) = \sum_{r=1}^{N} \sum_{j=1}^{n+1} (\triangle \mathbf{r}_r^j - \mathbf{f}_r^T A \mathbf{u}^j)^2 \tag{4.51}$$

where $\triangle \mathbf{r}_r^j$ is the measured and $\mathbf{h}_r^j = \mathbf{f}_r^T A \mathbf{u}^j = \mathbf{u}^j A \mathbf{f}_r$ is the predicted path distance for baseline r and GNSS satellite j. In this expression, Cohen assumed that the integer

ambiguity vector was resolved and that the line bias was removed by calibration (thus the observable is a single difference observation with the line bias term removed (see section 2.4.2)).

Cohen estimated attitude by minimizing the following linearized cost function (Cohen, 1996):

$$J(\triangle\theta) = \sum_{r=1}^{N}\sum_{j+1}^{n+1}(\delta r_r^j - \mathbf{h}_r^j \triangle\theta^x)^2 \tag{4.52}$$

where the attitude error and its skew-symmetric matrix are defined as (Shuster, 1993):

$$\triangle\theta = \begin{bmatrix}\delta r\\ \delta p\\ \delta y\end{bmatrix} \triangle\theta^x = \begin{bmatrix}0 & y & -p\\ -y & 0 & r\\ p & -r & 0\end{bmatrix} \tag{4.53}$$

The iterative process applied is initialized with an a priori attitude matrix (which can be the identity matrix). The attitude error vector is calculated and the attitude matrix is updated until the final solution is obtained, although convergence of the process cannot be guaranteed. The minimizer of this cost function is the square root of the trace of the observation matrix and its transpose.

$$\sqrt{trace(H^T H)^{-1}} = \sqrt{trace(\sum_{j=1}^{n+1}\mathbf{u}^{jxT}A^T F F^T A\mathbf{u}^{jx})^{-1}} \tag{4.54}$$

where

$$\mathbf{u}^{jx} = \begin{bmatrix}0 & \mathbf{u}_z^j & -\mathbf{u}_y^j\\ -\mathbf{u}_z^j & 0 & \mathbf{u}_x^j\\ \mathbf{u}_y^j & -\mathbf{u}_x^j & 0\end{bmatrix} \tag{4.55}$$

For an orthogonal baseline configuration, $FF^T = l^2 I_3$, with l is the effective baseline length, this can be rewritten to

$$\sqrt{\frac{trace(\sum_{j=1}^{n+1}\mathbf{u}^{jxT}A^T A\mathbf{u}^{jx})^{-1}}{l^2}} = \sqrt{\frac{trace\big(\,(n+1)\,I_3 - GG^T\big)^{-1}}{l^2}} \tag{4.56}$$

In this last step, the invariance of the matrix trace with respect to rotations is applied.

The term

$$\sqrt{trace\big((n+1)I_3 - GG^T\big)^{-1}} \tag{4.57}$$

is in (Cohen, 1996) referred to as the Attitude DOP or ADOP. (to avoid confusion with the Ambiguity DOP, Attitude DOP will be written as AttDOP).
Another AttDOP definition found in literature (Sullivan, 1995)(Gomez, 2000)(Yoon and Lundberg, 2001)(Buist et al., 2003)(Park et al., 2006) can be derived by linearizing the observation equation h, for example by taking the derivative with respect to the Euler angles ($\theta = (r, p, y)$); $H = \frac{\partial h}{\partial \theta}$:

$$\sqrt{trace(H^T Q^{-1} H)^{-1}} \tag{4.58}$$

where Q is a v-c matrix which differs for single and double difference models (see chapter 2).

For an orthogonal baseline configuration, $FF^T = l^2 I_q$, with l is the effective baseline length, an angular pointing error, according to (Cohen, 1996), can be written as:

$$\sigma_\theta = AttDOP \frac{\sigma_{\phi_f}}{l} \tag{4.59}$$

This AttDOP quantity is, assuming sufficient locked GNSS satellites and nominal geometry, in general close to one (Cohen, 1996)(Purivigraipong, 2000), and therefore the relationship can be simplified to:

$$\sigma_\theta \approx \frac{\sigma_{\phi_f}}{l} \tag{4.60}$$

This is the relationship that was shown in Fig. 4.2.

Next, the obtained v-c matrices for the MC-LAMBDA approach are investigated, all of which depend on the $q \times q$ matrix $FP_B^{-1}F^T$.

The precision of the attitude float solution $\hat{R}$ was obtained in Eq. (4.46) as

$$Q_{\hat{R}\hat{R}} = \sigma_p^2 \left[[FP_B^{-1}F^T]^{-1} \otimes [U^T Q^{-1} U]^{-1} \right] \tag{4.61}$$

and the float ambiguity solution $\hat{Z}_R$ for the attitude model (see Eq. (4.47))

$$Q_{\hat{Z}_R \hat{Z}_R} = \frac{\sigma_\phi^2}{\lambda_f^2} \left[P_B \otimes \frac{\sigma_\phi^2}{\sigma_P^2} Q + F^T [FP_B^{-1}F^T]^{-1} F \otimes U [U^T Q^{-1} U]^{-1} U^T \right] \tag{4.62}$$

The precision of the conditional attitude $\hat{R}(Z)$ was found in Eq. (4.48) as

$$Q_{\hat{R}(Z)\hat{R}(Z)} \approx [FP_B^{-1}F^T]^{-1} \otimes \sigma_\phi^2 [U^T Q^{-1} U]^{-1} \tag{4.63}$$

Thus the precision of the estimations are functions of the GNSS satellite geometry ($U^T Q^{-1} U$) and the local baseline geometry ($FP_B^{-1}F^T$). An evaluation parameter capable

of capturing the influence of the geometry-dependent term $F^T\left[FP_B^{-1}F^T\right]^{-1}F$ is useful, since this term induces smaller entries of the float ambiguity v-c matrix. The following parameter has been suggested to evaluate the baseline geometry in (Giorgi, 2011):

$$\nu_F = 1+\left(e_N^T F^T\left(FF^T\right)^{-1}Fe_N\right)|P_B| \tag{4.64}$$

where e_N is a column vector with N elements equal to one. The factor ν_F accounts for the number of baselines and their relative geometry. This parameter evaluates the quality of the baseline geometry resulting in higher values ν_F for less favorable antenna configurations.

For precise attitude determination, larger values for the $FP_B^{-1}F^T$ entries are desired to minimize the attitude v-c matrices $Q_{\hat{R}\hat{R}}$ as given by Eq. (4.46) and $Q_{\hat{R}(Z)\hat{R}(Z)}$ by Eq. (4.48). This can be achieved by employing longer baselines.
With respect to the baseline lengths, it is useful to consider the qth root of the determinants of v-c matrices, which read

$$|Q_{\hat{R}\hat{R}}|^{\frac{1}{q}} = \sigma_p^{\frac{6}{q}}|F^TP_B^{-1}F|^{-1}|U^TQ^{-1}U|^{-1} \tag{4.65}$$

$$|Q_{\hat{R}(Z)\hat{R}(Z)}|^{\frac{1}{q}} = \frac{\sigma_\phi^2}{\left(\frac{\sigma_\phi^2}{\sigma_p^2}+1\right)^{\frac{3}{q}}}|F^TP_B^{-1}F|^{-1}|U^TQ^{-1}U|^{-1} \tag{4.66}$$

Longer baselines result in larger determinants, hence smaller entries for the matrices $Q_{\hat{R}\hat{R}}$ and $Q_{\hat{R}(Z)\hat{R}(Z)}$.

4.3.4 Influence of baseline geometry on ambiguity resolution

This section discusses impact of antenna geometry on ambiguity resolution. The advantage of using the attitude model in Eq. (4.36) for ambiguity resolution when $n > q$ can be partially quantified through the ADOP factor (Teunissen, 2000). To evaluate the effect of the number of baselines, let us consider both the baseline model of Eq. (4.28) and the attitude model in Eq. (4.36). By substituting $F \rightarrow I$ into Eq. (4.47), the variance-covariance matrix of ambiguity float solution of model (Eq. 4.28) can deduced as (the single baseline equivalence was given in Eq. (3.52))

$$Q_{\hat{Z}_B\hat{Z}_B} = \frac{\sigma_p^2}{\lambda_f^2}P_B^{-1}\otimes\left(\frac{\sigma_\phi^2}{\sigma_p^2}Q+U\left(U^TQ^{-1}U\right)^{-1}U^T\right) \tag{4.67}$$

To quantify the effect of the number of baselines applied in the solution, a gain factor is defined in (Giorgi, 2011):

$$\zeta = \frac{ADOP\left(Q_{\hat{Z}_B\hat{Z}_B}\right)}{ADOP\left(Q_{\hat{Z}_R\hat{Z}_R}\right)} = \left(1+\frac{\sigma_p^2}{\sigma_\phi^2}\right)^{\frac{3(N-q)}{2nN}} \tag{4.68}$$

For $n = q$, the ratio ζ is always equal to one, and there is no gain in using the attitude model over the multi-baseline model. When the number of baselines is higher than q, the gain factor increases. The gain factor ζ is independent of the actual local baseline coordinates F, and it only quantifies the advantage of having a higher number of baselines on the platform when using the attitude model instead of the multi-baseline model.

4.3.5 The constrained float solution

The constrained float solution of the MC-LAMBDA problem is the solution of

$$\begin{aligned} vec(\hat{R}_c) &= \min_{R_c \in \mathbb{O}^{3\times q}} \|vec(\hat{R} - R)\|^2_{Q_{\hat{R}\hat{R}}} \\ vec(\hat{Z}_c) &= vec(\hat{Z}(\hat{R}_c)) = vec(\hat{Z}) - Q_{\hat{Z}\hat{R}} Q^{-1}_{\hat{R}\hat{R}} vec(\hat{R} - \hat{R}_c) \end{aligned} \tag{4.69}$$

These equations are similar to what was found in section 4.2.2 for the single baseline problem. Now due to the imposition of the orthogonal constraint, the constrained float solution $\hat{Z}_c$ must be closer to the optimal ambiguity $\check{Z}$ than the unconstrained float solution $\hat{Z}$. First the unconstrained float solutions $\hat{Z}$ and $\hat{R}$ are obtained by Eq. (4.38). Second, the attitude constrained float solution $\hat{R}_c$ is obtained by applying the Lagrangian multipliers methods in a similar way as described in section 4.2.2. Denoting the set of Lagrangian multiplier with μ_q (see section 4.2.1), the relationship between the constrained and unconstrained solution is:

$$vec(\hat{R}_c) = [Q^{-1}_{\hat{R}\hat{R}} - \mu_q \otimes I_3]^{-1} Q^{-1}_{\hat{R}\hat{R}} vec(\hat{R}) \tag{4.70}$$

From the unconstrained float solution Eq. (4.38), it follows that

$$Q^{-1}_{\hat{R}\hat{R}} vec(\hat{R}) = \left[F P_B^{-1} \otimes \overline{G}^T Q^{-1}_{yy} \right] vec(Y) \tag{4.71}$$

and thus Eq. (4.70) can be rewritten to

$$vec(\hat{R}_c) = [Q^{-1}_{\hat{R}\hat{R}} - \mu_q \otimes I_3]^{-1} \left[F P_B^{-1} \otimes \overline{G}^T Q^{-1}_{yy} \right] vec(Y) \tag{4.72}$$

The Lagrange multiplier can be obtained by applying the Lagrangian method for the solution of $vec(\hat{R}_c)$ in Eq. (4.69) utilizing the Lagrange function defined by

$$\Lambda(\hat{R}(Z), \mu_q) = vec(\hat{R} - R)^T Q^{-1}_{\hat{R}\hat{R}} vec(\hat{R} - R) - trace\left[\mu_q (R^T R - I_q)\right] \tag{4.73}$$

with μ_q is the q by q matrix of Lagrangian multipliers:

$$\mu_1 = \mu, \quad \mu_2 = \begin{bmatrix} \mu_1 & \frac{1}{2}\mu_3 \\ \frac{1}{2}\mu_3 & \mu_2 \end{bmatrix}, \quad \mu_3 = \begin{bmatrix} \mu_1 & \frac{1}{2}\mu_4 & \frac{1}{2}\mu_5 \\ \frac{1}{2}\mu_4 & \mu_2 & \frac{1}{2}\mu_6 \\ \frac{1}{2}\mu_5 & \frac{1}{2}\mu_6 & \mu_3 \end{bmatrix} \tag{4.74}$$

Assuming that R is known, Eq. (4.37) becomes

$$\begin{aligned} E\left(vec(Y) - (F^T \otimes G)vec(R)\right) &= (I_N \otimes A)vec(Z_c) \\ D\left(vec(Y) - (F^T \otimes G)vec(R)\right) &= P_B \otimes Q_{yy} \end{aligned} \tag{4.75}$$

and the constrained float solution Z_c

$$vec(Z_c) = \left[P_B^{-1} \otimes A^T Q_{yy}^{-1} A\right]^{-1} \left[P_B^{-1} \otimes A^T Q_{yy}^{-1}\right] \left[vec(Y) - (F^T \otimes G)vec(R)\right] \tag{4.76}$$

Combining Eq. (4.72) with Eq. (4.76) gives

$$\begin{bmatrix} P_B^{-1} \otimes A^T Q_{yy}^{-1} A & P_B^{-1} F^T \otimes A^T Q_{yy}^{-1} G \\ 0 & Q_{\hat{R}\hat{R}}^{-1} - \mu_q \otimes I_3 \end{bmatrix} \begin{pmatrix} vec(\hat{Z}_c) \\ vec(\hat{R}_c) \end{pmatrix} = \begin{bmatrix} P_B^{-1} \otimes A^T Q_{yy}^{-1} \\ F P_B^{-1} \otimes \overline{G}^T Q_{yy}^{-1} \end{bmatrix} vec(Y) \tag{4.77}$$

Multiplying both sides with

$$\begin{bmatrix} I & 0 \\ F \otimes G^T Q_{yy}^{-1} A [A^T Q_{yy}^{-1} A]^{-1} & I \end{bmatrix} \tag{4.78}$$

results in the following normal equations:

$$\begin{bmatrix} P_B^{-1} \otimes A^T Q_{yy}^{-1} A & F P_B^{-1} \otimes G^T Q_{yy}^{-1} A \\ P_B^{-1} F^T \otimes A^T Q_{yy}^{-1} G & F P_B^{-1} F^T \otimes G^T Q_{yy}^{-1} G - \mu_q \otimes I_3 \end{bmatrix} \begin{pmatrix} vec(\hat{Z}_c) \\ vec(\hat{R}_c) \end{pmatrix} = \\ = \begin{bmatrix} P_B^{-1} \otimes A^T Q_{yy}^{-1} \\ F P_B^{-1} \otimes G^T Q_{yy}^{-1} \end{bmatrix} vec(Y) \tag{4.79}$$

Thus it can be concluded that by rewriting the normal equations using the Langranian multiplier, the constrained float solution can be obtained by solving the equations

$$\begin{pmatrix} vec(\hat{Z}_c) \\ vec(\hat{R}_c) \end{pmatrix} = \begin{bmatrix} Q_{\hat{Z}_c\hat{Z}_c} & Q_{\hat{Z}_c\hat{R}_c} \\ Q_{\hat{R}_c\hat{Z}_c} & Q_{\hat{R}_c\hat{R}_c} \end{bmatrix} \left[I_N \otimes A \quad F^T \otimes G\right]^T \left[P_B \otimes Q_{yy}\right]^{-1} vec\left(Y\right) \tag{4.80}$$

where an approximation of the v-c matrix is obtained:

$$\begin{bmatrix} Q_{\hat{Z}_c\hat{Z}_c} & Q_{\hat{Z}_c\hat{R}_c} \\ Q_{\hat{R}_c\hat{Z}_c} & Q_{\hat{R}_c\hat{R}_c} \end{bmatrix} = \Big(\left[I_N \otimes A \quad F^T \otimes G\right]^T \left[P_B \otimes Q_{yy}\right]^{-1} \left[I_N \otimes A \quad F^T \otimes G\right] + \\ + \begin{bmatrix} 0 & 0 \\ 0 & -\mu_q \otimes I_3 \end{bmatrix} \Big)^{-1} \tag{4.81}$$

We switch back to the unconstrained float solution of Eq. (4.38) if the normal matrix Eq. (4.79) becomes singular.

4.3.6 Multi-epoch model

The model introduced in Eq. (4.36) is the single epoch GNSS attitude model. Here we will introduce the multi-epoch model (Teunissen, 2007)(Giorgi et al., 2010).

$$E(Y_i) = AZ + G_i R_i F \tag{4.82}$$

in which the unknowns are Z and R_i and i is the epoch counter $i = 1, 2, \ldots, N_e$. Again application of the vec-operator gives:

$$\begin{aligned} E(vec(Y_i)) &= (I_N \otimes A)vec(Z) + (F^T \otimes G_i)vec(R_i) \\ D(vec(Y_i)) &= Q_{YY} \end{aligned} \tag{4.83}$$

The ambiguities are assumed to be constant during the considered time period, but the observation matrices Y_i, the geometry matrices G_i and the rotation matrices R_i are assumed to vary with time: G changes over time due to the changing relative receiver-satellite geometry and the orthonormal matrix R could change over time, because of the changing attitude of the platform. Similar to the multi-epoch single baseline model derived in sections 3.3.3.1 and 4.2.3 the multi-epoch single frequency model can be written as:

$$\begin{aligned} E\begin{bmatrix} vec(Y_1) \\ vec(Y_2) \\ \vdots \\ vec(Y_{N_e}) \end{bmatrix} &= \begin{bmatrix} I_N \otimes A & F^T \otimes G_1 & 0 & \ldots & 0 \\ I_N \otimes A & 0 & F^T \otimes G_2 & \ldots & 0 \\ \vdots & & & \ddots & \vdots \\ I_N \otimes A & 0 & 0 & \ldots & F^T \otimes G_{N_e} \end{bmatrix} \begin{bmatrix} vec(Z_{N_e}) \\ vec(R_1) \\ \vdots \\ vec(R_{N_e}) \end{bmatrix} \\ &= M_{N_e} \begin{bmatrix} vec(Z_{N_e}) \\ vec(R_1) \\ \vdots \\ vec(R_{N_e}) \end{bmatrix} \\ D\begin{bmatrix} vec(Y_1) \\ vec(Y_2) \\ \vdots \\ vec(Y_{N_e}) \end{bmatrix} &= D\left[\underline{Y}\right] = Q_{\underline{YY}} \end{aligned} \tag{4.84}$$

Again $\underline{(\cdot)}$ indicates multi-epoch variable.

The associated v-c matrix for this multi-epoch float solution is derived as:

$$\begin{bmatrix} Q_{\hat{Z}_{N_e}\hat{Z}_k} & Q_{\hat{Z}_k\underline{\hat{R}}} \\ Q_{\underline{\hat{R}}\hat{Z}_{N_e}} & Q_{\underline{\hat{R}}\underline{\hat{R}}} \end{bmatrix} = \left[\quad M_{N_e}^T (I_{N_e} \otimes Q_{YY}^{-1}) M_{N_e} \right]^{-1} \tag{4.85}$$

where

$$Q_{\underline{\hat{R}}\underline{\hat{R}}} = \begin{bmatrix} Q_{\hat{R}_1\hat{R}_1} & Q_{\hat{R}_1\hat{R}_2} & \cdots & Q_{\hat{R}_1\hat{R}_{N_e}} \\ Q_{\hat{R}_2\hat{R}_1} & Q_{\hat{R}_2\hat{R}_2} & \cdots & Q_{\hat{R}_2\hat{R}_{N_e}} \\ \vdots & & \ddots & \vdots \\ Q_{\hat{R}_{N_e}\hat{R}_1} & Q_{\hat{R}_{N_e}\hat{R}_2} & \cdots & Q_{\hat{R}_{N_e}\hat{R}_{N_e}} \end{bmatrix} \tag{4.86}$$

and

$$Q_{\hat{Z}_{N_e}\hat{Z}_{N_e}} = \begin{bmatrix} Q_{\hat{Z}_{N_e}\hat{R}_1} & Q_{\hat{Z}_{N_e}\hat{R}_2} & \cdots & Q_{\hat{Z}_{N_e}\hat{R}_{N_e}} \end{bmatrix} \tag{4.87}$$

The float solution $\hat{Z}_{N_e}$ is the real-valued least-squares estimator of Z, based on all the data up to and including epoch N_e, but without taking the integerness of Z and the orthonormality of the R_i into account. Matrix $\hat{R}_i(Z)$ is the least-squares estimator of R_i, again based on all the data up to and including epoch N_e and without taking the orthonormality constraints into account, but now assuming that Z is known.

The sum-of-squares decomposition of the squared norm of the residuals is obtained for the multi-epoch model Eq. (4.83) as:

$$\begin{aligned} \left\| \begin{bmatrix} vec(Y_1) \\ \vdots \\ vec(Y_{N_e}) \end{bmatrix} - M_{N_e} \begin{bmatrix} vec(Z_1) \\ vec(R_1) \\ \vdots \\ vec(R_{N_e}) \end{bmatrix} \right\|^2_{Q_{\underline{YY}}} &= \left\| \begin{bmatrix} \hat{E}_1 \\ \vdots \\ \hat{E}_{N_e} \end{bmatrix} \right\|^2_{Q_{\underline{YY}}} + \\ &+ \|vec(\hat{Z}_{N_e} - Z)\|^2_{Q_{\hat{Z}_{N_e}\hat{Z}_{N_e}}} + \left\| \begin{bmatrix} vec(\hat{R}_1(Z) - R_1) \\ \vdots \\ vec(\hat{R}_{N_e}(Z) - R_{N_e}) \end{bmatrix} \right\|^2_{Q_{\underline{\hat{R}}(Z)\underline{\hat{R}}(Z)}} \end{aligned} \tag{4.88}$$

where the baseline solution assuming the integer ambiguities Z as known is applied:

$$\begin{bmatrix} vec(\hat{R}_1(Z)) \\ vec(\hat{R}_2(Z)) \\ \vdots \\ vec(\hat{R}_{N_e}(Z)) \end{bmatrix} = \begin{bmatrix} vec(\hat{R}_1) \\ vec(\hat{R}_2) \\ \vdots \\ vec(\hat{R}_{N_e}) \end{bmatrix} - Q_{\underline{\hat{R}}\hat{Z}_{N_e}} Q^{-1}_{\hat{Z}_{N_e}\hat{Z}_{N_e}} (vec(\hat{Z}_{N_e} - Z)) \tag{4.89}$$

with

$$Q_{\underline{\hat{R}}(Z)\underline{\hat{R}}(Z)} = Q_{\underline{\hat{R}}\underline{\hat{R}}} - Q_{\underline{\hat{R}}\hat{Z}_{N_e}} Q^{-1}_{\hat{Z}\hat{Z}} Q_{\hat{Z}_{N_e}\underline{\hat{R}}} \tag{4.90}$$

This last matrix has a block diagonal structure

$$Q_{\underline{\hat{R}}(Z)\underline{\hat{R}}(Z)} = \begin{bmatrix} Q_{\hat{R}_1(Z)\hat{R}_1(Z)} & 0 & \dots & 0 \\ 0 & Q_{\hat{R}_2(Z)\hat{R}_2(Z)} & \dots & 0 \\ \vdots & & \ddots & \vdots \\ 0 & 0 & \dots & Q_{\hat{R}_{N_e}(Z)\hat{R}_{N_e}(Z)} \end{bmatrix} \tag{4.91}$$

$$Q_{\hat{R}_i(Z)\hat{R}_i(Z)} = \left[(F^T \otimes G_i)^T Q_{YY}^{-1} (F^T \otimes G_i)\right]^{-1} \tag{4.92}$$

The least-squares criterion for this multi-baseline problem reads, written in the same form as Eq. (3.39), as:

$$\min_{Z\in\mathbb{Z}^{n\times N},\left[R_1 \dots R_{N_e}\right]\in\mathbb{O}^{3\times q\times N_e}} \left\| \begin{bmatrix} vec(Y_1^{DD}) \\ \vdots \\ vec(Y_{N_e}^{DD}) \end{bmatrix} - M_{N_e} \begin{bmatrix} vec(Z_1) \\ vec(R_1) \\ \vdots \\ vec(R_{N_e}) \end{bmatrix} \right\|^2_{Q_{\underline{YY}}} = \sum_{i=1}^{N_e} \|\hat{E}_i\|^2_{Q_{YY}} +$$

$$+ \min_{Z\in\mathbb{Z}^{n\times N},\left[R_1 \dots R_{N_e}\right]\in\mathbb{O}^{3\times q\times N_e}} \left(\|vec(\hat{Z}_{N_e} - Z)\|^2_{Q_{\hat{Z}_{N_e}\hat{Z}_{N_e}}} + \sum_{i=1}^{N_e} \|vec(\hat{R}_i(Z) - R_i)\|^2_{Q_{\hat{R}(Z)\hat{R}(Z)}} \right) \tag{4.93}$$

Due to the structure of Eq. (4.84) and the block diagonality of $D(\underline{Y})$, that $\hat{R}_i(Z)$ only depend on Y_i and not on observations from other epochs. This is also the reason why the last term in Eq. (4.93) can be written as a summation of N_e terms.

4.3.6.1 Unconstrained model

Without the orthogonality constraint on R, the last term of Eq. (4.93) can be made zero for any ambiguity vector, and thus the minimizer is obtained by minimizing the second term by the LAMBDA method.

$$\check{Z} = \arg \min_{Z\in\mathbb{Z}^{n\times N}} \left(\|vec(\hat{Z}_{N_e} - Z)\|^2_{Q_{\hat{Z}_{N_e}\hat{Z}_{N_e}}} \right) \tag{4.94}$$

As the entries of $Q_{\hat{Z}_{N_e}\hat{Z}_{N_e}}$ for the multi-epoch solution are reduced compared to the single-epoch case, the probability of correctly fixing the integer ambiguity vector increases. The attitude solutions can be obtained using

$$\check{R}_i = \arg \min_{R_i\in\mathbb{O}^{3\times q}} \|vec(\hat{R}_i(\check{Z}) - R_i)\|^2_{Q_{\hat{R}_i(Z)\hat{R}_i(Z)}} \tag{4.95}$$

4.3.6.2 Constrained model

When the orthonormality of R is taken into account the solution becomes:

$$\check{Z} = \arg \min_{Z \in \mathbb{Z}^{n \times N}} \left(\|vec(\hat{Z}_{N_e} - Z)\|^2_{Q_{\hat{Z}_{N_e}\hat{Z}_{N_e}}} + \sum_{i=1}^{N_e} \|vec(\hat{R}_i(Z) - \check{R}_i(Z))\|^2_{Q_{\hat{R}_i(Z)\hat{R}_i(Z)}} \right) \tag{4.96}$$

with

$$\check{R}_i(Z) = \arg \min_{R_i \in \mathbb{O}^{3 \times q}} \left(\|vec(\hat{R}_i(Z) - R_i)\|^2_{Q_{\hat{R}_i(Z)\hat{R}_i(Z)}} \right) \tag{4.97}$$

Now the minimization is the sum of two terms: the distance with respect to the float solution in the metric $Q_{\hat{Z}\hat{Z}}$ and various distances between $\hat{R}_i(Z)$ and their projection on the curved manifold defined by $R_i \in \mathbb{O}^{3 \times q}$.
This minimization can be performed using the steps described in section 4.3.2.

4.4 Verification by simulations

In this section, we will analyze by simulation ambiguity resolution for a single platform with a single or dual baseline configuration. The simulation conditions are provided in Appendix A.1. The results are presented in four tables containing empirical success rates as a function of the number of tracked satellites (N_{SV}) and the undifferenced phase and code noise (σ_ϕ, σ_p). The results for the LAMBDA and C-LAMBDA methods applied to the single baseline on the platform are shown in the Tables 4.3 and 4.4 for 3 and 1 mm undifferenced carrier phase noise respectively. The results for the LAMBDA and MC-LAMBDA methods applied to the dual baseline on the platform are shown in Tables 4.5 and 4.6 again for 3 and 1 mm undifferenced carrier phase noise respectively. The empirical success rate is defined as the ratio of occurrences that the computed integer solution is equal to the known true integer vector. We will analyze single epoch, single frequency success rates as the most challenging application. The difference in performance for the approaches for single epoch solutions, is a good indication of the strength of the underlying models.
The C- and MC-LAMBDA methods clearly provide better results than the unconstrained method. The difference is particularly pronounced when the underlying model is weaker (i.e. fewer satellites and or higher measurement noise). Making use of a single geometrical constraint in Tables 4.3 and 4.4 improves the success rate considerably: already 5 satellites and phase standard deviation of 3 mm result in a success rate of more than 70%. The difference in success rate becomes less pronouced when the strength in the underlying model increases: with 8 satellites and σ_ϕ =1 mm, standard LAMBDA will obtain a close to 100% success rate.

Table 4.3: Single baseline simulation results for σ_ϕ=3 [mm]: LAMBDA and C-LAMBDA single-frequency, single-epoch overall success rates

N_{SV}	LAMBDA			C-LAMBDA		
	σ_p [cm]			σ_p [cm]		
	30	15	5	30	15	5
5	0.03	0.20	0.87	0.72	0.89	0.99
6	0.25	0.67	0.97	0.96	0.99	1.00
7	0.50	0.77	0.99	0.99	1.00	1.00
8	0.86	0.94	1.00	1.00	1.00	1.00

Table 4.4: Single baseline simulation results for σ_ϕ=1 [mm]: LAMBDA and C-LAMBDA single-frequency, single-epoch overall success rates

N_{SV}	LAMBDA			C-LAMBDA		
	σ_p [cm]			σ_p [cm]		
	30	15	5	30	15	5
5	0.06	0.27	0.95	0.97	1.00	1.00
6	0.49	0.87	1.00	1.00	1.00	1.00
7	0.74	0.93	1.00	1.00	1.00	1.00
8	1.00	1.00	1.00	1.00	1.00	1.00

Table 4.5 and 4.6, shows the success rate for a two-baseline configuration. For standard LAMBDA, the baselines are processed using the correlation between the baselines, but this correlation is weak. If they would be processed independently, the overall success rate for the two baseline would be equal to the product of the success rates of each baseline. Since probabilities are always smaller or equal to one, the overall success rate decreases with increasing number of baselines. For MC-LAMBDA, the baselines are solved in an integrated approach which makes the model much stronger, therefore we observe an increase in success rate. The improvement for the weaker scenarios is even more outstanding than was observed for the single baseline configuration: for all 24 scenarios, a success rate of 100% is obtained with MC-LAMBDA.
So the simulations confirm that, as expected, including geometrical constraints in the LAMBDA method will improve the ability of correctly fixing the ambiguity vector. Next, this will be tested using data collected in field experiments.

Table 4.5: Dual baseline simulation results for σ_ϕ=3 [mm]: LAMBDA and MC-LAMBDA single-frequency, single-epoch overall success rates

N_{SV}	LAMBDA			MC-LAMBDA		
	σ_p [cm]			σ_p [cm]		
	30	15	5	30	15	5
5	0.00	0.06	0.84	1.00	1.00	1.00
6	0.10	0.57	0.97	1.00	1.00	1.00
7	0.32	0.73	1.00	1.00	1.00	1.00
8	0.82	0.93	1.00	1.00	1.00	1.00

Table 4.6: Dual baseline simulation results for σ_ϕ=1 [mm]: LAMBDA and MC-LAMBDA single-frequency, single-epoch overall success rates

N_{SV}	LAMBDA			MC-LAMBDA		
	σ_p [cm]			σ_p [cm]		
	30	15	5	30	15	5
5	0.01	0.10	0.95	1.00	1.00	1.00
6	0.30	0.81	1.00	1.00	1.00	1.00
7	0.61	0.91	1.00	1.00	1.00	1.00
8	1.00	1.00	1.00	1.00	1.00	1.00

4.5 Verification by field experiments

In this section, we will analyze the C- and MC-LAMBDA methods using field data from a static configuration, a vessel, an aircraft, a balloon and a spacecraft (hardware-in-the-loop simulation).
The experiments themselves are described in more detail in appendix A.3: Static, A.4: Vessel, A.5: Aircraft, A.6: Balloon-based Operation Vehicle and A.7: Spacecraft.

4.5.1 Multi-Antenna experiment (MAx)

For a static experiment with a large number of GPS receivers/antennas (see appendix A.3 for details) the success rate is analyzed for configurations with different numbers of baselines. These configurations, containing subgroups of GPS receivers/antennas, are shown in Fig. 4.8. 5400 epochs are processed as subsets of all the locked GNSS satellites, varying between 5 and 9. In the Table 4.7, the number of baseline in the solution is described by C. In the third column, the single constraint baseline ($C = 1$) represents C-LAMBDA, $C > 1$ MC-LAMBDA results.
For standard LAMBDA, more than 8 satellites are required to obtain a success rate higher than 99%, and the success rate is decreasing if more baselines are included in the solution. This was also observed in the simulations of section 4.4 and due to the fact that a large number of ambiguities at the different baselines have to be resolved, making correctly fixing all of them less likely, which decreases the overall success rate.
For C-LAMBDA, 7 satellites are required to obtain an overall success rate of 100%, for MC-LAMBDA a dual baseline is sufficient to obtain the same with even 5 satellites.

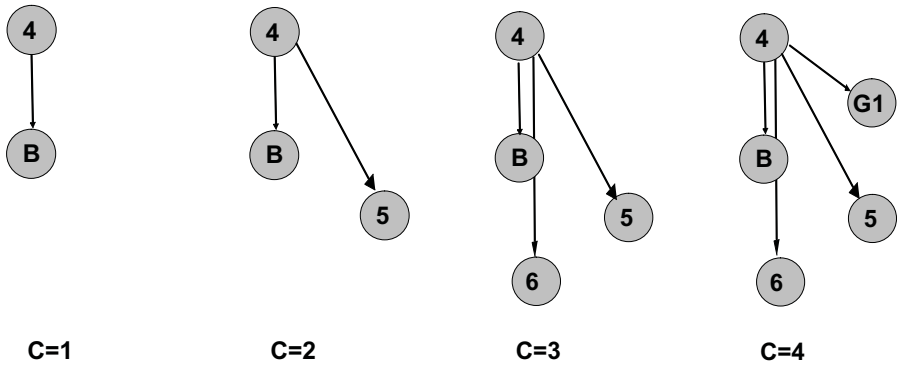


Figure 4.8: Multi-antenna experiment

Table 4.7: Field experimental results: LAMBDA and (M)C-LAMBDA single-frequency, single-epoch overall success rates for all the baselines, $\#C$ is total number of (constrained) baselines

N_{SV}	$\#C$	LAMBDA	(M)C-LAMBDA
5	1	0.12	0.85
	2	0.04	1.00
	3	0.01	1.00
	4	0.00	1.00
6	1	0.22	0.96
	2	0.12	1.00
	3	0.11	1.00
	4	0.04	1.00
7	1	0.64	1.00
	2	0.60	1.00
	3	0.58	1.00
	4	0.58	1.00
8	1	0.93	1.00
	2	0.94	1.00
	3	0.94	1.00
	4	0.94	1.00
9	1	1.00	1.00
	2	1.00	1.00
	3	1.00	1.00
	4	1.00	1.00

4.5.2 Vessel Application: Schie 2003

We will start this section with estimating a single baseline between two antennas, A1 and A2, using data collected in the Schie experiment of 2003 (Appendix A.4). The horizontal relative vector between the antennas A1 and A2 is shown in *North* and *East* coordinates in Fig. 4.9. The left hand side of Fig. 4.9 shows the float solutions as a function of time. The ship moves up and down on the same trajectory for 4 times and, as it is a vessel, all movements and rotations are done in the horizontal plane. The right hand side of Fig. 4.9 shows the float and fixed solutions. It is observed that correctly fixed solutions are positioned on a circle with a radius equal to the distance between the two antennas. So one can think of this figure as representing the master or reference antenna as being in the origin and the second antenna is moving on a circle around the origin at a distance equal to the distance between the two antennas, as both antennas are attached to the same moving body. Their relative position is only changing if the vessel makes a turn.
On epochs for which the algorithm failed to find the correct ambiguity solution, the fixed solution is, because of the baseline constraint, still positioned on the known distance from the reference antenna but the solution is -most of the time- situated out of the horizontal plane.
The overall empirical success rate and success rate subdivided for the number of locked GPS satellites at each epoch are summarized in Table 4.8 for both baseline A1-A2 and A2-A3. As can be seen in this table, the success rate increases with the number of available observations but even with 6 locked GPS satellites, the success rate with C-LAMBDA is higher than 93%.
Also the success rate of the standard LAMBDA method using single frequency and single epoch observations is shown in Table 4.8. As expected, the success rate for the standard LAMBDA method also increases with the number of available measurements. The overall success rate of the standard LAMBDA method is 82% on the baseline between antenna A1 and A2, whereas for the C-LAMBDA method this is improved to 100%. For the baseline between antenna A2 and A3 this is 40% and 95% respectively. Hence, especially when a limited number of observations is available, the success rate increases significantly for the C-LAMBDA method. Moreover, note that the success rates for the second baseline are lower than those on the first baseline, especially when employing LAMBDA. This is due to the fact that the lower grade receiver (A3) is used in the second baseline. It is interesting that the C-LAMBDA method can compensate the reduced quality of the observations by strengthening the underlying model, resulting in much improved success rates.
The MC-LAMBDA result combining the two baselines is included in Table 4.8 and this achieves a success rate close to 100%.
Next, we will have a closer look at how the search space is initiated and expanding. As was explained in section 4.2.1, at first the integer search space χ^2 is computed based on the bootstrapped solution. If the search space is found to be empty, which means that the unconstrained least-squares solution is and baseline constrained integer least-squares solution is not located in the applied search space, the search process is repeated after increasing the search space. The initial values and final values of χ^2 when a solution was accepted (i.e. both unconstrained and the constrained integer solution are located in the same search space) are shown in Fig. 4.10. It is clear from the figure that most of the time, the search space was not increased for this data.

Table 4.8: Single Frequency, Epoch by Epoch Ambiguity Resolution: Empirical success rates (%) with LAMBDA and (M)C-LAMBDA: 2003 Schie experiment

	A1-A2		A2-A3		A1-A2-A3	
	LAMBDA	C-LAMBDA	LAMBDA	C-LAMBDA	LAMBDA	MC-LAMBDA
Overall	0.82	1.00	0.40	0.95	0.28	0.99
6 sats	0.28	0.97	0.19	0.93	0.28	0.99
7 sats	0.81	1.00	0.32	0.95	0.15	1.00
8 sats	0.97	1.00	0.49	0.96	0.37	1.00

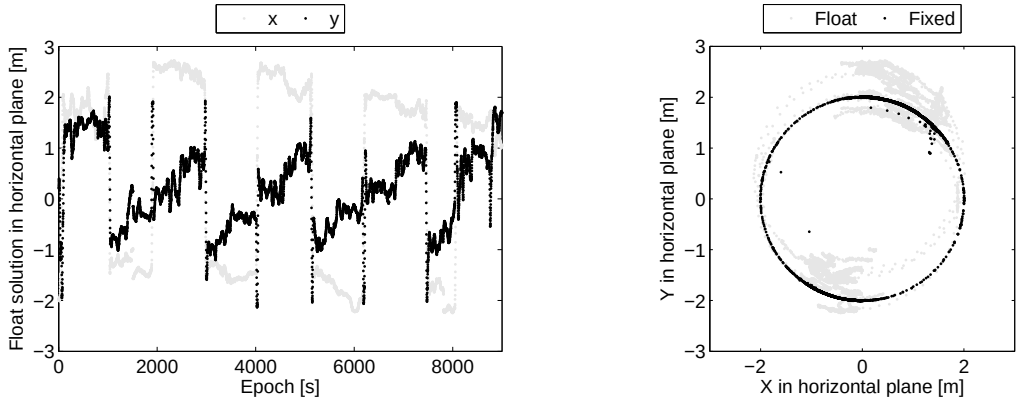


Figure 4.9: (left) The float solution of x and y in the horizontal plane as a function of experiment time (right) The float and the fixed solution of y as a function of the x solution in the horizontal plane

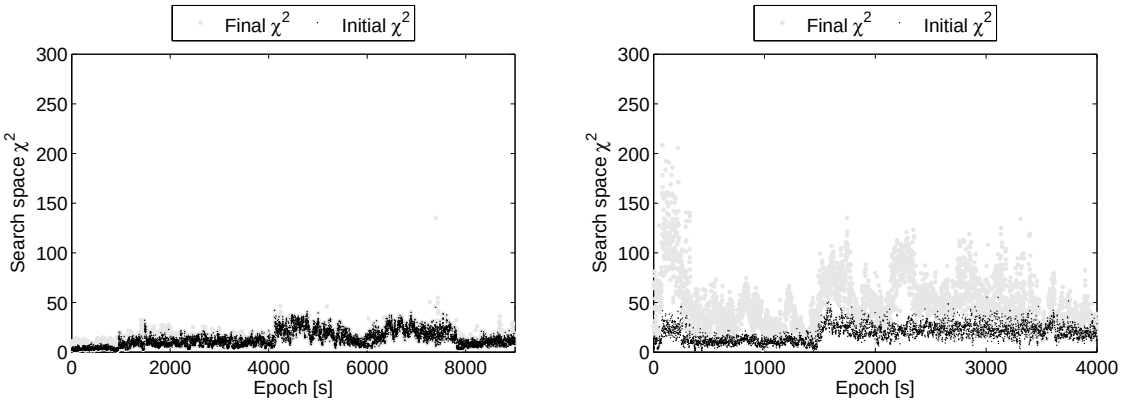


Figure 4.10: The initial and final integer search space: (left) 2003 Schie experiment (right) Cessna Citation II 2005 flight

Table 4.9: Single Frequency, Epoch by Epoch Ambiguity Resolution: Empirical success rates (%) with LAMBDA and (M)C-LAMBDA: 2005 flight

	main-nose		main-nose-wing	
	LAMBDA	C-LAMBDA	LAMBDA	MC-LAMBDA
Overall	0.14	0.58	0.06	0.82

4.5.3 Aircraft Application: Cessna Citation II 2005 and 2007

In this section, data collected during two different flights of a Cessna Citation II aircraft are analyzed. Details of the experiments can be found in appendix A.5. A difference with the vessel application of the previous section is that the attitude of an aircraft varies in three dimensions (two planes), and therefore the baseline solutions will not be placed on a single (horizontal) plane.

The overall empirical success rate is shown in Table 4.9 for the 2005 flight. Also the success rate of the standard LAMBDA method is shown in Table 4.9. Overall success rate of the standard LAMBDA method using single frequency, single epoch observations is 14%, for the constrained LAMBDA method this is improved to 58% for the baseline between the main and nose antenna during the 2005 flight. By including the second baseline and applying MC-LAMBDA, the success rate is improved to 82%. Hence the success rate increases significantly. However, as will be discussed later in more detail, compared with the vessel experiment, the success rate is lower.
The initial values and the applied values of χ^2 when a solution was accepted are shown in Fig. 4.10. By comparing left hand and the right hand side of Fig. 4.10, it is clear that the initial values are very similar, but that for the aircraft experiment, because of the less accurate observations, more often no solution was found for the initial search space and therefore the search space was increased. The reason for the lower success rate on the first baseline is of course the poorer data quality, due to multipath and higher noise levels. This is a result of the fact the GPS antennas are mounted directly on the aircraft, and that the aircraft application is much more dynamic than the vessel application. Especially in the first 500 seconds before take-off, multipath errors from the surroundings of the aircraft are dominant. Also the location of the antenna on the nose has to be considered with higher multipath levels due to the proximity of the cockpit window.
Similar results can be observed for the 2007 flight presented in Table 4.10, with much higher success rates on the baseline between the main and wing antenna than on the baseline between the main and nose antenna. Moreover, with 9 satellites the success rate is lower than with 8 satellite for the main-nose baseline with LAMBDA, C-LAMBDA and MC-LAMBDA. In (Giorgi et al., 2012), it was demonstrated to be a result of multipath on observations from GNSS satellites placed at low elevation in the direction of the cockpit.

4.5.4 Aerospace application: BOV 2009

In May 2009, a flight of the Balloon-based Operation Vehicle (BOV) was performed. The GPS receiver with three antennas and the other attitude sensors were placed on the

Table 4.10: Single Frequency, Epoch by Epoch Ambiguity Resolution: Empirical success rates (%) with LAMBDA and (M)C-LAMBDA: 2007 flight

	main-wing		main-nose		main-nose-wing	
	LAMBDA	C-LAMBDA	LAMBDA	C-LAMBDA	LAMBDA	MC-LAMBDA
Overall	0.61	0.94	0.25	0.61	0.25	0.88
8	0.31	0.90	0.28	0.78	0.06	0.92
9	0.67	0.95	0.25	0.61	0.29	0.87

Gondola hanging in-between the balloon and BOV. At the end of the flight, first the BOV is released and later the Gondola. For a more detailed description of the experiment, see Appendix (A.6.1).
The configuration used on the balloon experiment is also applied to collect static data before the flight in order to compare the influence of the balloon environment on the GPS experiment. For the balloon experiment, we will also compare the C-LAMBDA results with results based on a Kalman filter as provided by the GPS receiver. As discussed in section 4.1.3, the solution provided by the receiver also makes use of the standard LAMBDA method for ambiguity resolution (Kuylen et al., 2006).

4.5.4.1 Preflight static test

Before the flight of the balloon, a ground test using the actual antenna frame of the Gondola (see Fig. 4.11) was performed. The roll, pitch and heading angles for this static test are shown on the right side of this figure. Due to geometry of the baselines, the heading angle is more accurate (see section 4.3.3).
For this static test, the standard deviation of the three angles is calculated to confirm the accuracy achievable for the flight test. These results are summarized in Table 4.11. For the baselines with a length of about 1.4 meter, an accuracy of about 0.25° for roll and pitch and 0.1° for heading is achieved, which is as expected from the length and geometry of the baselines (see section 4.1).
Using single epoch data and applying C-LAMBDA, the ambiguities are resolved correctly for more than 99% of the epochs, and by MC-LAMBDA even 99.8% on both baselines (overall success rate).
Also the standard devation of the Kalman filter based attitude estimate (KF) is included in the table. The accuracy, after convergence of the filter, is similar to the C-LAMBDA result, although the applied method is very different (see Appendix A.6). The Kalman filter takes about 10 seconds to converge for this static experiment, whereas the C-LAMBDA method provides this accuracy from the very first epoch.

4.5.4.2 Gondola nominal flight

Next the same GPS antenna configuration was applied in the flight test on the gondola. An important difference from the static field experiment is that the antennas are now placed under the balloon and inside waterproof bags (see picture on the left side of Fig. A.15).
The right side of Fig. A.15 shows the flight trajectory (altitude) of the experiment. At

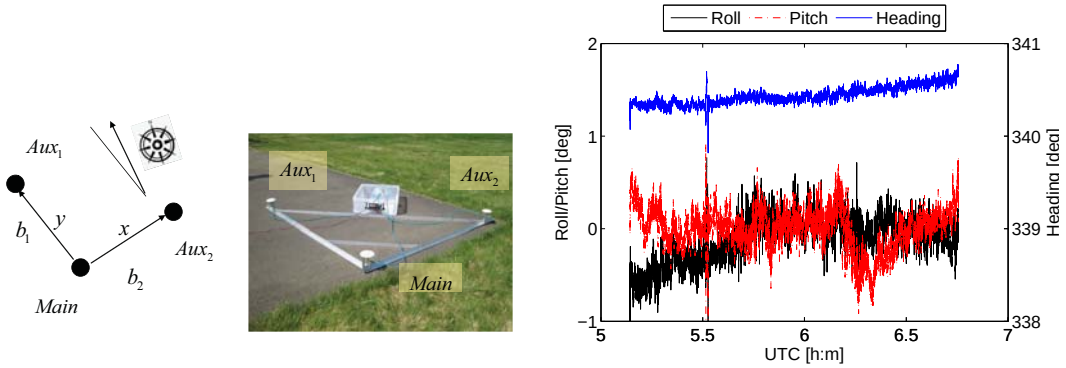


Figure 4.11: BOV preflight static test

Table 4.11: BOV preflight static test (*after convergence of filter)

	Baseline	Length	*Attitude angles* [°]		
			Roll	Pitch	Heading
KF*	1&2	1.413	0.25	0.28	0.12
C-LAMBDA			0.25	0.24	0.10
			Success rate [%]		
LAMBDA			0.66		
C-LAMBDA			0.99		
MC-LAMBDA			1.00		

21:05 UTC (7:05 JST), the balloon was released from the sliding launcher (Fig. A.12). The balloon reached an altitude of more than 41 kilometers from which the BOV was dropped. At 23:55, the BOV was released from the Gondola, and at 23:59 the Gondola was separated from the balloon.

During this flight, the attitude determination package and the GPS system were installed on the gondola of the balloon to confirm the nominal performance of all the sensors. Using a GPS receiver with three antennas, the full attitude of the gondola could be calculated. The roll and pitch estimates, both C-LAMBDA and KF, are shown in Fig. 4.12. The heading angle from the GPS C-LAMBDA and KF, Geomagnetic Aspect Sensor (GAS) and Sun Aspect Sensor (SAS) sensors are shown in Fig. 4.13. As explained in section A.6.2, the four SAS sensors will only output an attitude estimate, if the sun is in the field of view of this sensor. Therefore four distinct bands in the heading estimate of the SAS are observed, corresponding to the individual sensors (indicated in Fig. A.15 as SAS1 till SAS4).

The number of locked GPS satellites at the main antenna is shown in the right side of Fig. A.15. Before take off, the number of locked channels varies rapidly due to obstructions, but after take off the number is rather constant till the BOV is separated from the Gondola. Before take off, the GPS observations are affected by the obstruction of the sliding launcher and therefore ambiguity resolution is only possible on the second baseline (left side of Fig. 4.12). Also the receiver does not provide an attitude estimation during this phase of the experiment. During take off, large variations (up to 20 degrees (+/- 10 degrees) for both roll and pitch) in orientation of the gondola are observed which can be estimated well by both C-LAMBDA and KF GPS. Again the Kalman filter takes a few epochs to converge (in

this case 15 seconds from take off), whereas the C-LAMBDA method provides an accurate solution from the very first epoch. After take off, the attitude of the gondola stabilizes and the C-LAMBDA and KF attitude estimates are very similar.
During nominal flight, the difference between the attitude estimation from the different sensors is investigated. The mean and standard deviations of the differences are shown in Table 4.12. By comparing C-LAMBDA and KF GPS attitude, biases for all angles are observed. The most likely cause for this bias is, as observed in the static experiment in the form of convergence time, the time delay of the Kalman filter in response to changes in attitude. The standard deviation for roll, pitch and heading is as expected. For the comparison with the other sensors the C-LAMBDA GPS attitude is used as the reference. The difference between C-LAMBDA and KF is shown in Fig. 4.14. Between C-LAMBDA GPS and GAS / SAS, a bias is observed, most likely due to minor misalignment issues between the sensors. The standard deviations in Table 4.12 are in line with the expectation based on the sensors specifications as described in section A.6.2. During this part of the flight a single epoch, single frequency empirical success rate for ambiguity resolution using C-LAMBDA on the two baselines of 95 % was achieved. For MC-LAMBDA this success rate was improved to 100.00 %.

4.5.4.3 Gondola flight after BOV Separation

After the separation of the BOV from the Gondola, the Gondola starts to ascend and sweep. Fig. 4.15 contains roll and pitch estimates for this part of the flight until the Gondola separation. In the figure large variations (up to 40 (+/- 20) degrees for roll and 20 (+/- 10) degrees for pitch) in orientation of the gondola are observed.
It is interesting that after BOV separation, during the large manoeuvres of the Gondola caused by the separation, both C-LAMBDA and KF estimates are available but to a certain extent different.
Table 4.12 also contains standard deviations and biases between C-LAMBDA and KF for this part of the flight. It is clear from the table that the difference (standard deviation but also mean) between C-LAMBDA and KF - both for roll and pitch - is increased compared to the nominal part of the flight. As expected, the Kalman filter based result is lagging behind the true attitude in this dynamic situation, whereas the C-LAMBDA result based on single epoch data, should be able to provide the same accurate estimate as during the other phases of the flight.

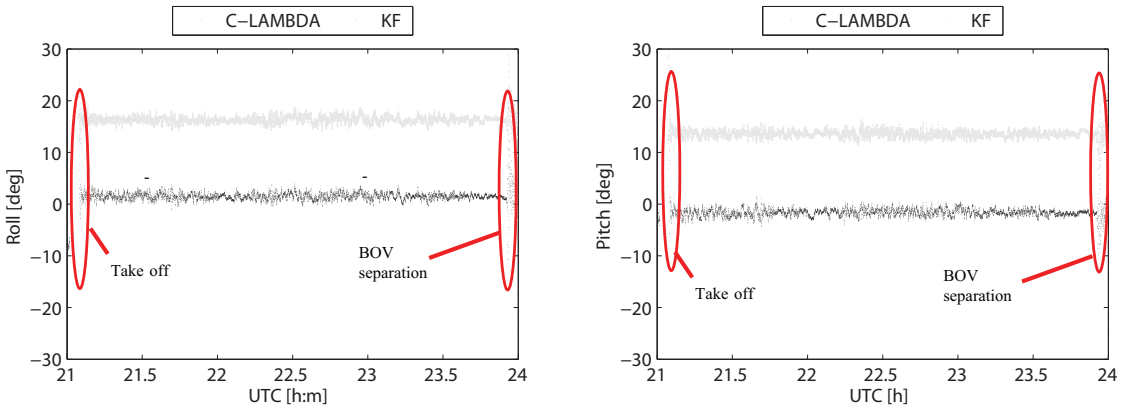


Figure 4.12: GPS Results for roll and pitch angles: BOV nominal flight (C-LAMBDA is offset for clarity)

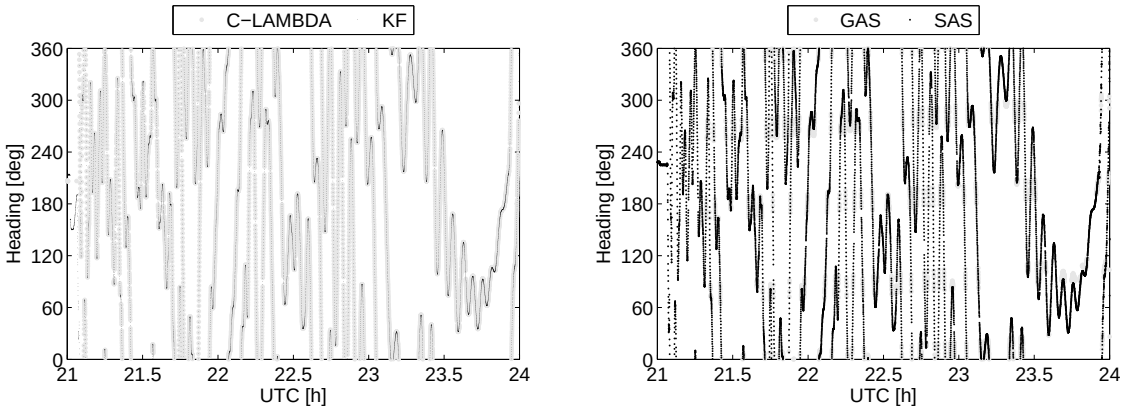


Figure 4.13: GPS (left), GAS and SAS (right) Results for heading angle: BOV nominal flight

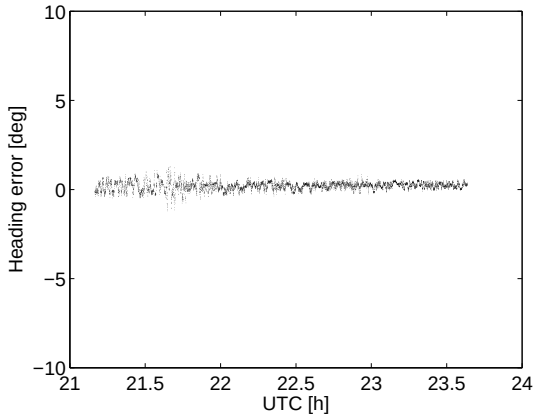


Figure 4.14: GPS C-LAMBDA minus KF: BOV nominal flight

Table 4.12: BOV Flight Test (nominal conditions) (*after convergence of filter)

	$Attitude\ errors\ mean/std\ [^\circ]$		
	Roll	Pitch	Heading
C-LAMBDA-KF*	0.18/0.43	-0.18/0.45	0.16/0.23
C-LAMBDA - GAS	N/A	N/A	0.81/1.50
C-LAMBDA - SAS1	N/A	N/A	3.12/1.28
C-LAMBDA - SAS2	N/A	N/A	-0.41/1.44
C-LAMBDA - SAS3	N/A	N/A	-0.39/1.69
C-LAMBDA - SAS4	N/A	N/A	0.53/1.24
	$Success\ rate\ [\%]$		
LAMBDA	0.58		
C-LAMBDA	0.95		
MC-LAMBDA	1.00		

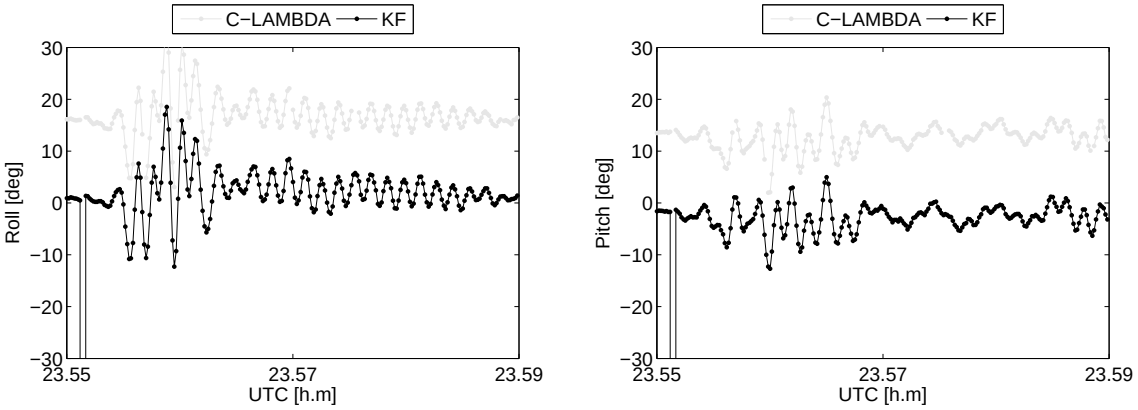


Figure 4.15: GPS Results for roll and pitch angles after BOV Separation (C-LAMBDA is offset for clarity)

Table 4.13: Formation flying: single platform, single frequency, single epoch, overall success rate [%]

	$PROBA-3$	$Garada$
LAMBDA	0.89	0.19
C-LAMBDA	0.99	0.81
MC-LAMBDA	1.00	0.96

4.5.5 Satellite Formation Flying: PROBA-3 and Garada

For the last experiments in this chapter on attitude determination, two spacecraft scenarios are analyzed using data collected in a hardware-in-the-loop simulation: PROBA-3 and Garada.
Two spacecraft were simulated using PROBA-3 characteristics, but in this chapter only a triple antenna configuration on one of the platforms is analyzed. An external reference clock is applied in this experiment.
During the part of the orbit where the spacecraft was below the GPS constellation, a single epoch, single frequency empirical success rate of more than 99% was achieved for ambiguity resolution using C-LAMBDA on the two baselines. This compared with about 89% for standard LAMBDA and for MC-LAMBDA a success rate of 100.0%.

Details about the Garada mission can be found in appendix A.8. The success rates for these baseline are shown in Table 4.13, for LAMBDA, C-LAMBDA and MC-LAMBDA. The Garada simulation used the Namuru receiver with relative large code noise (see discussion in section 3.6.3), resulting in a rather low success rate of around 20% for instantaneous ambiguity resolution. For C-LAMBDA this success rate is improved to more than 80%, for MC-LAMBDA it is dramatically improved to 96%.

4.6 Concluding remarks

Based on experience and literature review, it was shown that in terms of accuracy not much room for improvement is expected in GNSS attitude determination, as the theoretical limit has been reached. However, for ambiguity resolution still a number of open challenges remain. In this chapter, an ambiguity resolution method was developed based on a constrained extension of the popular LAMBDA method, known as the Multivariate Constrained (MC-) LAMBDA method. In contrast to existing methods that make use of the known baseline length, the method does full justice to the given information by fully integrating the nonlinear baseline constraint into the ambiguity objective function. As a result, the a priori information receives a proper weighting in the ambiguity objective function, thus leading to higher success rates.
The method was tested, using simulated as well as actual GPS data. The presented field tests cover static land experiments, and dynamic experiments such as a low-dynamics vessel, a high-dynamics aircraft and Balloon-based-Operation vehicle. Moreover hardware-

in-the-loop simulated spacecraft scenarios were applied to test the method.
The rigorous inclusion of the baseline length constraint into the ambiguity objective function shows dramatic improvements in the success rates and more reliable attitude estimations. The improved instantaneous ambiguity resolution will result in an even stronger reduction in time to fix (TTF).

Integrated Positioning and Attitude Determination

5

In this chapter, we will combine relative positioning (chapter 3) and attitude determination (chapter 4). Fig. 3.1 showed the relationship between the topics covered in these chapters and the current chapter. The chapter begins with a literature review of previous work that has been done in this field. Section 5.2 contains an extensive discussion on an integrated approach for triple and quadruple antenna configurations. In this section models for the optimal solution and suboptimal (or vectorial bootstrapping) solution are developed. This section ends with simulation results for the two approaches based on which it is concluded that the bootstrapping solution can be applied for the applications of interest for this research, as the performance is very similar to the optimal solution. In section 5.3, we will develop a general model for configurations with any number of antennas. In section 5.4 and 5.5, the developed methods are tested using simulated and actual GPS data. Extracts of this chapter were published in (Buist et al., 2008, 2009,a,b, 2010,a,c) and (Giorgi et al., 2011).

5.1 Overview of Previous Work/Methods

In (Lachapelle et al., 1993), the use of a quadruple receiver system consisting of two static GPS receivers and two GPS receivers mounted on a single platform was considered for improved On The Fly (OTF) ambiguity resolution with single frequency receivers. The ambiguities between the two static receivers and between the two receivers on the same platform could be determined within a few seconds due to the short and fixed baselines between them. These ambiguities could, in turn, be used as constraints to reduce the number of potential ambiguity solutions for the unconstrained baseline between the static station and the platform and, therefore, to reduce the time to resolution from 810 to about 470 seconds for a configuration without choke ring antennas, and from 355 to 180 seconds for a configuration with this type of antenna. The research used the relationship between the ambiguities but did not model the correlation between the observations at the antennas.

In (Pinchin et al., 2008), a system was proposed which provides carrier based positioning and two axis attitude measurements using three single frequency GPS receivers (i.e. a triple antenna configuration). The aim of this triple antenna configuration was to increase the success rate of the integer ambiguity resolution process when estimating the baseline between the base station and the platform. This was achieved by utilizing knowledge of the integer ambiguities obtained from a constrained baseline in the attitude determination system. As demonstrated in chapter 4, the use of baseline length or geometry constraints in the attitude determination problem increased the integer ambiguity success rate. In

(Pinchin et al., 2008), the knowledge of the integer ambiguities from the attitude determination system is used to reduce the number of candidates during the search for the integer ambiguities arising when the third receiver is included. When these ambiguities are resolved, the unknown baselines between the roving (attitude) receivers and base receiver may be determined and the relative position obtained. The relation between the work of (Pinchin et al., 2008) and this thesis will be discussed in more detail in section 5.2.4.

Also commercial products are starting to use multi-antenna data in their relative positioning solutions. One example is the TRIUMPH-4X from JAVAD, which uses quadruple antennas at both the base station and rover to calculate Real-Time Kinematic (RTK) solutions, in what they call *cluster RTK* (JAVAD, 2009). As it is a commercial product, details about their processing strategy is not available.

Research relevance Traditionally the relative positioning and attitude determination problem are treated as independent. In this chapter the possibilities of using multiple antenna data, not only for attitude determination but also for relative positioning are investigated, especially for moving platforms. This is of relevance for applications where each platform has multiple antennas with known baseline lengths on its own surface and baseline vectors with unknown length to the other platforms.
The objective of this research is to develop a method that optimally makes use of all the information available (i.e., the integerness of the ambiguities, the relationship between the ambiguities on the different baselines, the known baseline lengths and relative orientation of the baselines at the platforms) to determine the relative position and orientation of a multiple antenna system. Rigorous methods are developed to improve especially ambiguity resolution on the baseline(s) between platforms and the overall success rate of ambiguity resolution between a number of antennas.
In section 2.6.2, it was shown that spaceborne GNSS receivers have a limited number of channels (typical 8 for the currently available receivers), therefore observations from a larger number of channels are not foreseen in the near future for spaceborne applications. As was shown in chapter 1, this type of application often has multiple GNSS antennas at each spacecraft, and therefore the integrated approach could have advantages.

5.2 Triple and Quadruple-antenna configurations

First a three- or triple- and four- or quadruple-antenna configuration are introduced, which will be used to investigate the developed processing strategies theoretically.

5.2.1 Multi-baseline setup

Consider three or four antennas on two platforms as shown in Fig. 5.1. The baselines between two antennas at the same platform are called baseline b_i^j, the superscript j indicates the platform number, the subscript i the baseline number. If the baseline is between two platforms, the superscript contains the indicator of both platforms. The unconstrained baselines between an antenna at one platform and the antennas onboard another platform are b_1^{12}, b_2^{12} and b_3^{12} and the constrained baselines are baseline b_1^1 and baseline b_1^2 with length

l_1^1 and l_1^2 respectively. The antennas are assumed to be sufficiently close, an assumption generally acceptable for the kind of applications discussed in section 1.1, so that the relative antenna-satellite geometry may be considered the same for all antennas.
If this assumption is not valid for an application then atmospheric models should be applied as discussed in section 2.5, for a-priori corrections or estimation of the atmospheric effects. For compactness in this section, the design matrices A and G and the variance-covariance matrix Q_{yy} are assumed to be identical for each baseline (see also discussion in section 5.3.1). The ordering of the antenna pairs is taken such that y_i^j is the difference of the single-differenced data of two antennas. As defined in section 3.3.2.1, y_i^j has the dimension $2n$.

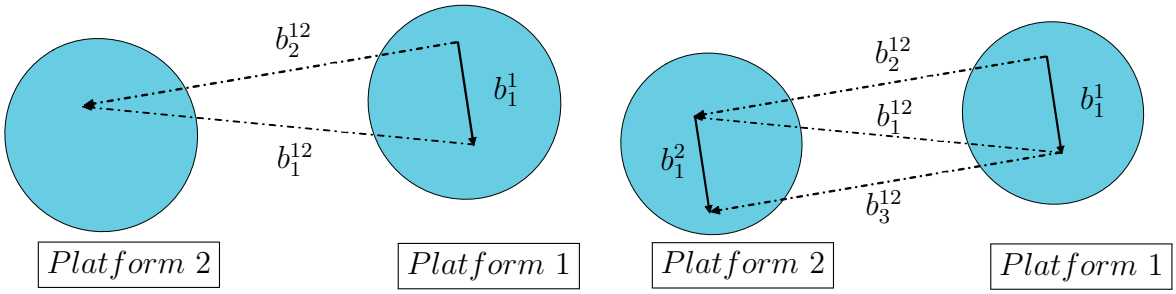


Figure 5.1: Definition of the (left) triple and (right) quadruple antenna configuration (solid arrows indicate baselines with known length)

5.2.2 Model and unconstrained float solution

5.2.2.1 Triple antenna configuration

For an integrated approach, the known relationship between constrained and unconstrained baselines can be utilized. For constrained baseline b_1^1 and unconstrained baselines b_1^{12}, b_2^{12} respectively, with common antennas the following relationship for the baseline, DD ambiguities and DD observation vectors apply:

$$\begin{aligned} b_2^{12} &= b_1^1 + b_1^{12} \\ z_2^{12} &= z_1^1 + z_1^{12} \\ y_2^{12} &= y_1^1 + y_1^{12} \end{aligned} \tag{5.1}$$

This equation shows that two out of three DD data vectors are sufficient to set up the GNSS model.

For the three antenna configuration, the model becomes for y_1^1 and y_1^{12}:

$$\begin{aligned} E\begin{bmatrix} y_1^1 \\ y_1^{12} \end{bmatrix} &= \begin{bmatrix} A & G & 0 & 0 \\ 0 & 0 & A & G \end{bmatrix} \begin{bmatrix} z_1^1 \\ b_1^1 \\ z_1^{12} \\ b_1^{12} \end{bmatrix} \\ D\begin{bmatrix} y_1^1 \\ y_1^{12} \end{bmatrix} &= \begin{bmatrix} -1 & 1 & 0 \\ 0 & -1 & 1 \end{bmatrix} \begin{bmatrix} \frac{1}{2}Q_{yy} & 0 & 0 \\ 0 & \frac{1}{2}Q_{yy} & 0 \\ 0 & 0 & \frac{1}{2}Q_{yy} \end{bmatrix} \begin{bmatrix} -1 & 0 \\ 1 & -1 \\ 0 & 1 \end{bmatrix} \\ &= \begin{bmatrix} Q_{yy} & -\frac{1}{2}Q_{yy} \\ -\frac{1}{2}Q_{yy} & Q_{yy} \end{bmatrix} \end{aligned} \tag{5.2}$$

Note the presence of the nonzero covariance matrix $C(y_1^1, y_1^{12}) = -\frac{1}{2}Q_{yy}$, which is due to the fact that the DD vectors y_1^1 and y_1^{12} have an antenna in common.

Applying $P_2 = \begin{bmatrix} 1 & -\frac{1}{2} \\ -\frac{1}{2} & 1 \end{bmatrix}$ and the Kronecker product $\otimes$ gives the following model:

$$\begin{aligned} E\begin{bmatrix} y_1^1 \\ y_1^{12} \end{bmatrix} &= I_2 \otimes \begin{bmatrix} A & G \end{bmatrix} \begin{bmatrix} z_1^1 \\ b_1^1 \\ z_1^{12} \\ b_1^{12} \end{bmatrix} \\ D\begin{bmatrix} y_1^1 \\ y_1^{12} \end{bmatrix} &= P_2 \otimes Q_{yy} \end{aligned} \tag{5.3}$$

A complete reference on the properties of the Kronecker product is provided in Appendix D.2. Now the least-squares solution and corresponding variance matrix of the three antenna configuration can be given as

$$\begin{aligned} \begin{bmatrix} \hat{z}_1^1 \\ \hat{b}_1^1 \\ \hat{z}_1^{12} \\ \hat{b}_1^{12} \end{bmatrix} &= \left[I_2 \otimes \left(\left[\begin{bmatrix} A & G \end{bmatrix}^T Q_{yy}^{-1} \begin{bmatrix} A & G \end{bmatrix} \right]^{-1} \begin{bmatrix} A & G \end{bmatrix}^T Q_{yy}^{-1} \right) \right] \begin{bmatrix} y_1^1 \\ y_1^{12} \end{bmatrix} \\ D\begin{bmatrix} \hat{z}_1^1 \\ \hat{b}_1^1 \\ \hat{z}_1^{12} \\ \hat{b}_1^{12} \end{bmatrix} &= P_2 \otimes \left[\begin{bmatrix} A & G \end{bmatrix}^T Q_{yy}^{-1} \begin{bmatrix} A & G \end{bmatrix} \right]^{-1} \end{aligned} \tag{5.4}$$

This shows that $\hat{z}_i^j$ and $\hat{b}_i^j$ are solely determined by the DD vector of the corresponding antenna pair, i.e. y_i^j, thus parallel processing is possible for the float solution.
In section 5.2.3, it will be demonstrated that this property is lost once the integer constraints are applied.
If we recall the variance-covariance matrix of $\hat{z}_i^j$ and $\hat{b}_i^j$ as (Eq. 3.41):

$$\begin{bmatrix} Q_{\hat{z}\hat{z}} & Q_{\hat{z}\hat{b}} \\ Q_{\hat{b}\hat{z}} & Q_{\hat{b}\hat{b}} \end{bmatrix} = \left[\begin{bmatrix} A & G \end{bmatrix}^T Q_{yy}^{-1} \begin{bmatrix} A & G \end{bmatrix} \right]^{-1} \tag{5.5}$$

then the dispersion of the three antenna model can also be written as:

$$D\begin{bmatrix}\hat{z}_1^1\\ \hat{b}_1^1\\ \hat{z}_1^{12}\\ \hat{b}_1^{12}\end{bmatrix} = P_2 \otimes \begin{bmatrix}Q_{\hat{z}\hat{z}} & Q_{\hat{z}\hat{b}}\\ Q_{\hat{b}\hat{z}} & Q_{\hat{b}\hat{b}}\end{bmatrix} \tag{5.6}$$

or after reordering

$$D\begin{bmatrix}\hat{z}_1^1\\ \hat{z}_1^{12}\\ \hat{b}_1^1\\ \hat{b}_1^{12}\end{bmatrix} = \begin{bmatrix}P_2 \otimes Q_{\hat{z}\hat{z}} & P_2 \otimes Q_{\hat{z}\hat{b}}\\ P_2 \otimes Q_{\hat{b}\hat{z}} & P_2 \otimes Q_{\hat{b}\hat{b}}\end{bmatrix} \tag{5.7}$$

If one wants to determine z_2^{12} and b_2^{12} from the above results, it can be obtained from (see Eq.(5.1)):

$$\begin{bmatrix}\hat{z}_2^{12}\\ \hat{b}_2^{12}\end{bmatrix} = \left[\begin{bmatrix}1 & 1\end{bmatrix} \otimes \begin{bmatrix}I_n & 0\\ 0 & I_3\end{bmatrix}\right]\begin{bmatrix}\hat{z}_1^1\\ \hat{b}_1^1\\ \hat{z}_1^{12}\\ \hat{b}_1^{12}\end{bmatrix} \tag{5.8}$$

Application of the variance propagation law shows that both the integer and baseline solutions on this baseline have the same precision as the integer and baseline solutions at the other baselines:

$$\begin{aligned} D\begin{bmatrix}\hat{z}_2^{12}\\ \hat{b}_2^{12}\end{bmatrix} &= \left[\begin{bmatrix}1 & 1\end{bmatrix} \otimes \begin{bmatrix}I_n & 0\\ 0 & I_3\end{bmatrix}\right]\left[P_2 \otimes \begin{bmatrix}Q_{\hat{z}\hat{z}} & Q_{\hat{z}\hat{b}}\\ Q_{\hat{b}\hat{z}} & Q_{\hat{b}\hat{b}}\end{bmatrix}\right]\left[\begin{bmatrix}1 & 1\end{bmatrix} \otimes \begin{bmatrix}I_n & 0\\ 0 & I_3\end{bmatrix}\right]^T\\ &= \begin{bmatrix}Q_{\hat{z}\hat{z}} & Q_{\hat{z}\hat{b}}\\ Q_{\hat{b}\hat{z}} & Q_{\hat{b}\hat{b}}\end{bmatrix} \end{aligned} \tag{5.9}$$

5.2.2.2 Quadruple antenna configuration

For constrained baselines b_1^1 and b_1^2 and unconstrained baselines b_1^{12}, b_2^{12}, b_3^{12} respectively, with common antennas, we have the following relationship for the baseline, ambiguities and observation vectors:

$$\begin{cases} b_2^{12} = b_1^1 + b_1^{12}\\ z_2^{12} = z_1^1 + z_1^{12}\\ y_2^{12} = y_1^1 + y_1^{12}\end{cases}$$
$$\begin{cases} b_3^{12} = b_1^{12} + b_1^2\\ z_3^{12} = z_1^{12} + z_1^2\\ y_3^{12} = y_1^{12} + y_1^2\end{cases} \tag{5.10}$$

This equation shows that now three out of five double difference data vectors are sufficient to set up the GNSS model: b_1^1, b_1^{12} and b_1^2 are the three independent baselines.

Using the Kronecker product, we can write also this model in a more compact form:

$$E\begin{bmatrix} y_1^1 \\ y_1^{12} \\ y_1^2 \end{bmatrix} = I_3 \otimes \begin{bmatrix} A & G \end{bmatrix} \begin{bmatrix} z_1^1 \\ b_1^1 \\ z_1^{12} \\ b_1^{12} \\ z_1^2 \\ b_1^2 \end{bmatrix}, \qquad D\begin{bmatrix} y_1^1 \\ y_1^{12} \\ y_1^2 \end{bmatrix} = P_3 \otimes Q_{yy} \tag{5.11}$$

with $P_3 = \begin{bmatrix} 1 & -\frac{1}{2} & 0 \\ -\frac{1}{2} & 1 & -\frac{1}{2} \\ 0 & -\frac{1}{2} & 1 \end{bmatrix}$.

The dispersion of float solution in the quadruple antenna model can again be written as:

$$D\begin{bmatrix} \hat{z}_1^1 \\ \hat{b}_1^1 \\ \hat{z}_1^{12} \\ \hat{b}_1^{12} \\ \hat{z}_1^2 \\ \hat{b}_1^2 \end{bmatrix} = P_3 \otimes \begin{bmatrix} Q_{\hat{z}\hat{z}} & Q_{\hat{z}\hat{b}} \\ Q_{\hat{b}\hat{z}} & Q_{\hat{b}\hat{b}} \end{bmatrix} \tag{5.12}$$

or again after reordering

$$D\begin{bmatrix} \hat{z}_1^1 \\ \hat{z}_1^{12} \\ \hat{z}_1^2 \\ \hat{b}_1^1 \\ \hat{b}_1^{12} \\ \hat{b}_1^2 \end{bmatrix} = \begin{bmatrix} P_3 \otimes Q_{\hat{z}\hat{z}} & P_3 \otimes Q_{\hat{z}\hat{b}} \\ P_3 \otimes Q_{\hat{b}\hat{z}} & P_3 \otimes Q_{\hat{b}\hat{b}} \end{bmatrix} \tag{5.13}$$

If one wants to determine z_2^{12}, z_3^{12} and b_2^{12}, b_3^{12} from the above results, it can be obtained from:

$$\begin{bmatrix} \hat{z}_2^{12} \\ \hat{b}_2^{12} \\ \hat{z}_3^{12} \\ \hat{b}_3^{12} \end{bmatrix} = \left[\begin{bmatrix} 1 & 1 & 0 \\ 0 & 1 & 1 \end{bmatrix} \otimes \begin{bmatrix} I_n & 0 \\ 0 & I_3 \end{bmatrix} \right] \begin{bmatrix} \hat{z}_1^1 \\ \hat{b}_1^1 \\ \hat{z}_1^{12} \\ \hat{b}_1^{12} \\ \hat{z}_1^2 \\ \hat{b}_1^2 \end{bmatrix} \tag{5.14}$$

5.2.3 Optimal solution of the fully integrated approach

5.2.3.1 Triple antenna configuration

For the derivation of the following integer least-squares solution, which is the optimal solution, we use the triple antenna configuration introduced in section 5.2.1, for which

the baseline b_1^1 is constrained and the baseline b_1^{12} is unconstrained. First, we write the sum-of-squares decomposition as (see section 3.3.2.1):

$$\left\| \begin{matrix} y_1^1 - Az_1^1 - Gb_1^1 \\ y_1^{12} - Az_1^{12} - Gb_1^{12} \end{matrix} \right\|^2_{P_2 \otimes Q_{yy}} = \left\| \begin{matrix} \hat{e}_1^1 \\ \hat{e}_1^{12} \end{matrix} \right\|^2_{P_2 \otimes Q_{yy}} + \left\| \begin{matrix} \hat{z}_1^1 - z_1^1 \\ \hat{z}_1^{12} - z_1^{12} \end{matrix} \right\|^2_{P_2 \otimes Q_{\hat{z}\hat{z}}} + \\ + \left\| \begin{matrix} \hat{b}_1^1(z_1^1, z_1^{12}) - b_1^1 \\ \hat{b}_1^{12}(z_1^1, z_1^{12}) - b_1^{12} \end{matrix} \right\|^2_{P_2 \otimes Q_{\hat{b}(z)\hat{b}(z)}} \tag{5.15}$$

The ambiguity-constrained baseline solution and its variance-covariance matrix are given as:

$$\begin{bmatrix} \hat{b}_1^1(z_1^1, z_1^{12}) \\ \hat{b}_1^{12}(z_1^1, z_1^{12}) \end{bmatrix} = \begin{bmatrix} \hat{b}_1^1 \\ \hat{b}_1^{12} \end{bmatrix} - (P_2 \otimes Q_{\hat{b}\hat{z}})(P_2 \otimes Q_{\hat{z}\hat{z}})^{-1} \begin{bmatrix} \hat{z}_1^1 - z_1^1 \\ \hat{z}_1^{12} - z_1^{12} \end{bmatrix} \\ = \begin{bmatrix} \hat{b}_1^1 \\ \hat{b}_1^{12} \end{bmatrix} - I_2 \otimes Q_{\hat{b}\hat{z}} Q_{\hat{z}\hat{z}}^{-1} \begin{bmatrix} \hat{z}_1^1 - z_1^1 \\ \hat{z}_1^{12} - z_1^{12} \end{bmatrix} = \begin{bmatrix} \hat{b}_1^1(z_1^1) \\ \hat{b}_1^{12}(z_1^{12}) \end{bmatrix} \tag{5.16}$$

and

$$D \begin{bmatrix} \hat{b}_1^1(z_1^1, z_1^{12}) \\ \hat{b}_1^{12}(z_1^1, z_1^{12}) \end{bmatrix} = P_2 \otimes Q_{\hat{b}(z)\hat{b}(z)} \tag{5.17}$$

Therefore it can be concluded that knowledge about z_1^1 does not improve the conditional baseline $\hat{b}_1^{12}(z_1^{12})$ and similarly, knowledge about z_1^{12} does not help to improve $\hat{b}_1^1(z_1^1)$. This is as expected from Eq.(5.2) assuming the integers are known.

In order to obtain the unknown parameters, we need to solve the following minimization problem:

$$F(z_1^1, z_1^{12}, b_1^1, b_1^{12}) = \min_{\substack{\left[z_1^1, z_1^{12}\right] \in \mathbb{Z}^{n\times 2}, \\ \left[b_1^1, b_1^{12}\right] \in \mathbb{R}^{3\times 2}, \\ ||b_1^1||_{I_3} = l_1^1}} \left\| \begin{matrix} y_1^1 - Az_1^1 - Gb_1^1 \\ y_1^{12} - Az_1^{12} - Gb_1^{12} \end{matrix} \right\|^2_{P_2 \otimes Q_{yy}} = \\ \left\| \begin{matrix} \hat{e}_1^1 \\ \hat{e}_1^{12} \end{matrix} \right\|^2_{P_2 \otimes Q_{yy}} + \min_{\substack{\left[z_1^1, z_1^{12}\right] \in \mathbb{Z}^{n\times 2}, \\ \left[b_1^1, b_1^{12}\right] \in \mathbb{R}^{3\times 2}, \\ ||b_1^1||_{I_3} = l_1^1}} \left(\left\| \begin{matrix} \hat{z}_1^1 - z_1^1 \\ \hat{z}_1^{12} - z_1^{12} \end{matrix} \right\|^2_{P_2 \otimes Q_{\hat{z}\hat{z}}} + \left\| \begin{matrix} \hat{b}_1^1(z_1^1) - b_1^1 \\ \hat{b}_1^{12}(z_1^{12}) - b_1^{12} \end{matrix} \right\|^2_{P_2 \otimes Q_{\hat{b}(z)\hat{b}(z)}} \right) \tag{5.18}$$

The last term on the right hand side can be rewritten as:

$$\left\| \begin{matrix} \hat{b}_1^1(z_1^1) - b_1^1 \\ \hat{b}_1^{12}(z_1^{12}) - b_1^{12} \end{matrix} \right\|^2_{P_2 \otimes Q_{\hat{b}(z)\hat{b}(z)}} = \left\| \hat{b}_1^1(z_1^1) - b_1^1 \right\|^2_{Q_{\hat{b}(z)\hat{b}(z)}} + \left\| \hat{b}_1^{12}(z_1^{12}, b_1^1) - b_1^{12} \right\|^2_{\frac{3}{4} Q_{\hat{b}(z)\hat{b}(z)}} \tag{5.19}$$

With the constraint on the baseline b_1^1 and the ambiguities, the conditional solution of the baseline b_1^{12} becomes:

$$\begin{aligned}\hat{b}_1^{12}(z_1^{12}, b_1^1) &= \hat{b}_1^{12}(z_1^{12}) - \left(-\frac{1}{2}Q_{\hat{b}(z)\hat{b}(z)}\right)\left(Q_{\hat{b}(z)\hat{b}(z)}\right)^{-1}\left(\hat{b}_1^1(z_1^1) - b_1^1\right) \\ &= \hat{b}_1^{12}(z_1^{12}) + \frac{1}{2}\left(\hat{b}_1^1(z_1^1) - b_1^1\right)\end{aligned} \tag{5.20}$$

The variance matrix for this ambiguity constrained baseline is $D\left(\hat{b}_1^{12}(z_1^{12}, b_1^1)\right) = \frac{3}{4}Q_{\hat{b}(z)\hat{b}(z)}$, and hence the knowledge of the constrained baseline allows us to improve the precision of the ambiguity constrained baseline from $Q_{\hat{b}(z)\hat{b}(z)}$ to $\frac{3}{4}Q_{\hat{b}(z)\hat{b}(z)}$.

The integer least-squares solution of Eq. (5.18) then becomes:

Optimal solution for triple antenna configuration

$$\begin{aligned}\begin{bmatrix}\check{z}_1^1 \\ \check{z}_1^{12}\end{bmatrix} &= \arg\min_{\left[z_1^1, z_1^{12}\right]\in\mathbb{Z}^{n\times 2}}\left(\left\|\begin{matrix}\hat{z}_1^1 - z_1^1 \\ \hat{z}_1^{12} - z_1^{12}\end{matrix}\right\|^2_{P_2\otimes Q_{\hat{z}\hat{z}}} + \min_{\substack{b_1^1\in\mathbb{R}^3, \\ ||b_1^1|| = l_1^1}}\left(\left\|\hat{b}_1^1(z_1^1) - b_1^1\right\|^2_{Q_{\hat{b}(z)\hat{b}(z)}}\right)\right) \\ \check{b}_1^1 &= \arg\min_{\substack{b_1^1\in\mathbb{R}^3, \\ ||b_1^1|| = l_1^1}}\left(\left\|\hat{b}_1^1(\check{z}_1^1) - b_1^1\right\|^2_{Q_{\hat{b}(z)\hat{b}(z)}}\right) \\ \check{b}_1^{12} &= \hat{b}_1^{12}(\check{z}_1^{12}, \check{b}_1^1) = \hat{b}_1^{12}(\check{z}_1^{12}) + \frac{1}{2}\left(\hat{b}_1^1(\check{z}_1^1) - \check{b}_1^1\right)\end{aligned} \tag{5.21}$$

For which the ambiguity vector can also be written as:

$$\begin{aligned}\begin{bmatrix}\check{z}_1^1 \\ \check{z}_1^{12}\end{bmatrix} = \arg\min_{\left[z_1^1, z_1^{12}\right]\in\mathbb{Z}^{n\times 2}}\Bigg(&\|\hat{z}_1^1 - z_1^1\|^2_{Q_{\hat{z}\hat{z}}} + \\ &+ \min_{\substack{b_1^1\in\mathbb{R}^3, \\ ||b_1^1|| = l_1^1}}\left(\|\hat{b}_1^1(z_1^1) - b_1^1\|^2_{Q_{\hat{b}(z)\hat{b}(z)}}\right) + \|\hat{z}_1^{12}(z_1^1) - z_1^{12}\|^2_{\frac{3}{4}Q_{\hat{z}\hat{z}}}\Bigg)\end{aligned} \tag{5.22}$$

The first two terms of the right hand side of the equation form the ambiguity objective function for the constrained baseline as described in section 4.2 (see Eq. (4.5)). The third term is due to the correlation between the ambiguities at the two baselines, where

$$\hat{z}_1^{12}(z_1^1) = \hat{z}_1^{12} - \left(-\frac{1}{2}Q_{\hat{z}\hat{z}}\right)Q_{\hat{z}\hat{z}}^{-1}\left(\hat{z}_1^1 - z_1^1\right) = \hat{z}_1^{12} + \frac{1}{2}\left(\hat{z}_1^1 - z_1^1\right) \tag{5.23}$$

This term contributes to the optimal solution, but because of the low correlation this contribution is expected to be small.

The processing strategy makes use of the steps explained in section 3.3.2.1 and 4.2 of the standard LAMBDA and the C-LAMBDA methods. C-LAMBDA is applied to enumerate

the ambiguities of the constrained baseline b_1^1 in combination with ambiguity vectors for baseline b_1^{12} using the correlation between the ambiguities on the two baselines. In the final step, Eq. (5.21) is used to find the integer least-squares solution.

5.2.3.2 Quadruple antenna configuration

For the quadruple antenna configuration with a constrained baseline, b_1^1 and b_1^2 respectively, on both sides of the ambiguity constrained baseline b_1^{12}, we can write:

$$\begin{aligned}\left\| \begin{matrix} \hat{b}_1^1(z_1^1) - b_1^1 \\ \hat{b}_1^{12}(z_1^{12}) - b_1^{12} \\ \hat{b}_1^2(z_1^2) - b_1^2 \end{matrix} \right\|^2_{P_3 \otimes Q_{\hat{b}(z)\hat{b}(z)}} &= \left\|\hat{b}_1^1(z_1^1) - b_1^1\right\|^2_{Q_{\hat{b}(z)\hat{b}(z)}} + \\ &+ \left\|\hat{b}_1^{12}(z_1^{12}, b_1^1, b_1^2) - b_1^{12}\right\|^2_{\frac{1}{2}Q_{\hat{b}(z)\hat{b}(z)}} + \left\|\hat{b}_1^2(z_1^2) - b_1^2\right\|^2_{Q_{\hat{b}(z)\hat{b}(z)}}\end{aligned} \tag{5.24}$$

With the constraint on the baselines b_1^1, b_1^2 and the ambiguities, the conditional solution of the baseline b_1^{12} becomes:

$$\hat{b}_1^{12}(z_1^{12}, b_1^1, b_1^2) = \hat{b}_1^{12}(z_1^{12}) + \frac{1}{2}\left(\hat{b}_1^1(z_1^1) - b_1^1\right) + \frac{1}{2}\left(\hat{b}_1^2(z_1^2) - b_1^2\right) \tag{5.25}$$

By choosing $\hat{b}_1^2(z_1^2) = b_1^2$ the second term on the right hand side of Eq.(5.24) becomes zero, and therefore we can write the minimization problem as:

$$\min_{\substack{\left[z_1^1, z_1^{12}, z_1^2\right] \in \mathbb{Z}^{n\times 3}, \\ \left[b_1^1, b_1^2\right] \in \mathbb{R}^{3\times 2}, \\ ||b_1^1||_{I_3} = l_1^1, \\ ||b_1^2||_{I_3} = l_1^2}} \left(\left\| \begin{matrix} \hat{z}_1^1 - z_1^1 \\ \hat{z}_1^{12} - z_1^{12} \\ \hat{z}_1^2 - z_1^2 \end{matrix} \right\|^2_{P_3 \otimes Q_{\hat{z}\hat{z}}} + \left\| \begin{matrix} \hat{b}_1^1(z_1^1) - b_1^1 \\ \hat{b}_1^2(z_1^2) - b_1^2 \end{matrix} \right\|^2_{I_2 \otimes Q_{\hat{b}(z)\hat{b}(z)}} \right) \tag{5.26}$$

The optimal solution becomes for the four antenna configuration:

Optimal solution for Quadruple antenna configuration

$$
\begin{aligned}
\begin{bmatrix} \check{z}_1^1 \\ \check{z}_1^{12} \\ \check{z}_1^2 \end{bmatrix} &= \arg \min_{\left[z_1^1, z_1^{12}, z_1^2\right] \in \mathbb{Z}^{n\times 3}} \left(\left\| \begin{matrix} \hat{z}_1^1 - z_1^1 \\ \hat{z}_1^{12} - z_1^{12} \\ \hat{z}_1^2 - z_1^2 \end{matrix} \right\|^2_{P_3 \otimes Q_{\hat{z}\hat{z}}} + \right. \\
&\quad \left. + \min_{\substack{b_1^1 \in \mathbb{R}^3, \\ ||b_1^1|| = l_1^1}} \left(\left\| \hat{b}_1^1(z_1^1) - b_1^1 \right\|^2_{Q_{\hat{b}(z)\hat{b}(z)}} \right) + \min_{\substack{b_1^2 \in \mathbb{R}^3, \\ ||b_1^2|| = l_1^2}} \left(\left\| \hat{b}_1^2(z_1^2) - b_1^2 \right\|^2_{Q_{\hat{b}(z)\hat{b}(z)}} \right) \right) \\
\check{b}_1^1 &= \arg \min_{\substack{b_1^1 \in \mathbb{R}^3, \\ ||b_1^1|| = l_1^1}} \left(\left\| \hat{b}_1^1(\check{z}_1^1) - b_1^1 \right\|^2_{Q_{\hat{b}(z)\hat{b}(z)}} \right) \\
\check{b}_1^2 &= \arg \min_{\substack{b_1^2 \in \mathbb{R}^3, \\ ||b_1^2|| = l_1^2}} \left(\left\| \hat{b}_1^2(\check{z}_1^2) - b_1^2 \right\|^2_{Q_{\hat{b}(z)\hat{b}(z)}} \right) \\
\check{b}_1^{12} &= \hat{b}_1^{12}(\check{z}_1^{12}, \check{b}_1^1, \check{b}_1^2) = \hat{b}_1^{12}(\check{z}_1^{12}) + \frac{1}{2}\left(\hat{b}_1^1(\check{z}_1^1) - \check{b}_1^1 \right) + \frac{1}{2}\left(\hat{b}_1^2(\check{z}_1^2) - \check{b}_1^2 \right)
\end{aligned}
\tag{5.27}
$$

Now the variance for this ambiguity constrained baseline is $D\left(\hat{b}_1^{12}(z_1^{12}, b_1^1, b_1^2)\right) = \frac{1}{2} Q_{\hat{b}(z)\hat{b}(z)}$, and hence the knowledge of two constrained baselines, one at each side of the unconstrained baseline, improves the precision of this baseline from $Q_{\hat{b}(z)\hat{b}(z)}$ to $\frac{1}{2} Q_{\hat{b}(z)\hat{b}(z)}$.

Intermezzo: Alternative quadruple antenna configuration In the previous section, a quadruple antenna configuration was considered, assuming that each platform has two antennas. The baseline lengths between the antennas on both platforms were assumed known (b_1^1 and b_1^2 in the right hand side of Fig. 5.1).
For completeness, now a quadruple antenna configuration with three antennas on one platform is discussed, again with known baseline lengths between the antennas, and one antenna on another platform.
A solution for this configuration is given where both constrained baselines are placed at the same side of the unconstrained baseline (see Fig. 5.2). For a quadruple antenna configuration with the two constrained baselines b_1^1 and b_2^1 and the unconstrained baseline as b_1^{12} we can write:

$$
\begin{aligned}
\left\| \begin{matrix} \hat{b}_1^1(z_1^1) - b_1^1 \\ \hat{b}_2^1(z_2^1) - b_2^1 \\ \hat{b}_1^{12}(z_1^{12}) - b_1^{12} \end{matrix} \right\|^2_{P_3 \otimes Q_{\hat{b}(z)\hat{b}(z)}} &= \left\| \hat{b}_1^1(z_1^1) - b_1^1 \right\|^2_{Q_{\hat{b}(z)\hat{b}(z)}} + \\
+ \left\| \hat{b}_2^1(z_2^1, b_1^1) - b_2^1 \right\|^2_{\frac{3}{4} Q_{\hat{b}(z)\hat{b}(z)}} &+ \left\| \hat{b}_1^{12}(z_1^{12}, b_1^1, b_2^1) - b_1^{12} \right\|^2_{\frac{2}{3} Q_{\hat{b}(z)\hat{b}(z)}}
\end{aligned}
\tag{5.28}
$$

With the constraint on both the baselines b_1^1 and the ambiguities, the conditional solution of the baseline b_2^1 becomes:

$$
\hat{b}_2^1(z_2^1, b_1^1) = \hat{b}_2^1(z_2^1) + \frac{1}{2}\left(\hat{b}_1^1(z_1^1) - b_1^1 \right) \tag{5.29}
$$

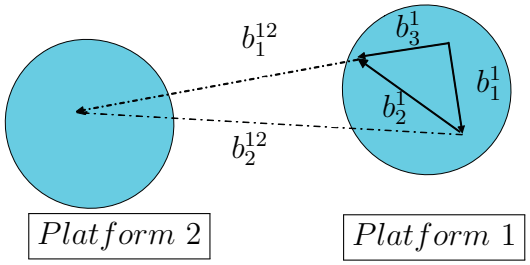


Figure 5.2: Definition of a different quadruple antenna configuration (solid arrows indicate baseline with known length)

With the constraint on the baselines b_1^1,b_2^1 and the ambiguities, the conditional solution of the baseline b_1^{12} becomes:

$$\hat{b}_1^{12}(z_1^{12}, b_1^1, b_2^1) = \hat{b}_1^{12}(z_1^{12}) + \frac{1}{3}\left(\hat{b}_1^1(z_1^1) - b_1^1\right) + \frac{2}{3}\left(\hat{b}_2^1(z_2^1) - b_2^1\right) \tag{5.30}$$

The third term on the right hand side of Eq.(5.28) can be made zero for every z_1^{12}, and therefore the minimization problem, using the decomposition of Eq. (5.19), becomes:

$$\min_{\substack{\left[z_1^1, z_1^2, z_1^{12}\right]\in\mathbb{Z}^{n\times 3},\\ \left[b_1^1, b_2^1\right]\in\mathbb{R}^{3\times 2},\\ ||b_1^1||_{I_3}=l_1^1,\\ ||b_2^1||_{I_3}=l_2^1}} \left(\left\| \begin{matrix} \hat{z}_1^1 - z_1^1 \\ \hat{z}_2^1 - z_2^1 \\ \hat{z}_1^{12} - z_1^{12} \end{matrix} \right\|^2_{P_3\otimes Q_{\hat{z}\hat{z}}} + \left\| \begin{matrix} \hat{b}_1^1(z_1^1) - b_1^1 \\ \hat{b}_2^1(z_2^1) - b_2^1 \end{matrix} \right\|^2_{P_2\otimes Q_{\hat{b}(z)\hat{b}(z)}} \right) \tag{5.31}$$

The optimal solution becomes for this four antenna configuration :

$$\begin{bmatrix} \check{z}_1^1 \\ \check{z}_2^1 \\ \check{z}_1^{12} \end{bmatrix} = \arg \min_{\left[z_1^1, z_2^1, z_1^{12}\right]\in\mathbb{Z}^{n\times 3}} \left(\left\| \begin{matrix} \hat{z}_1^1 - z_1^1 \\ \hat{z}_2^1 - z_2^1 \\ \hat{z}_1^{12} - z_1^{12} \end{matrix} \right\|^2_{P_3\otimes Q_{\hat{z}\hat{z}}} + \min_{\substack{\left[b_1^1, b_2^1\right]\in\mathbb{R}^{3\times 2},\\ ||b_1^1||_{I_3}=l_1^1,\\ ||b_2^1||_{I_3}=l_2^1}} \left(\left\| \begin{matrix} \hat{b}_1^1(z_1^1) - b_1^1 \\ \hat{b}_2^1(z_2^1) - b_2^1 \end{matrix} \right\|^2_{P_2\otimes Q_{\hat{b}(z)\hat{b}(z)}} \right) \right)$$

$$\begin{bmatrix} \check{b}_1^1 \\ \check{b}_2^1 \end{bmatrix} = \arg \min_{\substack{\left[b_1^1, b_2^1\right]\in\mathbb{R}^{3\times 2},\\ ||b_1^1||_{I_3}=l_1^1,\\ ||b_2^1||_{I_3}=l_2^1}} \left(\left\| \begin{matrix} \hat{b}_1^1(z_1^1) - b_1^1 \\ \hat{b}_2^1(z_2^1) - b_2^1 \end{matrix} \right\|^2_{P_2\otimes Q_{\hat{b}(z)\hat{b}(z)}} \right)$$

$$\check{b}_1^{12} = \hat{b}_1^{12}(\check{z}_1^{12}, \check{b}_1^1, \check{b}_2^1) = \hat{b}_1^{12}(\check{z}_1^{12}) + \frac{1}{3}\left(\hat{b}_1^1(\check{z}_1^1) - \check{b}_1^1\right) + \frac{2}{3}\left(\hat{b}_2^1(\check{z}_2^1) - \check{b}_2^1\right) \tag{5.32}$$

Now the variance for this ambiguity constrained baseline is $D\left(\hat{b}_1^{12}(z_1^{12}, b_1^1, b_2^1)\right) = \frac{2}{3}Q_{\hat{b}(z)\hat{b}(z)}$, and hence the knowledge of two constrained baselines, at the same side

of the unconstrained baseline, improves the precision of the ambiguity constrained baseline from $Q_{\hat{b}(z)\hat{b}(z)}$ to $\frac{2}{3}Q_{\hat{b}(z)\hat{b}(z)}$. This means that the improvement is larger than for the triple antenna configuration, as the model becomes stronger due to the two constrained baselines at one side, and less than the quadruple antenna configuration of the previous section. This is also as expected as the unconstrained baseline is now only constrained at one side; the other side is left free.

5.2.4 Vectorial bootstrapping of the fully integrated approach

5.2.4.1 Triple antenna configuration

An approximation of the optimal solution as given in section 5.2.3.1 can be obtained by first solving the first two terms on the right hand side of Eq. (5.22) for z_1^1, and then the third term for z_1^{12}, as if the correlation would be absent. The result is a vectorial bootstrapping approach in which we first solve the ambiguity on the constrained baseline and apply the found ambiguity vector in the solution of the unconstrained baseline. This is also the difference with the uncoupled approach from section 5.2.5 in which the solutions are found completely independent of each other. As it is based on an approximation, it is referred to as a suboptimal solution. This solution, hereafter coined the vectorial bootstrapping solution, is then given as:

Vectorial bootstrapped Solution for triple antenna configuration

$$\check{z}_1^1 = \arg\min_{z_1^1\in\mathbb{Z}^n}\left(\|\hat{z}_1^1 - z_1^1\|^2_{Q_{\hat{z}\hat{z}}} + \min_{\substack{b_1^1\in\mathbb{R}^3,\\ ||b_1^1||=l_1^1}}\left(\left\|\hat{b}_1^1(z_1^1) - b_1^1\right\|^2_{Q_{\hat{b}(z)\hat{b}(z)}}\right)\right)$$

$$\check{z}_1^{12} = \arg\min_{z_1^{12}\in\mathbb{Z}^n}\left(\|\hat{z}_1^{12}(\check{z}_1^1) - z_1^{12}\|^2_{\frac{3}{4}Q_{\hat{z}\hat{z}}}\right) \tag{5.33a}$$

$$\check{b}_1^1 = \arg\min_{\substack{b_1^1\in\mathbb{R}^3,\\ ||b_1^1||=l_1^1}}\left(\left\|\hat{b}_1^1(\check{z}_1^1) - b_1^1\right\|^2_{Q_{\hat{b}(z)\hat{b}(z)}}\right) \tag{5.33b}$$

$$\check{b}_1^{12} = \hat{b}_1^{12}(\check{z}_1^{12}) + \frac{1}{2}\left(\hat{b}_1^1(\check{z}_1^1) - \check{b}_1^1\right) \tag{5.33c}$$

For this approach in the first step, the C-LAMBDA is applied to estimate the ambiguities of the constrained baseline b_1^1. In the second step, the standard LAMBDA is used with $\hat{z}_1^{12}(\check{z}_1^1)$ and $\frac{3}{4}Q_{\hat{z}\hat{z}}$ on the unconstrained baseline.
From Eq. (5.33) and (5.22), it is expected that the success rate of the optimal approach is better than the vectorial bootstrapping (suboptimal) approach, but because of the low correlation between the two baselines the difference is anticipated to be minimal as discussed in the previous section. This is analyzed using simulated data in section 5.2.6.

Next, it is demonstrated that the suboptimal solution is the same as the solution from (Pinchin et al., 2008) in which the ambiguity vector for b_1^{12} that minimizes the cost

function in the metric of $Q_{\hat{z}\hat{z}}$ was found as:

$$\check{z}_1^{12} = \arg\min_{z_1^{12}\in\mathbb{Z}^n} \left(\|\hat{z}_1^{12} - z_1^{12}\|^2_{Q_{\hat{z}\hat{z}}} + \|(\hat{z}_2^{12} - z_1^1) - z_1^{12}\|^2_{Q_{\hat{z}\hat{z}}} \right) \tag{5.34}$$

Recall from section 5.2.3.1 that $\hat{z}_1^{12}(z_1^1) = \hat{z}_1^{12} + \frac{1}{2}(\hat{z}_1^1 - z_1^1)$, which can be rewritten using $\hat{z}_1^1 = \hat{z}_2^{12} - \hat{z}_1^{12}$, to:

$$\hat{z}_1^{12}(z_1^1) = \frac{1}{2}\left(\hat{z}_1^{12} + \hat{z}_2^{12} - z_1^1\right) \tag{5.35}$$

Thus $\hat{z}_1^{12}(z_1^1)$ is the average of $\hat{z}_1^{12}$ and $\hat{z}_2^{12} - z_1^1$. Next, the following identity is introduced, which is valid for any $u, v, x \in \mathbb{R}^n$ and arbitrary positive definite matrix M:

$$\|\frac{1}{2}(u+v) - x\|^2_M = \frac{1}{2}\|u-x\|^2_M + \frac{1}{2}\|v-x\|^2_M - \frac{1}{4}\|u-v\|^2_M \tag{5.36}$$

With this identity the following is obtained:

$$\begin{aligned} \|\hat{z}_1^{12}(z_1^1) - z_1^{12}\|^2_{Q_{\hat{z}\hat{z}}} =& \|\frac{1}{2}(\hat{z}_1^{12} + (\hat{z}_2^{12} - z_1^1) - z_1^{12})\|^2_{Q_{\hat{z}\hat{z}}} \\ =& \frac{1}{2}\|\hat{z}_1^{12} - z_1^{12}\|^2_{Q_{\hat{z}\hat{z}}} + \frac{1}{2}\|(\hat{z}_2^{12} - z_1^1) - z_1^{12}\|^2_{Q_{\hat{z}\hat{z}}} + \\ & - \frac{1}{4}\|\hat{z}_1^{12} - (\hat{z}_2^{12} - z_1^1)\|^2_{Q_{\hat{z}\hat{z}}} \end{aligned} \tag{5.37}$$

As the last term on the right hand side is constant, the following solution is obtained:

$$\check{z}_1^{12} = \arg\min_{z_1^{12}\in\mathbb{Z}^n} \left(\|\hat{z}_1^{12}(\check{z}_1^1) - z_1^{12}\|^2_{Q_{\hat{z}\hat{z}}} \right) \tag{5.38a}$$

$$= \arg\min_{z_1^{12}\in\mathbb{Z}^n} \left(\|\hat{z}_1^{12} - z_1^{12}\|^2_{Q_{\hat{z}\hat{z}}} + \|(\hat{z}_2^{12} - z_1^1) - z_1^{12}\|^2_{Q_{\hat{z}\hat{z}}} \right) \tag{5.38b}$$

Eq. (5.38a) is the same as Eq. (5.33a) with $Q_{\hat{z}\hat{z}}$ instead of $\frac{3}{4}Q_{\hat{z}\hat{z}}$. This difference in scaling will not affect the outcome of the minimization. The second expression (i.e. Eq. (5.38b)) is the one used in (Pinchin et al., 2008).

5.2.4.2 Quadruple antenna configuration

An approximation of the optimal solution as given in section 5.2.3.2 can again be obtained by solving the unconstrained baselines, after the constrained baselines have been resolved. This would result in three minimizations, one for z_1^1 and z_1^2 and one for z_1^{12}, if the correlation would be absent. The result is a vectorial bootstrapping approach in which we first solve the ambiguity on the constrained baselines b_1^1 and b_1^2 and apply the found ambiguity vector in the solution of the unconstrained baseline z_1^{12}. Hence, the vectorial bootstrapping solution for the four antenna configuration is given as:

Vectorial bootstrapped Solution for Quadruple antenna configuration

$$
\begin{aligned}
\check{z}_1^1 &= \arg \min_{z_1^1 \in \mathbb{Z}^n} \left(\|\hat{z}_1^1 - z_1^1\|^2_{Q_{\hat{z}\hat{z}}} + \min_{\substack{b_1^1 \in \mathbb{R}^3, \\ ||b_1^1|| = l_1^1}} \left(\left\| \hat{b}_1^1(z_1^1) - b_1^1 \right\|^2_{Q_{\hat{b}(z)\hat{b}(z)}} \right) \right) \\
\check{z}_1^2 &= \arg \min_{z_1^2 \in \mathbb{Z}^n} \left(\|\hat{z}_1^2 - z_1^2\|^2_{Q_{\hat{z}\hat{z}}} + \min_{\substack{b_1^2 \in \mathbb{R}^3, \\ ||b_1^2|| = l_1^2}} \left(\left\| \hat{b}_1^2(z_1^2) - b_1^2 \right\|^2_{Q_{\hat{b}(z)\hat{b}(z)}} \right) \right) \\
\check{z}_1^{12} &= \arg \min_{z_1^{12} \in \mathbb{Z}^n} \left(\|\hat{z}_1^{12}(\check{z}_1^1, \check{z}_1^2) - z_1^{12}\|^2_{\frac{1}{2}Q_{\hat{z}\hat{z}}} \right) \\
\check{b}_1^1 &= \arg \min_{\substack{b_1^1 \in \mathbb{R}^3, \\ ||b_1^1|| = l_1^1}} \left(\left\| \hat{b}_1^1(\check{z}_1^1) - b_1^1 \right\|^2_{Q_{\hat{b}(z)\hat{b}(z)}} \right) \\
\check{b}_1^2 &= \arg \min_{\substack{b_1^2 \in \mathbb{R}^3, \\ ||b_1^2|| = l_1^2}} \left(\left\| \hat{b}_1^2(\check{z}_1^2) - b_1^2 \right\|^2_{Q_{\hat{b}(z)\hat{b}(z)}} \right) \\
\check{b}_1^{12} &= \hat{b}_1^{12}(\check{z}_1^{12}) + \frac{1}{2}\left(\hat{b}_1^1(\check{z}_1^1) - \check{b}_1^1 \right) + \frac{1}{2}\left(\hat{b}_1^2(\check{z}_1^2) - \check{b}_1^2 \right)
\end{aligned}
\tag{5.39}
$$

For this approach in the first step C-LAMBDA is used to estimate the ambiguities of the two constrained baselines b_1^1 and b_1^2. In the second step we use standard LAMBDA with $\hat{z}_1^{12}(\check{z}_1^1, \check{z}_1^2)$ and $\frac{1}{2}Q_{\hat{z}\hat{z}}$ on the unconstrained baseline.

5.2.5 Uncoupled approach using unconstrained and constrained baselines

The simplest way to combine constrained and unconstrained baselines is the uncoupled approach in which the baselines are treated completely independently. This approach provides a lower bound for the empirical success rate of the optimal and vectorial bootstrapping approaches described in the previous two sections. For a discussion on lower bounds of the probability of obtaining the correct integer ambiguity vector, see section 3.4.2 and (Teunissen, 1998b).

5.2.6 Verification by simulation

In this section, the introduced optimal, vectorial bootstrapping and uncoupled approaches are tested using simulated data, for the most challenging application of single-epoch, single-frequency ambiguity resolution. We will investigate the experimental or empirical success rate, which depends on the strength of the underlying GNSS model. Information about the simulation setup can be found in Appendix A.1.
For analysis of the performance of the described approaches, we compare the true integer ambiguity vector (the 'true solution' known in the simulations) and the estimated integer ambiguity vector at every sample. The empirical success rate is defined as the number of epochs where the obtained integer ambiguity vector was equal to the true integer ambiguity vector divided by the total number of epochs.
The baseline length will not influence the performance of the ambiguity resolution method,

as long as the atmospheric affects on the GNSS observations are negligible (typically if the baseline is shorter than 10 km, see section 2.5 and (Buist, 2008)).
We will analyze both performance on individual baselines and on the solution of combined baselines (the "overall" solution). The first result is important as the information of the constrained baseline could improve the solution of the unconstrained baseline, and furthermore we would like to confirm that the success rate for the constrained baseline is not changed in the integrated solution compared to the uncoupled solution. The second result is important, as for some applications as described in section 1.1, we are interested in the estimation of a number of baseline vectors on or between a number of platforms.

In this section, we will analyze the proposed integrated approaches. For the vectorial bootstrapped solution, we observed a maximum difference in the empirical success rate with the optimal solution of 0.1%, therefore there is only a marginal difference between the two and we include only the optimal solution's results.
We analyze the optimal solution using one constrained baseline (as in the triple antenna configuration described in section 5.2.3.1) and two constrained baselines (as in the quadruple antenna configuration described in section 5.2.3.2). The results are presented in three tables. Table 5.1, 5.2 and 5.3 contain empirical success rates as a function of the number of tracked satellites (N_{SV}) and the phase and code undifferenced level noise (σ_ϕ, σ_p). In Table 5.1 and 5.2, we analyze the success rate on individual baselines, both uncoupled and as part of the optimal solution.
In these tables $P(\tilde{z}_1^1 = z_1^1)$ and $P(\check{z}_1^1 = z_1^1)$ stands for the success rate on the constrained baseline b_1^1, and $P(\tilde{z}_1^{12} = z_1^{12})$ and $P(\check{z}_1^{12} = z_1^{12})$ for the success rate on the unconstrained baseline b_1^{12} in the uncoupled and optimal solution, respectively. For the unconstrained baseline, we will analyze the uncoupled case $P(\tilde{z}_1^{12} = z_1^{12})$, the case where one constrained baseline is utilized ($C = 1$) and the case where two constrained baselines are utilized ($C = 2$).
In Table 5.3, we look at the overall empirical success rate, which is the success rate on both baselines ($P(\check{z}_1^1 = z_1^1, \check{z}_1^{12} = z_1^{12})$) for the triple antenna configuration or on all three baselines ($P(\check{z}_1^1 = z_1^1, \check{z}_1^{12} = z_1^{12}, \check{z}_1^2 = z_1^2)$) for the quadruple antenna configuration in a combined solution. Again the uncoupled and optimal approach using one or two constrained baseline(s) are considered.

Uncoupled vs. Optimal Solution

In Table 5.2, the unconstrained baseline b^{12} is presented as uncoupled ($C = 0$) and as part of the the optimal solution using a single constrained baseline ($C = 1$) and using two constrained baselines ($C = 2$). For the unconstrained baseline in Table 5.2, we observe that the optimal solution has a better performance than uncoupled. The improvement is between 0 and 13% using a single constrained baseline ($C = 1$), and between 0 and 30% using two constrained baselines ($C = 2$), with a larger improvement for weaker GNSS models.

In Table 5.3, the improvement of the empirical success rate for the optimal solution compared to the uncoupled approach ($C = 0$) is between 0 and 13% if a single constrained baseline ($C = 1$) is used, and between 0 and 29% if two constrained baselines ($C = 2$) are used. Again we observe a larger improvement for weaker GNSS models.

Table 5.1: Simulation results: single-frequency, single-epoch success rates for the constrained baseline b_1^1 using one constrained baseline ($C = 1$, i.e. two antennas for uncoupled and triple antenna configuration for the optimal solution)

N_{SV}	$\#C$	σ_ϕ [mm]=3			σ_ϕ [mm]=1		
		σ_p [cm]			σ_p [cm]		
		30	15	5	30	15	5
	1	*Uncoupled* $P(\check{z}_1^1 = z_1^1)$					
	1	*Optimal* $P(\check{z}_1^1 = z_1^1)$					
5	1	0.72	0.89	1.00	0.97	1.00	1.00
	1	0.72	0.89	1.00	0.97	1.00	1.00
6	1	0.96	0.99	1.00	1.00	1.00	1.00
	1	0.96	0.99	1.00	1.00	1.00	1.00
7	1	0.99	1.00	1.00	1.00	1.00	1.00
	1	1.00	1.00	1.00	1.00	1.00	1.00
8	1	1.00	1.00	1.00	1.00	1.00	1.00
	1	1.00	1.00	1.00	1.00	1.00	1.00

Vectorial bootstrapped vs. Optimal Solution

As already mentioned in the introduction of this section, the vectorial bootstrapped results are not included in the tables as these were almost the same as optimal. Nevertheless, we would like to report some observations. In the vectorial bootstrapped solution, the constrained baseline is not influenced by the unconstrained baseline, hence the result for the constrained baseline will be exactly the same as the uncoupled solution. We observed that the optimal solution and the vectorial bootstrapped solution have almost the same performance for the success rate on individual baselines (i.e. Table 5.2): the maximum difference was 0.1% in the empirical success rates. Also for the overall success rate (i.e. results in Table 5.3), the optimal solution and the vectorial bootstrapped solution have the same performance. This result is expected from the low correlation between the constrained and unconstrained baselines as discussed in section 5.2.3 and 5.2.4.

Triple vs. Quadruple Antenna Configuration

For the constrained baseline, the success rate for the uncoupled and optimal solution was found to be exactly the same (see Table 5.1), for the quadruple antenna configuration the same observation was made. The probability of obtaining the correct integer value increases as the precision of $\hat{z}$ improves. For the unconstrained baseline in the quadruple antenna configuration (the case for $C = 2$ in Table 5.2, and 5.3), we observe a higher success rate than for the same baseline in the triple antenna configuration ($C = 1$ case in Table 5.2 and 5.3), which is as expected as the variance-covariance matrix is scaled by $\frac{1}{2}$ and $\frac{3}{4}$ with respect to the original $Q_{\hat{z}\hat{z}}$ of the uncoupled solution. Therefore we can say that the quadruple antenna configuration is a stronger model than the triple antenna configuration.

Table 5.2: Simulation results: single-frequency, single-epoch success rates for the unconstrained baseline b^{12} using zero ($C = 0$), one ($C = 1$, i.e. triple antenna configuration) or two ($C = 2$, i.e. quadruple antenna configuration) constrained baselines

N_{SV}	$\#C$	σ_ϕ [mm]=3			σ_ϕ [mm]=1		
		σ_p [cm]			σ_p [cm]		
		30	15	5	30	15	5
	0	*Uncoupled* $P(\check{z}_1^{12} = z_1^{12})$					
	1	*Optimal* $P(\check{z}_1^{12} = z_1^{12})$					
	2	*Optimal* $P(\check{z}_1^{12} = z_1^{12})$					
5	0	0.03	0.19	0.87	0.06	0.27	0.95
	1	0.04	0.26	0.93	0.09	0.36	0.98
	2	0.09	0.42	0.98	0.15	0.52	1.00
6	0	0.25	0.67	0.97	0.49	0.87	1.00
	1	0.36	0.80	0.99	0.59	0.92	1.00
	2	0.55	0.92	1.00	0.74	0.97	1.00
7	0	0.50	0.80	1.00	0.75	0.93	1.00
	1	0.61	0.89	1.00	0.81	0.97	1.00
	2	0.74	0.96	1.00	0.89	0.99	1.00
8	0	0.86	0.95	1.00	1.00	1.00	1.00
	1	0.92	0.97	1.00	1.00	1.00	1.00
	2	0.97	0.99	1.00	1.00	1.00	1.00

Table 5.3: Simulation results: single-frequency, single-epoch overall success rates for two baselines or three baselines using zero ($C = 0$), one ($C = 1$, i.e. triple antenna configuration) or two ($C = 2$, i.e. quadruple antenna configuration) constrained baselines

N_{SV}	$\#C$	σ_ϕ [mm]=3			σ_ϕ [mm]=1		
		σ_p [cm]			σ_p [cm]		
		30	15	5	30	15	5
	0	*Uncoupled* $P(\check{z}_1^1 = z_1^1, \check{z}_1^{12} = z_1^{12})$					
	1	*Optimal* $P(\check{z}_1^1 = z_1^1, \check{z}_1^{12} = z_1^{12})$					
	2	*Optimal* $P(\check{z}_1^1 = z_1^1, \check{z}_1^{12} = z_1^{12}, \check{z}_1^2 = z_1^2)$					
5	0	0.02	0.17	0.86	0.05	0.27	0.95
	1	0.04	0.25	0.93	0.09	0.36	0.98
	2	0.06	0.38	0.98	0.15	0.52	1.00
6	0	0.24	0.66	0.97	0.49	0.87	1.00
	1	0.36	0.79	0.99	0.59	0.92	1.00
	2	0.53	0.92	1.00	0.74	0.97	1.00
7	0	0.50	0.80	1.00	0.75	0.93	1.00
	1	0.61	0.89	1.00	0.81	0.97	1.00
	2	0.74	0.96	1.00	0.89	0.99	1.00
8	0	0.86	0.95	1.00	1.00	1.00	1.00
	1	0.92	0.97	1.00	1.00	1.00	1.00
	2	0.97	0.99	1.00	1.00	1.00	1.00

5.2.7 Concluding remarks

In order to obtain more insight into the multi-baseline problem with unconstrained baselines between platforms and constrained baselines on platforms, an uncoupled and two integrated strategies (coined the optimal, and vectorial bootstrapping or suboptimal approach) were investigated, both theoretically and experimentally. As was expected from the low correlation between baselines, the success rate of the optimal approach is similar to the vectorial bootstrapping approach. This was confirmed with simulated data for the single-epoch, single-frequency application. This is an important result as the vectorial bootstrapped solution is more computational efficient and in general could be sufficient for the type of applications discussed in this thesis. In the reminder of this chapter, bootstrapping approaches will be further investigated.

5.3 General Model with both constrained and unconstrained baselines

Section 5.2 developed a model for two platforms with a total number of three (triple) or four (quadruple) antennas. In this section, a general model is developed for any number of antennas at the two platforms and so expanding the vectorial bootstrapping approach described in section 5.2. As a last step in this section, the Multivariate Constrained LAMBDA Method developed in section 4.3 is applied on each individual platform and the outcome is used for an ambiguity constrained solution on the unconstrained baseline. In this way the solution for the unconstrained baseline is bootstrapped from the MC-LAMBDA's solutions of each platform and therefore this method is called: multivariate bootstrapped relative positioning.

5.3.1 Multi-baseline Setup

As is shown in Fig. 5.3, in the multi-antenna configuration the number of antennas at a single platform is $N+1$ and the number of independent baselines is therefore N. The total number of constrained baselines at platform 1 is N^1. The first constrained baseline on platform 1 is called baseline b_1 and the last baseline b_N. In order to distinguish between antennas and baselines at different platforms, a superscript indicating the platform is introduced (same notation as applied in section 5.2.1), e.g. the first constrained baseline on platform 1 is written as b_1^1 in Fig. 5.3. The unconstrained baseline connecting the two platforms is then written as b^{12}. For simplicity, the baselines in Fig. 5.3 are shown as aligned, but generally a different antenna configuration will be used for attitude determination (see section 4.3.3).
For compactness in this theoretical discussion, the design matrices A and G and the variance-covariance matrix Q_{yy} are assumed to be identical. This is a reasonable assumption if only L1 observations are used and the antennas are sufficiently close, so that the relative antenna-satellite geometry may be considered the same for all antennas. In a software implementation, the design matrices can be assumed to be identical only if they apply to antennas at the same platform.

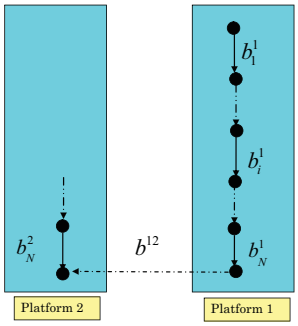


Figure 5.3: Illustration of the multi-antenna configuration on two platforms

Next, a matrix formulation for this multi-baseline problem is introduced based on section 4.3.2. A $2n \times N^1$ data matrix $Y = \left[y_1, \ldots, y_{N^1}\right]$ is used where each column corresponds to one baseline, an $n \times N^1$ matrix $Z = \left[z_1, \ldots, z_{N^1}\right]$ of N DD integer ambiguity vectors and a $3 \times N^1$ matrix $B = \left[b_1, \ldots, b_{N^1}\right]$ of N^1 unknown baseline vectors.

In section 4.3.2, we have obtained a multi-baseline model described in Eq. (4.29):

$$\begin{aligned} E(vec(Y)) &= (I_{N^1} \otimes A)vec(Z) + (I_{N^1} \otimes G)vec(B) \\ D(vec(Y)) &= P_{N^1} \otimes Q_{yy} \end{aligned} \tag{5.40}$$

To describe the dispersion of the observations at all baselines, $P_{N^1} \otimes Q_{yy}$ is used, where matrix P_{N^1} takes care of the correlation that follows from the fact that consecutive baselines have one antenna in common. For a discussion on the tridiagonal matrix P_{N^1}, we refer to section 4.3.2 and (Buist et al., 2008)(Buist et al., 2009b). In this section, an $N^1 \times N^1$ tridiagonal matrix is applied:

$$P_{N^1} = \begin{bmatrix} 1 & -\frac{1}{2} & 0 & \ldots & 0 \\ -\frac{1}{2} & 1 & -\frac{1}{2} & & \vdots \\ 0 & -\frac{1}{2} & 1 & \ddots & 0 \\ \vdots & & \ddots & \ddots & -\frac{1}{2} \\ 0 & \ldots & 0 & -\frac{1}{2} & 1 \end{bmatrix} \tag{5.41}$$

The least-squares solution and corresponding v-c matrix of the $N^1 + 1$-antenna configuration, which includes the unconstrained baseline b^{12} to the other platform, can be given as (Buist et al., 2009b):

$$\begin{aligned} \begin{bmatrix} vec(\hat{Z}^1) \\ \hat{z}^{12} \\ vec(\hat{B}^1) \\ \hat{b}^{12} \end{bmatrix} &= \begin{bmatrix} I_{N^1+1} \otimes (Q_{\hat{z}\hat{z}}A^T Q_{yy}^{-1} + Q_{\hat{z}\hat{b}}G^T Q_{yy}^{-1}) \\ I_{N^1+1} \otimes (Q_{\hat{b}\hat{z}}A^T Q_{yy}^{-1} + Q_{\hat{b}\hat{b}}G^T Q_{yy}^{-1}) \end{bmatrix} \begin{bmatrix} vec(Y^1) \\ y^{12} \end{bmatrix} \\ D \begin{bmatrix} vec(\hat{Z}^1) \\ \hat{z}^{12} \\ vec(\hat{B}^1) \\ \hat{b}^{12} \end{bmatrix} &= \begin{bmatrix} P_{N^1+1} \otimes Q_{\hat{z}\hat{z}} & P_{N^1+1} \otimes Q_{\hat{z}\hat{b}} \\ P_{N^1+1} \otimes Q_{\hat{b}\hat{z}} & P_{N^1+1} \otimes Q_{\hat{b}\hat{b}} \end{bmatrix} \end{aligned} \tag{5.42}$$

This shows, as was expected from Eq. (5.4) for a triple antenna configuration, that $\hat{z}_i$ and $\hat{b}_i$ are solely determined by the DD observation vector of the corresponding antenna pair, that is y_i. Thus also for any number of antennas, as was found in section 5.2 for triple and quadruple antenna configurations, parallel processing is possible for the float solution.

5.3.2 Vectorial bootstrapping using C-LAMBDA

In order to obtain the unknown parameters, the following minimization problem is solved for a single platform with N^1 constrained baselines, and a single unconstrained baseline to an antenna at another platform.

$$\begin{aligned}
&\min_{\substack{\left[Z^1,\, z^{12}\right]\in\mathbb{Z}^{n\times(N^1+1)} \\ \left[B^1,\, b^{12}\right]\in\mathbb{R}^{3\times(N^1+1)} \\ \left\|b_j^1\right\|=l_j^1,j=1\ldots N^1}} \left\| \begin{matrix} vec(Y^1) - (I_{N^1}\otimes A)vec(Z^1) - (I_{N^1}\otimes G)vec(B^1) \\ y^{12} - Az^{12} - Gb^{12} \end{matrix} \right\|^2_{P_{N^1+1}\otimes Q_{yy}} = \\
&= \left\| \begin{matrix} vec(\hat{E}^1) \\ \hat{e}^{12} \end{matrix} \right\|^2_{P_{N^1+1}\otimes Q_{yy}} + \\
&+ \min_{\substack{\left[Z^1,\, z^{12}\right]\in\mathbb{Z}^{n\times(N^1+1)} \\ \left[B^1,\, b^{12}\right]\in\mathbb{R}^{3\times(N^1+1)} \\ \left\|b_j^1\right\|=l_j^1,j=1\ldots N^1}} \left(\left\| \begin{matrix} vec(\hat{Z}^1 - Z^1) \\ \hat{z}^{12} - z^{12} \end{matrix} \right\|^2_{P_{N^1+1}\otimes Q_{\hat{z}\hat{z}}} + \left\| \begin{matrix} vec(\hat{B}^1(Z^1,z^{12}) - B^1) \\ \hat{b}^{12}(Z^1,z^{12}) - b^{12} \end{matrix} \right\|^2_{P_{N^1+1}\otimes Q_{\hat{b}(z)\hat{b}(z)}} \right)
\end{aligned} \tag{5.43}$$

where $\hat{e} = y - A\hat{z} - G\hat{b}$ is the least-squares residual vector of the float solution $\hat{z}, \hat{b}$ and $\hat{E} = Y - A\hat{Z} - G\hat{B}$ is the least-squares residual matrix in which $\hat{Z}$ and $\hat{B}$ are the least-squares estimators of Z and B, respectively, without taking the integer and baseline length constraints into account.

The ambiguity-constrained baseline solution with associated variance-covariance matrix is given as:

$$\begin{aligned}
&\begin{bmatrix} vec(\hat{B}^1(Z^1,z^{12}) - B^1) \\ \hat{b}^{12}(Z^1,z^{12}) - b^{12} \end{bmatrix} = \\
&= \begin{bmatrix} vec(\hat{B}^1) \\ \hat{b}^{12} \end{bmatrix} - (P_{N^1+1}\otimes Q_{\hat{b}\hat{z}})(P_{N^1+1}\otimes Q_{\hat{z}\hat{z}})^{-1} \begin{bmatrix} vec(\hat{Z}^1 - Z^1) \\ \hat{z}^{12} - z^{12} \end{bmatrix} \\
&= \begin{bmatrix} vec(\hat{B}^1) \\ \hat{b}^{12} \end{bmatrix} - I_{N^1+1}\otimes Q_{\hat{b}\hat{z}}Q_{\hat{z}\hat{z}}^{-1} \begin{bmatrix} vec(\hat{Z}^1 - Z^1) \\ \hat{z}^{12} - z^{12} \end{bmatrix} \\
&= \begin{bmatrix} vec(\hat{B}^1(Z^1) - B^1) \\ \hat{b}^{12}(z^{12}) - b^{12} \end{bmatrix} \\
&D\begin{bmatrix} vec(\hat{B}^1(Z^1,z^{12}) - B^1) \\ \hat{b}^{12}(Z^1,z^{12}) - b^{12} \end{bmatrix} = P_{N^1+1}\otimes Q_{\hat{b}(z)\hat{b}(z)}
\end{aligned} \tag{5.44}$$

As was demonstrated in section 5.2.2 and (Buist et al., 2008)(Buist et al., 2009b) for the triple and quadruple antenna configuration, it follows that each conditional baseline depends only on its own ambiguity vector, thus knowledge about z_i^1 does not contribute directly to the subsequent conditional baseline estimates $\hat{b}_{i+1}^1(z_{i+1}^1)$ and $\hat{b}^{12}(z^{12})$. Therefore the last term of Eq. (5.54) is equal to $\left\| \begin{matrix} vec(\hat{B}^1(Z^1) - B^1) \\ \hat{b}^{12}(z^{12}) - b^{12} \end{matrix} \right\|^2_{P_{N^1+1} \otimes Q_{\hat{b}(z)\hat{b}(z)}}$ and can be decomposed as:

$$\begin{aligned} \left\| \begin{matrix} vec(\hat{B}^1(Z^1) - B^1) \\ \hat{b}^{12}(z^{12}) - b^{12} \end{matrix} \right\|^2_{P_{N^1+1} \otimes Q_{\hat{b}(z)\hat{b}(z)}} &= \left\| \hat{b}_1^1(z_1^1) - b_1^1 \right\|^2_{Q_{\hat{b}(z)\hat{b}(z)}} + \\ + \sum_{i=2}^{N^1} \left\| \hat{b}_i^1(z_i^1, b_I^1) - b_i^1 \right\|^2_{X_i^1 Q_{\hat{b}(z)\hat{b}(z)}} &+ \left\| \hat{b}^{12}(z^{12}, b_{N^1}^1, \ldots, b_1^1) - b^{12} \right\|^2_{X_{N^1+1}^1 Q_{\hat{b}(z)\hat{b}(z)}} \end{aligned} \tag{5.45}$$

with $\hat{b}_i^1(z_i^1, b_I^1)$ is the ith baseline conditioned on the ambiguity z_i and the previous baselines $b_I^1 = \cup_{j=1}^{i-1} b_j^1$.

As explained in Appendix C.1 and using the relations found, the scaling factor X for the v-c matrix for the i-th baseline can be written as:

$$\begin{aligned} X_1^1 &= 1 \\ X_i^1 &= \frac{i+2}{2(i+1)}, \quad i = 2, \ldots, N^1 + 1 \end{aligned} \tag{5.46}$$

It is observed that the scaling factor for the ith baseline can be calculated directly, i.e. it is not necessary to do this sequentially.
The optimal solution becomes for this N^1 constrained and one unconstrained baseline configuration:

$$\begin{aligned} \begin{bmatrix} vec(\check{Z}^1) \\ \check{z}^{12} \end{bmatrix} = \arg \min_{z \in \mathbb{Z}^{n \times (N^1+1)}} \Bigg(& \left\| \hat{z}_1^1 - z_1^1 \right\|^2_{Q_{\hat{z}\hat{z}}} + \left\| \hat{b}_1^1(z_1^1) - \check{b}_1^1(z_1^1) \right\|^2_{Q_{\hat{b}(z)\hat{b}(z)}} + \\ + \sum_{i=2}^{N^1} \Bigg(& \left\| \hat{z}_i^1(z_I^1) - z_i^1 \right\|^2_{X_i^1 Q_{\hat{z}\hat{z}}} + \left\| \hat{b}_i^1(z_i^1, b_I^1) - \check{b}_i^1(z_i^1, b_I^1) \right\|^2_{X_i^1 Q_{\hat{b}(z)\hat{b}(z)}} \Bigg) + \\ & + \left\| \hat{z}^{12}(z_{N^1}^1, \ldots, z_1^1) - z^{12} \right\|^2_{X_{N^1+1}^1 Q_{\hat{z}\hat{z}}} \Bigg) \end{aligned} \tag{5.47}$$

for which $z_I^1 = \cup_{j=1}^{i-1} z_j^1$ and

$$\left\|\hat{b}_1^1(z_1^1) - \check{b}_1^1(z_1^1)\right\|^2_{Q_{\hat{b}(z)\hat{b}(z)}} + \sum_{i=2}^{N^1} \left\|\hat{b}_i^1(z_i^1, b_I^1) - \check{b}_i^1(z_i^1, b_I^1)\right\|^2_{X_i^1 Q_{\hat{b}(z)\hat{b}(z)}} =$$
$$\min_{\substack{b_j^1 \in \mathbb{R}^3, \\ ||b_j^1|| = l_j^1 \\ j=1,\ldots,N^1}} \left(\left\|\hat{b}_1^1(z_1^1) - b_1^1\right\|^2_{Q_{\hat{b}(z)\hat{b}(z)}} + \sum_{i=2}^{N^1} \left\|\hat{b}_i^1(z_i^1, b_I^1) - b_i^1\right\|^2_{X_i^1 Q_{\hat{b}(z)\hat{b}(z)}} \right)$$

An approximation of the optimal solution can be obtained again by solving the baselines sequentially where the solution of baseline i is applied on the next, as if the correlation between baselines would be absent (Buist et al., 2009b). The result is the vectorial bootstrapping approach as developed in section 5.2.4 in which first the ambiguities on the constrained baselines are solved and finally the found ambiguity vector is applied in the solution of the unconstrained baseline. This solution is then given as:

$$\check{z}_1^1 = \arg \min_{z_1^1 \in \mathbb{Z}^n} \left(\|\hat{z}_1^1 - z_1^1\|^2_{Q_{\hat{z}\hat{z}}} + \min_{\substack{b_1^1 \in \mathbb{R}^3, \\ ||b_1^1|| = l_1^1}} \left(\left\|\hat{b}_1^1(z_1) - b_1^1\right\|^2_{Q_{\hat{b}(z)\hat{b}(z)}} \right) \right)$$
$$\check{z}_2^1 = \arg \min_{z_2^1 \in \mathbb{Z}^n} \left(\|\hat{z}_2^1(\check{z}_1^1) - z_2^1\|^2_{\frac{3}{4}Q_{\hat{z}\hat{z}}} + \min_{\substack{b_2^1 \in \mathbb{R}^3, \\ ||b_2^1|| = l_2^1}} \left(\left\|\hat{b}_2^1(z_2^1) - b_2^1\right\|^2_{\frac{3}{4}Q_{\hat{b}(z)\hat{b}(z)}} \right) \right)$$
$$\vdots$$
$$\check{z}_{N^1}^1 = \arg \min_{z_{N^1}^1 \in \mathbb{Z}^n} \left(\|\hat{z}_{N^1}^1(\check{z}_I^1) - z_{N^1}^1\|^2_{X_{N^1}^1 Q_{\hat{z}\hat{z}}} + \min_{\substack{b_{N^1}^1 \in \mathbb{R}^3, \\ ||b_{N^1}^1|| = l_{N^1}^1}} \left(\left\|\hat{b}_{N^1}^1(z_{N^1}^1) - b_{N^1}^1\right\|^2_{X_{N^1}^1 Q_{\hat{b}(z)\hat{b}(z)}} \right) \right)$$
$$\check{z}^{12} = \arg \min_{z^{12} \in \mathbb{Z}^n} \left(\left\|\hat{z}^{12}(\check{z}_{N^1}^1, \ldots, \check{z}_1^1) - z^{12}\right\|^2_{X_{N^1+1}^1 Q_{\hat{z}\hat{z}}} \right)$$

With the constraint on the baseline and the ambiguities, the conditional solution of the baselines becomes:

$$\check{b}_1^1 = \arg \min_{\substack{b_1^1 \in \mathbb{R}^3, \\ ||b_1^1|| = l_1^1}} \left(\left\|\hat{b}_1^1(\check{z}_1) - b_1^1\right\|^2_{Q_{\hat{b}(z)\hat{b}(z)}} \right)$$
$$\check{b}_2^1 = \hat{b}_2^1(\check{z}_2^1, \check{b}_1^1)$$
$$\vdots$$
$$\check{b}_{N^1}^1 = \hat{b}_{N^1}^1(\check{z}_{N^1}^1, \check{b}_I^1)$$
$$\check{b}^{12} = \hat{b}^{12}(\check{z}^{12}, \check{b}_{N^1}^1, \ldots, \check{b}_1^1)$$

For example, the solution of the second constrained baseline conditioned on its ambiguity

Table 5.4: Scaling factor for the v-c matrix as a function of the number of constrained baselines, the grey color indicates cases that will be simulated

$\#C$	1	2	3	4	5	6	7	8	9	10
One side	3/4	2/3	5/8	3/5	7/12	4/7	9/16	5/9	11/20	6/11
$\#C$	2	4	6	8	10	12	14	16	18	20
Two side	1/2	1/3	1/4	1/5	1/6	1/7	1/8	1/9	1/10	1/11

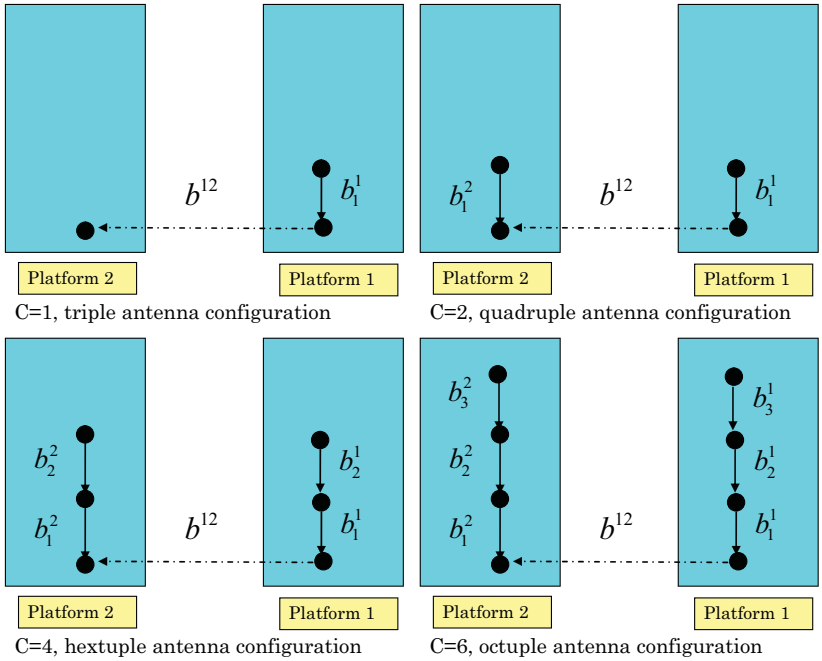


Figure 5.4: Definition of two platforms and C antenna configuration

vector and the previous baseline (follows from Eq. (5.20)):

$$\hat{b}_2^1(\check{z}_2^1, \check{b}_1^1) = \arg \min_{\substack{b_2^1 \in \mathbb{R}^3, \\ ||b_2^1|| = l_2^1}} \left(\left\| \hat{b}_2^1(\check{z}_2^1) - b_2^1 \right\|^2_{Q_{\hat{b}(z)\hat{b}(z)}} \right) + \frac{1}{2}(\hat{b}_1^1 \left(\check{z}_1^1\right) - \check{b}_1^1) \tag{5.48}$$

From Eq. (5.45) and Eq. (5.47), it is clear that the reduction on the dispersion (i.e. the scaling factor X) on the baseline and ambiguity vectors is the same. This relationship is consistent with the scaling factors obtained in section 5.2 and (Buist et al., 2009b).
The first two rows in Table 5.4 shows this scaling factor of $Q_{\hat{z}\hat{z}}$ and $Q_{\hat{b}(z)\hat{b}(z)}$ for a platform with up to 11 antennas (i.e. 10 baselines). For convenience, C is introduced, which indicates the total number of constrained baselines in the configuration (here $C = N^1$ for the case with constrained baselines on only one side of the in-between baseline). As discussed in section 1.1, the three and four antenna configurations are most relevant for our application and therefore the cases $C = 1$, $C = 2$, $C = 4$ and $C = 6$ marked in Table 5.4 are investigated further by simulation in the next section. These cases are shown in Fig. 5.4.

A similar general formula can be derived if the unconstrained baseline between the two platforms is constrained by constrained baselines at both sides (Buist et al., 2009b). Then

this theory can be extended to a general model for a multi-antenna configuration at both platforms with N^1 constrained baselines $b_1^1, \ldots, b_{N^1}^1$ at the first platform, N^2 constrained baselines $b_1^2, \ldots, b_{N^2}^2$ at the other platform and the unconstrained baseline between both platforms defined as b^{12}. The conditional solution can be decomposed as:

$$\begin{aligned}\left\| \begin{matrix} vec(\hat{B}^1(Z^1) - B^1) \\ vec(\hat{B}^2(Z^2) - B^2) \\ \hat{b}^{12}(z^{12}) - b^{12} \end{matrix} \right\|^2_{P \otimes Q_{\hat{b}(z)\hat{b}(z)}} &= \left\| \hat{b}_1^1(z_1^1) - b_1^1 \right\|^2_{Q_{\hat{b}(z)\hat{b}(z)}} + \\ + \sum_{i=2}^{N^1} \left\| \hat{b}_i^1(z_i^1, b_I^1) - b_i^1 \right\|^2_{X_i^1 Q_{\hat{b}(z)\hat{b}(z)}} &+ \left\| \hat{b}_2^2(z_2^2) - b_2^2 \right\|^2_{Q_{\hat{b}(z)\hat{b}(z)}} + \\ + \sum_{i=2}^{N^2} \left\| \hat{b}_i^2(z_i^2, b_I^2) - b_i^2 \right\|^2_{X_i^2 Q_{\hat{b}(z)\hat{b}(z)}} &+ \left\| \hat{b}^{12}(z^{12}, b_{N^1}^1, b_{N^2}^2, \ldots, b_1^1, b_1^2) - b^{12} \right\|^2_{X^{12} Q_{\hat{b}(z)\hat{b}(z)}}\end{aligned} \tag{5.49}$$

As explained in Appendix C.1, the scaling factor X^{12} for an unconstrained baseline connected to N^1 constrained baselines at a platform at one side and N^2 constrained baselines at a platform at the other side can be written as:

$$\begin{aligned} X^{12} &= \frac{N^1 + N^2 + 2}{2(1 + N^1)(1 + N^2)} \\ C &= N^1 + N^2 \end{aligned} \tag{5.50}$$

Again, it is observed that the scaling factor can be calculated directly if the number of constrained baselines at both platforms is known; so it is not necessary to calculate these factors sequentially.
If both platforms have the same number of constrained baselines (i.e. $N^1 = N^2 = N$), the scaling factor for the unconstrained baselines between the two platforms can be calculated as:

$$\begin{aligned} X^{12} &= \frac{1}{1 + N} \\ C &= 2N \end{aligned} \tag{5.51}$$

The last two rows in Table 5.4 shows the scaling factor for the v-c matrices of the ambiguity and baseline vectors for the unconstrained baseline between two platforms each with up to 11 antennas. The relation is shown as function of baseline number at one side or at two sides of the unconstrained baseline in Fig. 5.5. As this figure shows with constraints on one side, the scaling factor approaches $\frac{1}{2}$, and with constraints on both sides this factor will go to a very small value. This means that the improvement is larger with constraints at both sides as the model becomes stronger which is consistent with the conclusions obtained in section 5.2.

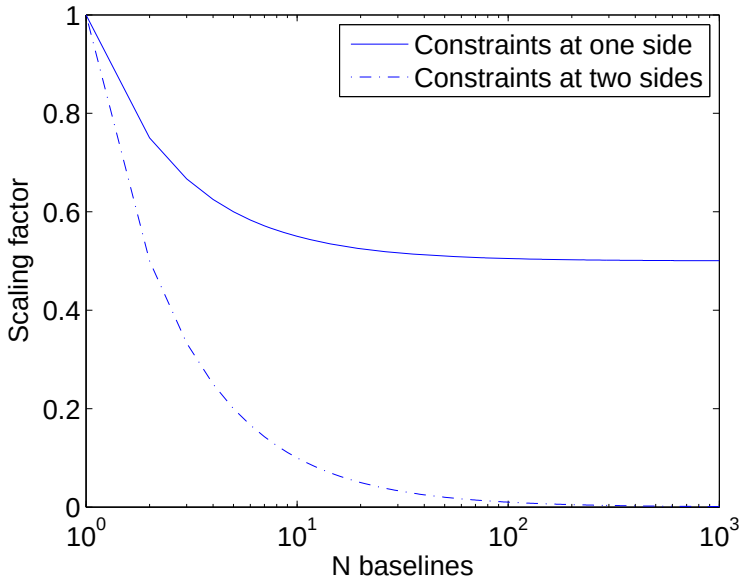


Figure 5.5: Theoretical relationship between number of constrained baselines at one (one side constrained) or both platforms (two sides constrained) and the scaling factor for the V-C matrix

These symmetrical configurations where both platforms have the same number of antennas, namely N, will be discussed further. A general model for a multi-baseline configuration at both platforms, can be written as:

$$\begin{aligned} E\begin{bmatrix} vec(Y^1) \\ vec(Y^2) \\ y^{12} \end{bmatrix} &= \begin{bmatrix} (I_N \otimes A)vec(Z^1) + (I_N \otimes G)vec(B^1) \\ (I_N \otimes A)vec(Z^2) + (I_N \otimes G)vec(B^2) \\ Az^{12} + Gb^{12} \end{bmatrix} \\ D\begin{bmatrix} vec(Y^1) \\ vec(Y^2) \\ y^{12} \end{bmatrix} &= P \otimes Q_{yy} \end{aligned} \tag{5.52}$$

The $(2N+1) \times (2N+1)$ P matrix of this model is no longer a tridiagonal matrix, but the block diagonal matrices P_N inside P describing the individual platforms are tridiagonal:

$$P = \begin{bmatrix} & P_N & & \mathbf{0} & 0 \\ & & & & \vdots \\ & & & & 0 \\ & & & & -\frac{1}{2} \\ & \mathbf{0} & & P_N & 0 \\ & & & & \vdots \\ & & & & 0 \\ & & & & -\frac{1}{2} \\ 0 & \dots & 0 & -\frac{1}{2} \; 0 \; \dots \; 0 & -\frac{1}{2} \; 1 \end{bmatrix}.$$

In this matrix P, a block matrix P_N can be recognized for the first platform and second platform as described in section 4.3.2 and the unconstrained baseline between the platforms. $\mathbf{0}$ is a $N \times N$ matrix with all entries being zero.

In order to estimate the unknown parameters, it is necessary to solve a minimization problem for two platforms with N constrained baselines, and a single unconstrained baseline between platforms. The ambiguity-constrained baseline solution with its associated v-c matrix are given as:

$$\begin{aligned}
&\begin{bmatrix} vec(\hat{B}^1(Z^1,Z^2,z^{12})) \\ vec(\hat{B}^2(Z^1,Z^2,z^{12})) \\ \hat{b}^{12}(Z^1,Z^2,z^{12}) \end{bmatrix} = \\
&= \begin{bmatrix} vec(\hat{B}^1) \\ vec(\hat{B}^2) \\ \hat{b}^{12} \end{bmatrix} - (P \otimes Q_{\hat{b}(z)\hat{b}(z)})(P \otimes Q_{\hat{z}\hat{z}})^{-1} \begin{bmatrix} vec(\hat{Z}^1 - Z^1) \\ vec(\hat{Z}^2 - Z^2) \\ \hat{z}^{12} - z^{12} \end{bmatrix} \\
&= \begin{bmatrix} vec(\hat{B}^1) \\ vec(\hat{B}^2) \\ \hat{b}^{12} \end{bmatrix} - I_{2N+1} \otimes Q_{\hat{b}(z)\hat{b}(z)} Q_{\hat{z}\hat{z}}^{-1} \begin{bmatrix} vec(\hat{Z}^1 - Z^1) \\ vec(\hat{Z}^2 - Z^2) \\ \hat{z}^{12} - z^{12} \end{bmatrix} \qquad (5.53) \\
&= \begin{bmatrix} vec(\hat{B}^1(Z^1) \\ vec(\hat{B}^2(Z^2)) \\ \hat{b}^{12}(z^{12}) \end{bmatrix} \\
&D \begin{bmatrix} vec(\hat{B}^1(Z^1,Z^2,z^{12})) \\ vec(\hat{B}^2(Z^1,Z^2,z^{12})) \\ \hat{b}^{12}(Z^1,Z^2,z^{12}) \end{bmatrix} = P \otimes Q_{\hat{b}(z)\hat{b}(z)}
\end{aligned}$$

Then the following minimization problem is obtained:

$$\begin{aligned}
&\min_{\substack{\left[Z^1,Z^2,z^{12}\right]\in\mathbb{Z}^{n\times(2N+1)} \\ \left[B^1,B^2,b^{12}\right]\in\mathbb{R}^{3\times(2N+1)} \\ ||b_j^1||=l_j^1, ||b_j^2||=l_j^2 \\ j=1,\ldots,N}} \left\| \begin{matrix} vec(Y^1) - (I_N \otimes A)vec(Z^1) - (I_N \otimes G)vec(B^1) \\ vec(Y^2) - (I_N \otimes A)vec(Z^2) - (I_N \otimes G)vec(B^2) \\ y^{12} - Az^{12} - Bb^{12} \end{matrix} \right\|_{P\otimes Q_{yy}}^2 = \\
&\qquad \left\| \begin{matrix} vec(\hat{E}^1) \\ vec(\hat{E}^2) \\ \hat{e}^{12} \end{matrix} \right\|_{P\otimes Q_{yy}}^2 + \min_{\substack{\left[Z^1,Z^2,z^{12}\right]\in\mathbb{Z}^{n\times(2N+1)} \\ \left[B^1,B^2,b^{12}\right]\in\mathbb{R}^{3\times(2N+1)} \\ ||b_j^1||=l_j^1, ||b_j^2||=l_j^2 \\ j=1,\ldots,N}} \left(\left\| \begin{matrix} vec(\hat{Z}^1 - Z^1) \\ vec(\hat{Z}^2 - Z^2) \\ \hat{z}^{12} - z^{12} \end{matrix} \right\|_{P\otimes Q_{\hat{z}\hat{z}}}^2 + \right. \\
&\qquad \left. + \left\| \begin{matrix} vec(\hat{B}^1(Z^1) - B^1) \\ vec(\hat{B}^2(Z^2) - B^2) \\ \hat{b}^{12}(z^{12}) - b^{12} \end{matrix} \right\|_{P\otimes Q_{\hat{b}(z)\hat{b}(z)}}^2 \right)
\end{aligned} \qquad (5.54)$$

where $\hat{e} = y - A\hat{z} - B\hat{b}$ is the least-squares residual of the float solution $\hat{z}, \hat{b}$ and $\hat{E} = Y - A\hat{Z} - G\hat{B}$ is the least-squares residual matrix in which $\hat{Z}$ and $\hat{B}$ are the least-squares estimators of Z and B respectively without taking the integer and baseline length constraints into account.

The last term in Eq. (5.54) can be decomposed using $V(B) = \left\|\hat{b}_1(z_1) - b_1\right\|^2_{Q_{\hat{b}(z)\hat{b}(z)}} + \sum_{i=2}^{N} \left\|\hat{b}_i(z_i, b_I) - b_i\right\|^2_{X_i Q_{\hat{b}(z)\hat{b}(z)}}$ with $\hat{b}_i(z_i, b_I)$ is the ith baseline conditioned on the ambiguity z_i and the previous baselines $b_I = \cup_{j=1}^{i-1} b_j$:

$$\left\| \begin{matrix} vec(\hat{B}^1(Z^1) - B^1) \\ vec(\hat{B}^2(Z^2) - B^2) \\ \hat{b}^{12}(z^{12}) - b^{12} \end{matrix} \right\|^2_{P \otimes Q_{\hat{b}(z)\hat{b}(z)}} = V(B^1) + V(B^2) + \left\|\hat{b}^{12}(z^{12}, B^1, B^2) - b^{12}\right\|^2_{X^{12} Q_{\hat{b}(z)\hat{b}(z)}} \tag{5.55}$$

X is a scaling factor for the v-c matrix. It is easy to see that for $N^1 = N^2 = N$, Eq. (5.49) becomes Eq. (5.55). The integer least-squares solution becomes for this $2N$ constrained and one unconstrained baseline configuration:

$$\begin{bmatrix} vec(\check{Z}^1) \\ vec(\check{Z}^2) \\ \check{z}^{12} \end{bmatrix} = \arg \min_{[Z^1, Z^2, z^{12}] \in \mathbb{Z}^{n \times (2N+1)}} \left(W(Z^1) + W(Z^2) + \left\|\hat{z}^{12}(Z^1, Z^2) - z^{12}\right\|^2_{X^{12} Q_{\hat{z}\hat{z}}} \right) \tag{5.56}$$

for which

$$W(Z) = \left\|\hat{z}_1 - z_1\right\|^2_{Q_{\hat{z}\hat{z}}} + \left\|\hat{b}_1(z_1) - \check{b}_1(z_1)\right\|^2_{Q_{\hat{b}(z)\hat{b}(z)}} + \\ + \sum_{i=2}^{N} \left(\left\|\hat{z}_i(z_I) - z_i\right\|^2_{X_i Q_{\hat{z}\hat{z}}} + \left\|\hat{b}_i(z_i, b_I) - \check{b}_i(z_i, b_I)\right\|^2_{X_i Q_{\hat{b}(z)\hat{b}(z)}} \right)$$

where $z_I = \cup_{j=1}^{i-1} z_j$.

From Eq. (5.49) and Eq. (5.56) it is clear that the reduction on the dispersion (i.e. the scaling factor) on the baseline and ambiguity vectors is the same. For the cases considered in this research, the scaling factor is shown in Table 5.4. This is an important result as the probability of obtaining the correct integer value in ambiguity resolution increases as the precision of $\hat{z}$ improves.

An approximation of the optimal solution can be obtained by solving the baselines sequentially where the solution of baseline i is applied on the next. The result is the suboptimal solution or vectorial bootstrapping approach in section 5.2.4 in which the ambiguity vectors on the constrained baselines are first solved sequentially and finally the found ambiguity

vectors are applied in the solution of the unconstrained baseline. This solution is given as:

$$
\begin{aligned}
\check{z}_1^1 &= \arg\min_{z_1^1\in\mathbb{Z}^n}\left(\|\hat{z}_1^1 - z_1^1\|^2_{Q_{\hat{z}\hat{z}}} + \min_{\substack{b_1^1\in\mathbb{R}^3,\\ ||b_1^1||=l_1^1}}\left(\left\|\hat{b}_1^1(z_1) - b_1^1\right\|^2_{Q_{\hat{b}(z)\hat{b}(z)}}\right)\right)\\
\check{z}_2^1 &= \arg\min_{z_2^1\in\mathbb{Z}^n}\left(\|\hat{z}_2^1(\check{z}_1^1) - z_2^1\|^2_{\frac{3}{4}Q_{\hat{z}\hat{z}}} + \min_{\substack{b_2^1\in\mathbb{R}^3,\\ ||b_2^1||=l_2^1}}\left(\left\|\hat{b}_2^1(z_2^1) - b_2^1\right\|^2_{\frac{3}{4}Q_{\hat{b}(z)\hat{b}(z)}}\right)\right)\\
&\vdots\\
\check{z}_N^1 &= \arg\min_{z_N^1\in\mathbb{Z}^n}\left(\|\hat{z}_N^1(\check{z}_I^1) - z_N^1\|^2_{X_N^1 Q_{\hat{z}\hat{z}}} + \min_{\substack{b_N^1\in\mathbb{R}^3,\\ ||b_N^1||=l_N^1}}\left(\left\|\hat{b}_N^1(z_N^1) - b_N^1\right\|^2_{X_N Q_{\hat{b}(z)\hat{b}(z)}}\right)\right)\\
\check{z}_1^2 &= \arg\min_{z_1^2\in\mathbb{Z}^n}\left(\|\hat{z}_1^2 - z_1^2\|^2_{Q_{\hat{z}\hat{z}}} + \min_{\substack{b_1^2\in\mathbb{R}^3,\\ ||b_1^2||=l_1^2}}\left(\left\|\hat{b}_1^2(z_1) - b_1^2\right\|^2_{Q_{\hat{b}(z)\hat{b}(z)}}\right)\right)\\
\check{z}_2^2 &= \arg\min_{z_2^2\in\mathbb{Z}^n}\left(\|\hat{z}_2^2(\check{z}_1^2) - z_2^2\|^2_{\frac{3}{4}Q_{\hat{z}\hat{z}}} + \min_{\substack{b_2^2\in\mathbb{R}^3,\\ ||b_2^2||=l_2^2}}\left(\left\|\hat{b}_2^2(z_2^2) - b_2^2\right\|^2_{\frac{3}{4}Q_{\hat{b}(z)\hat{b}(z)}}\right)\right)\\
&\vdots\\
\check{z}_N^2 &= \arg\min_{z_N^2\in\mathbb{Z}^n}\left(\|\hat{z}_N^2(\check{z}_I^2) - z_N^2\|^2_{X_N^2 Q_{\hat{z}\hat{z}}} + \min_{\substack{b_N^2\in\mathbb{R}^3,\\ ||b_N^2||=l_N^2}}\left(\left\|\hat{b}_N^2(z_N^2) - b_N^2\right\|^2_{X_N Q_{\hat{b}(z)\hat{b}(z)}}\right)\right)\\
\check{z}^{12} &= \arg\min_{z^{12}\in\mathbb{Z}^n}\left(\left\|\hat{z}^{12}(z_N^1,\ldots,z_1^1,z_N^2,\ldots,z_1^2) - z^{12}\right\|^2_{X^{12}Q_{\hat{z}\hat{z}}}\right)
\end{aligned}
\tag{5.57}
$$

With the constraint on the baseline and the ambiguities, the conditional solution of the

baselines becomes:

$$
\begin{aligned}
\check{b}_1^1 &= \arg \min_{\substack{b_1^1 \in \mathbb{R}^3, \\ ||b_1^1|| = l_1^1}} \left(\left\| \hat{b}_1^1(\check{z}_1^1) - b_1^1 \right\|^2_{Q_{\hat{b}(z)\hat{b}(z)}} \right) \\
\check{b}_2^1 &= \hat{b}_2^1(\check{z}_2^1, \check{b}_1^1) \\
&\vdots \\
\check{b}_N^1 &= \hat{b}_N^1(\check{z}_N^1, \check{b}_I^1) \\
\check{b}_1^2 &= \arg \min_{\substack{b_1^2 \in \mathbb{R}^3, \\ ||b_1^2|| = l_1^2}} \left(\left\| \hat{b}_1^2(\check{z}_1^2) - b_1^2 \right\|^2_{Q_{\hat{b}(z)\hat{b}(z)}} \right) \\
\check{b}_2^2 &= \hat{b}_2^2(\check{z}_2^2, \check{b}_1^2) \\
&\vdots \\
\check{b}_N^2 &= \hat{b}_N^2(\check{z}_N^2, \check{b}_I^2) \\
\check{b}^{12} &= \hat{b}^{12}(\check{z}^{12}, \check{b}_N^1, \ldots, \check{b}_1^2, \check{b}_N^2, \ldots, \check{b}_1^2)
\end{aligned}
$$

where, for example, the solution of the second constrained baseline conditioned on its ambiguity vector and the previous baseline (Eq. (5.20) in section 5.2.3.1) becomes:

$$
\hat{b}_2^1(\check{z}_2^1, \check{b}_1^1) = \arg \min_{\substack{b_2^1 \in \mathbb{R}^3, \\ ||b_2^1|| = l_2^1}} \left(\left\| \hat{b}_2^1(\check{z}_2^1) - b_2^1 \right\|^2_{Q_{\hat{b}(z)\hat{b}(z)}} \right) + \frac{1}{2}(\hat{b}_1^1 \left(\check{z}_1^1 \right) - \check{b}_1^1) \tag{5.58}
$$

This approach is visualized in Fig. 5.4. It is noted again that not all available information is applied, namely the relative geometry of the constrained baselines at the platforms. In the next section, a solution in which this information is utilized will be introduced.

5.3.3 MC-LAMBDA bootstrapped relative positioning

As a last step, the obtained solution from MC-LAMBDA at each platform is applied for an ambiguity constrained solution on the unconstrained baseline between the platforms. In this way the solution for the unconstrained baseline is bootstrapped from the MC-LAMBDA's solutions of each platform and therefore this method is called: multivariate bootstrapped relative positioning (Buist et al., 2010c). The applied baseline definition is visualized in Fig. 5.6 using the regular definition for attitude applications with a common antenna for all baselines at the same platform.

The model described in Eq. (4.37) for a single platform can be applied for both platforms and for the in-between baseline Eq. (5.5.1):

$$
\begin{aligned}
vec(Y^1) &= (I_N \otimes A)vec(Z^1) + (F^T \otimes G)vec(R^1) \\
vec(Y^2) &= (I_N \otimes A)vec(Z^2) + (F^T \otimes G)vec(R^2) \\
y^{12} &= Az^{12} + Gb^{12}
\end{aligned} \tag{5.59}
$$

$$D \begin{bmatrix} vec(Y^1) \\ vec(Y^2) \\ y^{12} \end{bmatrix} = P \otimes Q_{yy} \tag{5.60}$$

with the proper v-c matrix as derived in Eq. (4.31):

$$P = \begin{bmatrix} P_N & 0 & \frac{1}{2}e_N \\ 0 & P_N & -\frac{1}{2}e_N \\ \frac{1}{2}e_N^T & -\frac{1}{2}e_N^T & 1 \end{bmatrix} \tag{5.61}$$

where e_N is a column vector with dimension N with all elements equal to one. The difference in sign for the entries of e_N is due to the definition of the baselines at and between the two platforms (see difference in direction in Fig. 5.6). The assumption is made that all antennas track the same satellites (the number of observations and ambiguities are the same: $n^1 = n^2 = n$), and the baseline configurations on the platforms are the same (the number of baselines: $N^1 = N^2 = N$, the body frame vectors: $F^1 = F^2 = F$, thus $q^1 = q^2 = q$).

Following the same approach as applied to obtain Eq. (5.54), the minimization problem to be solved is

$$\min_{\substack{[Z^1,Z^2,z^{12}]\in\mathbb{Z}^{n\times(2N+1)} \\ R^1\in\mathbb{O}^{3\times q},R^2\in\mathbb{O}^{3\times q},b^{12}\in\mathbb{R}^3}} \left(\left\| \begin{matrix} vec(\hat{Z}^1 - Z^1) \\ vec(\hat{Z}^2 - Z^2) \\ \hat{z}^{12} - z^{12} \end{matrix} \right\|^2_{P\otimes Q_{\hat{z}\hat{z}}} + \left\| \begin{matrix} vec(\hat{R}^1(Z^1) - R^1) \\ vec(\hat{R}^2(Z^2) - R^2) \\ \hat{b}^{12}(z^{12}) - b^{12} \end{matrix} \right\|^2_{P\otimes Q_{\hat{R}(z)\hat{R}(z)}} \right) \tag{5.62}$$

To decouple the parameters at both platforms, the ambiguities are multiplied with the following matrix:

$$S_1 = \begin{bmatrix} I_N & 0 & 0 \\ 0 & I_N & 0 \\ -e_N^T P_N^{-1} & e_N^T P_N^{-1} & 1 \end{bmatrix} \otimes I_n \tag{5.63}$$

resulting in

$$\begin{bmatrix} vec(\mathrm{Z}^1) \\ vec(\mathrm{Z}^2) \\ \mathrm{z}^{12} \end{bmatrix} = S_1 \begin{bmatrix} vec(Z^1) \\ vec(Z^2) \\ z^{12} \end{bmatrix} = \begin{bmatrix} vec(Z^1) \\ vec(Z^2) \\ z^{12} - (\frac{1}{2}e_N^T P_N^{-1} \otimes I_n)vec(Z^1) + (\frac{1}{2}e_N^T P_N^{-1} \otimes I_n)vec(Z^2) \end{bmatrix}$$
$$= \begin{bmatrix} vec(Z^1) \\ vec(Z^2) \\ z^{12} - (\frac{e_N^T}{N+1} \otimes I_n)vec(Z^1) + (\frac{e_N^T}{N+1} \otimes I_n)vec(Z^2) \end{bmatrix}$$

(5.64)

The ambiguities Z_1 and Z_2 at the platform will remain unchanged by the transformation ($\mathrm{Z}_1 = Z_1$ and $\mathrm{Z}_2 = Z_2$), however the in-between ambiguity vector $\hat{\mathrm{z}}^{12}$ becomes a linear combination of the original in-between ambiguities $\hat{z}^{12}$ and the ambiguity matrices Z_1 and Z_2.

The v-c matrix of the decorrelated float ambiguities is then:

$$Q_{\hat{\mathrm{Z}}\hat{\mathrm{Z}}} = S_1 Q_{\hat{Z}\hat{Z}} S_1^T = \begin{bmatrix} Q_{\hat{\mathrm{Z}}^1\hat{\mathrm{Z}}^1} & 0 & 0 \\ 0 & Q_{\hat{\mathrm{Z}}^2\hat{\mathrm{Z}}^2} & 0 \\ 0 & 0 & Q_{\hat{\mathrm{z}}^{12}\hat{\mathrm{z}}^{12}} \end{bmatrix} \tag{5.65}$$

The conditional solution, as described by the right hand side of Eq. (5.62), can also be decorrelated through a transformation matrix:

$$S_2 = \begin{bmatrix} I_q & 0 & 0 \\ 0 & I_q & 0 \\ -e_N^T F^T & e_N^T F^T & 1 \end{bmatrix} \otimes I_3 \tag{5.66}$$

resulting in:

$$\begin{aligned} \begin{bmatrix} vec(\hat{\mathrm{R}}^1(Z^1)) \\ vec(\hat{\mathrm{R}}^2(Z^2)) \\ \hat{\mathrm{b}}^{12}(z^{12}) \end{bmatrix} &= S_2 \begin{bmatrix} vec(\hat{R}^1(Z^1)) \\ vec(\hat{R}^2(Z^2)) \\ b^{12} \end{bmatrix} \\ &= S_2 \begin{bmatrix} vec(\hat{R}^1) \\ vec(\hat{R}^2) \\ b^{12} \end{bmatrix} - S_2 Q_{\hat{R}\hat{Z}} Q_{\hat{Z}\hat{Z}} \begin{bmatrix} vec(\hat{Z}^1 - Z^1) \\ vec(\hat{Z}^2 - Z^2) \\ \hat{z}^{12} - z^{12} \end{bmatrix} \\ &= \begin{bmatrix} vec(\hat{R}_1(Z^1)) \\ vec(\hat{R}_1(Z^2)) \\ S_2 b^{12} - (G^T Q_{yy}^{-1} G)^{-1} G^T Q_{yy}^{-1} A(\hat{z}^{12} - z^{12}) \end{bmatrix} \end{aligned} \tag{5.67}$$

The v-c matrix of the corresponding decorrelated conditional solution is then:

$$Q_{\hat{\mathrm{R}}(\mathrm{Z})\hat{\mathrm{R}}(\mathrm{Z})} = S_2 Q_{\hat{R}(Z)\hat{R}(Z)} S_2^T = \begin{bmatrix} Q_{\hat{\mathrm{R}}^1(\mathrm{Z}^1)\hat{\mathrm{R}}^1(\mathrm{Z}^1)} & 0 & 0 \\ 0 & Q_{\hat{\mathrm{R}}^2(\mathrm{Z}^2)\hat{\mathrm{R}}^2(\mathrm{Z}^2)} & 0 \\ 0 & 0 & \frac{1}{1+N}[G^T Q_{yy}^{-1} G]^{-1} \end{bmatrix} \tag{5.68}$$

For the unconstrained baseline between the platforms, it is observed that the precision is the scaling factor Eq. (5.50) with respect to the precision that one would obtain by processing these baselines independently (Eq. (3.50)).

The transformation S_1 described by Eq. (5.63) can be applied on the dispersion matrix, Eq. (5.60), if the proper dimensions are taken into account,

$$S_3 = S_1 \otimes I_n = \begin{bmatrix} I_N & 0 & 0 \\ 0 & I_N & 0 \\ -e_N^T P_N^{-1} & e_N^T P_N^{-1} & 1 \end{bmatrix} \otimes I_{2n} \tag{5.69}$$

and by defining

$$\begin{aligned} \mathrm{y}^{12} &= y^{12} + (\frac{1}{2} e_N^T P_N^{-1} \otimes I_{2n}) vec(Y^2 - Y^1) \\ \mathrm{z}^{12} &= z^{12} + (\frac{1}{2} e_N^T P_N^{-1} \otimes I_{2n}) vec(Z^2 - Z^1) \\ \mathrm{b}^{12} &= b^{12} + (\frac{1}{2} e_N^T P_N^{-1} F \otimes I_3) vec(R^2 - R^1) \end{aligned} \tag{5.70}$$

the following decorrelated model is obtained

$$\begin{aligned} vec(Y^1) &= (I_N \otimes A) vec(Z^1) + (F \otimes G) vec(R^1) \\ vec(Y^2) &= (I_N \otimes A) vec(Z^2) + (F \otimes G) vec(R^2) \\ \mathrm{y}^{12} &= A\mathrm{z}^{12} + G\mathrm{b}^{12} \end{aligned} \tag{5.71}$$

with

$$D \begin{bmatrix} vec(Y^1) \\ vec(Y^2) \\ \mathrm{y}^{12} \end{bmatrix} = \begin{bmatrix} P_N & 0 & 0 \\ 0 & P_N & 0 \\ 0 & 0 & \frac{1}{N+1} \end{bmatrix} \otimes Q_{yy} \tag{5.72}$$

The result is that the observables at the two platforms and the in-between baseline are uncorrelated.

And as there is no correlation between the platforms we obtain the following solution:

$$\begin{aligned} vec(\check{Z}^1) = \arg \min_{Z^1 \in \mathbb{Z}^{n \times N}} \Big(& \left\| vec(\hat{Z}^1 - Z^1) \right\|^2_{Q_{\hat{Z}\hat{Z}}} + \\ & + \min_{R^1 \in \mathbb{O}^{3 \times q}} \left\| vec(\hat{R}^1(Z^1) - R^1(Z^1)) \right\|_{Q^2_{\hat{R}(Z)\hat{R}(Z)}} \Big) \\ vec(\check{Z}^2) = \arg \min_{Z^2 \in \mathbb{Z}^{n \times N}} \Big(& \left\| vec(\hat{Z}^2 - Z^2) \right\|^2_{Q_{\hat{Z}\hat{Z}}} + \\ & + \min_{R^2 \in \mathbb{O}^{3 \times q}} \left\| vec(\hat{R}^2(Z^2) - R^2(Z^2)) \right\|^2_{Q_{\hat{R}(Z)\hat{R}(Z)}} \Big) \\ \check{z}^{12} = \arg \min_{z^{12} \in \mathbb{Z}^n} \Big(& \left\| \hat{z}^{12}(Z^1, Z^2) - z^{12} \right\|^2_{X^{12} Q_{\hat{z}\hat{z}}} \Big) \end{aligned} \tag{5.73}$$

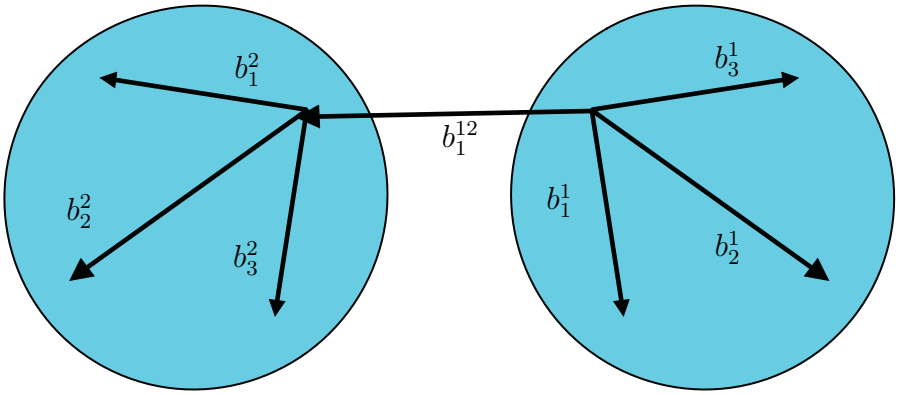


Figure 5.6: Multi-platform using attitude definition for baselines

The solution $\check{z}^{12}$ for the unconstrained baseline is the same as in Eq. (5.57) as $Z^1 = [z_N^1, \ldots, z_1^1]$ and $Z^2 = [z_N^2, \ldots, z_1^2]$. It is important to note that the scaling function of the v-c matrix for the unconstrained baseline is the same for the multivariate bootstrapping approach (Eq. (5.73)) as the vectorial bootstrapping approach (Eq. (5.57)). Therefore, as long as all constrained baselines are correctly fixed it is not expected that the success rate on the unconstrained baseline to improve. However, as the multivariate method is a stronger model (i.e. applies information of the relative geometry of the constrained baselines at the platforms), we expect the success rate of this method for the constrained baselines at each platform to be higher and therefore also a better performance on the unconstrained baseline for the weaker models (less observations/higher noise). This is investigated by simulation in section 5.4.

5.3.4 Discussion

The improvement for the precision of the v-c matrix in the multi-antenna configuration obtained mathematically in section 5.3.2 can be explained as follows. The symmetric case of having the same number of antennas $N + 1$ on each of the two platforms is discussed. First, consider a configuration with a single antenna at each platform ($C = 0$) implying no constrained baselines, and one unconstrained baseline between the two platforms. The variance of the conditional baseline estimate is given as $Q_{\hat{b}(z)\hat{b}(z)}$, thus the scaling factor for the v-c matrix of the ambiguity and baseline vectors is then 1.
Then, with two antennas at each platform ($C = 2$) assuming that the baseline lengths between antennas $1 - 2$ at each platform are known and the ambiguity vectors at these baselines can be determined successfully using the C-LAMBDA method, the baselines coordinates for b_1^1 and b_1^2 can be determined very precisely (mm-range). As a consequence, the baseline between the first two antennas at both platforms can be estimated by either differencing between these antennas, or by estimating the baseline between the remaining two antennas at both platforms and then forming the baseline $b_1^{12} = b_2^{12} + b_1^1 - b_1^2$, where $b_1^1 - b_1^2$ is known precisely. Hence the 'same' unconstrained baseline (namely b_1^{12} and b_2^{12} in the left hand side of Fig. 5.7) is observed twice and thus the variance of the baseline estimate is improved by a factor of $1/2$.
This discussion can be extended to a larger number of constrained baselines at each plat-

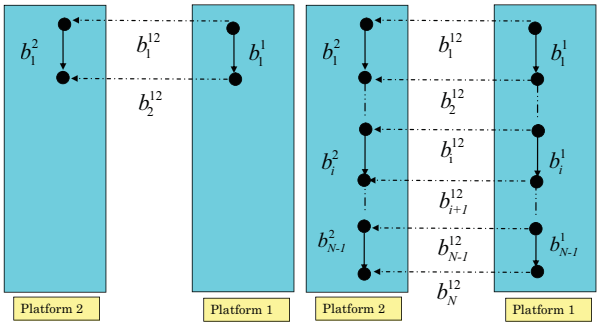


Figure 5.7: Definition of unconstrained baselines for the two platforms with (left) 2 and (right) C constrained baselines

form (right hand side of Fig. 5.7) but also for the non-symmetric case with a different number of antennas at each platform. With more than two baselines on the platform, MC-LAMBDA can be applied resulting in even a stronger model for the constrained baselines. Of course for real applications, even for a very large number of baselines, the scaling factor will not become zero as there are remaining biases and errors not included in our model (e.g. absolute positioning errors, influence of ionosphere and multipath), but the improvement is evident. Another assumption is that we can solve the ambiguities on the constrained baselines with a success rate of close to 100% (a failure rate close to 0%) which seems feasible as was demonstrated in section 4.4, especially if we include the geometry of the antenna placement using the multivariate approach described in 5.3.3.

5.3.5 Multi-frequency, multi-antenna relative positioning

Next, an extension of the integrated approach is derived with multi-frequency observations. We will only consider symmetrical configurations in which both platforms have the same number of baselines, namely N. For a general model of a multi-baseline configuration at both platforms where only the main antennas at each platform are dual frequency, we can write:

$$
\begin{aligned}
E\begin{bmatrix} vec(Y_{L1}^1) \\ vec(Y_{L1}^2) \\ y_{L1}^{12} \\ y_{L2}^{12} \end{bmatrix} &= \begin{bmatrix} (I_N \otimes A_{L1})vec(Z_{L1}^1) + (I_N \otimes G^1)vec(B^1) \\ (I_N \otimes A_{L1})vec(Z_{L1}^2) + (I_N \otimes G^2)vec(B^2) \\ A_{L1}z_{L1}^{12} + G^{12}b^{12} \\ A_{L2}z_{L2}^{12} + G^{12}b^{12} \end{bmatrix} \\
D\begin{bmatrix} vec(Y_{L1}^1) \\ vec(Y_{L1}^2) \\ y_{L1}^{12} \\ y_{L2}^{12} \end{bmatrix} &= P \otimes Q_{yy}
\end{aligned}
\tag{5.74}
$$

The $(2N+2) \times (2N+2)$ P matrix contains block diagonal matrices P_N describing the individual platforms:

$$P = \begin{bmatrix} & & & & & & & & 0 & 0 \\ & & P_N & & & & \mathbf{0} & & \vdots & \vdots \\ & & & & & & & & 0 & 0 \\ & & & & & & & & -\frac{1}{2} & 0 \\ & & & & & & & & 0 & 0 \\ & & \mathbf{0} & & & & P_N & & \vdots & \vdots \\ & & & & & & & & 0 & 0 \\ & & & & & & & & -\frac{1}{2} & 0 \\ 0 & \dots & 0 & -\frac{1}{2} & 0 & \dots & 0 & -\frac{1}{2} & P_{L_1L_2} & \\ 0 & \dots & 0 & 0 & 0 & \dots & 0 & 0 & & \end{bmatrix} \tag{5.75}$$

In this matrix P, we can recognize a block P_N for the single frequency observations at the first platform and second platform as described in section 4.3.2 and a block $P_{L_1L_2}$ for the unconstrained baseline with dual frequency observations between the platforms (see section 4.2.1). $\mathbf{0}$ is a $N \times N$ matrix with all entries being zero. The G matrix contains the DD line-of-sight vectors, and in our implementation we use a different G for the first and second platform (G^1 and G^2), and for the baseline in-between the platforms (G^{12}).

The model described in Eq. (4.29) can be applied with the proper v-c matrix as derived in Eq. (4.31):

$$P = \begin{bmatrix} P_N & 0 & \frac{1}{2}e_N & 0 \\ 0 & P_N & -\frac{1}{2}e_N & 0 \\ \frac{1}{2}e_N^T & -\frac{1}{2}e_N^T & 1 & 0 \\ 0 & 0 & 0 & 1 \end{bmatrix} \tag{5.76}$$

Decorrelation as applied in section 5.5.1 gives

$$P = \begin{bmatrix} P_N & 0 & 0 & 0 \\ 0 & P_N & 0 & 0 \\ 0 & 0 & \frac{1}{N+1} & 0 \\ 0 & 0 & 0 & 1 \end{bmatrix} \tag{5.77}$$

For the dual frequency case, assuming the ambiguities of the two platforms known, the ambiguity resolution process for the between-platform ambiguities can be seen as if the phase and code data on the first frequency has an improved precision with a factor $\frac{1}{1+N}$. This is an important result as the probability of obtaining the correct integer value in ambiguity resolution increases as the precision of $\hat{z}$ improves.
If all antennas are of the dual-frequency type, then all the phase and code on the unconstrained baseline can be considered to have an improved precision with the factor $\frac{1}{1+N}$. We will investigate its performance both for single- and dual-frequency observations on the unconstrained baseline by simulation in section 5.4.

5.3.6 Multi-epoch, multi-antenna relative positioning

As was demonstrated by section 5.3.3, there is no correlation between the platforms, so each platform could be solved by Eq. (4.96) in a multi-epoch solution and finally bootstrapping the unconstrained baseline from the ambiguity vector at both platforms:

$$\begin{aligned}
\check{Z}^1 &= \arg\min_{Z^1\in\mathbb{Z}^{n\times m}} \left(\|vec(\hat{Z}^1_{N_e} - Z^1)\|^2_{Q_{\hat{Z}_{N_e}\hat{Z}_{N_e}}} + \sum_{i=1}^{N_e} \|vec(\hat{R}^1_i(Z) - \check{R}^1_i(Z))\|^2_{Q_{\hat{R}_i(Z)\hat{R}_i(Z)}} \right) \\
\check{Z}^2 &= \arg\min_{Z^2\in\mathbb{Z}^{n\times m}} \left(\|vec(\hat{Z}^2_{N_e} - Z^2)\|^2_{Q_{\hat{Z}_{N_e}\hat{Z}_{N_e}}} + \sum_{i=1}^{N_e} \|vec(\hat{R}^2_i(Z) - \check{R}^2_i(Z))\|^2_{Q_{\hat{R}_i(Z)\hat{R}_i(Z)}} \right) \\
\check{z}^{12} &= \arg\min_{z^{12}\in\mathbb{Z}^n} \left(\|vec(\hat{z}^{12}_{N_e}(Z^1, Z^2) - z^{12})\|^2_{X^{12}Q_{\hat{Z}_{N_e}\hat{Z}_{N_e}}} \right)
\end{aligned} \tag{5.78}$$

with

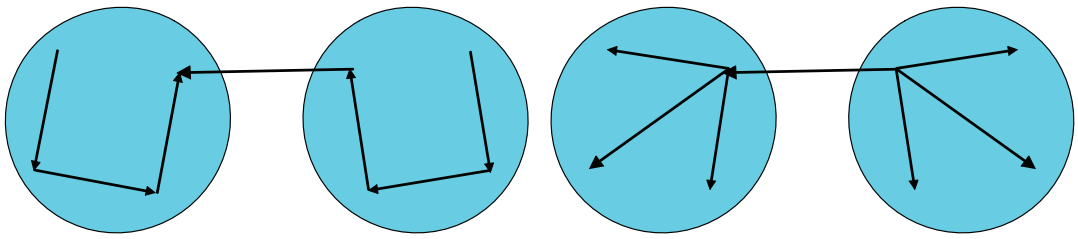
$$\begin{aligned}
\check{R}^1_i(Z^1) &= \arg\min_{R^1_i\in\mathbb{O}^{3\times q}} \left(\|vec(\hat{R}^1_i(Z^1) - R^1_i)\|^2_{Q_{\hat{R}_i(Z)\hat{R}_i(Z)}} \right) \\
\check{R}^2_i(Z^2) &= \arg\min_{R^2_i\in\mathbb{O}^{3\times q}} \left(\|vec(\hat{R}^2_i(Z^2) - R^2_i)\|^2_{Q_{\hat{R}_i(Z)\hat{R}_i(Z)}} \right)
\end{aligned} \tag{5.79}$$

However, as was demonstrated in section 4.5, the constrained baseline solution -especially the MC-LAMBDA method applied on multi-baseline configuration- is often strong enough to apply instantaneously in which case one could opt to solve the constrained baselines epoch-by-epoch, and only solve the unconstrained baseline using multi-epoch data:

$$\begin{aligned}
\check{Z}^1 &= \arg\min_{Z^1\in\mathbb{Z}^{n\times m}} \left(\|vec(\hat{Z}^1 - Z^1)\|^2_{Q_{\hat{Z}^1\hat{Z}^1}} + \|vec(\hat{R}^1(Z^1) - \check{R}^1(Z^1))\|^2_{Q_{\hat{R}^1(Z^1)\hat{R}^1(Z^1)}} \right) \\
\check{Z}^2 &= \arg\min_{Z^2\in\mathbb{Z}^{n\times m}} \left(\|vec(\hat{Z}^2 - Z^2)\|^2_{Q_{\hat{Z}^2\hat{Z}^2}} + \|vec(\hat{R}^2(Z^2) - \check{R}^2(Z^2))\|^2_{Q_{\hat{R}^2(Z^2)\hat{R}^2(Z)^2}} \right) \\
\check{z}^{12} &= \arg\min_{z^{12}\in\mathbb{Z}^n} \left(\|vec(\hat{z}^{12}_{N_e}(Z^1, Z^2) - z^{12})\|^2_{X^{12}Q_{\hat{Z}_{N_e}\hat{Z}_{N_e}}} \right)
\end{aligned} \tag{5.80}$$

with

$$\begin{aligned}
\check{R}^1(Z^1) &= \arg\min_{R^1\in\mathbb{O}^{3\times q}} \left(\|vec(\hat{R}^1(Z^1) - R^1)\|^2_{Q_{\hat{R}^1(Z^1)\hat{R}^1(Z^1)}} \right) \\
\check{R}^2(Z^2) &= \arg\min_{R^2\in\mathbb{O}^{3\times q}} \left(\|vec(\hat{R}^2(Z^2) - R^2)\|^2_{Q_{\hat{R}^2(Z^2)\hat{R}^2(Z^2)}} \right)
\end{aligned} \tag{5.81}$$



(a) Vectorial C-LAMBDA (b) MC-LAMBDA

Figure 5.8: Illustration of a multi-antenna configuration for bootstrapped relative positioning (illustration does not reflect local geometry of antennas)

5.4 Verification by simulation

In this section, the influence of various factors on the ambiguity resolution in the integrated approach is investigated. In sections 5.4.1 and 5.4.2, the geometry is kept constant while the number of GNSS satellites, observation noise and number of baselines at each platform is varied. In section 5.4.3, the influence of the geometry is investigated while the number of baselines at each platform and the observation noise is kept constant.

5.4.1 Multi-platform Ambiguity resolution

In this section, ambiguity resolution will be analyzed by simulation for all the constrained baselines at two platforms for the configurations shown in Fig. 5.8. The simulation conditions are provided in Appendix A.1. The data sets were processed applying the vectorial C-LAMBDA and the MC-LAMBDA methods as described in this chapter. The stochastic model does not apply elevation weighting and -as code and carrier phase noise- the same values as the simulations are used. Again single-epoch, single-frequency success rates are analyzed as the most challenging application. The difference in performance for the approaches for single-epoch solutions is a good indication of the strength of the underlying models. The strength will be important, as in the next step, the obtained solutions for the constrained baselines at each platform will be applied to improve relative positioning between the platforms.
The MC-LAMBDA results are based on independently processing data from two platforms, therefore the presented results are the square of the success rates reported in section 4.4 (the same simulation data is used as input). In this section, simulations are performed with code noises up to 0.9 meter (in section 4.4 up to 0.3 meter) to emphasize the difference in performance between vectorial C-LAMBDA and MC-LAMBDA. As will be shown later, for small noise values the difference in performance will be marginal.
Tables 5.5 and 5.6 show the single-frequency, single-epoch overall success rates for all the constrained baselines at both platforms as a function of the total number of constrained baselines at the two platforms ($\#C$), the number of tracked satellites (N_{SV}) and the undifferenced carrier phase and code noise (σ_ϕ, σ_p). In both tables, three rows for each value of N_{SV} show the overall success rate on a single baseline, on two baselines, and on three baselines, respectively, on two platforms using the C-LAMBDA method. The same results are also included on the right sides of Tables 5.5 and 5.6 for MC-LAMBDA. In the

Table 5.5: Simulation results for σ_ϕ=3 [mm]: Vectorial C-LAMBDA and MC-LAMBDA single-frequency, single-epoch overall success rates for all the constrained baselines at two platforms, $\#C$ is total number of constrained baselines at the two platforms where both have an equal number of antennas

N_{SV}	$\#C$	Vectorial C-LAMBDA						MC-LAMBDA					
		σ_p [cm]						σ_p [cm]					
		90	60	45	30	15	5	90	60	45	30	15	5
5	2	0.14	0.22	0.35	0.50	0.77	0.99	$-\ -\ -\ -$ *Same as Vectorial* $-\ -\ -\ -$					
	4	0.02	0.08	0.16	0.37	0.73	0.99	0.81	0.91	0.94	0.95	0.97	1.00
	6	0.01	0.03	0.08	0.24	0.63	0.99	1.00	1.00	1.00	1.00	1.00	1.00
6	2	0.51	0.67	0.79	0.92	0.98	1.00	$-\ -\ -\ -$ *Same as Vectorial* $-\ -\ -\ -$					
	4	0.25	0.49	0.68	0.88	0.99	1.00	0.96	0.99	1.00	1.00	1.00	1.00
	6	0.15	0.38	0.60	0.84	0.98	1.00	1.00	1.00	1.00	1.00	1.00	1.00
7	2	0.88	0.92	0.95	0.99	1.00	1.00	$-\ -\ -\ -$ *Same as Vectorial* $-\ -\ -\ -$					
	4	0.91	0.95	0.97	0.99	1.00	1.00	1.00					
	6	0.82	0.88	0.93	0.98	1.00	1.00						
8	2	0.95	0.97	0.98	1.00	1.00	1.00	$-\ -\ -\ -$ *Same as Vectorial* $-\ -\ -\ -$					
	4	0.96	0.98	0.99	1.00	1.00	1.00	1.00					
	6	0.91	0.95	0.97	0.99	1.00	1.00						
$\geq$9	2	1.00						1.00					
	4												
	6												

solution using two constrained baselines (i.e. one constrained baseline at each platform), the multivariate constrained solution becomes the same as the vectorial bootstrapped solution and therefore this result is not repeated in the tables.

If baselines would be processed independently, the overall success rate would be equal to the product of the success rates per baseline. Since probabilities are always smaller or equal to one, the overall success rate decreases with increasing number of baselines. Vectorial bootstrapping means that the fixed solution of the previously processed baselines are used for solving the next baseline. If the success rate of the previously fixed baselines is high, this will enhance the overall success rate compared to the case where the baselines are processed independently, but the overall success rate will always be lower than the success rate of the individual baselines.

For MC-LAMBDA, as is reported in section 4.4, it is observed that the overall success rates will always increase if more baselines are included. This is also as expected as this method makes use of a stronger model by including all baselines and their geometry into an optimal solution. The improvement is large especially for the weaker scenarios (lower number of satellites and/or higher levels of noise), where the difference between the methods is significant.

For example, the weakest simulated data set, with five available satellites and high noise values, shows an improvement from 2% for the vectorial C-LAMBDA to 81% for MC-LAMBDA with two constrained baselines. The number of correctly fixed samples for the MC-LAMBDA method with two baselines is always higher than 81% on all the data sets processed, obtaining a 100% success rate on 29 out of 36 data sets simulated. For three baselines per platform the success rate is even 100% for all 36 datasets.

With seven GNSS satellites, the MC-LAMBDA method always achieves a 100% success rate with two or more constrained baselines per platform. For the C-LAMBDA method with two constrained baselines at least nine GNSS satellites are required to achieve the same result.

Table 5.6: Simulation results for σ_ϕ=1 [mm]: Vectorial C-LAMBDA and MC-LAMBDA single-frequency, single-epoch overall success rates for all the constrained baselines at two platforms, $\#C$ is total number of constrained baselines at the two platforms where both have an equal number of antennas

N_{SV}	$\#C$	Vectorial C-LAMBDA						MC-LAMBDA					
		σ_p [cm]						σ_p [cm]					
		90	60	45	30	15	5	90	60	45	30	15	5
5	2	0.54	0.71	0.82	0.93	1.00	1.00	$---- Same\ as\ Vectorial ----$					
	4	0.32	0.59	0.78	0.94	1.00	1.00	1.00					
	6	0.22	0.47	0.68	0.89	1.00	1.00						
6	2	0.99	1.00	1.00	1.00	1.00	1.00	$---- Same\ as\ Vectorial ----$					
	4	0.75	0.88	0.95	0.99	1.00	1.00	1.00					
	6	0.79	0.91	0.97	1.00	1.00	1.00						
≥7	2	1.00						1.00					
	4												
	6												

5.4.2 Bootstrapped Relative Positioning

In this section, the relative positioning result is analyzed by simulation as part of the integrated approach for the antenna configurations in Fig. 5.8. The simulation conditions are provided in Appendix A.1. The stochastic model does not apply elevation weighting and -as code and carrier phase noise- the same values as the simulations are used. The results for the vectorial and Multivariate Constrained methods applied on all the constrained baselines at both platforms were shown in Tables 5.5 and 5.6. For the unconstrained baseline between the platforms, results of the vectorial and multivariate bootstrapping approach are, again for 3 and 1 mm carrier phase noise respectively, included in Tables 5.7 and 5.8. These tables contain empirical success rates as a function of the total number of constrained baselines at the two platforms ($\#C$), the number of tracked satellites (N_{SV}) and the undifferenced carrier phase and code noise (σ_ϕ, σ_p). We will analyze again single-epoch, single-frequency success rates as the difference in performance for the approaches in this most challenging application is a good indication of the strength of the underlying models.
The choice for simulation parameters (i.e. code noise) was made to show the improvement of the integrated method compared to uncoupled. The large code noise simulations are also an indication of the influence of multipath on the approach, as we are analyzing single-epoch solutions. Especially 90 cm is a conservative value for the standard deviation of the code noise that could also include other error sources than thermal noise as for example multipath. The 90 cm for code multipath is especially a valid number for space applications, where the signals can only reflect from the near surroundings (at the vehicle itself) of the GNSS antenna. For multi-epoch (filtered) solutions, the multipath error cannot be considered as Gaussian as there will be time correlation. However, for single-epoch processing this time correlation is not relevant as each epoch is considered independent from the previous and following epochs.

In Tables 5.7 and 5.8, the success rate for the unconstrained baseline between the two platforms is investigated. This unconstrained baseline b^{12} is presented as standalone ($C = 0$) and as part of the combined solution using two constrained baseline ($C = 2$) and using four or six constrained baselines, respectively ($C = 4$ and $C = 6$). In the

solution using two constrained baseline (i.e. one constrained baseline at each platform), the multivariate bootstrapped solution becomes the same as the vectorial bootstrapped solution and therefore this result is not repeated in Tables 5.7 and 5.8.
For the unconstrained baseline in Tables 5.7 and 5.8 on the left side, it is observed that the vectorial bootstrapping approach has a much better performance than standalone LAMBDA. The improvement is between 0 and 34% using two constrained baselines, between 0 and 46% using four constrained baselines, and between 0 and 51% using six constrained baselines with a larger improvement for weaker GNSS models.

For the unconstrained baseline on the right side in Table 5.7, it is observed that the multivariate bootstrapping approach has an even better performance. The improvement is between 0 and 50% using four constrained baselines, and between 0 and 59% using six constrained baselines again with a larger improvement for weaker GNSS models. If both sides of Table 5.7 are compared, it is observed that especially the weaker models are improved by applying the multivariate bootstrapping approach compared to vectorial bootstrapping. The maximum difference in improvement for the multivariate bootstrapping approach compared with the vectorial bootstrapping approach is 16% for the four constrained baselines and 20% for the six constrained baselines.

Another important result is that the availability of a fixed solution for the unconstrained baseline will increase remarkably for both the vectorial and multivariate bootstrapping approaches compared with standalone. Normally only if the lower bound of the success rate is higher than a certain threshold an attempt will be made to fix the ambiguities (see section 3.4.2). In Tables 5.7 and 5.8, the cases are colored grey for which success rate with the standard LAMBDA method is below a threshold of 95%, but those with the integrated approaches are higher than this threshold. It has to be noted that for most applications a success rate of 95% will not be acceptable.
For the standard LAMBDA method at least twelve GNSS satellites are required to achieve a 100% success rate for all cases (Tables 5.7 and 5.8). For the unconstrained baseline between the platforms, if constrained baselines are included in an integrated approach, at least ten GNSS satellites for a success rate of 100% are needed.
The simulation results can also be used in the opposite way: if nine GNSS satellites are locked, at least one constrained baseline at each platform is needed to achieve a success rate of more than 95 % on the unconstrained baseline between the platforms. With eight GNSS satellites, each platform needs three constrained baseline to achieve the same success rate. It has to be noted that the discussed numbers of required baselines are only valid for this particular GNSS satellite geomtry. In section 5.4.3, the influence of the GNSS satellite geometry will be investigated further.
To visualize the performance of the ambiguity resolution in the integrated methods, a logarithmic scale is preferable using the failure rate which is *1 - success rate*. The bootstrapped relative positioning results, now in the form of empirical failure rates, are presented in Fig. 5.9 and 5.10 as a function of the number of tracked satellites (N_{SV}) and the undifferenced carrier phase (σ_ϕ) and code noise (σ_p). Carrier phase noise varies from 3 to 1 mm, code noise between 90, 60, 45, 30, 15 and 5 centimeter. In Fig. 5.10, the threshold for the failure rate of 5% (the success rate of 95%) is indicated with a bold red line.

Table 5.7: Simulation results for σ_ϕ=3 [mm]: Single-frequency, single-epoch success rates for the unconstrained baseline between platforms using standard LAMBDA ($C = 0$), and bootstrapped solution from Vectorial C-LAMBDA and MC-LAMBDA ($C > 0$), $\#C$ is total number of constrained baselines at the two platforms, gray colored cases: success rate with the standard LAMBDA method $\leq 95\%$, the integrated approaches $\geq 95\%$

N_{SV}	$\#C$	Vectorial C-LAMBDA σ_p [cm]						MC-LAMBDA σ_p [cm]					
		90	60	45	30	15	5	90	60	45	30	15	5
5	0	0.00	0.01	0.01	0.03	0.19	0.87	$-\ -\ -\ -$ *Same as Vectorial* $-\ -\ -\ -$					
	2	0.00	0.01	0.02	0.06	0.42	0.98						
	4	0.00	0.01	0.02	0.09	0.51	0.99	0.01	0.03	0.07	0.17	0.62	1.00
	6	0.00	0.01	0.02	0.10	0.56	1.00	0.02	0.05	0.10	0.25	0.74	1.00
6	0	0.02	0.06	0.10	0.25	0.67	0.97	$-\ -\ -\ -$ *Same as Vectorial* $-\ -\ -\ -$					
	2	0.05	0.13	0.25	0.55	0.92	1.00						
	4	0.06	0.18	0.36	0.68	0.97	1.00	0.14	0.30	0.47	0.75	0.98	1.00
	6	0.06	0.21	0.42	0.75	0.98	1.00	0.21	0.41	0.60	0.84	1.00	1.00
7	0	0.10	0.21	0.33	0.50	0.80	1.00	$-\ -\ -\ -$ *Same as Vectorial* $-\ -\ -\ -$					
	2	0.26	0.42	0.55	0.74	0.96	1.00						
	4	0.39	0.55	0.68	0.85	0.99	1.00	0.42	0.58	0.70	0.86	0.99	1.00
	6	0.46	0.62	0.75	0.91	1.00	1.00	0.52	0.67	0.78	0.92	1.00	1.00
8	0	0.44	0.64	0.76	0.86	0.95	1.00	$-\ -\ -\ -$ *Same as Vectorial* $-\ -\ -\ -$					
	2	0.78	0.89	0.94	0.97	0.99	1.00						
	4	0.90	0.96	0.98	0.99	1.00	1.00	0.93	0.98	0.99	0.99	1.00	1.00
	6	0.95	0.97	0.99	1.00	1.00	1.00	0.98	0.99	1.00	1.00	1.00	1.00
9	0	0.75	0.82	0.87	0.90	0.95	1.00	$-\ -\ -\ -$ *Same as Vectorial* $-\ -\ -\ -$					
	2	0.95	0.96	0.96	0.97	0.99	1.00						
	4	0.99	0.99	0.99	0.99	1.00	1.00	1.00					
	6	1.00	1.00	1.00	1.00	1.00	1.00						
10	0	0.95	0.99	0.99	1.00	1.00	1.00	$-\ -\ -\ -$ *Same as Vectorial* $-\ -\ -\ -$					
	2	1.00	1.00	1.00	1.00	1.00	:						
	4	1.00	1.00	1.00	1.00	:							
	6	1.00	1.00	1.00	:								
11	0	0.99	1.00	:				$-\ -\ -\ -$ *Same as Vectorial* $-\ -\ -\ -$					
	2	1.00	:										
	4	:											
	6												
12	0	1.00						$-\ -\ -\ -$ *Same as Vectorial* $-\ -\ -\ -$					
	2												
	4												
	6												

Relationship with developed theory

The probability of obtaining the correct integer value increases as the precision of the float ambiguity estimation ($\hat{z}$) improves. As described in section 5.3.3, the scaling factor for the v-c matrix is the same for both the vectorial and multivariate bootstrapping approaches. Therefore the difference between the bootstrapped solutions in Tables 5.7 and 5.8 has to be explained by the difference in empirical success rate for ambiguity resolution on the constrained baselines at each platform (see section 5.4.1).
The probability of obtaining the correct integer value increases, thus the probability of failure decreases, as the precision of $\hat{z}$ improves. For the unconstrained baseline in the quadruple antenna configuration (case $C = 2$ in Fig. 5.10), a lower failure rate than for the same baseline in the triple antenna configuration ($C = 1$) is observed, which is

Table 5.8: Simulation results for σ_ϕ=1 [mm]: Single-frequency, single-epoch success rates for the unconstrained baseline between platforms using standard LAMBDA ($C = 0$), and bootstrapped solution from vectorial C-LAMBDA and MC-LAMBDA ($C > 0$), $\#C$ is total number of constrained baselines at the two platforms, gray colored cases: success rate with the standard LAMBDA method $\leq 95\%$, the integrated approaches $\geq 95\%$

N_{SV}	$\#C$	Vectorial C-LAMBDA σ_p [cm]						MC-LAMBDA σ_p [cm]					
		90	60	45	30	15	5	90	60	45	30	15	5
5	0	0.00	0.01	0.03	0.07	0.27	0.95	$-\ -\ -\ -$ *Same as Vectorial* $-\ -\ -\ -$					
	2	0.01	0.03	0.06	0.14	0.52	1.00						
	4	0.01	0.04	0.09	0.23	0.69	1.00	0.03	0.06	0.11	0.25	0.69	1.00
	6	0.01	0.05	0.12	0.31	0.79	1.00	0.04	0.09	0.16	0.34	0.79	1.00
6	0	0.09	0.10	0.28	0.49	0.87	1.00	$-\ -\ -\ -$ *Same as Vectorial* $-\ -\ -\ -$					
	2	0.26	0.41	0.54	0.74	0.97	1.00						
	4	0.34	0.52	0.66	0.85	0.99	1.00	0.40	0.57	0.69	0.85	0.99	1.00
	6	0.41	0.60	0.73	0.91	1.00	1.00	0.51	0.67	0.78	0.91	1.00	1.00
7	0	0.48	0.57	0.64	0.75	0.93	1.00	$-\ -\ -\ -$ *Same as Vectorial* $-\ -\ -\ -$					
	2	0.74	0.78	0.82	0.89	0.99	1.00						
	4	0.84	0.87	0.90	0.95	1.00	1.00						
	6	0.90	0.92	0.95	0.98	1.00	1.00						
8	0	0.94	0.99	1.00	1.00	:	:	$-\ -\ -\ -$ *Same as Vectorial* $-\ -\ -\ -$					
	2	0.99	1.00	1.00	:								
	4	1.00	1.00	:									
	6	1.00	:										
>9	0	1.00						$-\ -\ -\ -$ *Same as Vectorial* $-\ -\ -\ -$					
	2												
	4												
	6												

as expected as the variance-covariance matrix is scaled with $\frac{1}{2}$ and $\frac{3}{4}$ respectively of the original $Q_{\hat{z}\hat{z}}$ of the standalone solution. The unconstrained baseline in respectively the hextuple and octuple antenna configuration is scaled with $\frac{1}{3}$ and $\frac{1}{4}$. Therefore it can said that the larger number of constrained baselines in an antenna configuration results in a stronger model.

Relationship to Reported Observation Noise Values

In this section, the simulation results are linked to the observation noise of GNSS receivers, so that an expected performance in terms of success rate can be provided. In section 5.5, a comparison is made with field experiments.

For typical noise values of the surveying grade receiver (see section 2.6.1) with legacy GPS signals and observations from six GNSS satellites, in Table 5.7 for relative positioning using the vectorial bootstrapping approach ($C = 6$), a success rate of 75% for an undifference code noise of 0.3 meter and carrier noise of 3 millimeter, and 91% for a carrier noise of 1 millimeter is obtained. This is much better than the 25% and 49% respectively for standalone relative positioning using standard LAMBDA. For the multivariate bootstrapping approach in the Tables 5.7 and 5.8, a success rates of 84% and 91% for a code noise of 0.3 meter and 3 and 1 millimeter respectively for carrier noise is observed. Representing modernized GPS and Galileo in Table 5.1, a success rate of 98% (for 0.15 meter code and 3 millimeter carrier noise) and 100% (for 0.15 meter

undifferenced code and 1 millimeter carrier noise) for the vectorial bootstrapped solution is observed, compared with 67% and 87% for standalone solution. For the same code noise, a success rate of 100% for the multivariate bootstrapped approach in the Tables 5.7 and 5.8 for both 3 and 1 millimeter carrier noise is shown.
A similar discussion can be done for the typical noise values of the spaceborne receiver. As described in section 2.6.1, a typical space receiver has only a limited number of channels with for legacy GPS a undifferenced code noise up to 0.9 meter. For Galileo E1BC and GPS L1C, the expected code noise is smaller: around 0.55 meter. For both legacy and modernized signals, a carrier phase noise of about 2 millimeter is expected.
For an undifferenced code noise of 0.9 meter, at least twelve satellites are necessary for this GNSS satellite geometry to achieve 100 % success rate with the standard LAMBDA method for this particular GNSS satellite geometry. With two and four constrained baselines at two platforms, at least ten GNSS satellites are required and with six constrained baselines at least nine. With expected worst code noise of 0.55 meter for modernized GPS and Galileo, eleven satellites are required for standard LAMBDA. With two, four and six constrained baselines, the required number of GNSS satellites are respectively 10, 10 and 9. Based on these results it can be concluded that for the Galileo E1BC and GPS L1C signals, single-frequency, single-epoch relative positioning could be feasible as long as other errors can be neglected.

Time-To-Fix

In this section, Time-To-Fix (TTF) is defined as the number of epochs required to obtain a success rate of 100% for ambiguity resolution. TTF is an important number for real world applications as only after fixing the ambiguities, the higher accuracy of the carrier phase observations can be exploided. After the ambiguities are correctly fixed and as long as no cycle slips occur, the ambiguities vectors will not change. As was shown in Eq. (3.99), a multi-epoch solution based on four epochs has the same v-c matrix as a solution using observations with two times smaller standard deviations for both code and carrier.
Applying this relationship, an approximation of the Time-To-Fix will be provided based on the simulation results for bootstrapped relative positioning. Tables 5.9 and 5.10 show the expected Time-To-Fix for the simulation results presented in Tables 5.7 and 5.8. It is observed that for the weakest models more than 300 epochs are required to fix the ambiguities. For cases with large code and carrier noise but 8 or 9 GNSS satellites available, the bootstrapped solution using four or six constrained baselines is improved considerable over the standard LAMBDA method. Instead of requiring more than 300 epochs, a fix is expected after 36 epochs. An instantaneous fix should be feasible for this GNSS satellite geometry when there are three constrained baselines at each platform ($C = 6$).
Note that for Eq. (3.99), the assumption was made that the geometry does not change between the epochs. In reality, especially for space application where the user moves with high velocity, the geometry will change considerable making the multi-epoch solution even stronger. The influence of the geometry is investigated in the next section.

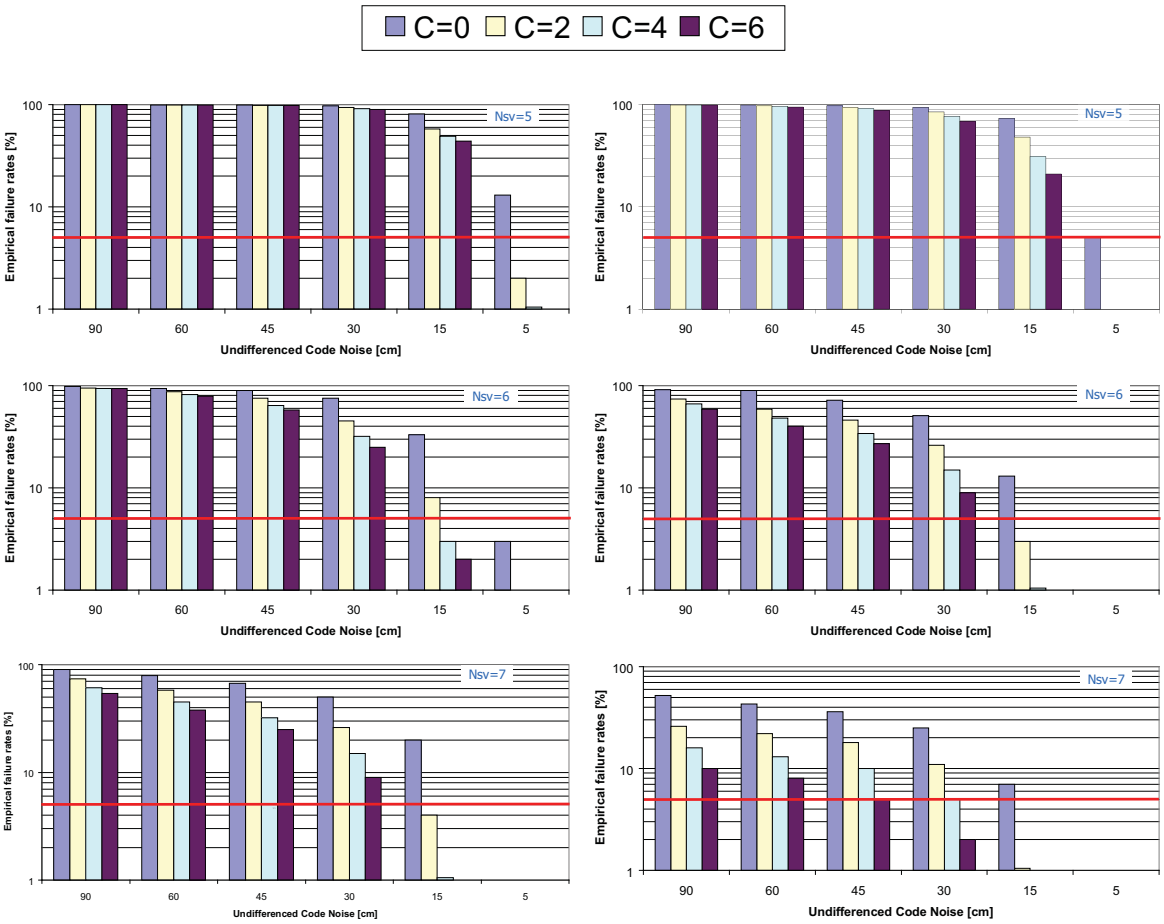


Figure 5.9: Single-frequency, single-epoch failure rates for undifferenced carrier noise of 3 mm (left) and 1 mm (right) for the unconstrained baseline using zero ($C = 0$), two ($C = 2$), four ($C = 4$) or six ($C = 6$) constrained baselines, red line indicates threshold of 5% for the failure rate

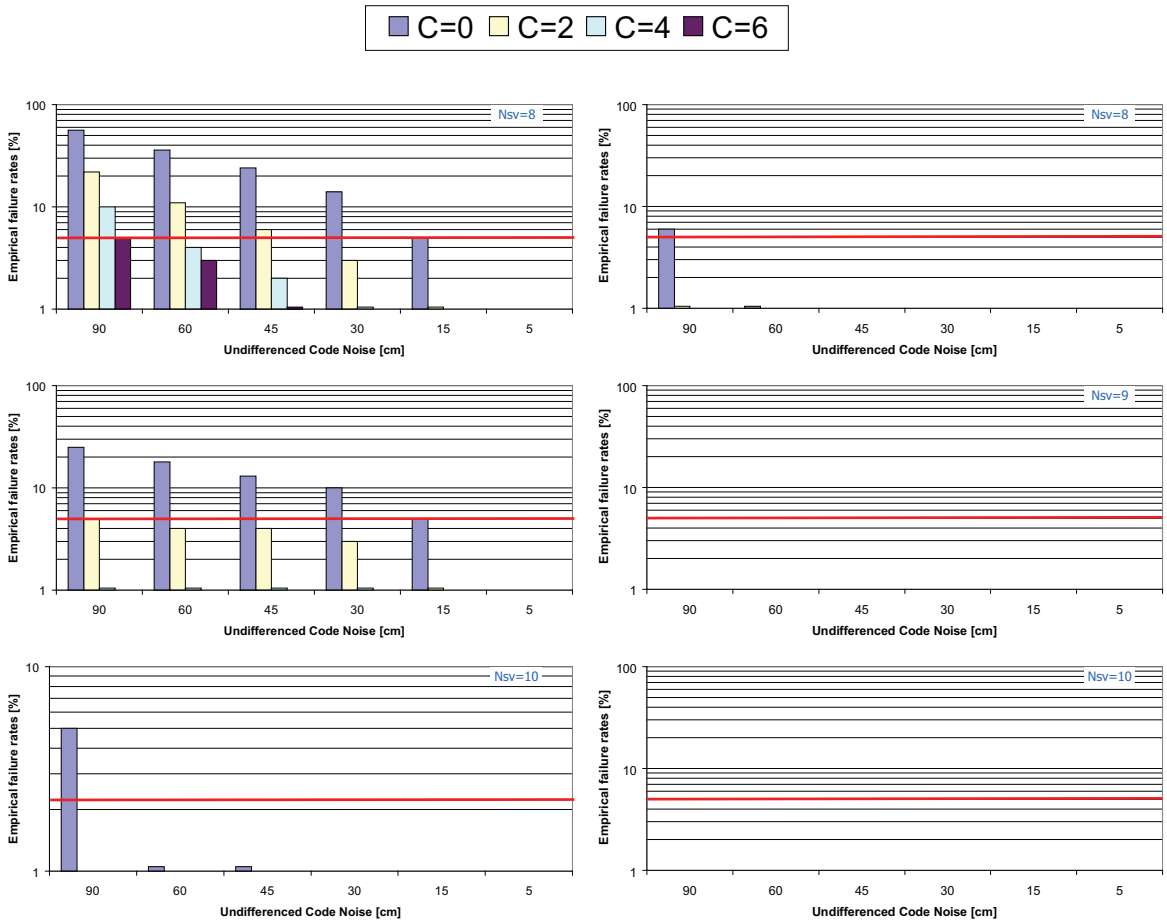


Figure 5.10: Single-frequency, single-epoch failure rates for undifferenced carrier noise of 3 mm (left) and 1 mm (right) for the unconstrained baseline using zero ($C = 0$), two ($C = 2$), four ($C = 4$) or six ($C = 6$) constrained baselines, red line indicates threshold of 5% for the failure rate

Table 5.9: Simulation results for σ_ϕ=3 [mm]: Single-frequency, single-epoch Time-To-Fix for the unconstrained baseline between platforms using standard LAMBDA ($C = 0$), and bootstrapped solution from Vectorial C-LAMBDA and MC-LAMBDA ($C > 0$), $\#C$ is total number of constrained baselines at the two platforms

N_{SV}	$\#C$	Vectorial C-LAMBDA σ_p [cm]						MC-LAMBDA σ_p [cm]					
		90	60	45	30	15	5	90	60	45	30	15	5
5	0							$- - - - \; Same\ as\ Vectorial \; - - - -$					
	2	≥324	≥144	≥81	≥36	≥9	≥1						
	4							324	144	81	36	9	1
	6	324	144	81	36	9	1						
6	0	≥324	≥144	≥81	≥36	≥9	≥1	$- - - - \; Same\ as\ Vectorial \; - - - -$					
	2												
	4	324	144	81	36	9	1	324	144	81	36	9	1
	6							36	16	9	4	1	1
7	0							$- - - - \; Same\ as\ Vectorial \; - - - -$					
	2	324	144	81	36	9	1						
	4							324	144	81	36	9	1
	6	36	16	9	4	1	1	36	16	9	4	1	1
8	0	324	144	81	36	9	1	$- - - - \; Same\ as\ Vectorial \; - - - -$					
	2												
	4	36	16	9	4	1	1	36	16	9	4	1	1
	6	9	4	3	1	1	1	4	2	1	1	1	1
9	0	324	144	81	36	9	1	$- - - - \; Same\ as\ Vectorial \; - - - -$					
	2												
	4	36	16	9	4	1	1						
	6	1	1	1	1	1	1				1		
10	0	9	4	3	1	1	1						
	2						:	$- - - - \; Same\ as\ Vectorial \; - - - -$					
	4	1	1	1	1	1							
	6												
11	0	3	1	:									
	2	1	:					$- - - - \; Same\ as\ Vectorial \; - - - -$					
	4	:											
	6												
12	0												
	2							$- - - - \; Same\ as\ Vectorial \; - - - -$					
	4				1.00								
	6												

Table 5.10: Simulation results for σ_ϕ=1 [mm]: Single-frequency, single-epoch Time-To-Fix for the unconstrained baseline between platforms using standard LAMBDA ($C = 0$), and bootstrapped solution from vectorial C-LAMBDA and MC-LAMBDA ($C > 0$), $\#C$ is total number of constrained baselines at the two platforms

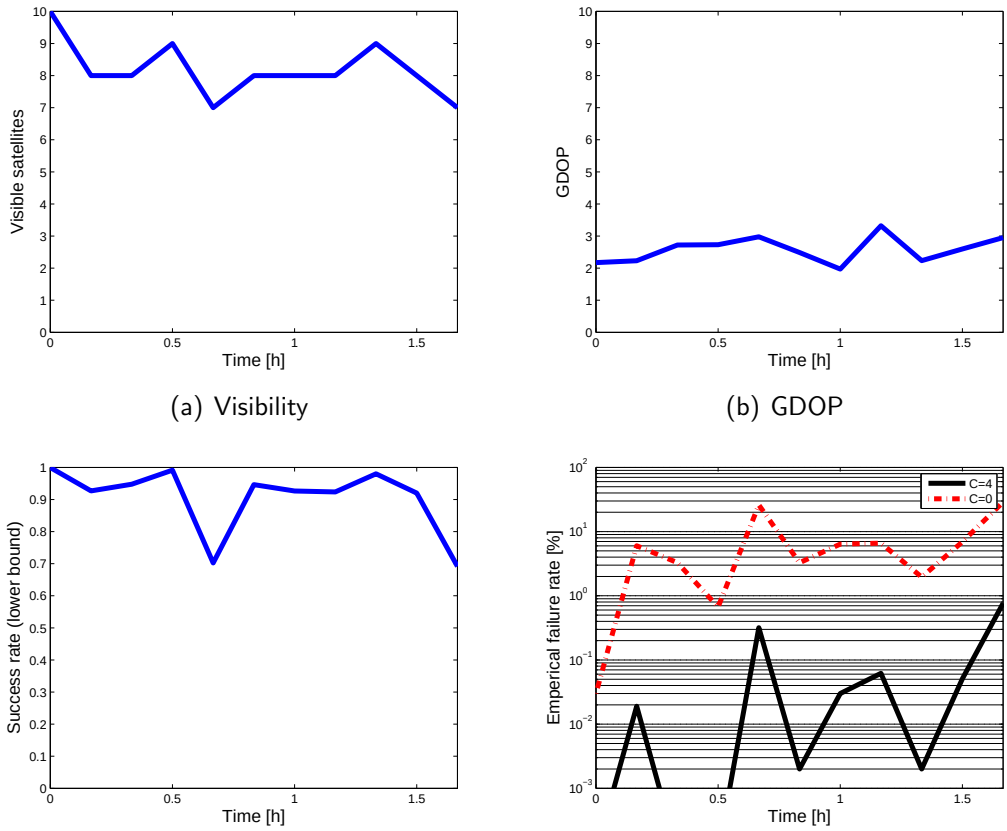
N_{SV}	$\#C$	Vectorial C-LAMBDA						MC-LAMBDA					
		σ_p [cm]						σ_p [cm]					
		90	60	45	30	15	5	90	60	45	30	15	5
5	0	≥324	≥144	≥81	≥36	≥9	≥1	$-\ -\ -\ -$ *Same as Vectorial* $-\ -\ -\ -$					
	2												
	4												
	6	324	144	81	36	9	1	324	144	81	36	9	1
6	0							$-\ -\ -\ -$ *Same as Vectorial* $-\ -\ -\ -$					
	2	324	144	81	36	9	1						
	4							324	144	81	36	9	1
	6	36	16	9	4	1	1	36	16	9	4	1	1
7	0	324	144	81	36	9	1	$-\ -\ -\ -$ *Same as Vectorial* $-\ -\ -\ -$					
	2												
	4												
	6	36	16	9	4	1	1						
8	0	4	2	1	1	:	:	$-\ -\ -\ -$ *Same as Vectorial* $-\ -\ -\ -$					
	2	3	1	1	:								
	4	1	1	:									
	6	1	:										
>9	0	1.00						$-\ -\ -\ -$ *Same as Vectorial* $-\ -\ -\ -$					
	2												
	4												
	6												

5.4.3 Influence of geometry

In this section, the relative positioning result is analyzed by simulation as part of the integrated approach. The orbit of the Garada mission is simulated with three antennas placed on each of the two spacecraft flying in close formation. With three antennas on the spacecraft, the antenna configuration is C=4 in Fig. 5.8. The simulation conditions are provided in Appendix A.2. In this section, the total number of constrained baselines at the two platforms ($\#C$) and undifferenced carrier phase and code noise (σ_ϕ, σ_p) are kept constant. The number of tracked satellites (N_{SV}) and the GNSS satellite geometry are determined by the user location, time and applied elevation mask.
The GNSS satellite visibility, GDOP, theoretical lower bound and empirical success rates for ambiguity resolution are shown in Fig. 5.11. The definition of the theoretical lower bound of the success rate was provided in Eq. (3.104).
With an elevation mask of 15 degrees and assuming that the spacecraft remains earth pointing, the number of visible GNSS satellites for the space pointing GNSS antennas is between 7 and 10. The geometry of the GNSS satellites is shown in Fig. A.1 and A.2.
For the unconstrained baseline between the platforms, results of the multivariate bootstrapping approach are shown on the bottom right hand side of Fig. 5.11. The figure contains empirical failure rates for the case with single GNSS receivers/antennas at each platform (C=0) and the case where there are three GNSS receivers/antennas at each platform (C=4). As expected, the success rate is lower for epochs where a lower number of GPS satellites is locked, and the improvement by applying the integrated approach is largest for these epochs.
Hence again, it is observed that especially the weaker models (for this simulation this means lower number of locked GNSS satellites) can be improved by applying the bootstrapping approach. The maximum difference in improvement by employing three antennas at each platform for the multivariate bootstrapping approach is 28%. The success rate for standard LAMBDA is higher than 71% in this simulation, whereas for the integrated approach with two constrained baselines at each platform, the success rate is always higher than 99%.

5.4.4 Dual Frequency

Next, the multi-frequency model introduced in section 5.3.5 where only the in-between baseline is dual frequency is analysed using simulated data. Table 5.11 shows empirical success rates for standard LAMBDA and MC-LAMBDA bootstrapped solutions. It is important that for this weak model with no more than five GNSS satellites, only with 90 cm code noise the success rates of standard LAMBDA is lower than 95 % and if $\sigma_p > 0.45$ [m] the standard LAMBDA method will achieve a success rate of about 99 % or more. Normally, only if the lower bound of the success rate is higher than a certain threshold an attempt will be made to fix the ambiguities. In Tables 5.11 and 5.12, the cases are colored grey for which success rate with the standard LAMBDA method is below a threshold of 99%, but those with the integrated approaches are higher than this threshold.
For the dual frequency unconstrained baseline, the success rate will increase if there are more than two constrained baselines at each platform ($C > 4$). However with $C \leq 4$, the success rate on the unconstrained baseline could decrease compared with dual frequency LAMBDA ($C = 0$). This can be explained by comparing Table 5.5 with the result for stan-



(a) Visibility

(b) GDOP

(c) Lower bound success rate

(d) Empirical failure rate

Figure 5.11: Garada simulation for one orbital period

dard LAMBDA in Table 5.11. We observe in these tables that the dual frequency model is stronger than the single frequency constrained baseline model, in case $C = 2$ or $C = 4$. For example the case $C = 4$, $\sigma_p = 90$ cm: the overall success rate of all constrained baselines at the two platforms is 81%, while the success rate for the unconstrained baseline is already 86%. In this case we do not expect a larger improvement by bootstrapping from the constrained baselines. For a bootstrapping solution it is important to start with the most precise solution and bootstrap the other solution from there.

For the unconstrained baseline in Table 5.11 applying dual frequency observations, it is observed that the MC-LAMBDA bootstrapping approach also has a better performance than standalone LAMBDA if more than four constrained baselines are applied at the two platforms, so two constrained baselines at each platform. To investigate this further we did another simulation for the dual frequency unconstrained baseline assuming that the ambiguities at the constrained baselines are correctly fixed. This result is included in Table 5.12. In this simulation, including ambiguity constraints on the dual frequency b^{12} baseline will always increase the success rate of the ambiguity resolution on this baseline. The improvement is strongest for the largest code noise: 4% using two constrained baselines, 11 % using four constrained baselines, and 13% using six constrained baselines. If we compare Tables 5.11 and 5.12, we observe for $C = 6$ that the emperical success rates becomes the same in both tables. This as expected as the MC-LAMBDA method will

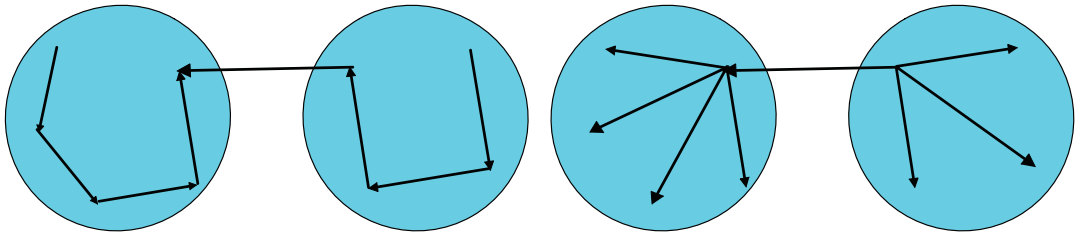
Table 5.11: Simulation results: Dual-frequency, single-epoch success rates for the unconstrained baseline between platforms using standard LAMBDA ($C = 0$), and bootstrapped solution from MC-LAMBDA ($C > 0$), $\#C$ is total number of constrained baselines at the two platforms, gray colored cases: success rate with the standard LAMBDA method $\leq 95\%$, the integrated approaches $\geq 95\%$

N_{SV}	$\#C$	MC-LAMBDA					
		σ_p [cm]					
		90	60	45	30	15	5
5	0	0.86	0.96	0.99	1.00	1.00	1.00
	2	0.87	0.95	0.98	1.00	1.00	1.00
	4	0.88	0.96	0.98	1.00	1.00	1.00
	6	0.99	1.00	1.00	1.00	1.00	1.00

Table 5.12: Simulation results assuming that the ambiguities at the constrained baselines are fixed correctly: Dual-frequency, single-epoch success rates for the unconstrained baseline between platforms using standard LAMBDA ($C = 0$), and bootstrapped solution from MC-LAMBDA ($C > 0$), $\#C$ is total number of constrained baselines at the two platforms, gray colored cases: success rate with the standard LAMBDA method $\leq 95\%$, the integrated approaches $\geq 95\%$

N_{SV}	$\#C$	MC-LAMBDA					
		σ_p [cm]					
		90	60	45	30	15	5
5	0	0.86	0.96	0.99	1.00	1.00	1.00
	2	0.90	0.98	0.99	1.00	1.00	1.00
	4	0.97	0.99	1.00	1.00	1.00	1.00
	6	0.99	1.00	1.00	1.00	1.00	1.00

achieve 100 % success in these simulations (Table 5.5).
Comparing the Table 5.1 and 5.11 it is clear that the dual frequency model is stronger than the single frequency model. If more than six constrained baselines at the platforms are available it can conclude that the bootstrapped solution cannot only enhance the single frequency but also dual frequency relative positioning.



(a) Vectorial C-LAMBDA (b) MC-LAMBDA

Figure 5.12: Illustration of a multi-antenna configuration for bootstrapped relative positioning in MAx experiment (illustration does not reflect local geometry of antennas)

5.5 Verification by field experiments

In this section, data collected in field experiments is used to confirm the developed theory on integrated relative positioning and attitude determination. The results of the field experiments are compared with the results of the software simulations described in section 5.4.

5.5.1 MAx Experiment

In the first field experiment described in this section, the simulation results from section 5.4 are confirmed using field data from the static experiment described in Appendix A.3 with a larger number of receivers/antennas. A sketch of the setup of the experiment is shown in Fig. 5.12. All receivers applied are Trimble R7s and in total 5400 epochs (sampling frequency 1 Hz) are processed. The receivers were placed in two distinguished groups, each representing a platform. In the first group, four receivers were placed (forming three independent baselines at the platform), separated from the first group, five receivers are placed in the second group (forming four independent baselines at the platform). So in total seven constrained baselines at the two platforms can be applied in the integrated approach to enhance relative positioning. The stochastic model does not apply elevation weighting but an elevation mask of 10° and -as code and carrier phase noise- the 0.3[m] and 3 [mm] are used.

Multi-platform Ambiguity Resolution

Table 5.13 shows the empirical success rates using C-LAMBDA and MC-LAMBDA as function of the number of constrained baselines included at both platforms. If one constrained baseline is used on each platform, the results obtained by applying C-LAMBDA and MC-LAMBDA are the same, therefore these are not repeated in the table. Compared with Table 4.7 in chapter 4, the success rates of (M)C-LAMBDA are squared, which is as expected as both platforms are processed independently. As observed for simulated data in Tables 5.5 and 5.6, the overall success rate will always increase if more baselines are included in the MC-LAMBDA solution. For vectorial C-LAMBDA, the overall success rate will decrease if more baselines are included in the solution.

In section 5.5.1, it was concluded that the standard deviation of the double difference code observations of the Trimble R7 receiver is between 0.3 and 0.6[m]. In Table 5.5, undifferenced code noise is given, thus following the propagation described in Eq. (2.177), an undifferenced code noise of 0.15 and 0.3[m] corresponds to double difference code noise of 0.3 and 0.6[m] respectively. An undifferenced carrier phase noise of 1[mm] corresponds to double difference carrier phase noise of 2[m]. If the success rates in Table 5.5 for code noise levels of 0.3∼0.15[m] and a carrier phase noise of 3 millimeter are compared to the values reported in Table 5.13, the success rates correspond as will be discussed in more next. The column containing the vectorial C-LAMBDA results reports a success rate of 65% for $N_{SV} = 5,\ C = 2$ which is in between the 50% and 77% reported for $\sigma_p = 0.3$ and 0.15[m] respectively in Table 5.5. Moreover, the success rate of 48% reported for the field experiment is between 37% and 73% for $C = 4$ reported for $\sigma_p = 0.3$ and 0.15[m] in the simulations, and 40% is between 24% and 63% for $C = 6$. The same correspondence holds for the cases with more GPS satellites included in the solution and the bootstrapped solution from MC-LAMBDA.

Bootstrapped Relative Positioning

The relative positioning result is analyzed as part of the integrated approach for the antenna configurations in Fig. A.3. The results are presented in Table 5.14, which contains empirical success rates as a function of the number of tracked satellites (N_{SV}) and the number of constrained baselines C at both platforms. The unconstrained baseline b^{12} is again presented as standalone ($C = 0$) and as part of the integrated solution using two till seven constrained baselines ($C = 2, \ldots, C = 7$).
It is confirmed with actual GPS data that the integrated approach has a better performance than standalone for the unconstrained baseline. The improvement is up to 23% using two constrained baselines ($C = 2$), 38% using four constrained baselines ($C = 4$), 67% using six constrained baselines ($C = 6$), and 65% using seven constrained baselines ($C = 7$) with a larger improvement for weaker GNSS models. For this experiment a weaker model means a lower number of satellites N_{SV}, as the code and carrier phase noise are given for this specific receiver and experimental setup.
In Table 5.14, the cases are colored grey for which success rate with the standard LAMBDA method is below a threshold of 95%, but those with the integrated approaches are higher than this threshold.
As was found for overall success rates for all the constrained baselines, the results for the unconstrained baseline in Tables 5.7 and 5.14 for undifferended code noise of $0.3 \sim 0.15$ [m] and a carrier phase noise of 3 [mm], correspond to the results obtained for the field experiment. The column containing the vectorial C-LAMBDA results reports a success rate of 9% for $N_{SV} = 5,\ C = 0$ which is in between the 3% and 19% reported for $\sigma_p = 0.3$ [m] and 0.15 [m] respectively in Table 5.7. Moreover, the success rate of 27% reported for the field experiment is between 6% and 42% for $C = 2$ reported for $\sigma_p = 0.3$ [m] and 0.15 [m] in the simulations, 33% is between 9% and 51% for $C = 4$ and 36% is between 10% and 56% for $C = 6$.
The exception is $N_{SV} = 6,\ C = 2, \ldots, 6$ where the success rate for the unconstrained baseline bootstrapped from the vectorial C-LAMBDA is lower than the simulation results

for $\sigma_p = 0.3$ [m]. Moreover, the success rate for the solution bootstrapped from MC-LAMBDA for $N_{SV} = 6,\ C = 4$ is lower than the success rate in the simulation with $\sigma_p = 0.3$[m]. This is indication that erroneous observations from one or more GNSS satellite is dominant in these solutions, for example due to multipath.
Analyses have shown that the receiver 10 is causing these difficulties: if data from this receiver is excluded from the solution, the success rate will always increase when a larger number of baselines is utilized in the solution. In appendix A.3, Figures A.6 till A.7 show the multipath combination for receiver 10 and the SNR values. In Figures A.8 till A.9, the single difference code and carrier phase residuals are shown calculated using the procedure described in appendix F. Especially carrier phase multipath for low elevation GNSS satellites is apparent.

Fig. 5.13 shows the estimate of the in-between baseline for all the epochs where the ambiguity vector was fixed correctly. The first three figures show the East, North and Up components as function of time. The last two figures show the North and Up component as function of the East component. The figures contain the integrated (C=4) and the LAMBDA results (C=0). It is clear from the figures that the integrated solution is more accurate, but also that there is time-varying multipath influencing the baseline estimates. This is confirming the early obtained conclusion that multipath, especially carrier phase multipath, is present on the observations.
Table 5.15, shows the accuracy of the baseline estimate as function of number of constrained baselines ($\#C$) and number of GNSS satellites (N_{SV}) applied in the solution. As the integrated solution is more accurate, it can be concluded that this approach is more robust for multipath. However, for this field data, a larger number of GNSS satellites does not garantuee a more accurate baseline estimation, again due to different multipath at the observations from the various GNSS satellites.
Based on the presented results from the field experiment, it can be concluded that an integrated approach can improve both ambiguity resolution and accuracy of the unconstrained baseline between platforms. The advantage of more epochs with correctly fixed ambiguities is that the precise baseline estimate is more often available.

Table 5.13: MAx field experimental results: vectorial C-LAMBDA and MC-LAMBDA single-frequency, single-epoch overall success rates for all the constrained baselines at two platforms, $\#C$ is total number of constrained baselines at the two platforms

N_{SV}	$\#C$	Vectorial C-LAMBDA	MC-LAMBDA
5	2	0.65	$Same\ as\ Vectorial$
	4	0.48	0.98
	6	0.40	1.00
	7	0.38	1.00
6	2	0.94	$Same\ as\ Vectorial$
	4	0.76	0.99
	6	0.61	1.00
	7	0.57	1.00
7	2	0.99	$Same\ as\ Vectorial$
	4	0.97	1.00
	6	0.94	1.00
	7	0.94	1.00
8	2	1.00	$Same\ as\ Vectorial$
	4	0.99	1.00
	6	0.99	1.00
	7	0.99	1.00
$\geq$9	2	1.00	$Same\ as\ Vectorial$
	4	1.00	1.00
	6	1.00	1.00
	7	1.00	1.00

Table 5.14: MAx field experimental results: Single-frequency, single-epoch success rates for the unconstrained baseline between platforms using standard LAMBDA ($C = 0$), and bootstrapped solution from vectorial C-LAMBDA and MC-LAMBDA ($C > 0$), $\#C$ is total number of constrained baselines at the two platforms, gray colored cases: success rate with the standard LAMBDA method $\leq 95\%$, the integrated approaches $\geq 95\%$

N_{SV}	$\#C$	Vectorial C-LAMBDA	MC-LAMBDA
5	0	0.09	$Same\ as\ Vectorial$
	2	0.27	
	4	0.33	0.38
	6	0.36	0.46
	7	0.36	0.43
6	0	0.25	$Same\ as\ Vectorial$
	2	0.48	
	4	0.63	0.68
	6	0.62	0.79
	7	0.60	0.80
7	0	0.71	$Same\ as\ Vectorial$
	2	0.86	
	4	0.95	0.96
	6	0.95	0.99
	7	0.95	0.98
8	0	0.94	$Same\ as\ Vectorial$
	2	0.99	
	4	0.99	1.00
	6	1.00	1.00
	7	1.00	1.00
$\geq$9	0	0.99	$Same\ as\ Vectorial$
	2	0.99	
	4	0.99	0.99
	6	0.99	0.99
	7	0.99	0.99

Table 5.15: MAx field experimental results: Standard deviation [mm] of the unconstrained baseline between platforms using standard LAMBDA ($C = 0$), and bootstrapped solution ($C = 4$), $\#C$ is total number of constrained baselines at the two platforms

N_{SV}	C=0	C=4
6	5.5	4.9
7	2.0	2.0
8	2.0	1.8
$\geq$9	2.7	2.6

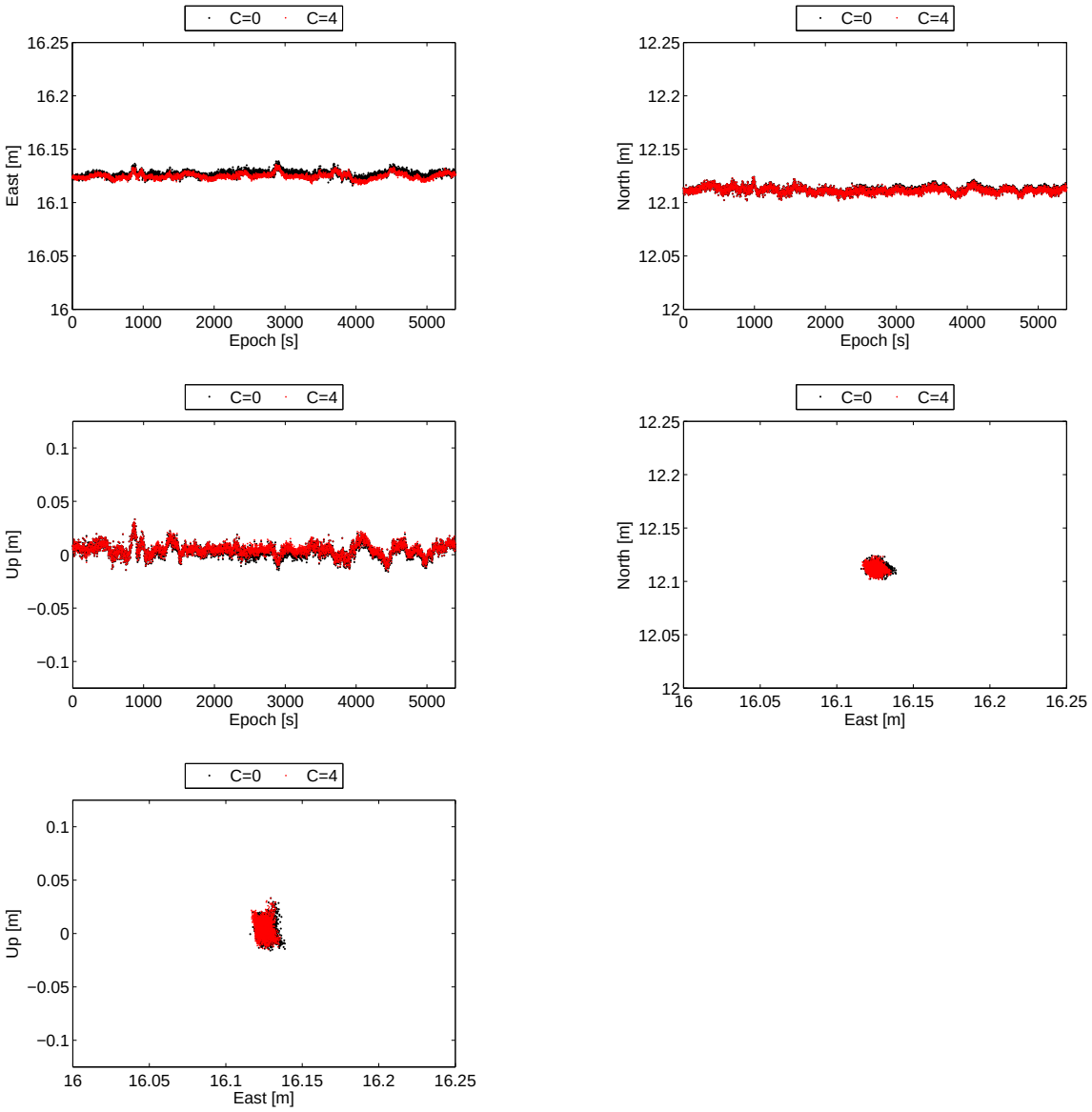
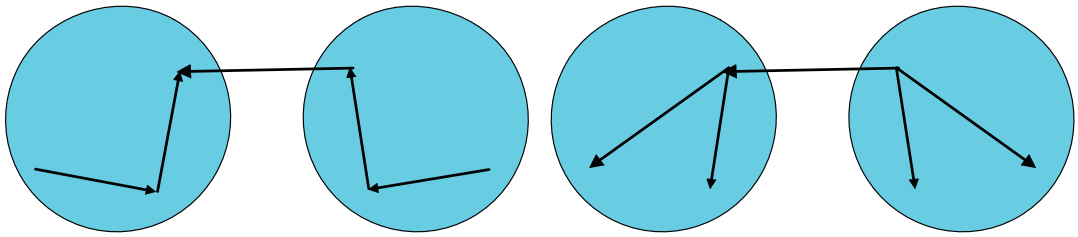


Figure 5.13: MAx baseline estimate ($\#C$ is total number of constrained baselines at the two platforms)

Figure 5.14: Illustration of a multi-antenna configuration for bootstrapped relative positioning in PROBA-3 experiment (illustration does not reflect local geometry of antennas)



(a) Vectorial C-LAMBDA (b) MC-LAMBDA

5.5.2 Satellite Formation Flying: PROBA-3

Next, the success rate for the hardware-in-the-loop simulations using a triple antenna configuration at each spacecraft of the PROBA-3 mission is analyzed. The mission itself is introduced in appendix A.7, relative positioning and attitude results were reported in section 3.6.1 and 4.5.5, respectively. A sketch of the experiment setup is shown in Fig. 5.14. 1500 epochs of observations are available to analyse, this is the duration the PROBA-3 spacecraft are below the GPS constellation (see Fig. A.16(b)).
The number of locked GPS satellites at each of the three antennas on both the PROBA-3 spacecraft are shown in Fig. 5.15. A so-called cold start is used for these receivers and in the figures it is observed that it took longer at the first spacecraft to initialize. The analysis is started if more than four GPS satellites are locked at both spacecraft. The stochastic model does not apply elevation weighting and -as the receiver's GNSS satellite selection algorithm is not adjusted for the space application and therefore a large number of tracked GPS satellites are at low elevation, no elevation mask was applied. As code and carrier phase noise, 0.3[m] and 3 [mm] are used. For the attitude determination result at both platforms, an empirical success rate for single-epoch ambiguity resolution of close to 100% is obtained (see section 4.5.5), so the failure rate is almost 0 %.
Empirical ambiguity success rates for the unconstrained baseline between the spacecraft are shown in Table 5.16. The increase in success rate from 85 to 91% for the unconstrained baselines in this hardware-in-the-loop experiment is in line with the expectation from the theory developed in the previous sections and the simulation results presented in section 5.4. It is observed that with vectorial C-LAMBDA and MC-LAMBDA, the same results are obtained. This is as expected as for this strong model already the single constrained baseline solution achieves a 100% success rate (see section 4.5.5).
The single-epoch relative positioning solutions ($C = 0$ and $C = 4$) for the hardware-in-the-loop test are shown in Fig. 5.16 for all the epochs where the ambiguity vector was fixed correctly. From the figure it is clear that the integrated solution is more accurate. Another advantage is that the more precise baseline estimate is more often available due the higher success rate for the integrated approach.
Table 5.16 also contains the standard deviation of the baseline estimates. Here it is observed, again in line with the theory developed in section 5.3.2, that the accuracy of the baseline estimate increases if more constrained baselines are included in the integrated so-

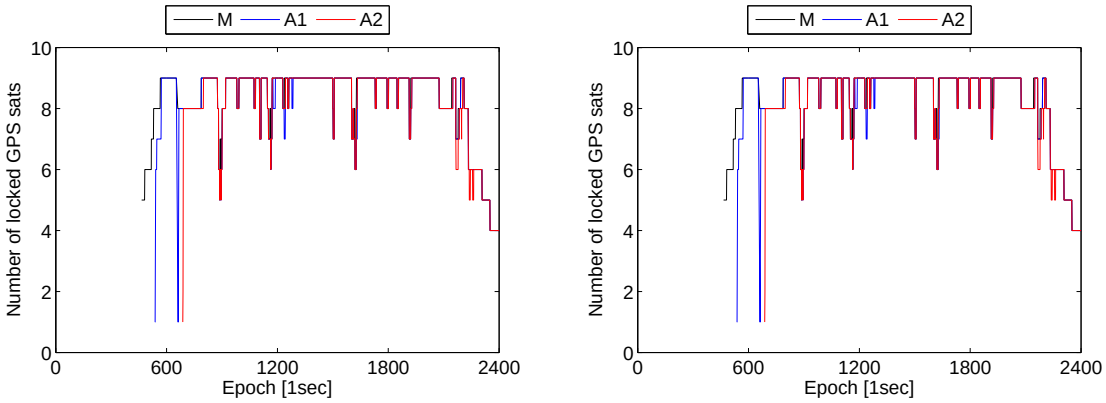


Figure 5.15: Number of locked GPS satellites vs. GPS time (PROBA-3)

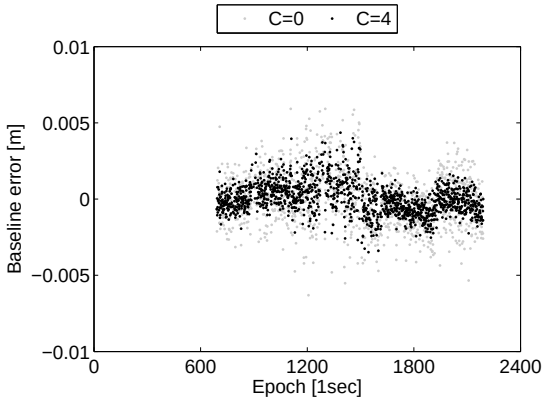


Figure 5.16: Baseline error for hardware-in-the-loop test using zero (C = 0) and four (C = 4) constrained baselines (PROBA-3)

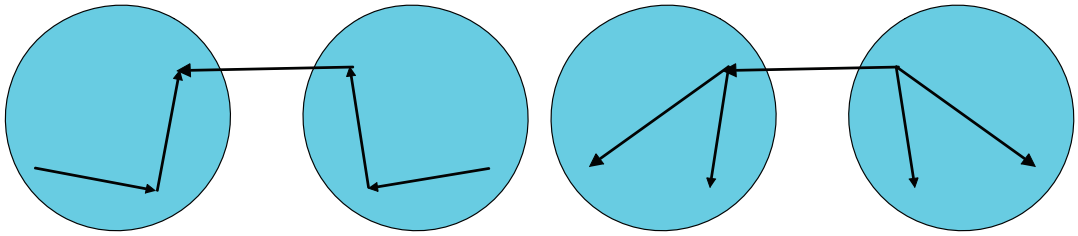
lution.
Next the theoretical improvement is compared with the results obtained from the PROBA-3 experiment. For example for case $C = 1$, $C = 2$ and $C = 4$, as was shown in Table 5.4, that the standard deviation of the fixed baseline should improve compared to standard LAMBDA with $\sqrt{(\frac{3}{4})} \approx 0.9$, $\sqrt{(\frac{1}{2})} \approx 0.7$ and $\sqrt{(\frac{1}{3})} \approx 0.6$ respectively. If these numbers are compared with the empirical results in Table 5.16, an improvement, as expected from the theory, is observed of $\frac{1.5}{1.8} \approx 0.8$, $\frac{1.2}{1.8} \approx 0.7$ and $\frac{1.1}{1.8} \approx 0.6$, respectively.
Based on the presented results from hardware-in-the-loop simulations, it can be concluded that an integrated approach can improve both ambiguity resolution and accuracy of the unconstrained baseline between platforms.

5.5.3 Satellite formation flying: Garada mission

In this section, the success rate for the hardware-in-the-loop simulations using the Garada mission is analyzed. The mission itself is introduced in appendix A.8, relative positioning and attitude results were reported in section 3.6.3 and 4.5.5 respectively. As explained in Appendix A.8, data from the same Namuru receiver is used, collected in different runs of

	Vectorial C-LAMBDA				*MC-LAMBDA*
$\#C$	0	1	2	4	4
Success rate	0.85	0.89	0.91	0.91	0.91
Standard deviation [mm]	1.8	1.5	1.2	1.1	1.1

Table 5.16: Hardware-in-the-loop simulation results: single-frequency, single-epoch success rates and standard deviation for the unconstrained baseline b^{12} using standard LAMBDA ($C = 0$), and a bootstrapped solution using constrained baselines with C is the total number of constrained baselines at the two spacecraft (PROBA-3)



(a) Vectorial C-LAMBDA (b) MC-LAMBDA

Figure 5.17: Illustration of a multi-antenna configuration for bootstrapped relative positioning in Garada experiment (illustration does not reflect local geometry of antennas)

the same simulation. A sketch of the experiment setup is shown in Fig. 5.17. In total 14935 epochs were applied in this analysis. The stochastic model does not apply elevation weighting and -as also the Namuru receiver's GNSS satellite selection algorithm is not adjusted for the space application and therefore large number of tracked GPS satellites are at low elevation, no elevation mask was applied. As code and carrier phase noise, 3 [m] and 3 [mm] were used. The code noise values were obtained in a detailed analysis of the receiver in (Buist et al., 2011b), where it was shown that the Namuru receiver has relative larger values for standard deviation. This could be explained by the knowledge that the applied firmware version does not use a narrow chip space and has a tracking loop design that keeps the code and carrier observations independent as is common for spaceborne receivers (see section 2.6.1). The accuracy for code observations is in line with the results for other spaceborne receivers based on the literature review in section 2.6.1.

Empirical ambiguity success rates for the unconstrained baseline between the spacecraft are shown in Table 5.17 as function of the number of constrained baselines applied in the solution.

A increase in success rate from 18% to 35% for the unconstrained baseline in this hardware-in-the-loop experiment is observed. The success rate becomes 44% for a unconstrained baseline solution bootstrapped from the MC-LAMBDA results at both platforms. The Namuru receiver applied in this experiment still had some issues with its code observations (Buist et al., 2012), therefore the standard deviation of the unconstrained baseline estimation did not improve when more constrained baselines were applied in the solution.

By comparing the results of Table 5.17 with the simulations in Table 5.7 for the maximum value of 0.9 [m] undifferenced code noise, the conclusion is that the success rate for the hardware-in-the-loop simulation is lower due to the larger code noise of the Namuru receiver.

Table 5.17: Hardware-in-the-loop simulation results: single-frequency, single-epoch success rates for the unconstrained baseline b^{12} using standard LAMBDA ($C = 0$), and a bootstrapped solution using constrained baselines with C is the total number of constrained baselines at the two spacecraft (Garada)

	Vectorial C-LAMBDA				*MC-LAMBDA*
$\#C$	0	1	2	4	4
Success rate	0.18	0.22	0.30	0.35	0.44

5.6 Concluding remarks

In this chapter, the possibility was investigated to use multi-antenna data, not only for attitude determination, but also to improve the relative positioning between spacecraft in an integrated approach. The method makes use of the following information to determine the relative position and orientation of a multi-antenna system with unconstrained and constrained baselines: the integerness of the ambiguities, the relationship between the ambiguities on the different baselines and the known geometry of the baselines at the platforms.

The outcome of the attitude determination problem was applied in the ambiguity constrained solution on the unconstrained baseline between the platforms. In this way the solution for the unconstrained baseline is bootstrapped from either the solutions of single baselines based on vectorial C-LAMBDA or the MC-LAMBDA solution of each platform in what is called vectorial or multivariate bootstrapped relative positioning respectively. As the multivariate bootstrapping approach is a stronger model by applying information on the geometry of the constrained baselines, the success rate of this approach is higher and this will also result in a better performance on the unconstrained baseline. The difference is profound for the weaker models and absent for the stronger models and thus for the latter we observe, as expected from the developed model, that both the approaches have the same performance.

It was showed the theoretical improvement achievable for the unconstrained baseline between the platforms as a function of the number of antennas on each platform, both for ambiguity resolution and accuracy of the baseline solution. The obtained mathematical relationship between the improvement achievable and the number of antennas was verified by software based and hardware-in-the-loop simulations.

It was demonstrated that the solution cannot only enhance single frequency relative positioning but can be applied to improve the multi-frequency relative positioning solution as well.

The rigorous inclusion of multiple antennas into the ambiguity objective function shows dramatic improvements in the success rates on the in-between baseline. The improved instantaneous ambiguity resolution will result in an even stronger reduction in time to fix (TTF). Additional benefits of the method is an improved robustness against multipath and the improved precision of the baseline estimation.

6 Conclusions and recommendations

There is trend in spacecraft engineering toward distributed systems where a number of smaller spacecraft work as a larger satellite. However, in order to make the small satellites work together as a single large platform, the precise relative positions and orientations of the elements of the formation have to be estimated. Global Navigation Satellite System (GNSS) receivers can be utilized to provide baseline estimates with centimeter to millimeter level accuracy.
While precise relative positioning using GNSS for surveying has been around for some time, precise relative navigation for moving applications on land, on water, in the air and even in space is still under development. The developed method can also be applied for these applications as it is independent of the user motion.

6.1 Kinematic relative positioning

For spaceborne applications, often an extensive dynamics model in combination with a filter and GNSS observations is used. One of the objectives of this thesis was to investigate the capabilities of formation flying using kinematic GNSS for relative positioning. The main advantage of this kinematic approach is that information about dynamics of the system is not applied, which gives more flexibility and furthermore could increase the scientific significance of the observations made by the spacecraft of -for example- gravimetry missions. Therefore a functional kinematic approach could be of importance for future space missions, but also for terrestrial applications and aviation.
A functional model was developed, in which the difference between the topocentric distance at the GNSS system time and at the GNSS receiver time is taken into account. For users with high dynamics and/or large clock offsets, not taking this effect into account can cause time-varying offsets in the baseline estimate. In the hardware-in-the-loop simulation presented in Chapter 3 of the Proba-3 spacecraft flying in formation in a very eccentric orbit, this error can be up to 16 centimeters. In the proposed functional model, this error can be corrected and the accuracy of the baseline estimate approaches the theoretical limitation resulting from the carrier phase accuracy.
The derived functional and stochastic models were applied for absolute and relative positioning. It was demonstrated that the Doppler is not an independent observation and correlated with the carrier phase. In the analysis, emphasis was on the effects of large receiver clock errors and user dynamics on absolute and relative positioning.
For relative positioning applications, it was shown that inclusion of the Doppler observations in the model is only desirable

1. if the GNSS receivers have large clock offsets. Especially in a dynamic environment, the standard DD model will result in an offset in the baseline estimation.

2. for applications where the relative position between two platforms is actively controlled, the relative velocity is generally required as input for the control loop.

The Doppler observation will not improve the float solution of the relative positioning problem and therefore will not improve ambiguity resolution. The drawback of using the Doppler for relative velocity estimation is the effect from the relative motion and the clock drift cannot be separated. If the relative velocity can be obtained offline, taking the time derivative of the baseline estimate can provide a more accurate relative velocity estimation.
A single and multi-epoch data processing strategy was introduced that exploits the capability of the current GPS system, however, the tests are focused on its stand-alone, unaided, single-frequency, single-epoch performance, as this is the most challenging case for ambiguity resolution. A stronger model (larger number of observations, lower observation noise) will improve the performance of the developed approach in terms of the probability of correctly fixing the ambiguities.
In the near future, a GNSS multi-constellation will become available providing a large number of visible satellites to the user on and above the Earth. With multi-frequency, multi-constellation (modernized GPS, Galileo, etc.) spaceborne GNSS receivers, which are expected to become more common in the near future, an instantaneous kinematic approach for relative navigation over short baselines could become feasible.

6.2 Attitude Determination

Multiple GNSS antennas mounted on one platform may be used to determine the attitude of the platform as well. As was concluded in chapter 4 in terms of accuracy not much room for improvement is expected in GNSS attitude determination, as the theoretical limit has been reached by the available techniques. However, for ambiguity resolution still a number of open challenges remain. Ideally, one would like to have an ambiguity resolution method with a high probability of correctly fixing the ambiguities even when a limited number of observations is available (weak models) which could work instantaneously, eliminating the need for a dynamics model, and is computational efficient. In this thesis such a method was developed based on a constrained extension of the popular LAMBDA method, known as the Multivariate Constrained (MC-) LAMBDA method.
The MC-LAMBDA method is a nontrivial modification of the standard LAMBDA method. In contrast to existing methods that make use of the known baseline length, the MC-LAMBDA method does full justice to the given information by fully integrating the nonlinear baseline constraint into the ambiguity objective function. As a result, the a priori information receives a proper weighting in the ambiguity objective function, thus leading to higher success rates.
The method was tested, using simulated as well as actual GPS data. The simulations cover a large number of different measurement scenarios, where the impact of measurement precision and receiver-satellite geometry was analysed.

The presented field tests, with receivers of different manufacturers and type, cover static land experiments, and dynamic experiments, a low-dynamics vessel experiment, a high-dynamics aircraft, a Balloon-based Operation Vehicle and (hardware-in-the-loop simulated) spacecraft. All these tests show consistent results: the method's excellent single-frequency, single-epoch performance. The rigorous inclusion of the baseline length constraint into the ambiguity objective function shows dramatic improvements in the success rates and more reliable attitude estimations. The improved instantaneous ambiguity resolution will result in an even stronger reduction in time to fix (TTF). Additionally, it was demonstrated that this also resulted in an increase in robustness against multipath and receiver-satellite geometry changes.

6.3 Attitude bootstrapped relative positioning

GNSS-based precise relative positioning between spacecraft normally requires dual frequency observations, whereas attitude determination of the spacecraft can be performed precisely using only single frequency observations. The possibility was investigated to use multi-antenna data, not only for attitude determination, but also to improve the relative positioning between spacecraft in an integrated approach. The integrated method makes use of the following information to determine the relative position and orientation of a multi-antenna system with unconstrained and constrained baselines: the integerness of the ambiguities, the relationship between the ambiguities on the different baselines and the known geometry of the baselines at the platforms.
In order to obtain more insight into the multi-baseline problem with unconstrained baselines between platforms and constrained baselines on platforms, an uncoupled and two integrated strategies (coined the optimal, and vectorial bootstrapping or suboptimal approach) were investigated, both theoretically and experimentally. As was expected from the low correlation between baselines, the success rate of the optimal approach is similar to the vectorial bootstrapping approach. This was confirmed with simulated data for the single-epoch, single-frequency application. This is an important result as the vectorial bootstrapped solution is more computational efficient and in general could be sufficient for the type of applications discussed in this thesis.
In the bootstrapping approach, the outcome of the attitude determination problem was applied in the ambiguity constrained solution on the unconstrained baseline between the platforms. In this way the solution for the unconstrained baseline is bootstrapped from either the solutions of single baselines based on vectorial C-LAMBDA or the MC-LAMBDA solution of each platform in what is called vectorial or multivariate bootstrapped relative positioning respectively. The theoretical improvement for the unconstrained baseline is the same for the multivariate bootstrapping approach as the vectorial bootstrapping approach. As the multivariate bootstrapping approach is a stronger model by applying information on the geometry of the constrained baselines, the success rate of this approach is higher and this will also result in a better performance on the unconstrained baseline. The difference is profound for the weaker models and absent for the stronger models and thus for the latter we observe, as expected from the developed model, that both the approaches have the same performance.
The theoretical improvement achievable for the unconstrained baseline between the plat-

forms as a function of the number of antennas on each platform was shown, both for ambiguity resolution and accuracy of the baseline solution. The obtained mathematical relationship between the achievable improvement and the number of antennas was verified by software based and hardware-in-the-loop simulations.
In simulations the single epoch, single frequency success rates were analyzed as the most challenging application and the difference in performance for single epoch solutions, is a good indication of the strength of the underlying models. For these simulations we used mission parameters of the European PROBA-3 and the Australian Garada mission.
It was demonstrated that the solution cannot only enhance single frequency relative positioning but can be applied to improve the multi-frequency relative positioning solution as well.
The rigorous inclusion of multiple antennas into the ambiguity objective function shows dramatic improvements in the success rates on the in-between baseline. The higher success rate on the unconstrained baseline between the platforms comes without extra computational load as the constrained baseline(s) problem has to be solved for attitude determination and this information can be applied for relative positioning. The improved instantaneous ambiguity resolution will result in an even stronger reduction in time to fix (TTF). Additional benefits of the method is an improved robustness against multipath and the improved precision of the baseline estimation.

6.4 Recommendations for future work

With the LAMBDA method it is known that it achieves the maximum probability of obtaining the correct ambiguities. It is believed, in analogy with the standard LAMBDA method, that it will be difficult to devise a method that, with the same information, is capable of achieving higher success rates than MC-LAMBDA. Further improvements on the speediness of the method are, however, possible. In addition, further research is needed so as to be able to describe the probabilistic properties of the ambiguity-resolved parameters of the GNSS compass model, this in analogy with the existing theory of the unconstrained GNSS model.
MC-LAMBDA is an efficient method for solving the constrained integer least squares problem, suitable for application such as attitude, attitude bootstrapped relative positioning and GNSS performance analysis (all described in this thesis, the latter in appendix F), but also for other applications. One example is array-aided Precise Point Positioning (A-PPP). A-PPP is a measurement concept that uses GNSS data, from multiple antennas in an array of known geometry, to realize improved GNSS parameter estimation (position, attitude, time and atmospheric delays) (Teunissen, 2012).
Another example is the multi-antenna RF-based navigation instrument such as the Formation Flying Radio Frequency sensor (FFRF) on the PRISMA mission. For this type of application, integer ambiguity resolution is challenging as only a limited number of observations are available with very weak geometry (i.e. only along the line-of-sight between the spacecraft). An attitude bootstrapping approach as presented in this thesis will result in a much stronger model and thus higher (instantaneous) probabilities of correct integer estimation and shorter TTF.

Simulation and field experiments

A

A.1 Simulations, observation accuracy, number of GNSS satellites and baselines

In order to investigate the performance of the proposed approaches, the empirical success rates are analysed using simulated data. Table A.1 summarizes the conditions of the simulations. Utilizing the VISUAL software (Verhagen, 2006), based on the location of the receivers and an actual GNSS constellation, the design matrices of the model are calculated. In order to obtain good approximations, the number of samples must be sufficiently large (Teunissen, 1998a). Assuming different levels of noise on the undifferenced phase (from 1 mm to 3 mm) and undifferenced code (from 5 cm to 90 cm) data and keeping the same GNSS satellite geometry, a set of 10^5 data was generated. The subsets of GNSS satellites were selected, varying between 5 and 12, based on elevation angles.

Table A.1: Software simulation specification

Date and time	22 Jan 2008 00:00
GPS week	439
Scenario (Total number of constrained baselines at the two platforms: #C)	Quadruple (2), Hextuple (4) and Octuple (6) antenna configuration
Frequency	L1/E1
Number of Satellites	5 - 6 - 7 - 8 - 9 - 10 - 11 - 12
Undifferenced code noise σ_p [cm]	90 - 60 - 45 - 30 - 15 - 5
Undifferenced phase noise σ_ϕ [mm]	3 - 1
Baseline length $\|b_i^1\| = \|b_i^2\| = \|b_i^3\| = l_i$	2.0 m
$\|b^{12}\|$	150.0 m
Samples	10^5

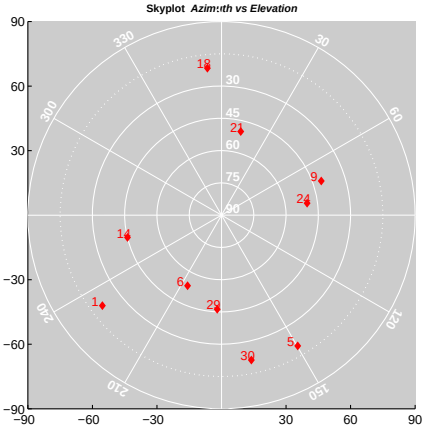
A.2 Simulations, influence of geometry

In order to investigate the influence of geometry on the proposed approaches, empirical success rate are analysed using a simulation in which the number of antennas at each

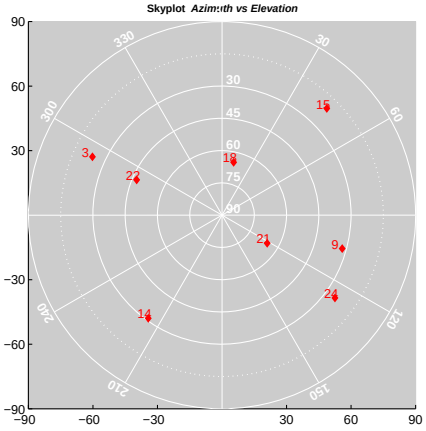
platform and the undifferenced code and carrier phase noise is kept constant, but the user spacecraft is moving through its orbit. Table A.2 summarizes the conditions of this simulation. The orbit is visualized in Fig. A.16(a), the same orbit is also applied in the hardware-in-the-loop simulation described in Appendix A.8. The setup of the experiment is shown in Fig. 5.8. The geometry of the GNSS satellites is shown in Fig. A.1 and A.2.

Table A.2: Software simulation specification

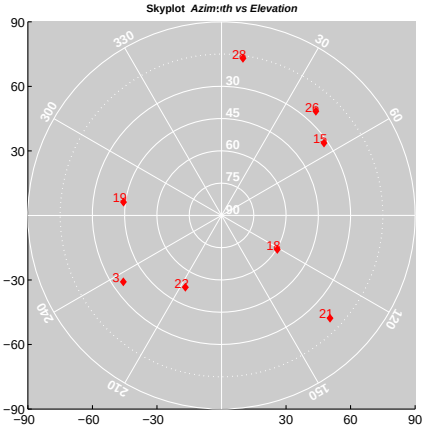
Date and time	22 Jan 2008 00:00
GPS week	439
Simulation duration	One orbital period
Scenario (Total number of constrained baselines at the two platforms: #C)	Hextuple (4) antenna configuration
Frequency	L1/E1
Number of Satellites	All visible with mask angle of 15°
Undifferenced code noise σ_p [cm]	30
Undifferenced phase noise σ_ϕ [mm]	3
Baseline length $\|b_i^1\| = \|b_i^2\| = l_i$	2.0 m
$\|b^{12}\|$	150.0 m
Samples	10^5
Orbital Period	$\pm$ 1.6 hours
Semi major axis (altitude)	7,058.14 (680.14) km
Inclination	98.0443°
Right ascension	-90.046°
Eccentricity	0
Mean anomaly at start of simulation	0°
Argument of perigee	0 °



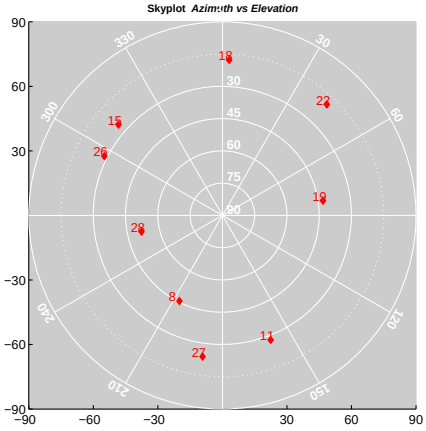
(a) Simulation epoch: 0h00m



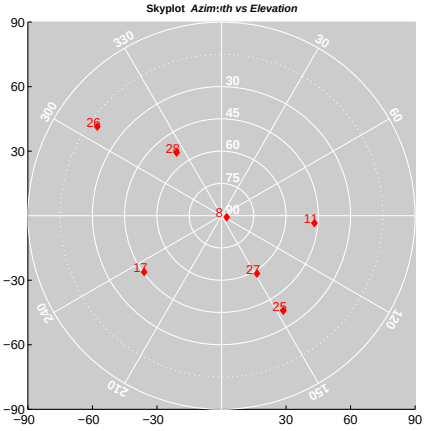
(b) Simulation epoch: 0h10m



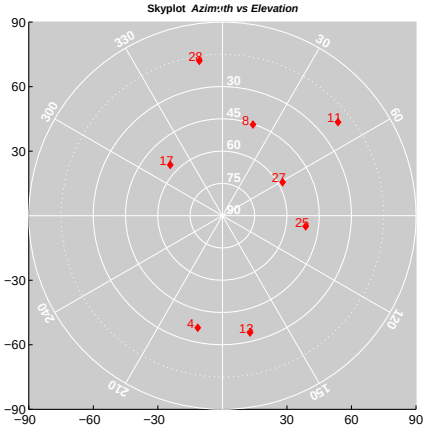
(c) Simulation epoch: 0h20m



(d) Simulation epoch: 0h30m

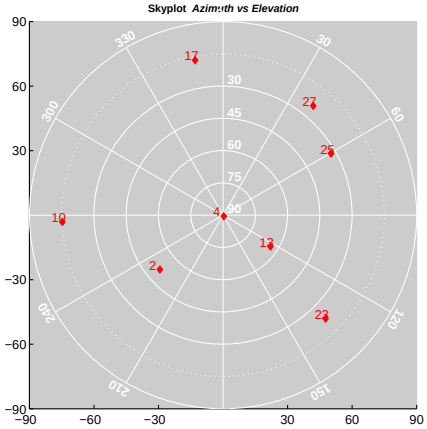


(e) Simulation epoch: 0h40m

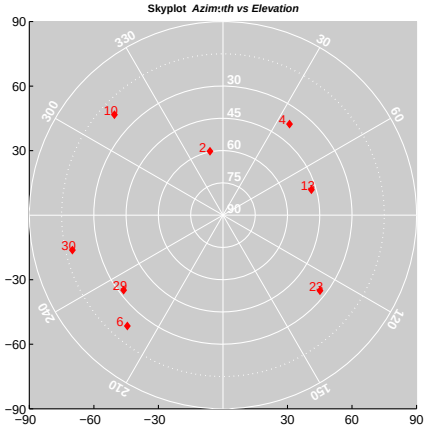


(f) Simulation epoch: 0h50m

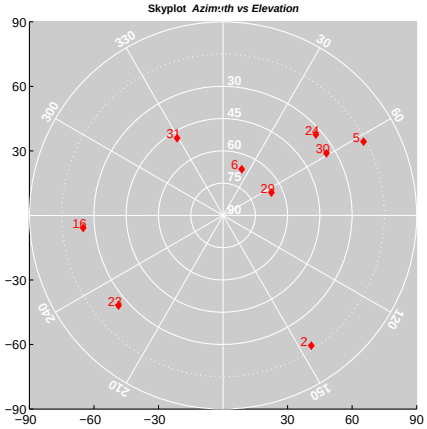
Figure A.1: Skyplots at different positions for the Garada spacecraft



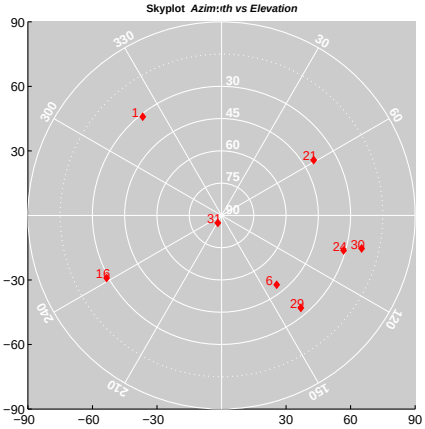
(a) Simulation epoch: 1h00m



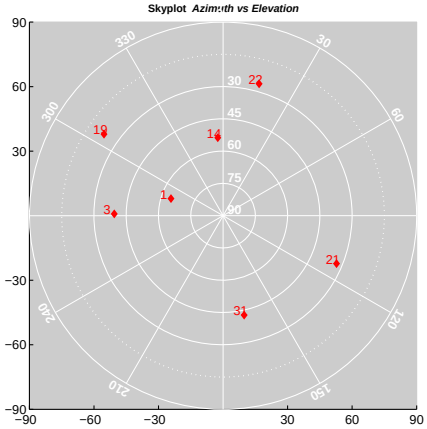
(b) Simulation epoch: 1h10m



(c) Simulation epoch: 1h20m



(d) Simulation epoch: 1h30m



(e) Simulation epoch: 1h40m

Figure A.2: Skyplots at different positions for the Garada spacecraft

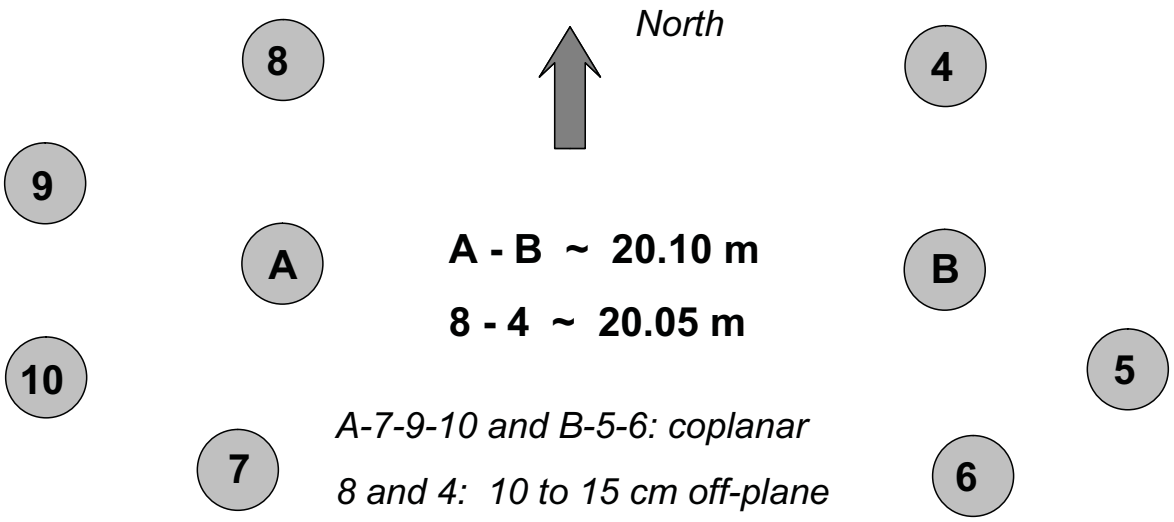


Figure A.3: Experimental set-up for the multi-antenna experiment



Figure A.4: Multi-baseline Experiment in September 2010

A.3 Static Experiment: Multi-Antenna experiment (MAx)

On 6th of September 2010, data was collected from nine Trimble R7 receivers. Raw data was logged at 10 Hz, but will be processed at 1 Hz. Each receiver has its own antenna and was placed in one of two groups: each representing a platform. The setup itself is shown in Fig. A.3 where letters/numbers indicate the different receivers/antenna combinations. Fig. A.4 shows the setup of the experiment at the end of the A4 freeway in the south-west of Delft. A and B are the master receivers/antennas, and these are place roughly in the same plane as receiver 7, 9, 10, and 5, 6, respectively. Antennas 4 and 8 are deliberately placed out of this plane.
Of these receivers, receiver 4 till 10 were connected to a Trimble Zephyr L1/L2 antenna, A and B were connected to a Trimble Zephyr Geodetic L1/L2 antenna. Data collected from 8h30 till 10h is analyzed in sections 4.5 and 5.5.
Table A.3 shows the GPS satellites applied in the different subgroups. Fig. A.5 shows the Skyplots of these GPS satellites.
Figures A.6 till A.7 show the multipath combination for receiver 10 and the SNR values. In Figures A.8 till A.9, the single difference code and carrier phase residuals are shown calculated using the procedure described in appendix F.

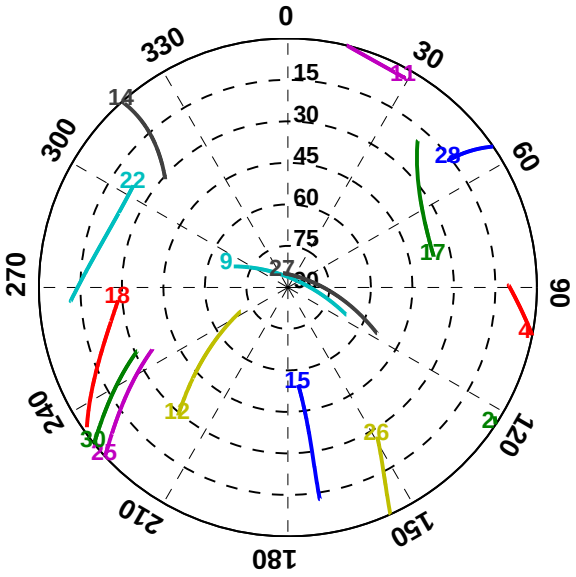


Figure A.5: Skyplot for the entire duration of the applied data collected at the multi-antenna experiment

Table A.3: PRN's of the used GPS satellites in the different subgroups

5	9- 12- 15- 17- 27
6	12- 15- 18 (replaced by 14 @2878)- 22- 28(replaced by 25 @1096) - 26 (replaced by 30 @2387)
7	12- 15- 17- 18 (replaced by 14 @2878)- 22- 28(replaced by 25 @1096) - 26 (replaced by 30 @2387)
8	9- 12- 15- 17- 18 (replaced by 14 @2878)- 22- 28(replaced by 25 @1096) - 26(replaced by 30 @2387)
9	9- 12- 15- 17- 27- 18(replaced by 14 @2878)- 22- 28(replaced by 25 @1096) - 26(replaced by 30 @2387)

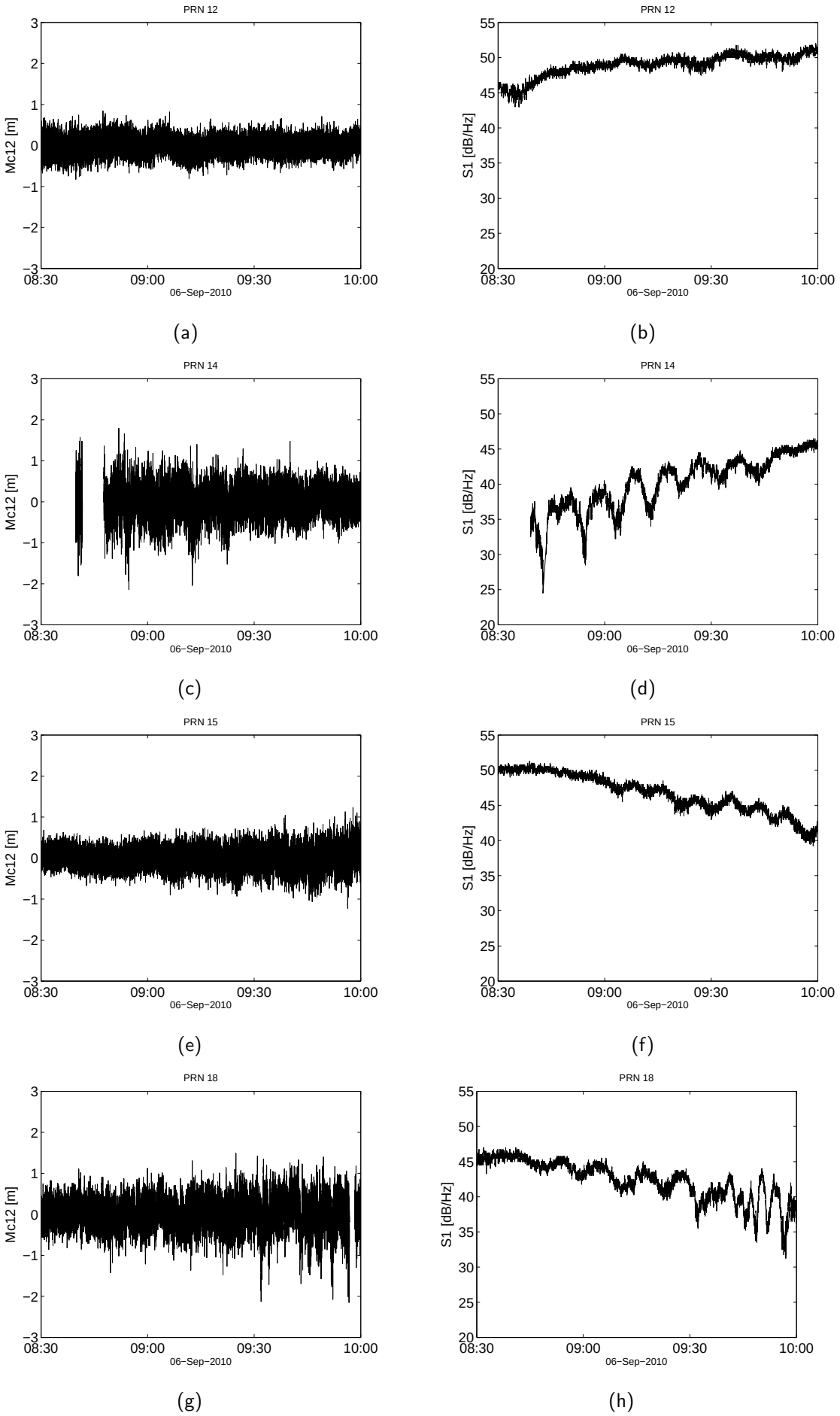


Figure A.6: Multipath combination and SNR for various channels of Receiver 10

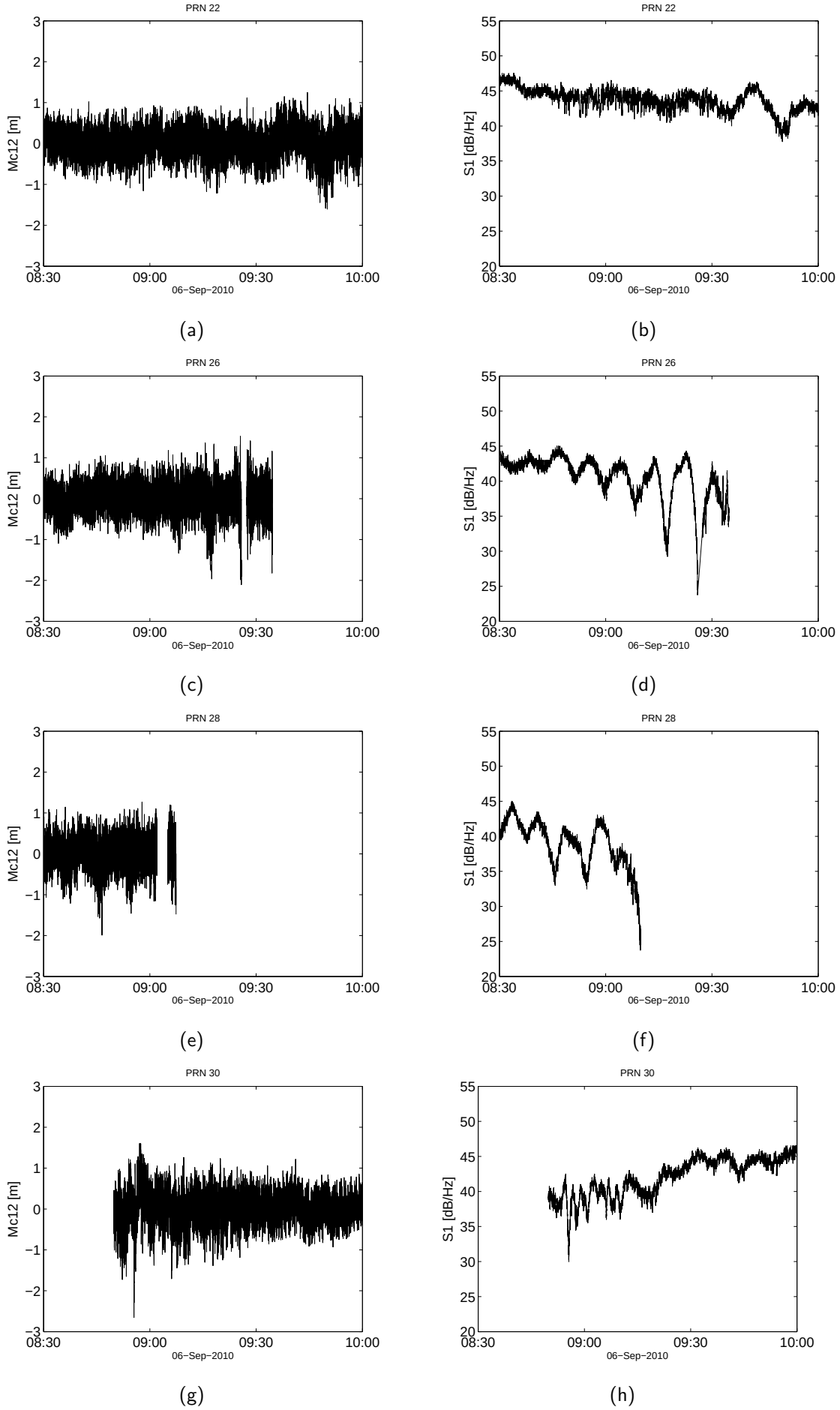


Figure A.7: Multipath combination and SNR for various channels of Receiver 10

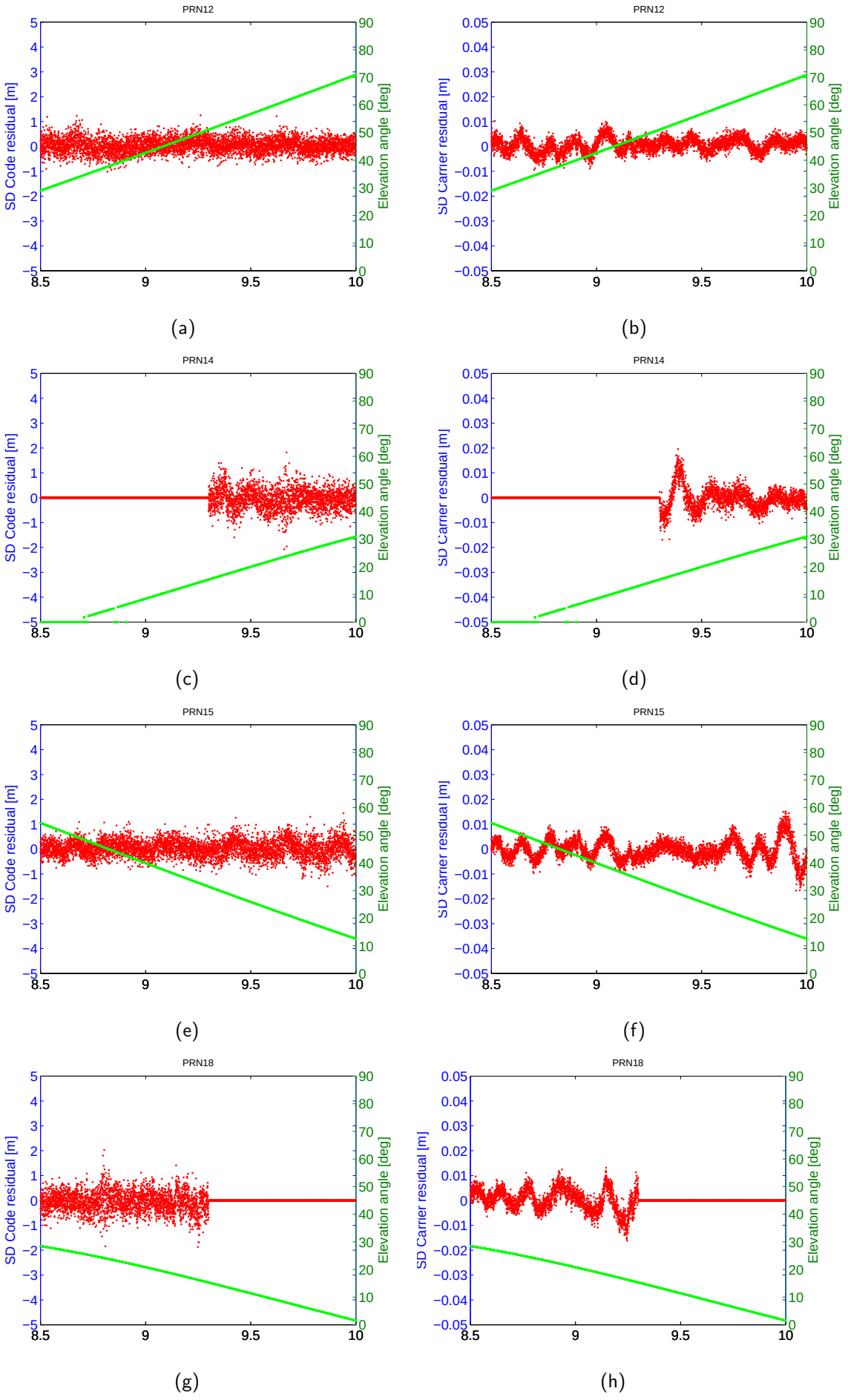


Figure A.8: Elevation angle, SD code and carrier residuals for the various channels at the baseline between receiver 7 and 10

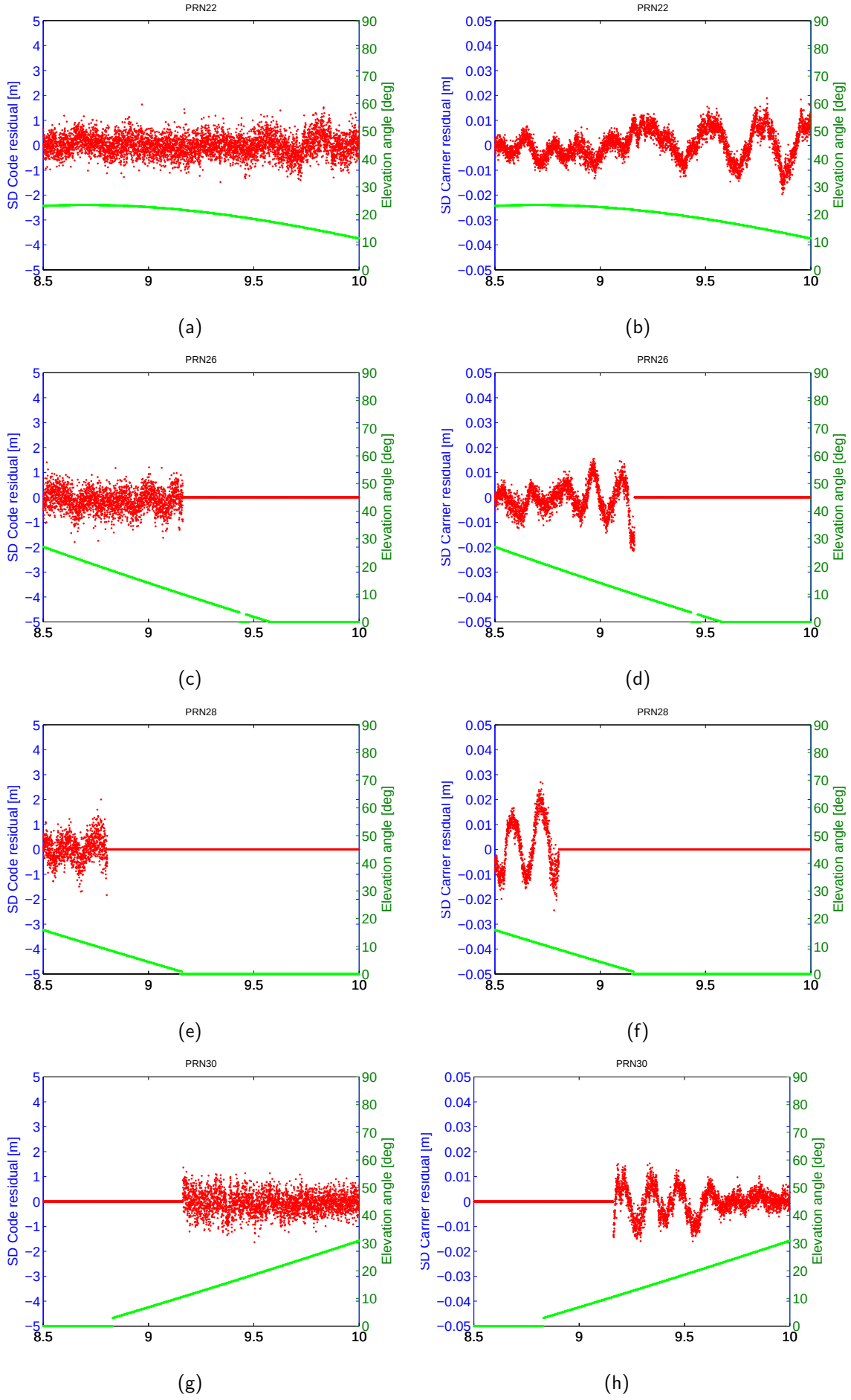


Figure A.9: Elevation angle, SD code and carrier residuals for the various channels at the baseline between receiver 7 and 10

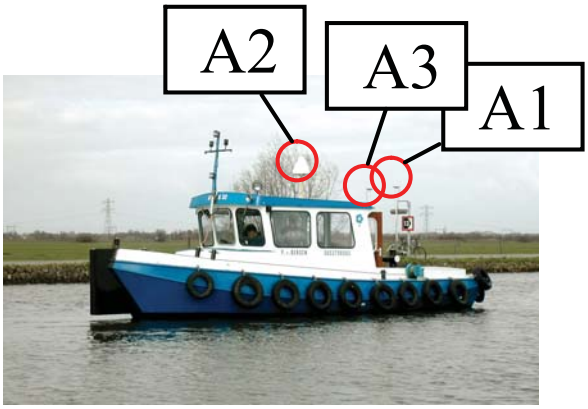


Figure A.10: Experimental set-up for the vessel experiment

A.4 Vessel Application: Schie 2003

In this experiment, the orientation of the baseline vector between vehicle is relatively slowly changing. This data was collected onboard a vessel on the 3rd of April 2003 (Kechine et al., 2003). Fig. A.10 shows the test setup of the experiment. For this experiment three dual frequency GPS receivers, two geodetic grade (Ashtech Z12 and Leica SR530 connected to antenna A2 and A1 in A.10 respectively) and one navigational type of receiver (NovAtel OEM3 connected to antenna A3 in fig A.10) were utilized. Data was collected at 1 Hz.

A.5 Aircraft Application:

A.5.1 Cessna 2005

The Cessna Citation II aircraft, owned and operated jointly by Delft University of Technology and National Aerospace Laboratory (NLR), was utilized in this experiment which was performed on the 2nd of June 2005. The multi-antenna GPS receiver (Septentrio PolaRx2@) collected data from three antennas. The main antenna on the fuselage was dual frequency (AIL DM-C L1-L2) and two slave antennas were single frequency (Sensor systems).

The local baseline matrix was:

$$F = \begin{bmatrix} 5.45 & -0.34 \\ 0 & 7.60 \end{bmatrix} [m] \tag{A.1}$$

A.5.2 Cessna 2007

The same Cessna Citation II aircraft was used in another experiment (Fig. A.11). This data was collected as part of the airborne gravimetry experiment GAIN (Alberts et al., 2010) on the 1st of November 2007. Compared with the vessel experiment described section A.4, which was performed about 4.5 years earlier, and the aircraft experiment from 2005, the

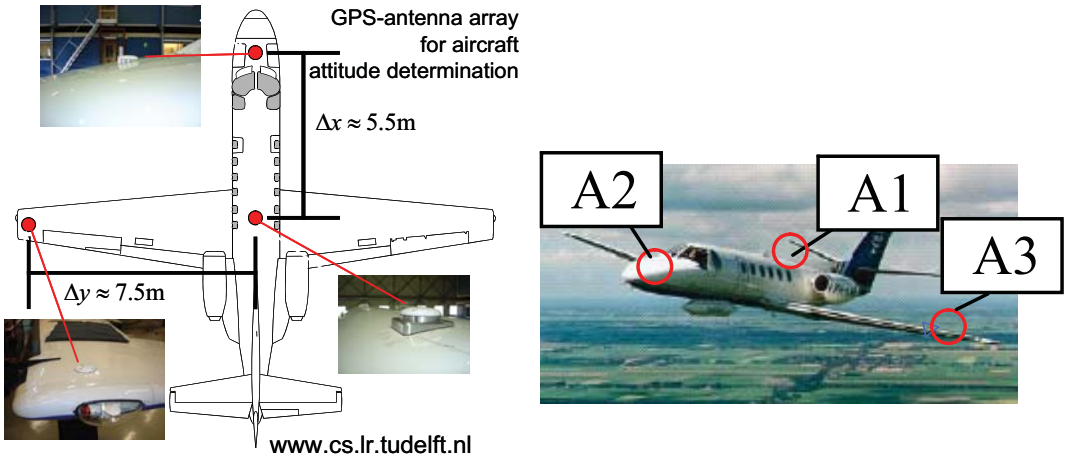


Figure A.11: Experimental Setup and antenna definition onboard airplane

GPS constellation is extended and therefore the average number of visible satellites has increased.
A multi-antenna navigational receiver (Septentrio PolaRx2@, for which the main antenna is A1 and aux antennas are A2 and A3 in Fig. A.11) were used onboard the aircraft. The local baseline matrix was:

$$F = \begin{bmatrix} 4.90 & -0.39 \\ 0 & 7.60 \end{bmatrix} [m] \tag{A.2}$$

Compared with the local baseline matrix of the 2005 experiment, the baseline between main and nose antenna is shorter due to the use of extension on the nose in the 2005 experiment.



Figure A.12: Take-off of BOV Experiment: at the left side BOV and Gondola hanging at the sliding launcher, on the right side the Balloon in front of the hanger

A.6 Aerospace application: Balloon-based Operation Vehicle

In this appendix a short introduction on the balloon-based experiments is provided. Scientific balloons have been launched in Japan by ISAS/JAXA since 1965, and JAXA currently has the world record for highest altitude reached with a balloon (53 km) (Yamagami et al., 2004). Recently balloon launches are performed from the Multipurpose Aviation Park (MAP) in Taiki, Hokkaido (Fuke et al., 2009). The balloons are launched using a so called *sliding launcher* (Fuke et al., 2009). The sliding launcher and the hanger of MAP are shown in Fig. A.12.

A.6.1 Balloon-based Operation Vehicle

JAXA has been developing a system to provide a long duration, good quality microgravity environment based on a capsule that can be released from a balloon (Hashimoto et al., 2008)(Hashimoto et al., 2009). The procedure of this micro gravity experiment is shown in Fig. A.13. The capsule, coined the Balloon-based Operation Vehicle (BOV), is launched with a balloon till an altitude of more than 40 kilometers where it is separated from the balloon. After separation, the BOV is in free fall until the parachute is released that makes a controlled landing in the sea possible. The BOV is recovered by helicopter and can be reused. The capsule has a double shell drag free structure and it is controlled not to collide with the inner shell. The flight capsule, shown hanging at the sliding launcher in Fig. A.12, consists of a capsule body (the outer shell), an experiment module (the inner shell) and a propulsion system. The inner shell is kept in free falling condition after release of the BOV from the balloon, and no disturbance force is working on this shell and the microgravity experiment it contains. The outer shell has a rocket shape to reduce aerodynamic disturbance. The distance between the outer and inner shell is measured using four laser range sensors. The propulsion system is controlling, besides the attitude, the outer shell not to collide with the inner shell. The propulsion system is using 16 dry-air gas-jet thrusters of 60 N each, controlling it not only in vertical direction but also in the horizontal direction to compensate disturbances from, for example, wind.
Flight experiments with the BOV were carried out in 2006 (BOV1) and in 2007 (BOV2),

Table A.4: Sensor specifications

Experiment	Abbreviation	Description
ADP	GAS	Geomagnetic Aspect Sensor
	SAS	Sun Aspect Sensor
	INC	Inclinometer
	gyro	Gyroscope
GPS	KF	Kalman filter based attitude provided by the receiver
	C-LAMBDA	C-LAMBDA based attitude, post-processed

when a fine microgravity environment was established successfully for more than 30 seconds (Hashimoto et al., 2008)(Sawai et al., 2008).

A.6.2 Attitude Determination and Control for Balloon Gondolas

Balloon experiments are performed for a large number of applications, some of which require attitude control. Observations from balloon-based telescopes are an example of an application in which stratospheric balloons have to carry payloads of hundreds of kilograms to an altitude of more than 30 kilometers to be reasonable free of atmospheric disturbances. Moreover in this application, the requirement for the control of the azimuth angle is within 0.1 degrees.
JAXA is developing an Attitude Determination Package (ADP, see Table A.4) containing a Sun Aspect Sensor (SAS), a Geomagnetic Aspect Sensor (GAS), Inclinometer, and gyro for a future version of the Balloon-based Operation Vehicle. The SAS determines the attitude with a resolution of one degree around one axis and ADP has four of these sensors pointing in different directions. Inherently this type of sensor can only provide attitude information if the sun is within the field of view of the sensor. The GAS determines also one axis attitude. 50ppm is the resolution of magnetic flux density which is measured by the GAS and applied to obtain an attitude estimate. The attitude determination accuracy of the GAS is 1.5 degrees with dynamic bias compensation. The Inclinometer determines a two axis attitude with a resolution of 0.2 degrees.

A.6.3 Background GPS Experiment

Delft University of Technology was involved in a precise attitude determination experiment onboard the gondola of the balloon. Not only the BOV, but also the gondola is a challenging environment, because of the rather rapidly varying attitude (due to wind and, especially at take-off and separation, rotation) and high altitude.
For a GPS experiment, the altitude of around 40 km is interesting as not many experiments have been performed at this height, which is higher than the altitude reachable by an aircraft but below Low Earth Orbits for spacecraft.
An altitude of about 40 km is a harsh environment for electrical devices because the pressure is about 1/1000 atm and the temperature ranges from -60 deg to 0 degrees Celsius.

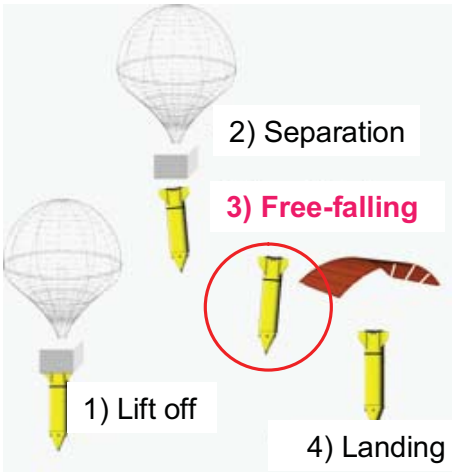


Figure A.13: Procedure of the micro gravity experiment

Furthermore the antennas are placed under the balloon, which will affect the GPS signals. The GPS receivers on the third flight of the BOV in 2008 were of a navigational type of receiver, not especially adjusted for such an experiment. For the fourth flight in 2009, an Septentrio PolaRx2@ (Septentrio, 2007) was used, for which the altitude restrictions were removed. This receiver has three RF inputs that can be connected to three antennas. In this experiment three Aero antennas from Sensor Systems Inc were used. Hence, the GPS experiment was using the same type of receiver as the aircraft experiment described in sections A.5.1 and A.5.2.

A.6.4 Initial Flights performed in 2008

In September 2008, we performed a test for a new the Attitude Determination Package (containing a SAS, a GAS, Inclinometer, and gyro) for a future version of the BOV and a GPS system containing two navigational GPS receivers (Buist et al., 2008)(Shimizu et al., 2009). The purpose of this flight was to test the equipment on the gondola without launching the BOV. By this test, nominal performance of some of the sensors in the real environment was confirmed.
The data from the single baseline is used to determine the pointing direction of the gondola, an application referred to as the GNSS compass (see section 4.1.1). The data was collected on the single baseline with two dual frequency GPS receivers. The receivers are controlled by, and the data stored on a ARM-linux board over a RS232 connection. The receivers and the controller are stored in a water proof container (Fig. A.14).
Also the antennas are sealed in waterproof bags. The location of the two GPS antennas on the gondola is shown in Fig. A.14. The baseline length is 1.95 [m].
Both receivers have their own clocks, so observations were not synchronized. The flight trajectory (altitude) of this flight is shown in the right side of Fig. A.14. This is a typical flight profile for the balloon applications from JAXA. The flight takes about three hours and reaches an altitude of more than 40 kilometer. At the end of the flight, there is a parachute guided fall over 40 kilometers to sea level which takes about 30 minutes. In this experiment, we could confirm nominal operation of some of the sensors and reception

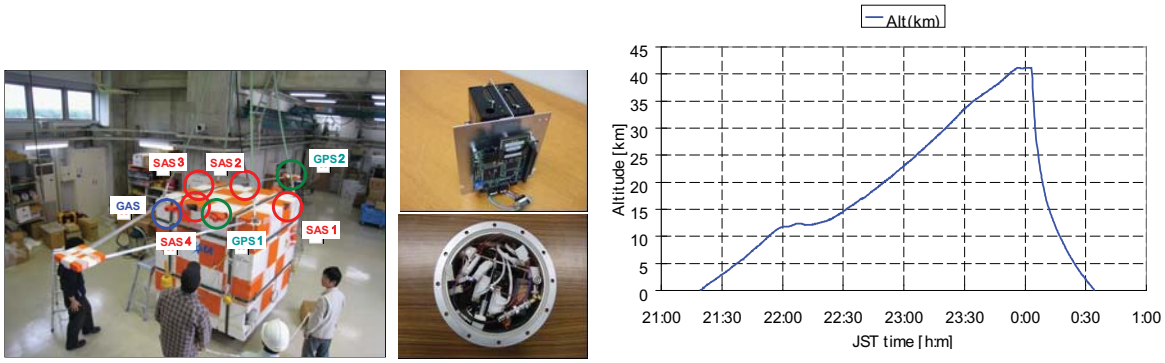


Figure A.14: Experiment single baseline in September 2008

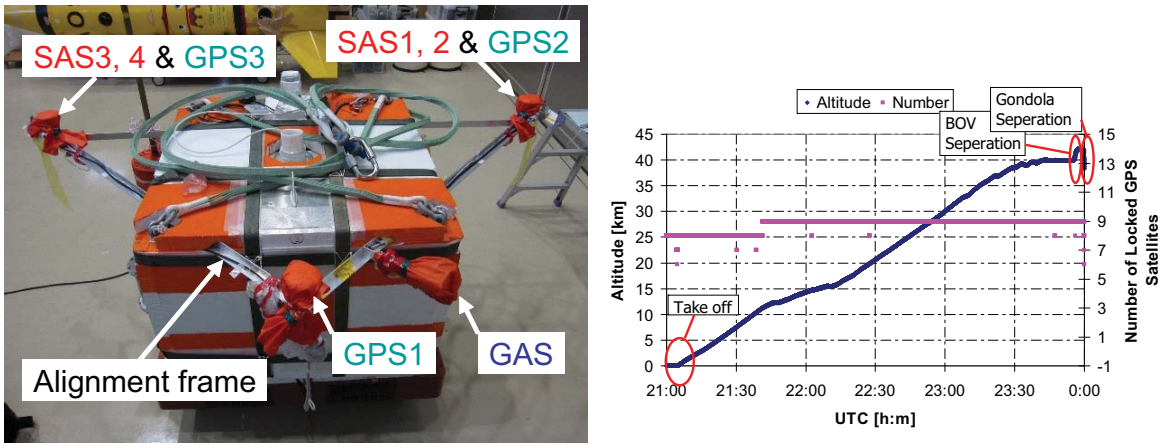


Figure A.15: Experiments full attitude in May 2009, Flight trajectory (Altitude)

of the GPS signals on the Gondola under the large balloon. For a more detailed discussion of this experiment, see (Shimizu et al., 2009).

A.6.5 Gondola Experimental Flight performed in 2009

In May 2009, the fourth flight of the BOV was performed. The GPS receiver with three antennas and the other attitude sensors were placed on the Gondola as shown in Fig. A.15. All the sensors were placed on an alignment frame for stiffness.

The local baseline matrix was:

$$F = \begin{bmatrix} \sqrt{2} & 0 \\ 0 & \sqrt{2} \end{bmatrix} [m] \tag{A.3}$$

Table A.5: Orbit specification for the Formation Flying spacecraft

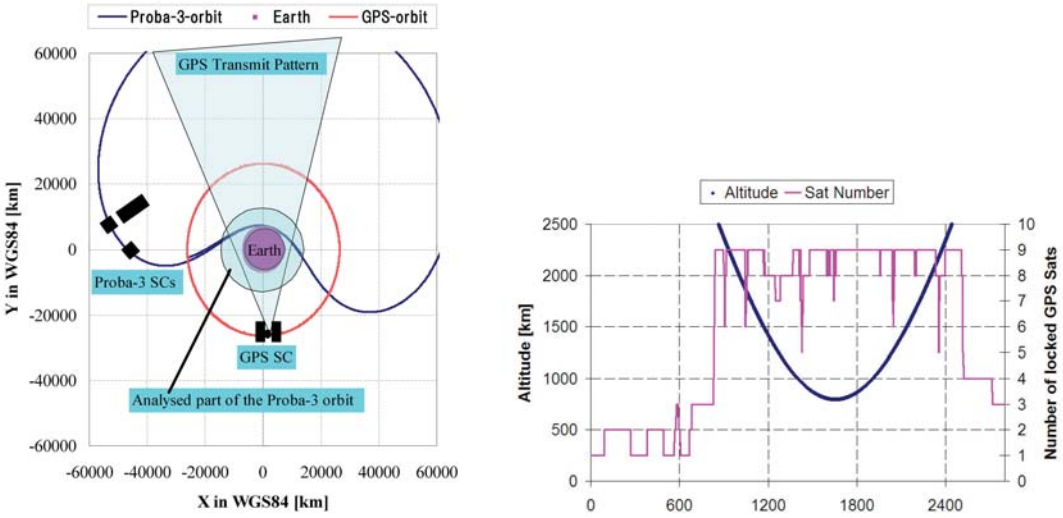
Orbital Period	$\pm$ 24.1 hours
Apogee (altitude)	77,578 (71,200) km
Perigee (altitude)	7,178 (800) km
Inclination	17.8°
Mean Anomaly at start of simulation	352°
Nominal ISD	0.150 km

A.7 Satellite Formation Flying: PROBA-3

In this appendix an introduction on the hardware-in-the-loop tests using the PROBA-3 scenario is provided. The tests were performed at the navigational laboratory of ESTEC, ESA in the Netherlands. In the formation flying experiment simulating two spacecraft, two PolaRx2@ receivers (Leyssens and Markgraf, 2005) were utilized. Both satellites have, in addition to the master antenna, two single frequency auxiliary antennas. This type of receiver is the same as applied in the aircraft experiments described in sections A.5.1 and A.5.2 and the balloon experiment of section A.6.
A scenario was simulated with the orbital parameters of the PROBA-3 mission as shown in Table A.5 and a nominal inter-satellite distance (ISD) of 150 meter. For the PROBA-3 scenario only the part of orbit where the satellites are below the GPS constellation was simulated (see Fig. A.16(a)), as the PolaRx2@ receivers are not modified for an orbit higher than the GPS constellation. According to (Manzano-Jurado et al., 2008), this matches well with the real mission requirements as the relative GPS equipment will be used during the period where the satellites are below 5000 km. The velocity of the satellites passing through the perigee is about 10 km/s (≈40.000 km/hr).
In Fig. A.17 the simulation set-up at the ESTEC navigation laboratory is shown. It consisted of one Spirent GPS simulator (4760) with three radio frequency outputs and two Septentrio Polarx2@ receivers, adjusted to acquire and track the GPS signals in a LEO environment. More information about the test set-up can be found in (Manzano-Jurado et al., 2008).

The local baseline matrix applied for both platforms is:

$$F^j = \begin{bmatrix} 1 & 0 \\ 0 & 1 \end{bmatrix} [m] \tag{A.4}$$



(a) Orbits of PROBA-3 and GPS SC

(b) Number of locked GPS SC and altitude vs. simulation time

Figure A.16: PROBA-3 mission [SC: spacecraft]



Figure A.17: Spirent GPS Simulator and Septentrio PolaRx2 Receivers applied in the PROBA-3 experiment

A.8 Satellite Formation Flying: Garada

For the Garada mission, a bistatic Synthetic-aperture radar (SAR) mission is under consideration consisting of a constellation of formation flying satellites with 3 or 4 satellites flying in each formation. Bistatic is the name given to a radar system which comprises a transmitter (Tx) and receiver (Rx) which are separated by a distance that is comparable to the expected target distance. Conversely, a radar in which the transmitter and receiver are collocated is called a monostatic radar. SAR is a form of radar using relative motion, between an antenna and its target region, to provide distinctive long-term coherent-signal variations.

In the proposed Garada mission, two observations are made from the same terrestrial area with a time separation (typically in the order of 50 ms (Romeiser et al., 2002)) and processed to determine the coherence between them. *Good* coherence will indicated stable areas, whereas *poor* coherence will indicate less stable areas such as water. The motion of water (due to wind, current, etc) can be observed if the time interval between the observations is long enough. The Garada system could in this way distinguish between flooded and non-flooded areas, enabling flood detection.

The required time separation is so short that two monostatic SAR payloads would interference with each other, therefore a bistatic SAR configuration is proposed, whereby one transmitter transmits the radar signal and two receivers separated along track acquire the reflected signal. The transmitter could be either placed on the same spacecraft as one of the receivers or on a separate spacecraft. The baseline to be estimated is between the two receiving spacecraft, therefore the actual implementation using two (one Tx/Rx and one Rx) or three spacecraft (one Tx, two Rx) does not change the requirement for relative positioning.

A requirement for rapid identification of flooded areas results in a solution with a constellation of spacecraft, where the revisit time determines the number of spacecraft required. The proposed SAR technique requires a formation flying concept.

In Fig. A.18 the red dot, *Platform 1*, represents the transmitting spacecraft and the two blue dots, *2* and *3*, the receiving spacecraft. The distance (b^{12}) between the transmitter and receiver spacecraft is about 80-100 km. The baseline between the two receiving spacecraft (b^{23}) has a 0.5-1 km separation along track and is to be estimated by GNSS. In total there might be 15-30 spacecraft sets (so times 3 is the total number of satellites of the mission).

In the hardware-in-the-loop experiment, the NamuruV2Rx receiver (Grillenberger et al., 2008) was connected to a Spirent GSS6560 simulator simulating GPS signals. The simulated scenario consists of two receiving spacecraft and is based on orbital parameters of a LEO satellite as shown in Table A.6. The tests were conducted at University of New South Wales (UNSW). It has to be mentioned that although the hardware is the same, the firmware used with the Namuru receiver at UNSW and DLR is different.

In the analysis described in chapter 3 till 5, data from the same receiver is used, collected in different runs of the same simulation. The clock errors obtained as part of absolute positioning are shown in Fig. A.19 for the receivers forming baseline 1 and 3. The figures contain the clock error of both receivers and the difference between the two. As can be seen in these figures, the clock behavior is the same (as expected as all data is collected with the same receiver) but the start time varies. The local baseline matrix applied for

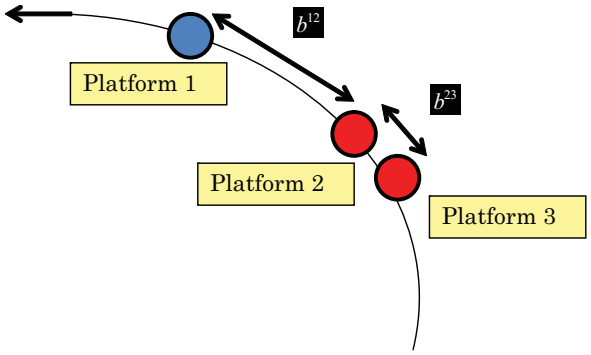


Figure A.18: Garada mission

Table A.6: Orbit specification for the simulated Garada platforms

Orbital Period	$\pm$ 1.6 hours
Semi major axis (altitude)	7,058.14 (680.14) km
Inclination	98.0443°
Right ascension	-90.046°
Eccentricity	0
Mean anomaly at start of simulation	0°
Argument of perigee	0 °
Nominal ISD	0.5 km

both platforms is:

$$F^j = \begin{bmatrix} 1 & 0 \\ 0 & 1 \end{bmatrix} [m] \tag{A.5}$$

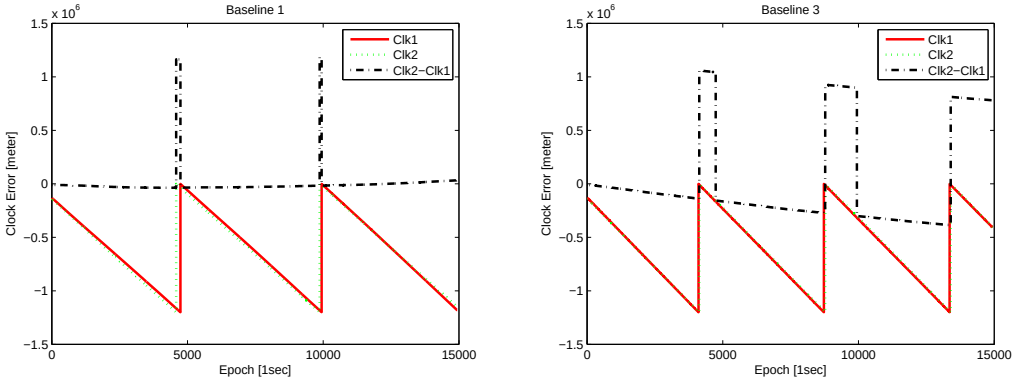


Figure A.19: Clock error for the receivers forming baseline 1 and 3 (Garada)

Orbits of GNSS Satellites

B

B.1 $r(t), \dot{r}(t), \ddot{r}(t)$ in ECEF WGS-84

We will follow the steps described in (GPS-ICD-200, 1993) and the derivations from (de Jonge, 1998).

Corrected mean motion, Time from ephemeris reference epoch, and Mean anomaly:

$$\begin{aligned} n &= \sqrt{\frac{\mu}{A^3}} + \Delta n \\ t_k &= t - t_{oe} \\ M_k &= M_0 + n t_k \end{aligned} \tag{B.1}$$

Eccentric anomaly which is solved by iteration:

$$\begin{aligned} E_k &= M_k + e \sin E_k \\ \dot{E}_k &= \frac{n}{1 - e \cos E_k} \end{aligned} \tag{B.2}$$

True anomaly:

$$\begin{aligned} \nu_k &= \arctan \frac{\sqrt{1-e^2} \sin E_k}{\cos E_k - e} \\ \dot{\nu_k} &= \frac{\sqrt{1-e^2}\dot{E}_k}{1 - e \cos E_k} \\ \ddot{\nu_k} &= \frac{-2e\sqrt{1-e^2} \sin E_k}{(1 - e \cos E_k)^2} \dot{E}_k^2 \end{aligned} \tag{B.3}$$

Argument of latitude:

$$\phi_k = \nu_k + \omega \tag{B.4}$$

Argument of latitude correction for second harmonic perturbations:

$$\begin{aligned} \delta u_k &= C_{us} \sin 2\phi_k + C_{uc} \cos 2\phi_k \\ \dot{\delta} u_k &= 2\dot{\nu_k}(C_{us} \cos 2\phi_k - C_{uc} \sin 2\phi_k) \\ \ddot{\delta} u_k &= -4\dot{\nu_k}^2 C_{us} \sin 2\phi_k + C_{uc} \cos 2\phi_k + 2\ddot{\nu_k}(C_{us} \cos 2\phi_k - C_{uc} \sin 2\phi_k) \end{aligned} \tag{B.5}$$

Radius correction for second harmonic perturbations:

$$\begin{aligned}
\delta r_k &= C_{rs}\sin 2\phi_k + C_{rc}\cos 2\phi_k \\
\dot{\delta} r_k &= 2\dot{\nu}_k(C_{rs}\cos 2\phi_k - C_{rc}\sin 2\phi_k) \\
\ddot{\delta} r_k &= -4\dot{\nu}_k^2 C_{rs}\sin 2\phi_k + C_{rc}\cos 2\phi_k + 2\ddot{\nu}_k(C_{rs}\cos 2\phi_k - C_{rc}\sin 2\phi_k)
\end{aligned} \tag{B.6}$$

Inclination correction for second harmonic perturbations:

$$\begin{aligned}
\delta i_k &= C_{is}\sin 2\phi_k + C_{ic}\cos 2\phi_k \\
\dot{\delta} i_k &= 2\dot{\nu}_k(C_{is}\cos 2\phi_k - C_{ic}\sin 2\phi_k) \\
\ddot{\delta} i_k &= -4\dot{\nu}_k^2 C_{is}\sin 2\phi_k + C_{ic}\cos 2\phi_k + 2\ddot{\nu}_k(C_{is}\cos 2\phi_k - C_{ic}\sin 2\phi_k)
\end{aligned} \tag{B.7}$$

Corrected argument of latitude:

$$\begin{aligned}
u_k &= \phi_k + \delta u_k \\
\dot{u}_k &= \dot{\nu}_k + \dot{\delta} u_k \\
\ddot{u}_k &= \ddot{\nu}_k + \ddot{\delta} u_k
\end{aligned} \tag{B.8}$$

Corrected radius:

$$\begin{aligned}
r_k &= A(l - e\cos E_k) + \delta r_k \\
\dot{r}_k &= Ae\dot{E}_k \sin E_k + \dot{\delta} r_k \\
\ddot{r}_k &= \frac{(\cos E_k - e)}{1 - e\cos E_k} Ae\dot{E}_k^2 + \ddot{\delta} r_k
\end{aligned} \tag{B.9}$$

Corrected inclination:

$$\begin{aligned}
i_k &= i_0 + i_{dot} t_k + \delta i_k \\
\dot{i}_k &= i_{dot} + \dot{\delta} i_k \\
\ddot{i}_k &= \ddot{\delta} i_k
\end{aligned} \tag{B.10}$$

Satellite position in orbital plane:

$$\begin{aligned}
\begin{bmatrix} x_k' \\ y_k' \end{bmatrix} &= r_k \begin{bmatrix} \cos u_k \\ \sin u_k \end{bmatrix} \\
\begin{bmatrix} \dot{x}_k' \\ \dot{y}_k' \end{bmatrix} &= \dot{r}_k \begin{bmatrix} \cos u_k \\ \sin u_k \end{bmatrix} + r_k \dot{u}_k \begin{bmatrix} -\sin u_k \\ \cos u_k \end{bmatrix} \\
\begin{bmatrix} \ddot{x}_k' \\ \ddot{y}_k' \end{bmatrix} &= (\ddot{r}_k - r_k \dot{u}_k^2) \begin{bmatrix} \cos u_k \\ \sin u_k \end{bmatrix} + (2\dot{r}_k \dot{u}_k + r_k \ddot{u}_k) \begin{bmatrix} -\sin u_k \\ \cos u_k \end{bmatrix}
\end{aligned} \tag{B.11}$$

Corrected longitude of ascending node:

$$\begin{aligned}
\Omega_k &= \Omega_0 + (\dot{\Omega} - \dot{\Omega}_e) t_k - \dot{\Omega} t_{oe} \\
\dot{\Omega}_k &= \dot{\Omega} - \dot{\Omega}_e
\end{aligned} \tag{B.12}$$

Rotation matrix from orbital plane to ECEF:

$$
\begin{aligned}
R_k &= \begin{bmatrix} \cos\Omega_k & -\cos i_k \sin\Omega_k \\ \sin\Omega_k & \cos i_k \cos\Omega_k \\ 0 & \sin i_k \end{bmatrix} \\
\dot{R}_k &= \begin{bmatrix} -\dot{\Omega}_k \sin\Omega_k & -\dot{\Omega}_k \cos i_k \cos\Omega_k + \dot{i}_k \sin i_k \sin\Omega_k \\ \dot{\Omega}_k \cos\Omega_k & -\dot{\Omega}_k \cos i_k \sin\Omega_k - \dot{i}_k \sin i_k \cos\Omega_k \\ 0 & \dot{i}_k \cos i_k \end{bmatrix} \\
\ddot{R}_k &= \begin{bmatrix} -\dot{\Omega}_k^2 \cos\Omega_k & (\dot{\Omega}_k^2 + \dot{i}_k^2)\cos i_k \sin\Omega_k + 2\dot{\Omega}_k \dot{i}_k \sin i_k \cos\Omega_k + \ddot{i}_k \sin i_k \sin\Omega_k \\ -\dot{\Omega}_k^2 \sin\Omega_k & -(\dot{\Omega}_k^2 + \dot{i}_k^2)\cos i_k \cos\Omega_k + 2\dot{\Omega}_k \dot{i}_k \sin i_k \sin\Omega_k - \ddot{i}_k \sin i_k \cos\Omega_k \\ 0 & -i_k^2 \sin i_k + \dot{i}_k \cos i_k \end{bmatrix}
\end{aligned}
\tag{B.13}
$$

Satellite position, velocity and accelaration in ECEF coordinates:

$$
\begin{aligned}
\begin{bmatrix} x_k \\ y_k \\ z_k \end{bmatrix} &= R_k \begin{bmatrix} x_k' \\ y_k' \end{bmatrix} \\
\begin{bmatrix} \dot{x}_k \\ \dot{y}_k \\ \dot{z}_k \end{bmatrix} &= \dot{R}_k \begin{bmatrix} x_k' \\ y_k' \end{bmatrix} + R_k \begin{bmatrix} \dot{x}_k' \\ \dot{y}_k' \end{bmatrix} \\
\begin{bmatrix} \ddot{x}_k \\ \ddot{y}_k \\ \ddot{z}_k \end{bmatrix} &= \ddot{R}_k \begin{bmatrix} x_k' \\ y_k' \end{bmatrix} + 2\dot{R}_k \begin{bmatrix} \dot{x}_k' \\ \dot{y}_k' \end{bmatrix} + R_k \begin{bmatrix} \ddot{x}_k' \\ \ddot{y}_k' \end{bmatrix}
\end{aligned}
\tag{B.14}
$$

C Scaling Factor

C.1 Derivation of the Scaling Factor for the v-c Matrix

For convenience we introduce the $(i-1)$-vector q_{i-1} with $-\frac{1}{2}$ as the $(i-1)^{th}$ element and zeros otherwise (so $q_{i-1} = \left[0, \ldots, 0, -\frac{1}{2}\right]$). Here we develop the scaling factor for the v-c matrix if the unconstrained baseline is on one side constrained by one or more constrained baseline. The same discussion can be extended to the case with constrained baselines at both platforms. We will make use of the expression Eq. C.1 found in Appendix C for the inverse of the tridiagonal matrix.

Using this notation we can write the ith baseline conditioned on the ambiguity z_i and the previous baselines $b_I = \cup_{j=1}^{i-1} b_j$ as:

$$\begin{aligned}\hat{b}_i(z_i, b_I) &= \hat{b}_i(z_i) - q_{i-1} P_{i-1}^{-1} vec(\hat{B}(Z) - B) \\ &= \hat{b}_i(z_i) + \frac{1}{2}\left[0, \ldots, 0, 1\right] P_{i-1}^{-1} vec(\hat{B}(Z) - B)\end{aligned}$$

and the associated variance-covariance matrix as:

$$\begin{aligned}Q_{\hat{b}_i(z_i,b_I)\hat{b}_i(z_i,b_I)} &= Q_{\hat{b}(z)\hat{b}(z)} - q_{i-1} P_{i-1}^{-1} q_{i-1}^T Q_{\hat{b}(z)\hat{b}(z)} \\ &= Q_{\hat{b}(z)\hat{b}(z)} - \frac{1}{4}\left[0, \ldots, 0, 1\right] P_{i-1}^{-1} \left[0, \ldots, 0, 1\right]^T Q_{\hat{b}(z)\hat{b}(z)} \\ &= \frac{i+2}{2(i+1)} Q_{\hat{b}(z)\hat{b}(z)}\end{aligned}$$

So we observe that the conditional baseline can be calculated from the last column of matrix P_{i-1}^{-1} divided by 2 and scaling factor from 1 minus the last element of P_{i-1}^{-1} divided by 4.

C.2 Inverse of Tridiagonal Matrix P

The inverse of tridiagonal matrices is often found in applied linear algebra, as for example in applications as genetics, finite elements analysis, partial differential equations, signal

processing (Richard, 1978). The analytic expression of the inverse $R(= P^{-1})$ for the tridiagonal matrix P introduced in this paper was, as far as we know, first published in (Maruyama, 1977) as:

$$r_{ij} = \begin{cases} \frac{2j(N+1-i)}{N+1} & i \geq j \\ \frac{2i(N+1-j)}{N+1} & i < j \end{cases} \tag{C.1}$$

In (Maruyama, 1977) this solution was provided without a theoretical proof. In (Meurant, 1992) expression (C.1) was derived, as far as we know, for the first time. For completeness we include another direct proof of the expression in this appendix.

Proof

Consider the jth column of the inverse matrix $R = P^{-1}$:

$$\begin{bmatrix} 1 & -\frac{1}{2} & & & & & \\ -\frac{1}{2} & 1 & -\frac{1}{2} & & & & \\ & \ddots & \ddots & \ddots & & & \\ & & -\frac{1}{2} & 1 & -\frac{1}{2} & & \\ & & & \ddots & \ddots & \ddots & \\ & & & & -\frac{1}{2} & 1 & -\frac{1}{2} \\ & & & & & -\frac{1}{2} & 1 \end{bmatrix} \begin{bmatrix} r_{1,j} \\ r_{2,j} \\ \vdots \\ r_{j-1,j} \\ r_{j,j} \\ r_{j+1,j} \\ \vdots \\ r_{N+1,j} \end{bmatrix} = \begin{bmatrix} 0 \\ 0 \\ \vdots \\ 0 \\ 1 \\ 0 \\ \vdots \\ 0 \end{bmatrix}.$$

In the basis step we will show that this holds for $i = 1$. In the inductive step we will show that this holds for $i > j$, $i < j$ and $i = j$.

Basis step

When $i = 1$, the first equation is $r_{1,j} - \frac{1}{2}r_{2,j} = 0$ for which we have $r_{2,j} = 2r_{1,j}$ and Eq. C.1 holds.

Induction step

We assume that Eq. C.1 hold for all j on the interval $i > j \geq k - 1 > 1$. We have $-\frac{1}{2}r_{k-1,j} + r_{k,j} - \frac{1}{2}r_{k+1,j} = 0$ and if we fill in elements from Eq. C.1 we see that the equation holds for $i \geq j$. Similarly we can show then when $i < j$ the equation also holds. The last thing left is to determine $r_{j,j}$. From the jth equation we have $-\frac{1}{2}r_{j-1,j} + r_{j,j} - \frac{1}{2}r_{j+1,j} = 1$. With $r_{j-1,j} = \frac{2(j-1)(N+1-j)}{N+1}$, $r_{j,j} = \frac{2j(N+1-j)}{N+1}$ and $r_{j+1,j} = \frac{2j(N+1-(j+1))}{N+1}$, we can show that the equation holds.

Mathematics

D

D.1 vec Operator

The vec-operator is a linear transformation which transforms a matrix into a vector by stacking the columns of the matrix one underneath the other:
$vec(A) = (a_1^T, a_2^T, \ldots, a_N^T)$.
A property of the vec-operator applied in this contribution is:
$vec(ABC) = (C^T \otimes A)vec(B)$.

D.2 Kronecker product

The Kronecker product is defined, with $M = \left[m_{ij}\right]$, as (Magnus, 1988):

$$M \otimes N = \begin{bmatrix} m_{11}N & \ldots & m_{1q}N \\ \vdots & & \vdots \\ m_{p1}N & \ldots & m_{pq}N \end{bmatrix} \tag{D.1}$$

It has the following properties:

$$\begin{aligned} (M \otimes N)^T &= M^T \otimes N^T \\ (M \otimes N)^{-1} &= M^{-1} \otimes N^{-1} \\ (M_1 \otimes N_1)(M_2 \otimes N_2) &= M_1 M_2 \otimes N_1 N_2 \end{aligned} \tag{D.2}$$

D.3 Trigonometric functions

$$\begin{aligned}
\sec(x) &= \frac{1}{\cos(x)} \\
\frac{\partial \arccos(x)}{\partial x} &= -\frac{1}{\sqrt{1-x^2}} \\
\frac{\partial \sec(x)}{\partial x} &= \sec(x)\tan(x) \\
\frac{\partial \tan^2(x)}{\partial x} &= \sec^2(x)
\end{aligned} \tag{D.3}$$

D.4 Inverse of block matrices

$$\begin{aligned}
\begin{bmatrix} A & B \\ C & D \end{bmatrix}^{-1} &= \begin{bmatrix} A^{-1} + A^{-1}B(D - CA^{-1}B)^{-1}CA^{-1} & -A^{-1}B(D - CA^{-1}B)^{-1} \\ -(D - CA^{-1}B)^{-1}CA^{-1} & (D - CA^{-1}B)^{-1} \end{bmatrix} \\
&= \begin{bmatrix} (A - BA^{-1}C)^{-1} & -(A - BD^{-1}C)^{-1}BD^{-1} \\ -D^{-1}C(A - BD^{-1}C)^{-1} & D^{-1} + D^{-1}C(A - BD^{-1}C)^{-1}BD^{-1} \end{bmatrix}
\end{aligned} \tag{D.4}$$

Transformations

E

E.1 ECEF to ECI

Earth Centered Earth Fixed (ECEF) is a Cartesian coordinate system representing positions as an X, Y, and Z coordinate. The point (0,0,0) is defined as the center of the Earth. The x-axis intersects the sphere of the Earth at $0\,\mathrm{deg}$ latitude (Equator) and $0\,\mathrm{deg}$ longitude (Greenwich). This means that the ECEF frame rotates with the earth. The z-axis is pointing towards the north but it does not coincide exactly with the instantaneous Earth rotational axis, which phenomenon is known as polar motion.
Earth-centered inertial (ECI) coordinate frames also have their origins at the center of mass of the Earth, but are a non-rotating frame specifying its axes towards the direction of celestial objects. One commonly used ECI frame, referred to as J2000, is defined with the Earth's Mean Equator and Equinox at 12:00 Terrestrial Time on 1 January 2000. The x-axis is aligned with the mean equinox. The z-axis is aligned with the Earth's spin axis or celestial North Pole.
In order to transfer a position vector from the ECI to ECEF coordinate system, a rotation around the z-axis (Misra and Enge, 2001). For more information on these transformations, see (Teunissen and Kleusberg, 1998)(Montenbruck and Gill, 2000).

E.2 ECEF to ENU

ECEF (X,Y,Z) coordinates can be transformed to the East, North, Up (ENU) coordinates by two rotations:

$$\begin{bmatrix} E \\ N \\ U \end{bmatrix} = R_x(\frac{\pi}{2} - \varphi)R_z(\frac{\pi}{2} + \lambda) \begin{bmatrix} X \\ Y \\ Z \end{bmatrix} \tag{E.1}$$

where φ is the latitude and λ is the longitude and

$$R_x(\frac{\pi}{2} - \varphi)R_z(\frac{\pi}{2} + \lambda) = \begin{bmatrix} -\sin(\lambda) & \cos(\lambda) & 0 \\ -\cos(\lambda)\sin(\varphi) & -\sin(\lambda)\sin(\varphi) & \cos(\varphi) \\ \cos(\lambda)\cos(\varphi) & \sin(\lambda)\cos(\varphi) & \sin(\varphi) \end{bmatrix} \tag{E.2}$$

E.3 ECEF to Local Orbit

The transformation matrix to the Local Horizon frame is defined:

$$R_{ECI}^{LH} = \begin{bmatrix} \frac{\mathbf{r}_r \times \dot{\mathbf{r}}_r}{\|\mathbf{r}_r \times \dot{\mathbf{r}}_r\|} \times \frac{\mathbf{r}_r}{\|\mathbf{r}_r\|} \\ -\frac{\mathbf{r}_r \times \dot{\mathbf{r}}_r}{\|\mathbf{r}_r \times \dot{\mathbf{r}}_r\|} \\ -\frac{\mathbf{r}_r}{\|\mathbf{r}_r\|} \end{bmatrix} \tag{E.3}$$

The local nadir (Nadir) is the direction towards the Earth's center. The local horizon (Right) is defined by the outer product of the position and velocity vectors. The Forward direction is Along track the orbital plane. See also Fig. (E.1).

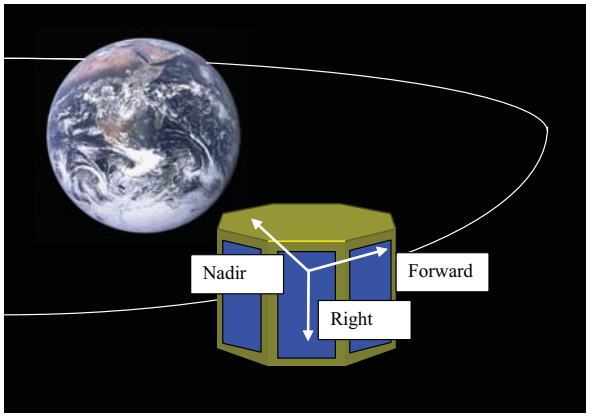


Figure E.1: Definition of Forward, Nadir and Right (FNR) coordinates Frame

E.4 Attitude representation: Euler

Euler angles (θ) are three angles to describe the orientation of a rigid body. These angles are often referred to as roll r, pitch p, yaw y. The Euler angles are easy to visualise, their disadvantage is that the trigonometric functions are relatively computationally demanding, and for certain orientations singularities might occur.

E.5 Attitude representation: quaternions

A quaternion $\overline{q}$ consist of four elements; a vector plus a scalar and it has to fulfill to following condition:

$$q_1^2 + q_2^2 + q_3^2 + q_4^2 = 1 \tag{E.4}$$

The use of quaternions has several advantages over the use of Euler angles. First of all they do not require the use of trigonometric functions making the calculations faster than Euler

angles. Secondly they do not have the singularities that might occur for certain rotations when Euler angles are applied. The main disadvantage of the use of quaternions is that there is no clear physical interpretation of the orientation.

E.6 Attitude rotation

Rotation matrices are square matrices, with real entries, which can be characterized as orthogonal matrices with determinant 1:

$$R^T = R^{-1}, det(R) = 1 \tag{E.5}$$

The three basic rotations are

$$R_x(\theta) = \begin{bmatrix} 1 & 0 & 0 \\ 0 & \cos(\theta) & \sin(\theta) \\ 0 & -\sin(\theta) & \cos(\theta) \end{bmatrix} \tag{E.6}$$

$$R_y(\theta) = \begin{bmatrix} \cos(\theta) & 0 & -\sin(\theta) \\ 0 & 1 & 0 \\ \sin(\theta) & 0 & \cos(\theta) \end{bmatrix} \tag{E.7}$$

$$R_z(\theta) = \begin{bmatrix} \cos(\theta) & \sin(\theta) & 0 \\ -\sin(\theta) & \cos(\theta) & 0 \\ 0 & 0 & 1 \end{bmatrix} \tag{E.8}$$

The combined matrix for three sequences of rotation is the product of the orthogonal matrices, for example:

$$R_{xyz} = R_z(y)R_y(p)R_x(r) \tag{E.9}$$

Test Procedure

F

The following 7 step procedure can be applied to evaluate noise characteristics of GNSS signals, receiver, etc. The first 3 steps are called preprocessing, step 4-7 form the analysis. The output of the preprocessing steps can be replaced by -for example- an *average* baseline vector calculated over all the correctly fixed epochs or the a-priori known baseline vector. For zero baseline analysis, the user could use $b = \begin{bmatrix} 0 & 0 & 0 \end{bmatrix}^T$. The default processing is epochwise pseudorange and carrier phase observation on a single frequency.

Preprocessing

1) First the float solution $\hat{z}$ and $\hat{b}$ is obtained from Eq. (3.40).
With this float solution ($\hat{z} \in \mathbb{R}^n, \hat{b} \in \mathbb{R}^3$), the solution of the linear system of observations becomes the squared norm of the least-squares DD residual vector:

$$\|y^{DD} - A\hat{z} - G\hat{b}\|^2_{Q_{yy}} = \|\hat{e}^{DD}\|^2_{Q_{yy}} \tag{F.1}$$

2) The vector of integer least-squares estimates of the ambiguities $\check{z}$ is solved using Eq. (3.43). where $\check{z}$ is the vector of integers that minimizes the term within the brackets. As we use the constraint that the solution of z has to be an integer ($\check{z} \in \mathbb{Z}^n, \check{b} = \hat{b}(\check{z}) \in \mathbb{R}^3$), the minimum solution becomes:

$$\|y^{DD} - A\check{z} - G\check{b}\|^2_{Q_{yy}} = \|\check{e}^{DD}\|^2_{Q_{yy}} = \|\hat{e}^{DD}\|^2_{Q_{yy}} + \|\hat{z} - \check{z}\|^2_{Q_{\hat{z}\hat{z}}} \tag{F.2}$$

where $\hat{e}^{DD} = y - A\hat{z} - G\hat{b}$ is the least-squares DD residual of the float solution $\hat{z}, \hat{b}$. The minimum of this equation is clearly equal to or larger than the float solution obtained in step 1.

Optional For baselines whose length $||b|| = l$ is known, the observation equations become Eq. (4.4). This model can be solved by applying Eq. (4.6).
As this model is much stronger than the unconstrained model, it might be preferred for the evaluation of noise characteristics of GNSS signals, receivers etc. However for typical receiver test set-up the unconstrained model could be strong enough.

---

3) The fixed baseline solution is obtained using the estimated integer ambiguities. The residual $\hat{z} - \check{z}$ is used to adjust the float solution $\hat{b}$ of the first step, which is $\check{b} = \hat{b}(\check{z})$. This fixed baseline solution is obtained from Eq. (3.46).

Analysis

4) Next, the observation vector y is adjusted with the baseline solution b read from a file using the original non-linear model described by Eq. (2.102)-(2.103) with the assumption that $Q_{\overline{yy}} = Q_{yy}$.

$$\overline{y} = y - Gb \tag{F.3}$$

5) The least-squares criterion for the new unconstrained problem reads as:

$$\min_{z \in \mathbb{Z}^n} \|\overline{y}^{DD} - Az\|^2_{Q_{\overline{yy}}} = \|\hat{\overline{e}}^{DD}\|^2_{Q_{\overline{yy}}} + \min_{z \in \mathbb{Z}^n} \left(\|\hat{\overline{z}} - z\|^2_{Q_{\hat{\overline{z}}\hat{\overline{z}}}} \right) \tag{F.4}$$

With the float solution ($\hat{\overline{z}} \in \mathbb{R}^n$), the solution of the linear system of adjusted observations becomes the squared norm of the least-squares DD residual vector:

$$\|\overline{y}^{DD} - A\hat{\overline{z}}\|^2_{Q_{\overline{yy}}} = \|\hat{\overline{e}}^{DD}\|^2_{Q_{\overline{yy}}} \tag{F.5}$$

6) As we use the constraint that the solution of z has to be an integer ($\check{z} \in \mathbb{Z}^n$), the minimum fixed solution for the adjusted problem becomes:

$$\|\overline{y}^{DD} - A\check{\overline{z}}\|^2_{Q_{\overline{yy}}} = \|\check{\overline{e}}^{DD}\|^2_{Q_{\overline{yy}}} = \|\hat{\overline{e}}^{DD}\|^2_{Q_{\overline{yy}}} + \|\hat{\overline{z}} - \check{\overline{z}}\|^2_{Q_{\hat{\overline{z}}\hat{\overline{z}}}} \tag{F.6}$$

The minimum of this adjusted problem is different than the minimum of original problem described by Eq. (F.2) if b is calculated as an average baseline estimate over a number of epochs.

Analysis

7) As a last step, the SD is calculated from the DD residuals of Eq. (F.6). The following transformation is used for every observation type between SD and DD residuals as described in (van der Marel and Gündlich, 2006):

$$\overbrace{\begin{bmatrix} w^1 & w^2 & w^3 & \dots & w^{n+1} \\ & & \overline{\mathbf{D}} & & \end{bmatrix}}^{D_{SD->DD}} \overbrace{\begin{bmatrix} \check{e}^1 \\ \check{e}^2 \\ \vdots \\ \check{e}^j \\ \vdots \\ \check{e}^{n+1} \end{bmatrix}}^{\check{e}^{SD}} = \overbrace{\begin{bmatrix} 0 \\ \check{e}^{12} \\ \vdots \\ \check{e}^{1,i} \\ \vdots \\ \check{e}^{1,n} \end{bmatrix}}^{\check{e}^{DD}} \tag{F.7}$$

Here $\overline{\mathbf{D}}$ is the matrix that forms the difference between GNSS satellites at the same frequency and observation type. The zero-mean property is applied that states that the weighted sum of SD residuals for a baseline is zero, i.e.:

$$\sum_{j=1}^{n+1} w^j \check{e}^j = 0 \tag{F.8}$$

with w^j is the weight of the SD observation. The equation states that the weighted sum of all the SD residuals to all tracked GNSS satellites for each baseline at each epoch should be zero. If no weighting is used for the observations than all the entries of w^j are one. The matrix $\overline{\mathbf{D}}$ itself is non-invertible, by adding the vector $\begin{bmatrix} w^1 & w^2 & w^3 & \dots & w^{n+1} \end{bmatrix}$ an invertible matrix $D_{SD->DD}$ is created.
In (van der Marel and Gündlich, 2006) where no attempted is made to fix the ambiguities, multi-epoch solutions are applied for which $\hat{e}^{DD}$ approaches $\check{e}^{DD}$.
Using these equations, the inverse transformation of the DD residuals to the SD residuals can be calculated:

$$\check{e}^{SD} = (D_{SD->DD})^{-1} \check{e}^{DD} \tag{F.9}$$

This SD residual vector can be applied to evaluate noise characteristics of GNSS signals, receivers, etc.

Curriculum Vitae

After completing his Aerospace Master at the Delft University of Technology, Peter Buist worked in the Japanese aerospace industry for 8 years, specializing in particular in Global Navigation Satellite System (GNSS). In Japan, he developed GPS receivers for -among others- the SERVIS-1, USERS, ALOS satellites and the H2A rocket. After his return to the Netherlands, Peter worked at Delft University of Technology before joining the National Aerospace Laboratory NLR. His current research interest includes all expects of navigation and (onboard) data processing.

Peter received the best paper award at the ION/IEEE PLANS 2010 conference in Indian Wells, CA for a paper titled "GPS Experiment on the Balloon-based Operation Vehicle" and was the regional winner for South-Holland in the European Satellite Navigation Competition 2011 (ESNC).

Peter is a board member of the Netherlands Space Society NVR, responsible for the magazine *Ruimtevaart* and a member of the Policy Advisory and Space Societies Committees of the International Astronautical Federation (IAF).

$1989 - 1992$	Atheneum, Augustinus College, Groningen, the Netherlands
$1992 - 1999$	Master Aerospace Engineering, Delft, the Netherlands
$1997 - 1998$	Internship at Surrey Satellite Technology, Guildford, UK
$1998 - 1999$	EU Vulcanus in Japan programme
$1999 - 2003$	Toshiba, Kawasaki, Japan
$2003 - 2006$	NEC Toshiba Space Systems, Kamoi/Fuchu, Japan
$2006 - 2012$	Delft University of Technology, Delft, the Netherlands
$2012-$	National Aerospace Laboratory NLR Amsterdam, the Netherlands

Bibliography

Alberts, B., B. Gunter, A. Muis, Q. Chu, G. Giorgi, L. Huisman, P. Buist, C. Tiberius, and H. Lindenburg (2010). *Correcting Strapdown GPS/INS Gravimetry Estimates with GPS Attitude Data, Gravity, Geoid and Earth Observation*. Springer.

Alfriend, K. T., S. R. Vadali, P. Gurfil, J. P. How, and L. S. Breger (2010). *Spacecraft Formation Flying*. Elsevier Astrodynamics Series.

Ardaens, J.-S., O. Montenbruck, and S. DAmico (2010). Functional and Performance Validation of the PRISMA Precise Orbit Determination Facility. *Proceedings of ION 2010, San Diego, CA, US, January 25-27*.

Ashby, N. and J. Spilker (1996). *Introduction to relativistic effects on the Global Positioning System, Global Positioning System: Theory and applications*, Volume 1. AIAA vol. 163.

Ashjaee, J. (1986). GPS Doppler processing for precise positioning in dynamic applications. *Navigation 32*(4), 370–385.

Ashjaee, J., R. Lorenz, R. Sutherland, J. Dutilloy, and J. Minazio (1989). New GPS developments and Ashtech M-XII. *Proceedings of ION 1989, Colorado Springs, CO, September 27-29*, 195–198.

Axelrad, P. and C. Behre (1999). Satellite attitude determination based on gps signal-to-noise ratio. *Proceedings of the IEEE 87*(1), 133–144.

Baby, H., P. Gole, and J. Lavergnat (1988). A model for the tropospheric excess path length of radio waves from surface meteorological measurements. *Radio science 23*(6), 1023–1038.

Bahrami, M. (2009). Getting Back on the Sidewalk: Doppler-aided Autonomous Positioning with Single-Frequency Mass Market Receivers in Urban Areas. *Proceedings of ION 2009, Savannah, GA, US, September 22-25*, 1716–1725.

Behre, C. (1997). *GPS-based attitude algorithms for low-cost satellite missions*. Ph.D. thesis, University of Colorado.

Bertiger, W., Y. Bar-Sever, S. Bettadpur, C. Dunn, B. Haines, G. Kruizinga, D. Kuang, S. Nandi, L. Romans, M. Watkins, and S. Wu (2002). GRACE: Millimeters and Microns in Orbit. *Proceedings of ION 2003, Portland, US, September 24-27*, 2022–2029.

Bona, P. (2000). Precision, cross corelation, and time correlation of GPS phase and code observations. *GPS Solutions 4*(2), 3–13.

Bona, P. and C. C. J. M. Tiberius (2000). An experimental assessment of observation cross-correlation in dual frequency GPS receivers. *Proceedings of ION 2000, Salt Lake City, UT, US, September 19-22*, 792–798.

Borre, K. and C. Tiberius (1999). Probability distribution of gps code and phase data. *Zeitschrift für Vermessungswesen 124*, 264–273.

Braasch, M. and A. Van Dierendonck (2002). GPS receiver architectures and measurements. *Proceedings of the IEEE 87*(1), 48–64.

Brock, J., R. Fuller, B. Kemper, D. Mleczko, J. Rodden, and A. Tadros (1995). Gps attitude determination and navigation flight experiment. *Proceedings of ION 1995, Palm Springs, CA, US, September 12-15*, 545–554.

Brown, R. A. (1992). Instantaneous GPS Attitude Determination. *Proceedings of IEEE Position Location and Navigation Symposium, Monterey, CA, US, March 24-27*, 113–120.

Buist, P., S. Kumagai, and K. Hama (2004). Flight Experience of the Integrated Navigation Unit; Combining GPS Attitude Determination with Star Sensor Measurements. *proceedings of NAVITEC, Noordwijk, The Netherlands, December 8-10*.

Buist, P., S. Kumagai, and K. Hama (2005). Gps-Based Attitude Determination in Different Attitude Modes: Experimenting with a GPS Receiver and a Star Sensor Onboard the SERVIS-1 Satellite. *proceedings of 6th International ESA Conference on Guidance, Navigation and Control Systems, ESA SP-606, Loutraki, Greece, October 17-20*.

Buist, P., S. Verhagen, T. Hashimoto, S. Sawai, S. Sakai, N. Bando, and S. Shimizu (2010). GPS experiment on the Balloon-based Operation Vehicle. *Position Location and Navigation Symposium (PLANS), 2010 IEEE/ION*, 1287–1294.

Buist, P. J. (2007). The Baseline Constrained LAMBDA Method for Single Epoch, Single Frequency Attitude Determination Applications. *Proceedings of ION 2007, Forth Worth, TX, US, September 25-28*, 2962–2973.

Buist, P. J. (2008). GNSS Kinematic Relative Positioning for Spacecraft: Data Analysis of a Dynamic Testbed. *Proceedings of the 26th ISTS (International Symposium on Space Technology and Science), Hamamatsu, Japan, June 1-8*.

Buist, P. J., Y. Hashida, M. Unwin, and M. Schroeder (1998). Spacecraft Full Attitude Determination from a Single Antenna: Experimentation with the PoSAT-1 GPS Receiver. *Proceedings of ION 1998, Nashville, TN, US, September 15-18*, 1811–1817.

Buist, P. J., S. Kumagai, T. Ito, K. Hama, and K. Mitani (2003). Development of the Integrated Navigation Unit; Combining a GPS Receiver with Star Sensor Measurements. *Proceedings of the 10th International Conference of Pacific Basin Societies (ISCOPS), vol. 117*.

Buist, P. J., S. Kumagai, M. Kasahara, K. Ijichi, K. Hama, and S. Nakamura (2004). Flight Experience of Single and Dual Frequency GPS Receivers Onboard of SERVIS-1 and USERS Satellites. *Proceedings of NAVITEC, Noordwijk, the Netherlands, December 8-10*.

Buist, P. J., N. Nadarajahand, P. J. G. Teunissen, and S. Verhagen (2011a). Algorithm development for the Garada project, Garada Milestone report, December 23.

Buist, P. J., N. Nadarajahand, P. J. G. Teunissen, and S. Verhagen (2011b). Stochastic Model for the Garada project, Garada Milestone report, September 30.

Buist, P. J., N. Nadarajahand, P. J. G. Teunissen, and S. Verhagen (2012). Analysis impact of configuration design, Garada Milestone report, March 29.

Buist, P. J., P. J. G. Teunissen, G. Giorgi, and S. Verhagen (2008). Instantaneous Multi-Baseline Ambiguity Resolution with Constraints. *Proceedings of the International Symposium on GPS/GNSS 2008, Tokyo, Japan, November 11-14*.

Buist, P. J., P. J. G. Teunissen, G. Giorgi, and S. Verhagen (2009a). Instantaneous GNSS-based Kinematic Relative Positioning and Attitude Determination using Multi-Antenna Configurations. *Proceedings of 2009 International Symposium on GPS/GNSS, Jeju, Korea, November 4-6*.

Buist, P. J., P. J. G. Teunissen, G. Giorgi, and S. Verhagen (2009b). Multiplatform Instantaneous GNSS Ambiguity Resolution for Triple- and Quadruple-Antenna Configurations with Constraints. *International Journal of Navigation and Observation, vol. 2009, Article ID 565426, 14 pages, doi:10.1155/2009/565426*.

Buist, P. J., P. J. G. Teunissen, G. Giorgi, and S. Verhagen (2010a). Attitude Bootstrapped Multi-frequency Relative Positioning. *Proceedings of IEEE/ION PLANS 2010, Indian Wells, CA, US, May 3-6*.

Buist, P. J., P. J. G. Teunissen, G. Giorgi, and S. Verhagen (2010b). Functional Model for Spacecraft Formation Flying using non-dedicated GPS/Galileo. *Proceedings of NAVITEC 2010, Noordwijk, the Netherlands, December*.

Buist, P. J., P. J. G. Teunissen, G. Giorgi, and S. Verhagen (2010c). Multivariate Bootstrapped Relative Positioning of Spacecraft Using GPS L1/Galileo E1 Signals. *Advances in Space Research, special issue: Galileo, doi:10.1016/j.asr.2010.10.001*.

Buist, P. J., P. J. G. Teunissen, and P. Joosten (2006). GNSS-Guided Relative Positioning and Attitude Determination for Missions with Multiple Spacecraft. *Proceedings of GPS/GNSS Symposium, Tokyo, Japan, November 15-17*.

Buist, P. J., P. J. G. Teunissen, S. Verhagen, and G. Giorgi (2009). Attitude Bootstrapped Relative Positioning for Spacecraft. *Proceedings of Fourth European Workshop on GNSS Signals and Signal Processing GNSS SIGNALS 2009, Oberpfaffenhofen, Germany, December 10-11*.

Buist, P. J., P. J. G. Teunissen, S. Verhagen, and G. Giorgi (2010). A Vectorial Bootstrapping Approach for Instantaneous GNSS-based Relative Positioning and Attitude Determination of Spacecraft. *Acta Astronautica, doi:10.1016/j.actaastro.2010.09.027*.

Buist, P. J., S. Verhagen, G. Giorgi, P. J. G. Teunissen, and N. Nadarajah (2011). Functional Model for the Garada project, Garada Milestone report, April 15.

Buist, P. J., S. Verhagen, T. Hashimoto, S. Sakai, and N. Bando (2008). GPS field experiment for the balloon-based operation vehicle. *Proceedings of the 18th Workshop on JAXA Astrodynamics and Flight Mechanics, Sagamihara, Japan, July*.

Buist, P. J., S. Verhagen, T. Hashimoto, S. Sawai, S.-I. Sakai, N. Bando, and S. Shimizu (2011). The right attitude. *GPS World 22*(9), 57–66.

Buys-Ballot, M. (1857). Note sur le rapport de l'intensite et de la direction du vent avec les ecarts simultanes du barometre. *Comptes Rendus 45*, 765–768.

Campa, G., M. Fravolini, A. Ficola, M. Napolitano, B. Seanor, M. Perhinschi, and P. Flaps (2004). Autonomous aerial refueling for UAVs using a combined GPS-machine vision guidance. In *AIAA Guidance, Navigation, and Control Conference and Exhibit*, pp. 1–11.

Cohen, C. E. (1996). *Attitude Determination, Global Positioning System: Theory and Applications*, Volume 2. AIAA vol. 163.

Cohen, C. E. and B. W. Parkinson (1992). Aircraft Applications of GPS-Based Attitude Determination. *Proceeding of ION 1992, Albuquerque, NM, CA, September 16 - 18*, 775–782.

Counselman III, C., H. Hinteregger, and I. Shapiro (1972). Astronomical Applications of Differential Interferometry. *Science 178*, 607–608.

Crassidis, J. L., F. L. Markley, and E. G. Lightsey (1999). Global Positioning System Integer Ambiguity Resolution without Attitude Knowledge. *AIAA Journal of Guidance, Control, and Dynamics 22*(2), 212–218.

de Jonge, P. (1998). *A processing strategy for the application of the GPS in networks*. Nederlandse Commissie voor Geodesie.

de Jonge, P. and C. Tiberius (1996). *The LAMBDA method for integer ambiguity estimation: implementation aspects, LGR Series 12, Publications of the Delft Geodetic Computing Centre*.

Draganov, S., B. Veytsman, and L. Haas (2002). Space Applications Algorithm and Initial Simulation Results for the ITT Low-Power Transceiver. *Proceedings of ION 2002, Portland, OR, US, September 24-27*.

Duncan, S. (2010). Development and Exploitation of GPS Attitude Determination for Microsatellites. *PhD Thesis, University of Surrey*.

Duncan, S., M. S. Hodgart, M. J. Unwin, and R. Hebden (2007). In-Orbit Results From a Space-borne GPS Attitude Experiments. *Proceedings of ION 2007, Forth Worth, TX, US, September 25-28*.

Ebinuma, T., E. Rooney, S. Gleason, and M. Unwin (2005). GPS receiver operations on the disaster monitoring constellation satellites. *The Journal of Navigation 58*(02), 227–240.

Ebinuma, T., M. Unwin, C. Underwood, and E. Imre (2004). A Miniaturised GPS Receiver for Space Applications. *16th IFAC Symposium on Automatic Control in Aerospace, St. Petersburg, Russia*.

ESA (2006). Galileo Open Service: Signal In Space Interface Control Document. Technical report, Galileo Joint Undertaking.

Euler, H. J. and C. Goad (1991). On optimal filtering of GPS dual frequency observations without using orbit information. *Bulletin Géodésique 65*, 130–143.

Fontana, R., W. Cheung, and T. Stansell (2001). The modernized L2 civil signal. *GPS world 12*(9), 28–35.

Freesland, D., K. Reiss, D. Young, J. Cooper, and C. Adams (1996). GPS Based Attitude Determination The REX II Flight Experience. *AIAA/USU Conference on Small Satellites, 10 th, Utah State Univ, Logan, UT*.

Fuke, H., D. Akita, I. Iijima, N. Izutsu, Y. Kato, J. Kawada, Y. Matsuzaka, E. Mizuta, M. Namiki, N. Nonaka, et al. (2009). Developments of the Sliding Launcher and Related Facilities for the New Japanese Balloon Base. *Transactions of the Japan Society for Aeronautical and Space Sciences, Space Technology Japan 7*.

Fuke, H., D. Akita, I. Iijima, N. Izutsu, Y. Kato, J. Kawada, Y. Matsuzaka, E. Mizuta, M. Namki, N. Nonaka, S. Ohta, Y. Saito, T. Sato, M. Seo, A. Takada, K. Tamura, M. Toriumi, K. Yamada, and T. Yoshida (2009). Opening of the New Japanese Balloon Base at the Taiki Aerospace Research Field. *Proceedings of the 27th ISTS (International Symposium on Space Technology and Science), Tsukuba, Japan, July 5-12*.

Geiger, A. (1990). Influence of Phase Center Variations on the Combination of Different Antenna Types. *Proceedings of GPS'90, the Second International Symposium on Precise Positioning with the Global Positioning System, Ottawa, Canada, September 3-7*, 466–476.

General Dynamics C4 (2005a). Specification sheet for Monarch GPS Spaceborne Receiver. *http://www.gdc4s.com/documents/monarch.pdf*.

General Dynamics C4 (2005b). Specification sheet for Viceroy Space GPS Receiver. *http://www.gdc4s.com/documents/viceroy.pdf*.

Gerlach, C., L. Földvary, D. Svehla, T. Gruber, M. Wermuth, N. Sneeuw, B. Frommknecht, H. Oberndorfer, T. Peters, M. Rothacher, et al. (2003). A champ-only gravity field model from kinematic orbits using the energy integral. *Geophysical Research Letters 30*(20).

Gill, E., O. Montenbruck, S. DAmico, and S. Persson (2006). Autonomous Satellite Formation Flying for the PRISMA Technology Demonstration Mission. *16th AAS/AIAA Space Flight Mechanics Conference, Tampa, Florida January 22-26*.

Gill, E., P. Sundaramoorthy, J. Bouwmeester, B. Zandbergen, and R. Reinhard (2012). Formation flying within a constellation of nano-satellites: The QB50 mission. *Acta Astronautica*.

Giorgi, G. (2011). GNSS Carrier Phase-based Attitude Determination: Estimation and Applications. *PhD thesis, Delft University of Technology*.

Giorgi, G. and P. J. Buist (2008). Single-Epoch, Single-Frequency, Standalone Full Attitude Determination: Experimental Results. *Proceedings of NAVITEC, Noordwijk, The Netherlands, December 10-12*.

Giorgi, G., P. J. Buist, S. Verhagen, and P. J. G. Teunissen (2011). GNSS based attitude determination: aerospace and formation flying. *Working paper, Inside GNSS 6*(4), 62–71.

Giorgi, G. and P. Teunissen (2009). On the Time-To-Fix for Single-Frequency GNSS-Based Attitude Determination. In *IGNSS Symposium, Queensland, Australia*, pp. 1–3.

Giorgi, G., P. Teunissen, D. Odijk, and P. Buist (2010). Enhancing the Time-To-Fix for the unaided single-frequency integer ambiguity resolution in GNSS attitude determination applications. *Position Location and Navigation Symposium (PLANS), 2010 IEEE/ION*, 236–244.

Giorgi, G., P. J. G. Teunissen, and P. J. Buist (2008). A Search and Shrink Approach for the Baseline Constrained LAMBDA: Experimental Results. *Proceedings of the International Symposium on GPS/GNSS 2008, Tokyo, Japan, November 11-14*.

Giorgi, G., P. J. G. Teunissen, S. Verhagen, and P. J. Buist (2009). Integer Ambiguity Resolution with Nonlinear Geometrical Constraints. *Presented at the VII Hotine-Marussi Symposium on Mathematical Geodesy, Rome, Italy, 2009*.

Giorgi, G., P. J. G. Teunissen, S. Verhagen, and P. J. Buist (2010). Testing a New Multivariate GNSS Carrier Phase Attitude Determination Method for Remote Sensing Platforms. *Advances in Space Research, special issue: GNSS Remote Sensing: New Roles and Progresses In Press, Accepted Manuscript, DOI: 10.1016/j.asr.2010.02.023, issn: 0273-1177*, –.

Giorgi, G., P. J. G. Teunissen, S. Verhagen, and P. J. Buist (2012). Instantaneous Ambiguity Resolution in Global-Navigation-Satellite-System-based Attitude Determination Applications: The Multivariate Constrained Least-Squares Ambiguity Decorrelation Adjustment Method. *Journal of Guidance Control and Dynamics 35*(1), 51–67.

Gleason, S. and D. Gebre-Egziabher (2009). *GNSS Applications and Methods*. Artech House Publishers.

Goad, C. and L. Goodman (1974a). A modified Hopfield tropospheric refraction correction model. In *Pr asentiert auf dem AGU Annual Fall Meeting, San Francisco, CA, Abstract: EOS*, Volume 55, pp. 1106.

Goad, C. and L. Goodman (1974b). A Modified Hopfield Tropospheric Refraction Correction Model. *Proceedings of the Fall Annual Meeting of the American Geophysical Union, San Francisco, California, December*, 12–17.

Gomez, S. (2000). Attitude Determination and Attitude Dilution of Precision (ADOP) Results for International Space Station Global Positioning System (GPS) Receiver. *Proceedings of ION 2000, Salt Lake City, UT, US, September 19-22*, 1995–2002.

Gomez, S. and M. Lammers (2004). Lessons Learned from Two Years of On-Orbit Global Positioning System Experience on International Space Station. *Proceedings of ION 2004, Long Beach, CA, US, September 21-24*.

GPS-ICD-200 (1993). Navstar GPS Space Segment / Navigation User Interface. Technical report.

Grillenberger, A., R. Rivas, M. Markgraf, P. Mumford, K. Parkinson, and C. Rizos (2008). The Namuru receiver as development platform for spaceborne GNSS applications. *Proceedings of NAVITEC, Noordwijk, The Netherlands, December 8-10*.

Guier, W. and G. Weiffenbach (1960). A satellite doppler navigation system. *Proceedings of the IRE 48*(4), 507–516.

Gundlich, B. and K.-R. Koch (2002). Confidence Regions for GPS Baselines by Bayesian Statistics. *Journal of Geodesy 76*, 55–62.

Gurtner, W., G. Beutler, S. Botton, M. Rothacher, A. Geiger, H. Kahle, D. Schneider, and A. Wiget (1987). The use of the Global Positioning System in mountainous areas. *Mitt. Satell.-Beobachtungsstn. Zimmerwald, Nr. 22, 21*.

Gurtner, W., G. Beutler, and M. Rothacher (1989). Combination of GPS observations made with different receiver types. *Proceedings of the 5th International Geodetic Symposium on Satellite Positioning, Las Cruces, NM, March*, 13–17.

Gurtner, W. and L. Estey (2006a). RINEX: The Receiver Independent Exchange Format, Version 2.11.

Gurtner, W. and L. Estey (2006b). RINEX: The Receiver Independent Exchange Format, Version 3.00.

Hansen, J., J. Murray, and N. Campos (2004). The NASA Dryden AAR Project: A Flight Test Approach to an Aerial Refueling System. *AIAA Atmospheric Flight Mechanics Conference and Exhibit, Providence, RI, US, August 16-19*, 103–115.

Harper, N. (2009). *Server-side GPS and Assisted-GPS in Java*. Artech House Publishers.

Hashida, Y. and M. Unwin (1993). Satellite Attitude from a Single GPS Antenna. *Proceedings of ION 1993, Salt Lake City, UT, September 22 - 24*, 355 – 363.

Hashimoto, T., S. Sawai, S. ichiro Sakai, N. Bando, S. Shimizu, P. J. Buist, and S. Verhagen (2009). Microgravity Research using a Balloon-based Operation Vehicle. *Leonardo Times, December issue, Delft University of Technology 13*(4), 12–14.

Hashimoto, T., S. Sawai, S. Sakai, N. Bando, H. Kobayashi, K. Fujita, Y. Inatomi, T. Ishikawa, T. Yoshimitsu, and Y. Saito (2008). Progress of Balloon-based Micro-gravity Experiment System. *The 26th ISTS (International Symposium on Space Technology and Science), Hamamatsu, Japan, June 1-8*.

Hatch, R. (1990). Instantaneous ambiguity resolution. *Proc. of KIS'90, Banff, Canada*, 290–308.

Hauschild, A. and O. Montenbruck (2007). GPS-Based Attitude Determination for Microsatellite. *Proceedings of ION 2007, Forth Worth, TX, US, September 25-28*.

Hodgart, M. S. and S. Purivigraipong (2000). New Approach to Resolving Instantaneous Integer Ambiguity Resolution for Spacecraft Attitude Determination using GPS signals. *Proceedings of IEEE PLANS 2000, San Diego, US, March*.

Hofmann-Wellenhoff, B., H. Lichtenegger, and J. Collins (2001). *Global Positioning System: Theory and Practice* (5 ed.). Springer-Verlag, Berlin.

Ifadis, I. M. (1992). The excess propagation path of radio waves: Study of the influence of the atmospheric parameters on its elevation depedence. *Survey Review 31*, 289–298.

IS-GPS-800 (2007). Interface Specification IS-GPS-800 Navstar GPS Space Segment/User Segment L1C Interfaces. *Available at http://www.losangeles.af.mil*.

IS-QZSS (2009). Quasi-Zenith Satellite System Navigation Service Interface Specification for QZSS (IS-QZSS) V1.1, japan aerospace exploration agency, july 31,. *Available at http://qzss.jaxa.jp/*.

Ishijima, Y., T. Miyano, T. Ito, and P. J. Buist (2000). GPS Attitude Determination Field Test and Preliminary Analysis Results using On-orbit GPS Data of ETS-VII. *International Workshop on Aerospace Applications of the Global Positioning System, Breckenridge, Co, US, January 31-February 2*.

Jaggi, A., U. Hugentobler, H. Bock, and G. Beutler (2007). Precise orbit determination for grace using undifferenced or doubly differenced gps data. *Advances in Space Research 39*(10), 1612–1619.

JAVAD (2009). http://www.javad.com/jgnss/products/receivers/triumph-4x.html.

Jin, X. (1995). Taylor Expansion of GPS Observation Equations. *LGR-Series* (11).

Jong, K. (2000). Quality control and precise kinematic GPS positioning-theory and applications. *Proceedings of Shallow Survey 99*, 18–20.

Jorgensen, P. (1980). Combined pseudo range and Doppler positioning for the stationary Navstar user. In *In: PLANS'80-Position Location and Navigation Symposium, Atlantic City, NJ, December 8-11, 1980, Record.(A82-18126 06-04) New York, Institute of Electrical and Electronics Engineers, Inc.*, pp. 450–458.

Julien, O., P. Alves, M. Cannon, and W. Zhang (2003). A tightly coupled GPS/GALILEO combination for improved ambiguity resolution. *Proceedings of the European Navigation Conference (ENC-GNSS03)*, 1–14.

Julien, O., M. Cannon, P. Alves, and G. Lachapelle (2004). Triple Frequency Ambiguity Resolution Using GPS/GALILEO. *European Journal of Navigation 2*(2), 51–57.

Kaplan, E. D. and C. J. Hegarty (2006). *Understanding GPS. Principles and Applications*. Artech House.

Kawano, I., M. Mokuno, T. Kasai, and T. Suzuku (1999). First Autonomous Rendezvous using Relative GPS Navigation by ETS-VII. *Proceedings of ION 1999, Nashville, TN, US, September 14-17*, 393–410.

Kawano, I., M. Mokuno, T. Miyano, and T. Suzuki (2000). Analysis and Evaluation of GPS Relative Navigation Using Carrier Phase for RVD Experiment Satellite of ETS-VII. *Proceedings of ION 2000, Salt Lake City, UT, US, September 19 - 22*, 1655–1660.

Kechine, M. O., C. C. J. M. Tiberius, and H. van der Marel (2003). Experimental Verification of Internet-based Global Differential GPS. *Proceedings of ION 2003, Portland, OR, US, September 24-27*, 28–37.

Khanafseh, S. and B. Pervan (2007). Autonomous Airborne Refueling of Unmanned Air Vehicles Using the Global Positioning System. *Journal of Aircraft 44*(5), 1670.

Kim, D. and R. B. Langley (1999). An Optimized Least-Squares Technique for Improving Ambiguity Resolution and Computational Efficiency. *Proceedings of ION 1999, Nashville, TN, US, September 14-17*, 1579–1588.

Kim, D. and R. B. Langley (2007). GPS RTK-Based Attitude Determination for the e-POP Platform onboard the Canadian CASSIOPE Spacecraft in Low Earth Orbit. *TimeNav'07 (ENC GNSS 2007), Geneva International Conference Center, Switzerland, May 29 - June 1*.

Kim, D., L. Serrano, and R. B. Langley (2005). Compensation of the Effects of Phase Wind-up for Improving the Performance of a GPS RTK-Based Vehicle Navigation System. *Proceedings of ION 2005, Long Beach CA, US, September 13-16*, 346–354.

Kleijer, F. (2004). *Troposphere modeling and filtering for precise GPS leveling*. Ph.D. thesis, Publications on Geodesy, 56, Netherlands Geodetic Commission, Delft.

Kleusberg, A. (1986). Kinematic Relative Positioning Using GPS Code and Carrier Beat Phase Observations. *Marine Geodesy: An International Journal of Ocean Surveys, Mapping and Sensing 10*(3/4).

Klobuchar, J. A. (1987). Ionospheric time-delay algorithm for single-frequency gps users. *Aerospace and Electronic Systems, IEEE Transactions on* (3), 325–331.

Knight, D. (1994). A New Method of Instantaneous Ambiguity Resolution. *Proceedings of ION 1994, Colorado Springs, CO, US, September 20-23*, 707–716.

Krauss, P., C. Kühl, M. Mittnacht, J. Heim, and E. Gottzein (2008). Modernized Spaceborne GNSS Receivers. *Proceedings of Proceedings of the 17th World Congress The International Federation of Automatic Control*, 4707–4712.

Krieger, G., I. Hajnsek, K. Papathanassiou, M. Younis, and A. Moreira (2010). Interferometric Synthetic Aperture Radar (SAR) Missions Employing Formation Flying. *Proceedings of the IEEE 98*(5), 816–843.

Krieger, G., A. Moreira, H. Fiedler, I. Hajnsek, M. Werner, M. Younis, and M. Zink (2007). TanDEM-X: A satellite formation for high-resolution SAR interferometry. *Geoscience and Remote Sensing, IEEE Transactions on 45*(11), 3317–3341.

Kroes, R. (2006). Precise Relative Positioning of Formation Flying Spacecraft using GPS. *PhD-thesis, Delft, The Netherlands, March*.

Kubo, N. (2009). Advantage of velocity measurements on instantaneous RTK positioning. *GPS solutions 13*(4), 271–280.

Kubo, N. and S. Pullen (2008). Instantaneous RTK Positioning Based on User Velocity Measurements. *Proceedings of ION 2008, Savannah, GA, US, September 16 - 19*, 1406–1417.

Kumagai, S., T. Ito, K. Toda, and T. Iwata (2001). Precision GPS Receiver for the Advanced Land Observing Satellite (ALOS). *Proceedings of the Space Sciences and Technology Conference, in Japanese 45*, 131–135.

Kuylen, L. V., P. Nemry, F. Boon, A. Simsky, and J. F. M. Lorga (2006). Comparison of Attitude Performance for Multi-Antenna Receivers. *European Journal of Navigation 4*(2).

Lachapelle, G., C. Liu, and G. Lu (1993). Quadruple Single Frequency Receiver System for Ambiguity Resolution On The Fly. *Proceedings of ION 1993, Salt Lake City, UT, September 22 - 24*, 1167–1172.

Larson, W. and J. Wertz (1992). Space mission analysis and design. *Second Edition, Space Technology Library, Kluwer Academic Publishers, Dordrecht, The Netherlands*.

Le, A. and C. Tiberius (2006). Phase wind-up effects in precise point positioning with kinematic platforms. *Proceedings of NAVITEC 2006, Noordwijk, the Netherlands, December*.

Lear, W. (1987). GPS Navigation for Low-Earth Orbiting Vehicles. Technical report, NASA 87-FM-2, Rev. 1.

Leick, A. (2003). *GPS Satellite Surveying* (3rd ed.). John Wiley and Sons, New York.

Leyssens, J. and M. Markgraf (2005). Evaluation of a Commercial-Off-The-Shelf dualfrequency GPS receiver for use on LEO satellites. *Proceedings of ION 2005, Long Beach, CA, US, September 13-16*.

Lightsey, E. (1997). Development and flight demonstration of a GPS receiver for space. *Ph.D.Thesis, Stanford University,*.

Lightsey, E., E. Ketchum, T. Flatley, J. Crassidis, D. Freesland, K. Reiss, and D. Young (1996). Flight results of GPS based attitude control on the REX II spacecraft. *Proceedings of ION 1996, Kansas City, MO, US, September 17 - 20 1*, 1037–1046.

Lin, D., L. K. Voon, and N. Nagarajan (2004). Real-time attitude determination for microsatellite by LAMBDA method combined with Kalman filtering. *22nd AIAA International Communications Satellite Systems Conference & Exhibit 2004*.

Lisano, M. E., J. R. Carpenter, and S. Gomez (1999). Navigation, Attitude Determination, and Multipath Analysis Results from the STS- 77 GPS Attitude and Navigation Experiment. *Navigation 46*(3).

Liu, X. (2002). A comparison of stochastic models for GPS single differential kinematic positioning. *Proceedings of ION 2002, Portland OR, US, September 24 - 27*, 1830–1841.

Liu, X., C. Tiberius, and K. de Jong (2004). Modelling of differential single difference receiver clock bias for precise positioning. *GPS Solutions 7*, 209–221. 10.1007/s10291-003-0079-x.

Llorente, J. S., A. Agenjo, B. Bereczki, L. Tarabini-Castellani, B. Jacobsson, and A. Cropp (2008). PROBA-3 Formation Flying System Perspectives. *3rd International Symposium on Formation Flying Missions and Technologies, ESTEC, 23-25 April 2008*.

Magnus, J. (1988). Linear Structures. London School of Economics and Political Science, Charles Griffin & Company LTD.

Manzano-Jurado, M., C. Carrascosa-Sanz, and A. Garcia-Rodrígues (2008). Formation Flying LEO Test Bed at the ESTEC Navigation Laboratory. *Proceedings of NAVITEC, Noordwijk, The Netherlands, December 10-12*.

Marcille, H., G. Moreau, and V. Pascal (1997). Relative GPS Navigation Design and Validation for ATV Rendez-Vous. *Proceedings of the 3rd ESA International Conference on Spacecraft Guidance, Navigation and Control Systems, ESTEC, Noordwijk, the Netherlands. ESA SP-381, November 26-29*, 77.

Marini, J. (1972). Correction of satellite tracking data for an arbitrary tropospheric profile. *Radio Science 7*(2), 223–231.

Maruyama, T. (1977). *Stochastic problems in population genetics*. Springer.

Memarzadeh, Y. (2009). *Ionospheric modeling for precise GNSS applications*. NCG, Nederlandse Commissie voor Geodesie.

Mendes, V. (1999). Modeling the neutral-atmosphere propagation delay in radiometric space techniques. *Ph.D. dissertation, University of New Brunswick*.

Meurant, G. (1992). A review on the inverse of symmetric tridiagonal and block tridiagonal matrices. *SIAM Journal on Matrix Analysis and Applications 13*, 707.

Misra, P. and P. Enge (2001). *Global Positioning System: Signals, Measurements, and Performance*. Ganga-Jamuna Press, Lincoln MA.

Mitani, S., T. Yamamoto, I. Kawano, S. Sakai, H. Tsunemi, and F. team (2009). FFAST : Formation Flight All Sky Telescope, Formation Flight System Analyses and Design. *Proceedings of the 27th ISTS (International Symposium on Space Technology and Science), Tsukuba, Japan, July 5-12*.

Monikes, R., J. Wendel, and G. F. Trommer (2005). A Modified LAMBDA Method for Ambiguity Resolution in the Presence of Position Domain Constraints. *Proceedings of ION 2005, Long Beach, CA, US, September 13 - 16*, 81–87.

Montenbruck, O., S. DAmico, J. Ardaens, and M. Wermuth (2011). Carrier phase differential gps for leo formation flying–the prisma and tandem-x flight experience. *AAS Astrodynamcis Specialist Conference, 31 July-4 Aug 2010, Girdwoord, USA*.

Montenbruck, O., M. Garcia-Fernandez, and J. Williams (2006). Performance comparison of semicodeless GPS receivers for LEO satellites. *GPS solutions 10*(4), 249–261.

Montenbruck, O. and E. Gill (2000). *Satellite orbits*. Springer, Berlin.

Montenbruck, O. and M. Markgraf (2008). User's Manual for the Phoenix GPS Receiver. *DLR/GSOC GTN-MAN-0120, Oberpfaffenhofen, version 1.9, July 14*.

Montenbruck, O., B. Nortier, and S. Mostert (2004). A Miniature GPS Receiver for Precise Orbit Determination of the SUNSAT2004 Micro-Satellite. *Proceedings of ION National Technical Meeting, San Diego, CA, US, January 26 - 28*, 636–642.

Montenbruck, O., P. W. L. van Barneveld, Y. Yoon, and P. N. A. M. Visser (2007). GPS-Based Precision Baseline Reconstruction for the TanDEM-X SAR-Formation. *20th International Symposium on Space Flight Dynamics, September 24-28, Annapolis, US*.

Montenbruck, O., M. Wermuth, and R. Kahle (2010). GPS Based Relative Navigation for the TanDEM-X Mission-First Flight Results. *Proceedings of ION 2010, Portland, OR, US, September 21 - 24*, 2797 – 2807.

Montenbruck, O., Y. Yoon, J. S. Ardaens, and D. Ulrich (2008). In-Flight Performance Assessment of the Single Frequency MosaicGNSS Receiver for Satellite Navigation. *7th International ESA Conference on Guidance, Navigation and Control Systems, 2-5 June, Tralee, Ireland*.

Moon, Y., R. Koenig, G. Michalak, and M. Rothacher (2008, july). Precise orbit and baseline determination for terrasar-x and tandem-x. In *Geoscience and Remote Sensing Symposium, 2008. IGARSS 2008. IEEE International*, Volume 2, pp. II–121 –II–124.

Nadarajah, N., P. J. G. Teunissen, and P. J. Buist (2012). Attitude determination of LEO satellites using an array of GNSS sensors. *IEEE Fusion, Singapore*, 7.

Nadarajah, N., P. J. G. Teunissen, P. J. Buist, and P. Steigenberger (2012). First Results of Instantaneous GPS/Galileo/COMPASS Attitude Determination. pp. 7.

Nadarajah, N., P. J. G. Teunissen, and G. Giorgi (2011). GNSS attitude determination for remote sensing: On the bounding of the multivariate ambiguity objective function. *Proceedings of International Association of Geodesy Symposia (IAGS-2011), Melbourne, Australia, 28 June - 7 July*.

Nakamura, S., T. Uchimura, S. Katagiri, A. Suzuki, M. Sawabe, and Y. Yamamoto (2004). Results of the Precise Orbit Determination Experiment with ADEOS-II. In *18th International Symposium on Space Flight Dynamics*, Volume 548, pp. 163.

Narmada (2005). ATV-Far rendez-vous navigation based on relative GPS. *Proceedings of ION 2005, Long Beach, Ca, US, September 13-16*, 1160–1166.

Neill, A. (1996). Global mapping functions for the atmosphere delay at radio wavelengths. *Journal of geophysical research 101*(B 2), 3227–3246.

Nguyen, T., J. Sinko, R. Galijan, S. Int, and M. Park (1997). Using differential carrier phase GPS to control automated vehicles. In *Circuits and Systems, 1997. Proceedings of the 40th Midwest Symposium on*, Volume 1.

Odijk, D. (2001). Weighting ionospheric corrections to improve fast gps positioning. *Proceedings of ION 2000, Salt Lake City, UT, US, September 19-22*, 1113–1123.

Odijk, D. (2002). Fast Precise GPS Positioning in the Presence of Ionospheric Delays. NCG Series, 52. *Netherlands Geodetic Commission, Delft, The Netherlands*.

Odijk, D. and P. Teunissen (2012). Characterization of between-receiver gps-galileo inter-system biases and their effect on mixed ambiguity resolution. *GPS Solutions*, 1–13.

Park, C., D. Cho, E. Cha, D. Hwang, and S. Lee (2006). Error analysis of 3-dimensional gps attitude determination system. *International Journal of Control Automation and Systems 4*(4), 480.

Park, C., I. Kim, J. G. Lee, and G. I. Jee (1996). Efficient Ambiguity Resolution Using Constraint Equation. *Proceedings of IEEE: Position, Location and Navigation Symposium PLANS96, Atlanta, Georgia, USA*.

Park, C. and P. J. G. Teunissen (2003). A New Carrier Phase Ambiguity Estimation for GNSS Attitude Determination Systems. *Proceedings of International GPS/GNSS Symposium, Tokyo, November 15-18*.

Parkinson, B. W., J. J. S. Jr, P. Axelrad, and P. Enge (1996). *Global Positioning System: Theory and Applications*. AIAA vol. 163.

Pasetti, A., P. Colmenarejo, and F. Gottifredi (1997). A Visibility-Based Algorithm for the GPS Initial Integer Ambiguity Problem. *Proceedings of the 3rd ESA International Conference on Spacecraft Guidance, Navigation and Control Systems, Noordwijk, the Netherlands. ESA SP-381, November 26-29 381*, 327.

Persson, S., S. Veldman, and P. Bodin (2009). PRISMA–A formation flying project in implementation phase. *Acta Astronautica 65*(9-10), 1360–1374.

Pervan, B., F. Chan, D. Gebre-Egziabher, S. Pullen, P. Enge, and G. Colby (2003). Performance Analysis of Carrier-Phase DGPS Navigation for Shipboard Landing of Aircraft. *Navigation 50*(3), 181–191.

Peters, T. V., L. Tarabini-Castellani, C. de Negueruela, and B. J. Salvador Llorente (2008). PROBA-3 FORMATION FLYING MISSION ANALYSIS. *3rd International Symposium on Formation Flying Missions and Technologies, ESTEC, April 23-25*.

Pinchin, J., C. Hide, D. Park, and X. Q. Chen (2008). Precise Kinematic Positioning Using Single Frequency GPS Receivers and an Integer Ambiguity Constraint. *Proceedings of IEEE PLANS 2008*.

Psiaki, M. and S. Mohiuddin (2007). Modeling, Analysis, and Simulation of GPS Carrier Phase for Spacecraft Relative Navigation. *Journal of Guidance, Control, and Dynamics 30*(6), 1628–1639.

Purivigraipong, S. (2000). Study of spacecraft attitude determination from phase information of gps signal. *Ph.D. Thesis, University of Surrey*.

Ray, J. and K. Senior (2005). Geodetic techniques for time and frequency comparisons using GPS phase and code measurements. *Metrologia 42*, 215.

Richard, L. (1978). Burden, J. *Douglas Faires, and Albert C. Reynolds. Numerical Analysis. Prindle, Weber and Schmidt, Boston*.

Romeiser, R., M. Schwäbisch, J. Schulz-Stellenfleth, D. Thompson, R. Siegmund, A. Niedermeier, W. Alpers, and S. Lehner (2002). Study on concepts for radar interferometry from satellites for ocean (and land) applications (koriolis). final report. *Univ. Hamburg, Germany*.

Saastamoinen, J. (1972). Atmospheric correction for the troposphere and stratosphere in radio ranging of satellites. *The use of artificial satellites for geodesy*, 247–251.

Sagnac, G. (1913). L'éther lumineux démontré par l'effet du vent relatif d'éther dans un interféromètre en rotation uniforme. *CR Acad. Sci. 157*, 708–710.

Saunders, P. and G. Barton (1995). GPS on the International Space Station Alpha. *Proceedings of the ION National Technical Meeting 1995, Anaheim, CA, US, January 18-20*.

Sawai, S., T. Hashimoto, S. Sakai, N. Bando, H. Kobayashi, K. Fujita, T. Yoshimitsu, T. Ishikawa, Y. Inatomi, H. Fuke, Y. Kamata, S. Hoshino, K. Tajima, S. Kadooka, S. Uehara, T. Kojima, S. Ueno, K. Miyaji, N. Tsuboi, K. Hiraki, K. Suzuki, and K. M. T. Nakata (2008). Development of Vehicle for Balloon-Based Microgravity Experiment and Its Flight Results. *Journal of the Japan Society for Aeronautical and Space Sciences 56*(654), 339–346.

Seeber, G. (2003). *Satellite geodesy*. Walter De Gruyter Inc.

Septentrio (2007). PolaRx2, User Manual, Version 2.7/3.2, January 30.

Shimizu, S., P. J. Buist, N. Bando, S. Sakai, S. Sawai, and T. Hashimoto (2009). Design of multi-sensor attitude determination system for balloon-based operation vehicle. *Proceedings of the 27th ISTS (International Symposium on Space Technology and Science), Tsukuba, Japan, July 5-12*.

Shivaramaiah, N. and A. Dempster (2009). The Galileo E5 AltBoC: Understanding the Signal Structure'. *IGNSS Symposium, 1-3 December, Holiday Inn Surfers Paradise, Qld, Australia*.

Shuster, M. (1993). A survey of attitude representations. *Journal of the Astronautical Sciences 41*(4), 439–517.

Shuster, M. and S. Oh (1981). Three-axis attitude determination from vector observations. *Journal of Guidance and Control 4*(1), 70–77.

Simsky, A. and F. Boon (2003). Carrier Phase and Doppler-Based Algorithms for Real-Time Standalone Positioning. In *Proceedings of ENC-GNSS 2003, Graz, April 25*.

Sleewaegen, J. and H. De Wilde (2004). Galileo Alt-BOC receiver. *Proceedings of ENC-GNSS, Rotterdam, the Netherlands*, 16–19.

SSTL (2009). Surrey supplies GPS unit for International Space Station. *http://www.spaceref.com/news/viewpr.html?pid=6243*.

SSTL (2010). Specification sheet for SGR-10 Space GPS Receiver. *available at www.sstl.co.uk*.

Stull, R. (1995). *Meteorology today for scientists and engineers*. Minneapolis/St. Paul: West Pub.

Sullivan, W. (1995). Performance analysis of an integrated gps/inertial attitude determination system. *Proceedings of ION National Technical Meeting 1995, Anaheim, CA, US, January 18-20*, 783–791.

Sutton, E. (1997). Optimal Search Space Identification for Instantaneous Integer Cycle Ambiguity Resolution. *Proceedings of ION 1997, Kansas City, MO, US, September 16-19*, 313–322.

Svehla, D. and M. Rothacher (2005). *Kinematic Precise Orbit Determination for Gravity Field Determination*, Volume 128. Springer Berlin Heidelberg.

Svehla, D., M. Rothacher, C. Salomon, G. Beyerle, J. Wickert, M. Ziebart, J. Dow, L. Cacciapuoti, T. Boerner, A. Rius, F. Cardellach, O. Montenbruck, R. Rivas, T. Gruber, C. Shum, P. Hoeg, T. Neubert, A. Helm, J. Hahn, I. Prochazka, U. Schreiber, P. Lauber, U. Hugentobler, and W. Schfer (2009). Galileo Onboard the International Space Station. *2nd Int. Colloquium on Scientific and Fundamental Aspects of the Galileo Program, Padua, Italy, October 14-16*.

Tancredi, U., A. Renga, and M. Grassi (2011). Ionospheric path delay models for spaceborne gps receivers flying in formation with large baselines. *Advances in Space Research*.

Teunissen, P. (1990a). Nonlinear inversion of geodetic and geophysical data: diagnosing nonlinearity. *Developments in Four-dimensional Geodesy*, 241–264.

Teunissen, P., P. de Jonge, and C. Tiberius (1994). On the spectrum of the GPS DD-ambiguities. *Proceedings ION 1994, Salt Lake City, UT, US, September 20-23*, 115–124.

Teunissen, P. J. (2012). A-ppp: Array-aided precise point positioning with global navigation satellite systems. *Signal Processing, IEEE Transactions on 60*(6), 2870–2881.

Teunissen, P. J. G. (1990b). An integrity and quality control procedure for use in multi-sensor integration. *Proceedings of ION 1990, Colorado Springs, CO, US, September 19-21*, 513–522.

Teunissen, P. J. G. (1993). Least Squares Estimation of the Integer GPS Ambiguities. *Invited lecture, Section IV Theory and Methodology, IAG General Meeting, Beijing*.

Teunissen, P. J. G. (1994). A New Method for Fast Carrier Phase Ambiguity Estimation. *Proceedings IEEE Position Location and Navigation Symposium, PLANS '94*, 562–573.

Teunissen, P. J. G. (1995). The Least-Squares Ambiguity Decorrelation Adjustment: a Method for Fast GPS Integer Ambiguity Estimation. *Journal of Geodesy 70*, 65–82.

Teunissen, P. J. G. (1998a). On the integer normal distribution of the GPS ambiguities. *Artificial Satellites 33*(2), 49–64.

Teunissen, P. J. G. (1998b). Success probability of integer GPS ambiguity rounding and bootstrapping. *Journal of Geodesy 72*, 606–612.

Teunissen, P. J. G. (1999). An Optimality Property of the Integer Least-Squares Estimator. *Journal of Geodesy 73*(11), 587–593.

Teunissen, P. J. G. (2000). ADOP based upperbounds for the bootstrapped and the least-squares ambiguity success rates. *Artificial Satellites 35*(4), 171–179.

Teunissen, P. J. G. (2001). Statistical GNSS Carrier Phase Ambiguity Resolution: a Review. *Proceedings of the 11th IEEE Signal Processing Workshop on Statistical Signal Processing, August*.

Teunissen, P. J. G. (2006). The LAMBDA Method for the GNSS Compass. *Artificial Satellites 41*(3), 89–103.

Teunissen, P. J. G. (2007). A General Multivariate Formulation of the Multi-Antenna GNSS Attitude Determination Problem. *Artificial Satellites 42*(2), 97–111.

Teunissen, P. J. G. (2008). GNSS Ambiguity Resolution for Attitude Determination: Theory and Method. *Proceedings of the International Symposium on GPS/GNSS, Tokyo, Japan, November 11-14*.

Teunissen, P. J. G. (2010). Integer Least Squares Theory for the GNSS Compass. *Journal of Geodesy, Springer, DOI: 10.1007/s00190-010-0380-8*.

Teunissen, P. J. G., G. Giorgi, and P. J. Buist (2010). Testing of a New Single-Frequency GNSS Carrier-Phase Attitude Determination Method: Land, Ship and Aircraft Experiments. *GPS Solutions, DOI: 10.1007/s10291-010-0164-x*.

Teunissen, P. J. G. and A. Kleusberg (1998). GPS for Geodesy. *Springer, Berlin Heidelberg New York*.

Teunissen, P. J. G., N. Nadarajah, G. Giorgi, and P. J. Buist (2011). Low-complexity instantaneous gnss attitude determination with multiple low-cost antennas. *Proceedings of ION 2011, Portland, OR, US, September 20 - 23*, 3874–3880.

Teunissen, P. J. G. and S. Verhagen (2004). On the foundation of the popular ratio test for GNSS ambiguity resolution. *Proceedings of ION 2004, Long Beach, CA, US, September 21-24*, 2529–2540.

Tiberius, C., P. Teunissen, and P. de Jonge (1997). Kinematic GPS: performance and quality control. In *Proceedings KIS97*, pp. 289–299.

Tiberius, C. C. J. M. (1998). *Recursive data processing for kinematic GPS surveying*. Ph.D. thesis. Publications on Geodesy, 45, Netherlands Geodetic Commission, Delft.

Tiberius, C. C. J. M., P. F. de Bakker, H. van der Marel, and R. J. P. van Bree (2009). Geometry-free Analysis of GIOVE-A/B E1 - E5a, and GPS L1 - L5 Measurements. *Proceedings of ION 2009, Savannah, GA, US, September 22-25*, 2911–2925.

Tsukui, J., S. Hotta, T. Imada, K. Yamanaka, and T. Kasai (2003). Automatic Rendezvous to the International Space Station. *Proceeding of the 7th International Symposium on Artificial Intelligence, Robotics and Automation in Space: i-SAIRAS 2003, NARA, Japan, May 19-23*.

Turner, K. J. and F. A. Faruqi (1997). Gaussian Sum Filtering Approach for Phase Ambiguity Resolution in GPS Attitude Determination. *1997 IEEE International Conference on Acoustics, Speech and Signal Processing, April*.

Um, J. and E. G. Lighsey (2000). Space Flight Test Results for the SOAR Experiment. *Proceeding of ION 2000, Salt Lake City, US, September 19-22*, 2243–2251.

Unwin, M., M. Oldfield, C. Underwood, and R. Harboe-Sorensen (1998). The use of commercial technology for spaceborne GPS receiver design. *Proceedings of ION 1998, Nashville, TN, US, September 15-18*, 1983–1989.

Vachon, M., R. Ray, K. Walsh, and K. Ennix (2003). F/A-18 Performance Benefits Measured During the Autonomous Formation Flight Project. *NASA Dryden Flight Research Center, Edwards, California., Tech. Rep. NASA/TM-2003-210734*.

van der Marel, H. and B. Gündlich (2006). Development of Models for Use of Slant Delays Slant Delay Retrieval and Multipath Mapping Software Report for WP6100 TOUGH Deliverable D33.

van Diggelen, F. (2009). *A-GPS: Assisted GPS, GNSS, and SBAS*. Artech House Publishers.

Vanicek, P. and E. Krakiwsky (1986). Geodesy, the concepts. *Elsevier Science Pub. Co., 1986. 2nd ed.*.

Verhagen, S. (2006). Visualization of GNSS-related design parameters: Manual for the Matlab user interface VISUAL. *Available at www.lr.tudelft.nl/mgp*.

Verhagen, S. and P. Joosten (2003). Algorithms for design computations for integrated GPS-Galileo. *Proceedings of the European Navigation Conference, 22-25 April, Graz, Austria*.

Verhagen, S. and P. J. Teunissen (2012). The ratio test for future gnss ambiguity resolution. *GPS Solutions*, 1–14.

Verhagen, S. and P. J. G. Teunissen (2006). New Global Navigation Satellite System Ambiguity Resolution Method Compared to Existing Approaches. *Journal of Guidance Control and Dynamics 29*(4).

Wahba, G. (1965). Problem 65-1: A Least Squares Estimate of Spacecraft Attitude. *SIAM Review 7*(3), 384–386.

Wang, B., L. Miao, S. Wang, and J. Shen (2009). A constrained LAMBDA method for GPS attitude determination. *GPS solutions, 13(2), 97-107*.

Ward, L. (1996). Spacecraft Attitude Determination Using GPS: Methodology and Results. *Ph.D. Thesis,University of Colorado*.

Wei, M. and K. P. Schwarz (1995). Fast ambiguity resolution using an integer nonlinear programming method. *Proceedings of ION 1995, Palm Springs, CA, US, September 12-15*, 1101–1110.

Weill, L. (1992). Sub-meter Positioning with a Low-Cost Hand-held Receiver. *Proceedings of ION 1992, Albuquerque, NM, September 16 - 18*, 647–653.

Wells, D. (1974). *Doppler satellite control*. Dept. of Surveying Engineering, University of New Brunswick.

Wertz, J. R. (1978). *Spacecraft Attitude Determination and Control*. Kluwer Academic Publishers.

Wu, J., S. Wu, G. Hajj, W. Bertiger, and S. Lichten (1992). Effects of antenna orientation on GPS carrier phase. *Manuscripta Geodaetica, Springer Verlag, New York 1*, 1647–1660.

Wu, S. and Y. Bar-Sever (2006). Real-time sub-cm differential orbit determination of two low-earth orbiters with gps bias fixing. *Proceedings of ION 2006, Forth Worth, TX, US, September 26-29*, 2515–2522.

Yamagami, T., Y. Saito, Y. Matsuzaka, M. Namiki, M. Toriumi, R. Yokota, H. Hirosawa, and K. Matsushima (2004). Development of the highest altitude balloon. *Advances in Space Research 33*(10), 1653–1659.

Yamamoto, T., Y. Ishijima, T. Itoh, H. Suzuki, S. Nakazato, S. Kumagai, and P. Buist (2006). Spaceborne GPS Receiver Prototype with New L2C Signal Tracking Capability. *IEIC Technical Report (Institute of Electronics, Information and Communication Engineers) 106*(1), 251–256.

Yoon, S. and J. Lundberg (2001). Euler angle dilution of precision in gps attitude determination. *Aerospace and Electronic Systems, IEEE Transactions on 37*(3), 1077–1083.

Zhang, J. (2006). Precise Velocity and Acceleration Determination Using a Standalone GPS Receiver in Real Time. *School of Mathematical and Geospatial Sciences, RMIT, Australia*.

Zhang, J., K. Zhang, R. Grenfell, and R. Deakin (2006). Short note: On the relativistic doppler effect for precise velocity determination using GPS. *Journal of Geodesy 80*(2), 104–110.